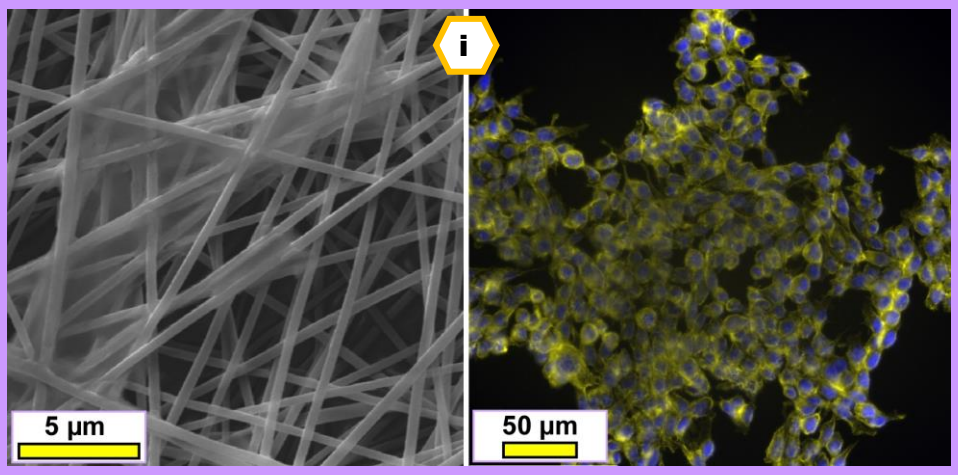

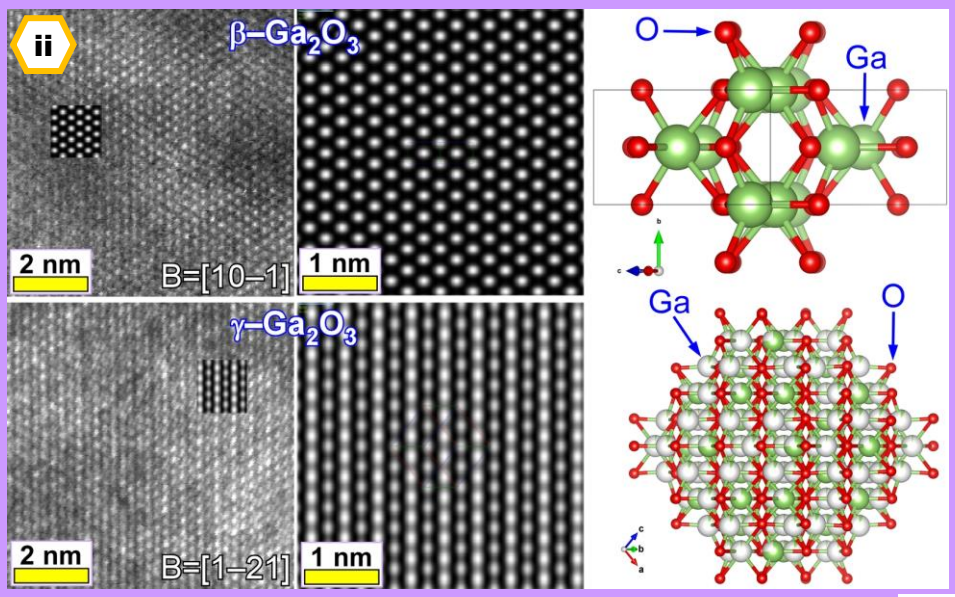

National Institute of Materials Physics

ANNUAL REPORT 2025

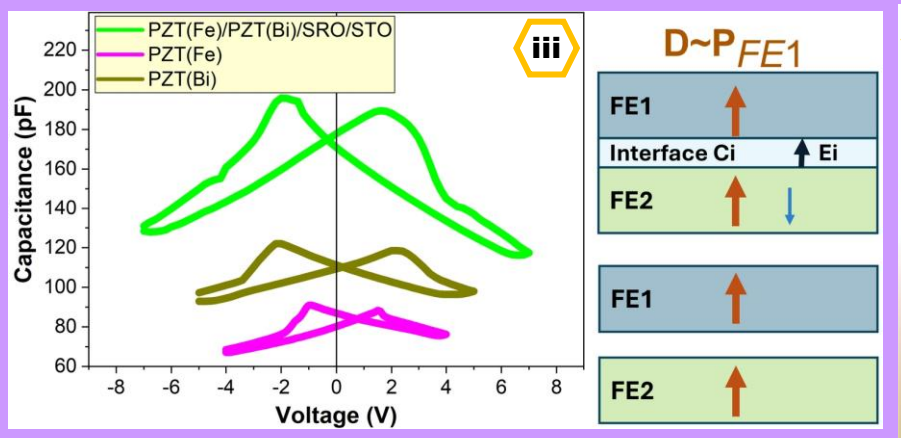

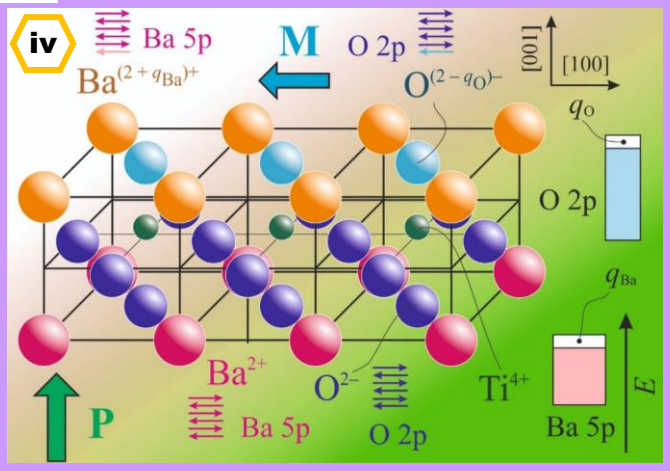

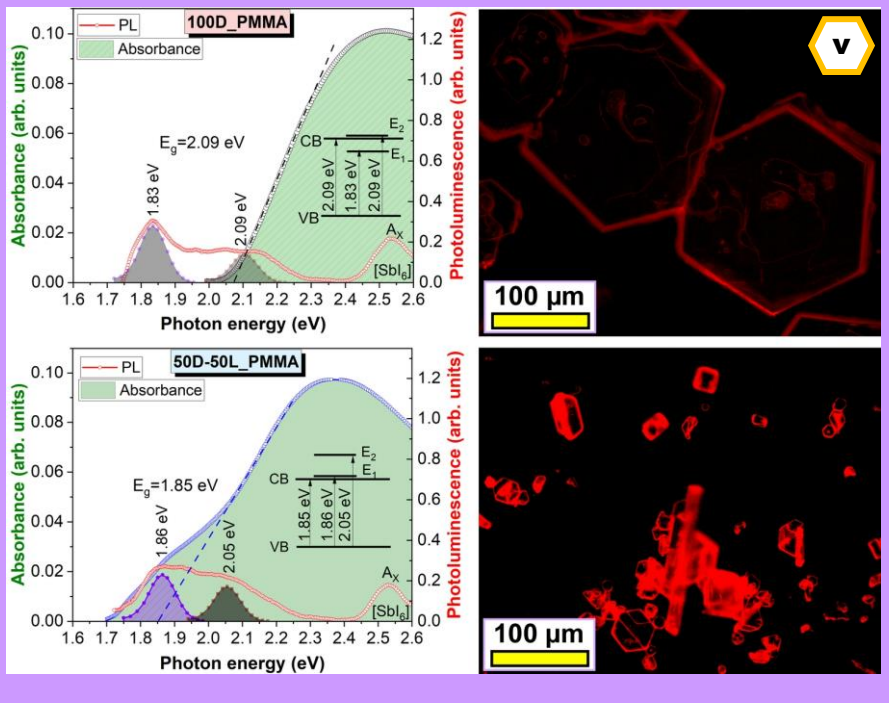

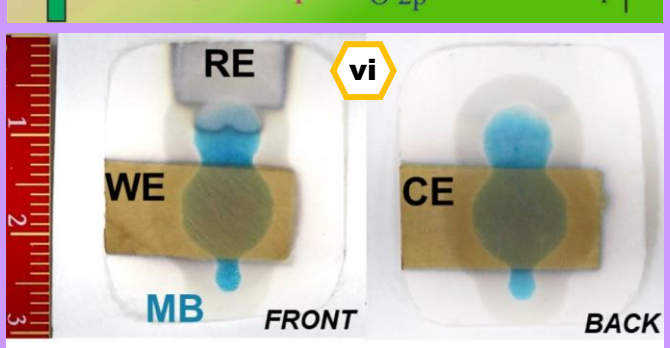

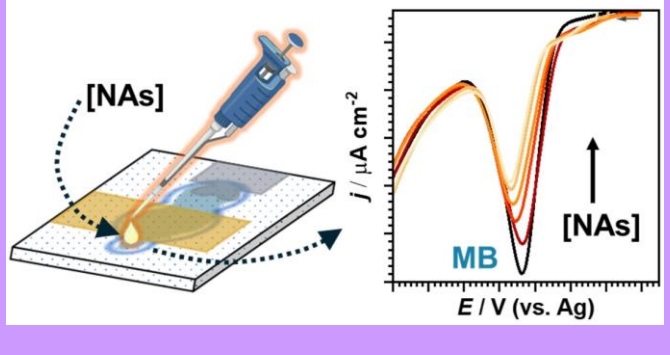

National Institute of Materials Physics

ANNUAL REPORT 2025

Cover page – Figures reproduced/adapted from:

i. M. Beregoi, S. Nistor, I.C. Ciobotaru, A. Nitescu, I. Zgura, M.C. Bunea, M. Enculescu, L. Nedelcu, C. Busuioc, T.A. Enache, *Cells proliferation on surfaces functionalized with amyloid beta peptide fibrils*, International Journal of Biological Macromolecules 309 (2025) 143160.

ii. A. Azarov, C. Radu, A. Galeckas, I.F. Mercioniu, A. Cernescu, V. Venkatachalapathy, E. Monakhov, F. Djurabekova, C. Ghica, J. Zhao, A. Kuznetsov, *Self-assembling of multilayered polymorphs with ion beams*, ACS Nano Letters 25 (2025) 1637–1643.

iii. A.G. Boni, C.F. Chirila, L.D. Filip, M.I. Botea, C. Radu, D.G. Popescu, M.A. Husanu, L. Hrib, L. Trupina, I. Pintilie, L. Pintilie, *Steady state negative capacitance in p-n ferroelectric junctions*, Acta Materialia 298 (2025) 121177.

iv. L.E. Borcan, A.-C. Iancu, N.G. Apostol, A. Nicolaev, C.M. Teodorescu, *Surface spin asymmetry of O 2p and Ba 5p states in $BaTiO_3(001)$*, Materials Advances 6 (2025) 8907–8920.

v. I.C. Ciobotaru, C.C. Ciobotaru, C. Bartha, M. Enculescu, M. Secu, S. Poloșan, C. Beșleagă, *Phase transitions in dimer/layered Sb-based hybrid halide perovskites: An in-depth analysis of structural and spectroscopic properties*, Advanced Optical Materials 13 (2025) 2402242.

vi. D. Botta, M. Beregoi, I.A. Cepleanu-Pascu, D.N. Crisan, A.-M. Ignat, E. Matei, I. Enculescu, V.C. Diculescu, *A paper-based device with submicronic fiber mesh electrodes for voltammetric quantification of nucleic acids*, Cell Reports Physical Science 6 (2025) 102781.

Background

The National Institute of Research and Development in Materials Physics (NIMP) was established in 1977 through the merger of laboratories from the Institute of Atomic Physics (IFA) and the Physics Institute of Bucharest (IFB), two entities emerged in 1956 from the Physics Institute of the Romanian Academy, founded in 1949. Initially named the Institute of Physics and Materials Technology, it received its current name in 1996 following a national accreditation process.

Since 2016, under Government Decision no. 1006/2015, NIMP has incorporated the International Centre for Advanced Training and Research in Physics (CIFRA), a UNESCO Category II Centre, functioning as a legally distinct subsidiary of the institute. CIFRA was established under the Government Decision no. 847/2013, based on the Agreement between the Government of Romania and the UNESCO for the creation, in Măgurele, Romania, of an International Centre for Advanced Training and Research in Physics. The agreement, originally signed in Paris on 21 November 2012, was renewed on 7 July 2022 for an additional eight years.

Located in Măgurele, Ilfov County, NIMP is part of the Măgurele Physics Platform, a reference scientific hub for both national and international research. Its facilities include several buildings, notably the new RITecC wing (Research Innovation and Technology Centre for New Materials) and the restored Oteteleșanu Hall, completed in 2020.

Today, NIMP performs both fundamental and applied research, with a strong emphasis on solid-state physics and materials science. It has established itself as a Centre of Excellence for international cooperation, participating in EU-funded and bilateral research projects, as well as in academic training programs for undergraduate, master's, doctoral, and postdoctoral researchers. The institute plays a key role in fostering interdisciplinary research in advanced materials.

NIMP comprises a Research Department with eight Laboratories and a Technology Transfer Unit, supported by administrative services, along with a small mechanical workshop.

Contents

Background II

CIFRA branch IV

NIMP's Research Labs IX

LABORATORY 10 X

LABORATORY 20 XV

LABORATORY 30 XXII

LABORATORY 40 XXVI

LABORATORY 50 XXXI

LABORATORY 60 XXXII

LABORATORY 70 XXXV

LABORATORY 80 XXXIX

List of Research Articles and Reviews Published in 2025 1

Highlighted Publications and Featured Covers 27

Key Scientific Achievements & Breakthroughs in *Materials and Devices for Electronics, Photonics & Optoelectronics* 32

Key Scientific Achievements & Breakthroughs in *Materials and Devices for Energy Systems, Extreme Environments, Space & Security* 78

Key Scientific Achievements & Breakthroughs in *Healthcare & Environmental Materials and Applications* 106

Key Scientific Achievements & Breakthroughs in *Theoretical and Computational Materials Physics* 134

Major R&D Projects 141

Contributions to Education and Society 194

CIFRA branch

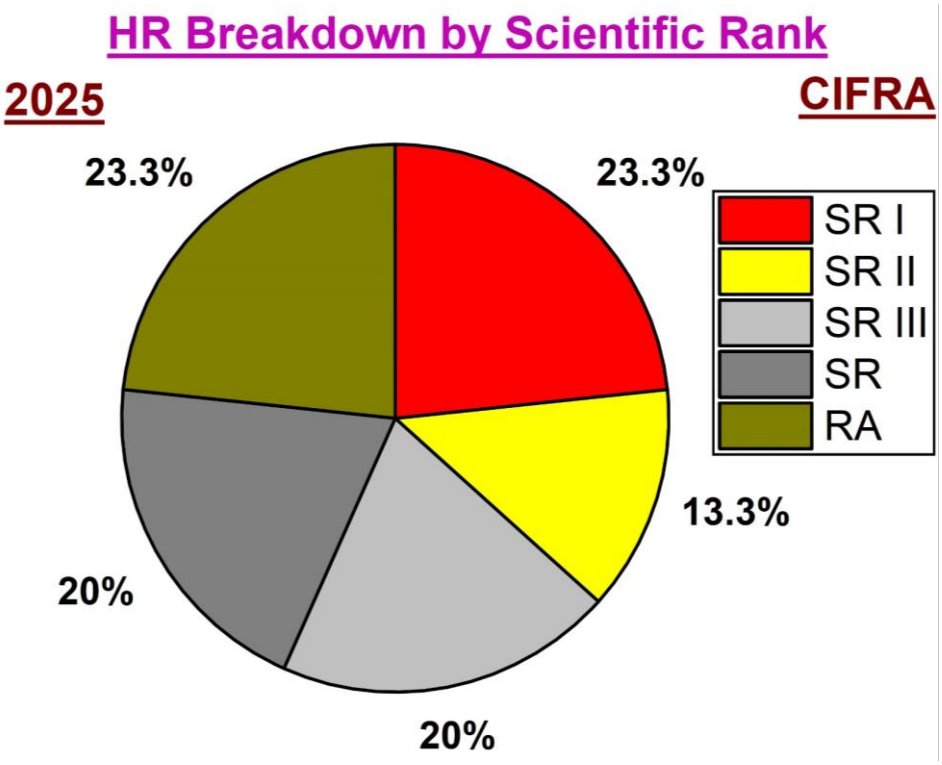

NIMP'S BRANCH
"International Centre for Advanced Training and Research in Physics"
CIFRA

Director of branch: CS I, Dr. Sabin STOICA (sabin.stoica@cifra-c2unesco.ro)

Personnel: 30 members (the majority employed part-time) – 7 × CS I; 4 × CS II; 6 × CS III; 6 × CS; 7 × ACS.
Out of the 30 CIFRA members, 24 hold a PhD degree in Physics.

Main research directions:
The structure of CIFRA's activities is established by the Agreement with UNESCO and comprises three main directions:

- ***Research***: Frontier scientific research carried out independently or in cooperation with national and international groups and institutions, on topics such as nuclear physics, elementary particle physics, astrophysics, computational physics, as well as interdisciplinary subjects at the interface between physics, chemistry, biology, and medicine.
  Within this direction, the CIFRA team has addressed two main topics:
  - ***i.*** The theoretical study of beta and double beta decays. In particular, we have developed computational methods for the quantities entering the decay rates, namely the phase space factors (PSF), nuclear matrix elements (NME), electron spectra, and the angular correlations between emitted electrons. These types of calculations provide essential theoretical support for dozens of large-scale experiments conducted in underground laboratories by consortia formed by leading research institutions and universities worldwide. The scientific interest focuses on elucidating neutrino properties and discovering new particles that may constitute dark matter (DM).
  - ***ii.*** Viromimetic particle physics represents a new interdisciplinary direction of CIFRA, aimed at initiating a research program dedicated to the study of viruses, specifically addressing questions related to their assembly mechanisms, their response to various physical and chemical factors, and, based on the understanding of these properties, the possibility of creating artificial particles with similar behaviour.
- ***Education***:
  Educational and training activities, including cooperation with UNESCO and UNESCO institutions (such as ICTP-Trieste), for the benefit of young people from Romania, Eastern and South-Eastern European countries, as well as from less developed countries, primarily in Africa.
  CIFRA carried out, in collaboration with UNESCO-Venice, the project entitled *"Integrating and Supporting STEM in the Educational Curriculum through UNESCO Microscience Experiments Project"*, which was awarded under the UNESCO call "*Revitalizing STEM Education to Equip Next Generations with STEM Competency".* This hands-on initiative enabled secondary and high school teachers and students to conduct experiments in the basic sciences (physics, chemistry, and biology) using dedicated experimental kits accompanied by user manuals. Within the framework of this project, we designed and developed educational kits for teaching fundamental concepts in physics, chemistry, and biology. The project introduced an experiment-based teaching and learning methodology aimed at improving the school curriculum, increasing students' interest in science, fostering critical thinking skills, and strengthening the

teacher–student relationship. A pilot phase was implemented in 10 schools in Bucharest and surrounding areas to test and validate the kits under real classroom conditions.

- ***Dissemination***: Organization of schools, workshops, and conferences; participation in research and educational networks; outreach activities:
  - Organization of the "*Măgurele Summer School for Computing in a Rapidly Evolving Society: Parallel Algorithms and Optimizations*", June 30 – July 11, 2025, Măgurele, Romania.
  - Participation in the Co-Creative Workshop entitled "*Revitalizing STEM Education to Equip Next Generations with STEM Competency*", March 13–15, 2025, Venice, Italy.
  - Participation in the organization of science outreach events, such as the *European Researchers' Night* or "*Young and Old Exploring the Universe*". CIFRA contributed to the organization of these events and conducted hands-on physics experiments for students and the general public.

Relevant infrastructure:

- High Performance Computing (HPC) System: The HPC system includes a computing capacity of 700 cores (1,062 threads) and 9.5 TB of RAM distributed across 19 compute nodes **(Fig. CIFRA**). For data storage, a usable capacity of 120 TB HDD is available for long-term storage and 12 TB SSD for temporary storage, providing fast read/write access during calculations. The nodes are interconnected via a 10 Gb/s Ethernet network and a low-latency 100 Gb/s InfiniBand network, the system being configured to run both parallel and serial computations. In addition, the NIMP–CIFRA HPC infrastructure includes one 100 Gb/s InfiniBand switch, two 10 Gb/s switches, two 20 kW UPS units, and two 20 kW air conditioning (AC) units. The entire system is mounted in a 19-inch rack, allowing for future expansion of the cluster.

Fig. CIFRA *The NIMP–CIFRA high performance computing (HPC) system.*

Highlights:

- ***Research***
  - ***i.*** *Contributions to the calculation of nuclear matrix elements (NME) for double beta decay.* A statistical model was developed to investigate the stability of the neutrinoless double beta decay nuclear matrix elements (0νββ NME) with respect to small random variations of the two-body matrix elements (TBME), calculated using three different Hamiltonians, as well as the correlations of 0νββ NME with 23 other observables. The study proposed a probability distribution function for the NME–0νββ values in the interval (1.55–2.65) at a 90% confidence level, with a most probable mean value of 1.99 and a standard deviation of 0.37. [*see* **AIP Conf. Proc. 3142 (2025) 020013**; **AIP Conf. Proc. 3143 (2025) 020020**].
  - ***ii.*** *Contributions to the description of the kinematic part of double beta decay processes.* New models and methods were developed that allow precise estimates of phase space factors and decay rates for beta, double beta, and electron capture processes (EC, 2EC), as well as a detailed description of the electron spectra and the correlations between the electrons emitted in these processes. The main novelties are as follows: (1) Inclusion of "exchange" effects between bound electrons and continuum electrons in the calculations; (2) Development of a method ensuring orthogonality between the wave functions of bound and continuum electrons. These improvements led to better agreement, particularly for very low decay energies ("Q-values"), where discrepancies between theory and experiment had previously been observed; (3) Development of a Dirac–Hartree–Fock–Slater (DHFS)–type method for obtaining electronic wave functions in electron capture (EC) processes; (4) A detailed investigation of EC rate ratios extended to a large number of atoms with atomic numbers Z in the range 1–92. The developed DHFS method incorporates electronic screening effects, electron correlations, overlap and exchange corrections, as well as atomic "shake-up" and "shake-off" effects. A key element of these calculations was the improvement of the energy balance of electron capture processes by using the atomic mass (experimentally determined with much higher precision than the nuclear mass). This approach allowed a more accurate determination of the energy available to the emitted neutrino (a quantity entering the EC rate formula), leading to improved predictions of EC rates in comparison with experimental measurements. [*see* **Phys. Rev. C 111 (2025) 035501**; **Phys. Lett. B 866 (2025) 139495**; **Phys. Lett. B 868 (2025) 139627**; **Eur. Phys. J C 85 (2025) 174**; **Phys. Rev. C 112 (2025) 035501**; **Phys. Rev. Lett. 134 (2025) 172501**].
- ***Education***

  Winning the project "Integrating and Supporting STEM in the Educational Curriculum through UNESCO Microscience Experiments Project" within the competition "REVITALIZING STEM EDUCATION TO EQUIP NEXT GENERATIONS WITH STEM COMPETENCY", launched by UNESCO–Venice, and its implementation in 10 schools in Bucharest and other regions of the country. The project led to the following achievements: (1) Selection, design, and production of approximately 100 educational kits (experimental sets), as well as the development of a pilot project for teaching and acquiring knowledge in physics, chemistry, and biology, in accordance with the national curriculum, using these kits; (2) Collaboration agreements with 10 schools for the continuation and expansion of the project; (3) Dissemination of project results, reflected in the official appreciation received from UNESCO and in media impact:
  - X.Com: https://x.com/cifra_c2unesco;

- LinkedIn: https://www.linkedin.com/company/cifra-c2unesco/
- Facebook: https://www.facebook.com/people/Centre-International-de-Formation-et-de-Recherche-Avanc%C3%A9es-en-Physique/61563541726319
- YouTube: https://www.youtube.com/watch?v=B2H00Xa46X0
- CIFRA website: https://cifra-c2unesco.ro/projects/integrating-and-supporting-stem-in-the-educational-curriculum-through-unesco-microscience-experiments-project/
- Other national press outlets: www.gandul.ro/actualitate/cum-pot-revolutiona-kit-urile-experimentale-procesul-educational-pentru-stem-problema-esentiala-este-cum-se-preda-si-cum-se-invata-20366100

Services provided: Realization of approximately 100 educational kits, accompanied by user manuals, and their distribution to the educational institutions involved in the project.

- ***Dissemination***

Outstanding results also include the impact of these achievements: (***a***) Publication of articles in highly ranked Web of Science®–indexed journals in the field, such as: *Physics Letters B; Journal of Physics G; Physical Review C; Universe*; (***b***) Dozens of citations in prestigious journals, including: *Reviews of Modern Physics; Nature Communications; Nature Astronomy; Physical Review Letters; Physics Letters B; Journal of High Energy Physics; Il Nuovo Cimento; European Physical Journal C; Astronomy & Astrophysics; Journal of Cosmology and Astroparticle Physics; Classical and Quantum Gravity; Annals of Physics; Physical Review A, B, C, and D*; *etc*. (***c***) Invited lectures and oral presentations at international conferences; (***d***) Requests for theoretical support from major international experiments (double beta decay and dark matter), such as LUX-ZEPLIN, CUORE, DARWIN, GERDA, MAJORANA, HOLMES, LEGEND, XENON-1T/nT, SuperNEMO, EXO-2000, nEXO, *etc*, which are carried out within large international collaborations that include prestigious.

- ***International recognition***
  - CIFRA was invited to become a founding member of SCIENSA, a UNESCO global science network. SCIENSA is a UNESCO initiative launched on October 21, 2025, to connect UNESCO Chairs and Category 2 Centres working in the fields of basic sciences, research, innovation, and engineering (https://www.unesco.org/en/sciensa-network). Its main objective is to promote global cooperation, support scientific research, and advance quality science education in order to build a more sustainable world.
  - S. Stoica was invited to serve as a panel member at the Science Diplomacy meeting where the strategy and roadmap for the field in Southeast Europe were defined (November 18, 2025, Ljubljana, Slovenia).
  - S. Stoica received an invitation to join the Editorial Board of the UNESCO Science Report, a strategic report published every five years.

NIMP's Research Labs

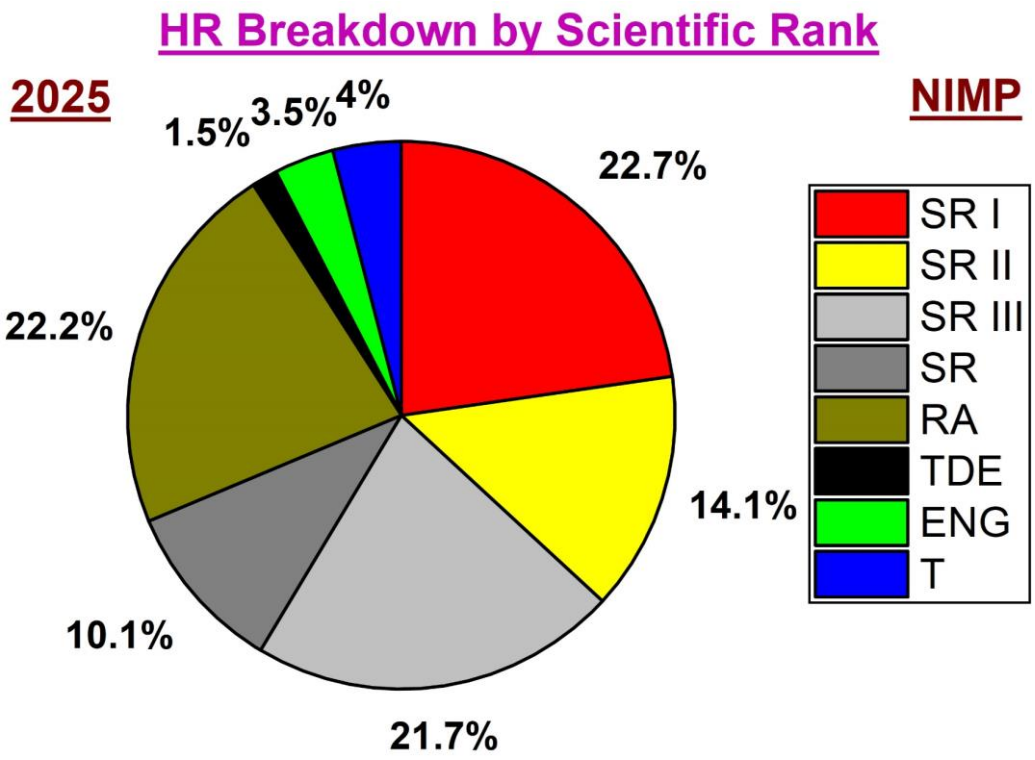

LABORATORY 10

"Functional Nanostructures"

Head of laboratory: Dr. Silviu Pavel POLOȘAN, Senior Researcher rank 1 (silv@infim.ro)

Personnel: 37 members – 11 × SR1, 1 × SR2, 10 × SR3, 2 × SR, 12 × RA, and 1 × technician (**SR stands for Senior Researcher; RA stands for Research Assistant*).
Beyond its scientific endeavours, the group actively participates in educational and training initiatives.
27 team members hold PhD titles in physics (12), chemistry (2), chemical engineering (6), biochemistry (3), materials engineering (1), energy engineering (1), biotechnology (1), and biomechanics (1). Additionally, the team includes 6 PhD students and 2 MSc students.

Main research directions:
The group deals with nanostructures and nanostructured materials preparation and development of applications. Both chemical/electrochemical (chemical bath deposition, electrochemical deposition with and without a template, chemical vapor deposition) and physical (magnetron sputtering, thermal evaporation in vacuum, electrospinning and forcespinning) methods are employed for nanostructures and nanostructured materials preparation. Different types of materials are used, including here metals, metal oxides, organometallic compounds and polymers. The nanostructures developed by this approach are used as building blocks for different types of functional devices (*e.g.*, transistors or diodes, biosensors, actuators). Several specific examples follow:

- Nanostructures and devices based on nanostructures – physical and chemical methods are employed for preparing nanostructures. Electrochemical or chemical deposition is used for preparing nanowires of zinc oxide with diameters down to 10 nm. Thermal oxidation of metal foils is used for obtaining metal oxide nanowires with diameters down to 20 nm. Further, the nanowires can be employed as building blocks for electronic devices such as diodes and transistors using microlithographic (photolithography and electron beam lithography). Devices complexity can be employed (*e.g.*, core shell devices can be fabricated) by covering the nanowires with thin-films employing methods such as magnetron sputtering or thermal evaporation. Chemical vapor deposition is employed for preparing thin nanostructured films such as metal oxides or graphene.
- Materials for applications in optics, optoelectronics and photonics for devices which include diodes and transistors for light emitting applications, glasses or modular composition fibres for photonic applications.
- Biosensors and biomedical devices based on nanostructures or on devices containing nanostructures as building blocks.

Nanostructures and nanostructured materials can be exploited successfully in biosensors, mainly due to the high specific surface but also due to other specific functionalities induced by the low dimensionality. Electrochemical sensors are developed based on nanostructured materials and are functionalized with different types of biomolecules in such a way in which both the desired sensitivity and selectivity are obtained. In this context, different types of substrates and configurations of functionalization are investigated with the goal of optimizing device performances. Novel applications are considered, including wearable sensors for physiologic parameters monitoring. Several specific examples follow:

- Submicrometer fibres; biomimetic devices based on microfiber web electrodes. In our group, methods of fabricating polymer submicrometric fibres were developed namely: electrospinning and forcespinning. By further functionalization, transparent and flexible

electrodes based on metal covered polymer fibre webs are obtained. These electrodes can be applied on a wide range of substrates including here materials such as textiles and paper and can become the functional element of devices such as biosensors or for applications such as artificial muscles. Functionality can be increased by covering with electroactive polymers, leading to devices with highly superior performances when compared to classic architectures.

- Biocompatible materials represent another research direction of the group, several approaches being developed, including both biopolymeric fibres (collagen or cellulose), natural membranes (eggshell membrane) or nanostructured materials such as hydroxyapatite. Further functionalization includes covering with different compounds or nanostructures or doping and leads to multiple fields of applications, the main one being that of medical devices.

The research directions of Lab. 10 are mostly interconnected for developing devices with direct applications. Equipment for fabricating fibres by means of electrospinning and forcespinning were designed and developed in the laboratory with the support of the engineers from the application department.

Relevant infrastructure:

The activity of Lab. 10 relies on several fully-equipped chemistry and electrochemistry laboratories (dedicated to different types of applications) as well as clean room infrastructure, essential for devices fabrication:

- Laboratory for the fabrication of submicrometric and nanostructured materials, equipped with electrospinning systems that allow high-precision control of process parameters (**Fig. 10-1**), as well as equipment for electrodeposition, anodization, and synthesis by wet-chemical methods. The laboratory is also equipped with facilities for thin film deposition by magnetron sputtering, hybrid thermal evaporation, and electron beam evaporation.

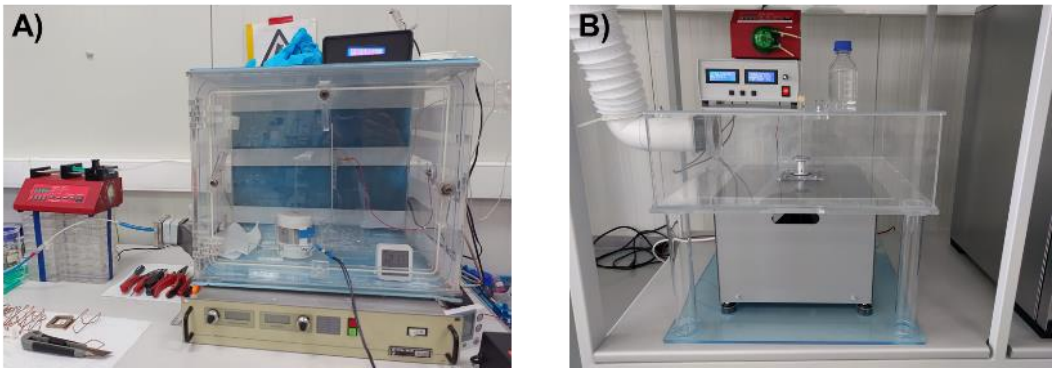

Fig. 10-1 *Equipment for (**A**) electrospinning and (**B**) centrifugal spinning, featuring chambers for high-precision control of process parameters.*

- Clean room (ISO 1000 and ISO 100 classes). The equipment available in the clean room are essential for the fabrication of electronic devices based on nanostructures:
  - Electron-beam nanolithography equipment with Raith Elphy systems with laser interferometers and Hitachi S3400 and Zeiss Merlin Compact scanning electron microscopes (**Fig. 10-2**);
  - Lithography/Mask Alignment EVG®620 NT system with nanoimprint capabilities;
  - CVD equipment for preparation of carbon-based nanostructures;
  - CVD equipment for deposition of semiconducting materials.

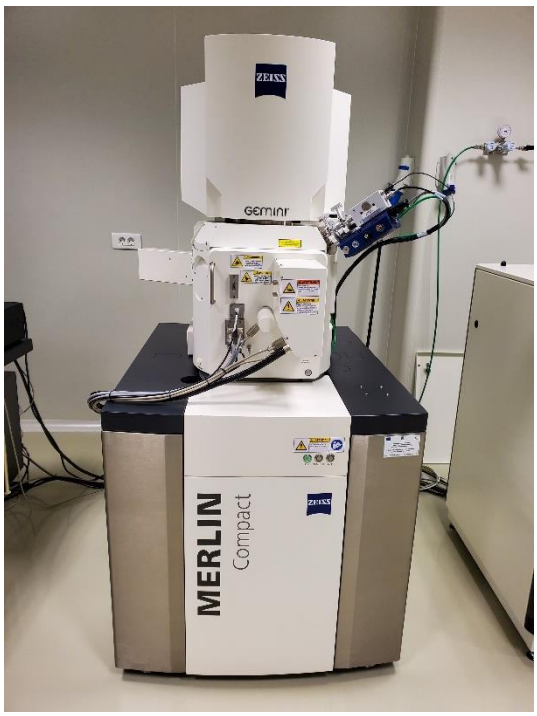

Fig. 10-2 Zeiss Merlin Compact scanning electron microscope.

- Electrochemistry and biosensors laboratory, equipped with approximately 10 potentiostats (Autolab, Vionic, Ivium, Ametek), some of which feature multiplexing capabilities and modules for electrochemical impedance spectroscopy (EIS), as well as a bipotentiostat and a quartz crystal microbalance (EC-QCM). This laboratory also includes a scanning electrochemical microscope (SECM) (**Fig. 10–3**).

Fig. 10-3 *Scanning electrochemical microscope with high-resolution mode.*

- Laboratory for optical characterization including UV – Vis absorption spectrometers (Carry 5 and Perkin Elmer 35), photoluminescence spectrometers (Edinburgh and Perkin Elmer LS55), near field photoluminescence microscope, stop-flow microspectrometer based on microfluidics and surface plasmon resonance (SPR) spectroscopy equipment with electrochemical control (**Fig. 10–4**).

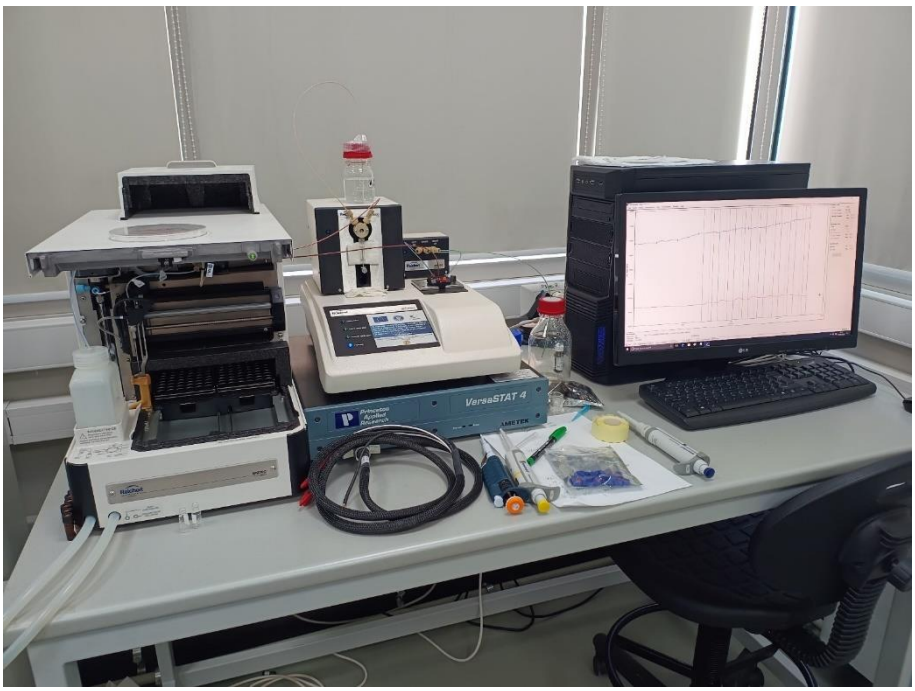

Fig. 10-4 *Surface plasmon resonance (SPR) spectroscopy equipment with electrochemical control.*

- High-performance liquid chromatograph (HPLC) with optical or electrochemical detection, coupled with a mass spectrometer;
- Laboratory for cytocompatibility testing, equipped with incubators for cell cultures, a flow cytometer, a spectrophotometer, a fluorescence microscope, and a Polymerase Chain Reaction (PCR) system, dedicated to studying and evaluating the *in vitro* biological response of materials of interest developed within NIMP.

Available services:

- Scanning electron microscopy characterization of materials (micro-morphology and elemental composition);
- Optical characterization by means of optical spectroscopy;
- Development of equipment for producing micrometric and submicrometric fibres by means of electrospinning and forcespinning.

Main results:

- 8 research projects (2 × PNRR; 3 × CoEx selected for funding; 2 × PED; and 1 × M-ERA.NET);
- 40 articles published in Web of Science®-indexed journals with impact factor (of which 23 with main author from Lab. 10);
- 1 EPO granted patent;
- 3 OSIM patent applications.

Highlights:

- Cells proliferation on surfaces functionalized with amyloid beta peptide fibrils [*see* **Int. J. Biol. Macromol**. **309 (2025) 143160**];
- Phase transitions in dimer/layered Sb-based hybrid halide perovskites: An in-depth analysis of structural and spectroscopic properties [*see* **Adv. Opt. Mater. 13 (2025) 2402242**];

- Bilayered metallic cathodes consisting of pure Mg and Zn:Al thin films optimized by Laser-induced Thermionic Vacuum Arc (LTVA) technology [*see* **Appl. Surf. Sci. Adv. 28 (2025) 100787**];
- Electrochemical assay for the quantification of anticancer drugs and their inhibition mechanism [*see* **Methods 241 (2025) 13–23**];
- Novel insights into the distinct magnetic configurations of polycrystalline Ni nanowires produced by a template approach at varying electrodeposition potentials [*see* **J. Alloys Compd. 1044 (2025) 183959**];
- Phosphorothioated oligonucleotides on gold-coated electrospun polymeric fibers for electrochemical genosensors [*see* **Electrochim. Acta 524 (2025) 146006**];
- A paper-based device with submicronic fiber mesh electrodes for voltammetric quantification of nucleic acids [*see* **Cell Rep. Phys. Sci. 6 (2025) 102781]**;
- Electrochemical bienzymatic biosensor for pyruvate kinase activity evaluation and inhibitor screening [*see* **Talanta 291 (2025) 127886**];
- Efficient and reusable 3D TiO_2@PDMS sponge composites for solar driven photocatalytic degradation of water pollutants [*see* **Results in Engineering 27 (2025) 107083**];
- Exploring the fabrication, properties, and morphology of fluorine substituted hydroxyapatite coatings [*see* **Ceram. Int. 51 (2025) 1929–1948**].

LABORATORY 20

"Complex Heterostructures and Multifunctional Materials"
HeCoMat

Head of laboratory: Dr. George E. STAN, Senior Researcher rank 1 (george_stan@infim.ro)

Personnel: 33 members – 8 × SR1, 3 × SR2, 7 × SR3, 3 × SR, 8 × RA, 3 × sub-engineer/engineer, and 1 × technician.
Beyond its scientific endeavours, the group actively participates in educational and training initiatives.
21 team members hold PhD titles in physics (17), chemistry (2), electrical engineering (2), and materials engineering (1), including 1 PhD supervisor. Additionally, the team comprised 4 PhD students and 3 MSc students.

Main research directions:

- Ferroelectric materials and related structures for electronic, optoelectronic and sensing applications (including non-volatile memories, UV and IR detectors, piezoelectric devices);
- Materials and devices with application in microelectronics, photovoltaic conversion and light/particle detection (including field-effect transistors, hybrid perovskite and chalcogenide solar cells, and silicon-based particle detectors);
- Superconducting and magnetic materials, strongly correlated electron systems;
- Dielectric and ferroelectric materials for microwave devices (*e.g.*, dielectric resonators, ferroelectric varactors, filters, antennas);
- Materials for healthcare applications.

Relevant infrastructure:

HeCoMat possesses a noteworthy infrastructure, covering the entire technological chain from the preparation of materials in the form of powders, bulk and thin layers and their complex physico-chemical characterization, to the integration of the optimized materials into functional devices. Amongst the most important systems and equipment one can mention:

- SURFACE SCIENCE pulsed lased deposition (PLD) work station (**Fig. 20–1a**) equipped with: 2 deposition chambers, each with 4-target carousels; a KrF excimer laser with 248 nm wavelength, repetition rate of 1 – 10 Hz, and maximum energy of 700 mJ; control of laser fluence; substrate heating up to 1000 °C; control of working gases pressure; *in-situ* reflection high-energy electron diffraction (RHEED) capabilities. One reaction chamber is used to deposit ferroelectric layers based on perovskites and other metal oxides (*e.g.*, doped ZnO, HfO_2), whilst the other chamber is used to prepare superconductor thin-films.
- SURFACE SCIENCE hybrid system for thin-films synthesis from temperature-sensitive materials by (*i*) matrix assisted pulsed laser evaporation (MAPLE) and (*ii*) PLD, constituted of: a deposition chamber with *in-situ* freezing facilities for targets (*e.g.*, frozen suspensions of organic materials or inorganic nanoparticles in a support matrix); a KrF excimer laser with 248 nm wavelength, 1 – 10 Hz repetition rate, and 700 mJ maximum power; maximum heating temperature of the substrate: 500 °C – MAPLE & 700 °C – PLD.

- Multi-cathode radio-frequency (RF), direct current (DC) and pulsed direct current (p-DC) magnetron sputtering (MS) systems with various facilities: bias, etching and heating (up to 800 ° C) of substrates; vacuum load-lock for sample transfer; vacuum systems (down to ~10^{-6} Pa); computerized control and process automation. The latest MS equipment, AJA PHASE II J, purchased in 2016, is shown in **Fig. 20–1b**. Each MS system in Laboratory 20 is dedicated to a distinct class of materials: metallic contacts; semiconductor and dielectric materials; biocompatible materials.
- Chemistry laboratory for the preparation of powders, bulk materials and thin-films by chemical (wet) methods, equipped with high-temperature annealing furnaces; spin-coating systems; fume hoods, aggregate mills; weighting scales; in-house made glove-boxes; glassware; *etc*.
- Doctor blade/Slot-die MTI system for large area deposition equipped with 100 mm width adjustable micrometre applicator, a slot-die head and an adjustable speed syringe pump. Additionally, two in-house built Doctor blade/Slot-die systems are also available.
- Spray pyrolysis facilities.
- Professional glove-box MBraun with two chambers (3 and 4 gloves), with integrated spin-coater and closed cycle gas purification system capable of maintaining an atmosphere with H_2O and O_2 under 0.1 ppm and with a solvent filter.
- Laboratory for the preparation of piezoelectric and superconducting materials, polycrystals and single crystals.
- Ceramic materials 3D printing laboratory, equipped with a NORDSON EFD, EV series, robocasting (direct ink writing) printing system, with Ultimus V dispenser; an ANTON PARR MCR302e modular rheometer; and a THINKY ARE-250 ceramic mixing & degassing machine.

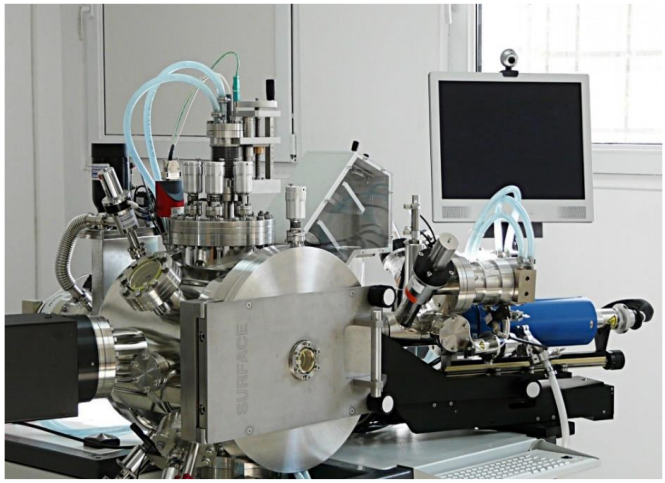

Fig. 20–1a PLD workstation assembly, SURFACE SCIENCE, for the deposition of ferroelectric thin-films.

Fig. 20–1b RF, DC and p-DC magnetron sputtering system, AJA PHASE II, for the deposition of semiconductor thin-films.

- X-ray diffraction systems for structure analysis of thin-films (a RIGAKU SmartLab 3 kW/2017 from room-temperature to 1100 °C and a BRUKER D8 Advance/2006) and powders (ANTON PAAR XRDynamic500 – from 600 °C to –180 °C and a BRUKER D8 Advance/2007).
- Optical and structural characterization systems, including a (*i*) variable angle spectroscopic ellipsometer (WOOLLAM) with wavelength range 200 – 1700 nm (6.2 – 0.73 eV), angle of incidence (35 – 90°), automated sample translation stage (for mapping) 150 mm × 150 mm, and an Instec temperature control stage (–160 – 600 °C) and (*ii*) a near infrared (NIR), infrared (midIR) and far infrared (farIR) Fourier

transform infrared (FTIR) JASCO spectrometry platform, encompassing the 12000 – 50 cm^{-1} spectral range. VASE Woollam can be used in the following modes: (*i*) reflection ellipsometry on semiconductor/dielectric thin-films or multilayers (inferred sample parameters: thicknesses, refractive index, extinction coefficient, absorption coefficient, dielectric function, band gap, critical point energies, electrical parameters for degenerate semiconductors – resistivity/conductivity, carrier density, scattering time, carrier mobility, phase transition in the temperature range –160 – 600 °C); and (*ii*) transmission ellipsometry on uniaxial/biaxial crystals, glasses and glass ceramics (derived sample parameters: linear birefringence and linear dichroism, Verdet constant/ Faraday rotation).

- Surface investigation by scanning probe microscopy (SPM) in contact or non-contact mode with piezoelectric (PFM), magnetic (MFM) or conductive (C-AFM) response.
- Electrical measurements laboratory, including: 2 LAKE SHORE cryo-probers for electrical measurements in the temperature range of 10 – 400 K; one with vertical magnetic field up to 2.5 T, and one with horizontal magnetic field up to 1.5 T, each with at least 3 micro-manipulated arms with contact needles allowing electrical measurements from liquid helium to 400 K under various electric/magnetic fields and illumination conditions; 4 cryostats, covering a temperature range between 10 – 800 K; DLTS (deep-level transient spectroscopy) and TSC (thermally stimulated current) systems for the investigation of electrically active defects (charge carrier traps) in materials and MOS-like structures; set-up for pyroelectric measurements; ferritesters; various instruments for measuring currents, resistances and voltages (electrometers, nanovoltmeters, Lock-In amplifiers); voltage and current sources; RLC bridges; and impedance analysers. These facilities are used to perform complex characterization of electrical (hysteresis loops; C–V and I–V characteristics; impedance spectroscopy; defect spectroscopies; *etc*.) and superconductive properties (electron transport, thermodynamics, magnetic-field penetration depth measurements); determination of the d_{33} piezoelectric coefficient; Kelvin probe and Hall measurements.
- Solar cells testing laboratory (**Fig. 20–2**), with two Newport LED solar simulators (aperture 50 mm × 50 mm), VeraSol-2 AAA Class and a MiniSol ABA Class), with AM 1.5G solar spectrum and adjustable power coupled with a Keithley source 2601. A measurement system for quantum conversion efficiency (EQE and IPCE) featuring a solar simulator with a Xe lamp and accessories, SCIENCETECH PTS-2-IQE, covering the spectral range of 250–2500 nm, is available.
- Microwave dielectric materials and devices testing laboratory, including:
  - Vector Network Analyser PNA 8361A from Agilent (0.01 – 67 GHz) for two-ports complex S parameters. It uses electronic calibrator Agilent N4694-60001 in the range of 0.01 – 67 GHz. For access, 1.9 mm, 2.9 mm, 2.4mm, 3.5 mm, SMA or N connectors or adaptors are used.
  - Vector Network Analyser PNA-X N5245A from Agilent (0.1 – 50 GHz standalone) with 4 ports and dual sources. It allows measurements of the S and X non-linear parameters. By using the millimetre wave extensions, the system covers a wide frequency band up to 500 GHz. Each extension pair allows the measurement of the two-ports parameter of waveguide devices. The millimetre wave extensions are from Agilent/OML (N5260A V10 VNA2, WR-10, 75-110 GHz; N5260A V06 VNA2, WR-06, 110-170 GHz; N5260A V05 VNA2, WR-05, 140-220 GHz; N5260A V03 VNA2, WR-03, 220-325 GHz; N5260A V02.2 VNA2, WR-02.2, 325-500 GHz).
  - Anechoic chamber with internal dimensions 3040 mm × 4100 mm × 2800 mm, for antenna characterizations (*e.g.*, directivity parameter) in the range of 0.9 – 40 GHz.

- Microprobe station for direct *on-wafer* measurements of two-ports in the frequency range 0.1 – 67 GHz by using GSG probes with 150 µm and 100 µm pitches.
- THz-TDS spectrometer from AISPEC Pulse IRS 2000 Pro, operating in the range of 200 GHz – 5 THz.

- In the framework of collaborative research activities, HeCoMat can access other NIMP infrastructures, such as: TEM and SEM equipment; XPS characterization (including at Elettra Synchrotron Trieste); magnetic measurements (SQUID, PPMS); other optical spectroscopy techniques (Raman, UV-Vis-NIR, luminescence); clean-room (photolithography, dry etching); and *in-vitro* preliminary biological testing of materials.

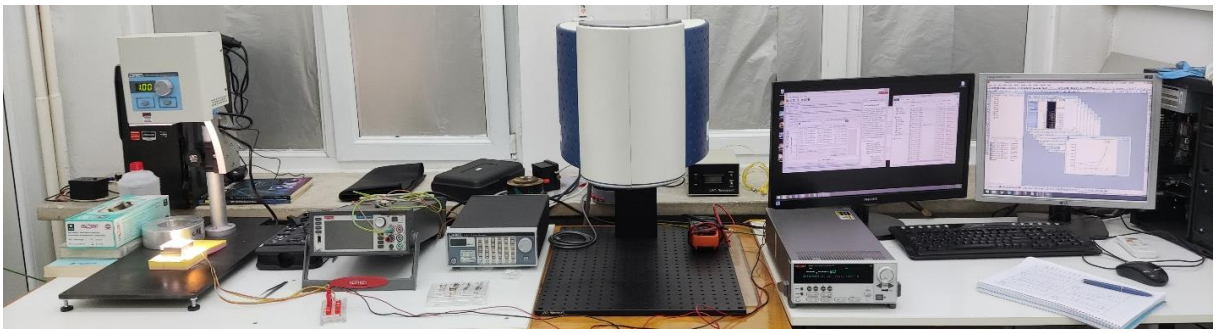

Fig. 20–2 Solar cells testing laboratory.

- High Performance Computing (HPC) system with a computing capacity of 352 cores and 2.5 TB RAM distributed across 9 compute nodes. For data storage, we have 120 TB of usable HDD capacity for long-term storage and 12 TB of SSD for temporary storage with fast read-write access during computations. The nodes are interconnected *via* a low-latency InfiniBand network, and the system is configured for both parallel and serial computing. The HPC system was built and is administered in collaboration with NIMP's branch CIFRA.

Available services:

- Preparation of materials (nano-powders; bulk ceramics; fabrication of thin-films by various techniques, including chemical methods, CVD and PVD techniques);
- Investigation of charge carrier traps by DLTS and TSC;
- Electric characterization of materials in a wide temperature range, under electric and magnetic fields;
- Investigation of pyroelectric properties;
- Fabrication and characterization of materials by electrochemistry;
- Fabrication and characterization of new generation solar cells;
- Fabrication and characterization of microelectronic devices (*e.g.*, FET, MOS);
- Characterization of microwave, millimetre waves and terahertz materials and devices;
- Antenna characterization (antenna directivity) in anechoic chamber in the frequency band from 900 MHz to 40 GHz;
- Electromagnetic design for microwaves devices/structures by using high accuracy software packages such as CST Studio Suite, Ansoft HFSS, and Ansoft Designer;
- Deposition of biocompatible (ceramic and glass) coatings on metallic implants;
- Characterizations by (*a*) reflection ellipsometry on semiconductor/dielectric thin-films or multilayers (thicknesses, refractive index, extinction coefficient, absorption coefficient, dielectric function, band gap, critical point energies, electrical parameters for degenerate semiconductors – resistivity/conductivity, carrier density, scattering time,

carrier mobility, phase transition in the temperature range -160 – 600 °C); and (*b*) transmission ellipsometry on uniaxial/biaxial crystals, glasses and glass ceramics (optical constants, linear birefringence and linear dichroism, Verdet constant/ Faraday rotation).

- XRD characterizations for crystalline phase identification and their quantitative analysis; determination of the lattice parameters, average size of crystallites, macro- and micro-strains, preferred orientation, *etc*; analysis of homo- and hetero-epitaxial structures; X-ray reflectometry analyses for inferring the thickness, density and roughness of the surface and interfaces of amorphous and crystalline layers and multi-layers; *etc*.
- FTIR spectroscopy analyses in transmission, specular reflectance (including at grazing incidence), attenuated total reflectance – ATR (RT – 180 °C), diffuse reflectance – DRIFT (RT – 500 °C) and integrating sphere modes.
- Morpho-compositional analyses by HR-SEM – EDXS;
- Surface characterization of materials by AFM, PFM, MFM, and c-AFM.

Main results:

- 9 research projects (1 × PNRR; 1 × CERN; 1 × M-ERA.NET; 1 × RONAQCI; 1 × Sectorial; 2 × PED; 1 × PTE; 1 × EUD);
- 43 articles published in Web of Science®-indexed journals with impact factor (of which 16 with main author from Lab. 20);
- 3 OSIM granted patents.

Highlights:

- NIMP, through Laboratory 20, is an active member of the international CERN collaboration DRD3 – Solid State Detectors, which brings together 137 institutions from 29 countries. Our current projects are strategically integrated within the DRD3 working groups: WG3 (Radiation Damage Characterization), WG4 (Simulation), and WG6 (Wide Band Gap and Innovative Materials). They contribute directly to WP3 – Sensors for Extreme Fluences, in which NIMP also holds a management role (elected Convener of WG3/WP3 and member of the DRD3 Steering Committee). By advancing the fundamental understanding of radiation damage in solid-state detectors, in alignment with the Roadmap DRDT 3.3 detector development strategy, this collaboration strengthens and consolidates our scientific expertise in detector physics, materials science, and device engineering. At the same time, participation in this high-level international framework enhances the visibility, credibility, and institutional prestige of NIMP, strengthening its position as a competitive and trusted partner in major European research initiatives.
- Progress toward steady-state negative capacitance was achieved in epitaxial ferroelectric/ferroelectric bilayers by controlling a polarization mismatch and, critically, by forming a ferroelectric p–n junction at the interface. The resulting built-in internal fields, established in PZT multilayers doped with Fe (p-type) and Nb or Bi (n-type), lead to a capacitance–voltage hysteresis that reveals a systematic enhancement of the effective capacitance beyond the value expected for a simple series connection. In thinner multilayers (50 nm/50 nm), strong frequency dispersion and Maxwell–Wagner relaxation point to an interfacial RC element that governs the high-frequency response and enables switchable capacitance at 0 V after pre-poling, highlighting the role of interfacial screening and transport in stabilizing negative capacitance in multilayers relevant for energy-efficient electronic components [*see* **Acta Materialia 298 (2025) 121177**].

- We demonstrated that the progressive substitution of barium (Ba^{2+}) with strontium (Sr^{2+}) is an efficient method for band-gap engineering in $Ba_{1-x}Sr_xTiO_3$ (BST) ferroelectric ceramics, thereby optimizing the material for optoelectronic applications [*see* **Ceram. Int. 51 (2025) 18166–18177**]. Samples (x = 0–1) were prepared by the conventional solid-state reaction method. Structural analysis (XRD) highlighted a phase transition from tetragonal to cubic symmetry at the x = 0.4 threshold, accompanied by a contraction of the unit cell volume from 64.29 $Å^3$ to 59.58 $Å^3$. We established a rigorous correlation between composition and optical properties, observing a reduction in the absorption threshold and a decrease in the band gap energy from 3.142 eV to 3.082 eV as the Sr content increases. The experimental results were validated through *ab initio* modelling using Density Functional Theory (DFT), confirming the accuracy of the PBE0 functional in predicting the electronic properties and stability of the perovskite phases. Sr substitution shifted the Curie temperature (T_c) from 132 °C toward the cryogenic range to −110 °C, while maintaining dielectric losses below 3.5%. The determined activation energies (E_a = 0.685–1.065 eV) suggest that doubly ionized oxygen vacancies dominate the conduction and relaxation processes. This compositional versatility and rigorous control of the Ba/Sr ratio open new perspectives for the development of self-powered UV photodetectors and high-performance energy storage systems.
- We demonstrated that the functional performance of $BaTi_{1-x}Hf_xO_3$ (BTH) ceramics can be precisely controlled through Hf-substitution combined with advanced Spark Plasma Sintering (SPS) processing [*see* **J. Eur. Ceram. Soc. 45 (2025) 117600** & **J. Mater. Res. Technol. 38 (2025) 5389–5408**]. We successfully established the phase diagram of composition and temperature for the BTH system. We found that Hf-substitution creates a phase coexistence region (R–O–T) at room-temperature, which is crucial for optimizing electromechanical properties. The use of SPS enabled the production of very fine grains (down to tens of nanometers). We observed that reducing the grain size below a critical threshold induces significant internal stress, stabilizes the cubic phase, and decreases switchable polarization. The substitution of Ti^{4+} by Hf^{4+} shifts the transition temperatures and broadens the dielectric maxima, maintaining low losses even at high frequencies. We highlighted the shift from classical ferroelectric behaviour to a relaxor-type response with a diffuse phase transition as the Hf content increases, thereby enhancing the thermal stability of the devices. Microstructural refinement allowed us to achieve high dielectric strength, positioning the BTH system as a sustainable alternative for tuneable electronic devices.
- We demonstrated the direct stabilization of the ferroelectric orthorhombic phase in 7.5 nm-thick $Hf_{0.5}Zr_{0.5}O_2$ thin films grown on TiN/Si substrates by pulsed laser deposition at a CMOS-compatible temperature of 400 °C, eliminating the need for post-deposition annealing or wake-up cycling. The study [*see* **Ceram. Int. 51 (2025) 50941–50950**] revealed robust intrinsic ferroelectricity in the as-grown films, with a remnant polarization of 12.5 $\mu C/cm^2$ at 1.9 MV/cm and a dielectric constant of ~38. Structural and microstructural analyses showed that as-grown films are dominated by the ferroelectric orthorhombic-phase, while annealing at 600 °C promotes monoclinic phase formation and structural relaxation toward thermodynamic equilibrium. Robust ferroelectric switching is achieved in the as-grown films, whereas high-temperature annealing increases coercive field, imprint, and leakage current, ultimately suppressing reliable polarization reversal. First-principles calculations supported a vacancy-mediated enhancement of polarization and clarified the defect–phase stability relationship. These findings establish a kinetic, defect-engineering pathway for metastable phase control in fluorite-structured ferroelectrics and provide a feasible

pathway for back-end-of-line integration of low-power, hafnia-based ferroelectric devices.

- The study was focused on synthesizing stable $MA_3Sb_2I_9$ micro-crystals with specific spatial arrangements [*see* **Adv. Opt. Mater. 13 (2025) 2402242**]. Comprehensive investigations demonstrated the presence of dimer (0D) and layered phases (2D), as well their structural phase transitions within the 85–573 K temperature range. Multiple complementary experimental techniques were employed, and the findings were validated through theoretical density functional theory simulations. It was revealed that the optical properties of dimer perovskites are more stable compared with the layering counterparts for which the self-trapped excitons emission combined with Sb^{3+} A_X and A_T emissions gives rise to overall white light phosphorescence.
- We explored the synthesis of quinary/quaternary chalcogenide light absorbers from molecular inks for efficient photovoltaic applications: (*i*) by alloying Cu_2ZnSnS_4 with Cd and employing higher sulphurisation temperatures, we achieved devices with power conversion efficiencies exceeding 10% [*see* **Prog. Photovoltaics 33 (2025) 628**]; (*ii*) we examined the impact of Ag alloying on the structural and optical properties of Cu_2ZnSnS_4 for potential indoor photovoltaic applications [*see* **Sustain. Energ. Fuels (2025) 6751**]; and (*iii*) using spray pyrolysis, we showed that the kesterite phase is obtained only under very short thermal treatments, whereas longer annealing times favour the formation of the disordered phase [*see* **Ceram. Int. 51 (2025) 47818]**.

LABORATORY 30

"Electronic Correlations, Magnetism, and Superconductivity"
ECMS

Head of laboratory: Dr. Victor Eugen KUNCSER, Senior Researcher rank 1, Habil. (kuncser@infim.ro)

Personnel: 34 members – 7 × SR1, 7 × SR2, 7 × SR3, 3 × SR, 3 × RA, 2 × technological development engineer (1 × TDE2 and 1 × TDE3), 1 engineer, and 4 × technician.
Beyond its scientific endeavours, the group actively participates in educational and training initiatives.
27 team members hold PhD titles in physics and chemistry, with one serving as PhD supervisor. Additionally, the team comprised 3 PhD students.

Main research directions:

- Fundamental and applied research in the field of magnetic and magneto-functional materials for actuator and sensoristic applications as well as in the field of superconductivity, mainly targeting materials with superconducting properties with potential for practical applications. The research process covers all stages, from preparation (bulk materials, thin-films or nanostructures) to structural and electronic characterization, completed with a deep analysis of the magnetic and superconducting properties, respectively.
- Related to the magnetic behaviour, mainly the functionalities mediated by magnetic reconfiguration controlled by temperature, magnetic and electric fields, applied or from interface interactions, are envisaged. The research is focused especially on the study of 0D, 1D and 2D nanostructures. In the case of magneto-functional structures, magnetic systems of nanoparticles, thin-films and multilayers, materials for colossal magnetoresistance (CMR), giant magnetoresistance (GMR) and tunnelling magnetoresistance (TMR), soft and hard magnetic materials, Heusler compounds with spin polarization, heterogeneous multiferroic systems, magneto-caloric materials, diluted magnetic oxides/semiconductors, thermo-electric systems, *etc* are envisaged. In addition, bulk materials, advanced hybrid systems and composites/nanocomposites destined to operate in extreme conditions such as the ones in fusion and fission reactors, particle accelerators and in space, are investigated. Interactions at the interface and functionalities induced by them in nanostructured hybrid systems such as soft magnet/hard magnet (exchange-spring), ferromagnet/antiferromagnet (exchange-bias), ferromagnet-ferroelectric (magneto-electric coupling) represent other fields of interest related to fundamental and applicative aspects of smart multi-functional systems. In specific cases, the experimental studies are completed by theoretical studies approaching electronic configurations based on Density Functional Theory (DFT) and magnetic configurations based on finite-element simulation programs.
- Related to the superconducting behaviour, studies of vortex matter, dynamics and pinning and nano-engineering of artificial pinning centres for high-magnetic field applications are envisaged. Exploration of fields of applicability of these materials and related ones considering, beyond superconductivity, other that may be important for applications, such as mechanical, biological, optical are also considered. The studied materials are mainly cuprate high temperature superconductors Y (rare earth)

$Ba_2Cu_3O_7$ (RE123) with nano-engineered pinning centres, Bi- and La-based superconducting cuprates, MgB_2 (with various additions for increasing pinning properties), iron-based pnictide and chalcogenide multicomponent superconductors and low temperature (classic) metallic and intermetallic superconductors. Other materials of interest are CeO_2, $SrTiO_3$, LiPdPtB, PdO, boron/carbide composites, selected steels, and archaeological ceramic materials. Most of the materials are obtained in the laboratory in various forms: powders, polycrystalline bulk samples, single crystals, wires/tapes, nanostructures, heterostructures and nanocomposites. The group uses advanced techniques for obtaining or processing materials: conventional powder synthesis in controlled atmosphere, cryochemistry or energy milling, crystal growth in flux or by melting zone, growth of thin films by laser ablation, sintering by spark plasma, lamination, arc melting, *etc*.

Relevant infrastructure:

Amongst important research equipment, considering preparation facilities as well as characterization ones, the following can be listed:

- Spark plasma sintering, hot pressing sintering, microwave sintering (**Fig. 30–1**);
- Melt-spinning and various ball mills;
- Nanoparticle preparation systems by hydrothermal / solvothermal synthesis in autoclave and centrifugation for separation by sizes);
- RF/DC sputtering deposition system for magnetic thin-films and multilayers with 4 sources and base pressure in the range of 10^{-7} Pa (**Fig. 30–1**);
- Facility for inducing thermal transfer in radiofrequency magnetic field to determine specific absorption rates in dispersed nanoparticle systems;
- Thermogravimetric and differential scanning calorimetry systems;
- Vibrating Sample Magnetometry system in magnetic fields up to 9 T;
- Mossbauer spectrometers with different accessories to perform measurements at variable temperatures (4.5 K – 1000 K) and in applied fields, *via* the detection of gamma radiation / X- rays / conversion electrons (the only group in Romania active in Mossbauer Spectroscopy) (**Fig. 30–1**);
- Complex system for measurements of physical properties (PPMS) with magnetic fields up to 14, DynaCool System in up to 9 T with various options for investigating conduction and magneto-conduction properties under applied fields and optical radiation, and a SQUID type magnetometer (**Fig. 30–1**) working in 7 T down to 2 K from Quantum Device with the corresponding facility for liquid He production (18 L/24 h);
- Magnetic texturing of thin-films is investigated by vectorial MOKE magnetometry;
- For high temperature domain, the laboratory possesses a Laser Flash Analyser system that allows the determination of thermal diffusivity, specific heat and thermal conductivity of the volume materials or multilayers (3 layers, including liquids) in the range 25 – 1100 °C, a dilatometer (Netzsch 402 C, 2015) to determine thermal expansion coefficients (25 – 1600 °C) and an equipment (Netzsch, Nemesis 2015) to determine electrical conductivity and Seebeck coefficient (25 – 800 °C);
- In order to determine the composition in bulk / powder systems, an X-ray fluorescence device is available, while for very low concentrations/quantities the group possesses an inductively coupled plasma mass spectrometer (ICP-MS) (**Fig. 30–1**), with an extension for thin film analysis by laser ablation (LA), the last one being acquired in 2019;
- Mechanical properties are determined in quasistatic regime up to 1700 °C, using a recently-acquired equipment (Instron);
- Glove box with an Ar atmosphere and an ARC/TIG welding device.

Fig. 30–1 RF magnetron sputtering system for thin film depositions/co-depositions using four targets, and a spark plasma sintering system used to obtain high-density materials while preserving nanostructural characteristics (left); ICP-MS system with laser ablation for thin film analysis and Mössbauer spectrometers equipped with closed-cycle helium cryostats (centre); High-sensitivity MPMS-SQUID and PPMS DynaCool devices from Quantum Design (right).

Available services:

- Preparation of metallic and intermetallic compounds in the geometry of thin-films, ribbons or bulk;
- Synthesis of materials that are important for applications using state-of-the-art powder metallurgy techniques;
- Lyophilization from frozen materials;
- Treatment of powders and thin-films at high pressures and temperatures in non-corrosive gas atmosphere (hydrogen, nitrogen, methane, carbon dioxide, helium) and measurement of the formation kinetics and thermodynamics of the materials obtained by gas-solid reaction;
- High sensitivity magnetometry to characterize the magnetic properties of the elements (bulk, powders and nano-powders, ribbons and nanocomposites, 0-, 1- and 2-dimensional nanostructures);
- Characterization of the thermodynamic and transport properties (thermal, electric) of the materials in a large temperature domain;
- Determination of the Debye temperature, specific heat and entropy variation of solid materials in the temperature range of 2 – 300 K and in a magnetic field between 0 and 14 T;
- Determination of thermal conductivity of solid materials in the temperature range of 2 – 300 K and in a magnetic field between 0 and 14 T;
- Complex characteristics and specific local configurations and magnetic interactions in materials containing iron, evidenced by all techniques of Mossbauer spectroscopy;
- Specific temperature-dependent properties evidenced by modern differential thermal analysis methods, differential calorimetry and mass spectrometry;
- Atomistic simulation within the DFT of the materials for advanced applications and finite element micromagnetic modelling;
- Preparation/processing by various techniques of powders, single-crystals, thin films/heterostructures/nanostructures, bulks, composites;

- Magnetic and transport measurements on superconducting materials;
- Analysis of experimental data obtained on superconductors with the determination and modelling of critical parameters (critical temperature, critical current density, irreversibility field, pinning force and pinning mechanisms, trapped field, vortex pinning energies, Debye temperature, and others);
- Mechanical measurements in quasistatic regime up to 1700 °C (bending/compression of hard materials);
- Analysis of mechanical properties and correlation with fractography aspects;
- Targets fabrication for thin film deposition.

The group also develops materials and technologies for a number of applications: superconducting thin layers and coated conductors from high critical temperature cuprates containing nano-engineered pinning centres; superconducting MgB_2 wires/tapes in metallic sheath; MgB_2-based magnetic storage devices, magnetic concentrators and magnetic shieldings; MgB_2-based powders, coatings and bulks for biomedical applications; boron-based super-hard materials for tools and extreme high temperature applications, integrated multifunctional devices.

Main results:

- 13 research projects (1 × Horizon; 1 × PNRR; 1 × CoEx selected for funding; 4 × EURATOM; 1 × PED; 2 × PCE; 1 × INUMMAT; 2 × PHE);
- 34 articles published in Web of Science®-indexed journals with impact factor (of which 14 with main author from Lab. 30);
- 3 OSIM granted patents;
- 6 OSIM patent applications.

Highlights:

- In depth analysis of cation distribution and its magnetic implications in gadolinium-iron garnets for an enhanced control of compensation temperature. A complex approach combining X-ray diffraction, magnetometry and Mössbauer spectroscopy was applied to such ferrimagnetic systems of interest in spintronic ultrafast spin storage devices [*see* **Phys. Chem. Chem. Phys. 27 (2025) 22894**];
- Preparation and complex investigation of structural, magnetic and THz emission properties of ultrathin Fe and Pt based spintronic heterostructures [*see* **Adv. Opt. Mater. 13(2025) e00874; Nanomaterials 15 (2025) 1099**];
- Preparation and complex investigation of ssynergistic effects of Ag-Bi co-doping on thermoelectric properties of $Mg_2Si_{0.3}Sn_{0.7}$ solid solutions [*see* **Journal of Alloys and Compounds, 1039 (2025) 183310**];
- Preparation and complex investigation of thermal memory effects and martensitic transformation dynamics in NiFeGa and NiMnGa shape memory systems obtained by different routes [*see* **J. Alloys Compd. 1043 (2025) 184056; Smart Mater. Struct. 34 (2025) 055012**];
- Evidencing the dependence of the magnetic configuration on the crystalline texture in polycrystalline Ni nanowires of high aspect ratio, produced by a template approach at different electrodeposition potentials [*see* **J. Alloys Compd. 1044 (2025) 183959**];
- Evidencing mixed singlet and triplet contributions with associated ground states in dimmers of DPPH stable radicals, by DC and AC SQUID magnetometry [*see* **ACS Omega 10 (2025) 36662**].

LABORATORY 40

"Surface and Interface Science"

Head of laboratory: Dr. Cristian Mihail TEODORESCU, Senior Researcher rank 1, Habil. (teodorescu@infim.ro; cristian@cmteodorescu.ro)

Personnel: 24 members – 2 × SR1, 4 × SR2, 6 × SR3, 5 × SR, 4 × RA, 1 × TDE3, and 2 × technician. Beyond its scientific endeavours, the group actively participates in educational and training initiatives.
18 team members hold PhD titles in physics (13), chemistry (1), materials engineering (3), and electronics (1), including 1 PhD supervisor. Additionally, the team comprised 3 PhD students in physics. Two of these PhD students are about to defend their theses in the first half of 2026.

Main research directions:

- Surface and interface analysis by photoelectron spectroscopies (XPS–ESCA, ARUPS, spin-resolved PES, PED) *in situ* electron diffraction (LEED, RHEED), AES, scanning tunnelling microscopy and spectroscopy STM–STS, photoelectron spectromicroscopy, low energy and photoemission electron microscopy (LEEM–PEEM);
- Surfaces, thin-films and heterostructure preparation by molecular beam epitaxy (MBE);
- Theoretical aspects of ferroic systems.

New subjects:

- Analysis of ferroelectric surfaces, band bending in heterostructures;
- Molecular reactions at ferroelectric surfaces;
- In plane conduction properties of 2D systems on ferroelectric surfaces;
- '2D nanoreactors', molecular reactions with reactants stabilized between graphene layers and substrates;
- Spin asymmetry in band structure of 2D systems;
- Photocatalysts with internal junctions;
- Multiferroic structures with indirect exchange or coupling through charge accumulation;
- Theoretical developments in the area of ferroic thin-films (ferroelectric, ferromagnetic);
- Ferromagnetic and ferroelectric domains;
- Use of NEXAFS to assess surface band bending and transitions of surface atoms in ferroelectric materials;
- Photoelectron spectromicroscopy and low-energy electron microscopy in ferroelectric materials;
- Theoretical (*ab-initio*) and experimental (angle-resolved photoelectron spectroscopy ARPES) band structure determinations;
- Development of new devices operating in ultrahigh vacuum (effusion cells, evaporators, manipulators);
- Development of software packages for data analysis.

Relevant infrastructure:

- A complex cluster for surface and interface science (Specs, **Fig. 40–1**), composed by: (*i*) a chamber for photoelectron spectroscopy (XPS, ESCA, UPS, AES); (*ii*) two molecular beam epitaxy (MBE) chambers, one of which is also equipped with low-energy (LEED) and high-energy (RHEED) electron diffraction *in situ* monitoring capabilities, with *in situ*

follow-up by low energy electron diffraction (LEED), reflection high energy electron diffraction (RHEED), Auger electron spectroscopy (AES), and residual gas analysis by mass spectroscopy; (*iii*) a chamber for scanning tunnelling microscopy and spectroscopy (STM/STS) and non-contact atomic force microscopy (AFM) with atomic resolution; (*iv*) load-lock and storage of samples in ultrahigh vacuum;

- An installation for X-ray photoelectron spectroscopy with possibilities of restricted area analyses (lateral resolution 2 μm) and automated change of samples / measuring areas, coupled to a reaction cell at high pressures and temperatures (Kratos, **Fig. 40–2**);
- A complex cluster for surface and interface science (Specs, **Fig. 40–3**), delocalized actually on the SuperESCA beamline at the Elettra synchrotron radiation facility in Trieste (Combined Spectroscopy and Microscopy on a Synchrotron – CoSMoS), composed by: (*i*) a chamber for photoelectron spectroscopy (XPS, ESCA, UPS, AES) with angle and spin resolution (ARPES, XPD, ARUPS, SR-UPS); (*ii*) a molecular beam epitaxy (MBE) chamber with *in situ* follow-up by low energy electron diffraction (LEED) and reflection high energy electron diffraction (RHEED) and residual gas analysis; (*iii*) a chamber for scanning tunnelling microscopy and spectroscopy (STM/STS); (*iv*) load-lock and storage of samples in ultrahigh vacuum , with the possibility of controlled in-situ application of a magnetic field. This installation has allocated each semester from Elettra 5 days of „in-house research" beamtime and 6 days of beamtime allocated based on research projects, reserved only from projects from Romania. In addition to synchrotron radiation beamtime, photoelectron spectroscopy using laboratory sources, or other experiments STM/STS, LEED, RHEED, Auger, *etc* are possible at any time, provided the personnel is able to travel at Elettra;
- An installation for low energy and photoemission electron microscopy: LEEM – PEEM, micro LEED, micro ARUPS (Specs). The installation is able to perform simultaneous imaging (*i.e.*, without scanning) of surfaces by using low energy electrons or photoelectrons produced by UV radiation. In the LEEM mode, the lateral resolution is about 5 nm, and in the PEEM mode about 50 nm. The advantages of using this installation are: (*i*) the possibility to record immediate imaging, to realize movies, to follow-up in real-time surface modifications; (*ii*) the fact that one uses low energy electrons makes this method suitable for delicate surfaces, which otherwise would be damaged by high energy electrons such as the ones used in scanning electron microscopy (SEM); (*iii*) one may obtain structural or electronic structure (densities of states, dispersion laws) information on nanometre scale.
- Setup for extended X-ray absorption fine structure (EXAFS). Excitations: Mo $K_{\alpha 1}$ (17479.34 eV), W $L_{\alpha 1}$ (8397.6 eV), power 3 kW (40 kV, 75 mA); Ge(220), Ge(400), Ge(840) monochromators; detectors: proportional counters, scintillation detectors; measurement in transmission or fluorescence; simulation and analysis software. Produced by Rigaku, Tokyo, Japan.
- Magneto-optical Kerr effect microscope with possibilities of in-plane and out-of-plane magnetic fields up to 1 T, resolution 500 nm.

Available services:

- Photoelectron spectroscopy-based techniques: X-ray photoelectron spectroscopy (XPS) and diffraction (XPD), ultraviolet photoelectron spectroscopy (UPS), angle-resolved UPS (ARUPS), spin-resolved ARUPS;
- Auger electron spectroscopy (AES) and diffraction (AED);
- Low energy electron diffraction (LEED) and reflection high energy electron diffraction (RHEED) characterization of surfaces;
- Scanning tunnelling microscopy (STM) and spectroscopy (STS) at variable temperature;
- Non-contact atomic force microscopy (AFM) with atomic resolution;

- Sample depth-profiling by ion sputtering assisted by XPS or AES;
- Surface cleaning and synthesis of epitaxial thin-films by molecular beam epitaxy (MBE);
- Thermally-programmed desorption of molecules from surfaces by residual gas analysis (RGA);
- Low energy electron microscopy (LEEM) and photoemission electron microscopy (PEEM), micro-LEED and micro-ARUPS;
- Extended X-ray absorption fine structure (EXAFS) and near-edge absorption fine structure (NEXAFS);
- Band structure calculations by density functional theory (Quantum ESPRESSO, WIEN2k, *etc*).

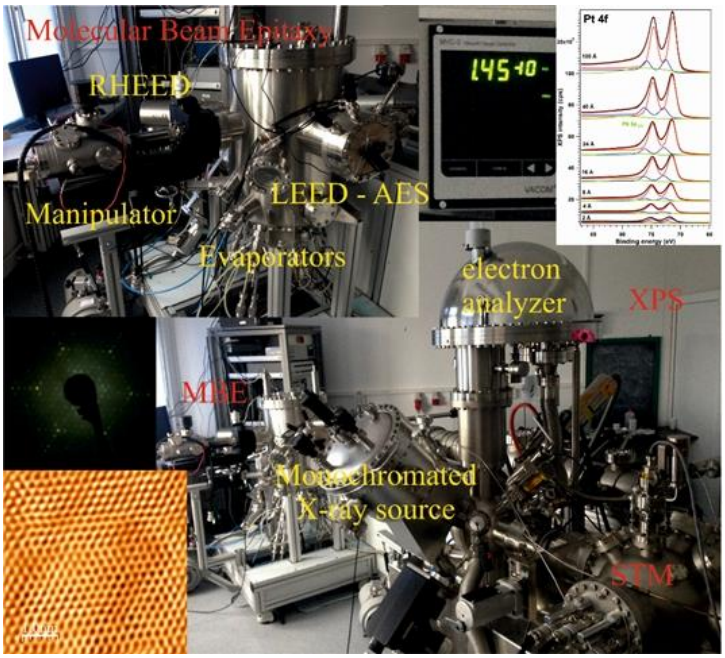

Fig. 40–1 The first cluster of surfaces and interfaces (the "multi-method system" coupled to MBE), located at NIMP. With red, the principal components are denoted (XPS, STM, MBE). With yellow, the main devices. Other photographs from this panel plot the working pressures, the quality of XPS spectra, LEED and STM images. Produced by Specs, Berlin, Germany.

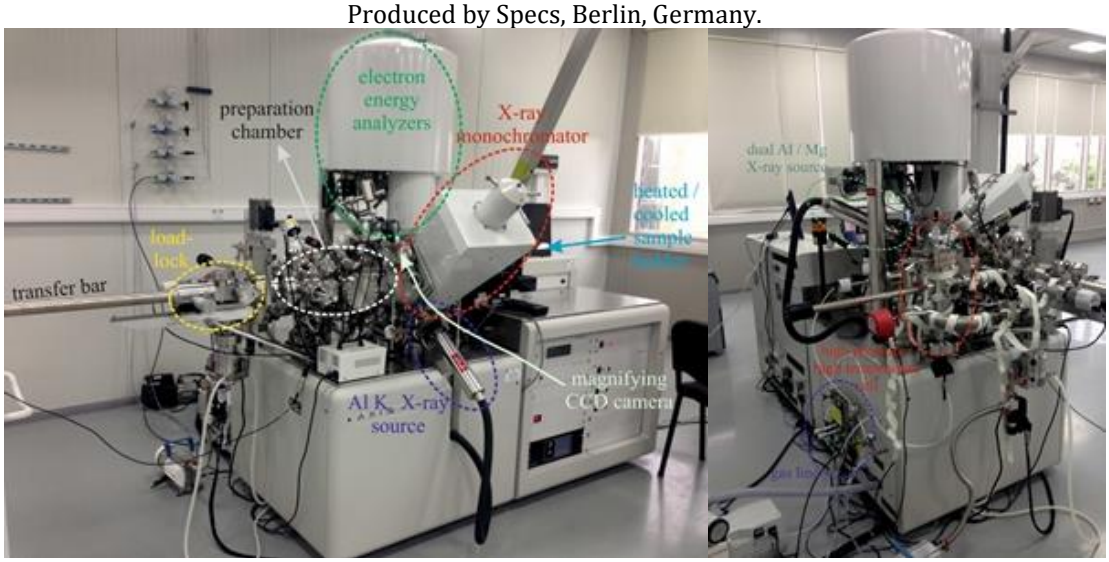

Fig. 40–2 The installation for photoelectron spectroscopy with possibilities of analysis on micrometre areas and provided with a cell for sample treatment at elevated pressures and temperatures (4 bar/1000 °C). Produced by Kratos, Manchester, United Kingdom.

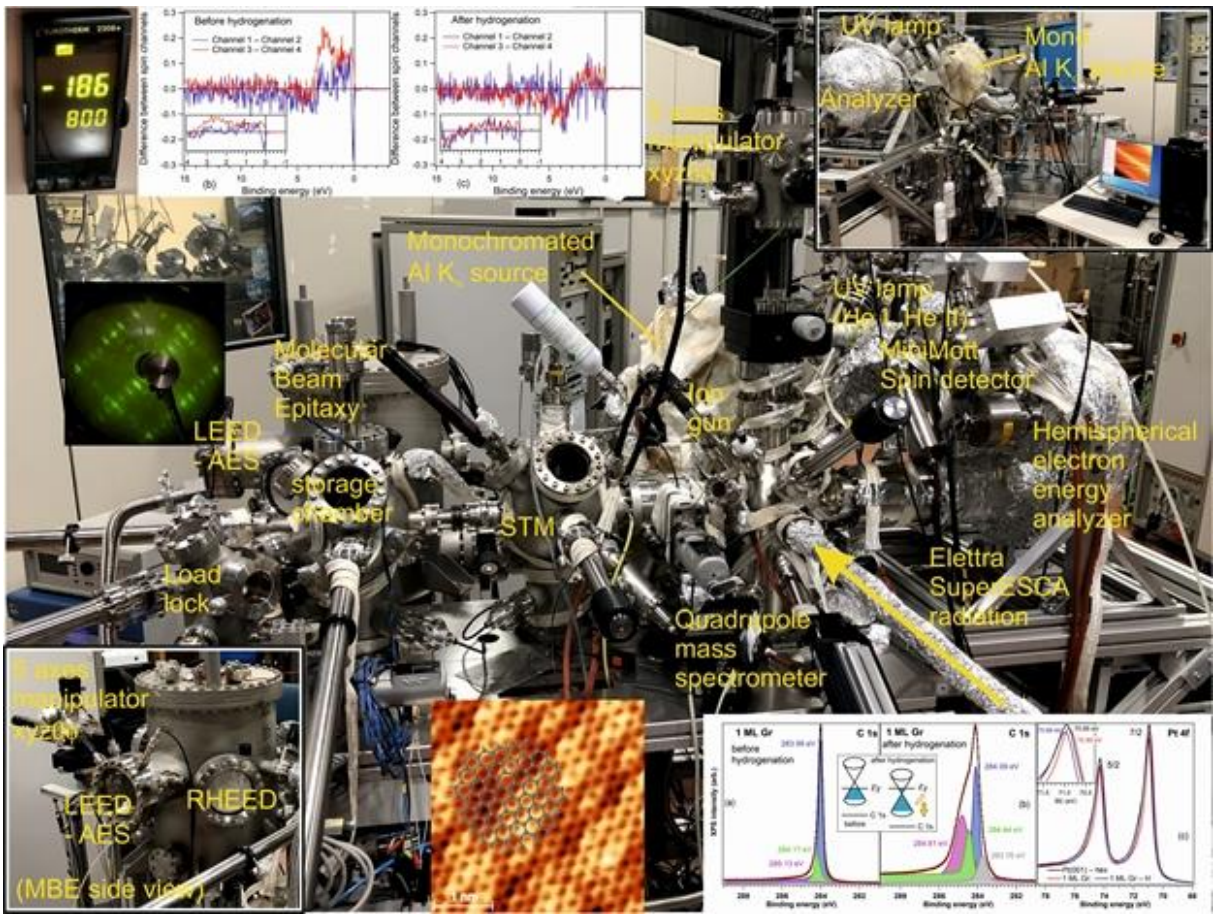

Fig. 40–3 The CoSMoS (combined spectroscopy and microscopy on a synchrotron) cluster coupled to the SuperESCA beamline at Elettra, Trieste. Produced by Specs, Berlin, Germany.

Main results:

- 2 research projects (1 × PCE; 1 × CoEx selected for funding);
- Sustained funding secured under the "Special Installations of National Interest" (IOSIN) national program.
- 44 articles published in Web of Science®-indexed journals with impact factor (of which 6 with main author from Lab. 40);
- 4 OSIM granted patents;
- 5 OSIM patent applications.

Highlights:

- Evidence of surface spin asymmetry in Pt(001) with hexagonal reconstruction [*see* **J. Phys. Mater. 8 (2025) 035010**]. This spin asymmetry is introduced by electron accumulations near the surface, such that the Fermi level is situated on a descending part of the density of states ($(dg/d\varepsilon)_{\varepsilon_F} < 0$). The Pt(001) single crystal was characterized by scanning tunnelling microscopy (STM) with atomic resolution, high resolution core level photoelectron spectroscopy and spin-resolved valence band photoelectron spectroscopy, after various procedures of *in-situ* magnetization. This is the first evidence of the prevalence of the criterion proposed a few years ago in [*see* **Res. Phys. 25 (2021) 104241**] against the Stoner criterion for ferromagnetism.
- Evidence of surface spin asymmetry of both O 2p and Ba 5p derived states in $BaTiO_3$(001) [*see* **Mat. Adv. 6 (2025) 8907**]. The deviation from completely filled O 2p and Ba 5p states is induced by the ferroelectric state which implies charge accumulation at surfaces: consequently, there is a clear interplay between the ferroelectricity and

surface magnetism of (001) barium titanate. A 'permanent inversion of population' is evidenced by the presence of Ba 5p holes on states lower in energy than occupied O 2p states. The stability of this situation stems in the fact that the corresponding states are not localized on the same kind of atom. Apart for the evidence of surface multiferroicity of barium titanate, this study offers the possibility of a tuneable source of extreme-UV radiation induced by the reversal of the ferroelectric state, with applications in semiconductor processing.

- Evidence of second-order Floquet topological phases and corner states based on spatial symmetries in honeycomb lattices in the presence of spin-orbit coupling, together with Floquet topological phase transitions in 2D Su-Schrieffer-Heeger model, with interplay between time reversal symmetry breaking and dimerization [*see* **Phys. Rev. B 111 (2025) 155128**; **New J. Phys. 27 (2025) 023010**]. These theoretical aspects have consequences not only in condensed matter physics, but also for cold gases trapped in optical lattices or topolectrical circuits.
- Study of HfO_2/GaAs(110) interfaces by using oxide-molecular beam epitaxy, X-ray photoelectron spectroscopy (XPS), energy loss electron spectroscopy (EELS), atomic force microscopy (AFM), X-ray diffraction and reflectivity (XRD, XRR), reciprocal space mapping and electrical measurements [*see* **Mater. Sci. Semicond. Process. 198 (2025) 109746**]. The main structural and phenomenological parameters (such as band offsets and dielectric constant) were determined and were found suitable for future MOS applications.

LABORATORY 50

"Theoretical Physics and Computational Modeling"

Head of laboratory: Dr. Valeriu MOLDOVEANU, Senior Researcher rank 1 (valim@infim.ro)

Personnel: 6 members – 1 × SR1, 1 × SR2, 3 × SR3, and 1 × SR.
Beyond its scientific endeavours, the group actively participates in educational and training initiatives.
All 6 team members hold PhD titles in physics.

Main research directions:

- Topological and transport properties of 2D materials and lattices;
- Hybrid quantum systems for nano-electronics and nano-optomechanics;
- Correlation effects in 2D lattices and artificial molecules.

Main results:

- 7 articles published in Web of Science®-indexed journals with impact factor (of which 3 with main author from Lab. 50).

Highlights:

- Antichiral edge states in a diatomic square lattice and quantum transport properties. In this study we move beyond the conventional honeycomb paradigm to show that antichiral edge states are a universal feature of topological systems rather than a geometry-specific effect. We demonstrate that a diatomic square lattice supports antichiral edge modes in which currents on opposite boundaries propagate in the same direction, forming a "one-way path" along both edges. This behaviour contrasts sharply with the quantum Hall effect, where edge currents counter-propagate. Charge conservation is maintained by a compensating return current flowing through the bulk, producing an intrinsic coupling between edge and bulk transport. This coupling leads to a striking anomaly: under specific local disorder, the longitudinal resistance becomes negative. Our results establish a robust and geometry-independent framework for realizing antichiral edge states and offer an alternative for designing photonic or acoustic metamaterials without dependence on hexagonal lattice geometry [*see* **Phys. Rev. B 112 (2025) 085416**].

LABORATORY 60

"Optical Processes in Nanostructured Materials"

Head of Laboratory: Dr. Mihaela Aneta BAIBARAC, Senior Researcher rank 1, Habil. (barac@infim.ro)

Personnel: 29 members – 8 × SR1, 3 × SR2, 5 × SR3, 3 × SR, and 10 × RA.
Beyond its scientific endeavours, the group actively participates in educational and training initiatives.
21 team members hold PhD titles in physics (20) and chemistry (1), including 1 PhD supervisor. Additionally, the team comprised 7 PhD students and 1 MSc student.

Main research directions:

- Optical properties of composite materials based on macromolecular compounds and carbon nanoparticles (graphene, including graphene oxide and reduced graphene oxide, carbon nanotubes, fullerene) and phosphorene, respectively, for applications in the field of eco-nanotechnologies, health and energy storage (supercapacitors, rechargeable batteries);
- Photoluminescence of 2D inorganic materials (including dichalcogenides) and their applications in information technology, sensors and energy storage;
- Optical properties of plasmonic materials, quantum dots and their applications in the fields of eco-nano-technologies and the pharmaceutical field;
- Optical properties of the inorganic micro/nano-particles for applications in the fields of heritage and optoelectronics.

Relevant infrastructure:

- An UV-VIS-NIR spectrophotometer, Lambda 950 model, from Perkin Elmer;
- A FTIR spectrophotometer, Vertex 80 model, from Bruker;
- A FT-Raman spectrophotometer, MultiRam model, from Bruker (**Fig. 60–1**);
- A Fluorolog FL-3.2.2.1 model with upgrade for the NIR range, from Horiba Jobin Yvon;
- A triple Raman spectrophotometer T64000 model, from Horiba Jobin Yvon, equipped with the lasers for the excitation in visible range;
- A FTIR imaging microscope SPOTLIGHT 400 from Perkin Elmer;
- A thermoluminescence reader Harshaw TLD 3500;
- A system for photoconductivity and I–V characteristics;
- A Scanning Near Field Optical Microscope (Multiview 4000 SNOM/SPM system from Nanonics) coupled with Atomic Force Microscope (AFM);
- A Fluoromax 4P with quantum efficiency and colorimetry options, for luminophores characterization, o system to measure surface/interfacial tension, contact angle and density;
- A Langmuir-Blodgett instruments, KSV 2000 system and KSV 5003 model;
- A potentiostat/galvanostat, Voltalab 80, from Radiometer Analytical;
- A multi-channel potentiostat/galvanostat, Origaflex model, from Origalys;
- An equipment for deposition by vacuum evaporation of organic materials;
- A broadband dielectric spectroscopy system from Novocontrol;
- An infrared spectro-microscope, Carry 600, from Agilent Scientific;
- A surface plasmons resonance (SPR) equipment from Reichert (**Fig. 60–2**);

- A hybrid Magnetron Sputtering – Pulsed Laser Deposition equipment for thin-films (**Fig. 60–3**);
- A Physical Vapor Transport equipment for transition metal dichalcogenides (**Fig. 60–4**).

Available services:

- Development of composite materials based on the conducting and insulating polymers and carbon nanoparticles of the type carbon nanotubes, graphene oxide, reduced graphene oxide, graphene quantum dots, fullerene and carbon nanohorns;
- Development of organic/inorganic hybrid materials based on conducting polymers and inorganic nanoparticles of the type ZnO, ZnS, CdS, TiO_2;
- Chemical and electrochemical functionalization of 2D materials (reduced graphene oxide, phosphorene, *etc*) with the organic and macromolecular compounds;
- Synthesis of transition metal dichalcogenides (TDMs) of the type MoS_2, WS_2, *etc*;
- The preparation of the surface-enhanced Raman scattering (SERS) supports of the type of rough metallic (Ag, Au, Cu) films, the colloidal suspensions of the metallic nanoparticles and the graphene sheets decorated with metallic nanoparticles;
- Deposition of thin layers using magnetron sputtering and Langmuir Blodgett;
- Realization of organic/organic and organic/inorganic structures by vacuum evaporation and from solution;
- Controlled crystallization of thin-films in various atmospheres;
- Functionalization of metallic surfaces for development of optical sensors *via* surface plasmons resonance;
- Analyses by the UV-VIS-NIR and IR absorption spectroscopy, Raman scattering, surface-enhanced Raman scattering (SERS), surface-enhanced infrared absorption (SEIRA) spectroscopy, photoluminescence, atomic force microscopy and broad-band dielectric spectroscopy;
- Structural characterization and phase identification in crystalline materials;
- Contact angle analysis for assessment of hydrophobic/hydrophile properties;
- Measurements of surface/interface tension and of the density of liquids;
- Colorimetry and quantum yield measurements for the characterization of phosphors;
- Calculated absorption coefficient of inorganic and macromolecular chain with density-functional theory (DFT);
- Electrochemical analysis by cyclic voltammetry, chronoamperometry, chronopotentiometry, electrochemical impedance spectroscopy, Tafel polarizations;
- Surface nano-patterning by UV Nano Imprint lithography (UV-NIL);
- Characterization of organic heterostructures for opto-electronic devices;
- Galvanostatic charge-discharge measurements for the testing nanomaterials as electrode active materials in supercapacitors and rechargeable batteries;
- The preparation of electrodes with the application in the field of the electrochemical sensors;
- Analysis concerning the stability of the drugs in the presence of UV light and various chemical agents by UV-VIS spectroscopy, photoluminescence, Raman scattering and FTIR spectroscopy.

Fig. 60–1 MultiRam FT-Raman spectrophotometer from Bruker.

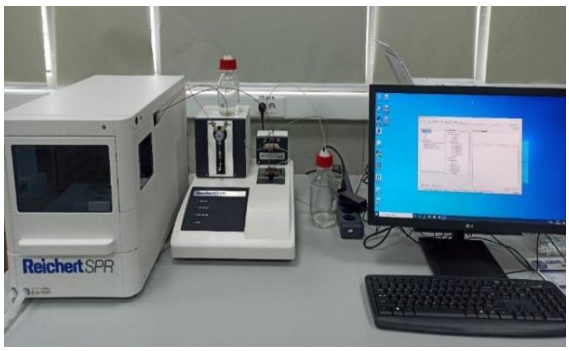

Fig. 60–2 Surface Plasmon Resonance equipment from Reichert.

Fig. 60–3 Hybrid Magnetron Sputtering – Pulsed Laser Deposition equipment for thin-films.

Fig. 60–4 Physical Vapor Transport equipment for transition metal dichalcogenides.

Main results:

- 12 research projects (1 × PNRR; 4 × M-ERA.NET; 3 × PED; 1 × PCE; 2 × TE; and 1 × RO-MD). In addition, Lab. 60's is involved in 2 COST actions;
- 39 articles published in Web of Science®-indexed journals with impact factor (of which 14 with main author from Lab. 60);
- 1 EPO patent application;
- 5 OSIM patent applications.

Highlights:

- DNA-RNA nucleobase-coated ZnO nanostructures for interface engineering in organic optoelectronics [*see* **ACS Appl. Nano Mater. 8 (2025) 16307–16320**];
- Optical, structural and electrical properties of composites based on MoS_2, WS_2, and poly(ortho-toluidine) [*see* **Mater. Today Commun. 46 (2025) 112469**];
- Unravelling the crystallization mechanism and structural evolution of Yb/Er doped SiO_2-GdF_3 nano-glass ceramics [*see* **Mater. Adv. 6 (2025) 5877–5883**];
- Ce-doped ZnO photoanode with enhanced photoelectrochemical performance [*see* **Int. J. Hydrog. Energy 114 (2025) 52–59**].

LABORATORY 70

"Atomic Structures and Defects in Advanced Materials"
LASDAM

Head of laboratory: Dr. Corneliu GHICA, Senior Researcher rank 1 (cghica@infim.ro)

Personnel: 28 members – 5 × SR1, 9 × SR2, 3 × SR3, 3 × SR, 5 × RA, and 3 × engineer.
Beyond its scientific endeavours, the group actively participates in educational and training initiatives.
22 team members hold PhD titles in physics (20), chemistry (1), and electrical engineering (1), including 2 PhD supervisors. Additionally, the team comprised 3 PhD students.

Main research directions:

Fundamental research

- Atomic scale structure-functionality correlations in advanced materials (nanostructures, thin-films, ceramics and special alloys);
- Paramagnetic point defects, either intrinsic or induced by impurities or radiations in insulators and wide-bandgap semiconductors;

Applied research

- Investigation of the physical-chemical mechanisms underpinning the detection process in nanostructured materials for gas sensing applications;
- Nanocrystalline materials and nanostructures based on SiGeSn, 2D-MoS_2 and ferroelectric HfZrO for applications in electronics, photonics and optoelectronics (*e.g.*, electronic and optoelectronic non-volatile memories, optical sensors, short-wave infrared photodetectors, neuromorphic devices);
- Cellular and non-cellular *in vitro* interactions and biomedical applications of inorganic nanomaterials and hybrid nanostructures;
- Nanostructured materials for post-Li-ion solid-state batteries;
- AI-based algorithms for TEM-generated data analysis.

Main research infrastructure:

- Aberration-corrected analytical transmission electron microscope (HRTEM/HRSTEM) provided with EDS and EELS microanalytical facilities for sub-Ångström resolution imaging and atomic-resolution elemental mapping;
- High-resolution analytical electron microscope for electron tomography, *in situ* and *operando* experiments by specimen heating/cooling/electrical biasing;
- SEM-FIB dual analytical system used for morpho-structural and microanalytical investigations (SEM, EDS, EBSD) as well as for ion beam micro- and nano-processing;
- Continuous wave (cw) X-band (9.8 GHz) EPR spectrometer with variable temperature (VT) accessories in the 80 – 500 K range; cw Q-band (34 GHz) EPR spectrometer with ENDOR (Electron-Nuclear Double Resonance) and VT accessories (5 – 300 K);
- Pulse X-band (9.7 GHz) EPR spectrometer equipped with pulse ENDOR, pulse ELDOR (Electron-Electron Double Resonance) and VT accessories (5 – 300 K);
- Automatic liquid He plant completed with a helium recovery system;
- Computer-controlled gas mixing station and associated electrical measurements chains for materials testing under controlled atmosphere;

- Chemical reactor and autoclave for hydrothermal and co-precipitation chemical synthesis;
- Magnetron sputtering equipment (substrate heating up to 850 °C, base pressure down to 10^{-8} Torr) for thin-film and multilayer deposition, equipped with *in situ* UV-VIS-NIR ellipsometry for monitoring film thickness and uniformity, as well as Auger electron spectroscopy (AES) and low-energy electron diffraction (LEED) for surface characterization;
- Three-inch rapid thermal processor (annealing – RTA, oxidation – RTO, nitridation – RTN) that allows running processes up to 1250 °C with ramp rates up to 300 °C/s, in gas flow (N_2, O_2, Ar, H_2);
- Three independent temperature zone horizontal split-tube furnace (up to 1200 °C) for thermal annealing and physical vapor deposition (PVD);
- Complex systems for electrical, photoelectrical, charge storage/memory, ferroelectric, Hall effect, and magnetoresistance measurements.

Fig. 70–1 (**a**) JEM ARM200F aberration-corrected analytical transmission electron microscope; (**b**) Bruker EPR spectrometer in CW Q-band with ENDOR accessory; (**c**) Setup for electrical measurements under controlled atmosphere gas mixing station; (**d**) Magnetron sputtering equipment for thin-film and multilayer deposition, equipped with *in situ* AES, LEED, and UV-VIS-NIR ellipsometry.

Available services:

- SEM morphological characterization of advanced materials;
- TEM characterization of nanostructured materials, thin-films, ceramics, alloys;
- Chemical elemental composition and elemental mapping by SEM-EDS and STEM-EDS;
- Multifrequency EPR characterization of bulk and nanostructured insulating and semiconductor materials: nature, concentration, localization, formation mechanism and stability of the paramagnetic centres in materials; chemical processes, structural or magnetic transitions;

- Controlled simulation of toxic and explosive gas environments (CO, CH_4, NO_2, H_2S, NH_3, SO_2) for gas sensors testing and calibration; temperature-voltage calibration for the optimization of power consumption for substrates and gas sensors;
- Deposition of thin films and multilayers by magnetron sputtering: semiconductors (Si, Ge, SiGe, GeSn, SiGeSn) and dielectrics (SiO_2, TiO_2, ZrO_2, HfO_2, Al_2O_3, Si_3N_4) on either heated substrates or substrates maintained at room-temperature;
- Rapid thermal annealing (RTA) and controlled oxidation (RTO) at temperatures within the 200 – 1250 °C range, with heating rates up to 200 °C/s in controlled gas flow (N_2, O_2, Ar, H_2) and thermal annealing in a three-zone horizontal split-tube furnace up to 1200 °C under vacuum or in Ar or N_2 flow;
- Electrical characterization under dark/illumination conditions, Hall effect measurements, and modelling of experimental curves: current-voltage (I–V) at different temperatures, in DC and AC; current-temperature (I-T) at different bias voltages; spectral photocurrent (I–λ) under modulated and continuous illumination; capacity-voltage (C–V); capacity-frequency (C–f); capacity-time (C–t); polarization-voltage (P–V); Hall investigations by V–I characteristics as a function of current, magnetic field, and temperature.

LASDAM operates as Partner Facility within CERIC-ERIC (https://www.ceric-eric.eu/) on behalf of NIMP, the Romanian Representing Entity in the ERIC along with research institutes and universities in Austria, Croatia, Czech Republic, Hungary, Italy, Poland, or Slovenia.

Main results:

- 1 research projects (1 × PCE);
- 33 articles published in Web of Science®-indexed journals with impact factor (of which 7 with main author from Lab. 70);
- 1 OSIM granted patent;
- 1 OSIM patent application.

Highlights:

- Microstructure of self-assembled Ga_2O_3 polymorph multilayers induced by ion beam irradiation. An in depth HRTEM investigation reveals the subsurface layering of (010) oriented β-Ga_2O_3 wafers after phase transitions induced by 400 keV $^{58}Ni^+$ ion beam irradiation at 350°C, generating an interlaced β-γ single-crystal 4-layer structure [*see* **ACS Nano Lett. 25 (2025) 1637–1643**].
- Evidence of the direct correlation between the NO_2 sensing properties of SnO_2 nanoparticles and the surface oxygen vacancy complexes. SnO_2 nanoparticles hydrothermally grown at 120 °C, 140 °C, and 160 °C were systematically investigated to establish the relationship between their morpho-structural features, defect properties, and NO_2 sensing performance under in-field-like conditions. The sample synthesized at 120 °C demonstrated the best performance, achieving a sensor signal of 74 at a NO_2 detection limit of 3 ppm, operating at 100 °C and 50% relative humidity, while exhibiting low cross-sensitivity to CH_4 and CO_2 and maintaining good stability over 20 months. Results corroborated from EPR, HRTEM, and electrical measurements highlight a direct correlation between NO_2 sensing performance and surface oxygen vacancy complexes, emphasizing the importance of the atomic-level control in the synthesis of application-oriented sensing materials [*see* **Surf. Interfaces 72 (2025) 107212**].
- The hydrogenation effect in the substantial enhancement of short-wave infrared (SWIR) photosensitivity of amorphous (a-) and nanocrystalline GeSn:H (nc-GeSn:H) films deposited by magnetron sputtering in a mixture of Ar and H_2 working atmosphere was reported for the first time. The key novelty lies in the successful hydrogenation that is

more effective in curing deep-level defects in the a-GeSn:H films than in the nc-GeSn:H ones. This leads to a remarkable two orders of magnitude increase in the spectral photocurrent in SWIR and an extension of photosensitivity up to 2.4 μm, the photocurrent being enhanced with increasing polarization due to the Poole-Frenkel effect by enhancing the carrier mobility by electric field. Still, the nc-GeSn:H shows improved sensitivity up to 1.8 μm compared to non-passivated nc-GeSn films [*see* **J. Alloy. Compd. 1010 (2025) 177065**].

- Field-effect devices with channel lengths of 15 μm and 20 μm have been obtained by Mo-CVD selective growth of 2D-MoS_2 between pre-deposited Mo source and drain finger electrodes on SiO_2/c-Si substrates. The interconnected MoS_2 flakes of few mono-layers cover the gap between Mo contacts. Such simple fabricated FET device is multifunctional, being very sensitive to changes of various external stimuli (gate and source-drain voltages, light, molecule adsorption, carrier trapping, temperature). We demonstrated the high sensitivity to the adsorption of molecules from air by gate-voltage dependence of source-drain current in dark and under illumination, spectral photocurrent, time dependence of the source-drain current and current-temperature dependence measurements. Depending on the orientation of adsorbed H_2O molecules from the air and adsorption sites on the 2D-MoS_2 layer, one can observe the accumulation or depletion of electrons in MoS_2 [*see* **Nanoscale Adv. 7 (2025) 2368**].
- Enhanced photocatalytic properties during incipient phase transformations in TiO_2. TiO_2 nanoparticles were synthesized *via* ultrasound-assisted excess hydrolysis of titanium tetra-isopropoxide. X-ray diffraction revealed that exposing the as-prepared powders to temperatures up to 500 °C induces a gradual transformation of brookite into anatase, followed by the formation of rutile. EPR measurements showed that synergistic action of charge-carrier trapping mechanisms leads to enhanced photocatalytic activity of TiO_2 at the temperature marking the onset of the anatase-to-rutile transformation [*see* **J. Alloys Compd. 1018 (2025) 179097**].

LABORATORY 80

"Catalytic Materials and Catalysis"
MATCA

Head of laboratory: Dr. Mihaela FLOREA, Senior Researcher rank 1, Habil. (mihaela.florea@infim.ro)

Personnel: 7 members – 3 × SR1, 2 × SR3, and 2 × RA.
Beyond its scientific endeavours, the group actively participates in educational and training initiatives.
6 team members hold PhD titles, including 1 PhD supervisor. Additionally, the team comprised 1 PhD student.

Designing advanced catalysts remains one of the most significant challenges at the forefront of modern science. The main objective of the MATCA group is to develop and engineer functional materials with precisely controlled structural and physicochemical properties and to contribute to the advancement of innovative catalytic systems addressing critical societal challenges in energy, sustainability, and environmental protection.

Main research directions:

- Pioneering advancements in catalytic and photocatalytic materials, addressing pressing challenges in sustainability, energy, and environmental protection. With a strong focus on the development, preparation, and characterization of heterogeneous catalytic materials, the group explores innovative solutions that enhance efficiency and performance in key chemical transformations.
- A significant part of their research is devoted to catalytic reactions, encompassing selective oxidation and hydrogenation processes that enable the synthesis of high-value compounds. Their work extends to the development of polymers derived from renewable and alternative resources, fostering sustainable materials for industrial applications. Moreover, MATCA researchers are at the forefront of depolymerization technologies, seeking efficient methods to break down plastics and contribute to circular economy strategies. In parallel, they investigate the reduction of volatile organic compounds (VOCs), aiming to minimize environmental pollutants and improve air quality.
- Photocatalysis represents another core research direction, harnessing solar energy to drive essential chemical reactions. The group is actively engaged in water splitting for green hydrogen production, a key component in the transition to clean energy. Additionally, their studies on photocatalytic CO_2 transformation and artificial photosynthesis explore ways to convert carbon dioxide into valuable fuels and chemicals, offering innovative approaches to carbon capture and utilization.
- In the field of energy, the MATCA team focuses on the synthesis of advanced materials for electrocatalysis in fuel cells. Their work aims to enhance the performance and durability of fuel cell components, contributing to the development of efficient, next-generation energy technologies that support decarbonization efforts.

Relevant infrastructure:

Lab. 80 has an infrastructure covering various methods of catalytic material preparation and physico-chemical characterization. Among the important infrastructures one can mention:

- Chemistry laboratory (**Fig. 80–1**) equipped with all necessary small equipment's for catalytic materials synthesis (ovens working in air or vacuum, rotavapors, magnetic stirrers, autoclaves for hydrothermal treatments, chemical niche, apparatus for milliQ water production, centrifuge, balances) and catalytic reactors (in house reactors for solid-gas phase and liquid-solid phase reactions);
- Thermo-programmed desorption and reduction equipment (TPD-TPR) – for determining the adsorption capacity and redox properties (**Fig. 80–2**);
- Spectroscopy analysis: UV-Vis and Raman portable (**Fig. 80–2**);
- Thermal analysis – to study the relationship between a sample property and its temperature as the sample is heated or cooled in a controlled manner (**Fig. 80–2**);
- Analysis of the reaction products – gas chromatograph with three detectors (TCD, FID, and BID) gas chromatograph coupled with mass spectrometer (**Fig. 80–2**);
- Adsorption analyser with high performance capabilities - utilized to quantify the surface area, pore size, and pore volume of powders and particulate materials. The equipment is outfitted with a chemisorption feature that expands the scope of its application to encompass both physical and chemical adsorption. This enables the characterization of catalyst texture and active surface properties in catalyst supports, sensors, and several other materials. By including an automated injection loop, the TCD analytical range can be expanded through the utilization of pulse chemisorption;
- Catalytic flow reactor – is a highly advanced modular laboratory system for determining in real time the selectivity and activity of catalysts for different catalytic applications through different configurations and options.

The group has access to other infrastructures located at NIMP, through collaborative research activities, such as: SEM; TEM; XPS; optical spectroscopies (Raman, UV-Vis-NIR, FTIR); X-ray diffraction; ICP-MS; photoluminescence.

Fig. 80–1 Chemistry laboratory.

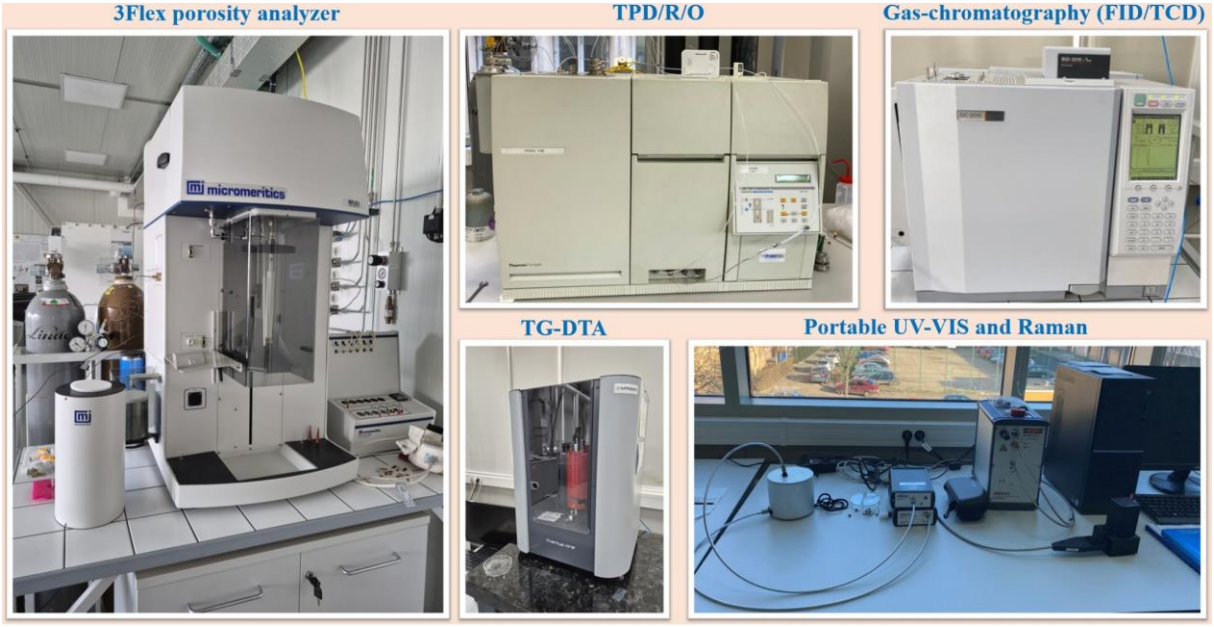

Fig. 80–2 Equipment for materials characterization and analysis.

Available services:

- Catalytic materials preparation;
- Gas-solid and gas-liquid catalytic reaction;
- H_2 production through water splitting;
- Surface characterization;
- Structural and textural characterization of the catalytic materials;
- Investigation of acid-base and redox properties;
- Determination of acid and basic properties (qualitatively and quantitatively).

Main results:

- 2 research projects (1 × PTE and 1 × PED);
- 9 articles published in Web of Science®-indexed with high-impact factor (of which 3 with the main author from Lab. 80).

Highlights:

- The development of active and selective materials for low-temperature oxidative activation of methane into value-added products remains a key challenge for the scientific community. We are actively involved in designing catalysts for selective methane oxidation to formaldehyde using molecular oxygen over MXene and MAX-based catalysts at low-temperature and ambient-pressure conditions. These studies were done in collaboration with Dr. L. Artiglia's group from the Paul Scherrer Institute, Switzerland [*see* **Catal. Today 443 (2025) 114959**].
- Developing 1D filaments of materials containing Ti, C, and O to split water under photocatalytic conditions and create H_2 gas is a straightforward, low-cost, and economically viable strategy [*see* **Cell Rep. Phys. Sci. 6 (2025) 102921**]. In collaboration with a team of researchers at Drexel University, led by Prof. M. Barsoum and a team from the University of Strasbourg, France, led by Dr. D. Constantin we are extending the research for CO_2 photocatalytic conversion to added value products. This partnership will continue into 2026.
- Plastics are indispensable materials for packaging and many products in our daily lives, and their recycling is essential to ensure a circular economy. We are continuing our efforts in developing efficient and stable catalysts, and therefore we have established a

new collaboration with group of Prof. J. Garcia Martinez from the University of Alicante, Spain.

Through their multidisciplinary approach, the MATCA research group is driving innovation in catalytic science, bridging fundamental research with practical applications that promote sustainability, cleaner energy solutions, and environmental resilience.

List of Research Articles and Reviews Published in 2025

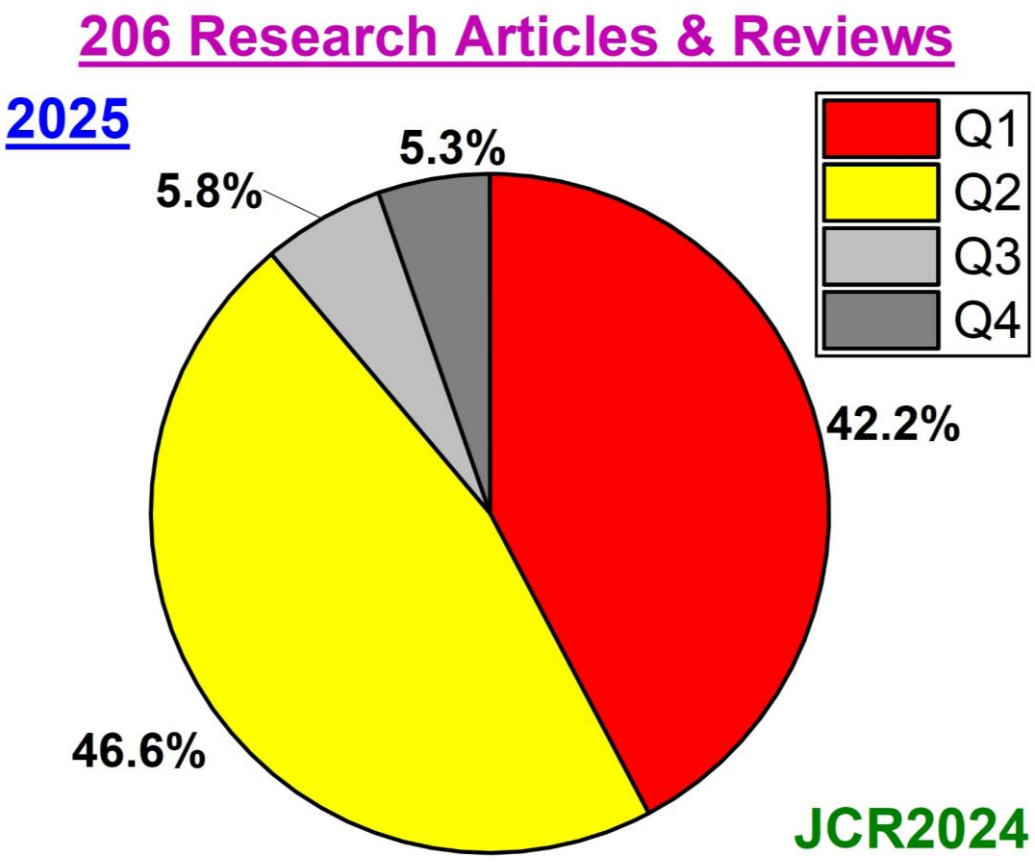

List of Research Articles and Reviews published by NIMP's authors in 2025 (*WoS®, 2025-02-28*)

No.	Authors	Article title	Journal	IF	Quartile	Cites WoS®	Year	Vol.	Pages/ Art. no.	DOI link	OA type
1.	Silva, NE; Jayakrishnan, AR; Kaim, A; Gwozdz, K; Domingues, L; Kim, JS; Istrate, MC; Ghica, C; Pereira, M; Marques, L; Gomes, MJM; Hoye, RLZ; MacManus-Driscoll, JL; Silva, JPB	Ultra-Sensitive, Self-powered, CMOS-Compatible Near-Infrared Photodetectors for Wide-Ranging Applications	ADVANCED FUNCTIONAL MATERIALS	19.0	Q1	17	2025	35	2416979	http://dx.doi.org/10.1002/adfm.202416979	Hybrid
2.	Ibrahim, MA; Walter, AD; Badr, HO; Schwenk, GR; Ibrahim, AMH; Morris, VR; Boukhris, S; Florea, M; Constantin, D; Barsoum, MW	Expanding the Processing Space of Quantum Confined, One-dimensional Titania-based Lepidocrocite Nanofilaments	MATTER	17.5	Q1	3	2025	8	102260	http://dx.doi.org/10.1016/j.matt.2025.102260	
3.	Grau, RR; Garcia-Aznar, P; Sastre, G; Goberna-Ferrón, S; Pavel, O; Tirsoaga, A; Cojocaru, B; Popescu, DG; Parvulescu, VI; Primo, A; García, H	MXenes as Heterogeneous Thermal Catalysts: Regioselective Anti-Markovnikov Hydroamination of Terminal Alkynes with 102 h-1 Turnover Frequencies	JOURNAL OF THE AMERICAN CHEMICAL SOCIETY	15.7	Q1	3	2025	147	3315–3332	http://dx.doi.org/10.1021/jacs.4c13481	Green submitted Hybrid
4.	Boukhris, S; Iacoban, AC; Ibrahim, M; Badr, H; Kuncser, AC; Neatu, S; Neatu, F; Barsoum, MW; Florea, M; Constantin, D	Structural Analysis of Colloidal Titania-Based Ribbons and Their Self-Assembly upon Drying	SMALL STRUCTURES	11.3	Q1	5	2025	6	2500017	http://dx.doi.org/10.1002/sstr.202500017	Green submitted Gold
5.	Sandu, N; Hanganu, A; Popescu, C; Demeter, AM; Mirea, AG; Kuncser, A; Tablet, C; Hadade, ND; Florea, M; Funeriu, DP; Matache, M	Synthesis of Dynamic N-acylhydrazone-based Macrocycles	JOURNAL OF MATERIALS CHEMISTRY A	9.5	Q1	0	2025	13	10232–10242	http://dx.doi.org/10.1039/d4ta09035g	
6.	Keshri, SR; Mandal, I; Gaddam, A; Ganisetti, S; Haque, S; Venkateswaran, C; Stan, GE; Tite, T; Ghosh, A; Gosvami, NN; Krishnan, NMA; Allu, AR	Mixed Network Former Effect on the Ion-dynamics of Sodium Alumino-Phospho-Silicate Glasses	ACTA MATERIALIA	9.3	Q1	1	2025	288	120837	http://dx.doi.org/10.1016/j.actamat.2025.120837	
7.	Boni, AG; Chirila, CF; Filip, LD; Botea, MI; Radu, C; Popescu, DG; Husanu, MA; Hrib, L; Trupina, L; Pintilie, I; Pintilie, L	Steady State Negative Capacitance in p-n Ferroelectric Junctions	ACTA MATERIALIA	9.3	Q1	0	2025	298	121177	http://dx.doi.org/10.1016/j.actamat.2025.121177	
8.	Azarov, A; Radu, C; Galeckas, A; Mercioniu, IF; Cernescu, A; Venkatachalapathy, V; Monakhov, E; Djurabekova, F; Ghica, C; Zhao, J; Kuznetsov, A	Self-Assembling of Multilayered Polymorphs with Ion Beams	NANO LETTERS	9.1	Q1	14	2025	25	1637–1643	http://dx.doi.org/10.1021/acs.nanolett.4c05727	
9.	Ruotsalainen, J; Stryjczyk, M; Ramalho, M; Eronen, T; Ge, Z;	Ultralow Qβ Value for the Allowed Decay of ^{110}Agm	PHYSICAL REVIEW LETTERS	9	Q1	1	2025	134	172501	http://dx.doi.org/10.1103/Ph	Green Submitted

No.	Authors	Article title	Journal	IF	Quartile	Cites WoS®	Year	Vol.	Pages/ Art. no.	DOI link	OA type
	Kankainen, A; Mougeot, M; Suhonen, J	Confirmed *via* Mass Measurements								ysRevLett.134.172501	
10.	Adams, DQ; Alduino, C; Alfonso, K; Armatol, A; Avignone, FT III; Azzolini, O; Bari, G; Bellini, F; Benato, G; Beretta, M; Biassoni, M; Branca, A; Brofferio, C; Bucci, C; Camilleri, J; Caminata, A; Campani, A; Cao, J; Capelli, C; Capelli, S; Cappelli, L; Cardani, L; Carniti, P; Casali, N; Celi, E; Chiesa, D; Clemenza, M; Copello, S; Cremonesi, O; Creswick, RJ; D'Addabbo, A; Dafinei, I; Dell'Oro, S; Di Domizio, S; Di Lorenzo, S; Dixon, T; Fang, DQ; Faverzani, M; Ferri, E; Ferroni, F; Fiorini, E; Franceschi, MA; Freedman, SJ; Fu, SH; Fujikawa, BK; Ghislandi, S; Giachero, A; Girola, M; Gironi, L; Giuliani, A; Gorla, P; Gotti, C; Guillaumon, P; Gutierrez, TD; Han, K; Hansen, E; Heeger, KM; Helis, DL; Huang, HZ; Hurst, MT; Keppel, G; Kolomensky, YG; Kowalski, R; Liu, R; Ma, L; Ma, YG; Marini, L; Maruyama, RH; Mayer, D; Mei, Y; Moore, MN; Napolitano, T; Nastasi, M; Nones, C; Norman, EB; Nucciotti, A; Nutini, I; o'Donnell, T; Olmi, M; Oregui, BT; Pagan, S; Pagliarone, CE; Pagnanini, L; Pallavicini, M; Pattavina, L; Pavan, M; Pessina, G; Pettinacci, V; Pira, C; Pirro, S; Pottebaum, EG; Pozzi, S; Previtali, E; Puiu, A; Quitadamo, S; Ressa, A; Rosenfeld, C; Schmidt, B; Serino, R; Shaikina, A; Sharma, V; Singh, V; Sisti, M; Speller, D; Surukuchi, PT; Taffarello, L; Tomei, C; Torres, A; Torres, JA; Vetter, KJ; Vignati, M; Wagaarachchi, SL; Welliver, B; Wilson, J; Wilson, K; Winslow, LA; Xie, F; Zhu, T; Zimmermann, S; Zucchelli, S;	Half-Life and Precision Shape Measurement of the 2νββ Decay of ^{130}Te	PHYSICAL REVIEW LETTERS	9	Q1	1	2025	135	82501	http://dx.doi.org/10.1103/jdhf-hn4l	Green Submitted

No.	Authors	Article title	Journal	IF	Quartile	Cites WoS®	Year	Vol.	Pages/ Art. no.	DOI link	OA type
	Castillo, D; Kotila, J; Menéndez, J; Nitescu, O; Simkovic, F										
11.	Petcu, IC; Negrea, R; Brandao, ATSC; Romanitan, C; Brincoveanu, O; Djourelov, N; Mihalache, I; Veca, LM; Isopencu, G; Pereira, CM; Anicai, L; Busuioc, C; State, S	Pulsed Reverse Electrochemical Synthesis of Ag-TiO_2 Composites from Deep Eutectic Solvents: Photocatalytic and Antibacterial Behaviour	APPLIED SURFACE SCIENCE ADVANCES	8.7	Q1	5	2025	27	100749	http://dx.doi.org/10.1016/j.apsadv.2025.100749	Green Submitted Gold
12.	Mandes, A; Vladoiu, R; Dinca, V; Tichy, M; Kudrna, P; Matei, E; Polosan, S	Bilayered Metallic Cathodes Consisting of Pure Mg and Zn:Al Thin Films Optimized by Laser-induced Thermionic Vacuum Arc (LTVA) technology	APPLIED SURFACE SCIENCE ADVANCES	8.7	Q1	1	2025	28	100787	http://dx.doi.org/10.1016/j.apsadv.2025.100787	Green submitted Gold
13.	Beregoi, M; Nistor, S; Ciobotaru, IC; Nitescu, A; Zgura, I; Bunea, MC; Enculescu, M; Nedelcu, L; Busuioc, C; Enache, TA	Cells Proliferation on Surfaces Functionalized with Amyloid Beta Peptide Fibrils	INTERNATIONAL JOURNAL OF BIOLOGICAL MACROMOLECULES	8.5	Q1	2	2025	309	143160	http://dx.doi.org/10.1016/j.ijbiomac.2025.143160	Hybrid
14.	Sima, M; Preda, N; Negrila, C; Matei, E; Sima, A; Stancu, V	Ce-doped ZnO Photoanode with Enhanced Photoelectrochemical Performance	INTERNATIONAL JOURNAL OF HYDROGEN ENERGY	8.3	Q1	3	2025	114	52–59	http://dx.doi.org/10.1016/j.ijhydene.2025.03.048	
15.	Spataru, N; Preda, L; Matei, E; Satulu, V; Mihai, MA; Radu, MM; Donath, C; Moga, OG; Spataru, T	Beneficial Role of Silicotungstic Acid Presence on the WO_3-modified Boron-doped Diamond Substrate on the Electrocatalytic Activity for Methanol Anodic Oxidation of Supported Platinum	INTERNATIONAL JOURNAL OF HYDROGEN ENERGY	8.3	Q1	2	2025	120	403–411	http://dx.doi.org/10.1016/j.ijhydene.2025.03.327	
16.	Gherca, D; Borhan, AI; Popescu, DG; Husanu, MA; Borca, CN; Stoian, G; Chiriac, H; Ababei, G; Lupu, N	Monophasic Titanate-based Photocatalyst with Heteroatom Mixed Iso-Aliovalency Enabling Water Oxidation	ACS APPLIED MATERIALS & INTERFACES	8.2	Q1	1	2025	17	30910–30923	http://dx.doi.org/10.1021/acsami.5c03417	
17.	Pavel, O; Tirsoaga, A; Cojocaru, B; Popescu, D; Ramírez-Grau, R; González-Durán, P; García-Aznar, P; Tian, L; Sastre, G; Primo, A; Parvulescu, V; Garcia, H	Nb_2C MXene as a Bifunctional Acid-Base and Oxidation/Hydrogenation Catalyst	EES CATALYSIS	8.1	Q1	2	2025	3	856–869	http://dx.doi.org/10.1039/d5ey00004a	Gold
18.	Elomari, G; Larhlimi, H; Oubaki, R; Elmaataouy, E; Aqil, M; Samih, Y; Makha, M; Negrila, C; Alami, J; Dahbi, M	Fast Charging and High-efficiency Sputter-deposited Silicon Thin Film Anodes for Li-ion Batteries	JOURNAL OF POWER SOURCES	7.9	Q1	3	2025	642	236967	http://dx.doi.org/10.1016/j.jpowsour.2025.236967	

No.	Authors	Article title	Journal	IF	Quartile	Cites WoS®	Year	Vol.	Pages/ Art. no.	DOI link	OA type
19.	Gilshtein, E; Gupta, HM; Enevoldsen, AMP; Besleaga, C; Galca, AC; Canulescu, S	Superstrate Structured Sb_2S_3 Thin-film Solar Cells by Magnetron Sputtering of Sb and Post-sulfurization	MATERIALS & DESIGN	7.9	Q1	3	2025	258	114621	http://dx.doi.org/10.1016/j.matdes.2025.114621	Green Submitted Gold
20.	Enculescu, M; Beregoi, M; Bunea, MC; Trandafir, MM; Enculescu, I	Efficient and Reusable 3D TiO_2@PDMS Sponge Composites for Solar Driven Photocatalytic Degradation of Water Pollutants	RESULTS IN ENGINEERING	7.9	Q1	1	2025	27	107083	http://dx.doi.org/10.1016/j.rineng.2025.107083	Green Submitted Gold
21.	Akabbouch, L; El Khouja, O; Assahsahi, I; Dassallem, S; Ait-alla, Y; Fahoume, M; Tite, T; Galca, AC; Nouneh, K	Charge Storage Mechanism and Supercapacitive Behavior of Transparent Vanadium Pentoxide Thin films in Various Aqueous Electrolytes	RESULTS IN ENGINEERING	7.9	Q1	1	2025	28	107836	http://dx.doi.org/10.1016/j.rineng.2025.107836	Gold
22.	El Khouja, O; Gong, YC; Jimenez-Arguijo, A; Guerra, MJ; Medaille, AG; Scaffidi, R; Basak, A; Radu, C; Flandre, D; Vermang, B; Giraldo, S; Placidi, M; Li-Kao, ZJ; Galca, AC; Saucedo, E	Exploring the Synthesis of $Cu_2(Zn,Cd)SnS_4$ at High Temperatures as a Route for High-Efficiency Solar Cells	PROGRESS IN PHOTOVOLTAICS	7.6	Q1	5	2025	33	628–643	http://dx.doi.org/10.1002/pip.3899	Green Submitted Hybrid
23.	Botta, D; Beregoi, M; Cepleanu-Pascu, IA; Crisan, DN; Ignat, AM; Matei, E; Enculescu, I; Diculescu, VC	A Paper-based Device with Submicronic Fiber Mesh Electrodes for Voltammetric Quantification of Nucleic Acids	CELL REPORTS PHYSICAL SCIENCE	7.3	Q1	1	2025	6	102781	http://dx.doi.org/10.1016/j.xcrp.2025.102781	Gold
24.	Hassig, MQ; Walter, AD; Ferrer, LM; Ibrahim, MA; Gordon, A; Morris, VR; Iacoban, AC; Neatu, F; Ibrahim, AMH; Schwenk, GR; Florea, M; Barsoum, MW	On the Alkaline Oxidation of Titanium Diboride into 1D Lepidocrocite Titanate Nanofilaments	CELL REPORTS PHYSICAL SCIENCE	7.3	Q1	0	2025	6	102921	http://dx.doi.org/10.1016/j.xcrp.2025.102921	Gold
25.	Papaioannou, ET; Scheuer, L; Torosyan, G; Dimitrakopulos, GP; Kret, S; Crisan, AD; Crisan, O; Beigang, R; Kehagias, T	Enhanced THz Emission from Ultrathin Ta/Fe/Pt Spintronic Trilayers	ADVANCED OPTICAL MATERIALS	7.2	Q1	2	2025	13	e00874	http://dx.doi.org/10.1002/adom.202500874	Hybrid
26.	Ciobotaru, IC; Ciobotaru, CC; Bartha, C; Enculescu, M; Secu, M; Polosan, S; Besleaga, C	Phase Transitions in Dimer/Layered Sb-Based Hybrid Halide Perovskites: An In-Depth Analysis of Structural and Spectroscopic Properties	ADVANCED OPTICAL MATERIALS	7.2	Q1	7	2025	13	2402242	http://dx.doi.org/10.1002/adom.202402242	Hybrid
27.	Ivan, R; Iordache, IU; del Pino, AP; Negrila, C; György, E	Mg Doped Ti Oxide/Reduced Graphene Oxide Nanohybrid Photocatalysts for Decomposition of Nucleic Acid Molecules and Saccharomyces	JOURNAL OF ENVIRONMENTAL CHEMICAL ENGINEERING	7.2	Q1	0	2025	13	116872	http://dx.doi.org/10.1016/j.jece.2025.116872	Hybrid

No.	Authors	Article title	Journal	IF	Quartile	Cites WoS®	Year	Vol.	Pages/ Art. no.	DOI link	OA type
		Cerevisiae Yeast Cells under Visible and Simulated Sunlight									
28.	do Nascimento, JLA; Rostas, AM; Silva, A; Kennedy, BJ; Barbu-Tudoran, L; Bocirnea, AE; dos Santos, IM; Alves, MCF; de Oliveira, ALM	Tailoring Structural Distortions and Ionic Defects as Alternative Strategy to Modulate Reactive Oxygen Species and Photocatalytic Activity in SnO_2 Nanoparticles	CHEMISTRY OF MATERIALS	7.0	Q1	7	2025	37	4963–4981	http://dx.doi.org/10.1021/acs.chemmater.4c03146	Hybrid
29.	Bordeiasu, M; Goscianska, J; Panek, R; Nicolaev, A; Jurca, B; Parvulescu, VI; Coman, SM	Magnetic Fe,Co-Nanocarbon Frameworks Derived from Fe-Doped Zeolitic Imidazolate Framework-67 as Highly Active Catalysts for 5-Hydroxymethylfurfural Oxidation	CHEMSUSCHEM	6.6	Q1	1	2025	18	e202500678	http://dx.doi.org/10.1002/cssc.202500678	Bronze
30.	Soare, EM; Stanciu, CA; Patru, RE; Surdu, VA; Padurariu, L; Horchidan, N; Nicoara, AI; Trupina, L; Vasile, BS; Trusca, RD; Mitoseriu, L; Ianculescu, AC	Grain Size Effects in $BaTi_{0.90}Hf_{0.10}O_3$ Ceramics with Phase Coexistence: The Influence of Nanostructuring and of the Internal Stress on the Functional Properties	JOURNAL OF MATERIALS RESEARCH AND TECHNOLOGY-JMR&T	6.6	Q1	0	2025	38	5389–5408	http://dx.doi.org/10.1016/j.jmrt.2025.08.195	Green submitted Gold
31.	Oprica, IMA; Beregoi, M; Popescu-Pelin, GF; Constantinoiu, I; Bacalum, M; Draghici, CI; Jinga, SI; Busuioc, C	Development of New Scaffolds for Bone Substitution by Electrospinning and Laser Ablation	JOURNAL OF MATERIALS RESEARCH AND TECHNOLOGY-JMR&T	6.6	Q1	0	2025	35	6087–6101	http://dx.doi.org/10.1016/j.jmrt.2025.02.225	Green Submitted Gold
32.	Gherca, D; Roman, T; Popescu, DG; Borhan, AI; Herea, DD; Stoian, G; Chiriac, H; Ababei, G; Lupu, N	Designing TiO_2@Fe_xO_y Magnetic Core-shell Catalyst with 3D Flower-like Surface Morphology Preservation for Enhanced Photocatalytic Performance	APPLIED SURFACE SCIENCE	6.3	Q1	3	2025	696	163003	http://dx.doi.org/10.1016/j.apsusc.2025.163003	Hybrid
33.	Craciun, C; Bercea, A; Radu, C; Stîngescu, ML; Bonciu, A; Satulu, V; Filipescu, M	Growth of Pyramidal Nanostructures in CeO_{2-x} Thin Films: Characterization and Morphology Modeling	APPLIED SURFACE SCIENCE	6.3	Q1	0	2025	705	163499	http://dx.doi.org/10.1016/j.apsusc.2025.163499	
34.	Dascalescu, I; Palade, C; Lungu, GA; Lepadatu, AM; Teodorescu, VS; Braic, M; Ciurea, ML; Stoica, T; Slav, A	Influence of *In-situ* Hydrogenation on Photoelectrical Properties of Amorphous and Nanocrystalline GeSn Deposited by Magnetron Sputtering	JOURNAL OF ALLOYS AND COMPOUNDS	6.3	Q1	2	2025	1010	177065	http://dx.doi.org/10.1016/j.jallcom.2024.177065	Hybrid

No.	Authors	Article title	Journal	IF	Quartile	Cites WoS®	Year	Vol.	Pages/ Art. no.	DOI link	OA type
35.	Ivekovic, A; Muralidharan, GK; Galatanu, A; Li, GC; Vanmeensel, K; Vleugels, J	Liquid-Copper Infiltration and Characterization of Additively Manufactured W-Lattice Structures	JOURNAL OF ALLOYS AND COMPOUNDS	6.3	Q1	4	2025	1011	178411	http://dx.doi.org/10.1016/j.jallcom.2024.178411	Green submitted
36.	Iacoban, AC; Rostas, AM; Mihalcea, CG; Vlaicu, ID; Culita, D; Ilas, MC; Florea, M; Neatu, S; Neatu, F; Secu, M; Popescu, T	Distortion of Charge Carrier Trapping Centers During Incipient Phase Transformations in TiO_2 Can Enhance its Photocatalytic Performance	JOURNAL OF ALLOYS AND COMPOUNDS	6.3	Q1	2	2025	1018	179097	http://dx.doi.org/10.1016/j.jallcom.2025.179097	Hybrid
37.	Manousou, DK; Atata, SB; Sohn, YJ; Tsipas, P; Grzechnik, A; Calamiotou, M; Friese, K; Gardelis, S	Phase Evolution in Low Fe Concentration $V_{1-x}Fe_xO_2$ compounds: Phase Diagram and Annealing Effects	JOURNAL OF ALLOYS AND COMPOUNDS	6.3	Q1	0	2025	1024	180081	http://dx.doi.org/10.1016/j.jallcom.2025.180081	
38.	Sadurni, MD; Timmo, K; Mikli, V; Krustok, J; Danilson, M; Suchodolskis, A; Radu, C; Bocirnea, AE; Galca, AC; Grossberg-Kuusk, M; Kauk-Kuusik, M	Effects of Cationic Substitution on the Properties of $Sb_{1-x}Bi_xSeI$ (x=0-1) Compounds	JOURNAL OF ALLOYS AND COMPOUNDS	6.3	Q1	1	2025	1037	182292	http://dx.doi.org/10.1016/j.jallcom.2025.182292	
39.	Assahsahi, I; Galatanu, A; El Bouayadi, R; Zejli, D; Popescu, B	Synergistic Effects of Ag-Bi Co-doping on Thermoelectric Properties of $Mg_2Si_{0.3}Sn_{0.7}$ Solid Solutions	JOURNAL OF ALLOYS AND COMPOUNDS	6.3	Q1	0	2025	1039	183310	http://dx.doi.org/10.1016/j.jallcom.2025.183310	Hybrid
40.	Onea, M; Iacob, N; Schinteie, G; Molares, MET; Matei, E; Kuncser, V; Enculescu, I	Novel Insights into the Distinct Magnetic Configurations of Polycrystalline Ni Nanowires Produced by a Template Approach at Varying Electrodeposition Potentials	JOURNAL OF ALLOYS AND COMPOUNDS	6.3	Q1	0	2025	1044	183959	http://dx.doi.org/10.1016/j.jallcom.2025.183959	
41.	Tolea, F; Nita, M; Tolea, M	Thermal Memory Effect in NiFeGa and NiMnGa Shape Memory Ribbons: Toward Maximum-temperature Recording Applications	JOURNAL OF ALLOYS AND COMPOUNDS	6.3	Q1	0	2025	1043	184056	http://dx.doi.org/10.1016/j.jallcom.2025.184056	Hybrid
42.	Boni, AG; Tsipas, P; Popescu,D; Radu, C; Laafar, S; Pintilie, P; Dimoulas, A	Tailoring Polarization and Dielectric Properties in HZO multilayers: Electrostatic Effects *vs.* Structural Instabilities	JOURNAL OF ALLOYS AND COMPOUNDS	6.3	Q1	0	2025	1044	184617	https://doi.org/10.1016/j.jallcom.2025.184617	Hybrid
43.	Lascu, I; Gheorghiu, CC; Bucur, IC; Tanase, AM; Dumitru, A	Influence of Polypyrrole-derived Nitrogen-doped Carbon Nanostructure Morphology on the Microbial Composition of	SURFACES AND INTERFACES	6.3	Q1	5	2025	56	105586	http://dx.doi.org/10.1016/j.surfin.2024.105586	Hybrid

No.	Authors	Article title	Journal	IF	Quartile	Cites WoS®	Year	Vol.	Pages/ Art. no.	DOI link	OA type
		Anodic Biofilms and Microbial Fuel Cell Performance									
44.	Andrei, F; Ion, V; Birjega, R; Ghitiu, I; Zamfir, M; Moldovan, A; Teodorescu, VS; Dinescu, M; Marcu, IC; Scarisoreanu, ND	Strain Engineering of Epitaxial Perovskite-type $LaFeO_3$/ $BiFeO_3$ Heterostructures for Photoelectrochemical Water Splitting	SURFACES AND INTERFACES	6.3	Q1	5	2025	62	106234	http://dx.doi.org/10.1016/j.surfin.2025.106234	Hybrid
45.	Gherca, D; Borhan, AI; Herea, DD; Minuti, AE; Stavila, C; Danceanu, CM; Popescu, DG; Borca, CN; Huthwelker, T; Stoian, G; Chiriac, H; Polo, CG; Ababei, G; Lupu, N	Ferrihydrite Surface Functionalization of Anatase TiO_2 Nanoparticles as Flower-like Core-shell Heterostructure with Enhanced Visible-light-driven Photocatalytic Properties	SURFACES AND INTERFACES	6.3	Q1	2	2025	69	106745	http://dx.doi.org/10.1016/j.surfin.2025.106745	
46.	Ghica, C; Stefan, M; Stanoiu, A; Simion, CE; Vlaicu, ID; Apostol, NG; Mihalcea, CG; Iacoban, AC; Florea, OG; Bulat, S; Ghica, D	Tailoring Surface Defects and Faceting in SnO_2 Nanocrystals to Improve their NO_2 Sensing Potential	SURFACES AND INTERFACES	6.3	Q1	0	2025	72	107212	http://dx.doi.org/10.1016/j.surfin.2025.107212	Hybrid
47.	Soare, EM; Stanciu, CA; Patru, RE; Surdu, VA; Horchidan, N; Mitoseriu, L; Pintilie, I; Vasile, BS; Nicoara, AI; Trusca, RD; Ianculescu, AC	Composition-dependent Structural, Microstructural and Functional Characteristics of Fine-grained $BaTi_{1-x}Hf_xO_3$ Ceramics Consolidated by Spark Plasma Sintering	JOURNAL OF THE EUROPEAN CERAMIC SOCIETY	6.2	Q1	0	2025	45	117600	http://dx.doi.org/10.1016/j.jeurceramsoc.2025.117600	Hybrid
48.	Alimenti, A; Silva, E; Torokhtii, K; Garcia, PV; Badica, P; Crisan, A; Grigoroscuta, MA; Pompeo, N	Microwave Surface Resistance in MgB_2: Effect of Te and Cubic-BN Addition on Flux Flow and Pinning	SUPERCONDUCTIVITY	6.2	Q1	0	2025	14	100170	http://dx.doi.org/10.1016/j.supcon.2025.100170	Green submitted Gold
49.	Leote, RJB; Barsan, MM; Sanz, CG; Diculescu, VC	Electrochemical Bienzymatic Biosensor for Pyruvate Kinase Activity Evaluation and Inhibitor Screening	TALANTA	6.1	Q1	3	2025	291	127886	http://dx.doi.org/10.1016/j.talanta.2025.127886	Hybrid
50.	Kolmas, J; Romaniuk, P; Predoi, D; Drobniewska, A; Burdan, K; Kolodziejska, B	Magnesium Ion Substitution in Various Calcium Phosphates: A Way Towards Bone Regeneration	CERAMICS INTERNATIONAL	5.6	Q1	4	2025	51	1153–1160	http://dx.doi.org/10.1016/j.ceramint.2024.11.096	
51.	Predoi, D; Iconaru, SL; Ciobanu, SC; Rokosz, K; Talu, S; Predoi, SA; Raaen, S; Motelica-Heino, M	Exploring the Fabrication, Properties, and Morphology of Fluorine Substituted Hydroxyapatite Coatings	CERAMICS INTERNATIONAL	5.6	Q1	8	2025	51	1929–1948	http://dx.doi.org/10.1016/j.ceramint.2024.11.168	Green submitted
52.	Mocanu, AC; Miculescu, F; Dondea, ES; Pandele, MA; Voicu, SI; Dobre, AA; Stan, GE; Ghebaur, A; Ciocan, LT	Induced Antibacterial Activity of Printable Composite Materials: Influence of the Conjoined Modulation of	CERAMICS INTERNATIONAL	5.6	Q1	1	2025	51	5181–5198	http://dx.doi.org/10.1016/j.ceramint.2024.11.492	Hybrid

No.	Authors	Article title	Journal	IF	Quartile	Cites WoS®	Year	Vol.	Pages/ Art. no.	DOI link	OA type
		Ampicillin/Hydroxyapatite/Graphene Nanoplatelets Ratios									
53.	Zidi, Y; Khaldi, O; Patru, RE; Leonat, LN; Enculescu, M; Toma, V; Stepanova, A; Ben Younes, R; Galca, AC	Experimental and Theoretical Perspective on Band Gap Modulation in Sr^{2+} Modified $BaTiO_3$ Capacitors	CERAMICS INTERNATIONAL	5.6	Q1	4	2025	51	18166–18177	http://dx.doi.org/10.1016/j.ceramint.2025.01.591	Hybrid
54.	Stanciu, G; Croitoru, G; Craciun, A; Voicu, F; Tihon, C; Dumitru, M; Enculescu, M; Pavel, N	Multilayered Yb^{3+}:Y_2O_3 Transparent Composite Ceramics Fabricated by Direct Dry Pressing-Characterization and Laser Emission Results	CERAMICS INTERNATIONAL	5.6	Q1	0	2025	51	37304–37311	http://dx.doi.org/10.1016/j.ceramint.2025.05.437	Hybrid
55.	El Khouja, O; Popescu, B; Assahsahi, I; Negrila, CC; Leonat, LN; Nouneh, K; Touhami, ME; Galatanu, A; Galca, AC	Improved Sulfurization Process for Enhancing the Microstructure and Transport Properties of Spray Pyrolysis-deposited Cu_2ZnSnS_4 Films	CERAMICS INTERNATIONAL	5.6	Q1	0	2025	51	47818–47829	http://dx.doi.org/10.1016/j.ceramint.2025.08.041	hybrid
56.	Chirila, CF; Boni, GA; Popescu, DG; Istrate, CM; Husanu, MA; Filip, LD; Besleaga, C; Pintilie, L; Dimoulas, A	Ferroelectric $Hf_{0.5}Zr_{0.5}O_2$ Thin Films on TiN/Si Substrates Grown by Pulsed Laser Deposition at CMOS-compatible Temperatures	CERAMICS INTERNATIONAL	5.6	Q1	1	2025	51	50941–50950	http://dx.doi.org/10.1016/j.ceramint.2025.08.321	
57.	Aldea, A; Onea, M; Matei, E; Apostol, N; Botta, D; Enculescu, I; Diculescu, VC	Phosphorothioated Oligonucleotides on Gold-coated Electrospun Polymeric Fibers for Electrochemical Genosensors	ELECTROCHIMICA ACTA	5.6	Q1	2	2025	524	146006	http://dx.doi.org/10.1016/j.electacta.2025.146006	
58.	Pusta, A; Tertis, M; Ciocan, B; Turcu, R; Craciunescu, I; Diculescu, VC; Stan, GE; Bulat, S; Porfire, A; Petru, AE; Fizesan, I; Mirel, S; Cristea, C	Aptamer-Modified Magnetic Nanoparticles as Targeted Drug Delivery Systems for Hepatocellular Carcinoma	PHARMACEUTICS	5.5	Q1	1	2025	17	1292	http://dx.doi.org/10.3390/pharmaceutics17101292	Green submitted Gold
59.	Khammar, F; Boukerche, S; Djaber, S; Boublia, A; Messabhia, A; Gharbi, A; Ferkous, H; Gomez, CV; Bellucci, S; Albrahim, M; Alam, M; Benguerba, Y	Synthesis, Characterization, and Photocatalytic Efficiency of Mg-doped ZnO Nanoparticles for Basic Fuchsin Dye Degradation: Experimental and Theoretical Insights	INORGANIC CHEMISTRY COMMUNICATIONS	5.4	Q1	9	2025	176	114274	http://dx.doi.org/10.1016/j.inoche.2025.114274	
60.	Iacoban, AC; Haldar, T; Neatu, F; Chirica, IM; Mirea, AG; Neatu, S; Barsoum, MW; Florea, M	Catalytic Behaviour of CuO_x and VO_x on Ti_3SiC_2 Support for Direct Oxidation of Methane	CATALYSIS TODAY	5.3	Q1	0	2025	443	114959	http://dx.doi.org/10.1016/j.cattod.2024.114959	Hybrid
61.	Petcu, G; Anghel, EM; Atkinson, I; Papa, F; Apostol, NG; Baran, A;	Ti-Zeolite Y Based Nanocomposites Modified with	CATALYSIS TODAY	5.3	Q1	2	2025	459	115403	http://dx.doi.org/10.1016/j.c	Hybrid

No.	Authors	Article title	Journal	IF	Quartile	Cites WoS®	Year	Vol.	Pages/ Art. no.	DOI link	OA type
	Petrescu, S; Trica, B; Tenchev, K; Todorova, S; Parvulescu, V	Au and CeO_2 with Photocatalytic Activity in Visible Light								attod.2025.115403	
62.	Rizescu, CE; Sun, C; Papa, F; Mereuta, P; Negrila, CC; Popescu, I; Da Costa, P; Urda, A; Marcu, IC	Effect of Mg/Al Molar Ratio on the Catalytic Performance of Cu-MgAlO Mixed Oxide Catalysts in the Hydrodeoxygenation of Benzyl Alcohol	ENERGY & FUELS	5.3	Q1	1	2025	39	7790–7804	http://dx.doi.org/10.1021/acs.energyfuels.5c00292	
63.	Stancu, AI; Ditu, LM; Oprea, E; Ficai, A; Badea, IA; Buleandra, M; Brîncoveanu, O; Mirea, AG; Voicu, SN; Musuc, AM; Aricov, L; Culita, DC; Mititelu, M	New Antimicrobial Gels Based on Clove Essential Oil-Cyclodextrin Complex and Plant Extracts for Topical Use	GELS	5.3	Q1	1	2025	11	653	http://dx.doi.org/10.3390/gels11080653	Green submitted Gold
64.	Dallas, P; Tzitzios, VK; Givalou, L; Tsipas, P; Basina, G; Sakellis, E; Boukos, N; Stergiopoulos, T	Effects of Ligand Coordination on Ag_8SnS_6 as a Photoabsorber for Thin Film Solar Cells	JOURNAL OF MATERIALS CHEMISTRY C	5.2	Q1	2	2025	13	7996–8005	http://dx.doi.org/10.1039/d5tc00397k	Green submitted Hybrid
65.	Chilom, CG; Iftimie, S; Balan, AE; Oprea, D; Enculescu, M; Enache, TA	Human Serum Albumin-based Nanoparticles for Targeted Intracellular Drug Delivery	INTERNATIONAL JOURNAL OF MOLECULAR SCIENCES	4.9	Q1	1	2025	26	8297	http://dx.doi.org/10.3390/ijms26178297	Green submitted Gold
66.	Groza, A; Hurjui, ME; Yehia-Alexe, SA; Staicu, C; Bleotu, C; Iconaru, SL; Ciobanu, CS; Ghegoiu, L; Predoi, D	Influence of Electron Beam Irradiation and RPMI Immersion on the Development of Magnesium-Doped Hydroxyapatite/Chitosan Composite Bioactive Layers for Biomedical Applications	POLYMERS	4.9	Q1	1	2025	17	533	http://dx.doi.org/10.3390/polym17040533	Green submitted Gold
67.	Predoi, D; Ciobanu, CS; Iconaru, SL; Petre, RA; Rokosz, K; Raaen, S; Predoi, MV	Development and Physico-Chemical and Antibacterial Characterization of Chromium-Doped Hydroxyapatite in a Chitosan Matrix Coating	POLYMERS	4.9	Q1	1	2025	17	2633	http://dx.doi.org/10.3390/polym17192633	Green submitted Gold
68.	Ciobanu, SC; Predoi, D; Iconaru, SL; Rokosz, K; Raaen, S; Bleotu, C; Predoi, MV	Development of Chrome-Doped Hydroxyapatite in a PVA Matrix Enriched with Amoxicillin for Biomedical Applications	ANTIBIOTICS-BASEL	4.6	Q1	1	2025	14	455	http://dx.doi.org/10.3390/antibiotics14050455	Green submitted Gold
69.	Sanz, CG; Aldea, A; Barsan, MM	Electrochemical Detection of Superoxide Anion in Living Systems: Recent Trends and Clinical Implications	BIOELECTROCHEMISTRY	4.5	Q1	1	2025	165	108998	http://dx.doi.org/10.1016/j.bioelechem.2025.108998	
70.	Manojlovic, M; Crnjac, A; Moffat, N; Villegas, J; Pintilie, I; Cabruja, E; Pellegrini, G; Hidalgo, S	Gain Response and Ion Beam-Induced Donor Removal in nLGAD Detector: Global Gain Quenching	IEEE SENSORS JOURNAL	4.5	Q1	0	2025	25	43985–43996	http://dx.doi.org/10.1109/JSEN.2025.3624206	Green accepted Green Submitted

No.	Authors	Article title	Journal	IF	Quartile	Cites WoS®	Year	Vol.	Pages/ Art. no.	DOI link	OA type
											Hybrid
71.	Civitarese, O; Kotila, J; Suhonen, J	Application of the Particle-number Projected Proton-Neutron QRPA to the Muon Capture on ^{136}Ba	PHYSICS LETTERS B	4.5	Q1	1	2025	866	139495	http://dx.doi.org/10.1016/j.physletb.2025.139495	Green submitted Gold
72.	Hellgren, M; Suhonen, J	Quenching of the Weak Axial Coupling Derived from the Scattering of Stopped-Pion Neutrinos on ^{127}I	PHYSICS LETTERS B	4.5	Q1	0	2025	866	139508	http://dx.doi.org/10.1016/j.physletb.2025.139508	Green submitted Gold
73.	Hellgren, M; Papoulias, DK; Suhonen, J	Inelastic Neutrino-Nucleus Scattering Off $^{203/205}$Tl In Terms of the Nuclear Recoil Energy Using a Hybrid Nuclear Model	PHYSICS LETTERS B	4.5	Q1	0	2025	868	139624	http://dx.doi.org/10.1016/j.physletb.2025.139624	Green submitted Gold
74.	Agnihotri, A; Suhonen, J	Novel Way of Evaluating gA Quenching in β^+/EC Decays: Introducing the Branching-Ratio Method (BRM)	PHYSICS LETTERS B	4.5	Q1	0	2025	868	139627	http://dx.doi.org/10.1016/j.physletb.2025.139627	Green submitted Gold
75.	Budaca, R; Budaca, AI	Harmonic Chiral Vibration in Triaxial Nuclei	PHYSICS LETTERS B	4.5	Q1	0	2025	868	139794	http://dx.doi.org/10.1016/j.physletb.2025.139794	Green submitted Gold
76.	Leote, RJB; Sanz, CG; Diculescu, VC; Barsan, MM	Electrochemical Assay for the Quantification of Anticancer Drugs and Their Inhibition Mechanism	METHODS	4.3	Q1	0	2025	241	13–23	http://dx.doi.org/10.1016/j.ymeth.2025.05.002	Hybrid
77.	Petrus, M; Popa, C; Bratu, AM; Joita, AC; Bercu, V	Evaluating Copper-Induced Oxidative Stress in Germinating Wheat Seeds Using Laser Photoacoustic Spectroscopy and EPR Techniques	TOXICS	4.1	Q1	0	2025	13	604	http://dx.doi.org/10.3390/toxics13070604	Green submitted Gold
78.	Lite, MC; Constantinescu, R; Chirila, L; Popescu, A; Kuncser, A; Romanitan, C; Brîncoveanu, O; Lacatusu, I; Badea, N	Antimicrobial Efficacy of Green Silver Nanoparticles Synthesized Using Crataegus Monogyna Extract	BIOMIMETICS	3.9	Q1	1	2025	10	737	http://dx.doi.org/10.3390/biomimetics10110737	Green submitted Gold
79.	Ydir, B; Ajdour, A; Antohe, I; Socol, G; Socol, M; Toderascu, LI; Saadaoui, D; Choulli, I; Leghrib, R; Lahlou, H	Aluminum Doped Zinc Oxide Nanoplatelets Based Sensor with Enhanced Hydrogen Sulfide Detection	SCIENTIFIC REPORTS	3.9	Q1	4	2025	15	8633	http://dx.doi.org/10.1038/s41598-025-93252-6	Green submitted Gold
80.	Abudeif, AM; Hamimi, Z; Gaber, GM; Kotb, A; Alarifi, N; Bellucci, S; Masoud, MM	Modeling of Potential Field Data for Detecting Structural and Tectonic Framework of Esh El Mellaha Area, Red Sea, Egypt	SCIENTIFIC REPORTS	3.9	Q1	2	2025	15	20131	http://dx.doi.org/10.1038/s41598-025-04674-1	Green submitted Gold

No.	Authors	Article title	Journal	IF	Quartile	Cites WoS®	Year	Vol.	Pages/ Art. no.	DOI link	OA type
81.	Ungeheuer, K; Bocirnea, AE; Marszalek, KW; Tokarz, W; Pikulski, DA; Kakol, Z; Galca, AC	XPS Study and Electronic Structure of Non-doped and Cr^{+} ion Implanted CuO Thin Films	SCIENTIFIC REPORTS	3.9	Q1	4	2025	15	25255	http://dx.doi.org/10.1038/s41598-025-08421-4	Green submitted Gold
82.	Abudeif, AM; Alarifi, N; Abdalla, F; Bellucci, S; Tawfik, FA	Clay Impact on Reservoir Quality in the Nubia Formation of Saqqara Field, Gulf of Suez, Egypt	SCIENTIFIC REPORTS	3.9	Q1	1	2025	15	26911	http://dx.doi.org/10.1038/s41598-025-07801-0	Green submitted Gold
83.	Neto, AS; Gaddam, A; Stan, GE; Ferreira, JMF	Multifunctional Cuttlefish Bone-derived Scaffolds: Smart Biomimetic Solutions for Bone Tissue Repair and Regeneration	JOURNAL OF THE AMERICAN CERAMIC SOCIETY	3.8	Q1	2	2025	108	e70044	http://dx.doi.org/10.1111/jace.70044	
84.	Popescu, B; Bartha, C; Enculescu, M; Tolea, F; Grigoroscuta, MA; Tolea, M; Badica, P; Sofronie, M	Martensitic Transformation Dynamics and Mechanical Properties Investigation in Spark Plasma Sintered Ni-Mn-Ga Shape Memory Alloys	SMART MATERIALS AND STRUCTURES	3.8	Q1	0	2025	34	55012	http://dx.doi.org/10.1088/1361-665X/add19d	Hybrid
85.	Gahramanli, L; Muradov, M; Baghirov, M; Eyvazova, G; Bellucci, S; Gomez, CV; Tene, T; Khankishiyeva, R	Synthesis, Characterization, and Photocatalytic Performance of 2D/1D Graphene/Ag-Ag_2S Hybrid Nanocomposites	DALTON TRANSACTIONS	3.3	Q1	1	2025	54	15118–15133	http://dx.doi.org/10.1039/d5dt01999k	
86.	Poleshchuk, K; Terentyev, D; Galatanu, A; Verbeken, K	Investigation of Neutron Irradiated W/CuCrZr Joints	JOURNAL OF NUCLEAR MATERIALS	3.2	Q1	4	2025	604	155496	http://dx.doi.org/10.1016/j.jnucmat.2024.155496	
87.	Predoana, L; Pandele-Cusu, J; Atkinson, I; Petrescu, S; Mocioiu, OC; Culiba, DC; Karajz, DA; Odhiambo, VO; Lemago, HH; Gomes, APB; Varady, ZI; Bohus, M; Costescu, RM; Szilágyi, IM; Pokol, G; Zaharescu, M	Comparative Study of the Cu-TiO_2 Nanostructures Obtained by Sol-Gel and Microwave Assisted Sol-Gel Methods	JOURNAL OF SOL-GEL SCIENCE AND TECHNOLOGY	3.2	Q1	0	2025	114	965–982	http://dx.doi.org/10.1007/s10971-025-06757-x	
88.	Breazu, C; Stanculescu, A; Socol, M; Rasoga, O; Preda, N; Costas, A; Stan, GE; Popescu, DG; Petre, G; Iftimie, S; Tite, T	DNA-RNA Nucleobase-coated ZnO Nanostructures for Interface Engineering in Organic Optoelectronics	ACS APPLIED NANO MATERIALS	5.5	Q2	0	2025	8	16307–16320	http://dx.doi.org/10.1021/acsanm.5c02516	
89.	Pantis-Simut, CA; Cosinschi, M; Allosh, A; Filipoiu, N; Preda, AT; Necula, G; Visan, C; Ghitiu, I; Nemnes, GA	Multiscale Modeling of Phosphorene-Based Sensing Devices for Volatile Organic Compounds	ACS APPLIED NANO MATERIALS	5.5	Q2	0	2025	8	16792–16801	http://dx.doi.org/10.1021/acsanm.5c02935	
90.	de Medeiros, SASL; de Oliveira, ALM; Duarte, TM; Kennedy, BJ; Rostas, AM; Negrila, CC; Galca, AC;	α-MoO_3 Micro- and Nanoparticles as Catalysts for Biofuel Production	ACS APPLIED NANO MATERIALS	5.5	Q2	11	2025	8	4339–4353	http://dx.doi.org/10.1021/acsanm.4c01239	Green submitted Hybrid

No.	Authors	Article title	Journal	IF	Quartile	Cites WoS®	Year	Vol.	Pages/ Art. no.	DOI link	OA type
	Maia, AD; Sambrano, JR; Dantas, MC; Farias, AF; dos Santos, IMG										
91.	Mirea, AG; Vlaicu, ID; Derbali, S; Neatu, F; Tomulescu, AG; Besleaga, C; Enculescu, M; Kuncser, AC; Iacoban, AC; Filipoiu, N; Cuzminschi, M; Nemnes, GA; Manolescu, A; Florea, M; Pintilie, I	Electron Transporting Bilayers for Perovskite Solar Cells: Spray Coating Deposition of c-TiO_2/m-SnO_2-Quantum Dots	COLLOIDS AND SURFACES A-PHYSICOCHEMICAL AND ENGINEERING ASPECTS	5.4	Q2	4	2025	705	135508	http://dx.doi.org/10.1016/j.colsurfa.2024.135508	
92.	Voicu, SN; Marinas, IC; Stoian, M; Kuncser, A; Neatu, F; Florea, M; Tudose, M; Gaboreanu, MD; Chifiriuc, MC	Bioinspired Gold-Titanium Dioxide Nanoparticles for Infection Control and Wound Healing Enhancement	COLLOIDS AND SURFACES A-PHYSICOCHEMICAL AND ENGINEERING ASPECTS	5.4	Q2	0	2025	725	137632	http://dx.doi.org/10.1016/j.colsurfa.2025.137632	Hybrid
93.	Boukhoubza, I; Achehboune, M; El Khouja, O; Basyooni-M Kabates, MA; Mindroc, M; Derkaoui, I; Enculescu, M; Matei, E	Enhanced Photocatalytic Performance of V_2O_5 NRs/RGO Nanocomposites for Rhodamine-B Decolorization Under Solar Irradiation: Experimental and Theoretical Study	JOURNAL OF PHYSICS AND CHEMISTRY OF SOLIDS	4.9	Q2	5	2025	201	112654	http://dx.doi.org/10.1016/j.jpcs.2025.112654	
94.	Comanescu, C	Ensuring Safety and Reliability: An Overview of Lithium-Ion Battery Service Assessment	BATTERIES-BASEL	4.8	Q2	15	2025	11	6	http://dx.doi.org/10.3390/batteries11010006	Green submitted Gold
95.	Burlanescu, T; Smaranda, I; Androne, A; Florica, CS; Cercel, M; Paraschiv, M; Udrescu, A; Lorinczi, A; Palade, P; Galatanu, A; Negrila, C; Matei, E; Dinescu, M; Cercel, R; Baibarac, M	Composites Based on Poly(ortho-toluidine) and WS_2 Sheets for Applications in the Supercapacitor Field	BATTERIES-BASEL	4.8	Q2	1	2025	11	37	http://dx.doi.org/10.3390/batteries11010037	Green submitted Gold
96.	Barabash, AS; Belli, P; Bernabei, R; Boiko, RS; Cappella, F; Caracciolo, V; Cerulli, R; Danevich, FA; Fang, DL; Ferella, F; Incicchitti, A; Kobychev, VV; Konovalov, SI; Laubenstein, M; Leoncini, A; Merlo, V; Nisi, S; Nitescu, O; Poda, DV; Polischuk, OG; Shcherbakov, IBK; Simkovic, F; Timonina, A; Tinkova, VS; Tretyak, VI; Umatov, VI	Double-beta decay of 150Nd to excited levels of 150Sm	EUROPEAN PHYSICAL JOURNAL C	4.8	Q2	3	2025	85	174	http://dx.doi.org/10.1140/epjc/s10052-025-13901-y	Green submitted Gold

No.	Authors	Article title	Journal	IF	Quartile	Cites WoS®	Year	Vol.	Pages/ Art. no.	DOI link	OA type
97.	Quaratesi, I; Calinescu, I; Chipurici, P; Dumbrava, EG; Cucos, A; Zaki, MY; La Manna, P; Bercea, A; Stan, MS; Michalik, S; Pearce, C; Odlyha, M; Burca, G; Badea, E	Ultrasound-assisted Synthesis of 3-Cyclodextrin/Hydroxyapatite Composites as a Green and Safe Additive for Enhancing Leather Properties	JOURNAL OF MOLECULAR STRUCTURE	4.7	Q2	5	2025	1328	141299	http://dx.doi.org/10.1016/j.molstruc.2024.141299	Green submitted Hybrid
98.	Borcan, LE; Iancu, AC; Apostol, NG; Nicolaev, A; Teodorescu, CM	Surface Spin Asymmetry of O 2p and Ba 5p States in $BaTiO_3$(001)	MATERIALS ADVANCES	4.7	Q2	0	2025	6		http://dx.doi.org/10.1039/d5ma00363f	Gold
99.	Secu, CE; Bartha, C; Secu, M	Unravelling the Crystallization Mechanism and Structural Evolution of Yb/Er-doped SiO_2-GdF_3 Nano-glass Ceramics	MATERIALS ADVANCES	4.7	Q2	1	2025	6	5877–5883	http://dx.doi.org/10.1039/d5ma00377f	Gold
100.	Aleinawi, MH; Saritas, E; Stefan, M; Ammar, AU; Hroub, A; Misirlioglu, FB; Bocirnea, A; Macavei, S; Tripon, S; Erdem, E; Mihai, RA	Supercapacitor Devices Based on Multiphase $MgTiO_3$ Perovskites Doped with Mn^{2+} Ions	MATERIALS CHEMISTRY AND PHYSICS	4.7	Q2	7	2025	329	130016	http://dx.doi.org/10.1016/j.matchemphys.2024.130016	Hybrid
101.	Radu, I; Borhan, AI; Gherca, D; Dirtu, AC; Dirtu, D; Popescu, DG; Husanu, MA; Pui, A	Cobalt Oxyhydroxide Co-catalyst Loaded onto Al:$SrTiO_3$ Surface to Boost Photocatalytic Performance	MATERIALS CHEMISTRY AND PHYSICS	4.7	Q2	4	2025	332	130274	http://dx.doi.org/10.1016/j.matchemphys.2024.130274	Hybrid
102.	Rostas, AM; Suciu, RC; Rosu, MC; Turza, A; Cosma, DV; Tripon, S; Fort, CI; Danciu, V; Baia, M; Bocirnea, A; Indrea, E	Annealing Temperature, A Key Factor in Shaping Ag-decorated TiO_2 Aerogels as Efficient Visible-light Photocatalysts	MATERIALS CHEMISTRY AND PHYSICS	4.7	Q2	4	2025	337	130557	http://dx.doi.org/10.1016/j.matchemphys.2025.130557	Hybrid
103.	Stavarache, I; Palade, C; Slav, A; Dascalescu, I; Lepadatu, AM; Matei, E; Besleaga, C; Ciurea, ML; Kardynal, BE; Stoica, T	Effect of Molecular Adsorption on the Conductivity of Selectively Grown, Interconnected 2D-MoS_2 Atomically Thin Flake Structures	NANOSCALE ADVANCES	4.7	Q2	1	2025	7	2368–2380	http://dx.doi.org/10.1039/d5na00138b	Green submitted Gold
104.	Scurtu, A; Dumitru, M; Garoi, P; Banici, AM; Radu, C; Ticos, D; Udrea, N; Mitu, ML; Ticos, CM	Enhancement of Luminescence of ZnS:Ag Treated in Low Power Radio Frequency Argon Plasma and Excited with an Electron Beam at 13 keV	MATERIALS SCIENCE IN SEMICONDUCTOR PROCESSING	4.6	Q2	3	2025	188	109259	http://dx.doi.org/10.1016/j.mssp.2024.109259	Hybrid
105.	Negrila, CC; Cotirlan, C; Iancu, AC; Popescu, DG; Palade, C; Trupina, L	Investigations on HfO_2/n-GaAs(110) Interface, In-situ Obtained by Oxide-MBE	MATERIALS SCIENCE IN SEMICONDUCTOR PROCESSING	4.6	Q2	1	2025	198	109746	http://dx.doi.org/10.1016/j.mssp.2025.109746	
106.	Iacob, N; Palade, P; Comanescu, C; Crisan, O; Toderascu, LI; Socol, G; Schinteie, G; Kuncser, V	Comprehensive Methodology for Evaluating the Drug Loading of Iron Oxide Nanoparticles	MOLECULES	4.6	Q2	1	2025	30	676	http://dx.doi.org/10.3390/m	Green submitted Gold

No.	Authors	Article title	Journal	IF	Quartile	Cites WoS®	Year	Vol.	Pages/ Art. no.	DOI link	OA type
		Using Combined Magnetometry and Mössbauer Spectroscopy								olecules30030676	
107.	Belciu, MI; Velea, A	Ensemble Machine Learning for the Prediction and Understanding of the Refractive Index in Chalcogenide Glasses	MOLECULES	4.6	Q2	0	2025	30	1745	http://dx.doi.org/10.3390/molecules30081745	Green submitted Gold
108.	Pavel, M; Cretu, L; Negrila, C; Culita, DC; Vasile, A; State, R; Balint, I; Papa, F	Mono-(Ni, Au) and Bimetallic (Ni-Au) Nanoparticles-Loaded ZnAlO Mixed Oxides as Sunlight-Driven Photocatalysts for Environmental Remediation	MOLECULES	4.6	Q2	0	2025	30	3249	http://dx.doi.org/10.3390/molecules30153249	Green submitted Gold
109.	Gulahmadov, O; Gahramanli, L; Muradov, M; Musayeva, N; Bellucci, S; Todorova, N; Trapalis, C	Porous Polysiloxane MWCNT Nanocomposites for High-performance and Scalable Triboelectric Nanogenerators	RSC ADVANCES	4.6	Q2	4	2025	15	31917–31930	http://dx.doi.org/10.1039/d5ra05894e	Green submitted Gold
110.	Aslan, ST; Arabaci, ED; Karakurt, O; Cevher, D; Yilmaz, EA; Yalvac, D; Yildiz, DE; Cirpan, A	Impact of Different Aromatic Side Units on Benzodithiophene on the Optical, Electronic, and Photovoltaic Properties for Organic Solar Cell Applications	SYNTHETIC METALS	4.6	Q2	0	2025	313	117890	http://dx.doi.org/10.1016/j.synthmet.2025.117890	
111.	Burlanescu, T; Cercel, M; Smaranda, I; Androne, A; Zgura, I; Ganea, CP; Negrila, C; Lorinczi, A; Bartha, C; Baibarac, M	Optical, Structural and Electrical Proprieties of Composites based on MoS_2, WS_2 and Poly(ortho-toluidine)	MATERIALS TODAY COMMUNICATIONS	4.5	Q2	4	2025	46	112469	http://dx.doi.org/10.1016/j.mtcomm.2025.112469	
112.	Boukhvalov, DW; Stefan, M; Joita, AC; Kuo, CN; Lue, CS; Politano, A	Charge Transfer-Driven Conversion of Molecular Oxygen to Doublet State on Vanadium Diselenide (VSe_2) Surface at Room Temperature	ADVANCED MATERIALS INTERFACES	4.4	Q2	0	2025	12	2400656	http://dx.doi.org/10.1002/admi.202400656	Green submitted Gold
113.	Das-Mohapatra, B; Rouzegar, R; Papaioannou, ET; Kampfrath, T; Schmidt, G	Controlling Charge Dynamics in Nanopatterned Spintronic Terahertz Emitters	PHYSICAL REVIEW APPLIED	4.4	Q2	1	2025	23	14024	http://dx.doi.org/10.1103/PhysRevApplied.23.014024	Green submitted
114.	Dinca, V; Mandes, A; Vladoiu, R; Tichy, M; Kudrna, P; Matei, E; Polosan, S	A Study of the Laser-aided TVA Plasma Applied for Deposition of Mg/Zn:Al Bilayers	RESULTS IN SURFACES AND INTERFACES	4.4	Q2	0	2025	21	100661	http://dx.doi.org/10.1016/j.rsurfi.2025.100661	Green submitted Gold
115.	Bika, P; Ioannidis, N; Tsipas, P; Papagiannis, S; Gatou, MA; Pavlatou, EA; Karydas, AG; Stergiopoulos, T; Dallas, P	Detection and Selective Sorption of Copper Ions by a COF-Modified Melamine Sponge	ACS OMEGA	4.3	Q2	2	2025	10	21755–21766	http://dx.doi.org/10.1021/acsomega.5c01393	Green submitted Gold

No.	Authors	Article title	Journal	IF	Quartile	Cites WoS®	Year	Vol.	Pages/ Art. no.	DOI link	OA type
116.	Dobre, AF; Lete, C; Kuncser, VE; Iacob, N; Madalan, AM; Ionita, G; Harada, M; Kitagawa, Y; Ionita, P	Dimer of the DPPH Stable Radical	ACS OMEGA	4.3	Q2	1	2025	10	36662–36671	http://dx.doi.org/10.1021/acsomega.5c05905	Green submitted Gold
117.	Gulahmadov, O; Gahramanli, L; Muradov, M; Musayeva, N; Bellucci, S; Trapalis, C	Optimization of MWCNT Concentration in Polysiloxane-Based Nanocomposites for Enhanced Performance of the TENGs	ACS OMEGA	4.3	Q2	2	2025	10	50511–50520	http://dx.doi.org/10.1021/acsomega.5c08067	Green submitted Gold
118.	Borcan, LE; Teodorescu, CM; Iancu, AC; Apostol, NG; Nicolaev, A; Costescu, RM; Husanu, MA; Popescu, DG; Lungu, GA; Bianchi, M	Surface Spin Asymmetry in Pt(001)-hex Induced by Electron Accumulation	JOURNAL OF PHYSICS-MATERIALS	4.3	Q2	1	2025	8	35010	http://dx.doi.org/10.1088/2515-7639/aded36	Green submitted Gold
119.	Ciobanu, CS; Predoi, D; Iconaru, SL; Negrila, CC; Leduc, D; Ghegoiu, L; Bleotu, C; El Kettani, MEC; Trusca, R; Zelmar, P; Predoi, MV	New Nanobioceramics Based on Hydroxyapatite for Biomedical Applications: Stability and Properties	NANOMATERIALS	4.3	Q2	3	2025	15	224	http://dx.doi.org/10.3390/nano15030224	Green submitted Gold
120.	Mihai, C; Simandan, ID; Sava, F; Tite, T; Bocirnea, A; Vaduva, M; Zaki, MY; Baibarac, M; Velea, A	Fabrication of High-Quality MoS_2/Graphene Lateral Heterostructure Memristors	NANOMATERIALS	4.3	Q2	1	2025	15	1239	http://dx.doi.org/10.3390/nano15161239	Green submitted Gold
121.	Locovei, C; Torosyan, G; Papaioannou, ET; Crisan, AD; Beigang, R; Crisan, O	Structural, Magnetic and THz Emission Properties of Ultrathin Fe/L10-FePt/Pt Heterostructures	NANOMATERIALS	4.3	Q2	1	2025	15	1099	http://dx.doi.org/10.3390/nano15141099	Green submitted Gold
122.	Tene, T; Gahramanli, L; Muradov, M; Baghirov, M; Eyvazova, G; Bellucci, S; Tixi, JAM; Gomez, CV; Khankishiyeva, R; Caputi, LS; Straface, S	Graphene/Ag-Ag_2S Based Hybrid Nanostructure for Methylene Blue Degradation	FRONTIERS IN CHEMISTRY	4.2	Q2	0	2025	13	1695385	http://dx.doi.org/10.3389/fchem.2025.1695385	Green submitted Gold
123.	Tamin, M; El Khouja, O; Guemmaz, M; Tamin, C; Bocirnea, AE; Asshsahi, I; Chaumont, D; Galca, AC	Towards a Wide Bandgap Absorber: Structural, Morphological, and Optical Investigation of Ag-alloyed Cu_2ZnSnS_4 Thin Films	SUSTAINABLE ENERGY & FUELS	4.1	Q2	0	2025	9	6751–6760	http://dx.doi.org/10.1039/d5se01303h	Hybrid
124.	Petcuta, OA; Guzo, NC; Bordeiasu, M; Nicolaev, A; Parvulescu, VI; Coman, SM	Ru/Beta Zeolite Catalysts for Levulinic Acid Hydrogenation: The Importance of Catalyst Synthesis Methodology	CATALYSTS	4.0	Q2	5	2025	15	80	http://dx.doi.org/10.3390/catal15010080	Gold
125.	Ivan, SB; Popescu, I; Negrila, C; Papa, F; Loridant, S; Marcu, IC	Effect of Modifying NiNbO Catalyst with Tetravalent (Sn, Ti) and Pentavalent (Sb, Ta) Cations on Its Ethane Oxidative Dehydrogenation Performance	INDUSTRIAL & ENGINEERING CHEMISTRY RESEARCH	3.9	Q2	0	2025	64	18692–18712	http://dx.doi.org/10.1021/acs.iecr.5c01954	Green submitted

No.	Authors	Article title	Journal	IF	Quartile	Cites WoS®	Year	Vol.	Pages/ Art. no.	DOI link	OA type
126.	Predoi, D; Ciobanu, CS; Iconaru, SL; Rokosz, K; Raaen, S; Predoi, SA; Talu, S; Motelica-Heino, M	Comprehensive Physicochemical and Biological Analysis of Hydroxyapatite/Dextran Powders before and after Immersion in Kokubo Solution	LANGMUIR	3.9	Q2	0	2025	41	17011–17034	http://dx.doi.org/10.1021/acs.langmuir.5c01585	
127.	Socol, M; Preda, N; Costas, A; Stanculescu, A; Rasoga, O; Stavarache, I; Petre, G; Popescu-Pelin, G; Toderascu, I; Breazu, C; Socol, G	Reduced Graphene Oxide-based Multilayer Transparent Conductive Electrodes	VACUUM	3.9	Q2	7	2025	233	113943	http://dx.doi.org/10.1016/j.vacuum.2024.113943	Hybrid
128.	Oprea, D; Crisan, D; Enache, A	Polyphenolic Extracts from Green Vegetables as Promoters of Fibroblast Viability and Reducers of Oxidative Stress	FOOD SCIENCE & NUTRITION	3.8	Q2	1	2025	13	e70230	http://dx.doi.org/10.1002/fsn3.70230	Green submitted Hybrid
129.	Tene, T; Bellucci, S; Guevara, M; Romero, P; Pérez, HSM; Gahramanli, L; Khankishiyeva, R; Sakher, E; Gomez, CV	Tuning Urine Glucose Sensing via Metal Films in Graphene-oxide-based SPR Architectures	FRONTIERS IN NANOTECHNOLOGY	3.8	Q2	0	2025	7	1702438	http://dx.doi.org/10.3389/fnano.2025.1702438	Green submitted Gold
130.	Socol, M; Preda, N; Costas, A; Petre, G; Stochioiu, A; Popescu-Pelin, G; Iftimie, S; Catargiu, AM; Socol, G; Stanculescu, A	Composite Films Based on Poly(3-hexylthiophene):Perylene Diimide Derivative:Copper Sulfide Nanoparticles Deposited by Matrix Assisted Pulsed Laser Evaporation on Flexible Substrates for Photovoltaic Applications	JOURNAL OF COMPOSITES SCIENCE	3.7	Q2	1	2025	9	172	http://dx.doi.org/10.3390/jcs9040172	Gold
131.	Ostahie, B; Aldea, A	Antichiral Edge States in Diatomic Square Lattice and Quantum Transport Properties	PHYSICAL REVIEW B	3.7	Q2	0	2025	112	85416	http://dx.doi.org/10.1103/3hc5-z3wt	
132.	Gudmundsson, V; Mughnetsyan, V; Goan, HS; Chai, JD; Abdullah, NR; Tang, CS; Moldoveanu, V; Manolescu, A	Spin Configuration of an Array of Quantum Rings Controlled by Cavity Photons	PHYSICAL REVIEW B	3.7	Q2	1	2025	111	115304	http://dx.doi.org/10.1103/PhysRevB.111.115304	
133.	Pena, A; Radu, C; Ostahie, B	Second-order Floquet Topological Phases and Corner States Based on Spatial Symmetries in Honeycomb Lattices in the Presence of Spin-orbit Coupling	PHYSICAL REVIEW B	3.7	Q2	0	2025	111	155128	http://dx.doi.org/10.1103/PhysRevB.111.155128	

No.	Authors	Article title	Journal	IF	Quartile	Cites WoS®	Year	Vol.	Pages/ Art. no.	DOI link	OA type
134.	Das-Mohapatra, B; Kanistras, N; Busse, A; Papaioannou, ET; Schmidt, G	On Chip Digital-to-Analog Converters for Ultrafast Signals using Spintronic Terahertz Emitters	APPLIED PHYSICS LETTERS	3.6	Q2	0	2025	127	204103	http://dx.doi.org/10.1063/5.0291032	Hybrid
135.	Nitescu, O; Simkovic, F	Radiative and Exchange Corrections for Two-neutrino Double-β Decay	PHYSICAL REVIEW C	3.4	Q2	1	2025	111	5501	http://dx.doi.org/10.1103/PhysRevC.111.035501	
136.	Kauppinen, E; Suhonen, J	Isoscalar and Isovector Multipole L=0 to 3 Strength Dunctions in Even-Even 90-94Zr and 92-100Mo Nuclei	PHYSICAL REVIEW C	3.4	Q2	0	2025	111	14309	http://dx.doi.org/10.1103/PhysRevC.111.014309	Green submitted
137.	Nitescu, O; Simkovic, F	Semi-empirical Formula for Two-neutrino Double-β Decay	PHYSICAL REVIEW C	3.4	Q2	1	2025	111	24307	http://dx.doi.org/10.1103/PhysRevC.111.024307	
138.	Kasurinen, J; Hellgren, M; Pirinen, P; Suhonen, J	Shell-model Description of Spin-dependent Elastic and Inelastic WIMP Scattering Off ^{203}Tl and ^{205}Tl	PHYSICAL REVIEW C	3.4	Q2	1	2025	112	14616	http://dx.doi.org/10.1103/59hn-5bsr	Green submitted
139.	Kauppinen, E; Kotila, J	Leading-order Short-range Nuclear Matrix Elements in Double-β Decay Using the Microscopic Interacting Boson Model	PHYSICAL REVIEW C	3.4	Q2	0	2025	112	34329	http://dx.doi.org/10.1103/6v3v-5fww	
140.	Ge, Z; Eronen, T; Sevestrean, VA; Ramalho, M; Nitescu, O; Ghinescu, S; Stoica, S; Suhonen, J; de Roubin, A; Nesterenko, D; Kankainen, A; Ascher, P; Andres, SAS; Beliuskina, O; Delahaye, P; Flayol, M; Gerbaux, M; Grevy, S; Hukkanen, M; Jaries, A; Jokinen, A; Husson, A; Kahl, D; Kostensalo, J; Kotila, J; Moore, I; Nikas, S; Ruotsalainen, J; Stryjczyk, M; Virtanen, V	High-precision Direct Decay Energy Measurements of the Electron-capture Decay of 97Tc	PHYSICAL REVIEW C	3.4	Q2	0	2025	112	35501	http://dx.doi.org/10.1103/g393-xx1w	
141.	Belli, P; Bernabei, R; Cappella, F; Caracciolo, V; Cerulli, R; Danevich, FA; Ferella, F; Incicchitti, A; Kasperovych, DV; Klavdiienko, VR; Kobychev, VV; Laubenstein, M; Leoncini, A; Nisi, S; Poda, DV;	Spectroscopy of 1^{13m}Cd	PHYSICAL REVIEW C	3.4	Q2	0	2025	112	45503	http://dx.doi.org/10.1103/yzlp-wcyf	

No.	Authors	Article title	Journal	IF	Quartile	Cites WoS®	Year	Vol.	Pages/ Art. no.	DOI link	OA type
	Polischuk, OG; Ramalho, M; Suhonen, J; Tretyak, VI										
142.	Badica, P; Grigoroscuta, MA; Kuncser, AC; Vasylkiv, O	High-Entropy Ti, Zr, Hf, Ta Multiphase Diboride with Deformation Resistance up to 2000 °C	ADVANCED ENGINEERING MATERIALS	3.3	Q2	1	2025	27	2402723	http://dx.doi.org/10.1002/adem.202402723	Hybrid
143.	Güner, SB; Badica, P; Miryala, M	Magnetic Levitation Performance of Superconducting Silver-Added MgB_2 Bulks Obtained by In Situ Spark Plasma Sintering	ADVANCED ENGINEERING MATERIALS	3.3	Q2	0	2025	27	2501616	http://dx.doi.org/10.1002/adem.202501616	
144.	Silva, A; Aleinawi, MH; Erdem, E; Kennedy, BJ; Galca, AC; dos Santos, IMG; Rostas, AM; de Oliveira, ALM	High-Performance and Ultrafast Symmetric Supercapacitors Based on Cu(II)-Doped $SrSnO_3$ Perovskites	JOURNAL OF PHYSICAL CHEMISTRY C	3.2	Q3	2	2025	129	15179–15195	http://dx.doi.org/10.1021/acs.jpcc.5c03126	Hybrid
145.	Hrib, LM; Trupina, L; Botea, MI; Chirila, CF; Boni, AG; Istrate, MC; Pintilie, L	Electrical Properties of Epitaxial PZT-LSMO Mmagnetoelectric Heterostructures: The Effect of the Interface with the Electrodes	JOURNAL OF PHYSICS D-APPLIED PHYSICS	3.2	Q2	0	2025	58	235304	http://dx.doi.org/10.1088/1361-6463/add542	
146.	Pereira, A; Martins, R; Monteiro, B; Correia, JB; Galatanu, A; Catarino, N; Belec, PJ; Dias, M	Thermal Stability and Irradiation Resistance of (CrFeTiTa)70W30 and VFeTiTaW High Entropy Alloys	MATERIALS	3.2	Q2	0	2025	18	1030	http://dx.doi.org/10.3390/ma18051030	Green submitted Gold
147.	Buruiana, AT; Mihai, C; Kuncser, V; Velea, A	Advances in 2D Group IV Monochalcogenides: Synthesis, Properties, and Applications	MATERIALS	3.2	Q2	4	2025	18	1530	http://dx.doi.org/10.3390/ma18071530	Green submitted Gold
148.	Caramitu, AR; Popescu, I; Grigoroscuta, M; Kuncser, A; Ganea, PC; Galatanu, A; Galatanu, M; Aldica, G; Badica, P; Burdusel, M; Bors, AM	Advanced Epoxy Resin/Boron Nitride Composites for High-Performance Electrotechnical Applications and Geological Instrumentation	MATERIALS	3.2	Q2	0	2025	18	4860	http://dx.doi.org/10.3390/ma18214860	Green submitted Gold
149.	Borcan, LE; Iancu, AC; Popescu, DG; Teodorescu, CM	Considerable Spin Asymmetry of Deep Valence States Induced by Partial Neutralization of Charged $SrTiO_3$(011) Surfaces	JOURNAL OF CHEMICAL PHYSICS	3.1	Q2	2	2025	162	54707	http://dx.doi.org/10.1063/5.0243885	Hybrid
150.	Aldica, G; Batalu, D; Nakamura, T; Ferbinteanu, M; Locovei, C; Vlaicu, MA; Pasuk, I; Badica, P	Structural and Thermal Analysis of the Linear Polygermoxane GeSP	JOURNAL OF THERMAL ANALYSIS AND CALORIMETRY	3.1	Q2	1	2025	150	2237–2247	http://dx.doi.org/10.1007/s10973-024-13962-3	
151.	Hattab, M; Oprea, OC; Cernea, M	Experimental Study on Thermal Evolution from Precursor Gel to Crystallized MgO for Biomedical Applications	JOURNAL OF THERMAL ANALYSIS AND CALORIMETRY	3.1	Q2	0	2025	150	3225–3236	http://dx.doi.org/10.1007/s10973-024-13951-6	

No.	Authors	Article title	Journal	IF	Quartile	Cites WoS®	Year	Vol.	Pages/ Art. no.	DOI link	OA type
152.	Tanska, J; Grigoroscuta, MA; Wiecinski, P; Ostrowski, A; Vasylkiv, O; Suzuki, TS; Wiecinska, P	Thermal Analysis of the Components Used in the Dabrication of Al_2O_3-Ni and Al_2O_3-Mo Composites via VAT Photopolymerization Followed by Spark Plasma Sintering	JOURNAL OF THERMAL ANALYSIS AND CALORIMETRY	3.1	Q2	0	2025	150	14811–14823	http://dx.doi.org/10.1007/s10973-025-14596-9	Green published Hybrid
153.	Avram, D; Patrascu, AA; Ghitu, I; Istrate, MC; Tiseanu, C	Energy Transfer in Tm, Gd, Eu Triple-doped $LiYbF_4$ Nanoparticles Enables Simplified Synthesis Design	OPTICAL MATERIALS EXPRESS	3.1	Q2	0	2025	15	2932–2947	http://dx.doi.org/10.1364/OME.567391	Gold
154.	Secu, C; Radu, C; Rostas, A; Secu, M	Structural, Up-Conversion Luminescence, and Electron Paramagnetic Resonance Investigations of Yb^{3+}/Er^{3+}-Doped $LiGdF_4$ Nanocrystals Dispersed in Silica Glassy Matrix	INORGANICS	3.0	Q2	0	2025	13	378	http://dx.doi.org/10.3390/inorganics13110378	Green submitted Gold
155.	Handor, S; Tomulescu, AG; Stancu, V; Razouk, A; Galca, AC; Leonat, LN	Gas-Assisted Spray Fabrication of Reticulated TiO_2 Scaffolds for Perovskite Solar Applications	MICROMACHINES	3.0	Q2	1	2025	16	685	http://dx.doi.org/10.3390/mi16060685	Green submitted Gold
156.	Anastasescu, M; Socoteanu, R; Bratan, V; Preda, S; Anastasescu, C; Gîfu, IC; Nistor, CL; Boscencu, R; Chifor, E; Negrila, C; Bordeianu, I; Zaharescu, M; Balint, I	Assessment of SiO_2 Nanotube Activity to Modify DL α-Tocopherol *via* 1O2 Generation Under Visible Light Irradiation	MICROMACHINES	3.0	Q2	0	2025	16	784	http://dx.doi.org/10.3390/mi16070784	Green submitted Gold
157.	Popescu, T	On the Motion of Classical and Quantum Complex Scalar Waves in Non-homogeneous Media	EUROPEAN PHYSICAL JOURNAL PLUS	2.9	Q2	0	2025	140	759	http://dx.doi.org/10.1140/epjp/s13360-025-06699-x	Hybrid
158.	Bartha, C; Locovei, C; Alexandru-Dinu, A; Comanescu, C; Grigoroscuta, MA; Kuncser, A; Iacob, N; Galatanu, M; Leca, A; Badica, P; Kuncser, V	Cation Distribution and its Magnetic Implications in Gadolinium-Iron Garnets for an Enhanced Control of Compensation Temperature	PHYSICAL CHEMISTRY CHEMICAL PHYSICS	2.9	Q2	0	2025	27	22894–22900	http://dx.doi.org/10.1039/d5cp02696b	Hybrid
159.	Husanu, MA; Popescu, DG	From Classical Ferroelectricity to Emerging Low-Dimensional Phases	ADVANCED PHYSICS RESEARCH	2.8	Q2	0	2025	4	e00107	http://dx.doi.org/10.1002/apxr.202500107	Green submitted Gold
160.	Socol, M; Preda, N; Costas, A; Petre, G; Stanculescu, A; Stavarache, I; Popescu-Pelin, G; Iftimie, S; Stochioiu, A; Catargiu, AM; Socol, G	Influence of Flexible Substrate Nature Covered with ITO on the Characteristics of Organic Heterostructures Fabricated by Laser Deposition Techniques	APPLIED PHYSICS A-MATERIALS SCIENCE & PROCESSING	2.8	Q2	3	2025	131	17	http://dx.doi.org/10.1007/s00339-024-08149-4	Hybrid

No.	Authors	Article title	Journal	IF	Quartile	Cites WoS®	Year	Vol.	Pages/ Art. no.	DOI link	OA type
161.	Ciobotaru, CC; Ciobotaru, IC; Nitescu, A; Polosan, S	Engineering of Thin Metallic Electrodes on OLED Performance	APPLIED PHYSICS A-MATERIALS SCIENCE & PROCESSING	2.8	Q2	0	2025	131	912	http://dx.doi.org/10.1007/s00339-025-09074-w	
162.	El Kanouny, A; Elotmani, R; El Manouni, A; El Khouja, O; Assahsahi, I; Almaggoussi, A; Galca, AC	Electrodeposition of SnSe Nanosheets: Effect of Deposition Potential on Structural, Morphological, and Optical Properties	APPLIED PHYSICS A-MATERIALS SCIENCE & PROCESSING	2.8	Q2	0	2025	131	979	http://dx.doi.org/10.1007/s00339-025-09116-3	
163.	Bleotu, C; Iconaru, SL; Ciobanu, CS; Groza, A; Predoi, D	Exploring the Effects of Dulbecco's Modified Eagle's Medium on Irradiated Layers of Magnesium-Doped Hydroxyapatite in a Chitosan Matrix for Biomedical Applications	COATINGS	2.8	Q2	3	2025	15	209	http://dx.doi.org/10.3390/coatings15020209	Gold
164.	Ciobanu, CS; Predoi, D; Iconaru, SL; Rokosz, K; Raaen, S; Negrila, CC; Ghegoiu, L; Bleotu, C; Predoi, MV	Chrome Doped Hydroxyapatite Enriched with Amoxicillin Layers for Biomedical Applications	COATINGS	2.8	Q2	7	2025	15	233	http://dx.doi.org/10.3390/coatings15020233	Gold
165.	Iacob, N	Pitfalls and Challenges in Specific Absorption Rate Evaluation for Functionalized and Coated Magnetic Nanoparticles Used in Magnetic Fluid Hyperthermia	COATINGS	2.8	Q2	4	2025	15	345	http://dx.doi.org/10.3390/coatings15030345	Gold
166.	Ghegoiu, L; Predoi, D; Iconaru, SL; Ciobanu, CS; Rokosz, K; Raaen, S; Badea, ML; Predoi, MV	Physicochemical and Preliminary Biological Properties of Thin Films Based on Fluoride-Doped Hydroxyapatite in a Dextran Matrix for Biomedical Applications	COATINGS	2.8	Q2	3	2025	15	565	http://dx.doi.org/10.3390/coatings15050565	Gold
167.	Ruotsalainen, J; Kauppinen, E; Eronen, T; Kankainen, A; Kotila, J; Mougeot, M	Probing the Double-Beta Decay of ^{104}Ru through Precise Q-value Measurements and Nuclear Matrix Element Calculations	EUROPEAN PHYSICAL JOURNAL A	2.8	Q2	3	2025	61	33	http://dx.doi.org/10.1140/epja/s10050-024-01481-6	Green submitted Hybrid
168.	Surender; Suhonen, J; Kumar, V	Comprehensive Shell Model Study of β-plus/EC-decay Properties for f5/2pg9/2 Space Nuclei	EUROPEAN PHYSICAL JOURNAL A	2.8	Q2	0	2025	61	265	http://dx.doi.org/10.1140/epja/s10050-025-01740-0	

No.	Authors	Article title	Journal	IF	Quartile	Cites WoS®	Year	Vol.	Pages/ Art. no.	DOI link	OA type
169.	Kauppinen, E; Ruotsalainen, J; Kumar, V; Suhonen, J; Kankainen, A; Eronen, T; Kotila, J; Mougeot, M	High-precision Q-value Measurement and Evaluation of Nuclear Matrix Elements for 122Sn and 124Sn Neutrinoless Double Beta Decays	EUROPEAN PHYSICAL JOURNAL A	2.8	Q2	0	2025	61	281	http://dx.doi.org/10.1140/epja/s10050-025-01744-w	Hybrid
170.	Velea, A; Simandan, ID; Mihai, C; Baibarac, M; Vaduva, M; Udrescu, A; Smaranda, I; Bocirnea, AE; Tite, T; Zaki, MY; Kuncser, A; Sava, F	Large-Scale Synthesis of Monolayer WS_2 by Low-temperature Sulfurization of Oxidized Magnetron Sputtered Monolayer W Precursors in a Microreactor	NANOTECHNOLOGY	2.8	Q2	0	2025	36	265601	http://dx.doi.org/10.1088/1361-6528/ade25f	Hybrid
171.	Pena, A; Ostahie, B; Radu, C	Floquet Topological Phase Transitions in 2D Su-Schrieffer-Heeger Model: Interplay Between Time Reversal Symmetry Breaking and Dimerization	NEW JOURNAL OF PHYSICS	2.8	Q2	3	2025	27	23010	http://dx.doi.org/10.1088/1367-2630/adac84	Green submitted Gold
172.	Prado, HSA; Cretu, N; Lörinczi, A; Badica, P; Bogomol, I	Magnetic Ordering Exploration by Study of the Magnetostriction	PHYSICA B-CONDENSED MATTER	2.8	Q2	1	2025	696	416659	http://dx.doi.org/10.1016/j.physb.2024.416659	
173.	Agnihotri, A; Kumar, V; Suhonen, J	Explosion Characteristics and Lethality Degree Evaluation from Improvised Explosive Device (IED) Detonation in Urban Area: Case of the Cylindrical Geometry	UNIVERSE	2.6	Q2	0	2025	11	138	http://dx.doi.org/10.3390/universe11050138	Green submitted Gold
174.	Ungeheuer, K; Rybak, J; Bocirnea, AE; Pikulski, DA; Galca, AC; Marszalek, KW	Influence of Proton Irradiation on Thin Films of AZO and ITO Transparent Conductive Oxides-Simulation of Space Environment	APPLIED SCIENCES-BASEL	2.5	Q2	5	2025	15	754	http://dx.doi.org/10.3390/app15020754	Green submitted Gold
175.	Ilie, A; Predoana, L; Anastasescu, C; Preda, S; Hosu, IS; Costescu, RM; Culita, DC; Bratan, V; Balint, I; Zaharescu, M	Layered Perovskite $La_2Ti_2O_7$ Obtained by Sol-Gel Method with Photocatalytic Activity	APPLIED SCIENCES-BASEL	2.5	Q2	0	2025	15	7665	http://dx.doi.org/10.3390/app15147665	Green submitted Gold
176.	Iacob, N; Kuncser, A; Stanciu, A; Palade, P; Schinteie, G; Leca, A; Ghicioi, E; Laszlo, R; Radermacher, L; Nicola, A; Kuncser, V	Explosion Characteristics and Lethality Degree Evaluation from Improvised Explosive Device (IED) Detonation in Urban Area: Case of the Cylindrical Geometry	APPLIED SCIENCES-BASEL	2.5	Q2	0	2025	15	11851	http://dx.doi.org/10.3390/app152211851	Green submitted Gold

No.	Authors	Article title	Journal	IF	Quartile	Cites WoS®	Year	Vol.	Pages/ Art. no.	DOI link	OA type
177.	Greculeasa, SG; Crisan, O	Rare-Earth-Free Exchange-Coupled Nanocomposites Based on M-Type Hexaferrites	MAGNETOCHEMISTRY	2.5	Q2	0	2025	11	99	http://dx.doi.org/10.3390/magnetochemistry11110099	Green submitted Gold
178.	Bertheaux, C; Grout, L; Ivan, IA; Borca, B; Dumont, F; Roux, JC; Fortunier, R	Emotional and Sensory Characterization of Thermoplastic Surfaces with Different Roughness	SURFACE TOPOGRAPHY-METROLOGY AND PROPERTIES	2.4	Q2	0	2025	13	25029	http://dx.doi.org/10.1088/2051-672X/ade5bc	Hybrid
179.	Gheorghe, DM; Mirea, AG; Chirica, IM; Madalan, AM; Popescu, CC; Matache, M; Ciuparu, DM; Florea, M	Synthesis and Investigation of Novel Nickel-based Metal Organic Frameworks	SYNTHESIS-STUTTGART	2.3	Q2	0	2025	57	3660–3668	http://dx.doi.org/10.1055/a-2720-5058	
180.	Giurgiu, D; Smaranda, I; Udrescu, A; Baibarac, M	Traceability of Diamonds Using UV-VIS-NIR Spectroscopy	MINERALS	2.2	Q2	0	2025	15	1091	http://dx.doi.org/10.3390/min15101091	Gold
181.	Ciupina, V; Vladoiu, R; Prodan, GC; Porosnicu, C; Lungu, C; Satulu, V; Mandes, A; Dinca, V; Andronescu, E; Vasile, B; Nicolescu, V; Polosan, S; Matei, E	N-doped C/Ti/C/Al/C/Si Multilayer and n-doped C+Ti/C+Al/C+Si Composite Thin Films: Synthesis and Characterization	ROMANIAN REPORTS IN PHYSICS	2.2	Q2	0	2025	77	503	http://dx.doi.org/10.59277/RomRepPhys.2025.77.503	
182.	De Luca, R; Cacciotti, E; Cerocchi, M; Crea, F; Roccella, S; Greuner, H; Hunger, K; Bonnekoh, C; Galatanu, A; Ivekovic, A; Jenus, P; Wirtz, M	Non-destructive Ultrasonic Inspections of Small-scale Mock-ups Provided with Advanced Tungsten Armours for DEMO Divertor Target	FUSION ENGINEERING AND DESIGN	2.0	Q2	0	2025	215	115007	http://dx.doi.org/10.1016/j.fusengdes.2025.115007	Hybrid
183.	Abudeif, AM; Mohammed, MA; Masoud, MM; Radwan, AE; Alarifi, N; Bellucci, S; Tawfik, FA	Influence of Shale on Petrophysical Properties and Reservoir Quality: Insights from the Matulla Formation, Saqqara Field, Gulf of Suez, Egypt	PURE AND APPLIED GEOPHYSICS	1.9	Q2	4	2025	182	2799–2820	http://dx.doi.org/10.1007/s00024-025-03711-4	Green submitted
184.	Suteu, T; Antohe, VA; Antohe, S; Stavarache, I; Balasin, MC; Socol, G; Socol, M; Rasoga, O; Iftimie, S	Induced Effects of Nano-Patterned Substrates on the Electrical and Photo-Electrical Properties of PTB7-Th:ICBA (1:1, wt.%) Bulk-Heterojunction Solar Cells	SURFACES	2.9	Q3	0	2025	8	30	http://dx.doi.org/10.3390/surfaces8020030	Green submitted Gold
185.	Mihai, MA; Preda, L; Negrila, C; Somacescu, S; Becherescu, ND; Velea, A; Zaki, MY; Spataru, N	Thermally Interpenetrated Co-Ni Mixed Oxide as Efficient Oxygen Evolution Electrodes	ELECTROCATALYSIS	2.8	Q3	1	2025	16	758–771	http://dx.doi.org/10.1007/s12678-025-00956-4	
186.	Gulahmadov, O; Gahramanli, L; Muradov, M; Musayeva, N; Bellucci, S; Trapalis, C	Controlled Dispersion of MWCNTs in Polysiloxane Nanocomposites for	JOURNAL OF POLYMER RESEARCH	2.8	Q3	0	2025	32	437	http://dx.doi.org/10.1007/s10965-025-04672-x	

No.	Authors	Article title	Journal	IF	Quartile	Cites WoS®	Year	Vol.	Pages/ Art. no.	DOI link	OA type
		Performance Enhancement in Triboelectric Nanogenerators									
187.	Gubbiotti, G; Barman, A; Ladak, S; Bran, C; Grundler, D; Huth, M; Plank, H; Schmidt, G; van Dijken, S; Streubel, R; Dobrovoloskiy, O; Scagnoli, V; Heyderman, L; Donnelly, C; Hellwig, O; Fallarino, L; Jungfleisch, MB; Farhan, A; Maccaferri, N; Vavassori, P; Fischer, P; Tomasello, R; Finocchio, G; Clérac, R; Sessoli, R; Makarov, D; Sheka, DD; Krawczyk, M; Gallardo, R; Landeros, P; d'Aquino, M; Hertel, R; Pirro, P; Ciubotaru, F; Becherer, M; Gartside, J; Ono, T; Bortolotti, P; Fernández-Pacheco, A	2025 Roadmap on 3D Nanomagnetism	JOURNAL OF PHYSICS-CONDENSED MATTER	2.6	Q3	35	2025	37	143502	http://dx.doi.org/10.1088/1361-648X/ad9655	Green submitted Green accepted Hybrid
188.	Nita, M; Tolea, M; Marinescu, DC	A General Algorithm for Determining the Conductivity Zeros in Large Molecular Nanostructures: Applications to Rectangular Graphene Sheets	JOURNAL OF PHYSICS-CONDENSED MATTER	2.6	Q3	0	2025	37	235301	http://dx.doi.org/10.1088/1361-648X/add77f	Green submitted Hybrid
189.	Bezzekhami, MA; Belkhir, NL; Zaoui, S; Harrane, A; Sid, ANE; Mostefai, A; Belalia, M; Bellucci, S	Boosting poly(ε-caprolactone) with Oleic Acid: A Green Catalyst-driven Approach for High-performance Antioxidant and Antibacterial Biodegradable Polymers	JOURNAL OF MACROMOLECULAR SCIENCE PART A-PURE AND APPLIED CHEMISTRY	2.4	Q3	1	2025	62	579–594	http://dx.doi.org/10.1080/10601325.2025.2518214	
190.	Mihalache, V	Fe-ZnO as an Oxide-dilute Magnetic Semiconductor in the Nanostructured ZnFeO Exchange Bias System	MATERIALS RESEARCH EXPRESS	2.2	Q3	0	2025	12	75003	http://dx.doi.org/10.1088/2053-1591/adee81	Green submitted Gold
191.	Diallo, A; Ndiaye, S; Tite, T; Yahsi, U; Diculescu, VC; Seck, A; Dioum, A; Ngom, BD; Ahmad, I; Galca, AC; Azizi, S	Bioengineered Y_2O_3 Nanorods and Their Potential Blue-emitting Phosphors	BULLETIN OF MATERIALS SCIENCE	2.1	Q3	0	2025	48	50	http://dx.doi.org/10.1007/s12034-025-03406-5	
192.	Sakher, E; Tahri, T; Bellucci, S; Bououdina, M	Unraveling Particle Folding in Nanostructured Shape Memory Alloy $Ni_{50}Ti_{50}$ Prepared by Mechanical Alloying	PHYSICA STATUS SOLIDI A-APPLICATIONS AND MATERIALS SCIENCE	1.9	Q3	0	2025	222	2500295	http://dx.doi.org/10.1002/pssa.202500295	Bronze

No.	Authors	Article title	Journal	IF	Quartile	Cites WoS®	Year	Vol.	Pages/ Art. no.	DOI link	OA type
193.	Sandu, V; Craciun, L; Ivan, I; Badea, AM; Chidthong, R; Mihai, F; Aldica, GV	Effect of Proton Energy on the Superconducting Properties of MgB2 Submitted to Proton Beams at a Constant Fluence	JOURNAL OF SUPERCONDUCTIVITY AND NOVEL MAGNETISM	1.7	Q3	0	2025	38	192	http://dx.doi.org/10.1007/s10948-025-07029-z	
194.	Burdusel, M; Aldica, GV; Pasuk, I; Grigoroscuta, MA; Kuncser, A; Badica, P	Trapped Magnetic Field of MgB_2 Machinable Disks with Different Additives	JOURNAL OF SUPERCONDUCTIVITY AND NOVEL MAGNETISM	1.7	Q3	0	2025	38	179	http://dx.doi.org/10.1007/s10948-025-07002-w	
195.	Laafar, S; Boumaaz, N; Elbacha, A; Lamuadni, B; Maali, A; Soulmani, A	Impact of the External Gate Resistance on the Power CoolMOS Transistor Transient Switching Dynamics	ANALOG INTEGRATED CIRCUITS AND SIGNAL PROCESSING	1.4	Q4	0	2025	125	9	http://dx.doi.org/10.1007/s10470-025-02487-w	Hybrid
196.	Cimpoiasu, E; Sandu, V; Rostem, K; Wollack, EJ; Brown, AD; Miller, KH; Mikula, V	Heat Capacity and Magnetic Properties of NbTiN Films in the Bulk Limit	PHYSICA C-SUPERCONDUCTIVITY AND ITS APPLICATIONS	1.0	Q4	0	2025	639	1354813	http://dx.doi.org/10.1016/j.physc.2025.1354813	
197.	Al-Azazi, NAS; Abudeif, AM; Mohammed, MA; Albaroot, MA; Alarifi, N; Bellucci, S; Basrada, FMQ; Masoud, MM	Application of Spectral Gamma-Ray Logs to Determine the Lithofacies and Depositional Environment of the Lam Member, Habban Oilfield, Sab'atayn Basin (Yemen)	RUSSIAN GEOLOGY AND GEOPHYSICS	1.0	Q4	0	2025	66	858–868	http://dx.doi.org/10.2113/RGG20254854	
198.	Gruyer, D; Baldesi, L; Barlini, S; Borderie, B; Bougault, R; Camaiani, A; Casini, G; Chbihi, A; Ciampi, C; Dueñas, JA; Fable, Q; Fabris, D; Frankland, JD; Frosin, C; Génard, T; Gramegna, F; Henri, M; Hong, B; Kim, S; Kordyasz, A; Kozik, T; Kweon, MJ; LE Neindre, N; Lombardo, I; Lopez, O; Marchi, T; Mazurek, K; Nam, SH; Park, J; Parlog, M; Pasquali, G; Piantelli, S; Poggi, G; Rebillard-Soulié, A; Stefanini, AA; Upadhyaya, S; Valdre, S; Verdé, G; Vient, E; Vigilante, M	Recent highlights from INDRA and FAZIA	NUOVO CIMENTO C-COLLOQUIA AND COMMUNICATIONS IN PHYSICS	0.4	Q4	0	2025	48	43	http://dx.doi.org/10.1393/ncc/i2025-25043-0	
199.	Ilie, A; Predoana, L; Anastasescu, C; Pandele-cusu, J; Preda, S; Rusu, A; Culita, DC; Bratan, V; Maraloiu, VA; Teodorescu, VS; Balint, I; Zaharescu, M	Photocatalytic Degradation of Ethanol Driven by Pristine and Metal-Modified TiO_2 Obtained by Sol-Gel Method	REVUE ROUMAINE DE CHIMIE	0.6	Q4	0	2025	70	385–394	http://dx.doi.org/10.33224/rrch.2025.70.7-8.02	Bronze

No.	Authors	Article title	Journal	IF	Quartile	Cites WoS®	Year	Vol.	Pages/ Art. no.	DOI link	OA type
200.	Alkali, M; Micutz, M; Ilis, M; Ganea, CP; Radulescu, M; Cîrcu, V	Dielectric and Rheological Characterization of Physical Gels Based on Liquid Crystals Mixture E7 and Thiourea Low Molecular Weight Gelators	UNIVERSITY POLITEHNICA OF BUCHAREST SCIENTIFIC BULLETIN-SERIES A-APPLIED MATHEMATICS AND PHYSICS	0.6	Q4	0	2025	87	175–190		
201.	Mekti, Z; Boutemedjet, A; Tahri, T; Benselhoub, A; Soliman, AM; Bellucci, S	Petrographic Characterization of the Uranium Ore of Tahaggart (El-Hoggar, Se Algeria)	VISNYK OF TARAS SHEVCHENKO NATIONAL UNIVERSITY OF KYIV-GEOLOGY	0.3	Q4	0	2025	2	64–72	http://dx.doi.org/10.17721/1728-2713.109.09	Hybrid
202.	Nicolae, SA	Current Trends in Synthesis and Characterization of Biomass-based Materials for CO_2 Capture	BIOMASS-SWITZERLAND	0.0	Q4	1	2025	5	70	http://dx.doi.org/10.3390/biomass5040070	Green submitted Gold
203.	Martins, R; Monteiro, B; Goncalves, AP; Correia, JB; Galatanu, A; Alves, E; Tejado, E; Pastor, JY; Dias, M	Influence of Cr on the Quaternary FeTaTiW Medium Entropy Alloy	JOURNAL OF MATERIALS SCIENCE-MATERIALS IN ENGINEERING	0.0	Q4	0	2025	20	52	http://dx.doi.org/10.1186/s40712-025-00256-1	Green submitted Gold
204.	Gulahmadov, O; Gahramanli, L; Muradov, M; Gilev, JB; Bellucci, S; Gomez, CV	Optimization of MWCNT Concentration in Nylon-based Nanocomposites for Enhanced Triboelectric Nanogenerator Performance	JOURNAL OF MATERIALS SCIENCE-MATERIALS IN ENGINEERING	0.0	Q4	5	2025	20	101	http://dx.doi.org/10.1186/s40712-025-00317-5	Green submitted Gold
205.	Tene, T; Gulahmadov, O; Gahramanli, L; Muradov, M; Gilev, JB; Hamzayeva, T; Bayramova, S; Bellucci, S; Gomez, CV	Influence of MWCNT Concentration on Performance of Nylon/MWCNT Nanocomposite-Based Triboelectric Nanogenerators Fabricated *via* Spin Coating Method	NANOENERGY ADVANCES	0.0	Q4	6	2025	5	9	http://dx.doi.org/10.3390/nanoenergyadv5030009	Green submitted Gold
			IF cumulat ≈	**890**							
			IF mediu ≈	**4.7**							

Highlighted Publications and Featured Covers

Readers respond

Correspondence

International treaties cannot be reformed through rational design

Your Comment article asserts rightly that the collapse of negotiations for the United Nations plastics treaty reflects broader systemic problems affecting international environmental law and governance (R. E. Kim and P. Bridgewater *Nature* **646**, 1054–1056; 2025). But in our view, the authors' suggested solution — a global scientific body that would assess and issue binding recommendations for environmental bodies and treaties — is wrong-headed.

Questions such as how to reduce plastic waste globally or, more broadly, how to overcome institutional paralysis, cannot be resolved by data or rationality alone. It is crucial to acknowledge that morals and politics are central to finding solutions.

What's more, this proposal seems impervious to the realities of international law. For example, most global treaties and conventions involve horizontal governance systems, in which top-down binding recommendations have no place. And treaty regimes can emerge and expire only through joint consent of the parties involved.

Finally, the proposal flies in the face of the current geopolitical situation, with the international liberal legal order under pressure and a marked move from multilateralism towards regionalism, if not outright nationalism. The world is not a unified organism that can be seamlessly managed or engineered through rational design.

Vito De Lucia, **Jan Solski**
Norwegian Centre for the Law of the Sea, The Arctic University of Norway, Tromsø, Norway.
vito.delucia@uit.no

Chile must preserve international science in Antarctica

For decades, Chile has helped scientists from across the world to study Antarctica, providing logistical support and rescue services from its southernmost region. But this role is under threat. These services are supported by annual short-term government funding. The two candidates who reached the second round of the ongoing presidential election have put little emphasis on Antarctica, suggesting a worrying lack of interest.

The government should take heed of the recent 'Mesa Antártica' consensus document (go.nature.com/3xmm3cd; in Spanish), produced by more than 40 Chilean Antarctic researchers and experts, including us, as part of a national initiative that seeks to develop a road map for Chile's future. It recommends modernizing the country's Antarctic governance model by creating a coordinated authority for logistics, science and diplomacy; ensuring multi-year funding for long-term observation systems; and deepening international scientific partnerships using Chilean infrastructure as a shared platform.

These changes would enable partner nations to plan joint field campaigns, interoperable logistics and long-term environmental monitoring, and allow Chile to continue its historic service to the international community.

Cristóbal Galbán Malagón, **Marcelo Leppe** Universidad Mayor, Santiago, Chile.
cristobal.galban@umayor.cl

Gustavo Chiang, **Paulina Bahamonde** Universidad Mayor, Temuco, Chile.

Help students faced with the death of a supervisor

The sudden loss of a PhD supervisor is a profound crisis, which can be magnified by a lack of institutional contingency plans. My experience, similar to that described by Cailyn McKay in your Career Column (C. McKay *Nature* https://doi.org/qdn4; 2025), highlights this. When my supervisor died of COVID-19, the ensuing chaos threatened my studies.

I was amazed to find that my university — like others I've heard about — lacked established protocols for when a principal investigator passes away. No administrative staff members or more-senior researchers could tell me what would happen next with certainty. I faced major hurdles, from the prospect of my laboratory closing to a lack of access to the documents I needed.

Universities must put formal plans in place to help others who find themselves in such circumstances. Decisions should be made quickly, to prevent students being left in limbo for months, and psychological support provided.

I found myself wondering whether choosing to do a PhD had been a good idea. Perhaps if I had joined a larger lab that had more PhD students and postdocs, I would have been more insulated from the shock. But, similar to McKay, I found that my PhD supervisor had left a network of collaborators and scientific friends who helped to guide me. In future, I hope that finding a path forward is made easier for others facing such circumstances.

Laura Zárraga-Vargas Sioltalife, Guadalajara, Mexico.
lczarragav@gmail.com

Without funding, Romanian research faces extinction

Over the past decade, Romania has spent less on research and development (R&D) relative to gross domestic product (GDP) than any other nation in the European Union, and has the fewest researchers per one million inhabitants. If no concrete measures are taken to increase funding in the next few years, the Romanian research system will collapse.

Although Romania's GDP has consistently increased in the past decade, the funds allocated for R&D in 2017–2022 have decreased relative to GDP. Public-sector funding represented just 0.16% of GDP in 2024, with 0.1% being allocated to R&D programmes in 2025. The funds from the private sector and EU projects are not enough to fill the gaps.

The government allotted a maximum of €12 billion (US$13.8 billion) for R&D between 2022 and 2027. But so far, only about €1 billion has been allocated, of which only €800 million has been paid out. Such shortfalls occur because of a tendency for the national authority for R&D to reduce the number and budget of project calls, or postpone handing out the contracts for new projects.

The government should increase R&D spending in 2026 to at least 0.15% of GDP, and then to at least 0.4% by 2028. This is far from the government's own target of 1% by 2030, but should be enough to prevent total collapse.

Lucian Pintilie National Institute of Materials Physics, Magurele, Romania.
pintilie@infim.ro

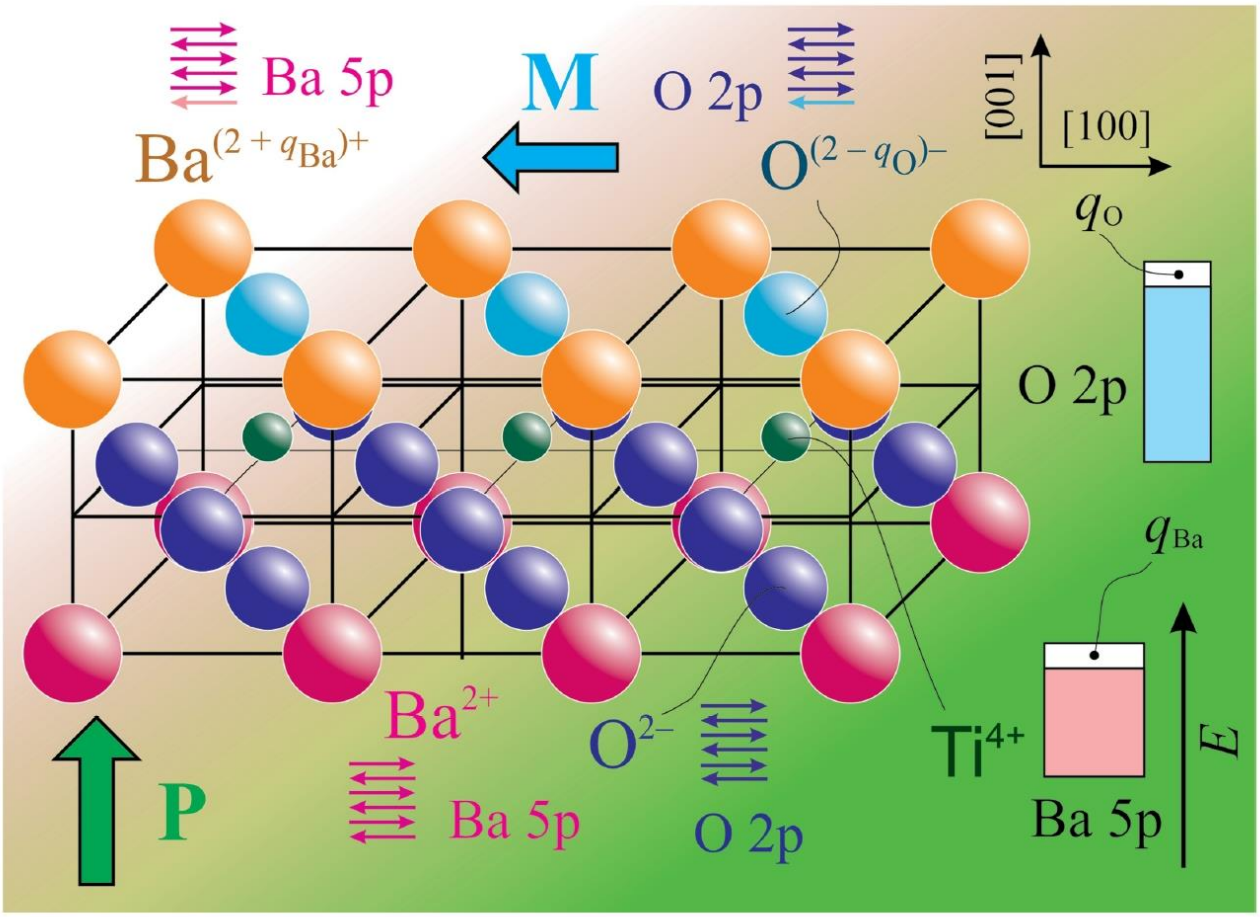

Showcasing research from Dr Cristian M. Teodorescu's laboratory, Surfaces and Interfaces, National Institute of Materials Physics, Măgurele, Romania.

Surface spin asymmetry of O 2p and Ba 5p states in $BaTiO_3$(001)

In its ferroelectric state, (001) oriented barium titanate with BaO termination features an electronic reconstruction with the surface layer positively charged. This positive charge is distributed almost evenly on the surface of Ba and O ions, yielding partially filled Ba 5p and O 2p orbitals. These orbitals feature uncompensated spins, enabling the formation of a detectable spin asymmetry. The fact that holes are stabilized on Ba 5p states, which are lower in energy than occupied O 2p states, may be regarded as a permanent population inversion induced by the ferroelectric state.

Image reproduced by permission of Cristian M. Teodorescu from *Mater. Adv.*, 2025, **6**, 8907.

As featured in:

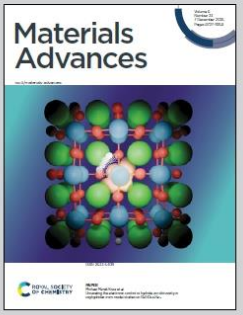

See Cristian M. Teodorescu *et al.*, *Mater. Adv.*, 2025, **6**, 8907.

ROYAL SOCIETY OF CHEMISTRY

rsc.li/materials-advances

Registered charity number: 207890

ADVANCED OPTICAL MATERIALS

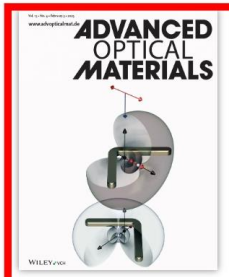

Volume 13, Issue 4
February 3, 2025
2402242
This article also appears in:
Celebrating Excellence in Advanced Optical Materials: Women in Photonics

Research Article | Open Access

Phase Transitions in Dimer/Layered Sb-Based Hybrid Halide Perovskites: An In-Depth Analysis of Structural and Spectroscopic Properties

Iulia Corina Ciobotaru, Claudiu Constantin Ciobotaru, Cristina Bartha, Monica Enculescu, Mihail Secu, Silviu Polosan, Cristina Besleaga

First published: 13 January 2025 | https://doi.org/10.1002/adom.202402242 | VIEW METRICS

SECTIONS PDF TOOLS SHARE

Figures References Related Information

Recommended

Phase Regulation of Layered Perovskites toward High-Performance Light-Emitting

Abstract

When used as the active layers—either as a light absorber in photovoltaic devices or as an electroluminescent material in light-emitting devices—lead-free perovskites significantly impact the performance of optoelectronic devices. This study focuses on antimony-based perovskites, which are promising for lighting applications. These types of perovskites enable the formation of self-trapped excitons (STEs) with higher dissociation energy than lead-based perovskites, which generate excitons with lower dissociation energy. The $(CH_3NH_3)_3Sb_2I_9$ crystals are synthesized using two methods, resulting in distinct spatial configurations – dimer and dimer/layered mixtures, each exhibiting unique structural and spectroscopic properties, as revealed by comprehensive multi-

Trends in Chemistry

CellPress

Volume 7, Issue 12, December 2025, Pages 737-739

Spotlight

Special Issue: The Chemistry of Nucleic Acids

Electrospun mesh electrodes advance paper-based nucleic acid detection

Thiago R.L.C. Paixão [1]

Show more

https://doi.org/10.1016/j.trechm.2025.10.004 ↗

Refers to

A paper-based device with submicronic fiber mesh electrodes for voltammetric quantification of nucleic acids

Cell Reports Physical Science, Volume 6, Issue 8, 20 August 2025, Pages 102781

Daciana Botta, Mihaela Beregoi, Ionut Adrian Cepleanu-Pascu, Daniel N. Crisan, Ana-Maria Ignat, Elena Matei, Ionut Enculescu, Victor C. Diculescu

Key Scientific Achievements & Breakthroughs in *Materials and Devices for Electronics, Photonics & Optoelectronics*

Steady state negative capacitance in p-n ferroelectric junctions

A.G. Boni, C.F. Chirilă, L.D. Filip, M.I. Botea, D.G. Popescu, M.A. Huşanu, L. Hrib, L. Trupină, I. Pintilie, L. Pintilie

National Institute of Materials Physics, 077125, Măgurele, Romania

Ferroelectrics exhibit a switchable spontaneous polarization, and near the coercive field their free-energy landscape can yield a negative differential permittivity, *i.e.*, negative capacitance (NC). In a standalone ferroelectric this NC region is intrinsically unstable, but it can be stabilized in multilayers when the electrostatic boundary conditions constrain the overall energy of the stack. In this report we focus on FE/FE bilayers with similar ferroelectric properties but a slight polarization mismatch, which generates internal fields that can bias one layer toward operation in the NC regime. *Fig. 2* summarizes the relevant electrostatic coupling scenarios, ranging from strongly screened to weakly screened interfaces, and the resulting internal-field distributions and parallel/antiparallel polarization configurations (*Fig. 1a–d*). A particularly important case arises when the interface behaves as a p–n junction between differently doped ferroelectrics, introducing a built-in field whose magnitude and sign depend on the polarization orientation (*Fig. 1e*). We tested these ideas in epitaxial $Pb(Zr_{0.2}Ti_{0.8})O_3$ bilayers doped with Fe (p-type) and with Nb or Bi (n-type), where both polarization mismatch and junction electrostatics can be engineered. By correlating switching behavior with capacitance measurements over temperature and frequency, we pinpoint conditions where the measured capacitance exceeds the series-capacitance expectation, consistent with a stabilized steady-state NC in at least one layer.

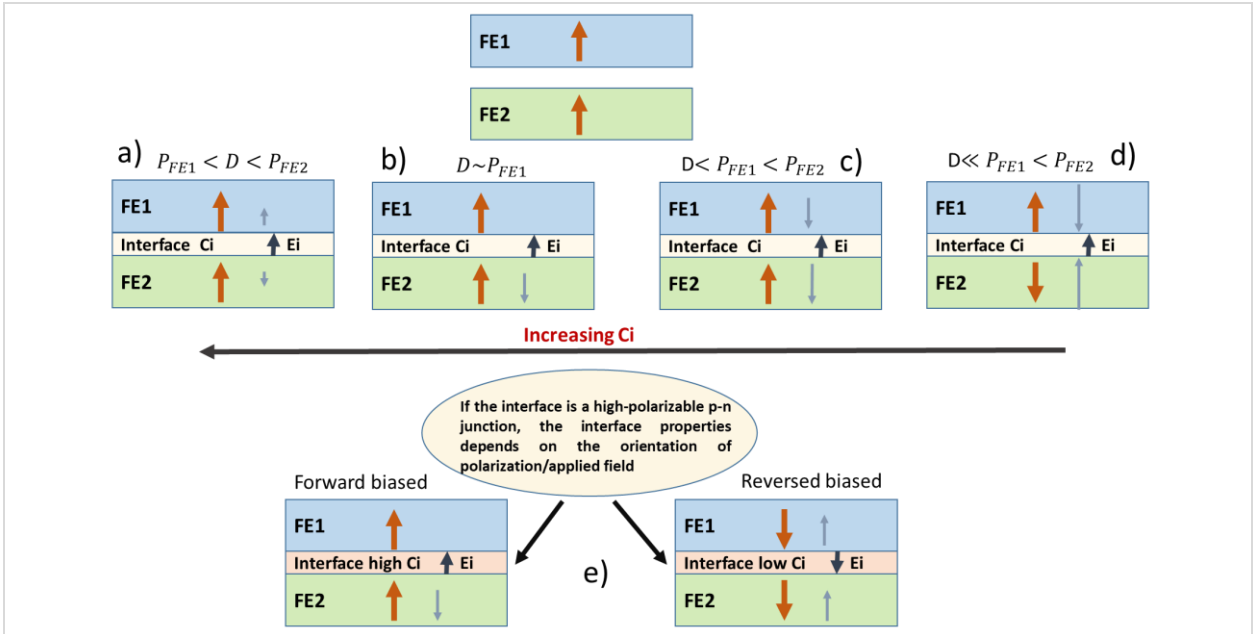

***Figure 1**: The schematic representation of polarization and internal fields in a bilayer FE structure for different properties of the interface. (**a**) High conductive or high polarizable interface; (**b,c**) Decreasing the capacitance of the interface; (**d**) Low capacitance of the interface; (**e**) Interface is a p-n junction of which properties depend on the polarization orientation. Reprinted from Ref. [1] with permission from Elsevier.*

Fig. 2 compares the capacitance–voltage hysteresis loops of the four bilayer stacks (Bi/Fe, Fe/Bi, Nb/Fe, and Fe/Nb), highlighting a clear order-dependent dielectric response. In all cases, the C–V curves are hysteretic, indicating two stable capacitance states linked to the polarization history of the bilayer. Most importantly, the measured capacitance was systematically higher than the value expected from a simple series connection of the two constituent ferroelectric layers: the strongest amplification was found in the Nb–Fe bilayers (≈195–215 pF measured *vs.* ≈84 pF series estimate), whereas the Bi–Fe bilayers showed a more moderate enhancement (≈120–170 pF measured vs ≈99 pF series estimate). Reversing the deposition sequence changed both the magnitude and the shape of the C–V hysteresis, evidencing

that the FE/FE interface is not electrostatically equivalent in the two growth orders. This order sensitivity supports the idea that interfacial screening and internal-field redistribution differ from one configuration to another, thereby biasing at least one layer closer to switching and enabling an effective capacitance boost consistent with stabilized NC contributions within the stack.

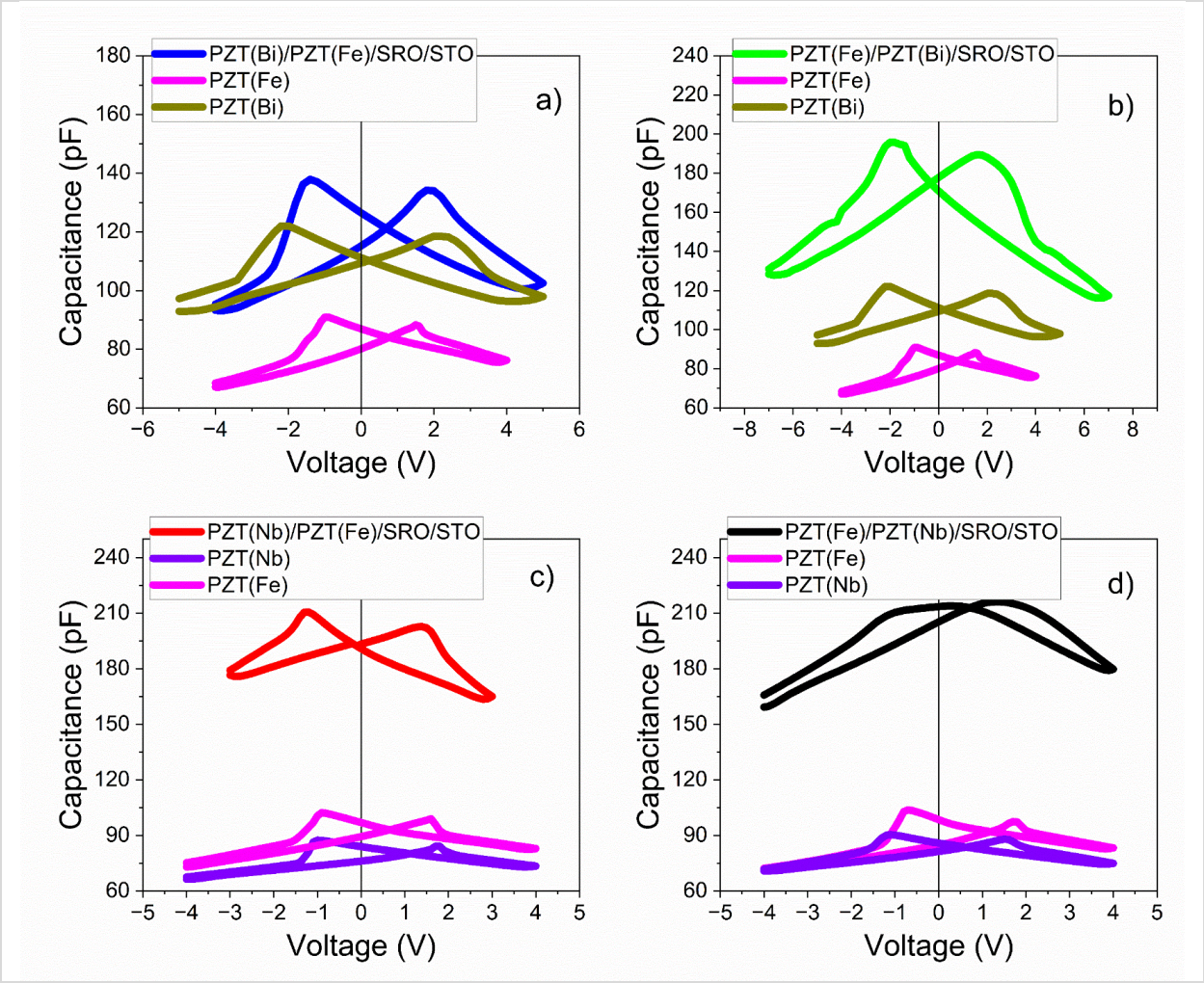

***Figure 2**: The hysteresis capacitance-voltage measurements for different bilayered structures: (**a**) PZT(Bi)/PZT(Fe)/SRO/STO; (**b**) PZT(Fe)/PZT(Bi)/SRO/STO; (**c**) PZT(Nb)/PZT(Fe)/SRO/STO; (**d**) PZT(Fe)/PZT(Nb)/SRO/STO. Reprinted from Ref. [1] with permission from Elsevier.*

Fig. 3 extends the dielectric analysis to the thinner 50 nm/50 nm PZT(Nb)/PZT(Fe) and PZT(Fe)/PZT(Nb) stacks, for which a simple series estimate based on the single-layer trend would give an overall capacitance of roughly ~200 pF. In these samples the response becomes strongly dispersive: the C–V curves depend markedly on frequency and exhibit an order-dependent shift along the voltage axis, most pronounced at low frequencies, so that at 0 V two different capacitance values can be obtained depending on the pre-poled polarization state (*Fig. 3a,d*). The Cp–f and loss–f characteristics reveal a clear Maxwell–Wagner (Debye-like) relaxation, with the high-frequency capacitance dropping to ~100 pF—well below the series estimate—consistent with the multilayer being limited by an additional interfacial contribution (of order ~200 pF) that sets the high-frequency equivalent value (*Fig. 3b,c,e,f*). The dielectric-loss peak occurs at lower frequency for the PZT(Fe)/PZT(Nb) sequence, indicating a larger RC time constant and therefore a higher resistance associated with the non-ferroelectric/interfacial element, in agreement with the trends inferred from the hysteresis behaviour. Overall, reducing the thickness amplifies the role of interfacial electrostatics and transport, pushing the capacitance enhancement into a polarization-history-dependent, relaxation-controlled regime rather than the comparatively less frequency-dispersive behaviour observed in the thicker bilayers.

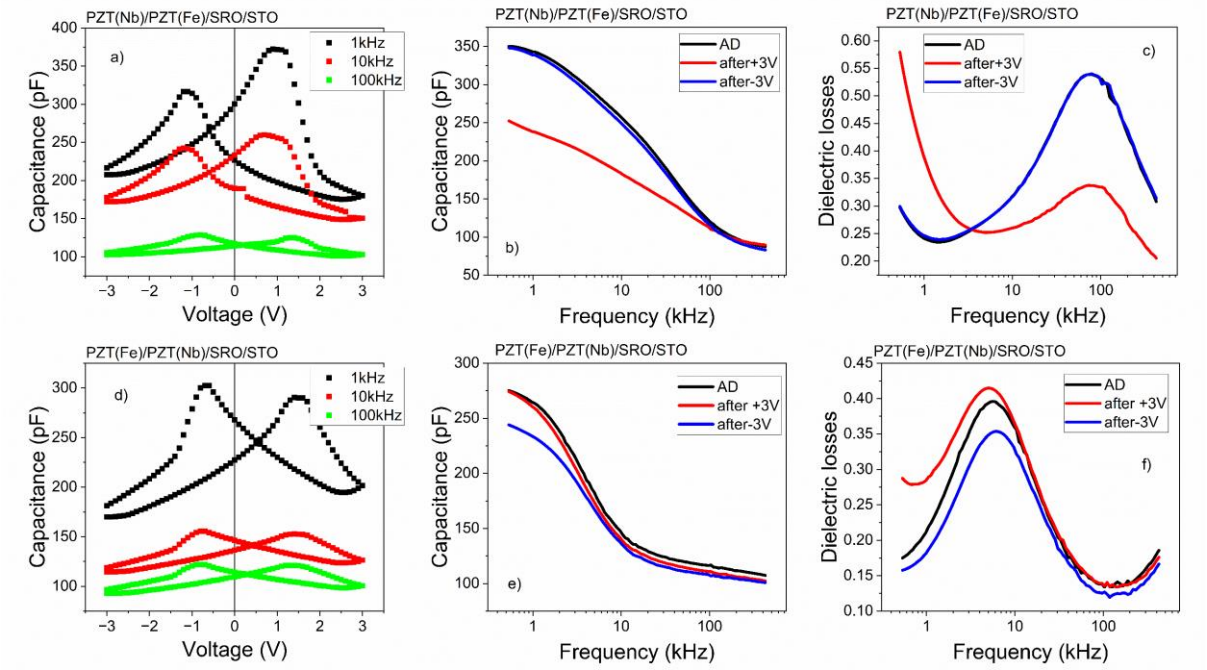

***Figure 3**: The dielectric characteristics of thinner PZT(Nb)/PZT(Fe) multilayers. (**a**) The CV characteristics for PZT(Nb)/PZT(Fe)/SRO at different frequency; (**b**) The capacitance-frequency characteristics after different pre-pulse pooling for PZT(Nb)/PZT(Fe)/SRO; (**c**) The dielectric losses-frequency characteristics after different pre-pulse pooling for PZT(Nb)/PZT(Fe)/SRO; (**d**) The CV characteristics for PZT(Fe)/PZT(Nb)/SRO at different frequency; (**e**) The capacitance-frequency characteristics after different pre-pulse pooling for PZT(Fe)/PZT(Nb)/SRO; (**f**) The dielectric loses-frequency characteristics after different pre-pulse pooling for PZT(Fe)/PZT(Nb)/SRO. Reprinted from Ref. [1] with permission from Elsevier.*

Reference:

[1] A.G. Boni, C.F. Chirila, L.D. Filip, M.I. Botea, C. Radu, D.G. Popescu, M.A. Husanu, L. Hrib, L. Trupina, I. Pintilie, L. Pintilie, *Steady state negative capacitance in p-n ferroelectric junctions*, Acta Materialia 298 (2025) 121177.

Phase transitions in dimer/layered Sb-based hybrid halide perovskites: An in-depth analysis of structural and spectroscopic properties

I.C. Ciobotaru, C.C. Ciobotaru, C. Bartha, M. Enculescu, M. Secu, S. Poloşan, C. Beşleagă

National Institute of Materials Physics, 077125, Măgurele, Romania

Halide perovskite (HP) materials have made significant advances in optoelectronics, thanks to their tuneable bandgap, good charge-carrier mobility, high photoluminescence quantum yield, and long carrier diffusion lengths [1]. They are widely used in light-emitting diodes (LEDs), with external quantum efficiency rising from 0.1% in 2014 [2] to over 20% in 2018 [3]. Despite these advances, perovskite electronics still struggle with two main issues: lead toxicity and instability under light, heat, and humidity [4,5]. Antimony is less toxic, abundant, and has a much higher safe exposure limit than lead, making it a good option for lead-free perovskites. However, replacing lead with antimony in halide perovskites creates only 0D or 2D structures [6]. Dimer (0D) perovskites are a subset of isolated metal-halide octahedral anions known for Stokes-shifted broadband emissions and high PLQYs, exclusively from self-trapped excitons (STEs), making them suitable for Light Emitting Devices and Scintillators. In contrast, 2D perovskites have corrugated layers with partially corner-sharing MX_6 octahedra, exhibit direct band gaps and better carrier transport, but are less stable and harder to synthesize [7]. In this work [8], we synthesized $MA_3Sb_2I_9$ powders using anti-solvent and ligand-assisted methods to achieve various dimer-to-layered phase ratios, enabling precise control over their optoelectronic properties. Adding OA and OLA surfactants promotes the formation of layered (2D) structures by reducing nucleation centres. Structurally, the dimer phase is hexagonal, featuring columns of two octahedra capped by three iodide ions, while the trigonal phase is layered and planar, with two octahedra capped by a single iodide ion.

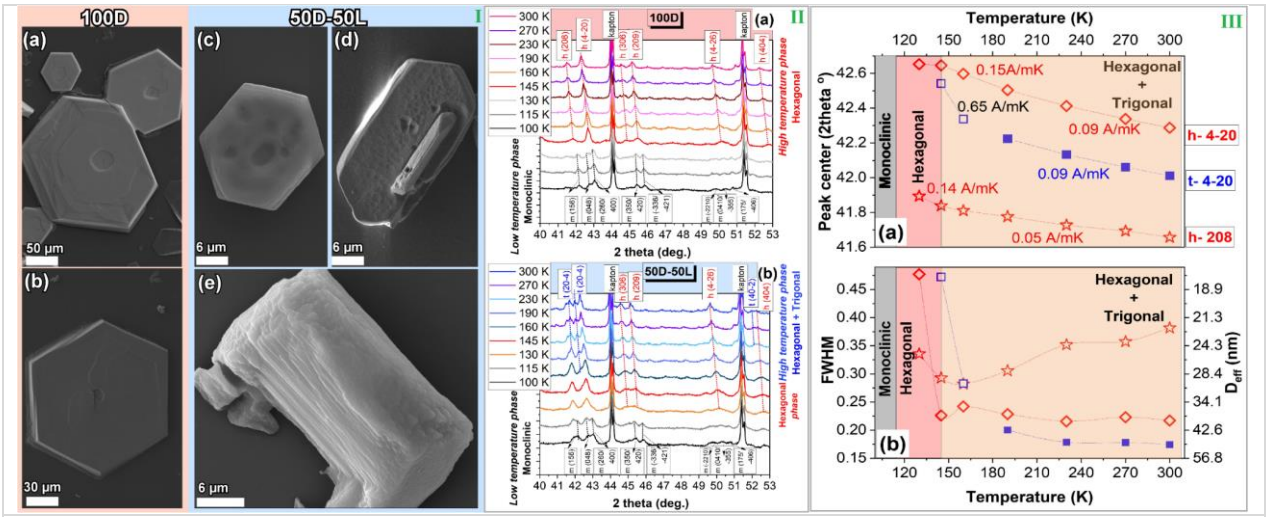

***Figure 1**: **I.** (**a**) SEM images for 100D: 0.8 kX magnification; (**b**) 1 kX magnification; and (**c**) for 50D-50L: hexagonal crystal, (**d**) top and (**e**) lateral view of trigonal layered crystal at 5 kX magnification; **II.** (**a**) XRD patterns vs. temperature for 100 D and (**b**) 50D-50 L; **III.** (**a**) Temperature dependences of XRD parameters: (4-20) and (208) peak's centre and FWHM of (4-20) and (208) reflections and (**b**) the equivalent D_{eff} for the 50D-50L sample; red and blue colour correspond to hexagonal and trigonal phase. Adapted from Ref. [8].*

SEM images (*Fig. 1.I*) revealed that 100D grains are ten times larger than those in 50D-50L and confirmed the layered arrangement of the crystalline planes from the trigonal phase (*Fig. 1.I (e)*). XRD measurements with Rietveld analysis revealed the presence of both layered and dimer phases when methylammonium iodide (MAI) is used as the A-site cation. The ratio of dimer to layered phase can be controlled by varying the OA:OLA surfactant ratio during synthesis. At room-temperature, 100D samples displayed a pure hexagonal structure (P63/mmc space group), while 50D-50L samples contained a mixture of hexagonal and trigonal (P-3m1 space group) phases, with the trigonal phase

~47%. Both 100D and 50D-50L samples undergo a monoclinic-to-hexagonal phase transition at approximately 145 K and 130 K, as confirmed by XRD (*Fig. 1.II*). At 190 K, the (4–20) peak indicated the formation of the trigonal phase, which is preceded by an intermediary phase observed between 145 K and 160 K, characterised by a larger (4–20) interplanar distance and smaller D_{eff} as illustrated in *Fig. 1.III (a)*. Above the transition temperature, D_{eff} values for the (4–20) peak remain constant at ~39 nm for the hexagonal phase and ~48 nm for the hexagonal and trigonal phases, while the (208) peak of the hexagonal phase showed a slight decrease in D_{eff} from 30 to 25 nm with increasing temperature (*Fig. 1.III (b)*).

Optical spectroscopy of $MA_3Sb_2I_9$ powder was performed using diffuse reflectance and absorption measurements, with samples either dispersed in PMMA or dissolved in gamma-butyrolactone (GBL). The results highlighted how varying Sb–Sb interatomic distances affect the material's optical response and demonstrated that spin-orbit coupling significantly influences self-trapped exciton (STE) behaviour. The absorption and emission spectra are determined by the ratio of dimer (Sb:I = 2:9) to layered (Sb:I = 4:11) phases. Increasing Sb^{3+} content shifts the absorption edge to the UV, consistent with observations in Sb-doped $(NH_4)_2SnCl_6$ [9].

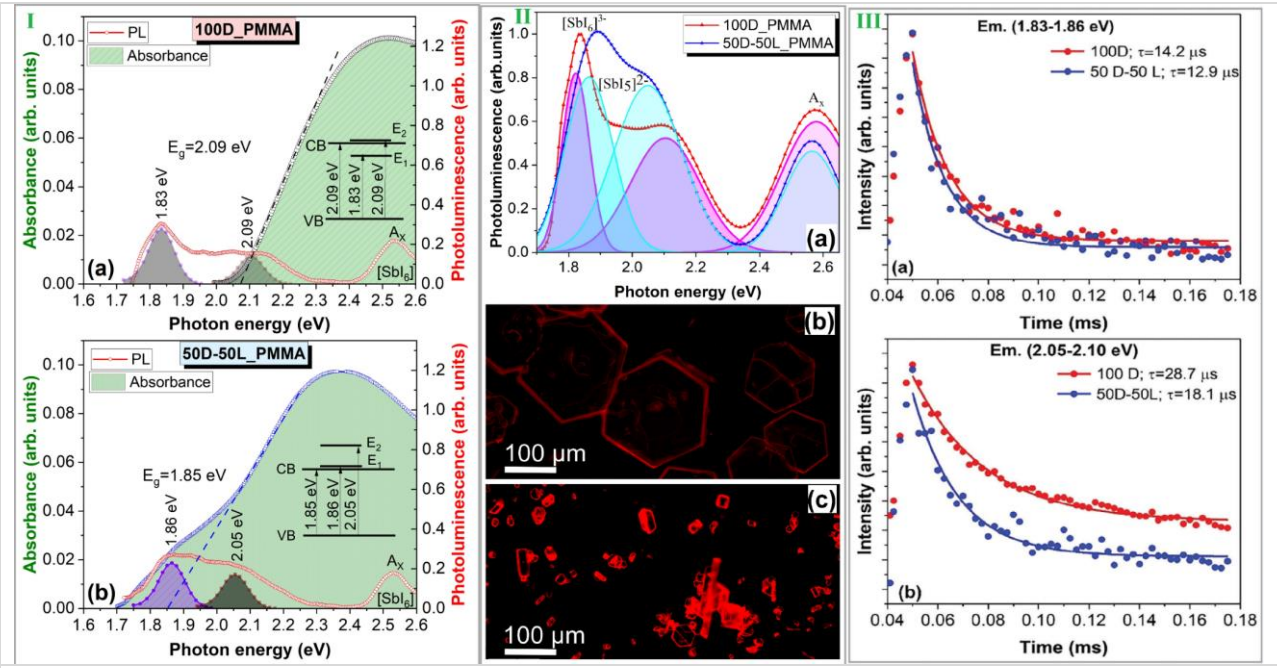

***Figure 2**: **I.** Comparison between the absorption and emission spectra for the (**a**) 100D and (**b**) 50D-50L samples. Inset: Sub-levels (E1 and E2) in comparison to bandgaps; **II.** (**a**) PL spectra of 100D and 50D-50L samples dispersed in PMMA, excited at 3.16 eV. (**b**,**c**) FM images for the (**b**) 100D and (**c**) 50D-50L samples; **III.** Lifetime measurements for (**a**) red and (**b**) yellow STE, excited at 392 nm (3.16 eV). Adapted from Ref. [8].*

The absorption edge tails in the 50D-50L structures revealed two distinct sub-gap energy levels, as shown in *Fig. 2.I*. These sublevels play a critical role in the photophysical behaviour of the material, influencing optical transitions and emission properties. When comparing $MA_3Sb_2I_9$ dispersed in PMMA to the synthesized powder, there is a slight shift in observed bandgap values, indicating that the chemical environment and matrix can subtly affect electronic properties. Strong electron-phonon coupling in Sb^{3+} ions leads to self-trapped exciton (STE) recombination, which is responsible for the appearance of two broad photoluminescence emissions triggered by the bandgap evolution from 100D (1.83 eV and 2.09 eV) to the mixed 50D-50L structure (1.86 eV and 2.05 eV) as illustrated in *Fig. 2.I*. The photoluminescence spectra of the 100D sample in PMMA (*Fig. 2.II (a)*), excited at 3.16 eV is mainly featuring dimer hexagonal structures, with two main emission bands at 2.09 eV and 1.83 eV by varying intensities, plus an additional band at 2.54 eV (Ax band). The 100D structure's predominant $[SbI_6]^{3-}$ octahedra result in shorter Sb–Sb distances, enhancing exciton-phonon interactions and leading to a significant Stokes shift from 3.16 to 1.83 eV (>200 nm), characteristic of STE emission. In contrast, the mixed 50D-50L structure displayed similar emission bands at 2.05 eV and 1.86 eV but featured a more relaxed Sb–Sb distance, which reduced exciton-phonon interaction and resulted in a smaller Stokes shift.

Fluorescence microscopy (*Fig. 2.II (b,c)*) confirmed the morphologies and emissions of the hexagonal and trigonal phases in the 100D and 50D-50L samples, aligning with SEM analysis and indicating that the 100D structure has a larger hexagonal grain size compared to the 50D-50L samples. The red STE emission, with lifetimes of approximately 13–14 μs, remains consistent between the 100D and 50D-50L samples (*Fig. 2.III*). However, the yellow-green excitons exhibit notably different decay dynamics: in the layered structure, their lifetime is 18.1 μs, which is significantly shorter than the 28.7 μs observed in the dimer-only sample. This longer lifetime in the 100D sample corresponds to its higher photoluminescence and greater exciton binding energies, experimentally measured at 97 meV at room-temperature and increasing to 106 meV at temperatures below the phase transition (~150 K). In contrast, the layered structure in 50D-50L resulted in reduced phosphorescence, as evidenced by lower exciton binding energies at 88 meV at RT and 95 meV below the phase transition point. To assess long-term structural stability, the 100D and 50D-50L samples were monitored for more than a year. After 382 days of exposure to air and ambient light, the XRD patterns of the powders showed no changes, and no new peaks indicating degradation products were observed.

In conclusion, this work introduces a reliable approach for synthesizing next-generation antimony-based perovskites and outlines strategies to tailor their structural configuration for specific lighting applications. It also offers important insights into the factors that improve their functionality and versatility, making it a valuable resource for future research and technological innovation.

References:

[1] S. Sun, M. Lu, X. Gao, Z. Shi, X. Bai, W.W. Yu, Y. Zhang, *0D perovskites: Unique properties, synthesis, and their applications*, Advanced Science 8 (2021) 2102689.

[2] Z.-K. Tan, R.S. Moghaddam, M.L. Lai, P. Docampo, R. Higler, F. Deschler, M. Price, A. Sadhanala, L.M. Pazos, D. Credgington, F. Hanusch, T. Bein, H.J. Snaith, R.H. Friend, *Bright light-emitting diodes based on organometal halide perovskite*, Nature Nanotechnology 9 (2014) 687–692.

[3] K. Lin, J. Xing, L.N. Quan, F.P.G. de Arquer, X. Gong, J. Lu, L. Xie, W. Zhao, D. Zhang, C. Yan, W. Li, X. Liu, Y. Lu, J. Kirman, E. H. Sargent, Q. Xiong, Z. Wei, *Perovskite light-emitting diodes with external quantum efficiency exceeding 20 per cent*, Nature 562 (2018) 245–248.

[4] D. Liang, S. M. H. Qaid, X. Yang, S. Zhao, B. Luo, W. Cai, Q. Qian, Z. Zang, *Luminescence regulation of Sb^{3+} in 0D hybrid metal halides by hydrogen bond network for optical anti-counterfeiting*, Opto-Electronic Advances 7 (2024) 230197.

[5] W. Ke, M.G. Kanatzidis, *Prospects for low-toxicity lead-free perovskite solar cells*, Nature Communications 10 (2019) 965.

[6] Y. Zhao, K. Cruse, M. Abdelsamie, G. Ceder, C.M. Sutter-Fella, *Synthetic approaches for thin-film halide double perovskites*, Matter 4 (2021) 1801–1831.

[7] Y. Peng, F. Li, Y. Wang, Y. Li, R. L. Z. Hoye, L. Feng, K. Xia, V. Pecunia, *Enhanced photoconversion efficiency in cesium-antimony-halide perovskite derivatives by tuning crystallographic dimensionality*, Applied Materials Today 19 (2020) 100637.

[8] **I.C. Ciobotaru, C.C. Ciobotaru, C. Bartha, M. Enculescu, M. Secu, S. Poloşan, C. Beşleagă, *Phase transitions in dimer/layered Sb-based hybrid halide perovskites: An in-depth analysis of structural and spectroscopic properties*, Advanced Optical Materials 13 (2025) 2402242.**

[9] H. Lin, Q. Wei, B. Ke, W. Lin, H. Zhao, B. Zou, *Excitation-wavelength-dependent emission behavior in $(NH_4)_2SnCl_6$ via Sb^{3+} dopant*, The Journal of Physical Chemistry Letters 14 (2023) 1460.

Novel insights into the distinct magnetic configurations of polycrystalline Ni nanowires produced by a template approach at varying electrodeposition potentials

M. Onea[1,2], N. Iacob[1], G. Schînteie[1], M.E. Toimil Molares[3], E. Matei[1], V. Kuncser[1], I. Enculescu[1]

1) *National Institute of Materials Physics, 077125, Măgurele, Romania*
2) *Faculty of Physics, University of Bucharest, 077125, Măgurele, Romania*
3) *GSI Helmholtzzentrum für Schwerionenforschung GmbH, 64291, Darmstadt, Germany*

Electrochemical replication of nanoporous membranes was employed for the fabrication of nickel nanowires. The fabrication process led to uniform arrays of quasi-1D nanoobjects with low diameters and high aspect ratios. Extensive characterization experiments were carried out for determining the morphological, structural and magnetic properties of the nanostructures. It was found that the working electrode potential employed during the electrochemical deposition fabrication experiments influences both the crystalline structure and the magnetic properties of the nanowires [1]. Accordingly, an in-depth investigation of the correlations between the morpho-structural and the magnetic parameters was performed [2]. It was shown that several structural factors, mainly crystalline texture and grain size and shape, quite sensitive to the deposition potential, influence also the specific magnetic configurations, which can be tuned from 3D Imry and Ma random anisotropy type to cooperative quasi-1D superspin type. Consequently, new possibilities in tailoring the magneto-functionalities of polycrystalline magnetic nanowires by adjusting fabrication parameters are revealed. In this paper the magnetic properties of Ni nanowires fabricated by means of template electrochemical route, using as templates chemically etched polycarbonate membranes irradiated with swift heavy ions, are reported. The aim is to prove the experimental possibility to tune the magnetic anisotropy of the wires by suitable choosing the electrodeposition potentials. The complexity of the obtained magnetic configurations is discussed, showing the role of the structural texture on the interplay between the different components of anisotropy. The SEM images confirm that the growth process took place as expected, with the wires growing as replicas of the pores' arrays (*Fig. 1*).

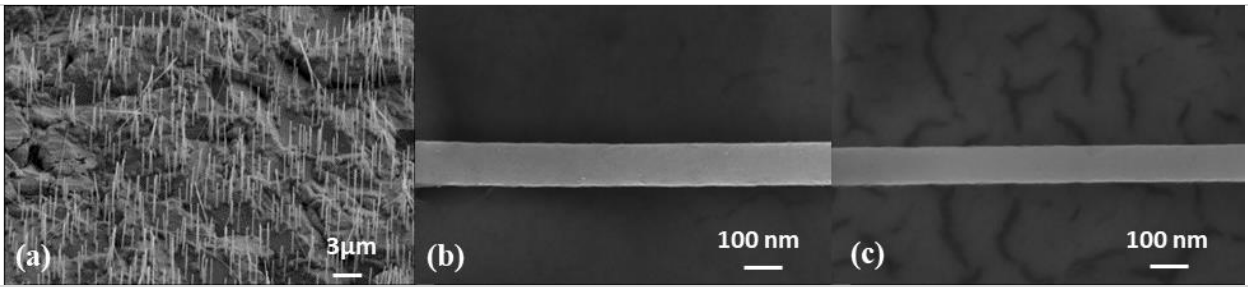

***Figure 1**: SEM images of (**a**) arrays of nanowires deposited at –1000 mV; (**b,c**) Detail of nanowires deposited at potentials of –1000 mV and –700 mV, respectively. Reproduced from Ref. [2].*

The XRD patterns showed the typical fcc structure of Ni for all samples. The lattice parameter remains nearly constant (~3.5195 Å), slightly (~0.3%) lower than the bulk Ni value, indicating that the density of Ni nanowires is independent of the deposition potential and close to that of bulk Ni.
Deviations in SQUID measurements explain the geometry-dependent saturation magnetization, with the perpendicular configuration providing the most reliable values [3]. At 300 K, the saturation magnetization decreases from ~40 emu/g (Sample 1) to ~20 emu/g (Sample 4), well below bulk Ni, despite similar crystal structure.
This reduction and its strong dependence on deposition potential are attributed to changes in magnetic texture rather than structural differences. The nanowires exhibit shape-anisotropy-dominated, uniaxial magnetism with the easy axis along the wire length, leading to rectangular hysteresis loops in parallel geometry and nearly linear ones in perpendicular geometry. Progressive, incomplete saturation and

reduced magnetization indicate non-collinear spin configurations and magnetic defects. Analysis of MR/MS ratios shows a strong decrease in magnetic texture with increasing (more negative) deposition potential, from highly textured nanowires (S1, S2) to weakly textured ones (S4) (*Fig. 2*).
Magnetic hysteresis loops measured at different temperatures in parallel and perpendicular field geometries show distinct loop shapes and an unexpected difference in saturation magnetization between the two configurations at the same temperature. The magnetization values are normalized to the Ni mass, estimated from the nanowire volume and bulk Ni density. The discrepancy in saturation magnetization is attributed to measurement artifacts and possible SQUID magnetometer limitations rather than intrinsic sample properties.

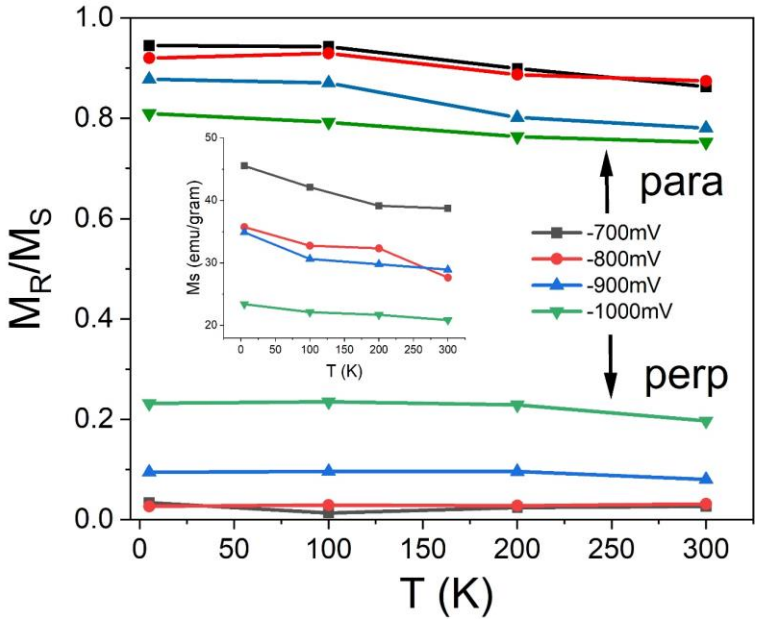

***Figure 2**: Evolution of the M_R/M_S ratio (M_S=saturation magnetization, M_R=remanent magnetization) function of temperature, for samples obtained at different electrodeposition potentials. The same two geometries, with the field applied parallel (para) and perpendicular (perp) to the nanowires are considered. The inset shows the temperature evolution of the saturation magnetization in perpendicular geometry which gives the best estimation for the real values of saturation magnetization. Reproduced from Ref. [2].*

The crystalline texture was quantified using a texture coefficient (TC) calculated from the (111), (200), and (220) Ni fcc reflections. TC values showed that samples deposited at potentials more positive than −900 mV exhibit a pronounced (220) texture, which progressively shifts toward a dominant (111) texture at more negative potentials. Crystallite size and strain analyses support this result: the largest crystallites and lowest strains occur along the (220) direction, consistent with elongated (ellipsoidal) crystallites whose aspect ratio decreases with deposition potential. As the potential approaches −1000 mV, both crystallite aspect ratio and texture coefficients approach unity, indicating nearly random polycrystalline growth, which correlates with the strongly reduced magnetic texture observed for sample S4 (*Fig. 3*). Magnetic texture was further characterized using the ratio R_C between coercive fields measured in parallel and perpendicular geometries. A high magnetic texture corresponds to large R_C values, while values close to 1 indicate weak or negligible texture. At 5 K, R_C decreases strongly from ~9 for nanowires deposited at −700 mV to ~0.9 at −1000 mV, confirming a progressive loss of magnetic texture with decreasing deposition potential.
The coercive fields in parallel geometry (≈970–1080 Oe) are significantly lower than the Stoner–Wohlfarth switching field for bulk Ni and increase slightly as the saturation magnetization decreases, supporting a localized domain-wall nucleation mechanism associated with structural imperfections and grain boundaries. Grain-size analysis and exchange-length considerations (*Fig. 4*) indicate a transition from cooperative quasi-1D superspin behaviour (samples S1–S2) to a 3D Imry–Ma random anisotropy configuration (sample S4), with sample S3 at the crossover [4].

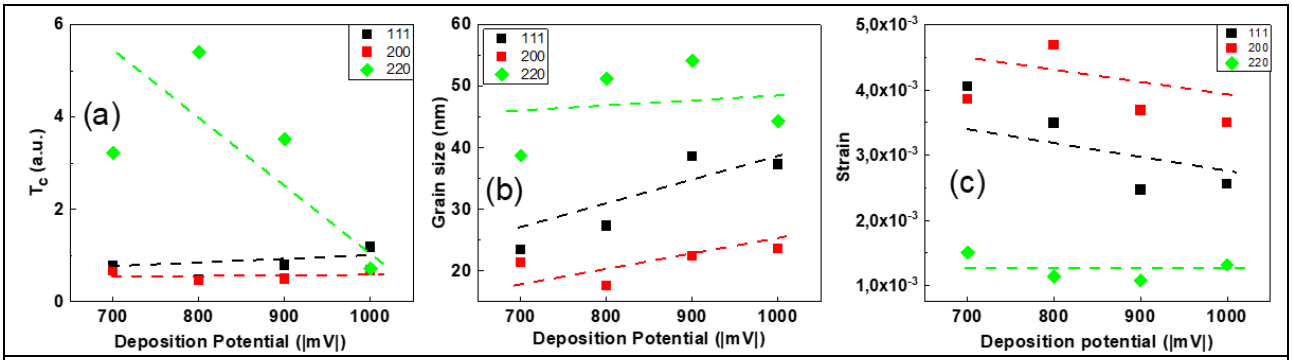

***Figure 3**: (**a**) Texture coefficient, (**b**) crystallite size; and (**c**) strain along perpendicular directions to the reflection planes as estimated for samples obtained at different deposition potentials. Reproduced from Ref. [2].*

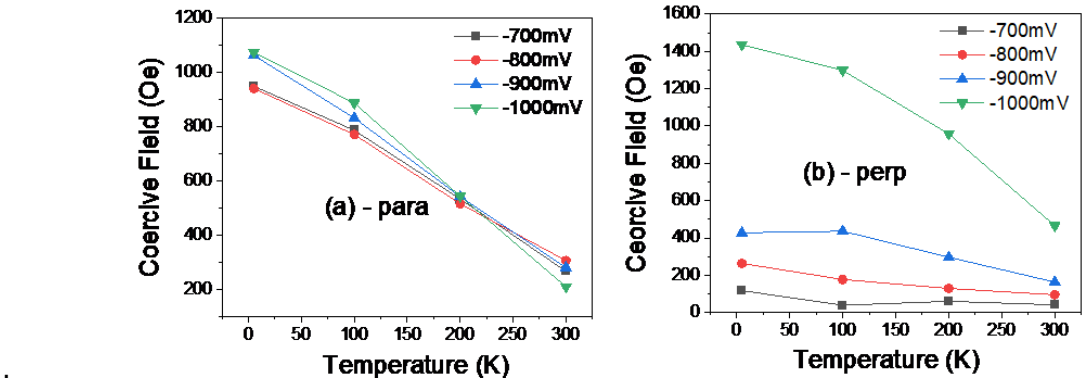

***Figure 4**: Coercive fields at different temperatures for the 4 samples obtained at electrodeposition potentials between –700 and –1000 mV. The same two geometries, with the field applied (**a**) parallel and (**b**) perpendicular to the nanowires are considered. Reproduced from Ref. [2].*

Uniform Ni nanowires (~100 nm diameter, ~30 μm length) were obtained by electrodeposition in polymer templates. While all samples are well-crystallized fcc Ni, the electrodeposition potential strongly controls grain size, crystalline texture, and magnetic defects, which in turn determine the magnetic behaviour.

At higher (more electropositive) potentials, the nanowires show strong magnetic texture and cooperative quasi-1D superspin behaviour. At more negative potentials, texture is lost and the system evolves toward a random anisotropy (Imry–Ma–type) magnetic configuration, accompanied by reduced saturation magnetization. Thus, the changes in magnetic properties originate from modifications of magnetic texture and spin configuration rather than from structural phase or density variations.

References:

[1] E. Matei, I. Enculescu, M.E. Toimil-Molares, A. Leca, C. Ghica, V. Kuncser, *Magnetic configurations of Ni–Cu alloy nanowires obtained by the template method*, Journal of Nanoparticle Research 15 (2013) 1863.

[2] **M. Onea, N. Iacob, G. Schinteie, M.E. Toimil Molares, E. Matei, V. Kuncser, I. Enculescu, *Novel insights into the distinct magnetic configurations of polycrystalline Ni nanowires produced by a template approach at varying electrodeposition potentials*, Journal of Alloys and Compounds 1044 (2025) 183959.**

[3] M. Sawicki, W. Stefanowicz, A. Ney, *Sensitive SQUID magnetometry for studying nanomagnetism*, Semiconductor Science and Technology 26 (2011) 064006.

[4] M. Imry, S. Ma, *Random-field instability of the ordered state of continuous symmetry*, Physical Review Letters 35 (1975) 1399–1401.

Ferroelectric $Hf_{0.5}Zr_{0.5}O_2$ thin films on TiN/Si substrates grown by pulsed laser deposition at CMOS-compatible temperatures

C.F. Chirilă[1], G.A. Boni[1], D.G. Popescu[1], C.M. Istrate[1], M.A. Huşanu[1], L.D. Filip[1], C. Beşleagă[1], L. Pintilie[1], A. Dimoulas[1,2]

1) *National Institute of Materials Physics, 077125, Măgurele, Romania*
2) *Institute of Nanoscience and Nanotechnology, National Centre for Scientific Research DEMOKRITOS, 15341, Athens, Attiki, Greece*

Ferroelectric hafnium–zirconium oxide ($Hf_{0.5}Zr_{0.5}O_2$, HZO) has become a key material for emerging non-volatile memories and low-power electronic devices due to its full compatibility with silicon technology, scalability to nanometre thickness, and lead-free composition. Unlike conventional perovskite ferroelectrics, hafnia-based materials retain ferroelectricity at extremely small thicknesses, making them attractive for highly scaled device architectures. However, stabilization of the ferroelectric orthorhombic phase typically requires high-temperature post-deposition annealing and electrical wake-up cycling, which increase process complexity and conflict with the strict thermal budgets imposed by back-end-of-line (BEOL) integration in advanced CMOS technologies.
In this study, we demonstrated direct stabilization of the ferroelectric orthorhombic phase in ultrathin HZO films grown by pulsed laser deposition (PLD) at a substrate temperature of only 400 °C on Si/TiN substrates, without the need for post-deposition annealing or wake-up treatments. This represents a significant reduction in thermal budget compared to standard fabrication routes and enables a simplified processing flow suitable for CMOS integration. The PLD process, characterized by highly energetic species and controlled oxygen partial pressure, allows kinetic stabilization of metastable crystalline phases that are difficult to achieve by equilibrium-driven deposition methods. The interdependence between processing conditions, defect chemistry, crystalline phase, and functional properties is summarized schematically in (*Fig. 1*).

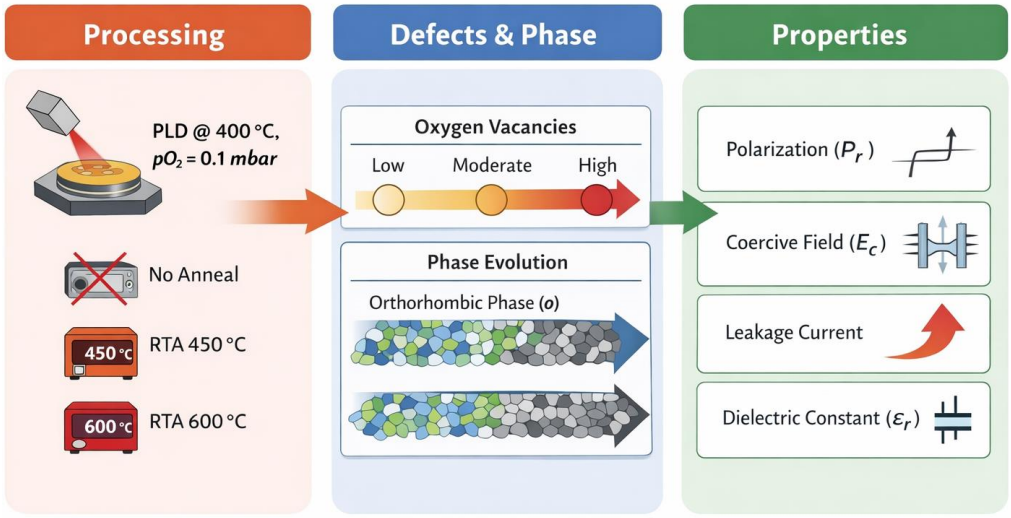

***Figure 1**: Schematic representation of the processing–defects–phase–properties relationship in HZO thin films grown by pulsed laser deposition.*

Structural and microstructural investigations revealed that the as-grown films are dominated by the ferroelectric orthorhombic phase, with only a minor contribution from the thermodynamically stable monoclinic phase. Moderate post-growth annealing at 450 °C slightly modifies the phase balance but preserves the dominance of the ferroelectric phase, while annealing at 600 °C promotes a clear increase in monoclinic phase content and reduced crystallinity. High-resolution transmission electron microscopy (HR-TEM) further confirmed the granular nature of the films and reveals a higher fraction of monoclinic crystallites after high-temperature annealing, indicating structural relaxation toward equilibrium. To summarize, the diffraction and microscopy results (*Fig. 2*) provided a schematic

representation of the qualitative phase evolution, highlighting the increased monoclinic phase fraction after annealing at 600 °C compared to the as-grown and moderately annealed films.

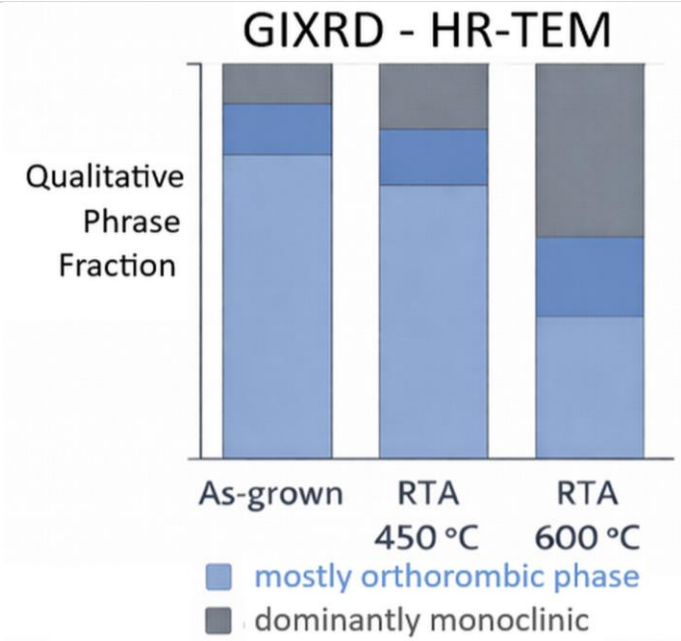

***Figure 2**: Schematic illustration of the qualitative phase composition of HZO thin films under different processing conditions, based on grazing incidence XRD and HR-TEM trends. Each stacked bar reflects the relative contribution of the orthorhombic (o-phase, light blue) and monoclinic (m-phase, grey) polymorphs for the as-grown film, the sample annealed at 450 °C, and the sample annealed at 600 °C. Adapted from the structural results presented in Ref. [1].*

Electrical measurements showed robust ferroelectric switching in the as-grown films, with remanent polarization values comparable to or higher than those previously reported for hafnia-based films grown on silicon by PLD. Moderate annealing increased polarization but also led to higher coercive fields and stronger imprint, which are undesirable for low-voltage device operation. In contrast, films annealed at 600 °C exhibited strong leakage currents that suppress reliable ferroelectric switching, indicating that excessive defect generation and phase transformation significantly degrade functional performance. These results highlighted the importance of maintaining an optimal balance between polarization strength and electrical insulation. Chemical analysis combined with first-principles calculations indicated that oxygen vacancies play a central role in stabilizing the ferroelectric phase. A moderate vacancy concentration promoted polar distortions and favours the orthorhombic structure, while excessive vacancy densities increased electronic conductivity and facilitate structural transformation toward the monoclinic phase. Theoretical modelling supported this interpretation by showing that oxygen vacancies enhance spontaneous polarization in the orthorhombic lattice but become detrimental when their concentration exceeds an optimal range. The trade-off between enhanced remanent polarization and increased coercive field after annealing, suggesting that the as-grown film offers a more favourable balance for low-voltage ferroelectric applications, is summarized in (*Fig. 3*). The oxygen vacancy axis is qualitative and inferred from XPS trends.

The combined structural, chemical, and electrical results indicated that ferroelectric phase stabilization in these ultrathin HZO films is governed primarily by kinetic effects during PLD growth rather than by post-deposition thermodynamic equilibration. The energetic species inherent to the PLD process and the low oxygen partial pressure promoted the formation of a moderate concentration of oxygen vacancies, which locally distort the fluorite lattice and favour the formation of the polar orthorhombic phase. This mechanism enabled direct crystallization of the ferroelectric phase at relatively low substrate temperatures, in contrast to ALD and CSD processes that typically require high-temperature annealing to induce crystallization and phase transformation. First-principles calculations support this interpretation by showing that oxygen vacancies enhance spontaneous polarization and stabilize polar distortions within the orthorhombic lattice. However, the calculations also suggested that increasing vacancy concentration beyond an optimal range, while potentially enhancing polarization locally, leads

to electronic states that facilitate charge transport and increase leakage current. Experimentally, this behaviour is observed in the RTA 600 °C sample, where elevated vacancy concentration coincides with phase transformation toward the monoclinic structure and loss of switchable ferroelectricity. Therefore, an optimal balance between defect-assisted phase stabilization and electrical insulation is required to achieve high-performance ferroelectric behaviour. The as-grown PLD films appear to lie within this optimal defect window, combining sufficient vacancy concentration to stabilize the orthorhombic phase with sufficiently low leakage to allow reliable polarization switching. These findings highlight the importance of defect engineering through deposition parameters rather than post-growth thermal treatments and provide a general strategy for stabilizing metastable ferroelectric phases in fluorite-structured oxide thin films.

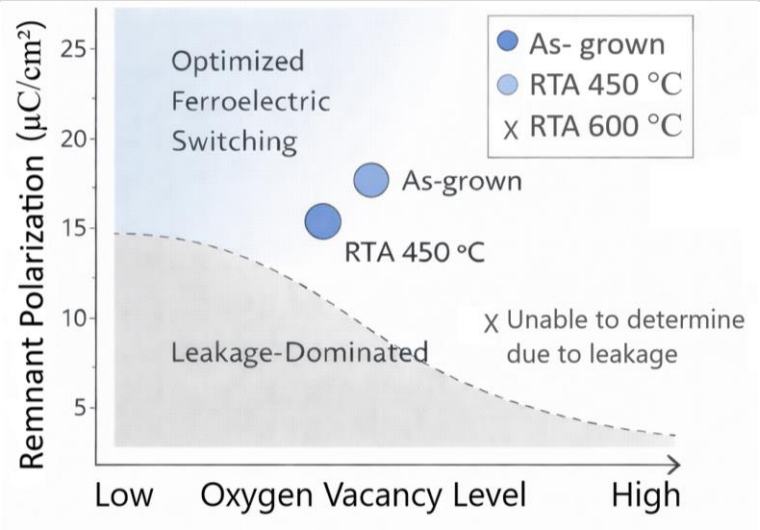

***Figure 3**: Schematic performance map correlating remanent polarization (P_r) with the qualitative level of oxygen vacancies in HZO thin films under different processing conditions. Adapted from the electrical measurements results presented in Ref. [1].*

Reference:

[1] C.F. Chirila, G.A. Boni, D.G. Popescu, C.M. Istrate, M.A. Husanu, L.D. Filip, C. Besleaga, L. Pintilie, A. Dimoulas, *Ferroelectric $Hf_{0.5}Zr_{0.5}O_2$ thin films on TiN/Si substrates grown by pulsed laser deposition at CMOS-compatible temperatures*, Ceramics International 51 (2025) 50941–50950.

Cation distribution and its magnetic implications in gadolinium-iron garnets for an enhanced control of compensation temperature

C. Bartha, C. Locovei, A. Alexandru-Dinu, M.A. Grigoroscuţă, A. Kuncser, N. Iacob, M. Galaţanu, A. Leca, P. Badică, V. Kuncser

National Institute of Materials Physics, 077125, Măgurele, Romania

Recent research in spintronic ultrafast spin storage devices have increasingly focused on ferrimagnetic rare-earth iron garnets with magnetization compensation properties. Among them, $Gd_3Fe_5O_{12}$ (gadolinium iron garnet) is considered a promising candidate due to its high compensation temperature (θ_c). Values of θ_c are between 286 and 295 K, *i.e.*, the highest among the rare-earth garnets. For practical applications, obtaining materials with θ_c near room-temperature is essential. All functional key spintronic characteristics, including the magneto-electric or magneto-optic control of the garnet systems are optimal around θ_c, hence understanding of the underlaying physics controlling θ_c is of paramount importance.

This work presents an in-depth analysis of the stoichiometry of $Gd_3Fe_5O_{12}$ synthesized by two distinct routes and its influence on the magnetic configurations and compensation temperatures, promoting various magneto-functionalities [1]. The complex study was carried out using a complex approach combining X-ray diffraction (XRD), magnetometry, and Mössbauer spectroscopy. The main results obtained by the mentioned methods showing the correlations between the effective magnetic structures and the corresponding compensation temperatures are presented in *Fig. 1*.

The proposed materials were obtained by: (*i*) an original processing route that combines a cheap and facile surfactant assisted hydrothermal method to prepare mesoporous garnet nano-powders followed by sintering, and (*ii*) solid state reaction.

Rietveld refinement of the XRD patterns confirmed that both analyzed samples consist exclusively of garnet phases with different stoichiometries deviating from the ideal composition. The ideal structure of a rare-earth iron garnet type ($RE_3Fe_5O_{12}$) is cubic, with two iron cations on the octahedral positions and three iron cations on the tetrahedral positions, the three RE cations being on the dodecahedral position according to the formula unit: $RE_3^{3+}Fe_2^{3+}Fe_3^{3+}O_{12}$ [2]. The changes in stoichiometry are due to the presence of small cationic inversions, as well as to defects, both generated by processing technologies.

Atomic-scale analysis supported mainly by Mössbauer spectroscopy revealed with unprecedent accuracy a cationic inversion between Fe^{3+} and Gd^{3+} at octahedral and dodecahedral sites in both samples, and their chemical compositions were determined as $Gd_{2.70}Fe_{4.76}O_{11.9}$ and $Gd_{2.96}Fe_{4.68}O_{11.5}$, respectively. Accordingly, local electronic and magnetic configurations investigated by temperature dependent Mössbauer Spectroscopy (see right side of *Fig. 1*) showed the presence of three different Fe positions, instead of the two specific positions assigned to an ideal garnet structure. Therefore, the three well-resolved sextet components observed in the 6 K Mössbauer spectra of both samples are assigned, based on their specific hyperfine parameters, to Fe^{3+} ions occupying distinct crystallographic sites: (*i*) the octahedral sites, (*ii*) the tetrahedral sites typical of the garnet structure, and (*iii*) a more distorted configuration involving seven oxygen neighbors, corresponding to Fe cations substituting at the dodecahedral Gd sites. The relative spectral areas of the sextet components at low temperature were consistent with Fe^{3+} populations of 31% in the octahedral sites and 60% in the tetrahedral sites for the garnet synthesized by the hydrothermal method, and 26% in the octahedral sites and 64% in the tetrahedral sites for the garnet obtained by the solid-state method. In both cases, the relative spectral area of the less intense sextet supports a fraction of approximately 9% of Fe ions occupying the Gd sites, in excellent agreement with the optimal compositional model obtained from the Rietveld refinement. Based on Mössbauer data, the magnetic moments per formula units (in μB) were calculated for both samples at low temperatures where magnetic relaxation effects are negligible, by using also the saturation magnetization values collected from the hysteresis loops at 5 K. The values obtained were 14.57 μB for $Gd_3Fe_5O_{12}$ obtained by hydrothermal method and 15.98 μB for $Gd_3Fe_5O_{12}$ synthetized by solid state reaction. Both magnetic moments are smaller than the theoretical value of 16 μB, but they

are consistent with the structures (chemical composition and atomic positions) determined through Rietveld analysis.

Hysteresis loops at different temperatures revealed that both samples exhibit significant ferrimagnetic behaviour at low temperatures. As the temperature increased up to 300 K, the saturation magnetization values decreased rapidly, due to thermal fluctuations that change the effective magnetic moments and coupling strength. The saturation magnetization values at low temperatures (5 K) are consistent with those reported in previous studies [3], *i.e.*, 94.5 emu/g for $Gd_3Fe_5O_{12}$ synthesized *via* solid-state reaction and 90.15 emu/g for $Gd_3Fe_5O_{12}$ obtained by the hydrothermal method. Again, the corresponding magnetic moments calculated for both samples are in good agreement with those calculated from the Mössbauer data, *i.e.*, 15.46 μB for the solid-state reaction sample and 14.08 μB for the hydrothermal sample.

Both ZFC-FC curves showed a relatively high magnetization at low temperatures where magnetic ordering of Gd^{3+} sublattice occurs. The compensation temperatures vary considerably. The $Gd3Fe5O_{12}$ synthesized by hydrothermal method had a θ_c of 290 K. The garnet produced through the solid-state reaction exhibited a 27 K increase in θ_c due to a higher occupancy of the dodecahedral Gd positions and consequently stronger Fe-Gd interactions.

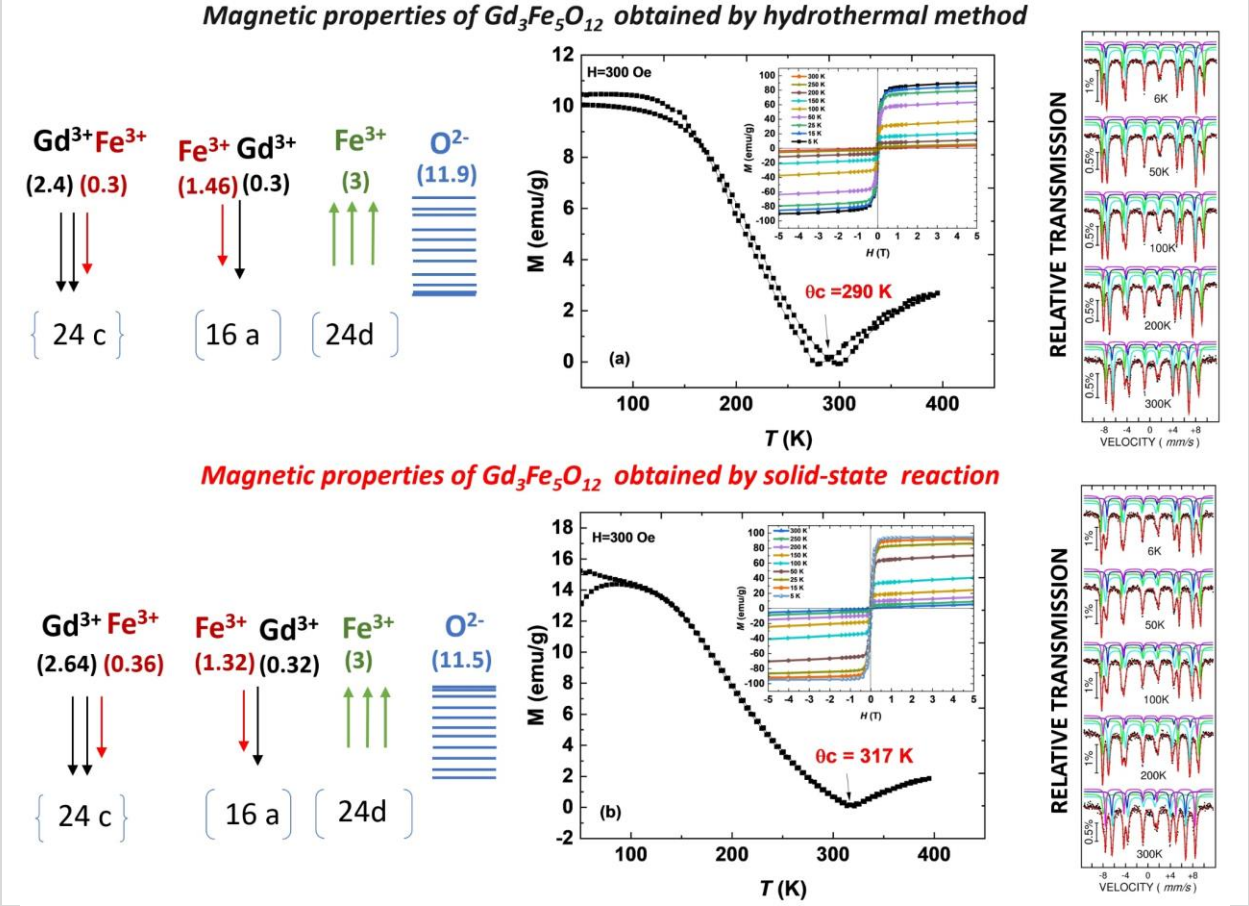

Figure 1: *Magnetic structures of the two garnets prepared by different synthesis routes, as determined from accurate structural and magnetic refinements. The ZFC-FC magnetization curves recorded under a magnetic field of 300 Oe, together with the hysteresis loops measured at different temperatures, are also shown. The Mössbauer spectra collected at various temperatures, providing direct evidence for the cation occupancy per formula unit shown on the left side. The less intense third sextet (about 9% relative area) in the low-temperature Mössbauer spectra offers direct support for Fe^{3+} cations on the dodecahedral sites, which are typically occupied by Gd^{3+} ions. Adapted from Ref. [1].*

Our results demonstrated that internal substitutions involving cation inversions, where iron ions migrate from the octahedral sites to the gadolinium (dodecahedral) positions and *vice versa*, are of paramount importance and exhibit the strongest dependence on the preparation method. Therefore, even for a fixed stoichiometry, due to different atomic arrangements leading to a different distribution of Fe–Fe and Fe–Gd magnetic couplings, compensation temperature changes significantly and this takes

place in the room-temperature range. The impact is remarkably high, promoting extended possibilities of design towards customizable advanced spintronic applications.

References:

[1] **C. Bartha, C. Locovei, A. Alexandru- Dinu, M.A. Grigoroscuta, A. Kuncser, N. Iacob, M. Galatanu, A. Leca, P. Badica, V. Kuncser, *Cation distribution and its magnetic implications in gadolinium-iron garnets for an enhanced control of compensation temperature*, Physical Chemistry Chemical Physics 27 (2025) 22894–22900.**

[2] S. Geller, *Crystal chemistry of the garnets*, Zeitschrift für Kristallographie – Crystalline Materials 125 (1967) 1–6.

[3] J. Sultana, J. Mohapatra, P.J. Liu, S.R. Mishra, *Structural, magnetic, and magnetocaloric properties of chromium doped $Gd_3Fe_{5-x}Cr_xO_{12}$ garnet compound*, AIP Advances 13 (2023) 025252.

Enhanced terahertz emission in ultrathin spintronic trilayers

E.Th. Papaioannou[1,2,3], C. Locovei[1], G. Torosyan[4], L. Scheuer[3], G.P. Dimitrakopulos[2], S. Kret[5], A.D. Crişan[1], R. Beigang[6], T. Kehagias[2], O. Crişan[1]

1) *National Institute of Materials Physics, 077125, Măgurele, Romania*
2) *Department of Physics, Aristotle University of Thessaloniki, 54124, Thessaloniki, Greece*
3) *Department of Physics and Research Center OPTIMAS Rheinland-Pfälzische Technische Universität Kaiserslautern-Landau, 67663, Kaiserslautern, Germany*
4) *Department of Electrical and Computer Engineering and Research Centre OPTIMAS, Rheinland-Pfälzische Technische Universität Kaiserslautern-Landau, 67663, Kaiserslautern, Germany*
5) *Institute of Physics Polish Academy of Sciences, 02-668, Warsaw, Poland*
6) *Department of Physics, Rheinland-Pfälzische Technische Universität Kaiserslautern-Landau, 67663, Kaiserslautern, Germany*

Recent advancements in ultrafast spin physics have catalysed the development of spintronic terahertz (THz) emitters (STEs). These devices, composed of ultrathin heterostructures of ferromagnetic (FM) and non-magnetic (NM) layers, convert spin currents into THz radiation through the inverse spin Hall effect (ISHE). The study explores optimizing this efficiency by engineering trilayer configurations that utilize novel alloy phases and specific non-magnetic material combinations.

Two distinct fabrication techniques are involved to achieve high-quality ultrathin interfaces. The magnetron co-sputtering deposition with direct current sources was used to fabricate Fe/L10-FePt/Pt heterostructures on MgO <001> substrates. This allowed for precise control over the L10-FePt alloy phase thickness with very low roughness over a large surface. The electron-beam evaporation technique was employed for preparation of ultrathin Ta/Fe/Pt trilayers in an ultrahigh vacuum (UHV) environment. Substrates were cleaned via annealing at 650 °C and plasma-etching to ensure high crystallinity.

Structural characterization revealed successfully grown tetragonal L10-FePt and fcc Pt phases with epitaxial growth on the MgO substrate (*Fig. 1*). Bragg lines attributable to the bcc Fe are not detected in either sample, regardless of the Fe thickness of the two samples (1.5 and 4 nm, respectively).

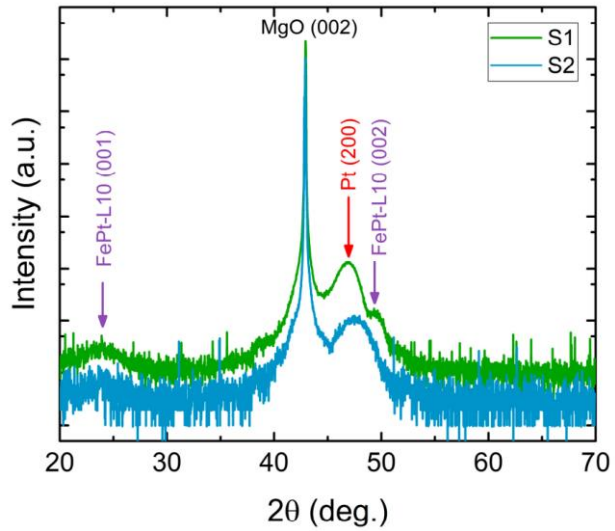

***Figure 1**: X-ray diffraction measurements of the S1:Fe(1.5)/FePt(2)/Pt(2) and S2:Fe(4)/FePt(2)/Pt(2) epitaxial nanosystems. Reproduced from Ref. [1].*

THz time-domain spectroscopy revealed that the Fe/L10-FePt/Pt configuration is superior to standard Fe/Pt bilayers. The emission amplitude of the optimized sample (S1) surpassed the reference Fe/Pt

bilayer by a factor of 1.44 (*Fig. 2*). It seems that the magnetic hardening of the Fe (4 nm)/L10-FePt (2nm)/Pt (2nm) that is attributed to the stronger coupling between Fe(4) and L10-FePt(2) does not facilitate the spin current transparency of the L10-FePt/Pt interface.

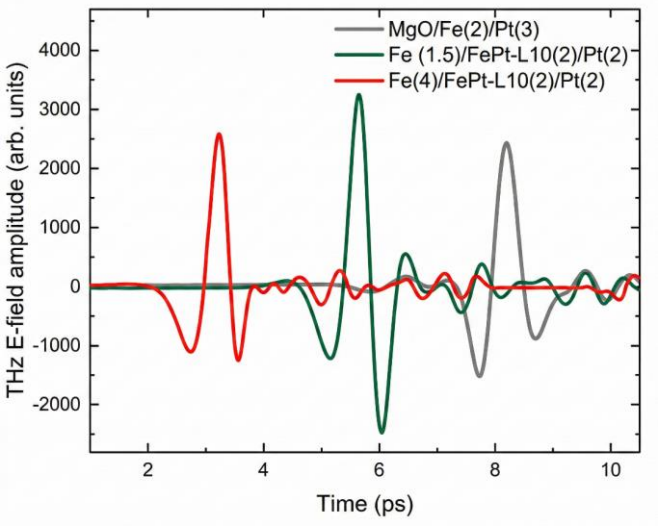

Figure 2: *THz E-field amplitude emission from the two Fe/L10 -FePt/Pt samples (S1 and S2) as well as the emission from a reference MgO/Fe(2)/Pt(3) bilayer. Reproduced from Ref. [1].*

In Ta/Fe/Pt trilayers, the tantalum layer was found to crystallize in a high-resistivity fcc phase rather than the expected bcc phase. This allotropic phase, combined with the use of NM layers with opposite spin Hall angles, leads to constructive interference of the emitted THz pulses (*Fig. 3*). THz emission was highly sensitive to layer thickness. For the Ta/Fe/Pt system, the maximum signal was achieved with a total NM thickness of approximately 3 nm, specifically in the Ta(1.5nm)/Fe(2nm)/Pt(2nm) configuration.

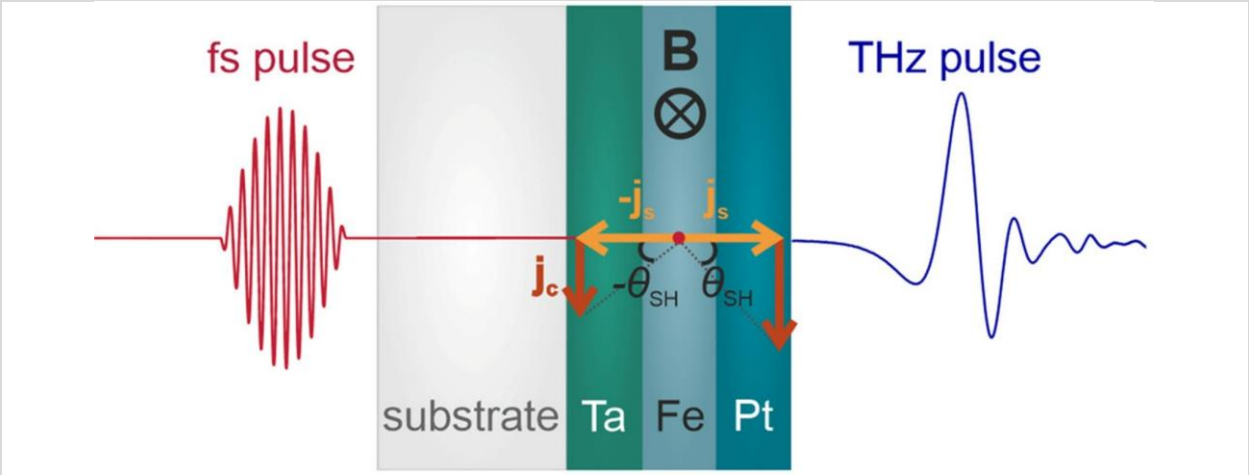

Figure 3: *Schematic of the best geometrical arrangement for the highest THz emission strength based on trilayer structures where the ferromagnetic (FM) Fe layer lies between two non-magnetic (NM) layers NM1/FM/NM2. Here, the NM1:Ta and NM2:Pt layers have opposite signs of their spin Hall angles. The opposite spin Hall angles and the opposite direction of the spin current entering the two layers results in the emission of two THz pulses of the same phase that can constructively add. Reproduced from Ref. [2].*

The STEM-EDXS analysis of the Ta/Fe/Pt trilayers revealed that elemental interdiffusion was a critical factor in the structural and optical performance of the emitter (*Fig. 4*). Intermixing is particularly pronounced at the Fe/Pt interface compared to the Ta/Fe interface, as was also observed in the Fe/FePt/Pt epitaxial nanosystems. This chemical diffusion is intrinsically linked to the THz emission efficiency as it governs the transparency of the interfaces to spin current. The build-up of oxygen at the

MgO substrate surface, likely due to the out-diffusion of Mg species during high-temperature growth, facilitates in this case the formation of the high-resistivity allotropic fcc-Ta phase. This specific phase, combined with the controlled interdiffusion that maintains a low total thickness of the non-magnetic materials, is identified as a key factor in achieving the significantly enhanced THz signal observed in these optimized trilayer configurations.

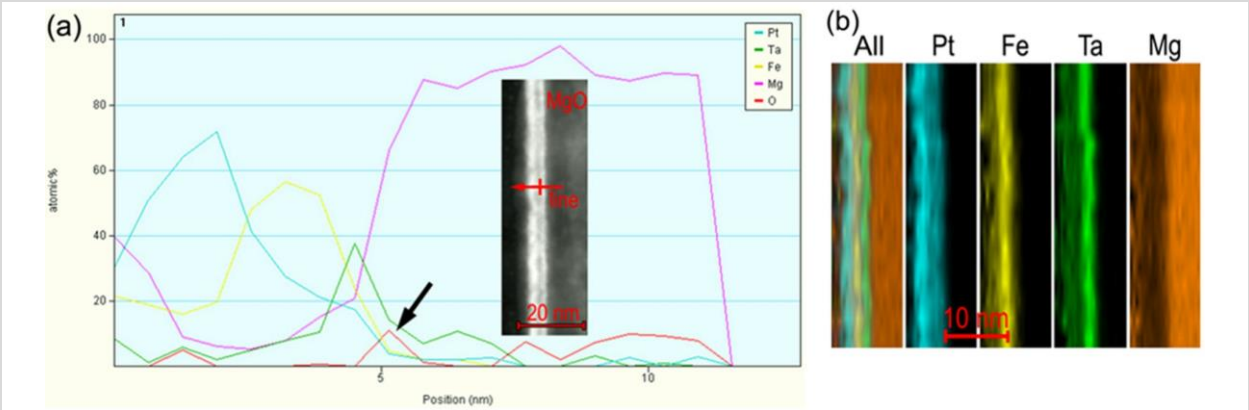

***Figure 4**: (**a**) EDXS line profile along the growth direction of the STEM image shown in the inset, depicting the interdiffusion of element species among interfaces of the trilayer. The arrow denotes the buildup of oxygen (red line) toward the surface of the MgO substrate. (**b**) Corresponding EDXS elemental maps illustrating the interdiffusion of elements and showing the full covering of MgO by the Ta layer. Reproduced from Ref. [2].*

References:

[1] C. Locovei, G. Torosyan, E.Th. Papaioannou, A.D. Crisan, R. Beigang, O. Crisan, *Structural, magnetic and THz emission properties of ultrathin Fe/L10-FePt/Pt heterostructures*, Nanomaterials 15 (2025) 1099.

[2] E.Th. Papaioannou, L. Scheuer, G. Torosyan, G. P. Dimitrakopulos, S. Kret, A.D. Crisan, O. Crisan, R. Beigang, T. Kehagias, *Enhanced THz emission from ultrathin Ta/Fe/Pt spintronic trilayers*, Advanced Optical Materials 13 (2025) e00874.

[3] M. Battiato, K. Carva, P.M. Oppeneer, *Theory of laser-induced ultrafast super diffusive spin transport in layered heterostructures*, Physical Review B 86(2012) 024404.

[4] G. Torosyan, S. Keller, L. Scheuer, R. Beigang, E.T. Papaioannou, *Optimized spintronic terahertz emitters based on epitaxial grown Fe/Pt layer structures*, Scientific Reports,8 (2018) 1311.

Surface spin asymmetry, natural multiferroicity and permanent inversion of population in (001) barium titanate

L.E. Borcan[1,2], A.-C. Iancu[1,2], N.G. Apostol[1], A. Nicolaev[1], C.M. Teodorescu[1]

1) *National Institute of Materials Physics, 077125, Măgurele, Romania*
2) *Faculty of Physics, University of Bucharest, 077125, Măgurele, Romania*

Barium titanate is one of the firstly discovered ferroelectrics and it still stimulates excitement in the community of ferroic physics. One of the sources of this excitement stems in the possibility to induce ferromagnetic ordering in the ferroelectric barium titanate, thus rendering it multiferroic [1]. In this contribution, we prove that ultraclean, well-prepared (001) barium titanate thin films possess a sizable spin asymmetry at least in their surface layers.

The experiments were performed in the CoSMoS (combined spectroscopy and microscopy on surfaces) setup connected to the SuperESCA beamline at the Elettra storage ring facility, which operates in low 10^{-10} hPa vacuum. $BaTiO_3$(001) thin films are grown on 0.5 % Nb-doped $SrTiO_3$(001) (STON) by pulsed laser deposition (PLD) in a Surface setup, using a KrF laser (248 nm wavelength) with repetition rate 5 Hz and laser fluence 1.5 J/cm^2. The substrate was heated at 970 K and the partial O_2 pressure was 14 Pa. After deposition, the sample was cooled down in a rich O_2 atmosphere, 0.1 MPa, with a rate of 10 K/min. The film was characterized by X-ray diffraction and X-ray reflectivity, yielding in-plane lattice constants identical to that of the substrate (Nb-doped strontium titanate), *i.e.*, 3.905 Å. The out-of-plane lattice constant is 4.121 Å, yielding a clear tetragonal structure, while the film thickness is derived as 12.5 nm [2]. The $BaTiO_3$(001) thin film was then introduced in the CoSMoS setup and cleaned by annealing in oxygen (5×10^{-7} hPa) to remove surface carbon. The maximum sample temperature reached was 1054 K, as measured with an optical pyrometer. During the annealing, time-resolved X-ray photoelectron spectra (XPS) were used to follow-up the carbon contamination. When the C 1s peak disappeared, the annealing was stopped and the sample was cooled down for about 10 minutes in 2×10^{-6} hPa oxygen. LEED images and XPS core-levels measurements were then recorded. These results are represented in *Fig. 1*. The Ba 4d (*Fig. 1a*) and O 1s (*Fig. 1c*) spectra present two components, ascribed to surface and bulk atoms, with the surface component shifted towards higher binding energies, due to both the different ionic environment and to the ferroelectric polarization. The Ti 2p spectrum (*Fig. 1b*) is simulated with a single component, thus no surface titanium is detected. This implies a single BaO termination of the film. This is further confirmed by LEED images recorded at different electron energies, where no spot extinction was detected (*Fig. 1f*): spot extinction at some energies would have been a sign of destructive interference of electrons diffracted on successive layers. In a different experiment with ultrafast XPS while heating the sample, it was derived that the ferroelectric polarization is oriented outwards, since above the Curie temperature all core level shift towards lower binding energies [2]. XPS data analysis revealed also a good stoichiometry of the barium titanate, about $BaTiO_{2.9}$, therefore with a detectable amount of oxygen vacancies. In summary, the $BaTiO_3$(001) film is perfectly clamped to the Nb:$SrTiO_3$(001) substrate, has a well-defined tetragonal structure, almost perfect surface stoichiometry, BaO termination and its polarization is oriented outwards.

The stabilization of the ferroelectric polarization is realized by accumulation of surface charges [3]. If the surface charges are positive, then one might expect that the surface Ba and O atoms feature incomplete shells of valence electrons (*i.e.*, O 2p and Ba 5p). In this case, one might expect uncompensated spins for these shells, which could become ferromagnetically ordered. Indeed, spin-resolved photoelectron spectroscopy evidenced that phenomenon, as it is clear from *Fig. 2a–c* [4]. The sample was *in situ* magnetized by using either a permanent magnet or an electromagnet with applied field in the range of 40 Am^{-1} in the (001) surface plane, roughly in the [110] direction. Different magnetization geometries yielded different spin asymmetry signals; also, the signal was shown to increase in time with the sample cooling down, which is also a sign of a permanent ferromagnetism. In conclusion, the BaO surface is magnetic and there are incomplete O 2p and Ba 5p shells.

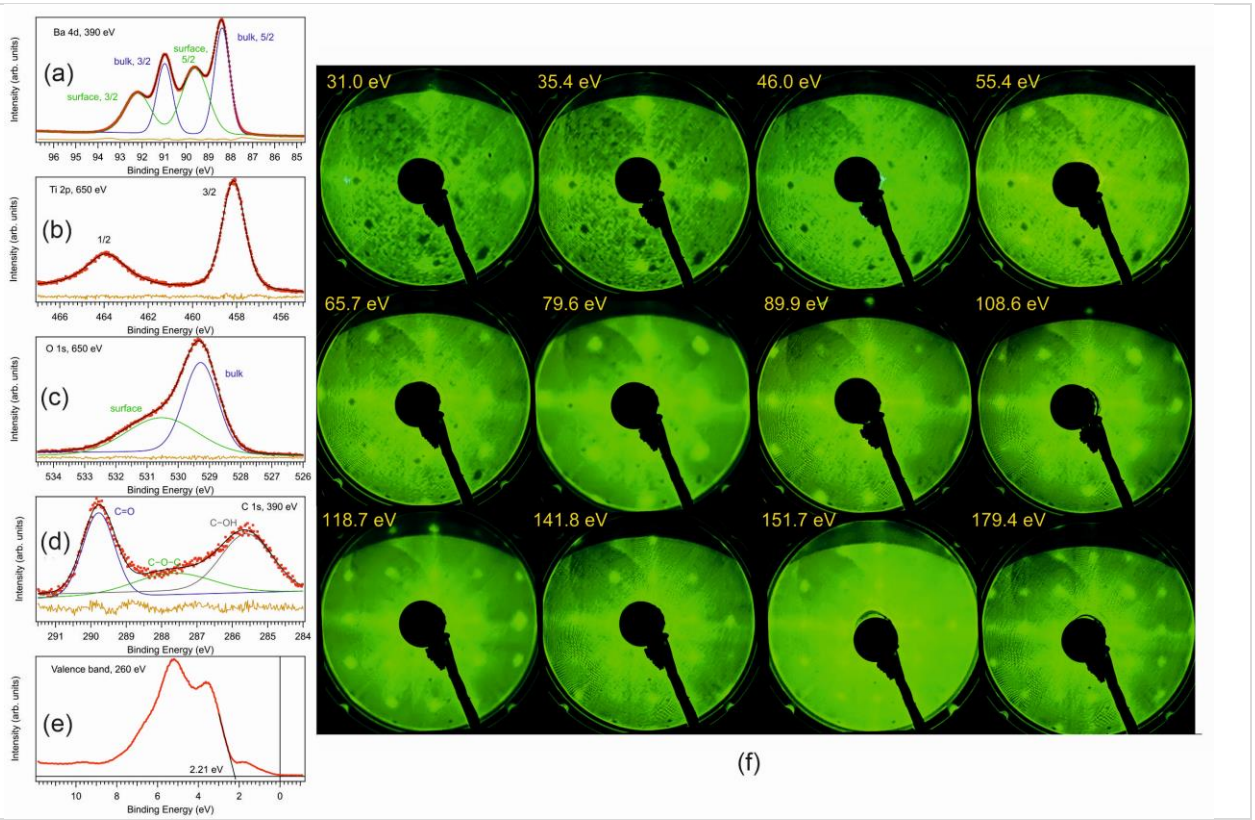

Figure 1: *Characterization of $BaTiO_3$(001) by X-ray photoelectron spectroscopy (XPS) and low energy electron diffraction (LEED). (**a**) Ba 4d high-resolution core-level spectrum; (**b**) Ti 2p high-resolution core level spectrum; (**c**) O 1s high resolution core level spectrum; (**d**) C 1s high-resolution core level spectrum; (**e**) valence band spectrum. (**f**) LEED images, taken at different incident electron energies, specified on each image. Adapted from Ref. [4].*

The fact that there are detected holes in the Ba 5p states which are situated at higher binding energies than filled O 2p states is counter-intuitive and might be regarded as a 'permanent inversion of population'. In fact, such phenomenon is possible due to the high degree of localization of these states, on barium or oxygen surface atoms, respectively. A detailed computation presented in Ref. [4] which takes into account chemical shifts due to the different ionization states of surface Ba and O, together with deviations in the crystal field at the two different atomic sites at the surface yielded to the conclusion that if some positive charge Q is distributed on a surface BaO unit cell, the most favourable situation is an almost equal share of this charge on surface barium and oxygen atoms (*Fig. 2d, e*). Thus, the O 2p and Ba 5p shells are both incomplete and give rise to the detected spin asymmetry in both states.

Apart for the discovery of surface multiferroicity of ultraclean barium titanate, the results obtained in this work are interesting since they suggest that the occurrence of holes in Ba 5p states, situated below occupied O 2p states, are intrinsically related to the surface charge accumulation, *i.e.*, to the ferroelectricity [3]. In these conditions, one might expect that when the ferroelectric polarization is switched, these holes will disappear, most probably by electron-hole recombination. There are big chances that this electron-hole recombination is radiative, hence photons in the extreme ultraviolet (EUV) range would be emitted (about 10 eV photon energy). This opens the possibility to design versatile EUV sources of use, *e.g.*, for deep UV lithography controlled electrically, by the ferroelectric polarization, or even magnetically, given the fact that there is an intrinsic coupling between long range magnetic order and ferroelectricity.

The article reporting this study (Ref. [4]) is highlighted on the back cover of the Materials Advances journal.

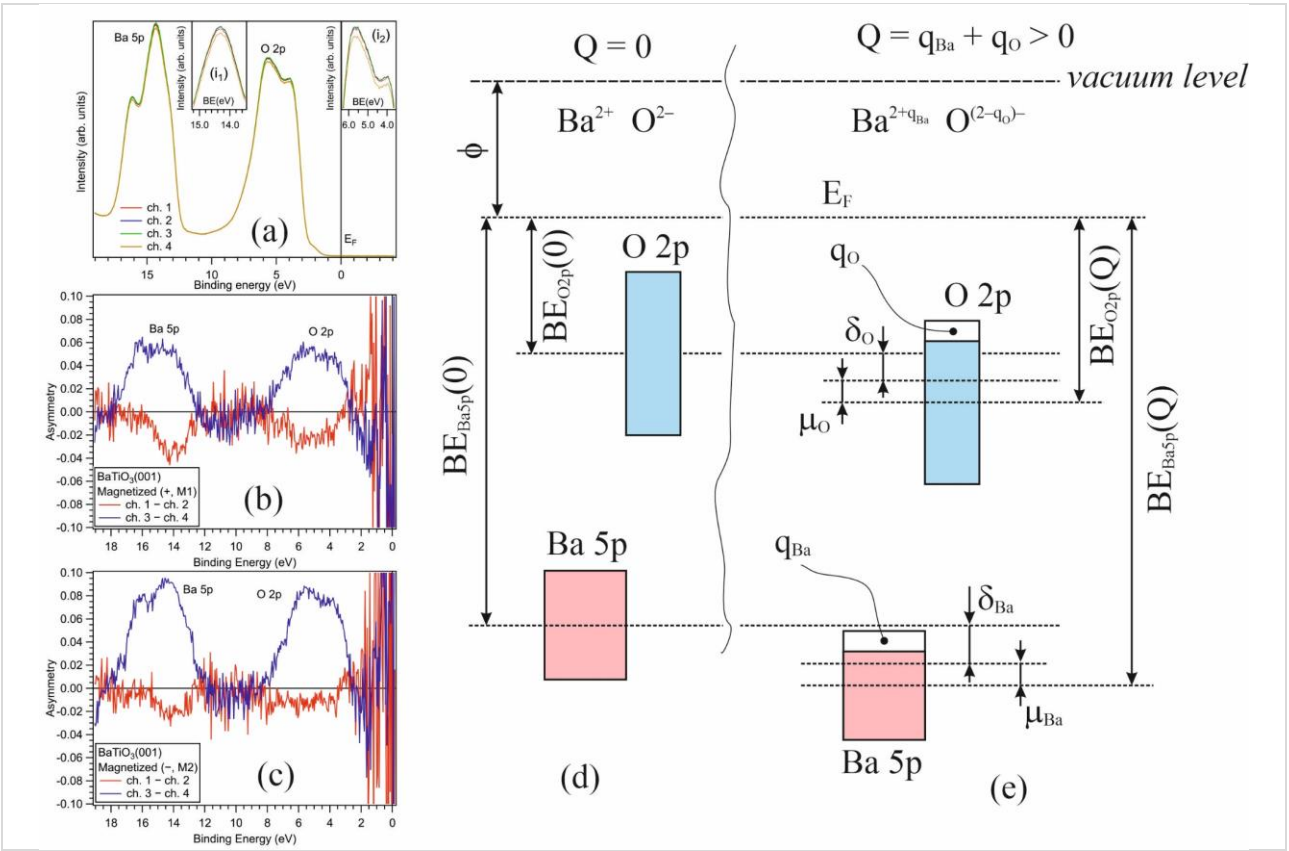

***Figure 2**: (**a**) Spin-resolved valence band photoelectron spectra of $SrTiO_3$(011). (**b,c**) Spin asymmetries between horizontally-oriented spins (red curve) and vertically-oriented spins (blue curve) for two different magnetizations of the sample. (**d**) Schematics of the O 2p and Ba 2p energy levels in a neutral paraelectric sample. (**e**) Schematics of the energy levels in a charged surface BaO layer of a ferroelectric sample. q are charges on the surface atoms, δ are chemical shifts and μ values of the crystal field. Adapted from Ref. [4].*

References:

[1] S. Valencia, A. Crassous, L. Bocher, V. Garcia, X. Moya, R.O. Cherifi, C. Deranlot, K. Bouzehouane, S. Fusil, A. Zobelli, A. Gloter, N.D. Mathur, A. Gaupp, R. Abrudan, F. Radu, A. Barthélémy, M. Bibes, *Interface-induced room-temperature multiferroicity in $BaTiO_3$*, Nature Materials 10 (2011) 753–758.

[2] A.-C. Iancu, N.G. Apostol, A. Nicolaev, L.E. Abramiuc, C.F. Chirilă, D.G. Popescu, C.M. Teodorescu, *Molecular adsorption–desorption of carbon monoxide on ferroelectric $BaTiO_3$(001)*, Materials Advances 5 (2024) 5709–5723.

[3] C.M. Teodorescu, *Ferroelectricity in thin films driven by charges accumulated at interfaces*, Physical Chemistry Chemical Physics 23 (2021) 4085–4093.

[4] **L.E. Borcan, A.-C. Iancu, N.G. Apostol, A. Nicolaev, C.M. Teodorescu, *Surface spin asymmetry of O 2p and Ba 5p states in $BaTiO_3$(001)*, Materials Advances 6 (2025) 8907–8920.**

Surface spin asymmetry in (001) and (011) strontium titanate

L.E. Borcan[1,2], A.-C. Iancu[1,2], D.G. Popescu[1], A. Nicolaev[1], R.M. Costescu[1], G.A. Lungu[1], C.A. Tache[1], M.A. Huşanu[1], C.M. Teodorescu[1]

1) *National Institute of Materials Physics, 077125, Măgurele, Romania*
2) *Faculty of Physics, University of Bucharest, 077125, Măgurele, Romania*

Strontium titanate is sometimes called "the silicon of future oxide electronics", since it is the most convenient template for the growth of perovskites thin films with ferroelectric, pyroelectric, multiferroic or even superconductor characteristics. However, this substrate features more fascinating properties when compared with silicon. Some of these properties are related to magnetism [1], spin asymmetry or two-dimensional electron gas stabilized at the surface [2]. There was a sound controversy as to whether the two-dimensional electron gas at $SrTiO_3$(001) surface exhibits or not a 'giant' spin asymmetry [3–5]. During the last two years, our team has investigated by spin-resolved photoelectron spectroscopy not only the valence states close to the Fermi level, but also the deeper valence states originating from O 2p orbitals [6,7]. A non-vanishing and sometimes consistent spin asymmetry of these states was detected and will be discussed in this contribution.

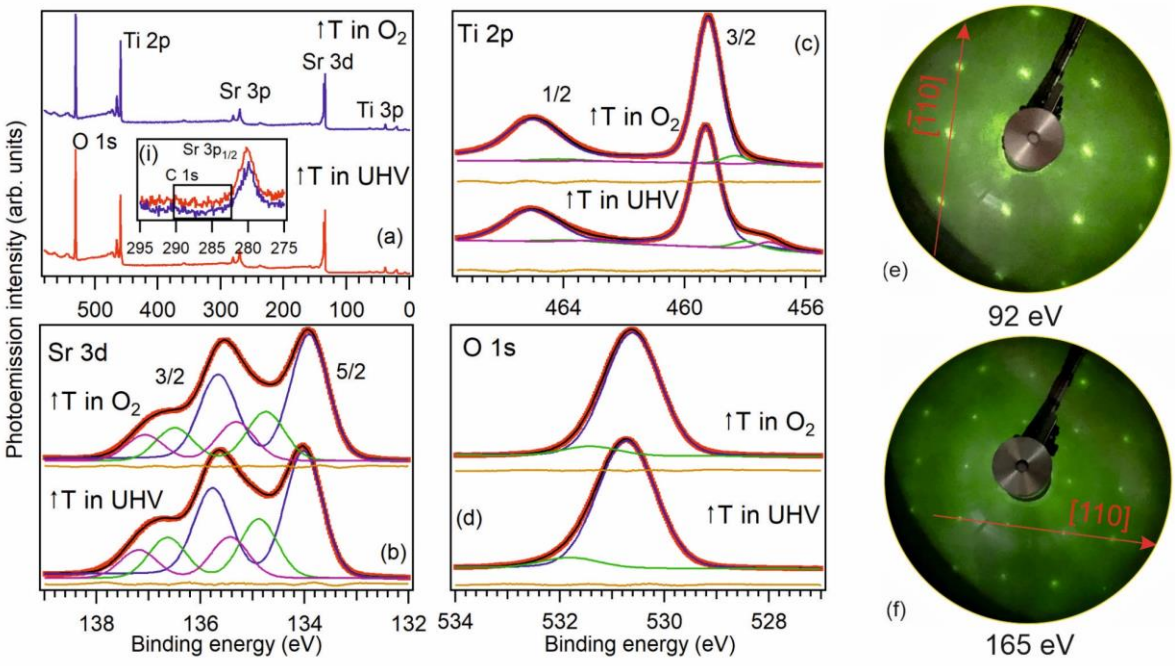

***Figure 1**: Characterization of $SrTiO_3$(001) by X-ray photoelectron spectroscopy (XPS) and low energy electron diffraction (LEED). (**a**) XPS survey spectra; (**b**) Sr 3d high-resolution core level spectra; (**c**) Ti 2p high-resolution core level spectra: (**d**) O 1s high resolution core level spectra of $SrTiO_3$(001) annealed in ultrahigh vacuum or in oxygen. (**e,f**) LEED patterns obtained at two kinetic energies of incident electrons. Adapted from Ref. [6].*

The experiments were performed by using the CoSMoS (combined spectroscopy and microscopy of surfaces) endstation connected to the SuperEsca beamline at the Elettra synchrotron radiation facility. $SrTiO_3$(001) and $SrTiO_3$(011) single crystals (CrysTec) are prepared in ultrahigh vacuum (UHV) conditions up to the removal of any contaminants, as follows: (*a*) for $SrTiO_3$(001) by sputtering with 2 keV Ar^+ ions (10 + 10 minutes from two opposite grazing directions, 10 μA ion current) and annealing at 1100 K for 30 minutes, then by annealing further in oxygen (5×10^{-7} hPa, 30 minutes, 1100 K), followed by cooling down for about 1 hour in 10^{-6} hPa oxygen. (*b*) $SrTiO_3$(011) single crystals are degassed up to 1000 K, then sputtered with 2 keV Ar^+ ions, 13 μA ion current (5 + 5 minutes from two opposite grazing directions) and annealed in ultrahigh vacuum in several steps, the most severe being at 1200 K for 15 minutes. The temperature is measured with an optical pyrometer. During the annealing step, time resolved XPS spectra allowed one to quantify the carbon contamination, and this was

negligible in all cases. X-ray photoelectron spectroscopy (XPS) and low energy electron diffraction (LEED) patterns confirmed the absence of contaminants and the good crystal structure of these surfaces (*Figs. 1, 2*). One can notice that for $SrTiO_3$(001) two kind of surface preparations were performed, with or without final annealing in oxygen atmosphere. The main differences between the two preparations is the presence of the Ti^{3+} component (*Fig. 1c*) and of in-gap states with binding energy of around 1 eV [6] for samples prepared just by sputtering and annealing in UHV, without further annealing in oxygen. The $SrTiO_3$(001) surfaces showed a very weak Ti^{3+} contribution (*Fig. 2d*) and there was a very weak signal of in-gap states in the valence band (*Fig. 2i$_b$*).

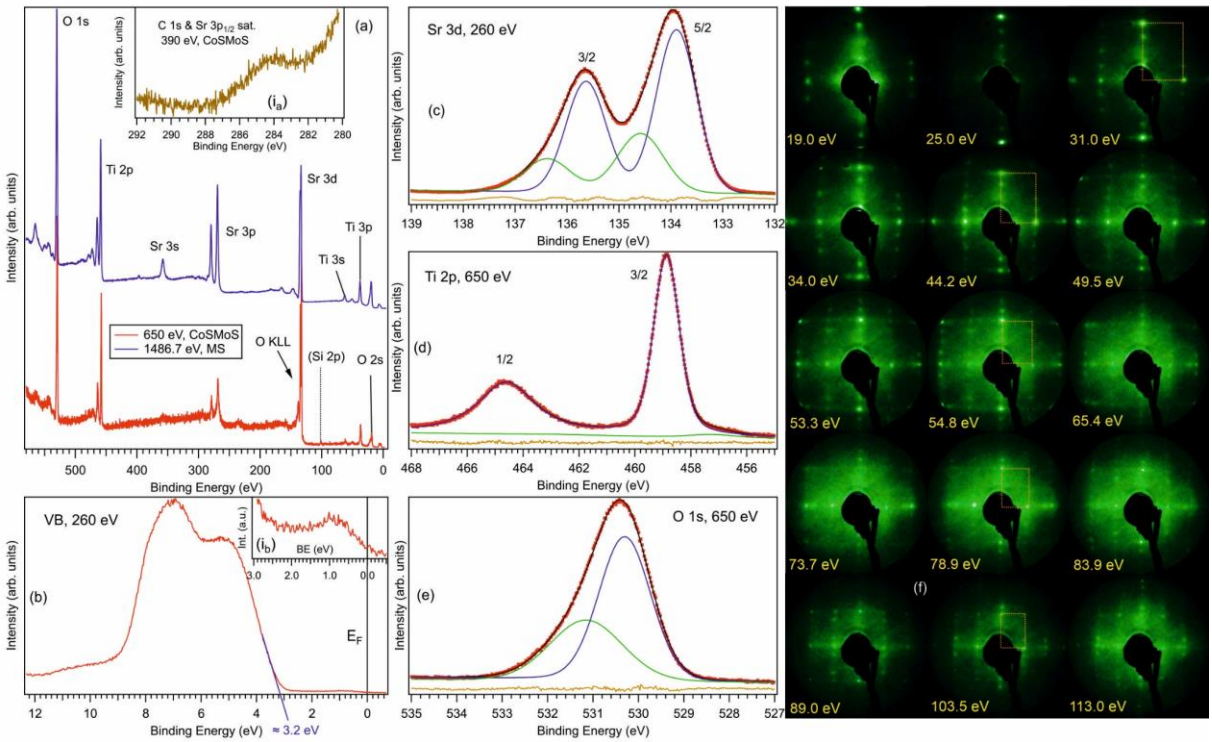

***Figure 2**: Characterization of $SrTiO_3$(011) by X-ray photoelectron spectroscopy (XPS) and low energy electron diffraction (LEED). (**a**) XPS survey spectra; (**b**) Valence band spectra; (**c**) Sr 3d high-resolution core level spectra; (**d**) Ti 2p high-resolution core level spectra; (**e**) O 1s high-resolution core level spectra; (**f**) LEED images, taken at different incident electron energies, specified on each image. Adapted from Ref. [7].*

Spin-resolved photoelectron spectroscopy was performed by using a 'mini-Mott' detector, where the detected electrons are accelerated at 25 keV kinetic energies, scattered on a Th target and detected at deflection angles of ±120° in two orthogonal planes. The detected spin asymmetries are in the plane orthogonal to the emission direction of the photoelectron. Photoelectrons are detected near normal emission (24° emission angle). The explored region from the reciprocal surface is slightly exceeding one surface Brillouin zone. Selected results are presented in *Fig. 3a,b*. The $SrTiO_3$(001) surface, when annealed in oxygen, did not show and detectable spin asymmetry. As soon as some oxygen vacancies are created, with some contribution of Ti^{3+} and presence of in-gap states, $SrTiO_3$(001) show a measurable sin asymmetry (dashed lines in *Fig. 3b*). Of the five scenarios proposed in Ref. [1], the Zener scenario of coupling of O 2p holes seems the most appropriate, especially if one supposes that the coupling is intermediated by the extended in-gap states.

The case of $SrTiO_3$(011) is slightly different. First of all, the spin asymmetry shown by this surface exceed largely that of $SrTiO_3$(001), see *Fig. 3b*. This crystal orientation supposes the alternance of charged planes $SrTiO^{(4+)}$ and $O_2^{(4-)}$, as represented in *Fig. 3c,d*. Such an alternance of planes would imply a divergence of the potential energy felt by one electron, see *Fig. 3e*. The solution to avoid this divergence is to admit an 'electronic reconstruction' at the surface, for instance O^{2-}terminated surfaces should have a charge of $^{(2-)}$ instead of $^{(4-)}$, see *Fig. 3f*. In this case, each oxygen from the surface is simply negatively charged, with electronic configuration 2p5 and therefore it should have a net spin (*Fig. 3g*). These spins order ferromagnetically and yield the high spin asymmetry signal that we detected.

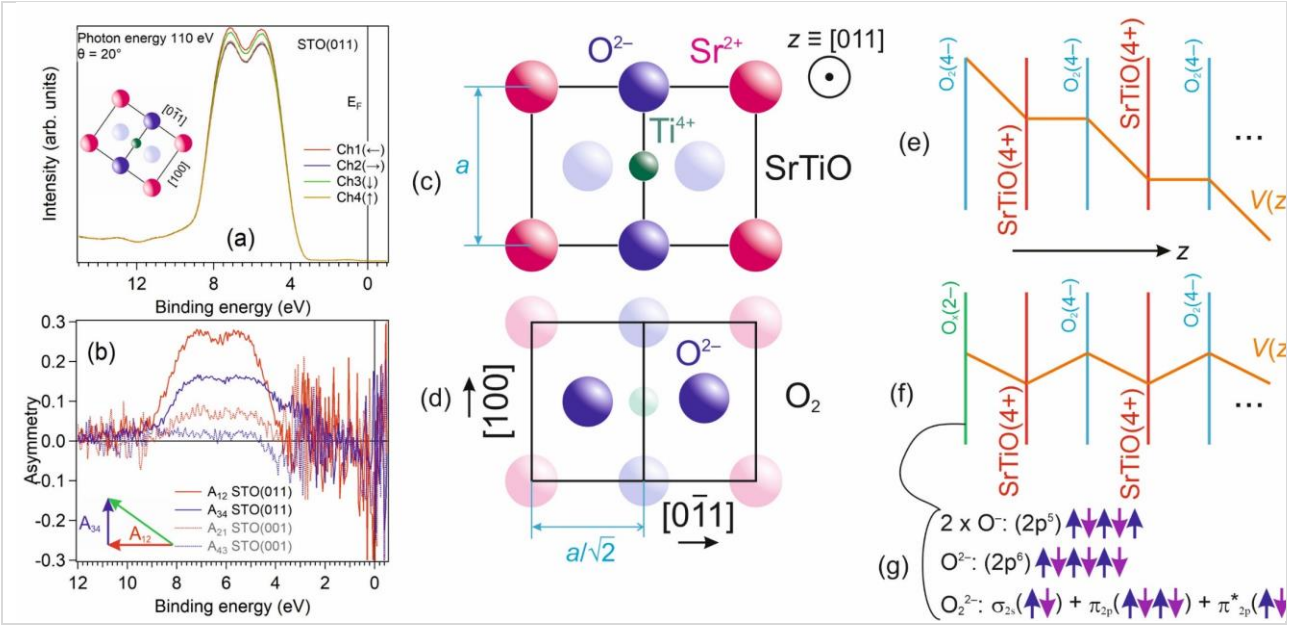

***Figure 3**: (**a**) Spin-resolved valence band photoelectron spectra of $SrTiO_3$(011). The orientation of the detected spins by the four detection channels is represented, together with the sample orientation during the measurement. (**b**) Spin asymmetry signals for $SrTiO_3$(011) – full lines – and for $SrTiO_3$(001). (**c,d**) Sketches of SrTiO and O_2 planes. (**e**) Potential energy variation in the case of an alternance $O_2(^{4-})/SrTiO(^{4+})/O_2(^{4-})/...$ (**f**) Potential energy variation for the case of a surface electronic reconstruction such as $O_2(^{2-})/SrTiO(^{4+})/O_2(^{4-})/...$ (**g**) Possible electronic configurations of the surface oxygens. Adapted from Ref. [7].*

References:

[1] J.M.D. Coey, M. Venkasetan, P. Stamenov, *Surface magnetism of strontium titanate*, Journal of Physics: Condensed Matter 28 (2016) 485001.

[2] A.F. Santander-Syro, O. Copie, T. Kondo, F. Fortuna, S. Pailhès, R. Weht, X.G. Qui, F. Bertran, A. Nicolaou, A. Taleb-Ibrahimi, P. Le Fèvre, G. Herranz, M. Bibes, N. Reyren, Y. Apertet, P. Lecoeur, A. Barthélémy, M.J. Rozenberg, Two-dimensional electron gas with universal subbands at the surface of $SrTiO_3$, Nature 469 (2011) 189–193.

[3] A.F. Santander-Syro, F. Fortuna, C. Bareille, T.C. Rödel, G. Landolt, N.C. Plumb, J.H. Dil, M. Radović, *Giant spin splitting of the two-dimensional electron gas at the surface of $SrTiO_3$*, Nature Materials 13 (2014) 1085–1090.

[4] S. McKeown Walker, S. Riccò, F.Y. Bruno, A. de la Torre, A. Tamai, E. Golias, A. Varykhalov, D. Marchenko, M. Hoesch, M.S. Bahramy, P.D.C. King, J. Sánchez-Barriga, F. Baumberger, *Absence of giant spin splitting in the two-dimensional electron liquid at the surface of $SrTiO_3$(001)*, Physical Review B 93 (2016) 245143.

[5] E.B. Guedes, S. Muff, M. Fanciulli, A.P. Weber, M. Caputo, Z.M. Wang, N.C. Plumb, M. Radović, J.H. Dil, *Single spin-polarized Fermi surface in $SrTiO_3$ thin films*, Physical Review Research 2 (2020) 033173.

[6] D.G. Popescu, A. Nicolaev, R.M. Costescu, L.E. Borcan, G.A. Lungu, C.A. Tache, M.A. Huşanu, C.M. Teodorescu, Spin asymmetry of O 2p–related states in $SrTiO_3$(001), Physica Scripta 99 (2024) 105925.

[7] L.E. Borcan, A.-C. Iancu, D.G. Popescu, C.M. Teodorescu, *Considerable spin asymmetry of deep valence states induced by partial neutralization of charged $SrTiO_3$(011) surfaces*, Journal of Chemical Physics 162 (2025) 054707.

Surface spin asymmetry in Pt(001)

L.E. Borcan[1,2], C.M. Teodorescu[1], A.-C. Iancu[1,2], N.G. Apostol[1], A. Nicolaev[1], R.M. Costescu[1], M.A. Huşanu[1], D.G. Popescu[1], G.A. Lungu[1], M. Bianchi[3]

1) *National Institute of Materials Physics, 077125, Măgurele, Romania*
2) *Faculty of Physics, University of Bucharest, 077125, Măgurele, Romania*
3) *Elettra Sincrotrone Trieste, 34149, Basovizza, Trieste, Italy*

The model of band ferromagnetism is probably the most convenient explanation of this phenomenon for metals. The Stoner model (1938) compares the energy variation between the ferromagnetic and the paramagnetic state due to the reduction of the overall Coulomb repulsion energy when electrons with opposite spins occupy the same atomic site with the kinetic energy increase when electrons are transferred from the sub-band of minority spin towards the sub-band of majority spin. It follows $g(\varepsilon_F)U > 1$, where $g(\varepsilon_F)$ is the one-electron (paramagnetic) density of states (DOS) at the Fermi level and U is the Coulomb repulsion term (the Hubbard parameter). The main drawback of the Stoner model stems in its inability to predict Curie temperatures. Recently, another criterion was proposed in Ref. [1], by considering that the Fermi level should be the same for majority and minority spin electrons, just the bottoms of the sub-bands are shifted. Based on the observation that the total (kinetic + potential) energy should be taken into account and not only the kinetic energy, it follows that for a constant DOS, without any Hubbard stabilization term, the ferromagnetic state has lower energy than the paramagnetic one. The fact that not all metals are ferromagnetic is in fact related to the shape of the DOS. By computing the total electronic energies in the ferromagnetic and in the paramagnetic state, one ends up with a criterion written as:

$$\left(\frac{dg}{d\varepsilon}\right)_{\varepsilon_F} \int_{\varepsilon_{min.}}^{\varepsilon_F} g(\varepsilon)d\varepsilon \leq g^2(\varepsilon_F) \qquad (1)$$

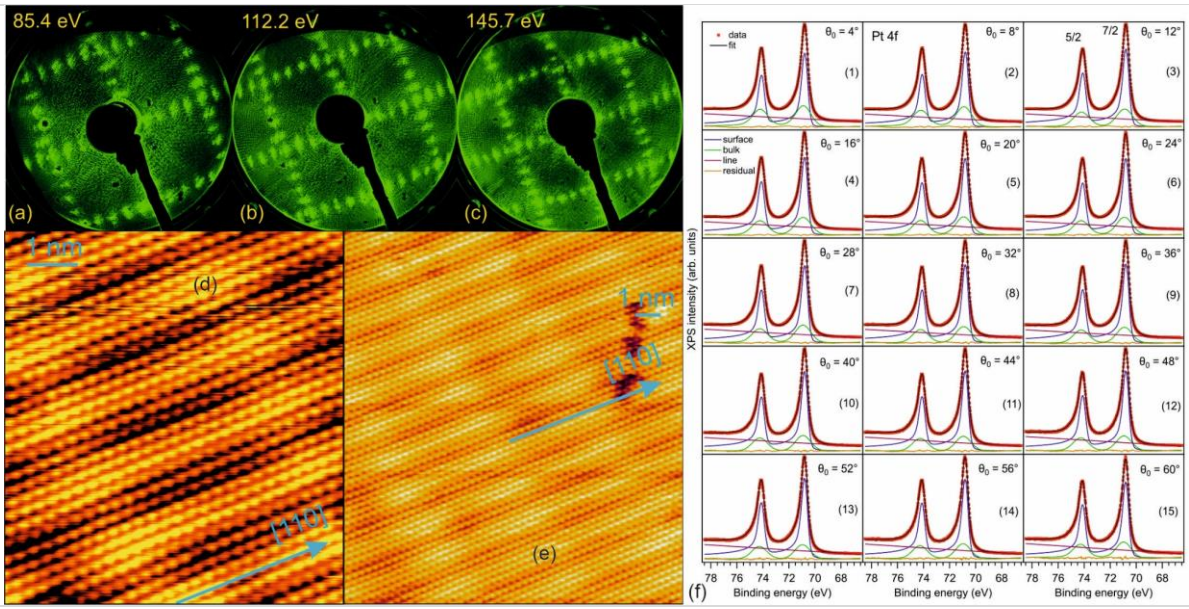

***Figure 1**: Characterization of Pt(001)–hex by (**a,b,c**) low energy electron diffraction (LEED), (**d,e**) scanning tunnelling microscopy (STM), and (**f**) high-resolution X-ray photoelectron spectroscopy (XPS) at different emission angles. Adapted from Ref. [4].*

where $\varepsilon_{min.}$ is the minimum energy for the paramagnetic DOS. Metals where the Fermi levels lie on the descending part of the DOS $(dg/d\varepsilon)_{\varepsilon_F} \leq 0$ are supposed to feature spin asymmetry. This explains why ferromagnetism is manifested mostly by metals towards the end of the 3d series (Fe, Co, Ni). The model also computes reasonable Curie temperatures, explains the ferromagnetism of some metastable

systems and predicts re-entrant ferromagnetism at ultrahigh temperatures, a possible explanation for geomagnetism.

Checks of the validity of this criterion imply systems where the Fermi level is shifted from a region with positive derivative of the DOS towards regions with negative $(dg/d\varepsilon)_{\varepsilon_F}$. The Pt(001) system is a good candidate for that. It exhibits a hexagonal reconstruction [2] with a considerable larger atomic density at the surface, hence the electronic density increases, as was reported by the existence of a surface state in the Pt 4f photoemission spectrum at lower binding energy [3]. Thus, this system will be used to check the validity of the Stoner criterion or of criterion given by *eq. (1)*. This was reported for the first time in Ref. [4].

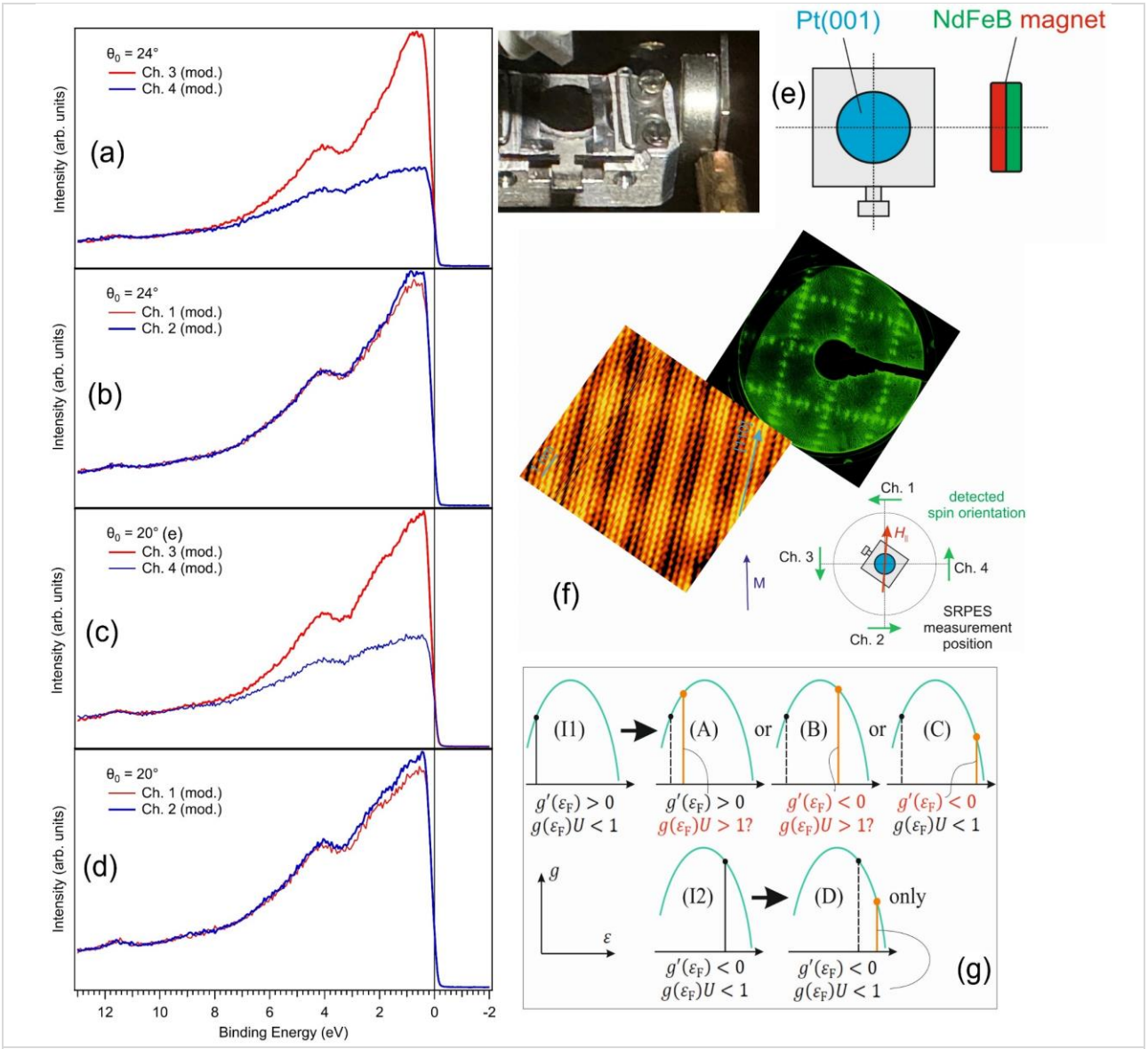

***Figure 2**: (**a–d**) Spin-resolved valence band photoelectron spectra of Pt(001)–hex. The spectra are represented for Channels 1 and 2 in (**a,c**) (horizontal spins – see (**f**)) and Channels 3 and 4 in (**b,d**) (vertical spins). Two emission angles were investigated, 24° for (**a,b**) and 20° for (**c,d**). (**e**) In-situ magnetization geometry (photograph and schematics). (**f**) Sample orientation during spin-resolved measurements, with LEED and STM images rotated by the corresponding azimuthal angle. (**g**) Simplified view of the lowest binding energy region of the density of states, with several scenarios related to electron accumulation near surface and the corresponding consequences regarding the Stoner criterion or the new criterion proposed in Ref. [1]. Adapted from Ref. [4].*

The experiments were not trivial, since the Pt(001), after its preparation by sputtering and annealing firstly in oxygen, then in ultrahigh vacuum, is still rapidly contaminated (within a few hours) even in vacuum of 10^{-10} hPa. The experiments were performed in the CoSMoS (combined spectroscopy and microscopy on surfaces) setup connected to the SuperESCA beamline at the Elettra storage ring facility.

The cluster features a photoemission chamber with high resolution X-ray photoelectron spectroscopy of core levels and spin-resolved photoelectron spectroscopy of the valence band, a chamber with low energy electron diffraction (LEED) and a chamber dedicated to scanning tunnelling microscopy (STM). *Fig. 1* presents the result of the extensive surface characterization. LEED images show the existence of reconstruction spots (approximately 5 × 1 [2]), see *Fig. 1a–c*, while STM with atomic resolution features the corresponding atomic rows of the hex. reconstruction, see *Fig. 1d,e*. Pt 4f core level spectra show two components, one narrower at lower binding energy and higher intensity and one broader at higher binding energy, in line with the observations of Ref. [3]. In order to demonstrate that the narrower (and more intense) component is indeed due to Pt surface atoms, a series of spectra were performed at various emission angles, as shown in *Fig. 1f*. The analysis of the relative intensities evidenced that the peak at lower binding energy indeed belongs to Pt surface atoms [4].

Next, spin-resolved photoelectron spectra were recorded. The total amount of experiments implied several tens of series, extended over four one-week beamtimes at Elettra during three years. For each series, the sample was freshly prepared. An example of result obtained after *in situ* magnetization of the sample is represented in *Fig. 2a–d*, where the magnetization geometry is represented in *Fig. 2e* and the sample orientation during spin-resolved measurements is given in *Fig. 2f*. A clear spin asymmetry is recorded, mostly in the direction of the surface atomic rows. Consequently, the intended experiment was a success. Additionally, by taking into account several scenarios for the variation of the DOS at the Fermi level, as schematized in *Fig. 2g*, it follows that the most reasonable scenario to explain the occurrence of the spin asymmetry is (C), which supposes a shift of the Fermi level from the ascending towards the descending part of the DOS, while the value of the DOS at the Fermi level decreases, hence the criterion from Ref. [1] is to be applied and not the Stoner criterion.

Note also that experiments performed with no previously applied magnetic field on the sample still evidenced a spin asymmetry signal, although the LEED patterns suggest that domains with the rows of atoms oriented along [110] and [$1\bar{1}0$] directions coexist. Nevertheless, in that case the asymmetry between spin orientation in the horizontal and in the vertical directions is comparable.

In conclusion, this study, published in Ref. [4], evidenced the surface spin asymmetry of Pt(001)–hex., whose explanation is the electron accumulation near surface, as revealed by high-resolution photoelectron spectroscopy, with the most prominent spin asymmetry oriented in the direction of the atomic rows formed by the hexagonal reconstruction. This is the first clear experimental proof of the validity of the criterion proposed in Ref. [1] against the Stoner criterion.

References:

[1] C.M. Teodorescu, *Spin asymmetry originating from densities of states: Criterion for ferromagnetism, structures and magnetic properties of 3d metals from crystal field based DOSs*, Results in Physics 25 (2021) 104241.

[2] R. Hammer, K. Meinel, O. Krahn, W. Widdra, *Surface reconstruction of Pt(001) quantitatively revisited*, Physical Review B 94 (2016) 195406.

[3] A. Baraldi, E. Vesselli, L. Bianchettin, G. Comelli, S. Lizzit, L. Petaccia, S. de Gironcoli, A. Locatelli, T. Onur Mentes, L. Aballe, J. Weissenrieder, J.N. Andersen, *The (1×1) → hexagonal structural transition on Pt(100) studied by high-energy resolution core level photoemission*, Journal of Chemical Physics 127 (2007) 164702.

[4] L.E. Borcan, C.M. Teodorescu, A.-C. Iancu, N.G. Apostol, A. Nicolaev, R.M. Costescu, M.A. Huşanu, D.G. Popescu, G.A. Lungu, M. Bianchi, *Surface spin asymmetry in Pt(001)–hex induced by electron accumulation*, Journal of Physics: Materials 8 (2025) 035010.

Investigations on HfO_2/n-GaAs(110) interface prepared *in-situ* by oxide molecular beam epitaxy

C.C. Negrilă[1], C. Cotîrlan1, A.-C. Iancu[1,2], D.G. Popescu[1], C. Palade[1], L. Trupină[1]

1) *National Institute of Materials Physics, 077125, Măgurele, Romania*
2) *Faculty of Physics, University of Bucharest, 077125, Măgurele, Romania*

High k dielectrics manage to attract an increased interest of researchers due to the considerable application potential they bring to the electronics industry. The HfO_2/GaAs heterojunction combines the qualities of the dielectric material with the carrier mobility properties of GaAs, promising a high potential compared to the Si/SiO_2 interface. GaAs has an electron mobility couple times higher than that of Si, hence GaAs devices have much higher switching speeds and consequently they work at much higher frequencies [1]. Intensely studied recently, the HfO_2/GaAs heterojunction presents specific features such as the presence of chemical reactions at the interface, high density of interface traps, high densities of leakage currents. In obtaining such interfaces, the main factors that determine their quality are primarily the state of the semiconductor surface and the deposition technique itself. In this work, HfO_2 thin films were deposited on n-type GaAs substrates by Oxide-Molecular Beam Epitaxy (Oxide-MBE) method using Hf metallic flow in an oxidizing atmosphere of 10^{-6} mbar molecular oxygen. The Hf metallic flow was provided by an e-beam evaporator and a deposition rate of ~10 nm/hour was established. Heterojunctions with HfO_2 thin layers of 1 nm, 3 nm, 10 nm and 20 nm thickness were fabricated in a SPECS multimethod system (*Fig. 1*).

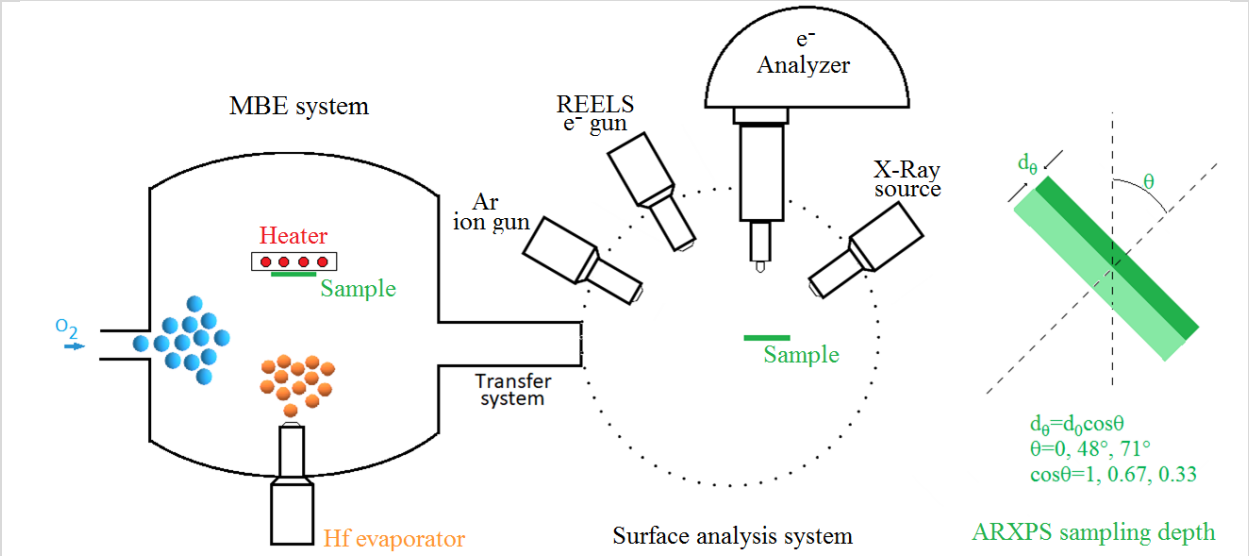

***Figure 1**: Facility for in-situ oxide-MBE deposition and characterization of HfO_2/GaAs heterojunctions. Reproduced from Ref. [2].*

The surface of n-GaAs (110) was prepared in two main steps – a wet chemical etching for 20 minutes in a solution of HF:H_2O 20%, followed by an *in-situ* stoichiometry adjustment by aggressive Ar ion etching. The ion etching removed the As capping and produced a stoichiometry close to the value of 1 but slightly in favour of Ga. The surface was subjected to HfO_2 layers deposition. In order to determine the chemical structure of the interface, a detailed ARXPS study was undertaken on the thinnest sample of 1 nm HfO_2/GaAs (*Fig. 2*). The XPS spectra and calculated values of Auger Parameters indicate a stable behaviour and the lack of chemical reactions between the GaAs substrate and the HfO_2 layer components [2].

The determination of the band structure of the HfO_2/GaAs interface was made by considering the Kraut method [3] corroborated with in-situ REELS measurements on thick layers of HfO_2 deposited on GaAs (*Fig. 3*). XPS measurements were performed on three types of surfaces: GaAs clean surface prior

deposition, thin HfO_2/GaAs interface, and thick layer of HfO_2/GaAs. Calculated band offsets of ΔE_C = 1.75 eV and ΔE_V = 2.62 eV confirmed a high application potential [2].

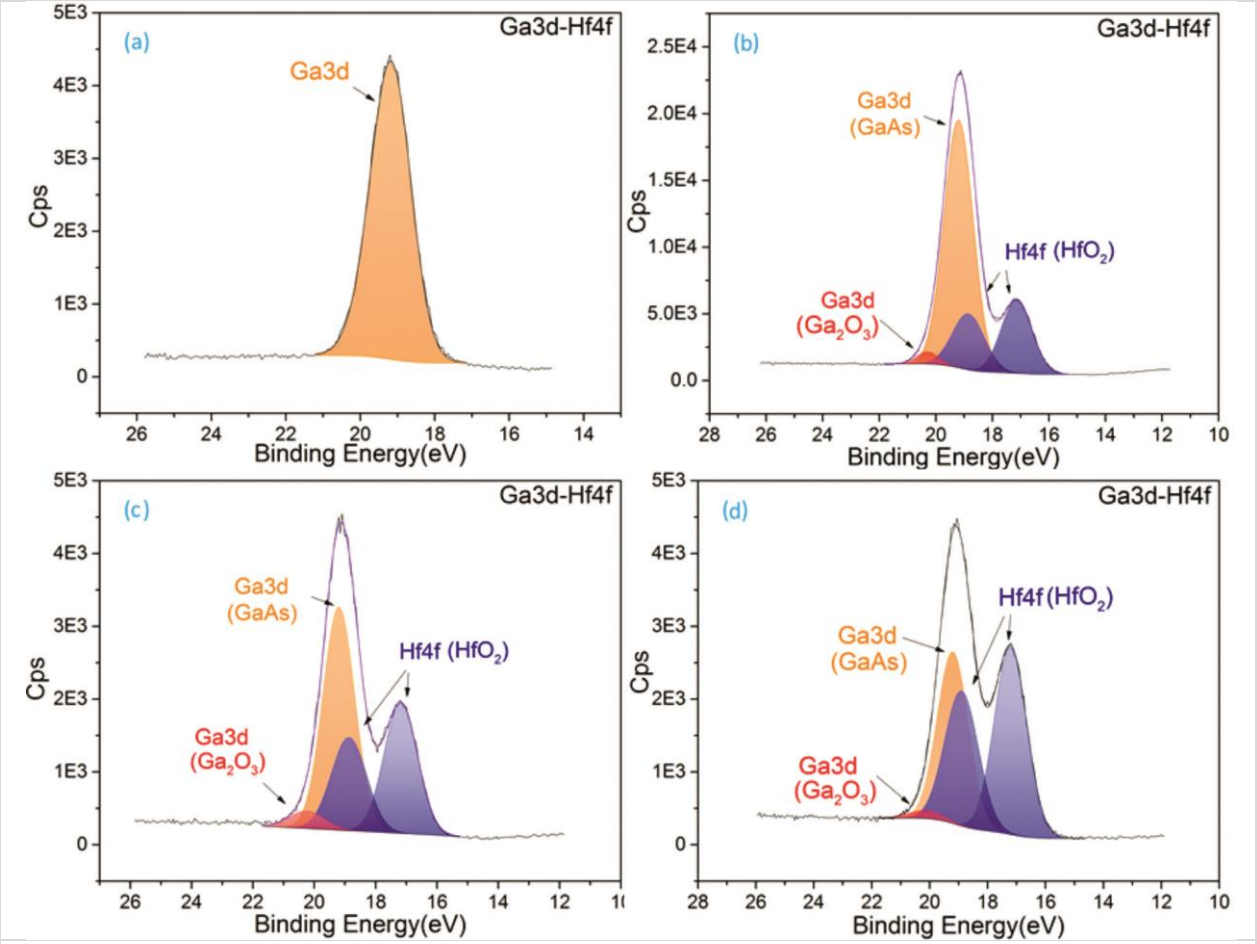

***Figure 2**: XPS spectra of Ga 3d-Hf 4f for (**a**) clean GaAs surface and (**b–d**) after deposition of 1 nm HfO_2 – measured at (**b**) 0°, (**c**) 48°, and (**d**) 71° emission angles. Reproduced from Ref. [2].*

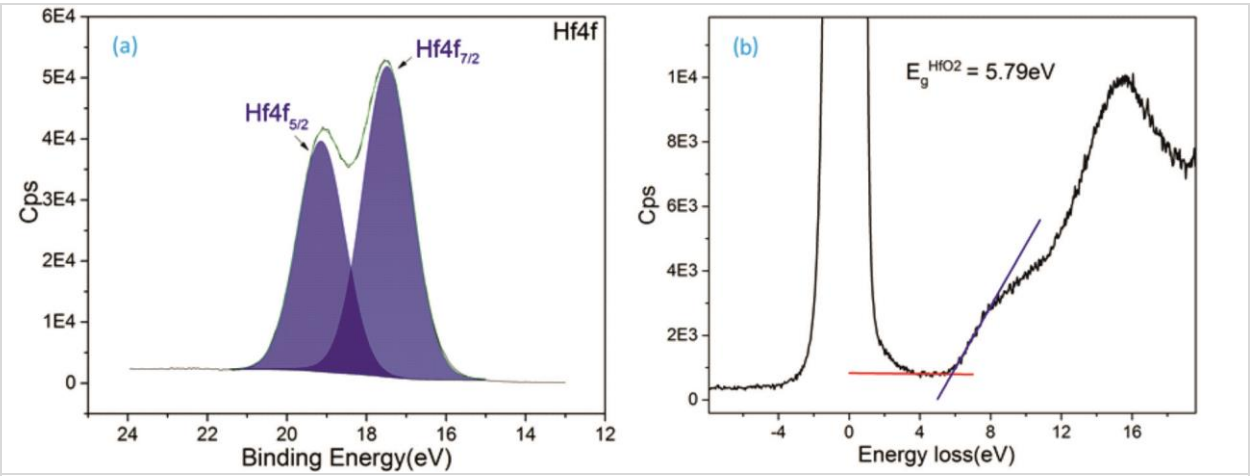

***Figure 3**: (**a**) XPS spectrum of Hf 4f and (**b**) REELS measurement on 20 nm thick HfO_2 layer. Reproduced from Ref. [2].*

The XRR, XRD, AFM, and XPS measurements simultaneously provided data on the structure of the deposited layers (*Fig. 4*). At low temperatures of GaAs substrate, HfO_2 deposition produces amorphous layers. XRD observations revealed the emergence of polycrystalline grains in the layer deposited on a substrate kept at more than 300 °C, hence this value served as a benchmark to avoid crossing. The XRR and AFM data showed a compact growth, starting from a smooth interface, without worsening the roughness towards the surface.

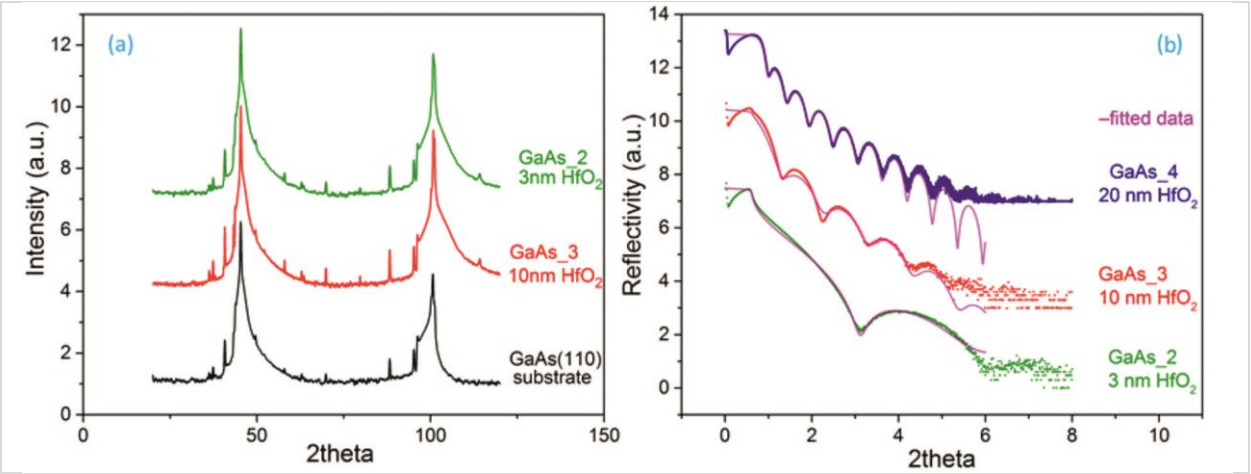

***Figure 4**: (**a**) XRD and (**b**) XRR patterns of GaAs samples. Reproduced from Ref. [2].*

C–V electrical measurements on MOS type capacitor devices allowed the determination of the dielectric constant k of the HfO_2 layers (*Fig. 5a*). The obtained values of k were in the range of 19–22 [2]. To further determine the defect density at the interface, room-temperature I–V characterizations were also performed on thick layers of HfO_2/GaAs. The interface was analysed considering the thermionic emission theory applied to a MIS Schottky type structure and the Cheung method for electrical parameters extraction (*Fig. 5b*). The measurements demonstrated the formation of an abrupt, highly stable interface with a minimal density of defect states [4].

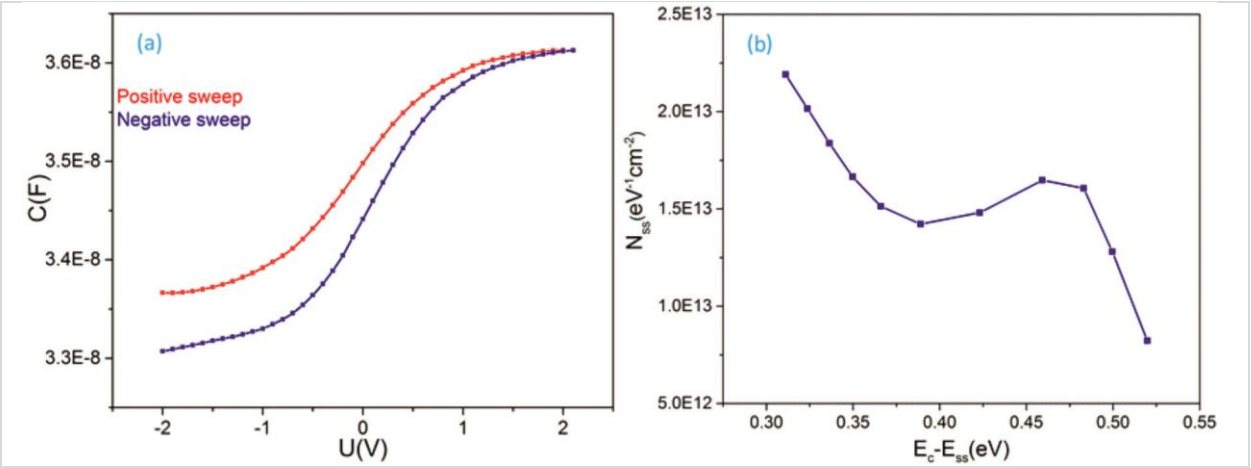

***Figure 5**: C–V characteristics at (**a**) 1MHz and (**b**) the density of interface states (N_{ss}) in the band gap for a 20 nm HfO_2/GaAs structure. Reproduced from Ref. [2].*

References:

[1] D.A. Usanov, A.E. Postelga, A.A. Kalyamin, I.V. Sharov, *Measurement of the charge-carrier mobility in gallium arsenide using a near-field microwave microscope by the microwave-magnetoresistance method*, Electronic Properties of Semiconductors 52 (2018) 1669–1671.

[2] C.C. Negrila, C. Cotirlan, A.-C. Iancu, D.G. Popescu, C. Palade, L. Trupina, *Investigations on HfO_2/n-GaAs(110) interface, in-situ obtained by Oxide-MBE*, Materials Science in Semiconductor Processing 198 (2025) 109746.

[3] E.A. Kraut, R.W. Grant, J.R. Waldrop, S.P. Kowalczyk, *Precise determination of the valence-band edge in X-ray photoemission spectra: Application to measurement of semiconductor interface potentials*, Physical Review Letters 44 (1980) 1620.

[4] W. Wang, K. Xiong, G. Lee, M. Hunag, R. Wallace, K. Cho, *Origin of HfO_2/GaAs interface states and interface passivation: A first principles study*, Applied Surface Science 256 (2010) 6569–6573.

Unravelling the crystallization mechanism and structural evolution of Yb/Er doped SiO_2-GdF_3 nano-glass ceramics

C.E. Secu, C. Bartha, M. Secu

National Institute of Materials Physics, 077125, Măgurele, Romania

Glassy nanocomposites where optically active nanocrystals are well dispersed within the amorphous matrix represent a novel class of nanostructured materials with high potential for various applications such as optical amplifiers, photovoltaic devices, scintillators, optical waveguides, optical refrigerator, and high-power white light-emitting diodes [1]. For the sol-gel derived glass ceramics, the main process is represented by the thermally activated chemical decomposition reaction of metal trifluoroacetates precursors followed by the precipitation and growth of nanocrystals [2]. Therefore, thermal behaviours that can be analysed through a complex thermal analysis, which can include TG-DSC measurements but also thermokinetic analysis.

The TG-DSC curves of the Yb^{3+}/Er^{3+}-doped SiO_2-GdF_3 xerogel co-doped with Li measured in synthetic air are shown in *Fig. 1*. The main process revealed by thermal analysis is the thermolysis of metal trifluoroacetate (M) revealed by a distinct exothermic DSC peak around 300 °C [3,4]; at higher heating rates, the crystallization maxima shift to higher temperatures, and their surface increase because faster heating leads to the production of higher number of crystals within the same time [4].

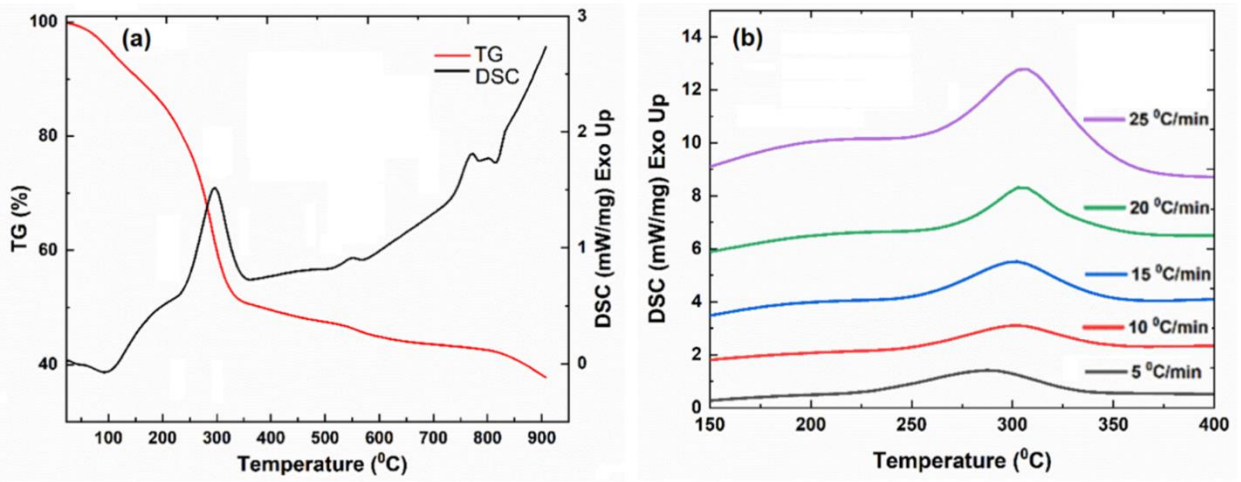

***Figure 1**: (**a**) TG-DSC curves of the Yb^{3+}/Er^{3+}-doped SiO_2-GdF_3 xerogel co-doped with Li measured in synthetic air with a heating rate of 10 °C/min and (**b**) crystallization peak highlighted at five different heating rates. Reproduced from Ref. [3].*

The XRD patterns analysis allowed to track the structural modifications during the annealing of the Yb^{3+}/Er^{3+}-doped SiO_2-GdF_3 xerogel (*Fig. 2*). The crystallization of the orthorhombic GdF_3 nanocrystals (ICDD-PDF no. 012-0788) can be observed in the 225 to 350 °C temperature range and agrees very well with the strong DSC peak at 300 °C. XRD pattern analysis of the glass-ceramic samples revealed a pronounced lattice relaxation effect compared to GdF_3, evidenced by a shift of the diffraction peaks toward higher angles [3,4]. This behavior was attributed to the incorporation of Li and Yb/Er ions into the lattice [5], along with a gradual increase in nanocrystal size up to approximately 40 nm.

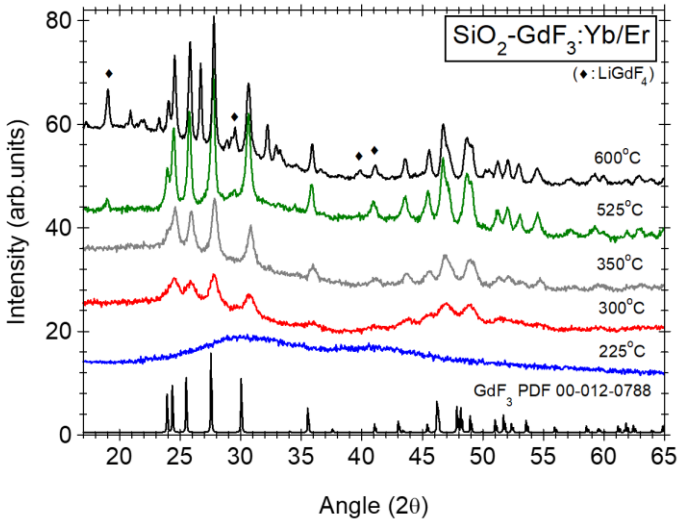

***Figure 2**: The XRD patterns recorded of GCLiYb/Er glass-ceramic samples after annealing at different temperatures. The XRD pattern of orthorhombic GdF_3 (ICDD-PDF no. 012–0788) is included. Reproduced from Ref. [3].*

The DSC curves recorded at different heating rates were analyzed and fitted using various reaction models with the Thermokinetics software. The Prout–Tompkins autocatalytic model provided the best description of the crystallization mechanism, in which the crystallization rate is governed by two principal factors: the degree of conversion and the presence of catalytic species. According to this model, the amorphous xerogel sample showed rapid self-accelerated crystallization, which occured due to the simultaneous formation of the Li-related metastable phases, as result of the thermal decomposition of metal trifluoroacetates at temperatures of around 300 °C. By lowering the activation energy, they facilitate the crystallization of the Yb^{3+}/Er^{3+}-doped SiO_2-GdF_3 phase, promoting rapid phase formation [3,4]. Furthermore, a reaction order value (n) greater than 1 (with n ≈ 1.57) suggests an accelerated nucleation and crystallite growth rate. This leads to a nonlinear increase in the crystallization rate, which can result in the formation of larger crystallites or rapid development of the crystalline phase.

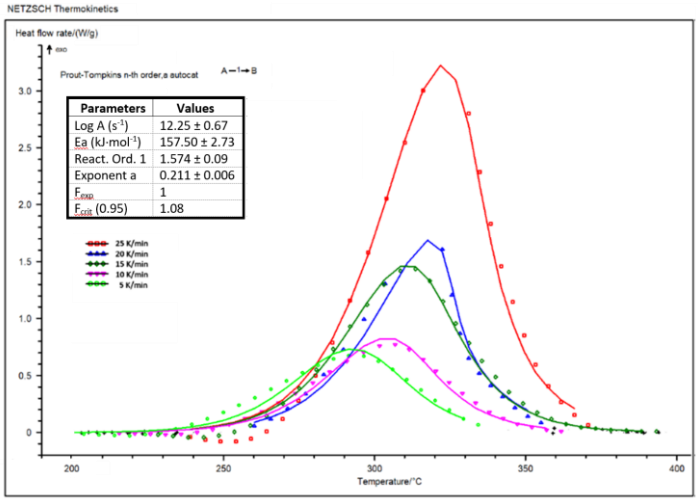

***Figure 3**: Experimental data recorded on Yb^{3+}/Er^{3+}-doped SiO_2-GdF_3 xerogel and the fitting curve of the 300 °C crystallization peak. The inset shows the kinetic model parameters. Reproduced from Ref. [3].*

We observed that Li-ions co-dopant influence is not limited only to the crystallization behaviour [5] but also on the up-conversion luminescence properties. Under 980 nm IR light pumping GCLiYb/Er glass-ceramic sample showed UC luminescence of Er^{3+} ions caused by the energy transfer Yb-Er within the GdF_3 nanocrystals (*Fig. 4*).

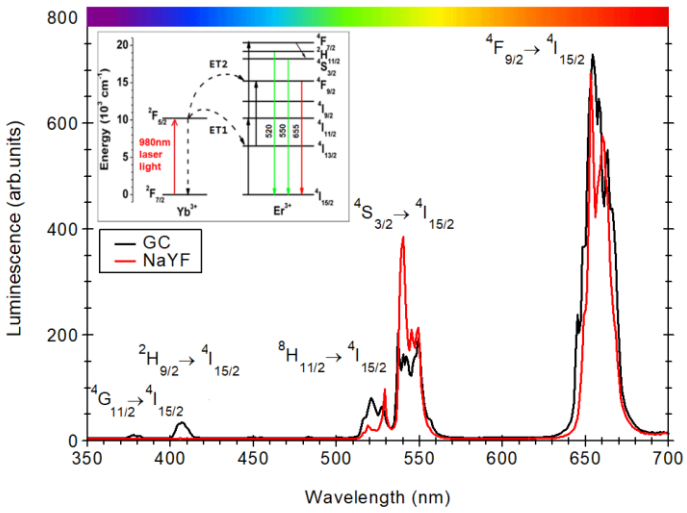

***Figure 4**: Normalized UC luminescence spectra recorded on GCLiYb/Er glass-ceramic and β-$NaYF_4$:18Yb/2Er polycrystalline powder recorded under 980 laser light pumping and the possible UC mechanism (inset). Reproduced from Ref. [3].*

The UC mechanism behind it has been extensively investigated in various host Yb^{3+}/Er^{3+} doped nanocrystalline materials and it relies on highly efficient IR light absorption by the Yb^{3+} ions at around 1000 nm ($^2F_{7/2} \rightarrow {}^2F_{5/2}$ transition). Higher energy Er^{3+} ions levels are feed by energy transfer (ET) process to neighbouring Yb^{3+} ions followed by its characteristic green (($^2H_{11/2}$, $^4S_{3/2}$) $\rightarrow {}^4I_{15/2}$) and red ($^4F_{9/2} \rightarrow {}^4I_{15/2}$) luminescence (inset). The substitutional Li^+ ions tailored the crystal field symmetry and altering the environment of Er^{3+} and led to an increase of the UC luminescence compared to undoped glass-ceramic [5].

For the quantitative measurement of absolute quantum yield QY of the up-conversion we used the method proposed in Ref. [6]. For comparison and verification, we measured a β-$NaYF_4$:18Yb/2Er polycrystalline powder, too. We obtained QY of 0.2±0.1% for GCLiYb/Er glass ceramic and 0.3±0.1% for the β-$NaYF_4$:18Yb/2Er that matches well with literature.

In conclusion, the crystallization mechanism of Yb/Er doped GdF_3 nanocrystals in silica nano-glass ceramics has been analysed by using model-free and model-fitting methods and thermal analysis data by correlation to the structural data. The formation of GdF_3 nanocrystals occurs at around 300 °C and their size is temperature dependent on the processing temperature. Model-free analysis showed an increase of both activation energy (E_a) and preexponential factor (log A) until the end of crystallization up to 175 kJ mol^{-1} and 14.8 s^{-1}, respectively. Model-fitting analysis indicated a crystallization process controlled by an autocatalytic-type reaction where a second metastable phase (LiF) is acting as a catalyst and facilitates a rapid and self-accelerated crystallization of the main GdF3 nanocrystalline phase. The ceramisation process boosted the UC luminescence up to values comparable to the $NaYF_4$:18Yb/2Er UC phosphor.

References:

[1] E.D. Zanotto, *A bright future for glass-ceramics*, American Ceramics Society Bulletin 89 (2010) 19–27.

[2] G. Gorni, J.J. Velázquez, J. Mosa, R. Balda, J. Fernández, A. Durán, Y. Castro, *Transparent glass-ceramics produced by sol-gel: A suitable alternative for photonic materials*, Materials 11 (2018) 212.

[3] **C.E. Secu, C. Bartha, M. Secu, *Unravelling the crystallization mechanism and structural evolution of Yb/Er-doped SiO_2-GdF_3 nano-glass ceramics*, Materials Advances 6 (2025) 5877–5883.**

[4] C.E. Secu, C. Bartha, C. Radu, M. Secu, *Crystallization processes of rare-earth doped GdF_3 nanocrystals in silicate glass matrix: Dimorphism and photoluminescence properties*, Ceramics International 20 (2024) 37518–37524.

[5] C. Secu, C. Bartha, C. Radu, M. Secu, *Up-conversion luminescence and magnetic properties of multifunctional Er^{3+}/Yb^{3+}-doped SiO_2-GdF_3/$LiGdF_4$ glass ceramics*, Magnetochemistry 9 (2023) 11.

[6] J.C. Boyer, F.C.J.M. van Veggel, *Absolute quantum yield measurements of colloidal $NaYF_4$: Er^{3+}, Yb^{3+} upconverting nanoparticles*, Nanoscale 2 (2010) 1417–1419.

Transfer-free fabrication of MoS_2/few-layer graphene lateral heterostructure memristors *via* confined sulfurization

C. Mihai, I.-D. Şimandan, F. Sava, T. Tite, A.E. Bocîrnea, M. Văduva, M.Y. Zaki, M. Baibarac, A. Velea

National Institute of Materials Physics, 077125, Măgurele, Romania

Two-dimensional (2D) semiconductor/conductor heterostructures are attractive building blocks for analogue memristors and neuromorphic computing hardware, because their switching characteristics can be engineered through interface-controlled charge trapping and defect dynamics. A key integration bottleneck is the formation of chemically clean van der Waals contacts over technologically relevant areas: conventional wet-transfer stacking typically leaves polymer residues that pin the Fermi level and broaden the device-to-device variability. We report a transfer-free and wafer-compatible route for centimetre-scale MoS_2/few-layer graphene (FLG) lateral heterostructures on SiO_2/Si, enabling direct evaluation of memristive behaviour in an in-plane electrode geometry [1]. The approach combined radio-frequency sputtering of an ultrathin amorphous MoS_2 precursor (≈0.8–1.0 nm) onto CVD FLG with a confined-space sulfurization step at 800 °C (graphite box, <30 mg sulphur), which crystallizes continuous 2H-MoS_2 while preserving the graphene layer (*Fig. 1*). Using a shadow mask during precursor deposition, the same coupon is partitioned into graphene-only, MoS_2-only, and overlap (MoS_2/graphene) regions, allowing same-wafer benchmarking of transport across each component and the heterointerface.

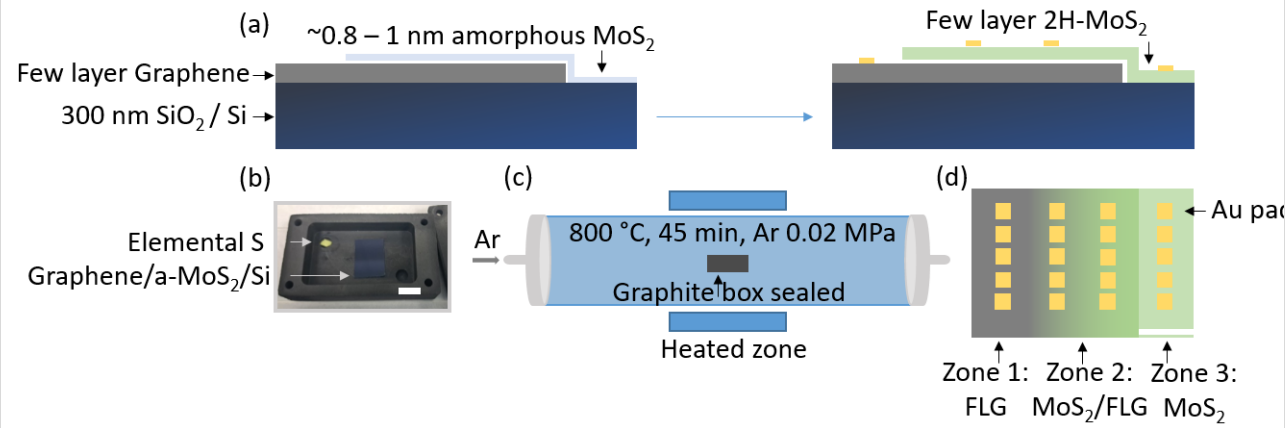

***Figure 1**: Two-step fabrication route of centimetre-scale MoS_2/graphene heterostructures. (**a**) Cross-sectional schematic of the FLG/SiO_2/Si stack coated with a ~0.8–1.0 nm sputtered amorphous MoS_2 precursor and crystallized into few-layer (3–4 L) 2H-MoS_2 during confined-space sulfurization; Au pads are added later for electrical measurements. (**b**) Photograph of the graphite box loaded with elemental sulphur and the MoS_2-coated FLG/Si coupon before annealing. (**c**) Quartz-tube furnace used for sulfurization at 800 °C in flowing Ar/S vapour (graphite box in the hot zone). (**d**) Top-view layout of the 1.5 cm × 2 cm coupon divided into graphene-only, MoS_2/graphene overlap, and MoS_2-only regions, each patterned with Au contacts. Adapted from Ref. [1].*

Structural and chemical characterization confirmed conversion of sub-nanometre amorphous precursors into continuous three-to-four-layer 2H-MoS_2 (Raman $\Delta\omega \approx 21$ cm^{-1}), with low areal roughness ($S_q \approx 0.8$–0.9 nm) and near-stoichiometric composition. Raman ID/IG ≈ 0.90 and a graphene sheet resistance of ~1.9 kΩ sq^{-1} after the 800 °C annealing indicate that the process does not introduce additional local disorder beyond the CVD-transfer baseline [1]. Electrical measurements performed through Ti/Au shadow-mask contacts reveal a clear conductance hierarchy (I(FLG–FLG) > I(FLG–MoS_2) > I(MoS_2–MoS_2)) at low bias (±3 V), together with a small volatile hysteresis for the mixed FLG–MoS_2 path indicative of reversible Schottky-barrier modulation at the heterojunction (*Fig. 2a*) [1]. When sweeping the FLG–MoS_2 pair to ±7 V, a non-volatile SET event occurs at ~+6 V, followed by partial RESET under negative polarity. The read current at 0.5 V changes by a factor of ≈2.1 at 10 mA compliance (ambient conditions), demonstrating true memristive switching localized in the crystallized MoS_2 layer (*Fig. 2b*) [1]. The switching window is consistent with an interface-controlled mechanism where bias-

driven sulphur-vacancy migration and trapping at the MoS_2/graphene boundary narrows the effective Schottky barrier (*Fig. 2c*), enabling analogue-like conductance tuning rather than metallic filament formation [1].

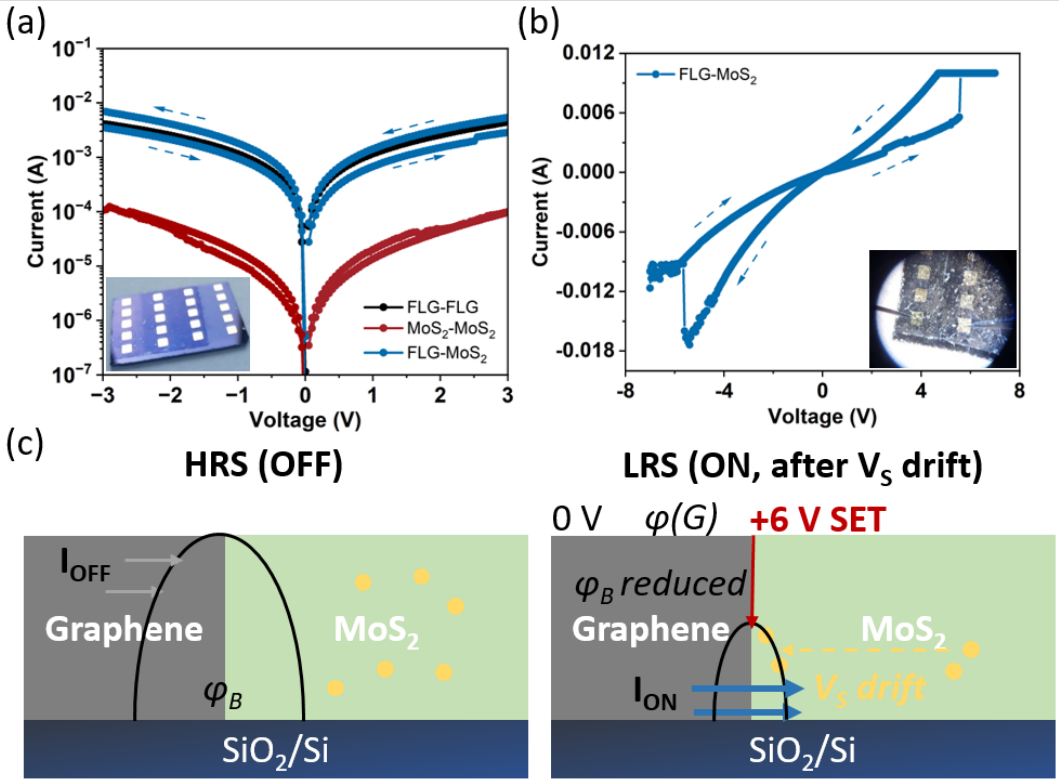

***Figure 2**: Memristive behavior of the MoS_2/graphene heterostructure and pathway toward BEOL-compatible 2D memristors. (**a**) Semi-log |I|–V characteristics (±3 V) for three in-plane contact configurations on the same coupon: FLG–FLG (quasi-ohmic), MoS_2–MoS_2 (high-resistance), and FLG–MoS_2 (intermediate, with a small volatile hysteresis). (**b**) Extended sweep (±7 V) for the FLG–MoS_2 configuration showing a non-volatile SET event at ~+6 V and partial RESET under negative polarity (read current ratio ~2.1 at 0.5 V). (**c**) Conceptual vacancy-mediated switching model: sulphur vacancies drift and accumulate at the MoS_2/graphene boundary under positive bias, reducing the Schottky barrier and switching the device from HRS to LRS. Adapted from Ref. [1].*

The present transfer-free concept provides a scalable path to 2D-material memristors compatible with industrial sputtering tools, while avoiding toxic H_2S chemistries and minimizing transfer-related residues/interfacial contamination. A complementary direction toward lowering the thermal budget is demonstrated by our microreactor-enhanced sulfurization of magnetron-sputtered oxidized W monolayer precursors, enabling electronics-grade monolayer WS_2 at 450 °C (*Fig. 3*), approaching the back-end-of-line (BEOL) temperature requirement of ~400 °C, and WS_2/FLG heterostructures that also exhibit resistive switching likely governed by vacancy migration [2]. Beyond transition-metal dichalcogenides, we have reviewed the rapidly expanding materials space of 2D group-IV monochalcogenides, highlighting synthesis strategies, property engineering, and device opportunities relevant to next-generation nanoelectronics and optoelectronics [3]. Together, these results establish an experimentally grounded, process-oriented roadmap for integrating defect-engineered 2D semiconductors with graphene electrodes toward reliable, scalable, and energy-efficient analogue computing devices.

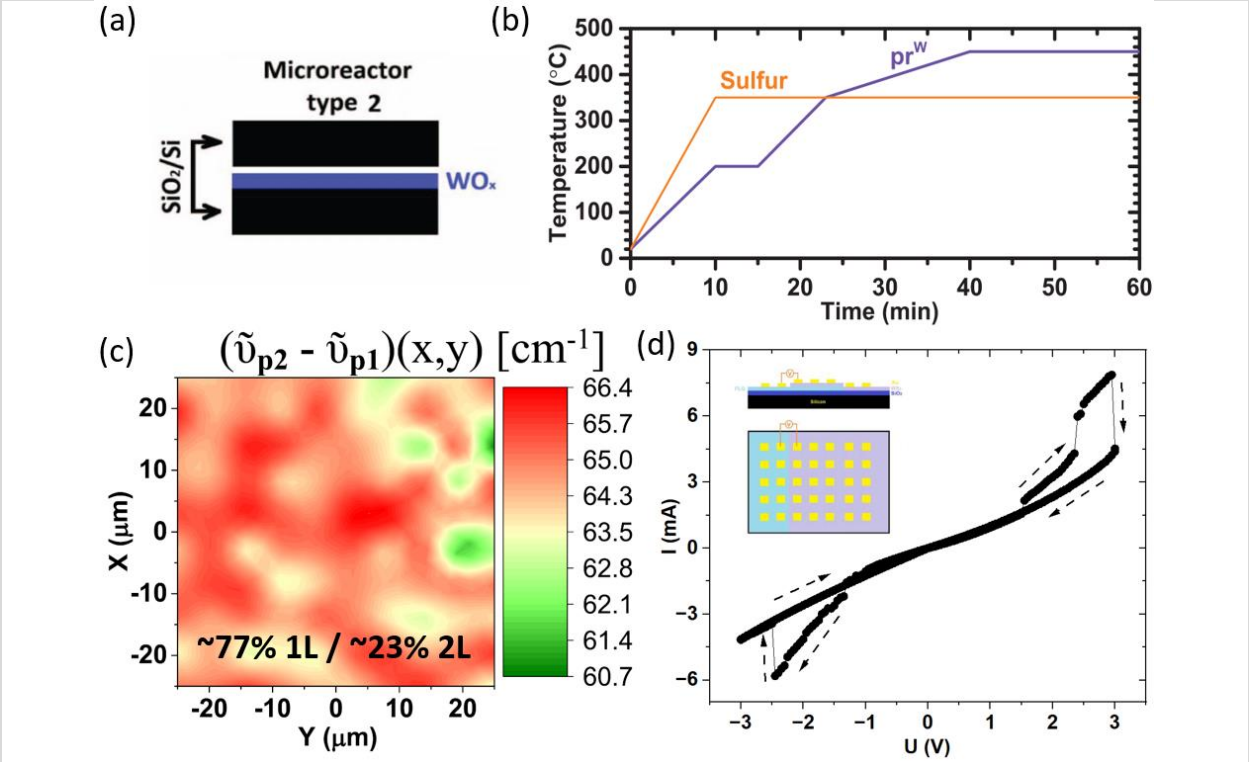

***Figure 3**: Microreactor-assisted low-temperature sulfurization route for monolayer WS_2 and WS_2/graphene memristive devices. (**a**) "Sandwich" microreactor (type 2) geometry: the oxidized magnetron-sputtered W monolayer precursor (WO_x) on SiO_2/Si is covered with a clean SiO_2/Si cap substrate to confine sulphur vapour and suppress precursor evaporation. (**b**) Representative stepwise thermal profile enabling conversion at 450 °C (sulphur source heated to 350 °C; substrate zone to 450 °C) in Ar. (**c**) Raman mapping of the p2–p1 second-order peak separation, highlighting monolayer-dominant WS_2 coverage (≈77% monolayer, ≈23% bilayer). (**d**) Resistive switching in Au/WS_2/FLG lateral devices with device layout/stack inset, consistent with vacancy-migration-assisted barrier modulation. Adapted from Ref. [2].*

A key next step is to merge the transfer-free MoS_2/FLG lateral device concept with microreactor-style confinement to reduce the crystallization temperature into the BEOL window while preserving a clean van der Waals interface. In parallel, controlling sulphur chemical potential and defect landscapes offers a direct handle to widen the switching window and stabilize multilevel conductance states. Wafer-level statistics on variability, retention/endurance, and analogue update linearity will be essential for positioning these heterostructures as reliable synaptic elements.

References:

[1] C. Mihai, I.-D. Simandan, F. Sava, T. Tite, A.E. Bocîrnea, M. Văduva, M.Y. Zaki, M. Baibarac, A. Velea, *Fabrication of high-quality MoS_2/graphene lateral heterostructure memristors*, Nanomaterials 15 (2025) 1239.

[2] A. Velea, I.-D. Simandan, C. Mihai, M. Baibarac, M. Văduva, A. Udrescu, I. Smaranda, A.E. Bocîrnea, T. Tite, M.Y. Zaki, A. Kuncser, F. Sava, *Large-scale synthesis of monolayer WS_2 by low-temperature sulfurization of oxidized magnetron sputtered monolayer W precursors in a microreactor*, Nanotechnology 36 (2025) 265601.

[3] A.-T. Buruiană, C. Mihai, A. Kuncser, A. Velea, *Advances in 2D group IV monochalcogenides: Synthesis, properties, and applications*, Materials 18 (2025) 1530.

Optical, structural and electrical proprieties of composites based on MoS_2, WS_2 and poly(ortho-toluidine)

T. Burlănescu[1,2], M. Cercel[1,2], I. Smaranda[1], A. Androne[1], I. Zgură[1], C.-P. Ganea[1], C. Negrilă[1], A. Lorinczi[1], C. Bartha[1], M. Baibarac[1]

1) *National Institute of Materials Physics, 077125, Măgurele, Romania*
2) *Faculty of Physics, University of Bucharest, 077125, Măgurele, Romania*

In this work [1], a method in two steps for the preparation of the composites based on poly(ortho-toluidine) (POT) and the MoS_2 and WS_2 sheets was reported. In the first step, by ball-milling of mixtures of MoS_2 and WS_2 particles, the sheets of MoS_2 and WS_2 (MoS_2:WS_2) with weight ratio equal to 3:1, 1:1 and 1:3 were prepared. In the second step, the interaction in solid-state of the MoS_2:WS_2 samples with POT in emeraldine-base (POT-EB) and emeraldine-salt (POT-ES) was used to obtain composites of the type MoS_2:WS_2/POT-EB and MoS_2:WS_2/POT-ES. The choice of POT-EB and POT-ES was essential for elucidating the role of polymer charge state in governing interfacial chemistry, charge transfer, and electrical transport. Using X-ray diffraction (XRD), FTIR spectroscopy, Raman scattering and X-ray photoelectron spectroscopy (XPS), we demonstrated that the ball-milling method can allow the preparation of the MoS_2 and WS_2 sheets with different stacking order. The interaction of POT-EB with the MoS_2:WS_2 samples involves the transformation of some repeating units of the type EB into ES. The interaction of POT-ES with the MoS_2:WS_2 samples leads to the appearance of new positive charges onto macromolecular chains which are compensated by S^{2-} ions. XRD diagrams (*Fig. 1*) showed a systematic decrease in the intensity of the peak at 14.30° assigned to the (002) crystalline planes of the two TMDs after the addition of POT-ES or POT-EB macromolecular compounds. This systematic and relevant intensity drop is most probably due to the decrease of the initial concentration of the MoS_2 and WS_2 crystallites per unit volume of the diffracting substance by the addition of the polymers. The decrease in the intensity of the maximum assigned to the crystalline plane (002) is a typical variation reported for the exfoliation of WS_2 [2] and MoS_2 [3].

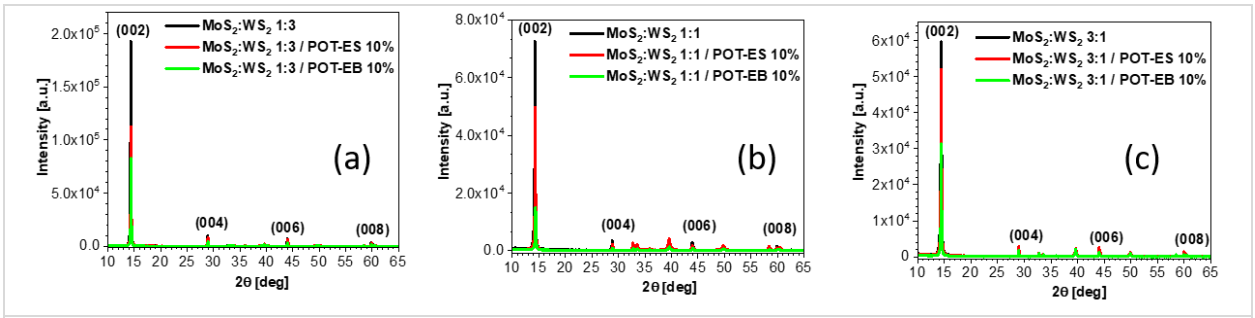

***Figure 1**: XRD diagrams of: (**a**) MoS_2:WS_2 1:3 (black curve), MoS_2:WS_2 1:3 /POT-ES 10 wt.% (red curve), MoS_2:WS_2 1:3 /POT-EB 10 wt.% (green curve); (**b**) MoS_2:WS_2 1:1 (black curve), MoS_2:WS_2 1:1/ POT-ES 10 wt.% (red curve), MoS_2:WS_2 1:1/ POT-EB 10 wt.% (green curve); (**c**) MoS_2:WS_2 3:1 (black curve), MoS_2:WS_2 3:1 /POT-ES 10 wt.% (red curve), and MoS_2:WS_2 3:1/POT-EB 10 wt.% (green curve). Reproduced from Ref. [1].*

FTIR spectra of the MoS_2:WS_2/POT-EB composites highlighted a down-shift of the IR band from 1242 cm^{-1} to 1211–1217 cm^{-1}, a gradual down-shift of the IR band from 816 cm^{-1} up to 806–802 cm^{-1} and an increase in the absorbance of the IR band situated at 1111–1107 cm^{-1}. Taking into account the vibrational modes of IR bands of POT-EB and POT-ES, the change of the absorbance ratio as well as the presence of IR bands close to those of POT-ES indicate clearly that the solid-state interaction of POT-EB with MoS_2:WS_2 led to the transformation of some repeating units of POT-EB into ES. FTIR spectra of the MoS_2:WS_2/POT-ES composites showed a significant decrease in the absorbance of the IR bands situated in the spectral ranges 1400–1500 and 1230–1300 cm^{-1}. The decrease in the absorbance of the IR bands assigned to the vibrational modes of the N–B–N bond and C–N stretching indicates that the interaction of POT-ES with MoS_2:WS_2 induced the generation of new positive charges onto macromolecular chains that are compensated by S^{2-} ions. The Raman spectra of the MoS_2:WS_2/POT-EB composites showed a decrease in the intensity of the Raman lines localized in the spectral ranges 1300–1400 and 1450–1520

cm^{-1}, simultaneously with shifts of characteristic bands. The presence of Raman lines close to those of POT-ES confirmed that interaction in solid-state of POT-EB with MoS_2:WS_2 leads to the transformation of some repeating units of EB into ES. In the case of MoS_2:WS_2/POT-ES composites, the change of the ratio between the intensities of characteristic Raman lines indicated a growth of the pseudo-protonated structure. The Raman lines of MoS_2 and WS_2 are observed in the low frequency range of the spectra of the composites. Small shifts of the E_2g^1 and A_1g vibrational modes are observed in the case of the composites. These variations were discussed considering the dependence of the Raman modes on stacking patterns and on the interaction between layers. XPS spectra of the MoS_2:WS_2 samples and their composites showed changes in the binding energies and intensities of Mo 3d, W 4f, and S 2p core levels (*Fig. 2*). The diminution of the intensities of the peaks assigned to sulphate species in the case of the MoS_2:WS_2/POT-EB composites indicated a chemical adsorption of sulphate ions present in the MoS_2:WS_2 samples into the macromolecular chain of POT-EB, when a part of repeating units of the type EB are transformed into ES. The presence of the peaks assigned to $C–N^+$ bonds confirmed the appearance of new positive charges onto macromolecular chains.

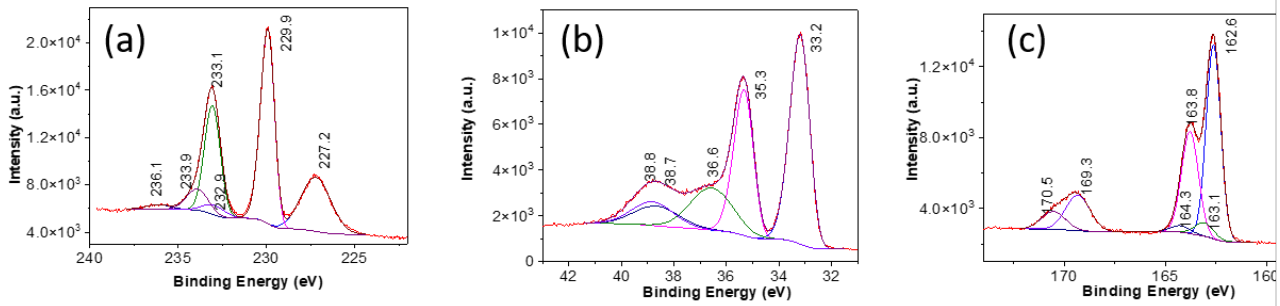

***Figure 2**: XPS spectra of the MoS_2:WS_2 1:1 sample: (**a**) Mo 3d; (**b**) W 4f; and (**c**) S 2p. Reproduced from Ref. [1].*

According to thermogravimetric analysis (TG) and differential scanning calorimetry (DSC), all samples are demonstrated to be stable up to 230 °C. Differences in thermal stability are observed depending on the polymer concentration and the type of macromolecular compound. Dielectric spectroscopy data revealed a complex dependence of DC electrical conductivity on frequency, temperature, and composite concentration. The conductivity spectra showed a frequency-independent region at low frequencies followed by a dispersive behaviour at higher frequencies. The temperature dependence of the conductivity revealed an increase in conductivity with rising temperature. The apparent activation energy was defined as the derivative of the logarithm of conductivity with respect to the inverse temperature. The obtained results (*Fig. 3*) indicate that the apparent activation energy is influenced by the system composition via filling factors.

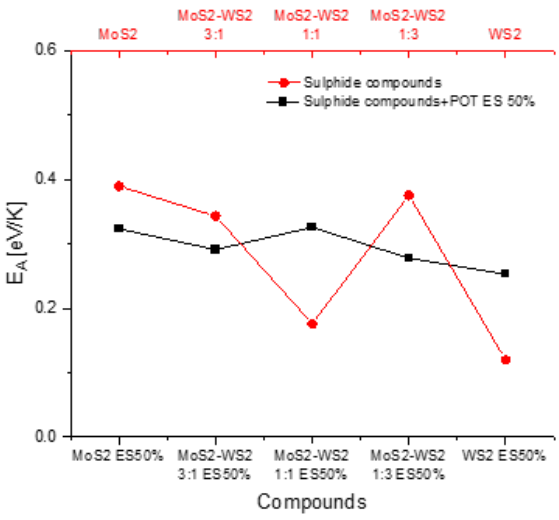

***Figure 3**: The apparent energies for several groups of samples. Reproduced from Ref. [1].*

The electrical properties of these heterogeneous materials are described using Lichtenecker's mixing laws [4]. The composite systems studied (two/three-component) exhibit complex behaviour in terms of effective conductivity, depending on both concentration and temperature. We applied Lichtenecker's mixing laws for effective electrical conductivity, which do not require extensive theoretical considerations and are supported by consistent empirical evidence. In the case of inhomogeneous systems made up of components with comparable electrical properties, the effective conductivity is represented by a weighted sum by means of filling factors (concentrations).
For the complex analysis of the temperature dependence of electrical conductivity, we used the "apparent activation energy". The procedure called "derivative with the inverse of temperature" allows the determination of the temperature-dependent functional relationship of the apparent activation energy and the identification of the intervals in which this exists. The apparent activation energy followed of a linear combination, in which the coefficients depend in a simpler or more complicated way on the filling factors and the conductivities of the components, if the inhomogeneous composite system is made up of elements that have comparable electrical properties. Qualitatively, the expressions were in acceptable agreement with the experimental data.

References:

[1] **T. Burlanescu, M. Cercel, I. Smaranda, A. Androne, I. Zgura, C.-P. Ganea, C. Negrila, A. Lőrinczi, C. Bartha, M. Baibarac, *Optical, structural and electrical proprieties of composites based on MoS_2, WS_2 and poly(ortho-toluidine)*, Materials Today Communications 46 (2025) 112469.**

[2] M.S. Loeian, D.A. Ziolkowska, F. Khosravi, J.B. Jasinski, B. Panchapakesan, *Exfoliated WS_2-nafion composite based electromechanical actuators*, Scientific Reports 7 (2017) 14599.

[3] G. Venu, J.S. Jayan, K. Joseph, A. Saritha, *Polyvinyl pyrrolidone mediated exfoliation of transition metal dichalcogenides: Comparative evaluation of exfoliated MoS_2 and WS_2 in epoxy toughening*, Polymer Composites 45 (2024) 9561–9572.

[4] A.V. Goncharenko, V.Z. Lozovski, E.F. Venger, *Lichtenecker's equation: applicability and limitations*, Optics Communications 174 (2000) 19–32.

Microstructure of self-assembled Ga_2O_3 polymorphs induced by ion beam irradiation

C. Ghica[1], C. Radu[1], I.F. Mercioniu[1], A. Kuznetsov[2], J. Zhao[3]

1) *National Institute of Materials Physics, 077125, Măgurele, Romania*
2) *University of Oslo, N-0316, Oslo, Norway*
3) *Southern University of Science and Technology, 518055, Shenzhen, China*

Combining materials into multilayers or composites down to a nanometric scale represents one of the strategies nowadays for modulating the physical and chemical properties of solids. In this article, we studied the impact of the dynamic defect annealing on the disorder-induced phase transitions in β-Ga_2O_3 by ion irradiation [1]. Single crystalline (010) oriented β-Ga_2O_3 wafers were irradiated with 400 keV $^{58}Ni^+$ ions keeping the ion fluence at a constant value of 1×10^{16} cm^{-2}. The irradiation temperature was varied in the range from RT to 400 °C keeping the ion flux constant at 6×10^{12} at./(cm^2 s). Advanced techniques of transmission electron microscopy have been used to extract and analyse the structural information regarding the induced subsurface layering of the irradiated material. A cross-section lamella has been prepared for TEM studies by focused ion beam using a Tescan Lyra III XMU instrument. Analytical TEM and high-resolution TEM (HRTEM) measurements were performed with a JEM ARM200F transmission electron microscope operated at 200 kV. On the STEM-ADF image and the EDS elemental maps of the FIB lamella extracted from the Ni implanted sample (*Fig. 1*) one can notice the profile of the Ni signal having its maximum concentration at ~190 nm below the surface, consistently with the SRIM predicted range.

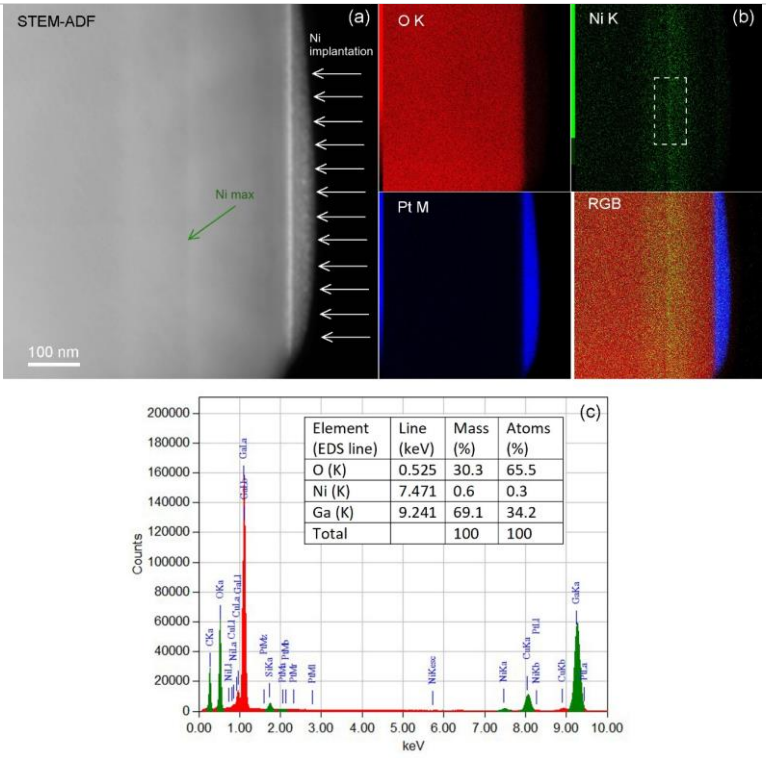

***Figure 1**: (**a**) STEM-ADF cross-section image of the FIB lamella close to the implanted surface of the Ga_2O_3 sample; (**b**) Elemental maps of O, Ni and Pt; (**c**) EDXS spectrum extracted from the Ni-rich area. Reproduced from Ref. [1].*

XRD and RBS/C data suggest the formation of a complex multilayered polymorph structure in the sample irradiated at 350 °C. Cross-section TEM imaging of this sample (*Fig. 2*) revealed several clearly defined layers of 25, 30, 150, and 130 nm delimited by interfaces I1, I2 and I3, as pointed out by white arrows.

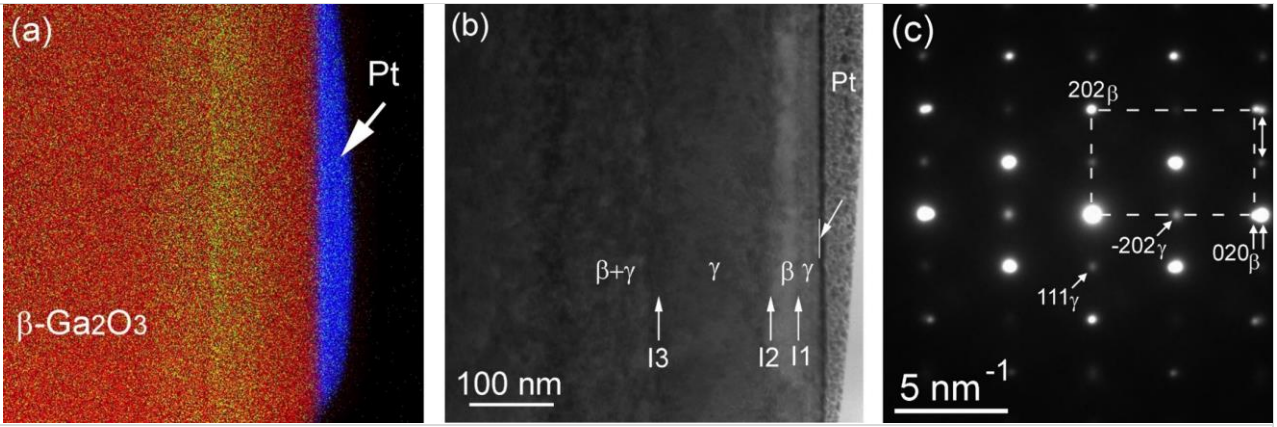

***Figure 2**: (**a**) Chemical elemental mapping of the lamella used for TEM investigations; (**b**) bright-field TEM image showing a layered subsurface contrast; (**c**) SAED pattern from the whole irradiated part of the sample. Reproduced from Ref. [1].*

The SAED pattern acquired from the whole cross-section is interpreted as an overlap of two lattice signatures having close lattice parameters. The dominant phase is assigned to the monoclinic β-Ga_2O_3 in [10−1] zone axis orientation. The weaker diffraction spots in intermediate positions with respect to the β-Ga_2O_3 pattern correspond to γ-Ga_2O_3.

Further insights into the multilayered polymorph structure were obtained by HRTEM investigations around each of the interfaces. The HRTEM image in *Fig. 3a* together with the corresponding FFTs taken in the vicinity of the I1 interface, confirms the separation of Ga_2O_3 into two layers, 25 and 30 nm thick.

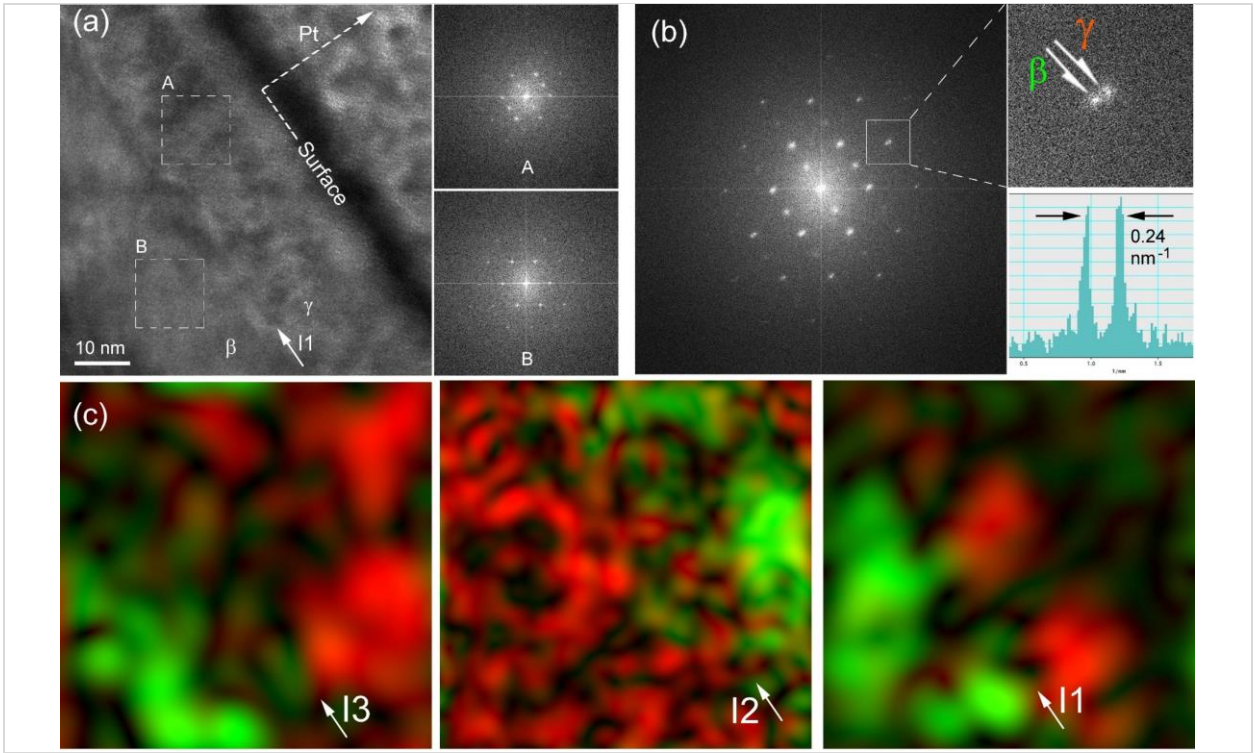

***Figure 3**: (**a**) HRTEM image and FFT patterns from areas labelled A and B on either side of the I1 interface verifying Ga_2O_3 phase separation; (**b**) FFT pattern taken over both sides of the I1 interface and zoom-in showing the 020_β spot splitting, correlated with the presence of the γ-phase; (**c**) structural maps around I1, I2, and I3 interfaces associated with 020_β and -404_γ spots in green and red, respectively. Reproduced from Ref. [1].*

The features observed in the SAED patterns acquired from the whole multilayer structure in *Fig. 2c* are now examined in the FFT patterns from smaller areas, labelled as A and B on either side of the I1 interface. These FFT patterns show two different families of spots. The FFT pattern from the B-area is indexed as the monoclinic β-Ga_2O_3 in the [10−1] orientation. In turn, the FFT pattern from the A-area

contains spots in nearly halfway positions with respect to that in the B-area and indexed as the cubic defective spinel γ-Ga_2O_3 [2,3]. The FFT diagram taken from a bigger area across the I1 interface validates that there are two adjacent characteristic spots clearly separated by $\Delta g/g \approx 3$ %, corresponding to the peak splitting of 0.24 nm^{-1}. Similar characterizations were carried out on areas around the I2 and I3 interfaces. The I2 interface separates a layer of pure β-phase above (~30 nm thick) from a layer of pure γ-phase below (~150 nm thick), while the I3 interface separates the single-phase γ-layer above from a mixed β−γ region deeper in the sample, containing predominantly β-phase with a minor portion of γ-phase. The phase colour maps around the I1, I2, and I3 interfaces with 020_β and -404_γ spots color-coded in green and red visualize the polymorph flips across the interfaces. The HRTEM data shows that the sample conserved the single-crystal structure, so that β- and γ-phases are well-aligned across the interfaces according to the crystallographic relation $[10-1]_\beta$ || $[1-21]_\gamma$, $(-101)_\gamma$ || $(010)_\beta$, and $(111)_\gamma$ || $(101)_\beta$. Simulated images were generated using the ReciPro software in $[10-1]_\beta$ and $[1-21]_\gamma$ zone axes (*Fig. 4*), respectively. Two simulated patterns are shown in Fig. 4b and 4e, as well as inserted into the experimental micrographs for direct comparison. Comparing images in Fig. 4, we observe a nearly doubling of periods between (202) planes in β-Ga_2O_3 ($d_{202\beta}$ = 0.236 nm) versus (111) planes in γ-Ga_2O_3 ($d_{111\gamma}$ = 0.476 nm).

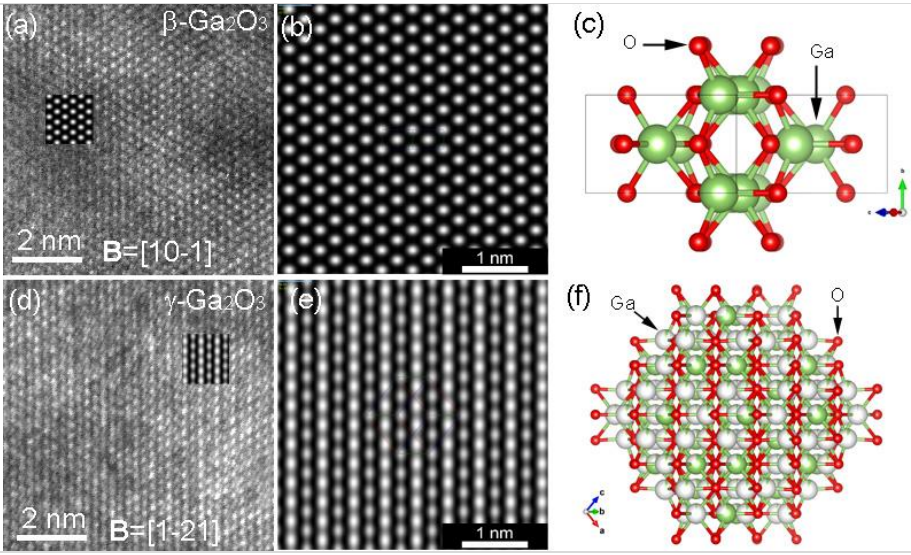

***Figure 4**: Atomic-resolution micrographs, simulated HRTEM patterns, and atomic structural model assigned to domains containing (**a–c**) β-Ga_2O_3 in [10−1] orientation and (**d–f**) γ-Ga_2O_3 in [1−21] orientation. Reproduced from Ref. [1].*

By exploring a wide range of sample temperatures and ion fluxes, we demonstrated that the system can be tuned toward self-assembling of several polymorph interfaces. The TEM investigation clearly refined the data from XRD and RBS/C measurements, providing atomic resolution information on the phase transitions and self-assembling of a multilayered structure below the irradiated surface. The finding reported in this article paves the way for fabrication of multilayered Ga_2O_3 polymorphs with ion beams, potentially emerging as a suitable technology for polymorph heterostructure fabrication.

References:

[1] A. Azarov, C. Radu, A. Galeckas, I.F. Mercioniu, A. Cernescu, V. Venkatachalapathy, E. Monakhov, F. Djurabekova, C. Ghica, J. Zhao, A. Kuznetsov, *Self-assembling of multilayered polymorphs with ion beams*, ACS Nano Letters 25 (2025) 1637–1643.

[2] H.Y. Playford, A.C. Hannon, E.R. Barney, R.I. Walton, *Structures of uncharacterised polymorphs of gallium oxide from total neutron diffraction*, Chemistry – A European Journal 19 (2013) 2803–2813.

[3] H.Y. Playford, A.C. Hannon, M.G. Tucker, D.M. Dawson, S.E. Ashbrook, R.J. Kastiban, J. Sloan, R.I. Walton, *Characterization of structural disorder in γ-Ga_2O_3*, Journal of Physical Chemistry C 118 (2014) 16188–16198.

Effect of molecular adsorption on the conductivity of selectively grown, interconnected 2D-MoS_2 atomically thin flake structures

I. Stavarache[1], C. Palade[1], A. Slav[1], I. Dăscălescu[1], A.-M. Lepădatu[1], E. Matei[1], C. Beşleagă[1], M.L. Ciurea[1,2], B.E. Kardynal[3,4], T. Stoica[1]

1) *National Institute of Materials Physics, 077125, Măgurele, Romania*
2) *Academy of Romanian Scientists, 050094, Bucharest, Romania*
3) *Peter Grünberg Institute 9, JARA-FIT, 52425 Jülich, Germany.*
4) *Department of Physics, RWTH Aachen University, 52074, Aachen, Germany*

The gas sensitivity of field-effect structures with 2D-MoS_2 channels selectively grown between Mo electrodes using the Mo-CVD method was investigated by measuring the effect of molecular adsorption from air on the source-drain current (I_{sd}) of the device. The channels were composed of interconnected atomically thin MoS_2 flakes, with their density and average thickness varied by choosing two different distances between the Mo contacts (15 and 20 μm).
As reported in literature, the atomically thin layers of transition metal dichalcogenides (2D-TMDs) show a high sensitivity to the light, that along with their good electronic transport properties, have led to a large number of potential applications. In particular, the atomically thin 2D-MoS_2 layers, with a high exciton binding energy, an enhanced dielectric confinement, a strong spin–orbit coupling and a large valence band spin-splitting, make them attractive for photonics and spintronics. A high response to the external stimuli, including molecule adsorption, illumination and gate voltage changes, we evidenced in our work [1]. The selective growth of atomically thin MoS_2 with Mo supplied from the deposited patterned layer on a SiO_2 (300 nm)/c-Si substrate was obtained by the Mo-CVD method in a three-zone horizontal quartz tube furnace (Carbolite HZS) [2]. The selective growth took place over 30 min by simultaneous surface diffusion of native MoO_2 formed on the surface of the 30 nm thick Mo deposited by sputtering and its chemical reaction with S vapor transported by 20 sccm Ar flux at 100 mbar pressure. An additional advantage of this growth method is its bottom-up approach for fabricating devices, where the source-drain Mo-electrodes are pre-deposited and the MoS_2 film is self-aligned and in intimate contact with them, without post-growth photolithographic process, avoiding the surface contamination with resists. The back contacted silicon substrate served as a gate electrode controlling the devise response to the external stimuli (*Fig. 1*).

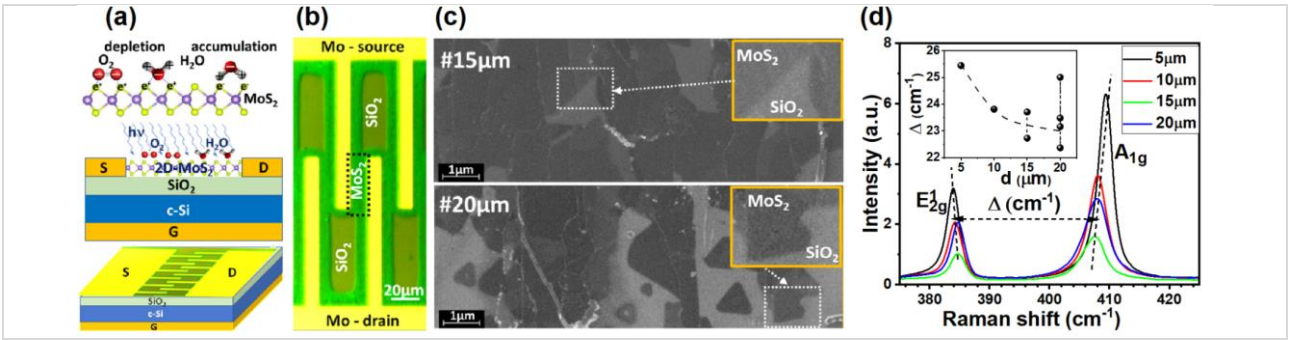

***Figure 1**: (**a**) Schematic of the electron depletion and accumulation in 2D-MoS_2 due to the adsorption of O_2 and H_2O molecules from air, showing the cross-section and bird's-eye view of the device with selectively grown MoS_2 between Mo finger contacts; (**b**) optical image detail of selectively grown 2D-MoS_2 around Mo finger contact patterns; (**c**) comparison of high-resolution SEM images of 2D-MoS_2 acquired from the gap between Mo electrodes for #15 μm and #20 μm samples (dark areas – MoS_2 MLs; lighter areas – SiO_2); (**d**) representative Raman spectra of 2D-MoS_2 for different gap lengths (inset shows the dependence of the distance and its fluctuations, between A_1g and E_1 2g peaks, as a function of gap length). Reproduced from Ref. [1].*

The gate voltage dependence of I_{sd} (V_{sd} = 1.0 V) in the dark and under illumination with monochromatic light, in vacuum of different pressures and in air (at atmospheric pressure) is presented in *Fig. 2a,b*, showing similar behaviour in the #15 μm and #20 μm samples, with I_{sd} increased under high vacuum (HV), for both in dark and under illumination. The relative dark current response to the transition from

air to HV reached up to 1000 % at the turn-on voltage (*Fig. 2c*). The #20 μm device had more electron traps; the lower density of interconnected MoS_2 flakes, forming separated conductive channels, some of which were interrupted in #20 μm, may also explain its lower surface conductance. Despite the screening of the disorder by extra electrons, the #20 μm sample remained more sensitive to air molecules on its surface, than the 15 μm sample. The mobility increased by an order of magnitude for gate voltages above the turn-on voltage, but the maximum value remained in the order of $10^{-4} cm^2 V^{-1} s^{-1}$ (*Fig. 2d*).

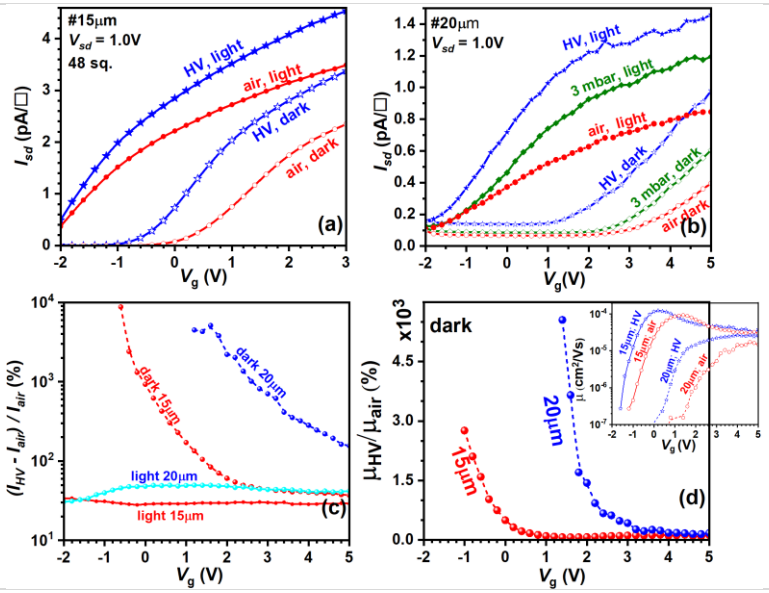

***Figure 2**: Gate-voltage dependence of source-drain currents in dark and under illumination with monochromatic light measured at room temperature: (**a**) #15 μm (λ = 600 nm) and (**b**) #20 μm (λ = 570 nm) under vacuum, at atmospheric and reduced pressures (current normalized to the number of squares (sq.)) of MoS_2 area; (**c**) relative differences between currents measured at HV of 2×10^{-5} mbar (I_{HV}) and in air (I_{air}) at atmospheric pressure on #15 μm and #20 μm samples; and (**d**) gate voltage dependence of mobility ratio μ_{HV}/μ_{air} obtained from the dark transfer curves in (**a**) and (**b**) (the absolute values are shown in the inset). Reproduced from Ref. [1].*

When monitored during the gradual change in air pressure, I_{sd} exhibited a non-monotonic function, sharply peaking at about 10^{-2} mbar, suggesting molecular adsorption on different defect sites and orientations of adsorbed H_2O molecules. Initially during the adsorption process, water molecules are electrostatically adsorbed, with their positive pole towards the MoS_2 surface due to the $H^+ - S^-$ attractive interaction, inducing the accumulation of electrons, which generates the current peak at 2×10^{-2} mbar. Over time and by increasing the pressure, the water molecules are adsorbed on the surface of the MoS_2 layer in a more stable position, which is the one with the depletion effect induced by charge transfer (*Fig. 1*).

The spectral dependences of the photocurrent (defined as the difference between the I_{sd} under illumination and in dark before spectral illumination) was measured at room-temperature on samples #15 μm and #20μm in vacuum at different pressures and in air at atmospheric for gate voltage V_g = 0 V. In #20 μm sample, the spectral photocurrent increases with decreasing the air pressure from the atmospheric (atm) to 2–4 mbar and to 2×10^{-5} mbar, as shown in *Fig. 3a*. For better comparison, the spectral responsivity in air, at atm pressure and in HV was computed by normalizing the photocurrent to the spectral illumination power (*Fig. 3b*). As can be seen, the spectral responsivity of sample #15μm is almost independent of the molecule adsorption, the atm and HV curves almost overlap, with a small blue-shift in energy for the measurements in vacuum. In sample #20μm, the photocurrent increases in HV by a factor of 2.1 and is lower than that of the #15 μm on the whole spectrum. The weak photocurrent response of sample #15 μm to the ambient pressure can be explained if we assume that the spectral photocurrent is mainly controlled by photo-excitation and recombination in the "bulk" of thicker 2D-MoS_2 multi layer.

The HV state was also investigated by annealing devices at temperatures up to 340 K in HV. Following this annealing, the dark source-drain current in the samples was measured as a function of temperature for both samples, by cooling down from 340 K to 100 K and then heating up back to 340 K (*Fig. 4a,b*).

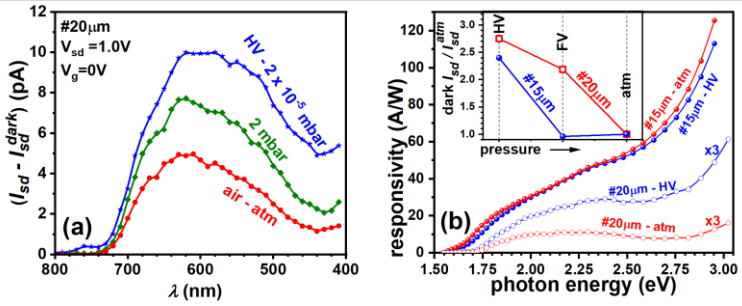

***Figure 3**: (**a**) Spectral photocurrent measured at room temperature in vacuum and different pressures on sample #20 μm; (**b**) Comparison of the spectral responsivity of both samples #20 μm and #15 μm. Reproduced from Ref. [1].*

The temperature dependence of the current in sample #15 μm showed extrinsic semiconducting-like behavior. When the sample was cooled down, the current was decreasing with variable rates for different temperature ranges, with activation energies of 230 meV, 85 meV, and 110 meV, corresponding to different trapping states. Based on literature data, we can attribute the activation energy of 230 meV to sulfur vacancies, while those of 85–120 meV possibly due to natural impurities, grain boundaries or disorder defects. The hysteresis of $T_{down} - T_{up}$ cycle is due to thermally stimulated current (TSC) phenomenon. Transport through the #20 μm sample (*Fig. 4b*) is almost independent of the temperature (activation energy of 12 meV) and the current is very low, suggesting a very low free carriers concentration and hopping transport on surface states or defects in the bulk.

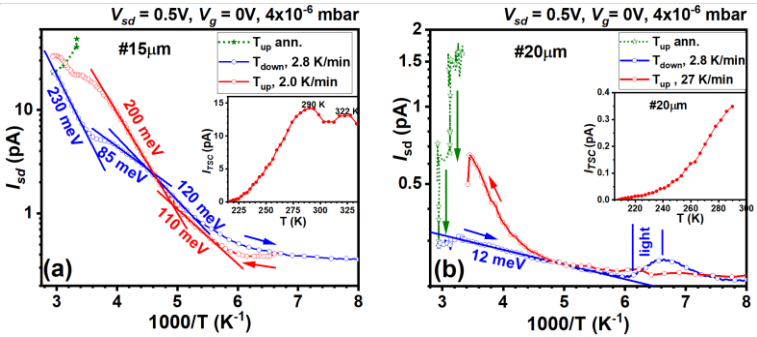

***Figure 4**: Temperature dependence of I_{sd} in high vacuum for samples (**a**) #15 μm and (**b**) #20 μm for cooling (T_{down}) and heating (T_{up}) at low temperatures. The insets of (**a**) and (**b**) show the corresponding thermally stimulated current (TSC). Reproduced from Ref. [1].*

The results demonstrated the high sensitivity of these devices to molecular adsorption, making the technology promising for the easy fabrication of chemical sensors. We also performed some tests exposing our devices to acetone vapor and found an exponential increase in the source-drain current during exposure toward a saturation value (~an order of magnitude), as well as unexpectedly large fluctuations in the dc current, which we interpreted as the effect of trapping–detrapping fluctuations of adsorbed polar molecules. The demonstration of a large number of structural and boundary defects in selectively grown 2D-MoS_2 interconnected flakes, which control the behaviour of the studied FET structures, can be of great interest for the future applications of this versatile device fabrication technique in optoelectronics or modern synaptic electronics.

References:

[1] I. Stavarache, C. Palade, A. Slav, I. Dascalescu, A.M. Lepadatu, E. Matei, C. Besleaga, M.L. Ciurea, B.E. Kardynal, T. Stoica, *Effect of molecular adsorption on the conductivity of selectively grown, interconnected 2D-MoS_2 atomically thin flake structures*, Nanoscale Advances 7 (2025) 2368–2380.

[2] I. Stavarache, C. Palade, A. Slav, I. Dascalescu, A.-M. Lepadatu, L. Trupina, E. Matei, M.L. Ciurea, T. Stoica, *Atomically thin MoS_2 layers selectively grown on mo patterned substrates for field-effect-controlled photosensors*, ACS Applied Nano Materials 7 (2024) 5051–5062.

Key Scientific Achievements & Breakthroughs in *Materials and Devices for Energy Systems, Extreme Environments, Space & Security*

Exploring the synthesis of $Cu_2(Zn, Cd)SnS_4$ from molecular inks as a route for high-efficiency solar cells

O. El Khouja[1,2], Y. Gong[3], A. Jimenez-Arguijo[3], M. Jimenez Guerra[3], A. Gon Medaille[3], R. Scaffidi[4], A. Basak[5], C. Radu[1], D. Flandre[4], B. Vermang[4], S. Giraldo[3], M. Placidi[3], Z. Jehl Li-Kao[3], A.C. Gâlcă[1], E. Saucedo[3]

1) *National Institute of Materials Physics, 077125, Măgurele, Romania*
2) *Ibn Tofail University, 14000, Kenitra, Morocco*
3) *Universitat Politècnica de Catalunya (UPC), 08019, Barcelona, Spain*
4) *Hasselt University, 3590, Hasselt, Belgium*
5) *KIIT-Deemed to Be University, 751024, Bhubaneswar, India*

In a recent study [1], we explored the complex relationship between sulfurization at unusually high temperatures (up to 700 °C) and the structural and optoelectronic characteristics of Cd-based Cu_2ZnSnS_4 (CZTS) films. First, pure CZTS absorbers were obtained using a Cu^+-Sn^{4+}-DMSO molecular ink. Photovoltaic cells based on Cd free CZTS absorber layers crystallized at different temperatures had a maximum PCE of 4.08% and a V_{oc} of 576 mV (*Fig. 1* and *Table 1*). The analysis revealed that high sulfurization temperatures induce a transformation in microstructure. By introducing Cd in the CZTS, along with band gap decrease, the improvement of CZCTS/CdS interface led to much better photovoltaic properties (*Fig. 1* and *Table 1*). The PCE increased, peaking at 10.4 % at an optimal sulfurization temperature of 680 °C, underlying the critical role of grain boundary passivation and interface engineering. Further increasing the sulfurization temperature to 700 °C led to secondary phase formation and interface degradation. We showed that the incorporation of 20% Cd into CZTS not only stabilized the conduction band offset but also significantly reduced the V_{oc} loss for CZCTS devices. This study established a novel approach for tuning kesterite-based thin films through a combination of Cd-alloying and sulfurization temperature optimization, providing valuable insights into achieving higher efficiencies and advancing the field of scalable, solution-processed photovoltaics.

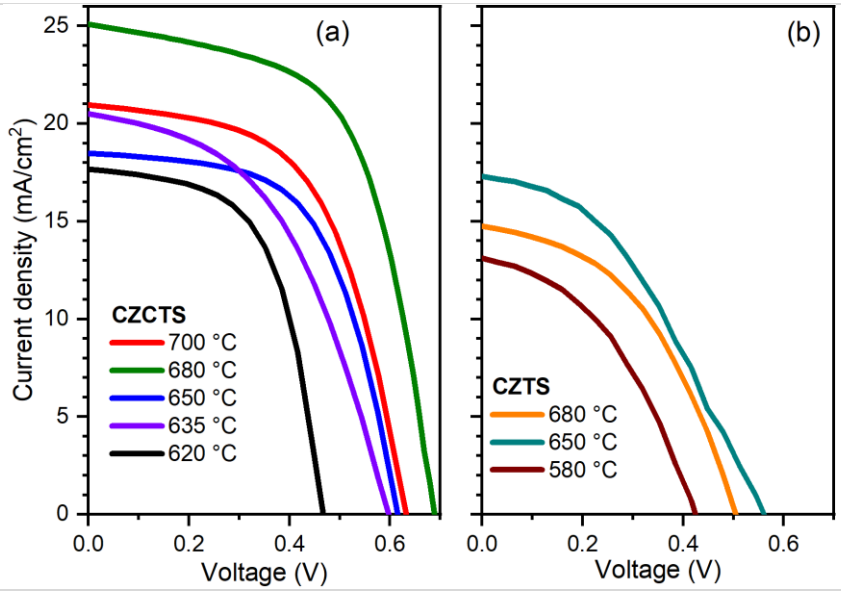

***Figure 1**: J–V curves of CZCTS-based devices (**a**) compared with those of (**b**) CZTS devices. Adapted from Ref. [1].*

The cross-sectional SEM images (*Fig. 2*) offered insights into both the absorber and the devices engineered from the high-performance CZCTS prepared at 680 °C. Notably, the images demonstrated a typical large-grain structure, with certain grains extending throughout the entire thickness of the CZCTS layer. The presence of such large grains holds intrinsic benefits for device performance, minimizing therefore the likelihood of recombination of photogenerated carriers at grain boundaries. This inherent

characteristic demonstrates the potential of CZCTS films synthesized at 680 °C, highlighting their capacity to facilitate superior charge transport and collection within the photovoltaic device

***Table 1**: Detailed photovoltaic parameters of the devices.*

Sample	J_{sc} (mA/cm²)	V_{oc} (mV)	FF (%)	PCE (%)
CZTS 680 °C	15.90	512	44.54	3.59
CZTS 650 °C	18.61	576	36.34	4.08
CZTS 580 °C	14.20	416	42.66	2.48
CZCTS 700 °C	23.1	624	59.1	8.5
CZCTS 680 °C	24.3	701	60.8	10.4
CZCTS 650 °C	19.8	608	59.3	7.1
CZCTS 635 °C	22.0	608	46.3	6.2
CZCTS 620 °C	18.8	480	56.7	5.1

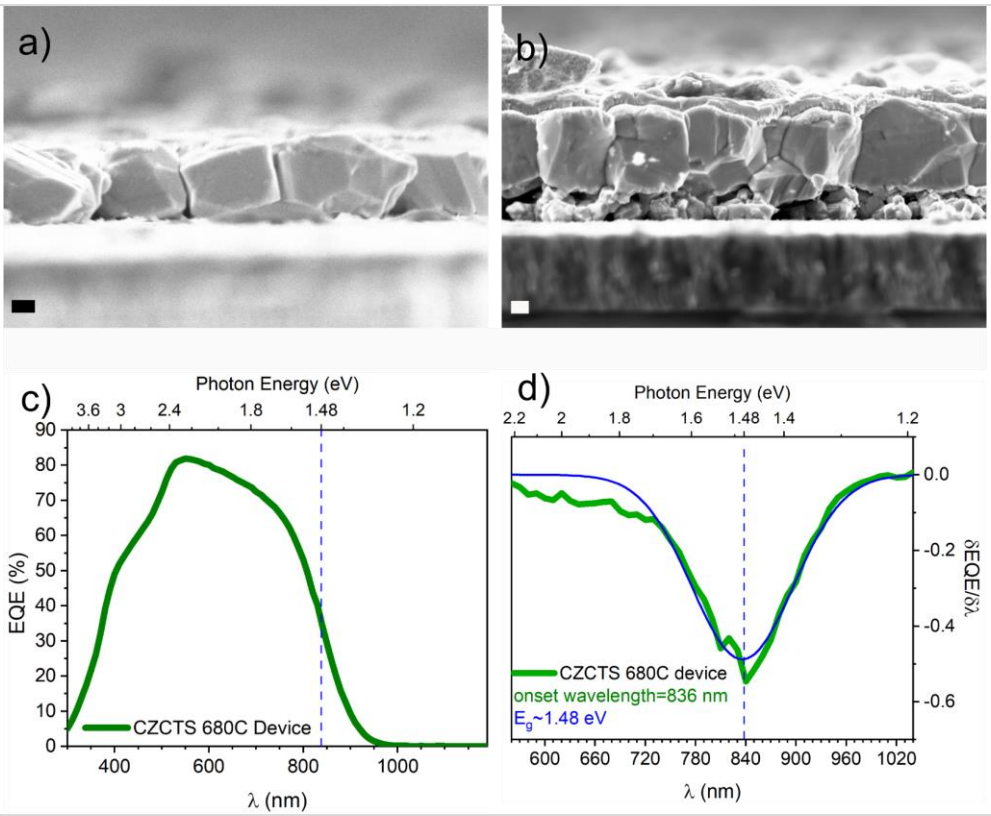

***Figure 2**: Cross-section micrographs of (**a**) the absorber layer and (**b**) the devices fabricated using CZCTS films sulfurized at 680 °C. Magnification bars: 200 nm. (c) EQE spectrum for the highest efficiency CZCTS device. (**d**) The bandgap extraction from the derivative of the EQE. Adapted from Ref. [1].*

In *Fig. 2* is also presented the external quantum efficiency (EQE) spectrum for the best device fabricated under standard conditions. The EQE spectrum bring out the device commendable carrier collection efficiency, particularly in the near-infrared range, which is a crucial indicator of the absorber's very good quality and the device's internal charge transport properties. As observed, the EQE spectrum exhibited over 80 % quantum efficiency across the entire visible light, peaking at 83.3 % at a wavelength of 580 nm. This performance is comparable to or exceeds that reported in previous studies on CZTS and Cd-alloyed CZTS absorbers, where typical EQE values peak between 75% and 85% for devices fabricated using optimized conditions. The current density, derived from the EQE data, is found to be 25.07 mA cm Reproduced from Ref. [1]., which is in close agreement with values typically observed in high-performance CZTS-based devices. The obtained results in an active area efficiency of 10.4%, which is in line with, and sometimes surpasses, efficiencies seen in recent studies of Cd-alloyed CZTS devices processed under similar conditions. The slight discrepancies between the measured and EQE-integrated current density are attributed to suboptimal mask design and metal contact grids. The bandgap of the CZCTS absorber material of 1.48 eV is also estimated from the EQE spectrum.

The study highlighted the pivotal role of alloying and of sulfurization temperature in shaping the structural and optical properties of $Cu_2(Zn,Cd)SnS_4$ (CZCTS) films. Employing a two-step process of spin coating and precise thermal treatment, a high-quality tetragonal structure aligned with the desired kesterite phase was achieved, as confirmed by X-ray diffraction and Raman spectroscopy. SEM imaging revealed a significant increase in grain size with elevated sulfurization temperatures, emphasizing the importance of temperature control for optimizing grain growth and minimizing recombination losses. The achieved power conversion efficiency (PCE) exceeding 10% can be attributed to improved crystallinity, uniform Cd distribution, and the suppression of deep-level defects.

Investigating the alloying of elements such as Se or Ag, which can reduce defect formation energy and modulate the bandgap (*e.g.*, in Ref [2]), as well as implementing light-trapping architectures or tandem designs, offers significant potential for further efficiency gains. Additionally, back interface engineering approaches are also important. Interestingly, we observed that the voids present at the CZCTS/Mo interface may act as rear-contact passivation regions, while the remaining contact areas facilitate charge collection and simultaneously maintain good adhesion of the absorber film, thereby minimizing recombination at the CZCTS/Mo interface.

References:

[1] O. El Khouja, Y. Gong, A. Jimenez-Arguijo, M. Jimenez Guerra, A. Gon Medaille, R. Scaffidi, A. Basak, C. Radu, D. Flandre, B. Vermang, S. Giraldo, M. Placidi, Z. Jehl Li-Kao, A.C. Galca, E. Saucedo, *Exploring the synthesis of $Cu_2(Zn, Cd)SnS_4$ at high temperatures as a route for high-efficiency solar cells*, Progress in Photovoltaics: Research and Applications 33 (2025) 628–643.

[2] M. Tamin, O. El Khouja, M. Guemmaz, C. Tamin, A.E. Bocirnea, I. Assahsahi, D. Chaumont, A.C. Galca, *Towards a wide bandgap absorber: structural, morphological, and optical investigation of Ag-alloyed Cu_2ZnSnS_4 thin films*, Sustainable Energy & Fuels 9 (2025) 6751–6760.

Microstructure and transport properties of Cu_2ZnSnS_4 films

O. El Khouja[1,2], B. Popescu[1], I. Assahsahi[1,2], C.C. Negrilă[1], L.N. Leonat[1], K. Nouneh[2], M. Ebn Touhami[2], A. Galaţanu[1], A.C. Gâlcă[1,3]

1) *National Institute of Materials Physics, 077125, Măgurele, Romania*
2) *Ibn Tofail University, 14000, Kenitra, Morocco*
3) *International Centre for Advanced Training and Research in Physics, 077125, Măgurele, Romania*

The Cu-based quaternary chalcogenide materials, such as $Cu_2M_IM_{II}X_4$ (where M_I= Zn, Co, Ni, Mn, and Fe; M_{II}= Sn, Ge, and Si; and X = S and/or Se), have gained significant attention for being environmentally friendly and for their suitability across a wide range of optoelectronic applications, the most targeted one being photovoltaics. The I2-II-IV-VI4 – $Cu_2ZnSn(S,Se)_4$ (CZTSSe) is derived from I-III-VI2 – $Cu(In,Ga)Se_2$ (CIGS) by replacing the more expensive In/Ga with the more abundant and less toxic Zn and Sn atoms, having similar properties, such as high absorption coefficients, which should compete with the already mature CIGS technology, considering also the prioritization of cost-effectiveness and environmental considerations.

The use of CZTSSe in such applications is closely tied to its structural, compositional, and transport properties, which can be significantly influenced by its synthesis and processing conditions. It is important to have precise control over these parameters to get the best performance across all energy conversion technologies. Sulfurization is a necessary post-deposition treatment that has been shown to improve the structural, morphological, and electrical characteristics of CZTS thin films. This high temperature treatment not only enhances the crystallinity of the films but also optimizes the distribution of elements within the material, resulting in the synthesis of the desired polymorph (kesterite), and consequently leading to improved charge carrier mobility. Sulfurization step plays also a critical role in reducing secondary phases, improving stoichiometry, and promoting grain growth.

Spray pyrolysis is considered as one of the best deposition methods due to its scalability, cost-effectiveness, and compatibility with large-area deposition, making it an excellent choice for large scale technology. Although this technique addresses some challenges, such as difficulty to use viscous solvents. NIMP researchers have been involved in such studies aiming to provide scientific insights on the Spray pyrolysis of Cu_2ZnSnS_4 [1], Cu_2CoSnS_4 [2], and Cu_2BaSnS_4 [3], addressing also the influence of the sulfurization parameters on the properties of these emerging p-type materials.

Here, we resume the major findings resulted from a recent study [1] where we investigated the effect of sulfurization duration (5, 15, 30, and 60 minutes) at 550 °C on the structural, morphological, optical, and thermoelectric properties of CZTS thin films synthesized using spray pyrolysis.

X-ray diffraction (XRD) cannot unambiguously determine the exact structural phase of CZTS because Cu^+ and Zn^{2+} are isoelectronic and possess very similar X-ray scattering factors. As a result, the obtained diffractograms can be indexed to the tetragonal CZTS structure corresponding to both the ordered kesterite phase (ICDD card no. 00-026-0575) and the disordered kesterite phase (ICDD card no. 04-015-7542). However, the method is required to possible observe secondary phases (within the method limits) as well as to assess the of average crystallite size (coherence length along certain crystallographic direction) and strain parameters (*Fig. 1*).

The variation in crystallite size along the [112], [204], and [312] directions are extracted using the Scherrer equation. The 5-minute sulfurization treatment yielded optimal microstructural evolution in CZTS thin films. Using this processing time, a robust nucleation and early-stage grain growth take place, minimizing therefore the onset of excessive grain growth or defect formation observed at longer sulfurization durations. Sulfurization times of 15 or 60 minutes led to larger grain sizes but also induced undesirable structural irregularities, potentially compromising film integrity.

The Raman spectroscopy is the complementary technique to probe the possible existence of minor phases and to discern the structure of CZTS among the polymorphs. The Raman spectra (*Fig. 2*) revealed a dominant peak at approximately 336 cm^{-1} (A1), characteristic of the CZTS structure. This confirmed the dominant presence of the CZTS in all sulfurized samples. The binary or ternary phases were not detected, suggesting that the sulfurization process effectively minimizes their formation and promotes the kesterite CZTS phase as the dominant structure. The most intense band for the 5 minutes

sulphurisation was observed at ≈336 cm^{-1}, being consistent with the A-symmetry mode of the CZTS kesterite structure, with a downward shift observed to longer thermal treatment times attributed to disorder in the cationic sublattice. The variation of the full width at half maximum (FWHM) of the most intense mode is correlated with structural properties, such as composition, grain size, and strain. The FWHM of the A-mode increased progressively with sulfurization time, underlining an increase in structural disorder and strain. Thus by Raman spectroscopy a difference between ordered kesterite and disordered/stannite phases can be easily be inferred, showing in this study that controlling the sulfurization time the ordered kesterite phase can be obtained, while prolonged annealing led to an increased fraction of disordered CZTS phase, culminating in an almost complete transition (60 min thermal treatment in this case).

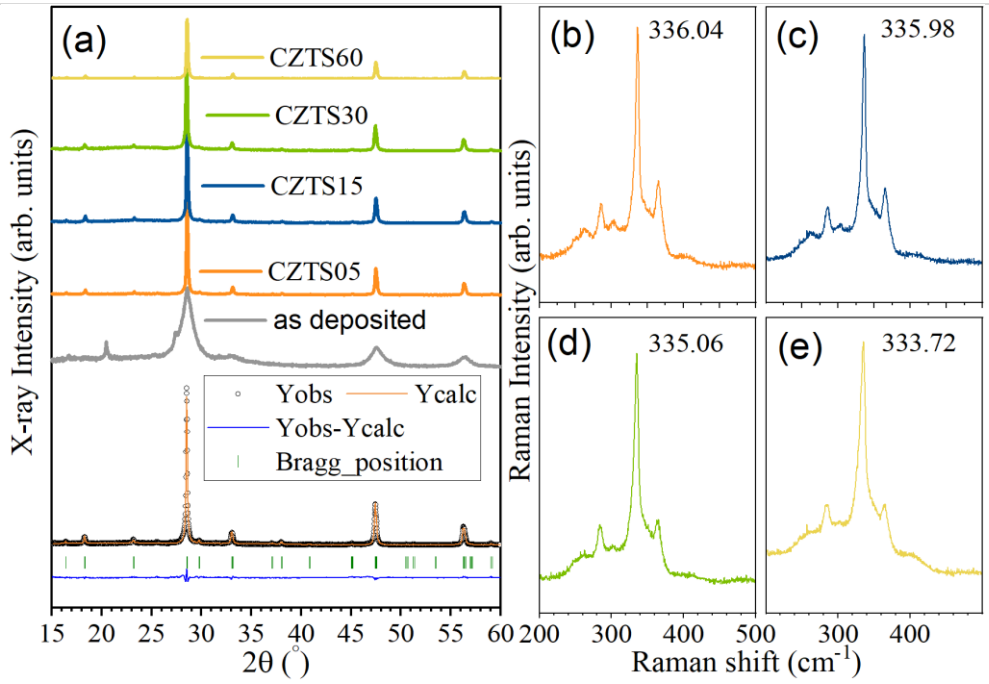

***Figure 1**: (**a**) XRD patterns of CZTS as deposited and sulfurized CZTS films; (**b–e**) Raman scattering spectra of the sulfurized CZTS films under 633 nm excitation wavelength. Adapted from Ref. [1].*

In the same study [1], we also investigated the transport properties by performing temperature-dependent measurements of the Seebeck coefficient (S), electrical conductivity (σ), and power factor (PF), with the results presented in *Fig. 2*. The Seebeck coefficient was positive for all the samples across the entire measured temperature range, indicating that the hole carriers are predominant (typical p-type semiconductor). The Seebeck coefficient increased with temperature, although it remained lower than the reported values for bulk counterparts, which are approximately 300 μV K^{-1} at room-temperature.

The behaviour of the transport coefficients is influenced by various types of defects in the samples, which may arise due to nanoscale compositional inhomogeneities, grain boundary effects, or minor structural imperfections, an increased number of the defects introducing additional charge carrier scattering centres, which in turn affects the electrical conductivity, not neglecting the charge carrier density which is strongly governed by sample stoichiometry. The annealing promoted grain growth and enhanced interfacial adhesion, effectively reducing carrier scattering at grain boundaries, leading to an overall increase in charge carrier density, which in turn lowers the Seebeck coefficient due to entropy-related effects.

A good thermoelectric material is characterized by higher values of the Seebeck coefficient, above ~150 μ K^{-1}, and electrical conductivity (~10^3 S cm^{-1}), with an optimal carrier concentration between 10^{19} cm^{-3} and 10^{21} cm^{-3}. Owing to the low electrical conductivity and Seebeck coefficient values, the PF attains low values. Thus, the highest PF values, ranging from 0.15 μW mK^{-2} at room-temperature to 0.36 μW mK^{-2} at 130 °C, were obtained for the film sulfurized for only 5 minutes.

By systematically investigating the influence of sulfurization duration on the structural, morphological, and thermoelectric properties of CZTS films, we emphasized the critical role of sulfurization conditions in obtaining the kesterite phase. Films sulfurized for 5 minutes exhibited the most desired properties, with high phase purity confirmed by XRD, Raman spectroscopy, and electrical measurements. Extended sulfurization durations (30–60 minutes) led to grain overgrowth, void formation, and the development of secondary phases, which negatively impacted electrical conductivity and PF values. The decline in thermoelectric performance with increasing sulfurization duration underscores the importance of balancing grain growth and defect minimization to optimize charge transport, while in absence of Raman spectroscopy, can be used to assess the kesterite phase.

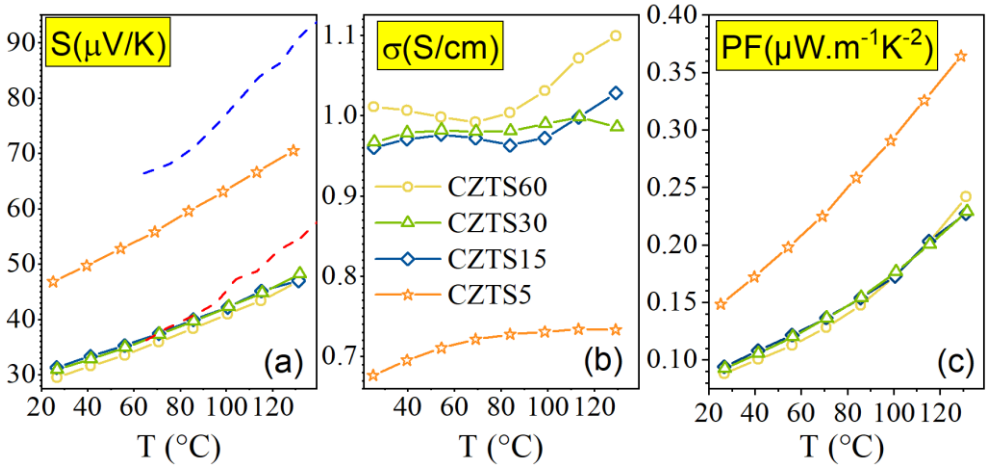

***Figure 2**: Temperature dependence of (**a**) Seebeck coefficient, (**b**) electrical conductivity, and (**c**) power factor. Adapted from Ref. [1].*

References:

[1] O. El Khouja, B. Popescu, I. Assahsahi, C.C. Negrila, L.N. Leonat, K. Nouneh, M. Ebn Touhami, A. Galatanu, A.C. Galca, *Improved sulfurization process for enhancing the microstructure and transport properties of spray pyrolysis-deposited Cu_2ZnSnS_4 films*, Ceramics International 51 (2025) 47818–47829.

[2] O. El Khouja, I. Assahsahi, K. Nouneh, M. Ebn Touhami, M. Secu, A. Talbi, Y. Khaaissa, E. Matei, V. Stancu, A. Galatanu, A.C. Galca, *Structural and transport properties of Cu_2CoSnS_4 films prepared by spray pyrolysis*, Ceramics International 48 (2022) 32418–32426.

[3] A.S. Kadari, A. Nebatti Ech-Chergui, P.R. Ghediya, A. Guendouz, M. Guezzoul, O. El Khouja, A.E. Bocirnea, K. Driss-Khodja, B. Amrani, A.C. Galca, *Growth and optimization of spray coated Cu_2BaSnS_4 thin films for solar photovoltaic application*, Materialia 36 (2024) 102178.

Experimental and theoretical perspective on band gap modulation in Sr^{2+} modified $BaTiO_3$ capacitors

Y. Zidi[1], O. Khaldi[2], R.E. Pătru[3], L.N. Leonat[3], M. Enculescu[3], V. Toma[3], A. Stepanova[3], R.B. Younes[1], A.C. Gâlcă[3,4]

1) *Laboratory of Technology, Energy and Innovative Materials, TEMI, Department of Physics, Faculty of Sciences of Gafsa, University of Gafsa, 2112, Gafsa, Tunisia*
2) *Laboratory of Materials, Organization and Properties, LMOP (LR99ES17), Faculty of Sciences of Tunis, University of Tunis El Manar, 2092, Tunis, Tunisia*
3) *National Institute of Materials Physics, 077125, Măgurele, Romania*
4) *International Centre for Advanced Training and Research in Physics, 077125, Măgurele, Romania*

Barium titanate ($BaTiO_3$) remains a benchmark material in the family of perovskite-structured dielectrics, being intensively investigated due to its remarkable ferroelectric, piezoelectric, and electro-optical properties [1]. In the current technological context, the development of photocatalytic devices and self-powered UV photodetectors requires precise band structure engineering to optimize the separation of photogenerated charge carriers. The main motivation for this study was to explore the mechanisms by which the progressive substitution of barium with strontium modulates the intrinsic properties of the $Ba_{1-x}Sr_xTiO_3$ (BST) system. Going beyond conventional approaches, the research establishes a rigorous correlation between chemical composition, phase transitions, and dielectric dynamics by combining advanced experimental methods with theoretical modelling using Density Functional Theory (DFT) [2]. The desired outcome is to obtain materials with an adaptable bandgap, capable of optimizing functional performance in emerging applications of photodetection.

Details regarding the technological flow, as well as preliminary results obtained by X-ray diffraction (XRD) and scanning electron microscopy (SEM) to confirm phase purity and evaluate initial morphology, are shown schematically (*Fig. 1*). The synthesis of BST ceramics with strontium content x = 0, 0.3, 0.4, 0.5, 0.7, and 1 was performed using the conventional solid-state reaction method (*Fig. 1a*). The process included grinding and homogenization of high-purity precursors ($BaCO_3$, $SrCO_3$, TiO_2) in ethanol, calcination at 1100 °C for 2 hours to form the perovskite phase and the sintering at 1400 °C to obtain well-densified, coarse-grained ceramics. XRD investigations revealed a significant structural transformation induced by doping (*Fig. 1b,c*). For compositions with $x \leq 0.3$, the system crystallized in the tetragonal phase, while increasing strontium content $x \geq 0.4$ favoured the transition to cubic symmetry. This evolution is marked by the contraction of the unit cell from 64.29 $Å^3$ to 59.58 $Å^3$ and the decrease of the tetragonal ratio *c/a* towards the unit value (*Fig. 1d,f*). The grains morphology changed from rounded polyhedral shapes to sharp-edged cubic geometries, with strontium acting as an inhibitor of grain growth in the tetragonal phase (*Fig. 1e*). The average grain size decreased progressively as the strontium concentration increases, confirming its role as a grain growth inhibitor, however, the size of the crystallites showed a non-monotonic evolution, marked by an initial decrease in the tetragonal phase followed by a sharp increase as the cubic symmetry stabilizes (*Fig. 1g*).

The analysis of dielectric behaviour as a function of temperature highlights the intrinsic correlation between chemical composition and phase transition dynamics in the BST system (*Fig. 2*).

The Sr addition shifted the Curie point to the cryogenic range (*Fig. 2a*) without degrading the dielectric quality of the material or the risk of energy dissipation, with losses remaining low (*Fig. 2b*). Analysis of the modified Curie-Weiss law (*Fig. 2c,d*) indicated an increase in the diffuse character of the transition. The Curie temperature (T_C) decreased with increasing strontium concentration, from 132 °C for pure samples to −110 °C for Sr-rich compositions (*Fig. 2e*). This trend of decreasing ferroelectric phase stability is attributed to changes in the distortions of the TiO_6 octahedra, a phenomenon induced by the chemical stress generated by the difference between the ionic radii of the two cations [3]. The chemical stress induced by the smaller ionic radius of the Sr^{2+} cation destabilized the long-range ferroelectric order and favoured cubic symmetry. Validation of the band-gap modulation mechanisms by DFT modelling confirmed the accuracy of the PBE0 functional in predicting electronic properties, revealing a decrease in E_g from 3.142 eV to 3.082 eV with increasing Sr content. This narrowing of the energy

barrier, coupled with the maintenance of low dielectric losses despite the T_C shifting towards the cryogenic range, demonstrated the versatility of the BST system for optoelectronic applications. Furthermore, the correlation between activation energies (E_a = 0.685 – 1.065 eV) and oxygen vacancy dynamics highlighted that rigorous control of the Ba/Sr ratio optimizes the dielectric response and the efficiency of charge carrier separation. Thus, the microstructural stability and adaptability of the band structure confirmed the potential of these materials in the development of UV photodetectors and high-performance energy storage systems (*Fig. 3*).

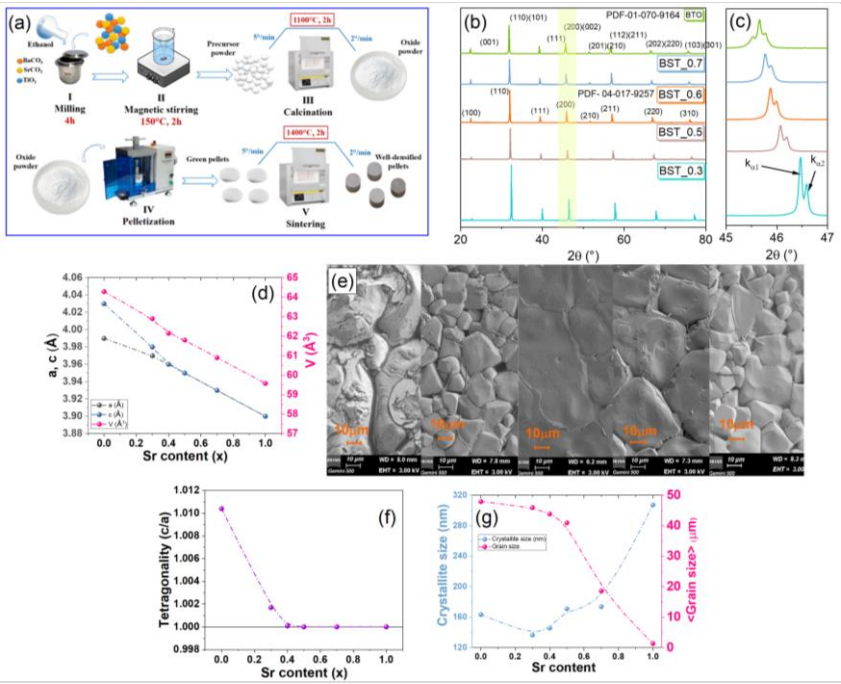

***Figure 1**: Analysis of the synthesis process and structural-morphological characterization of the BST ceramics: (**a**) technological flow diagram for the solid-phase reaction method, including the stages of homogenization, calcination and sintering; (**b**) XRD patterns recorded at room-temperature; (**c**) detail of the (200) reflection; (**d**) evolution of lattice parameters (a and c) and unit cell volume (V) as a function of Sr concentration; (**e**) micrographs obtained on fracture surfaces; (**f**) variation of the tetragonal coefficient (c/a); and (**g**) dependence of the average grain and crystallite size on strontium content. Reproduced from Ref. [2].*

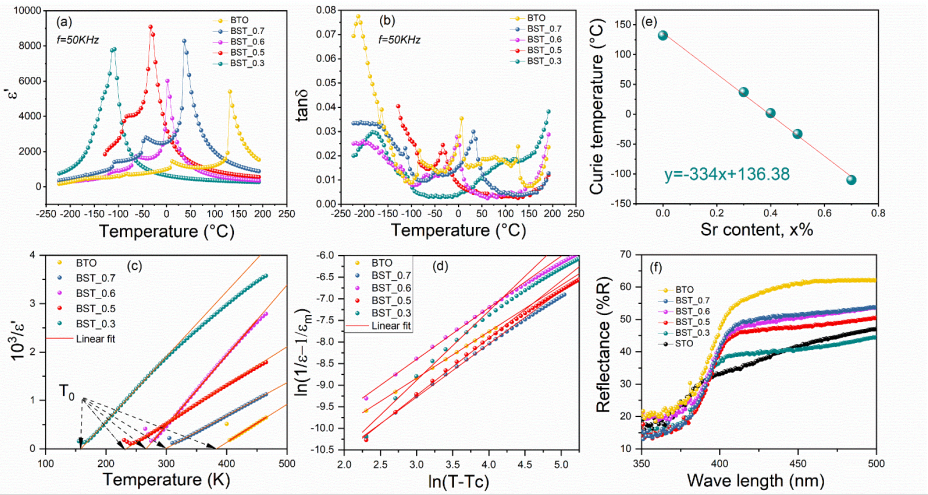

***Figure 2**: Characterization of the dielectric and optical properties of the BST ceramics as a function of temperature and composition: temperature dependence of (**a**) the real part of permittivity and (**b**) dielectric losses at a frequency of 50 kHz, together with analysis based on the (**c**) classical and (**d**) generalized Curie-Weiss law for the BST system; (**e**) Linear evolution of the T_C as a function of Sr content described by the regression equation; (**f**) UV-Vis reflectance spectra as a function of wavelength, illustrating the shift of the absorption threshold and the modulation of the band gap by Ba/Sr substitution. Reproduced from Ref. [2].*

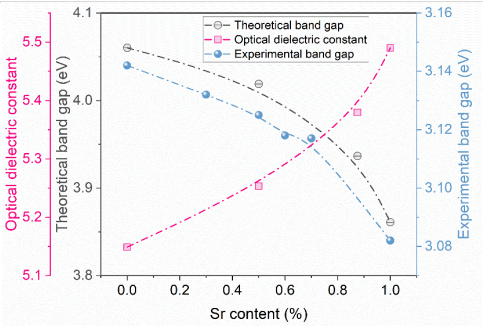

***Figure 3**: Correlation between optical parameters and band structure in the BST system as a function of strontium content. Reproduced from Ref. [2].*

The study demonstrated that the progressive substitution of Ba with Sr is an effective method of band structure engineering, reducing the band gap energy, and optimizing the material for optoelectronic applications. The rigorous correlation between experimental data and DFT modelling confirmed the accuracy of the PBEO functional in predicting the electronic properties and stability of perovskite phases. This compositional versatility, maintained without degradation of dielectric losses, underpined the use of the BST system in the development of self-powered UV photodetectors and high-performance energy storage systems.

References:

[1] A. Ianculescu, L. Mitoseriu, D. Berger, C.E. Ciomaga, D. Piazza, C. Galassi, *Composition-dependent ferroelectric properties of $Ba_{1-x}Sr_xTiO_3$ ceramics*, Phase Transitions 79 (2006) 375–388.

[2] Y. Zidi, O. Khaldi, R.E. Patru, L.N, Leonat, M, Enculescu, V. Toma, A. Stepanova, R. Ben Younes, A.C. Galca, *Experimental and theoretical perspective on band gap modulation in Sr^{2+} modified $BaTiO_3$ capacitors*, Ceramics International 51 (2025) 18166–18177.

[3] A. Ianculescu, I. Pintilie, C.A. Vasilescu, M. Botea, A. Iuga, A. Melinescu, N. Drăgan, L. Pintilie, *Intrinsic pyroelectric properties of thick, coarse grained $Ba_{1-x}Sr_xTiO_3$ ceramics*, Ceramics International 42 (2016) 10338–10348.

Composition-dependent structural, microstructural and functional characteristics of fine-grained $BaTi_{1-x}Hf_xO_3$ ceramics consolidated by Spark Plasma Sintering

E.M. Soare[1,2], C.A. Stanciu[2,3], R.E. Pătru[4], V.A. Surdu[5], N. Horchidan[6,7], L. Mitoșeriu[6], I. Pintilie[4], B.S. Vasile[2], A.I. Nicoară[2], R.D. Truşcă[2], A.C. Ianculescu[2]

1) *Institute of Physical Chemistry "Ilie Murgulescu", Romanian Academy, 060021, Bucharest, Romania*
2) *Faculty of Chemical Engineering and Biotechnologies, National University of Science and Technology POLITEHNICA Bucharest, 011061, Bucharest, Romania*
3) *National Institute for Lasers, Plasma and Radiation Physics, 077125, Măgurele, Romania*
4) *National Institute for Materials Physics, 077125, Măgurele, Romania*
5) *Faculty of Materials Science and Engineering, Transilvania University of Braşov, 500036, Braşov, Romania*
6) *Faculty of Physics, "Alexandru Ioan Cuza" University of Iaşi, 700507, Iaşi, Romania*
7) *RAMTECH Centre, Department of Exact and Natural Sciences, Institute of Interdisciplinary Research, 700507, Iaşi, Romania*

Lead-free $BaTi_{1-x}Hf_xO_3$ (BTH) ceramics represent a sustainable and versatile alternative for high-performance electromechanical applications, offering significant advantages in terms of environmental compatibility and functional tunability [1]. Starting from the base BTH system, this research branches into two distinct yet complementary directions to unlock its full potential. The first direction focuses on compositional engineering, specifically investigating how varying hafnium concentrations (x = 0.05, 0.10, 0.15, 0.20) induce a transition from a classical ferroelectric state to a relaxor-like behaviour [2]. The second direction explores microstructural optimization, analysing the grain size effects, ranging from the micronic to the nanometric scale, in stabilizing a coexistence of polymorphic rhombohedral-orthorhombic-tetragonal phases [3]. By employing advanced sintering techniques to precisely tailor the hafnium content and grain size, the research demonstrates that the interdependence of compositional modification by Hf-substitution and nanostructuring is fundamental to achieving superior dielectric and piezoelectric performance.

The structural and microstructural evolution of the BTH ceramics highlighted the dual influence of chemical composition and grain size refinement (*Fig. 1*). The investigation revealed that Hf substitution acts as a major driver for structural modification in the BTH ceramics (*Fig. 1a–h*). Increasing the Hf content from x = 0 to x = 0.20 induced a linear expansion of the unit cell volume due to the larger ionic radius of Hf^{4+} compared to Ti^{4+}. This chemical modification led to a systematic reduction in the Curie temperature (T_C) and a convergence of the low-temperature polymorphic transitions (R–O and O–T) towards a pinched region at approximately x = 0.10. As shown in the proposed phase diagram (*Fig. 1b*), this convergence facilitated a transition from classical ferroelectric order to a diffuse, relaxor-like state at higher concentrations. The use of the modified Pechini method combined with spark plasma sintering (SPS) proved instrumental in achieving dense ceramics while strictly inhibiting grain growth. As seen in the FE-SEM analysis (*Fig. 1c–f*), Hf addition further suppresses grain coarsening, shifting the microstructure from the micrometre range to the nanometre scale. The linear increase in unit cell volume and the tetragonality decrease in as the Hf content reaches x = 0.20 (*Fig. 1g*). Hafnium acted as a growth inhibitor; both mean crystallite and particle size decreased with increasing doping, while internal micro-strains rose due to hafnium-induced lattice distortions (*Fig. 1h*).

Landau-Devonshire simulations confirmed that grain size reduction and non-equilibrium stress fields disturb the energy barriers between symmetries, favouring the coexistence of rhombohedral and cubic phases in nanocrystalline BTH10 (*Fig. 1i*). This scale-driven phase modulation results in superior dielectric stability and a remarkable energy storage efficiency of 86.9%. Microstructural control in the consolidated ceramics was achieved by comparing conventional sintering (CS) with SPS. For the x = 0.10

composition, the average grain size was effectively tuned by adjusting the sintering temperature and method (*Fig. 1j*).

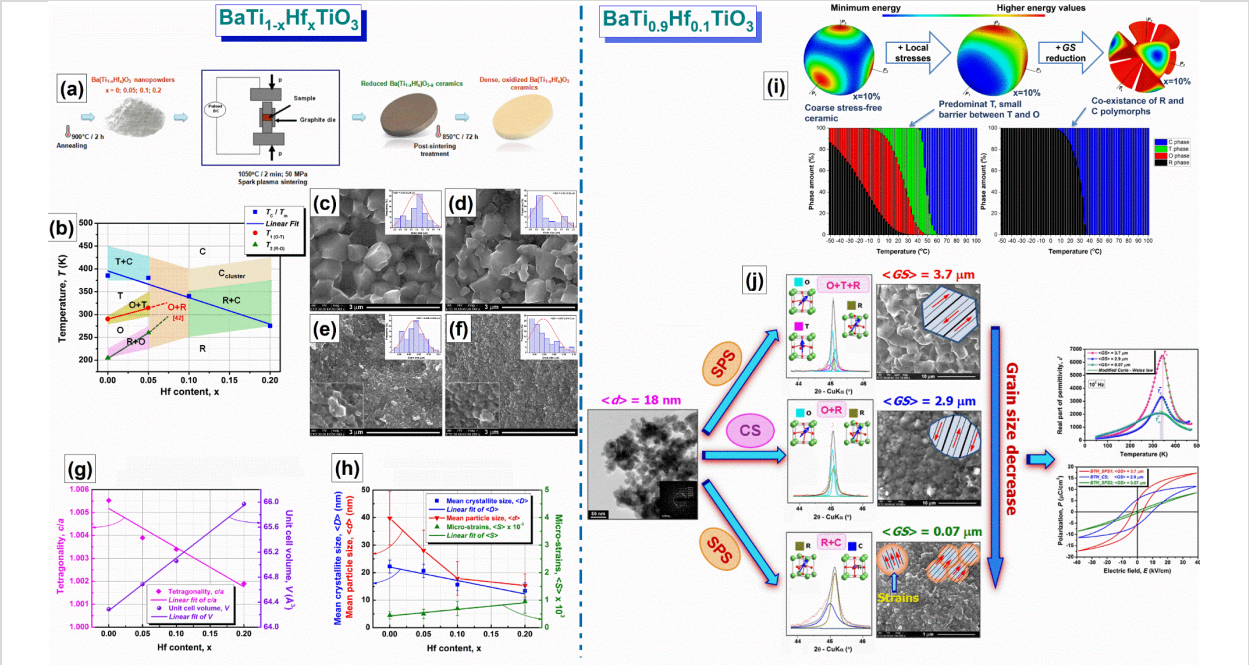

***Figure 1**: Compositional and microstructural design of the BTH ceramics: (**a**) schematic of the combined synthesis process from nanopowder obtained via modified Pechini, consolidation and post-sintering re-oxidation; (**b**) proposed phase diagram of the BTH ceramics; (**c–f**) FE-SEM micrographs of BTH ceramics with varying Hf-concentrations (x = 0, 0.05, 0.10, 0.20); (**g**) evolution of structural parameters as a function of Hf-content; (**h**) correlation between mean crystallite size, particle size, and internal micro-strain as a function of Ti-substitution by Hf; (**i**) theoretical representations based on the Landau-Devonshire model, illustrating the impact of local strain and grain size reduction on free energy minima and polymorphic phase stability for the x = 0.10 composition; (**j**) comparative scale-effect study for $BaTi_{0.90}Hf_{0.10}O_3$ and the influence of SPS sintering methods vs. conventional sintering on grain size, phase coexistence, and the resulting impact on dielectric permittivity and P–E hysteresis loops. Adapted from Refs. [2,3].*

The dielectric, ferroelectric properties, along with energy density, storage efficiency and tunability were systematically investigated as a function of both Hf composition and grain size effects (*Fig. 2*).
Dielectric investigations confirmed that Hf-substitution induces a ferroelectric-to-relaxor crossover, marked by a 5.5 K/at.% reduction in TC and a diffuse phase transition at BTH10. This compositional tuning, combined with <GS> refinement, significantly enhanced energy storage capabilities. For the BTH10 composition, reducing the <GS> to the nanocrystalline regime *via* low-temperature SPS resulted in a shift from orthorhombic to rhombohedral/cubic phase coexistence. This scale-induced phase modulation, coupled with the inhibition of domain wall motion in fine grains, led to slender P–E loops with reduced hysteresis. The nanocrystalline BTH10 ceramics exhibited a remarkable energy storage efficiency of 86.9% and improved thermal stability of the dielectric constant. Arrhenius analysis further confirmed that nanostructuring increases activation energies for conduction, effectively suppressing leakage currents and dielectric losses, which is vital for high-field electronic applications.
The experimental findings are strongly supported by Landau-Devonshire thermodynamic calculations, which provide a theoretical framework for the observed phase stabilization under local stress and nanostructuring. Furthermore, the systematic suppression of frequency-dependent losses through microstructural control confirmed the high reliability of these BTH ceramics for high-frequency microwave and energy storage applications.
These studies [2,3] demonstrated that the combined control of compositional engineering and microstructural refinement offers an effective strategy for tailoring the functional properties of BTH ceramics, establishing these lead-free materials as promising high-performance candidates for next-generation energy storage and tunable electronic devices.

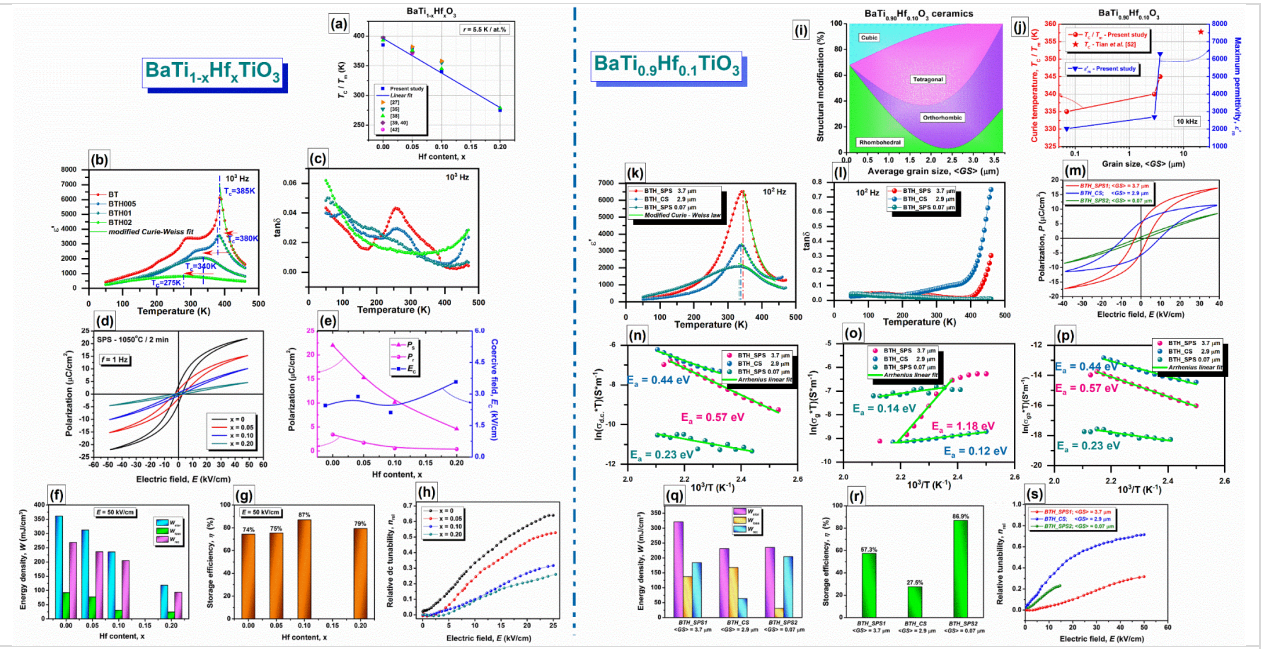

***Figure 2**: Dielectric, ferroelectric, and energy storage performance of BTH ceramics analysed based on compositional effects: (**a**) T_C dependence on Hf-content; (**b,c**) temperature-dependent dielectric properties showing the ferroelectric-relaxor crossover; (**d,e**) P–E loops and polarization/coercive field variation with Hf-content; (**f–h**) Hf-dependent energy density, storage efficiency and tunability; and based on size effects: (**i,j**) polymorphic phase stability (R, O, T, C) and dielectric parameters evolution vs. <GS>; (**k,l**) frequency-dependent dielectric response; (**m**) P–E loops. (**n–p**) Transport mechanisms: Arrhenius plots for AC conductivity and dielectric relaxations in bulk and grain boundaries. (**q–s**) Impact of nanostructuring on energy density, storage efficiency and tunability. Adapted from Refs. [2,3].*

References:

[1] J. Li, D. Zhang, S. Qin, T. Li, M. Wu, D. Wang, Y. Bai, X. Lou, *Large room-temperature electrocaloric effect in lead-free $BaHf_xTi_{1-x}O_3$ ceramics under low electric field*, Acta Materialia, 115 (2016) 58–67.

[2] **E.M. Soare, C.A. Stanciu, R.E. Patru, V.A. Surdu, N. Horchidan, L. Mitoseriu, I. Pintilie, B.S. Vasile, A.I. Nicoara, R.D. Trusca, A.C. Ianculescu, *Composition-dependent structural, microstructural and functional characteristics of fine-grained $BaTi_{1-x}Hf_xO_3$ ceramics consolidated by Spark Plasma Sintering*, Journal of the European Ceramic Society 45 (2025) 117600.**

[3] **E.M. Soare, C.A. Stanciu, R.E. Patru, V.A. Surdu, L. Padurariu, N. Horchidan, A.I. Nicoara, L. Trupina, B.S. Vasile, R.D. Trusca, L. Mitoseriu, A.C. Ianculescu, *Grain size effects in $BaTi_{0.90}Hf_{0.10}O_3$ ceramics with phase coexistence: the influence of nanostructuring and of the internal stress on the functional properties*, Journal of Materials Research and Technology 38 (2025) 5389–5408.**

Enhanced thermoelectric performance of $Mg_2Si_{0.3}Sn_{0.7}$ alloys *via* dual Ag–Bi doping

I. Assahsahi[1,2], A. Galaţanu[1], R. El Bouayadi[2], D. Zejli[2], B. Popescu[1]

1) *National Institute of Materials Physics, 077125, Măgurele, Romania*
2) *National School of Applied Sciences, Ibn Tofail University, 14000, Kenitra, Morocco*

Over the past decade, several classes of thermoelectric materials have been extensively investigated, including bulk compounds such as skutterudites, chalcogenides, oxides, and silicides, as well as low-dimensional systems such as thin films and nanostructured materials. Among these, magnesium silicide-based solid solutions, $Mg_2Si_{1-x}Sn_x$, are particularly attractive due to their abundance, low toxicity, thermal stability, and potential for medium-temperature applications.

The thermoelectric performance of a material is quantified by the dimensionless figure of merit, $ZT = S^2\sigma/\kappa T$, where S is the Seebeck coefficient, σ the electrical conductivity, κ the thermal conductivity, and T the absolute temperature. Enhancing ZT requires optimizing electronic transport and reducing lattice thermal conductivity, both of which are strongly influenced by crystal structure and microstructural features. In the $Mg_2Si_{1-x}Sn_x$ system, introducing lattice disorder through solid-solution formation enhances phonon scattering. Compositions near $x \approx 0.6–0.7$ also exhibit particularly favourable thermoelectric behaviour. This enhancement is attributed to conduction-band convergence, which improves electronic transport, and to phase separation within the miscibility gap, which increases phonon scattering. As a result, ZT values exceeding unity have been reported in appropriately doped compositions. Performance optimization of $Mg_2Si_{1-x}Sn_x$ primarily focused on controlling carrier concentration through doping, band-structure engineering *via* the Si/Sn ratio, and enhancing phonon scattering through point defects, nanoprecipitates, and microstructural refinement. For n-type $Mg_2Si_{1-x}Sn_x$, bismuth has been shown to effectively increase electrical conductivity while reducing lattice thermal conductivity, although excessive carrier concentrations may limit the Seebeck coefficient. In contrast, p-type $Mg_2Si_{1-x}Sn_x$ remains underdeveloped, with relatively low ZT values, mainly due to insufficient carrier concentration and high lattice thermal conductivity.

To address these limitations, dual-doping strategies have been proposed to exploit synergistic effects between dopants, enabling simultaneous tuning of electronic and thermal transport properties. While such approaches have been widely applied to n-type systems, recent studies have demonstrated their potential for improving p-type $Mg_2Si_{1-x}Sn_x$ by increasing hole concentration through combined substitutions at the Mg and Si/Sn sites. Within this research framework, our work initially focused on optimizing the synthesis and microstructural control of $Mg_2Si_{1-x}Sn_x$ solid solutions. A two-step synthesis route combining melting and spark plasma sintering was developed to ensure chemical homogeneity and limit magnesium losses [1]. Building on this optimized synthesis, p-type co-doping strategies were subsequently investigated, notably Ag-Ga co-doping, which led to a significant increase in hole carrier concentration, although the resulting thermoelectric performance remained limited [2]. The present study extends these efforts to n-type $Mg_2Si_{1-x}Sn_x$, co-doped with Ag and Bi, to investigate the effects of donor–acceptor co-doping on electronic and thermal transport. Bi substitutes Si/Sn sites as a donor, increasing electron concentration, while Ag occupies Mg sites as an acceptor, affecting carrier generation and lattice thermal conductivity. This co-doping strategy enables simultaneous tuning of electronic and thermal transport and regulation of carrier concentration, which is expected to contribute to an enhanced Seebeck coefficient [3].

Fig. 1a–c summarizes the electrical transport properties of $Mg_2Si_{0.3}Sn_{0.7}$ as a function of doping. The undoped sample exhibited increasing electrical conductivity with temperature, characteristic of intrinsic semiconducting behaviour, while Bi and Ag-Bi-doped samples show significantly higher conductivity and a monotonic decrease with temperature, indicating degenerate, extrinsic transport. Bi doping enhanced conductivity by nearly two orders of magnitude through increased electron concentration, whereas Ag co-doping reduced σ due to donor compensation and increased carrier scattering, with the highest conductivity obtained for $Mg_{1.98}Ag_{0.02}Si_{0.29}Sn_{0.69}Bi_{0.02}$ owing to its optimized carrier concentration and mobility (*Table 1*). Correspondingly, the Seebeck coefficient remained negative over the entire temperature range, confirming n-type conduction; Bi doping reduced |S|, while Ag–Bi co-doping enhanced the Seebeck coefficient by lowering the carrier concentration. The Pisarenko

analysis at room-temperature showed good agreement with the Single Parabolic Band model, with co-doped samples exhibiting intermediate effective masses, indicating that Ag–Bi co-doping effectively tuned the Fermi level and optimized the balance between electrical conductivity and Seebeck coefficient.

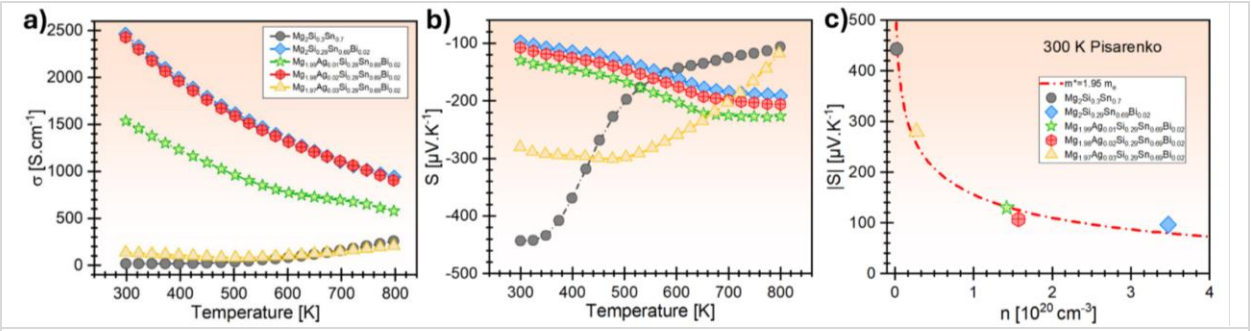

***Figure 1**: Temperature dependence of (**a**) electrical conductivity and (**b**) Seebeck coefficient. (**c**) Pisarenko plot at room-temperature. Reproduced and adapted from Ref. [3].*

***Table 1**: Room-temperature physical properties $Mg_{2-x}Ag_x(Si_{0.3}Sn_{0.7})_{1-y}Bi_y$.*

Sample	n (cm^{-3})	μ ($cm^2\ V^{-1}\ s^{-1}$)	S (μV K^{-1})	σ (S cm^{-1})	R_H ($cm^3\ C^{-1}$)	E_g (eV)	m*(m_e)
MSS	1.91×10^{18}	63.62	-442.96	18.32	-3.271	0.27	1.45
MSSB	3.47×10^{20}	49.12	-96.72	2463.75	-0.017	0.30	2.41
MASSB₁	1.42×10^{20}	52.91	-130.16	1537.60	-0.043	0.35	1.91
MASSB₂	1.57×10^{20}	92.44	-107.63	2429.18	-0.039	0.32	1.61
MASSB₃	2.71×10^{19}	32.39	-279.92	137.39	-0.229	0.28	2.35

Fig. 2 shows the temperature dependence of the total, electronic, and lattice thermal conductivities of $Mg_{2-x}Ag_x(Si_{0.3}Sn_{0.7})_{1-y}Bi_y$. Bi doping significantly reduces the lattice thermal conductivity through mass disorder, lattice distortion, and enhanced phonon scattering, while Ag co-doping lowers the electronic contribution via charge compensation. Overall, Bi and Ag co-doping widened the energy band gap, suppressed bipolar conduction at high temperatures, and reduced thermal conductivity, complementing the optimized electrical conductivity and Seebeck coefficient to improve thermoelectric performance. Consequently, the figure of merit ZT (*Fig. 3*) increased with temperature, reaching 1.07 for Bi-doped samples and 1.12–1.13 for Ag–Bi co-doped samples, with the highest average ZT obtained for $MASSB_1$ and $MASSB_2$.

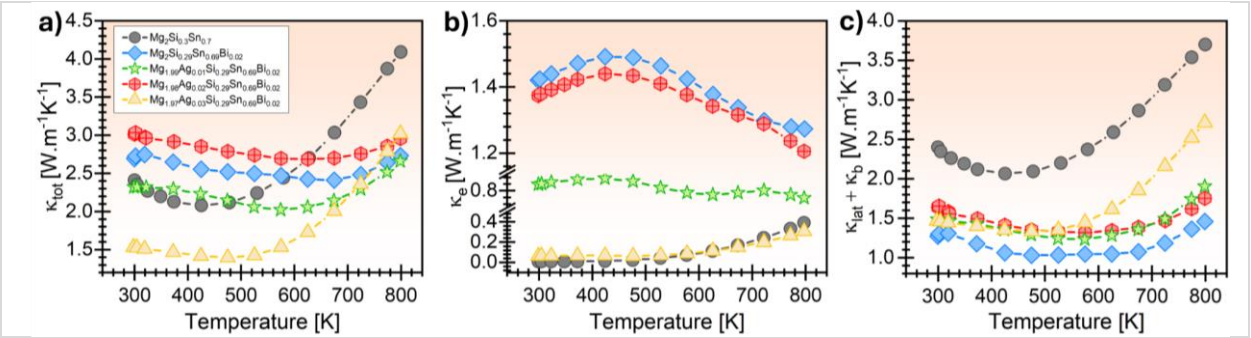

***Figure 2**: Temperature dependence of (**a**) total thermal conductivity; (**b**) Electronic thermal conductivity; and (**c**) lattice thermal conductivity. Reproduced and adapted from Ref. [3].*

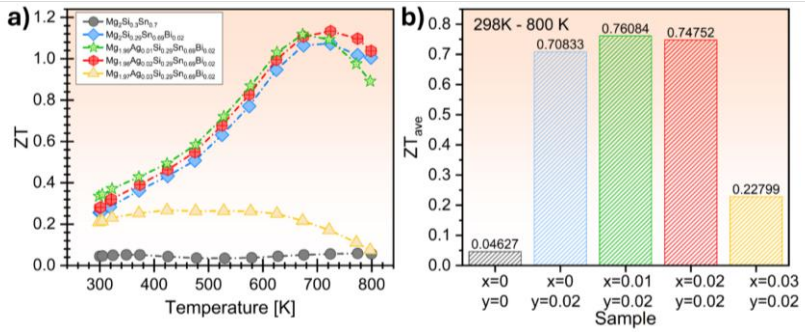

***Figure 3**: (**a**) Temperature dependent ZT and (**b**) average ZT as a function of Ag and Bi concentrations. Reproduced and adapted from Ref. [3].*

References:

[1] I. Assahsahi, B. Popescu, M. Enculescu, M. Galatanu, A.C. Galca, R. El Bouayadi, D. Zejli, A. Galatanu, *Influence of the synthesis parameters on the transport properties of $Mg_2Si_{0.4}Sn_{0.6}$ solid solutions produced by melting and spark plasma sintering*, Journal of Physics and Chemistry of Solids 163 (2022) 110561.

[2] I. Assahsahi, B. Popescu, R. El Bouayadi, D. Zejli, M. Enculescu, A. Galatanu, *Thermoelectric properties of p-type $Mg_2Si_{0.3}Sn_{0.7}$ doped with silver and gallium*, Journal of Alloys and Compounds 944 (2023) 169270.

[3] I. Assahsahi, A. Galatanu, R. El Bouayadi, D. Zejli, B. Popescu, *Synergistic effects of Ag-Bi co-doping on thermoelectric properties of $Mg_2Si_{0.3}Sn_{0.7}$ solid solutions*, Journal of Alloys and Compounds 1039 (2025) 183310.

Thermal memory effects and dynamics of martensitic transformation in Ni–(Mn,Fe)–Ga shape memory alloys

F. Țolea, M. Sofronie, B. Popescu, C. Bartha, M. Enculescu, M.A. Grigoroscuță, M. Niță, P. Badică, M. Țolea

National Institute of Materials Physics, 077125, Măgurele, Romania

Shape memory alloys (SMA) are known to undergo a solid-state phase transition from a high-temperature, high-symmetry phase (austenite) to a low-temperature, low-symmetry phase (martensite). The non-diffusive nature and low enthalpy of this phase transition allow it to be triggered by mechanical stress (or by an applied magnetic field in the case of ferromagnetic SMA) [1,2]. Interestingly, SMA have been shown to remember not only shapes, but also temperatures corresponding to incomplete phase transitions that occurred in the past. The Thermal Memory Effect (TME) in SMA [3,4], sometimes also referred to as "Thermal Arrest" (TA), is, however, less well understood and has received comparatively less attention. In short, the TME manifests as follows: a system initially in the martensite phase at low temperature is warmed to a point where the austenite transformation has begun but not completed — let us call this the "Arrest Temperature" (AT). The system is then fully cooled back into martensite and finally fully heated into austenite. If one records the calorimetric signal — *i.e.*, the heat flow — during this final martensite-to-austenite transformation, a dip will be observed at a temperature close to AT.

In this work [5], we demonstrated that NiFeGa and NiMnGa alloys, prepared as polycrystalline ribbons, exhibit a robust TME. This behaviour combined with the possibility to shift the transformation intervals, qualifies these alloys as potential “maximum thermometers”. Variations in chemical composition can significantly shift the transformation temperatures (*Fig. 1*), while thermal treatments (not shown in this summary) provide an additional degree of control over the transformation range.

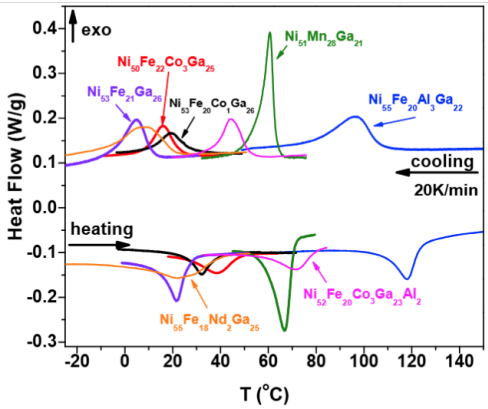

***Figure 1**: DSC heat-flow curves showing the transformation temperatures for the compositions $Ni_{50}Fe_{21}Ga_{26}$, $Ni_{55}Fe_{18}Nd_2Ga_{25}$, $Ni_{53}Fe_{20}Co_1Ga_{26}$, $Ni_{50}Fe_{22}Co_3Ga_{25}$, $Ni_{51}Mn_{28}Ga_{21}$, $Ni_{52}Fe_{20}Co_3Ga_{23}Al_2$, and $Ni_{55}Fe_{20}Al_3Ga_{22}$. All samples are as-quenched (AQ) ribbons. Reproduced from Ref. [5].*

Single and triple TME on NiFeGa alloy is presented in *Fig. 2* (details can be found in the figure’s caption). An SMA-based maximum thermometer would embody the concept “the material is the machine”. A few milligrams of alloy capable of recording the maximum temperature reached can be useful in food storage and transport, medicine handling, or industrial monitoring. Other potential uses include cold-chain logistics and overheating detection in electronics or batteries—situations where a small, passive, and robust indicator offers clear advantages.

We hope that our work will stimulate further research, both toward a deeper understanding of the TME and toward its development into a practical tool.

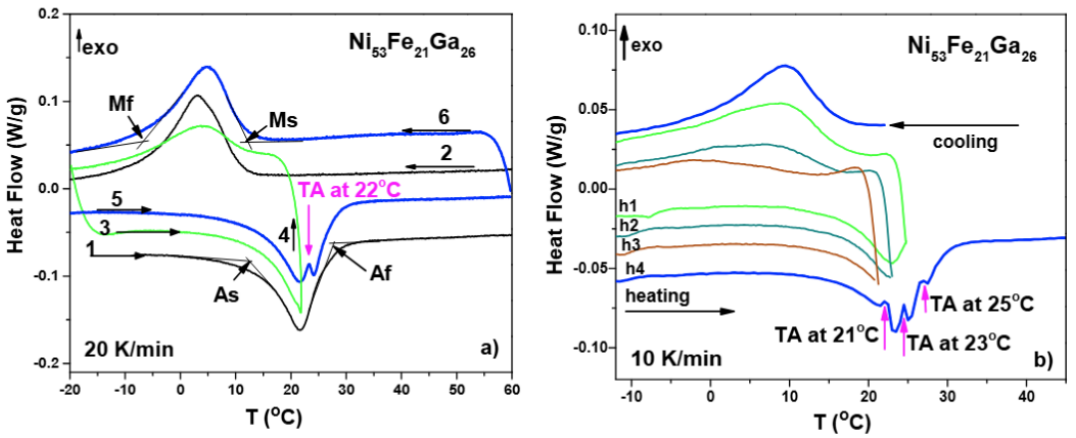

***Figure 2**: For the as-quenched (AQ) ribbons of the alloy $Ni_{53}Fe_{21}Ga_{26}$, we recorded: (**a**) complete direct and reverse martensitic transformations (curves labelled 1, 2, and 6; curve 6 corresponds to the final complete martensitic transformation and is shifted upward for clarity). The transformation temperatures M_s, M_f, A_s, and A_f were determined using the tangential method. A single thermal arrest at 22 °C was then performed: incomplete heating curve 3, followed by cooling back into martensite and the reading curve 4, which shows the characteristic dip. (**b**) three thermal arrests at 25 °C, 23 °C, and 21 °C, applied in decreasing order and denoted by h_1, h_2, and h_3 (heating curves). The final heating curve, h_4, reads the thermal memory, demonstrating the ability to record multiple temperatures. The heating/cooling rates were 20 K min^{-1} for (a) and 10 K min^{-1} for (**b**). Reproduced from Ref. [5].*

In Ref. [6], $Ni_{49+x}Mn_{32-2x}Ga_{19+x}$ (x = 0, 2) Heusler alloys were fabricated by SPS from melt-spun ribbon powders and characterized structurally, thermally, and mechanically. While ribbons and powders showed similar trends, the bulk sintered alloys exhibit opposite behavior: $Ni_{49}Mn_{32}Ga_{19}$ displays higher enthalpy, increased MT temperature (+9 K), and reduced hysteresis (5 K), whereas $Ni_{51}Mn_{28}Ga_{21}$ exhibited lower enthalpy, a strong MT temperature decrease (−40 K), and broadened hysteresis (26 K), attributed to microstructural effects.

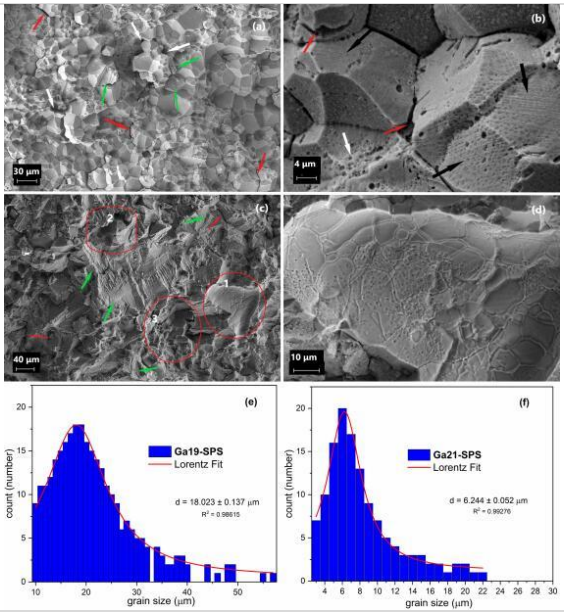

***Figure 3**: SEM images at different magnifications on the fractured cross-section in the bending test for (**a,b**) $Ni_{49}Mn_{32}Ga_{19}$ and (**c,d**) $Ni_{51}Mn_{28}Ga_{21}$ sintered samples. The arrows indicate martensitic microstructure (black arrow), cracks (red arrows), pores (white arrows), and cleavage zone (green arrows). The grain size distributions (fit is with a Lorentzian distribution) for the fractured cross-sections for Ga19-SPS (**e**) and on polycrystalline fused large unit (**d**) from sample Ga21-SPS (**f**). Reproduced from Ref. [6].*

$Ni_{51}Mn_{28}Ga_{21}$ sintered samples (denoted Ga_{21}-SPS) showed pronounced particle coarsening during SPS, forming large, nearly pore-free polycrystalline regions, unlike $Ni_{49}Mn_{32}Ga_{19}$ denoted Ga_{19}-SPS).

Structurally, $Ni_{49}Mn_{32}Ga_{19}$ is fully martensitic, while $Ni_{51}Mn_{28}Ga_{21}$ is biphasic (martensite + cubic austenite). Thermally, $Ni_{49}Mn_{32}Ga_{19}$ exhibited a higher MT temperature, higher enthalpy, narrow transformation range, and low hysteresis, whereas $Ni_{51}Mn_{28}Ga_{21}$ showed a strong MT temperature decrease, reduced enthalpy, broader MT range, and large hysteresis, typical of SPS-processed materials. Moreover, the activation energy and the pre-exponential factor of the MT, extracted through kinetic analysis within two non-isothermal models, Kissinger and Friedman, complement and sustain these findings. Fractography details of the sintered samples are discussed in relation to the stress-strain curves from the bending tests (see *Fig. 4*). These tests revealed a three-stage process with inter- and intra-granular cracks formation, which are deflected or arrested so that samples do not collapse at intermediate values of stress and strain The $Ni_{49}Mn_{32}Ga_{19}$ bulk sample exhibits a higher bending strength (260 MPa) and a lower strain (0.55%) than the $Ni_{51}Mn_{28}Ga_{21}$ sample (177 MPa and 0.61%).

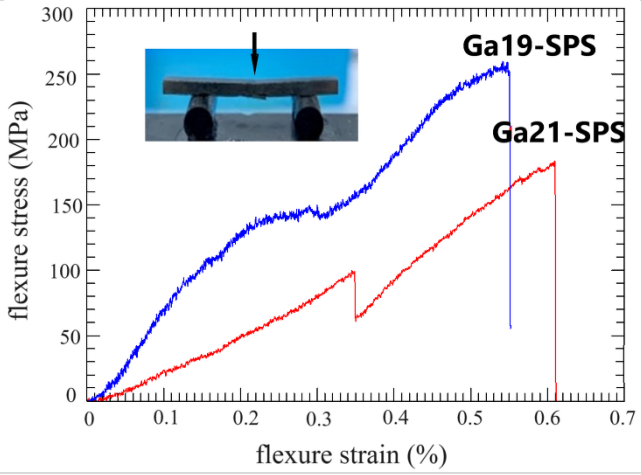

***Figure 4**: Bending stress–strain curves for Ga19-SPS and Ga21-SPS specimens. Inset: Ga21-SPS specimen after bending at intermediate stress, showing fracturing, but without collapsing. Reproduced from Ref. [6].*

The observed dependence of functional characteristics on preparation enables the possibility of property control required for various applications and suggests that the proposed route is promising in this regard for further investigations.

References:

[1] J.M. Jani, M. Leary, A. Subic, M.A. Gibson, *A review of shape memory alloy research, applications and opportunities*, Materials & Design (1980–2015) 56 (2014) 1078.

[2] A.N. Vasilev, A.D. Bozhko, V.V. Khovailo, I.E. Dikshtein, V.G. Shavrov, V.D. Buchelnikov, M. Matsumoto, S. Suzuki, T. Takagi, J. Tani, *Structural and magnetic phase transitions in shape-memory alloys* $Ni_{2+x}Mn_{1-x}Ga$, Physical Review B 59 (1999) 1113.

[3] J. Rodriguez-Aseguinolaza, I. Ruiz-Larrea, M.L. No, A. Lopez-Echarri, J. San Juan, *Temperature memory effect in Cu–Al–Ni shape memory alloys studied by adiabatic calorimetry*, Acta Materialia 56 (2008) 3711.

[4] A. Vidal-Crespo, A.F. Manchón-Gordón, J.M. Martín-Olalla, F.J. Romero, J.J. Ipus, M.C. Gallardo, J.S. Blázquez, C.F. Conde, *Phase dependence of the thermal memory effect in polycrystalline ribbon and bulk* $Ni_{55}Fe_{19}Ga_{26}$ *Heusler alloys*, Intermetallics 180 (2025),108695.

[5] F. Tolea, M. Nita, M. Tolea, *Thermal memory effect in NiFeGa and NiMnGa shape memory ribbons: Toward maximum-temperature recording applications*, Journal of Alloys and Compounds 1043 (2025) 184056.

[6] B. Popescu, C. Bartha, M. Enculescu, F. Tolea, M.A. Grigoroscuta, M. Tolea, P. Badica, M. Sofronie, *Martensitic transformation dynamics and mechanical properties investigation in spark plasma sintered Ni-Mn-Ga shape memory alloys*, Smart Materials and Structures 34 (2025) 055012.

DNA-RNA nucleobase-noated ZnO nanostructures for interface engineering in organic optoelectronics

C. Breazu[1], A. Stănculescu[1], M. Socol[1], O. Rașoga[1], N. Preda[1], A. Costaș[1], G.E. Stan[1], D.G. Popescu[1], G. Petre[1], S. Iftimie[2], T. Tite[1]

1) National Institute of Materials Physics, 077125, Măgurele, Romania
2) Faculty of Physics, University of Bucharest, 077125, Măgurele, Romania

Due to the importance of buffer layers in interface engineering, the development of more variants and the rational design of materials have a significant influence on the performance of optoelectronic devices. High-efficiency photovoltaic devices are continuously gaining attention and are widely studied to overcome the energy resource crisis [1,2]. The operational efficiency and lifetime of organic electronic devices are governed by the properties of both the active materials and their interfaces. Depending on the device architecture, the rational design of interfacial materials has a significant impact on the performance of optoelectronic devices (*Fig. 1a*). In addition to the optimization of active layers, interface engineering contributes significantly to improving interface contact and, consequently, enhancing device performance. Through interface engineering, the energy level alignment at the electrode–active layer interface can be tuned, the morphology controlled, and the stability enhanced [2]. Furthermore, selecting a suitable material for the transition layer and ensuring the quality of preparation can efficiently reduce interfacial charge carrier recombination and decrease the interfacial contact resistance at the electrode interface, which leads to an improvement in charge extraction capability. This study provides a strategy to increase device performance by facilitating efficient charge transfer and defect passivation by combining the properties of eco-friendly materials (adenine, cytosine, guanine, thymine, and uracil) with the physicochemical properties of metal oxides. Alignment of energy levels (*Fig. 1b*) in this hybrid junction determines charge transfer efficiency by influencing the electronic coupling of these states between ZnO and nucleobases. Generally, ZnO nanostructures interact with the ring nitrogen atom of nucleobases due to the electronic configuration of both ZnO and nucleobases [3,4].

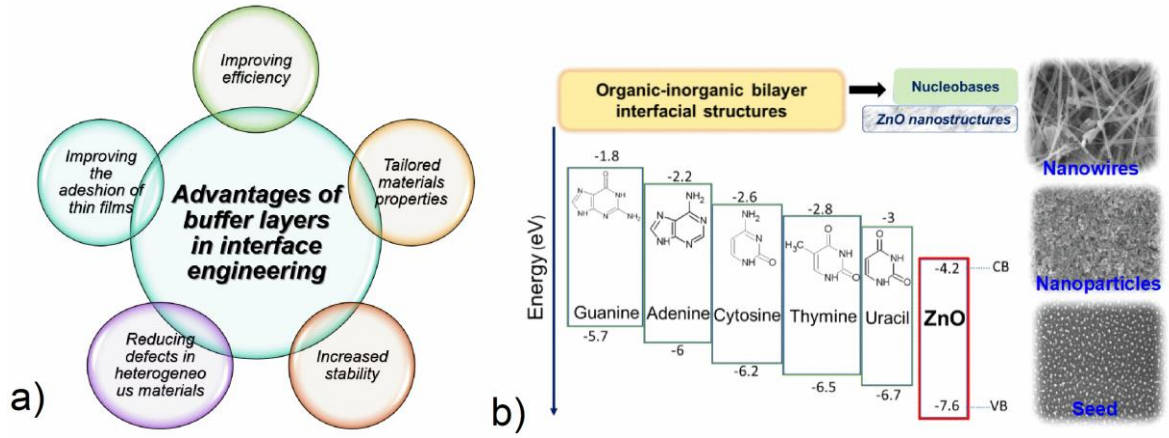

***Figure 1**: (**a**) Importance of buffer layers in interface engineering. (**b**) Energy levels of ZnO and nucleobases with inserted chemical structures and SEM images of ZnO nanostructures. Reproduced from Ref. [5].*

All deposited films exhibited a polycrystalline nature with a hexagonal wurtzite crystal structure, except for the ZnO seed layer, as evidenced by its XRD pattern (*Fig. 2a*). The low intensity of the diffraction peaks observed for the ZnO seed layer is most likely attributed to the small thickness of the deposited film. Owing to the high deposition rate and associated kinetic energy, three preferential orientations, (100), (002), and (101), are observed, resulting in parallel growth and a polycrystalline structure.
The Raman spectra were dominated by longitudinal optical (LO) phonon modes, which are characteristic of ZnO under resonant conditions. Periodic peak repetitions, assigned to multiphonon Raman scattering processes, are detected up to the third order of the LO phonon frequency, indicating the good crystallinity of the synthesized nanostructures [5].

Furthermore, comprehensive XPS analysis confirmed the presence, chemical integrity, and quantifiable amount of nucleobases on the ZnO nanostructures (*Fig. 2b*). The C 1s, N 1s, and O 1s core-level spectra of the functionalized samples display binding energies and chemical environments consistent with intact aromatic rings and amino groups, characteristic of unmodified nucleobases. The higher carbon and lower nitrogen concentrations observed on the nanowires suggest that the ZnO nanowire surfaces may preferentially expose or retain the carbon-rich moieties of the nucleobases, possibly due to reduced molecular packing between adjacent nanostructures. In contrast, the ZnO seed layer and ZnO nanoparticles appear to promote stronger or more accessible interactions with nitrogen-containing groups, likely due to their smaller dimensions and closer interparticle proximity.

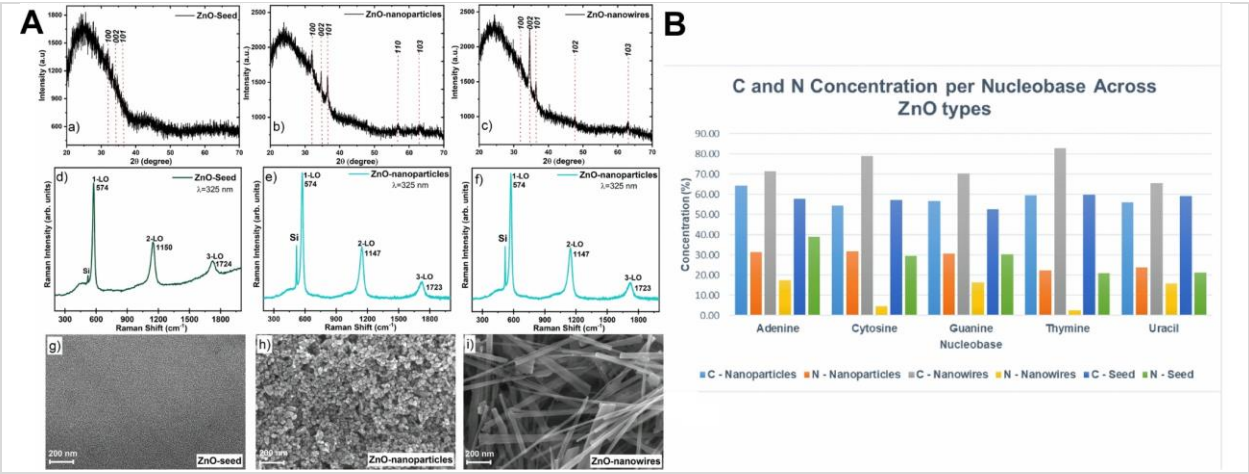

Figure 2: (**A**) *Characterization of the ZnO nanostructures: XRD pattern of (**a**) ZnO seed; (**b**) ZnO nanoparticles; and (**c**) ZnO nanowires. Raman spectra of (**d**) ZnO seed; (**e**) ZnO nanoparticles; and (**f**) ZnO nanowires. FE-SEM images of (**g**) ZnO seed; (**h**) ZnO nanoparticles; and (**i**) ZnO nanowires. (**B**) C% and N% concentrations for the nucleobases deposited on ZnO nanostructures. Reproduced from Ref. [5].*

Nucleobase coatings significantly modulate the PL properties of ZnO nanostructures by enhancing visible emissions through interactions with surface defects and introducing new optical transitions, as described in *Fig. 3*a. The degree of modulation varies with both the type of nucleobase and the morphology of the ZnO nanostructure. The differential responses observed for various nucleobases highlight the suitability of these materials for biosensing applications and justify further studies aimed at elucidating the fundamental mechanisms governing their interactions [5]. All the I–V characteristics plotted for nucleobase-coated ZnO nanostructures revealed distinct behaviours depending on the type of nucleobase and the morphology of the ZnO nanostructures. Adenine, thymine, and uracil exhibited linear I–V characteristics, indicating ohmic behaviour for all the ZnO morphologies: seed, nanoparticles, and nanowires, respectively. The enhancement in conductivity seemed to be higher in the case of ZnO nanoparticles and ZnO nanowires compared to the ZnO seed morphology, as evidenced by their I–V curves. A change in the shape of I–V characteristics from linear to a slightly nonlinear dependence is evidenced for the cytosine coated ZnO nanoparticles and guanine-coated ZnO nanoparticles and ZnO nanowires suggesting non-ohmic conduction mechanisms such as diode-like behaviour or field-enhanced charge transport. Guanine-coated ZnO nanoparticles and ZnO nanowires display the most significant deviation from linearity among all the studied nucleobases. Guanine, with a morphology characterized by nanoparticles, shows strong nonlinear behaviour and relatively low current ($\sim 10^{-8}$ A), while guanine with a morphology characterized by nanowires shows an improvement in the current value ($\sim 10^{-4}$ A) but a more asymmetric I–V characteristic associated with rectifying behaviour [5]. Based on the provided electrical measurements for the nucleobase thin films deposited on ZnO nanostructures, the conductivity follows the order: nanowires ≈ nanoparticles > seed. The interaction between nucleobases and ZnO nanostructures could improve interfacial properties, such as reducing charge carrier recombination at the photoanode interface.

A

Nucleobase-ZnO coating photoluminescence

Emission Type	ZnO-Peak (nm)	Nucleobases-Coating ZnO Behavior	Possible mechanism
UV	380-400	Enhanced intensity	Defect passivation
Violet	~400	Intensity modulation	Zn_i/surface interaction
Blue	426-440	Broadening or shifting	Charge-transfer transition
Green	~550	Suppresion or red shift	V_O passivation

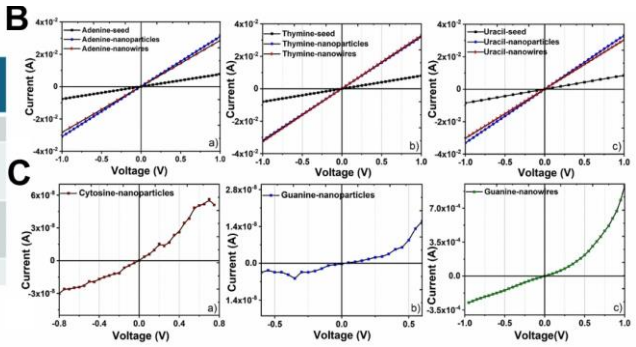

***Figure 3**: (**A**) Nucleobase–ZnO coating photoluminescence behaviour; (**B**) Dark I–V characteristics of (**a**) the adenine-coated ZnO nanostructures; (**b**) thymine-coated ZnO nanostructures; and (**c**) uracil-coated ZnO nanostructures; (**C**) Dark I–V characteristics of the (**a**) cytosine-coated ZnO nanoparticles, (**b**) guanine-coated ZnO nanoparticles; and (**c**) guanine-coated ZnO nanowires. Reproduced from Ref. [5].*

This makes the hybrid system particularly attractive for potential applications in solar cell architectures, such as dye-sensitized solar cells by improving light absorption and electron injection efficiency, or organic solar cells, where it can serve as efficient electron transport layer, enhancing the built-in potential and overall device performance [6].

References:

[1] B. Gajdzik, R. Wolniak, R. Nagaj, B. Žuromskaitė-Nagaj, W.W. Grebski, *The influence of the global energy crisis on energy efficiency: A comprehensive analysis*, Energies 17 (2024) 947.

[2] G.G. Njema, J.K. Kibet, S.M. Ngari, *A review of interface engineering characteristics for high performance perovskite solar cells*, Measurement: Energy 2 (2024) 100005.

[3] S. Saha, P. Sarkar, *Understanding the interaction of DNA-RNA nucleobases with different ZnO nanomaterials*, Physical Chemistry Chemical Physics 16 (2014) 15355–15366.

[4] V. Shewale, P. Joshi, S. Mukhopadhyay, M. Deshpande, R. Pandey, S. Hussain, S.P. Karna, *First-principles study of nanoparticle-biomolecular interactions: Anchoring of a $(ZnO)_{12}$ cluster on nucleobases*, The Journal of Physical Chemistry C 115 (2011) 10426– 10430.

[5] C. Breazu, A. Stanculescu, M. Socol, O. Rasoga, N. Preda, A. Costas, G.E. Stan, D.G. Popescu, G. Petre, S. Iftimie, T. Tite, *DNA–RNA nucleobase-coated ZnO nanostructures for interface engineering in organic optoelectronics*, ACS Applied Nano Materials 8 (2025) 16307–16320.

[6] S. Baruah, R.A. Afre, D. Pugliese, *Effect of size and morphology of different ZnO nanostructures on the performance of dye-sensitized solar cells*, Energies 17 (2024) 2076.

Ce-doped ZnO photoanode with enhanced photoelectrochemical performance

M. Sima[1], N. Preda[1], C. Negrilă[1], E. Matei[1], A. Sima[2], V. Stancu[1]

1) *National Institute of Materials Physics, 077125, Măgurele, Romania*
2) *National Institute for Lasers, Plasma and Radiation Physics, 077125, Măgurele, Romania*

The photoelectrochemical (PEC) water splitting is a clean method for generation of hydrogen by converting the abundant solar energy into chemical energy. Semiconductor photoelectrodes are typical components of PEC cell, the electron-hole pairs being generated as a result of light absorption. The separation of charge carriers allows electrons to reduce water to hydrogen while holes oxidize water to oxygen. The process of separation of carriers takes place both within the photoelectrode and at solid-liquid interface. The transport of the charge carriers inside the photoelectrode and their extraction at solid-electrolyte interface are important steps in PEC generation of products [1]. Among the semiconductors, metal oxides are very attractive due to their low toxicity, durability, cost-effective synthesis routes and their natural abundance. In the last decades, ZnO, a n-type semiconductor, was widely explored by many researchers as a promising photoanode material due to its high electron mobility, its favourable band edge energy positions with respect to the redox potential of water, and its synthesis in a wide variety of nanostructures. However, it was noted that ZnO is subject to photocorrosion in aqueous solution under UV illumination by hole trapping on its surface. Also, it is generally accepted that ZnO can respond only to UV light (4% of the solar spectrum) due to its wide band gap of 3.37 eV. Another disadvantage characteristic for the un-doped semiconductors is relatively high recombination rate of the photogenerated electron-hole pairs in ZnO. A strategy to increase the PEC performance for solar water splitting was to develop ZnO photoanodes more sensitive to visible light. Thus, the induction of point defects in ZnO lattice that affects the electron energy level structure and Fermi-level will narrow the bandgap width of the semiconductor increasing its visible light absorption. Oxygen vacancies (V_o) and zinc interstitials (Zn_i) are predominant defects in ZnO nanostructures, these being usually identified by photoluminescence. The absorption properties of ZnO are affected by both extrinsic dopants and native defects. It was observed an increase in the PEC efficiency of ZnO based photoanodes by introduction of V_o defects. Also, high photocatalytic activity in visible light was noted for ZnO nanostructures with intrinsic defects. A common approach to modify the optoelectronic properties of wide bandgap semiconductors consists in their doping with metal or non-metal elements. Among them, Ce^{4+} dopant has a radius similar to that of Zn^{2+} being easily inserted into ZnO lattice without modifying its wurtzite structure. However, Ce^{3+}/Ce^{4+} ratio in CeO_2 determines the oxygen vacancies, and an increased content of Ce^{3+} leads to narrowing of the bandgap and improves the visible light-induced photocatalytic activity. A method to increase Ce^{3+}in CeO_2 involves the annealing of the precursor in argon atmosphere. Modifying the ZnO surface with CeO_2 can enhance its photocatalytic activity and stability due to the improvement of reaction kinetics and stabilized surface. The transition between oxidation states Ce^{3+} and Ce^{4+} in CeO_2 is relative easily and the matching of its energy-level structure to that of ZnO favors the transfer of photogenerated electrons from the surface to the bulk [2].

This work is focused on the fabrication of ZnO and Ce-doped ZnO nanorod arrays on FTO substrates *via* a simple hydrothermal method and their evaluation as photoanodes for water splitting [3]. The investigated samples in this study are summarized in *Table 1*.

The optical properties of the p1, p2, p4, p5, and p6 samples are evaluated by UV-Vis spectroscopy (*Fig. 1a,b*). All the samples exhibit absorption in the UV region with sharp absorption edge at around 380 nm for p1, p4, p5, and p6 samples and at 385 nm for the p2 sample. The samples also show absorption in the visible region around 400 nm, more pronounced at p2 sample, correlated with the presence of oxygen vacancies. The direct band gap energy (E_g) of the samples was estimated according to the Tauc's formula.

***Table 1**: Sample labels and corresponding structural characteristics of the ZnO-based samples.*

Sample label	Sample structure description
p1	FTO/as-grown ZnO nanorods
p2	FTO/ZnO nanorods annealed at 500 °C in air
p3	FTO/ZnO nanorods annealed at 500 °C in air and immersed in Ce^{3+} solution (see [3])
p4	FTO/as-grown Ce-doped ZnO nanorods
p5	FTO/Ce-doped ZnO nanorods annealed at 500 °C in argon
p6	FTO/Ce-doped ZnO nanorods annealed at 500 °C in air
p7	FTO/CeO_2 film annealed at 500 ° in argon

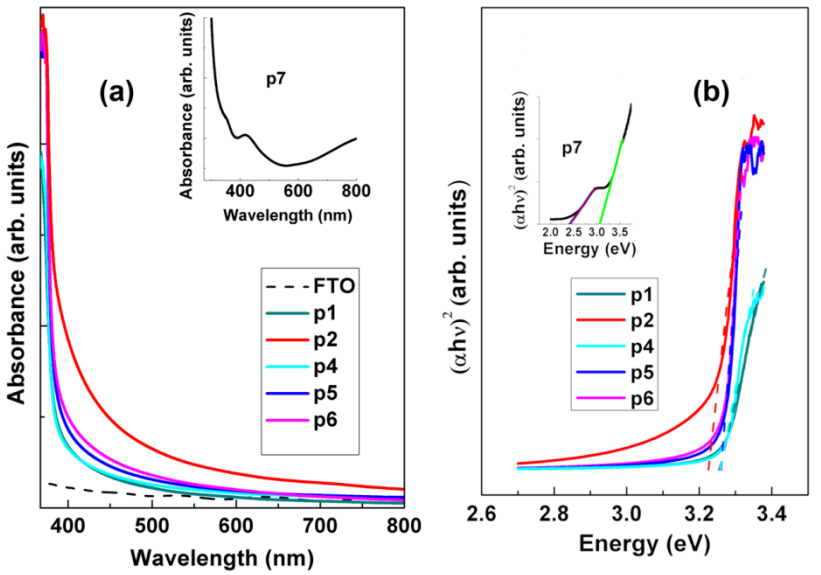

***Figure 1**: (**a**) UV-Vis absorption spectra and (**b**) Tauc plots of the p1, p2, p4, p5, and p6 samples. Inset shows UV-Vis absorption spectrum and Tauc plot of the p7 sample. Reproduced from Ref. [3].*

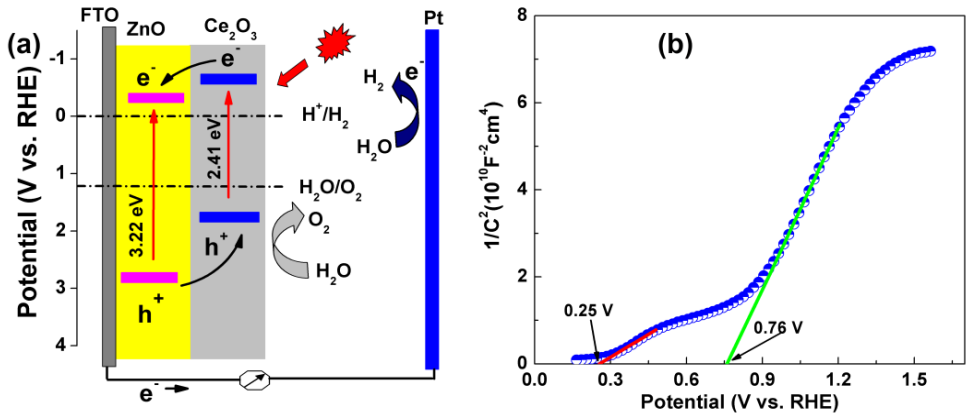

***Figure 2**: (**a**) Schematic diagram showing band level positions of ZnO and Ce_2O_3 and charge transfer path upon light absorption by the components of the photoanode; (**b**) Mott-Shottky plot of the p5 sample. Reproduced from Ref. [3].*

Based on collected results and related literature data [4], a mechanism for the photocatalytic improvement of p5 sample, considered a ZnO/CeO_2 heterojunction, is proposed in *Fig. 2a*. The valence band (VB) and the conduction (CB) edge positions of p2 sample (ZnO) and p7 sample (Ce2O3 + CeO_2) semiconductors at the point of zero charge were estimated using Mulliken's electronegativity equations. The Mott-Schottky plot of photoanode p5 (*Fig. 2b*) shows two linear portions attributed to ZnO and cerium oxide components, suggesting formation of a heterojunction between these n-type semiconductors.

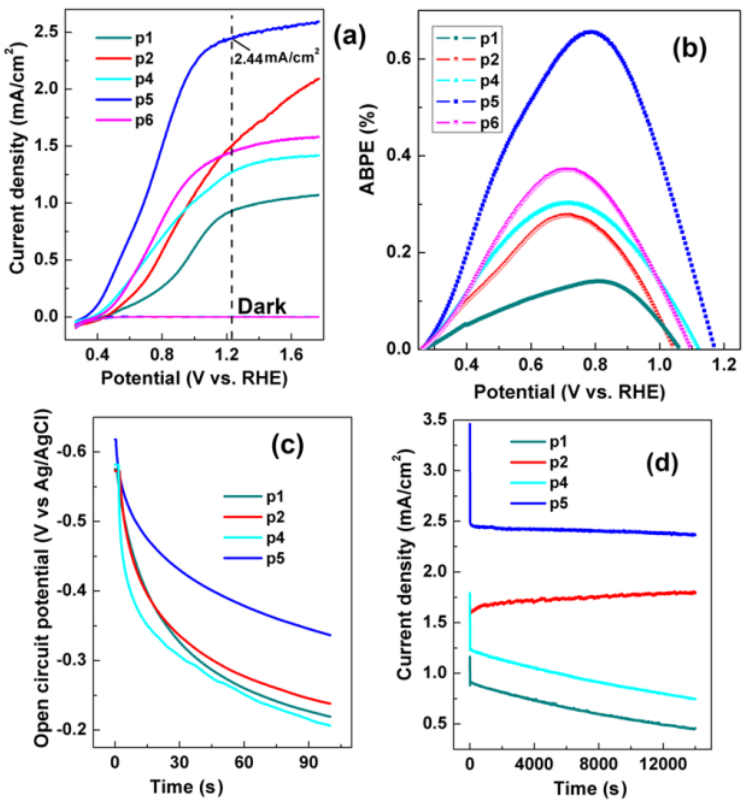

***Figure 3**: (a) Linear sweep voltammetry plots measured under dark and simulated solar illumination (AM 1.5, 100 mW/cm²; (**b**) the photoconverssion efficiency versus applied potential profile; (**c**) open circuit voltage decay with time, after stopping the illumination; and (**d**) stability test data measured at 1.23 V vs. RHE, under illumination for the p1, p2, p4, p5 samples. The measurements of the samples were carried out in solution 0.1 M KOH. Reproduced from Ref. [3].*

ZnO and Ce-doped ZnO nanorod arrays grown through a facile hydrothermal process were used as photoanodes for water splitting. The highest photocurrent density of 2.44 mA/cm^2 at 1.23 V *vs.* reversible hydrogen electrode (RHE) was achieved for Ce-doped ZnO sample annealed at 500 °C in argon atmosphere. This sample also showed the maximum applied bias photon-to-current efficiency (ABPE) value of 0.65 % at 0.81 V *vs.* RHE and excellent stability with photocurrent retention higher than 97%, under illumination for 14,000 s (Fig. 3). The presence of Ce^{3+} specie on the surface of sample determining formation of ZnO/Ce_2O_3 heterojunction. At the same time, Ce doping improved the charge transfer in the bulk. In summary, this study demonstrated that the doping ZnO with cerium ions modifies the charge transfer process in the bulk and induces formation of ZnO/cerium oxide heterojunction leading to an enhancement of PEC performance.

References:

[1] M. Ma, Y. Huang, J. Liu, K. Liu, Z. Wang, C. Zhao, S. Qu, Z. Wang, *Engineering the photoelectrochemical behaviors of ZnO for efficient solar water splitting*, Journal of Semiconductors 41 (2020) 091702.

[2] S. Rajendran, M.M. Khan, F. Garcia, J. Qin, V.K. Gupta, S. Arumainathan, *Ce^{3+}-ion-induced visible-light photocatalytic degradation and electrochemical activity of ZnO/CeO_2 nanocomposite*, Scientific Reports 6 (2016) 31641.

[3] M. Sima, N. Preda, C. Negrila, E. Matei, A. Sima, V. Stancu, *Ce-doped ZnO photoanode with enhanced photoelectrochemical performance*, International Journal of Hydrogen Energy 114 (2025) 52–59.

[4] R. Ma, M. Jahurul Islam, D. Amaranatha Reddy, K T. Kim, *Transformation of CeO_2 into a mixed phase CeO_2/Ce_2O_3 nanohybrid by liquid phase pulsed laser ablation for enhanced photocatalytic activity through Z-scheme pattern*, Ceramics International 42 (2016) 18495–18502.

Distortion of charge carrier trapping centres during incipient phase transformations in TiO_2 can enhance its photocatalytic performance

A.C. Iacoban[1], A.M. Rostaș[2], C.G. Mihalcea[1], I.D. Vlaicu[1], D. Culiță[4], M.C. Ilaș[1], M. Florea[1], Ș. Neațu[1], F. Neațu[1], M. Secu[1], T. Popescu[1]

1) *National Institute of Materials Physics, 077125, Măgurele, Romania*
2) *National Institute of Isotopic and Molecular Technologies, 400293, Cluj-Napoca, Romania*
3) *Interdisciplinary School of Doctoral Studies, University of Bucharest, 050067, Bucharest, Romania*
4) *"Ilie Murgulescu" Institute of Physical Chemistry, 060021, Bucharest, Romania*

In the present study, we addressed the behaviour of paramagnetic defect centres in multiphase TiO_2 materials obtained at temperatures of onset of polymorphic phase transformations and studied their effects on the photocatalytic activity of TiO_2 for hydrogen production by water splitting and generation of oxygen radicals [1].

TiO_2 nanoparticles (NPs) were synthesized *via* ultrasound-assisted excess hydrolysis of titanium tetra-isopropoxide ($Ti[OCH(CH_3)_2]_4$, TTIP). The excess hydrolysis was performed by adding TTIP dropwise to distilled water at a hydrolysis ratio (number of moles of water/number of moles of TTIP) r=245 under simultaneous bath ultrasonication and mechanical stirring. After adding TTIP, the mechanical stirring was stopped, and the reaction vessel remained under ultrasonication for 90 min at 50 °C. The resulting precipitate was separated by centrifugation and dried in atmospheric air for 72 h at 35 °C. The dry powders were gently ground, placed in covered alumina crucibles, and thermally treated in static atmospheric air for 2 h at 200, 300, 450, 500, 550, 600, 650, and 700 °C, using a heating rate of 2 °C/min. Following the thermal treatment, the samples were again gently ground for homogenization before being subjected to physicochemical characterization. The samples were labeled as "T–synthesis temperature" for materials synthesized at temperatures between 200 and 700 °C, whereas the untreated precipitate was designated as "T-NTT" (not thermally treated, NTT).

The X-ray diffraction (XRD) (*Fig. 1a*) shows that the exposure of T-NTT to temperatures up to 450 °C led to a gradual transformation of brookite into anatase, their v/v ratio becoming 87 % anatase / 13 % brookite at 450 °C (*Fig. 1b*) and their crystallite sizes increasing to ~ 19 nm in the case of anatase and ~16 nm for brookite (*Fig. 1c*). A rapid reverse transformation of anatase to brookite occurred in the temperature range of 450 – 500 °C, with the percentage of brookite increasing to 44 % at 500 °C. During this transformation, the average crystallite size of brookite did not change much (~19 nm at 500 °C). Still, significant crystallite growth was observed in the case of anatase, its average size becoming ~31 nm. The rutile phase also began to form at approximately 500 °C from the grown anatase phase, being observed in low amounts (< 2 v. %) with an average crystallite size of ~16 nm in T-500.

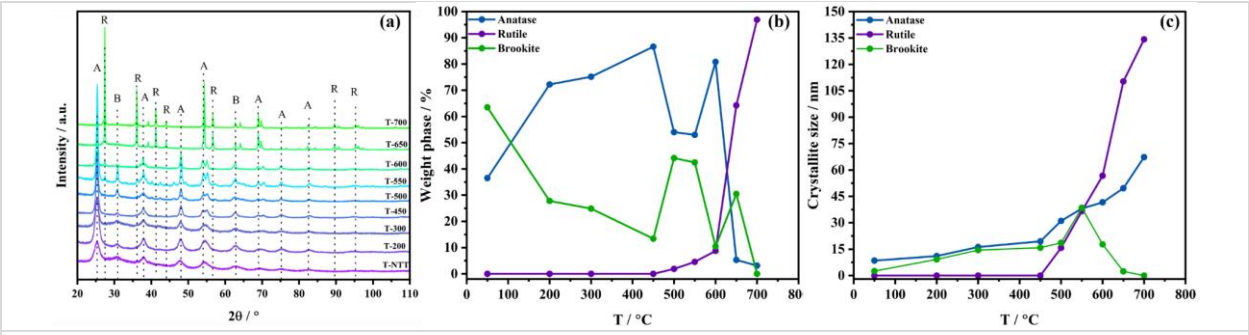

***Figure 1**: (**a**) XRD diagrams of the synthesized samples at different thermal treatment temperatures; (**b**) thermal evolution of constituent phases; and (**c**) average crystallite size. Reproduced from Ref. [1].*

The nucleation of rutile was followed by a significant decrease in the amount of brookite due to its transformation into both anatase and rutile during exposure to thermal treatment in the temperature range 550 – 600 °C (*Fig. 1b*). The phase composition of the sample T-600 was 81% anatase, 10%

brookite, and 9% rutile. A peculiar reduction of the crystallite size of the remaining brookite phase down to ~18 nm was determined at this temperature. Considering the physical significance of the size derived based on Scherrer's formula [2], we interpret this apparent crystallite size reduction as merely a decrease of the coherently scattering domain size in the brookite nanoparticles due to lattice disorder induced by the rapid brookite to anatase/rutile phase transition that occurred in the temperature range 550 – 600 °C. At temperatures beyond 600 °C, anatase transformed into rutile directly and through the intermediary brookite phase. This behaviour was assessed based on the higher amount of nanosized (~2 nm) brookite (30 %) found in the sample T-650. The presence of brookite in the T-650 sample was confirmed by SAED determinations (not shown). The small crystallite size of the newly formed brookite phase is not unexpected, considering its unstable, transitory character.

The paramagnetic centres present in the studied materials were characterized using EPR spectroscopy. The EPR Q-band spectra measured for the T-NTT precipitate and the samples calcined at different temperatures are depicted in *Fig. 2*. While no paramagnetic signal was detected in the case of T-NTT, the calcined samples showed a complex defect structure comprising three types of paramagnetic centres. One resonant line with an isotropic g-value of g_F = 2.003 was assigned to so called F^+-centres (an electron trapped in an oxygen vacancy (O_v)) present in the samples containing anatase and brookite phases in agreement with the literature data [3]. These centres were observed in the case of samples treated at temperatures between 200 – 450 °C and, surprisingly, for T-600. At this moment, we do not have a confirmed explanation for this behaviour. Based on existing literature, a second resonant line with g_V = 2.01 was associated with so-called V-centres (oxygen ions with trapped holes) [4]. The V-centres were found in the samples calcined between 200 and 600 °C that contained mostly anatase and brookite phases as determined by XRD (*Fig. 1b*). The third paramagnetic signal exhibited an axial g-tensor with g_{Ti}= [2.0017 2.0007] and was attributed based on previous literature reports to paramagnetic centres involving Ti^{3+} such as Ti^{3+}-O_v [5,6]. The assignment of F^+-centres and V-centres to the anatase and brookite phases and of the Ti^{3+}-related centres to the rutile phase based on the characteristics of the observed EPR signals was supported by the phase composition of the studied materials assessed by XRD (*Fig. 1b*). The intensity of the EPR signal was peculiarly diminished in the case of samples T-500 and T-550 and became maximum in the case of sample T-600 (*Fig. 2*).

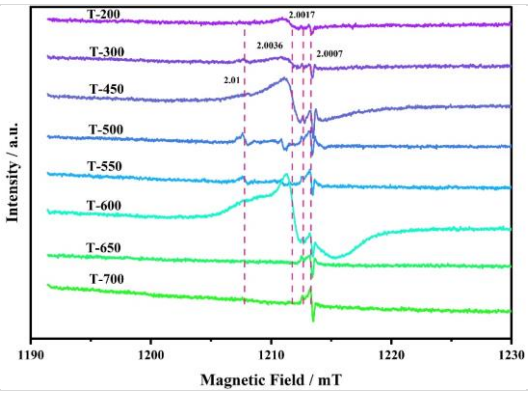

***Figure 2**: Q-band electron paramagnetic resonance spectra recorded for all the synthesized TiO_2 samples. Reproduced from Ref. [1].*

The spectra recorded for aqueous suspensions of each sample during exposure to UV radiation (365 nm) in the presence of DMPO are displayed in *Fig. 3a*. The spectra exhibited complex characteristics, representing the superposition between the dominant sextet attributed to •DMPO – CH_3 and the low-intensity signal produced by •DMPO – OH (marked with "*"), with slightly modified hyperfine coupling constants due to the presence of DMSO in the reaction medium. The hyperfine constants determined from the spectra are a_N = 16.3 G and a_H = 23.3 G for the •DMPO – CH_3 radical and $a_N = a_H$ = 14.8 G for the •DMPO – OH radical values that agree with those presented in the published literature [7]. The evolution of the EPR signal intensity with irradiation time, representing the kinetics of the ROS photogeneration reaction, is represented for each TiO_2 sample in *Fig. 3b*. To establish which type of photogenerated charge carrier (electrons or holes) was primarily involved in the formation of ROS, the activity of the T-600 sample for ROS photogeneration was determined again in the presence of EDTA, which acted as a

hole scavenger. The observed loss of paramagnetic signal induced by EDTA indicated that photogeneration of ROS underwent a hole-mediated pathway.

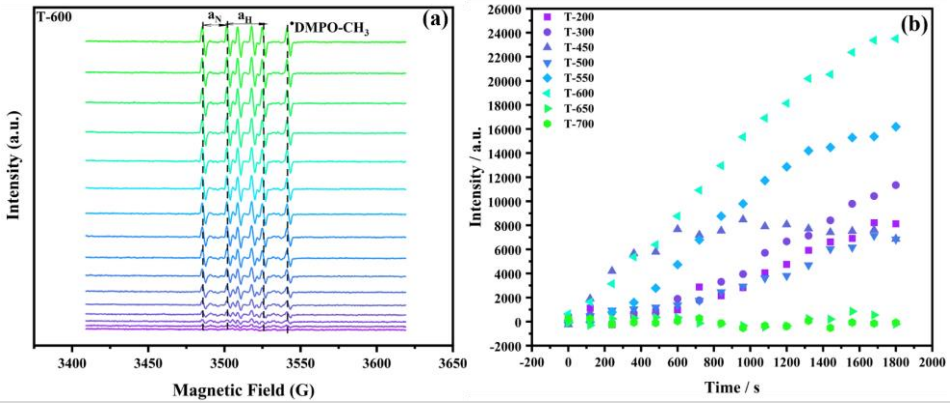

***Figure 3**: (**a**) The structure of the EPR spectra recorded during the ROS photogeneration for sample T-600. Each spectrum was recorded after 2 min of irradiation. (**b**) Evolution of the EPR signal intensity for all samples. Reproduced from Ref. [1].*

The photocatalytic hydrogen production by water splitting was assessed for the T-600 and T-500 samples, which exhibited significantly different ROS photogeneration efficiency (*Fig. 3b*). The T-600 material proved twice as efficient in producing hydrogen as the sample T-500. This result confirmed that oxygen vacancies did not trap electrons (at least not efficiently) in bulk. Moreover, the positive correlation between the efficiencies of the ROS photogeneration by holes and hydrogen production by electrons supported the findings regarding the photocatalytic activities of the studied materials.
The overall results of the present study suggested that synergistic action of the charge carrier trapping mechanisms led to enhanced photocatalytic activity of the TiO_2 nanomaterial obtained at the temperature marking the onset of the massive anatase to rutile formation in the studied multiphase system.

References:

[1] A.C. Iacoban, A.M. Rostas, C.G. Mihalcea, I.D. Vlaicu, D. Culiță, M.C. Ilas, M. Florea, S. Neatu, F. Neatu, M. Secu, T. Popescu, *Distortion of charge carrier trapping centers during incipient phase transformations in TiO_2 can enhance its photocatalytic performance*, Journal of Alloys and Compounds 1018 (2025) 179097.

[2] J. Hargreaves, *Some considerations related to the use of the Scherrer equation in powder X-ray diffraction as applied to heterogeneous catalysts*, Catalysis, Structure & Reactivity 2 (2016) 33–37.

[3] A. Naldoni, M. Altomare, G. Zoppellaro, N. Liu, S. Kment, R. Zboril, P. Schmuki, *Photocatalysis with reduced TiO_2: From black TiO_2 to cocatalyst-free hydrogen production*, ACS Catalysis 9 (2018) 345–364.

[4] O. Al-Madanat, B.N. Nunes, Y. AlSalka, A. Hakki, M. Curti, A.O.T. Patrocinio, D.W. Bahnemann, *Application of EPR spectroscopy in TiO_2 and Nb_2O_5 photocatalysis*, Catalysts 11 (2021) 1514.

[5] T. Rajaraman, S.P. Parikh, V.G. Gandhi, *Black TiO_2: A review of its properties and conflicting trends*, Chemical Engineering Journal 389 (2020) 123918.

[6] Z. Wang, C. Yang, T. Lin, H. Yin, P. Chen, D. Wan, F. Xu, F. Huang, J. Lin, X. Xie, M. Jiang, *Visible-light photocatalytic, solar thermal and photoelectrochemical properties of aluminium-reduced black titania*, Energy & Environmental Science 6 (2013) 3007–3014.

[7] D. Dvoranová, Z. Barbieriková, V. Brezová, *Radical intermediates in photoinduced reactions on TiO_2 (an EPR spin trapping study)*, Molecules 19 (2014) 17279–17304.

Key Scientific Achievements & Breakthroughs in *Healthcare & Environmental Materials and Applications*

A paper-based device with submicronic fibre mesh electrodes for voltammetric quantification of nucleic acids

D. Botta[1], M. Beregoi[1], I.A. Cepleanu-Pascu[1,2,3], D.N. Crișan[1], A.-M. Ignat[1], E. Matei[1], I. Enculescu[1], V.C. Diculescu[1]

1) *National Institute of Materials Physics, 077125, Măgurele, Romania*
2) *Faculty of Biology, University of Bucharest, 050095, Bucharest, Romania*
3) *S.C. ALA BIOLAB S.R.L., 030108, Bucharest, Romania*

This work presents a novel paper-based electrochemical sensor (FiberSens) for nucleic acid quantification, developed through the innovative assembly of chromatographic paper with metallized electrospun polymeric fibre electrodes [1]. The device addresses critical limitations of conventional paper-based sensors by introducing submicronic fibre mesh electrodes that maintain fluid permeability while providing excellent electrochemical performance. The sensor was designed in a sandwich-type architecture with a three-electrode configuration, where gold-coated electrodes serve as working and counter electrodes, while silver-coated fibres function as the reference electrode (*Fig. 1*). A 3D-printed hydrophobic barrier created from wax-like polymers defines precise injection and testing zones on the chromatographic paper, ensuring controlled fluid flow through capillary action.

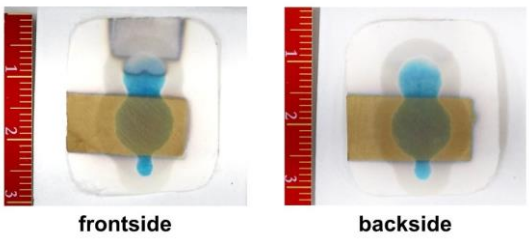

***Figure 1**: Photographs of the assembled device showing the electrode placement on each side of the fluidic channel (saturated with 1 mM methylene blue solution) patterned on the paper substrate. Reproduced from Ref. [1].*

The fabrication process employed three main steps: electrode preparation through electrospinning of poly(methyl methacrylate) solution followed by patterned metal deposition, paper patterning with 3D printing and thermal treatment, and thermal assembly of the components into the final device. The electrospun fibre meshes offer unique advantages including high surface-to-volume ratio, moderate surface roughness that enhances electron transfer, and electret-like behaviour that minimizes non-specific adsorption. Unlike traditional screen-printed electrodes that can block paper pores and hinder capillary flow, the permeable fibre mesh electrodes allow uniform fluid distribution across the entire sensing area, leading to more consistent and accurate measurements.

Comprehensive fluid diffusion analysis revealed that a minimum of 40 µL of solution is required for optimal sample distribution throughout the testing zone, with complete equilibration achieved within 10 seconds. The working electrode was strategically designed to cover the entire test zone, minimizing effects from microscopic concentration gradients. Electrochemical characterization using cyclic voltammetry with methylene blue as a redox probe (*Fig. 2*) revealed a diffusion coefficient of $D = 1.43 \times 10^{-6}$ cm^2 s^{-1} and a charge transfer rate constant of $k0 = 9.03 \times 10^{-3}$ cm s^{-1}. The quasi-reversible behaviour of methylene blue at the gold-coated fibre electrodes was confirmed through detailed analysis of peak potentials and currents as a function of scan rate. Complementary to cyclic voltammetry, electrochemical impedance spectroscopy was used to investigate the physical and interfacial properties of the FiberSens in pH 7. 0 0.1 M phosphate buffer in the presence of 2 mM MB (not shown) for different applied potential values.

Electrochemical detection of nucleic acids was tested using calf-thymus dsDNA. Under optimized conditions, FiberSens contained 40 µL of 1 mM MB in pH 7.0 phosphate buffer and equilibrated for 30 minutes. The SW voltammogram showed an MB reduction peak at $E_{pc} = -0.22$ V. With each addition of 2 µL dsDNA, the reduction peak current decreased due to MB intercalating into the dsDNA helix, which

impedes electron transfer compared to unbound MB near the electrode. This interaction reduces free MB molecules available for charge transfer, so remaining peaks after dsDNA addition reflect unbound MB.

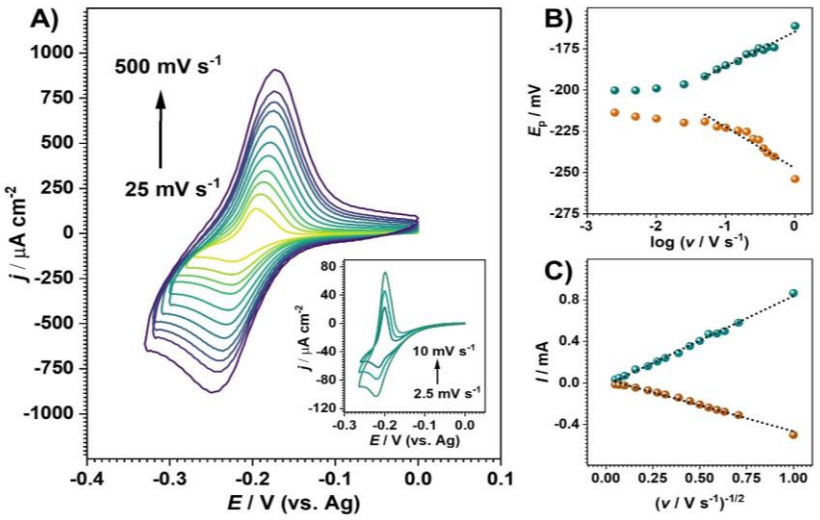

***Figure 2**: Electrochemical characterization of FiberSens. (**A**) Cyclic voltammograms at different scan rates after addition of 40 µL of 2 mM MB in pH 7.0 0.1M phosphate buffer. (**B**) Variation of peak potentials with scan rate. (**C**) Variation of peak currents with square root of scan rate. Reproduced from Ref. [1].*

This interaction between MB and dsDNA within FiberSens was also comprehensively characterized using complementary spectroscopic techniques. UV-Vis reflectance spectroscopy demonstrated a progressive increase in reflectance (decrease in absorbance) with increasing DNA concentration, consistent with methylene blue intercalation. Raman spectroscopy revealed characteristic spectral shifts in methylene blue bands upon DNA binding, with the C–N and C–C bond stretching vibrations shifting from 1392 to 1388 cm^{-1} and from 1627 to 1622 cm^{-1}, respectively, along with the appearance of new bands at 1580 and 1495 cm^{-1} (*Fig. 3*). Energy dispersive X-ray spectroscopy of the working electrode after use confirmed the absence of DNA or methylene blue adsorption, eliminating electrode fouling as a concern and validating the solution-phase interaction mechanism.

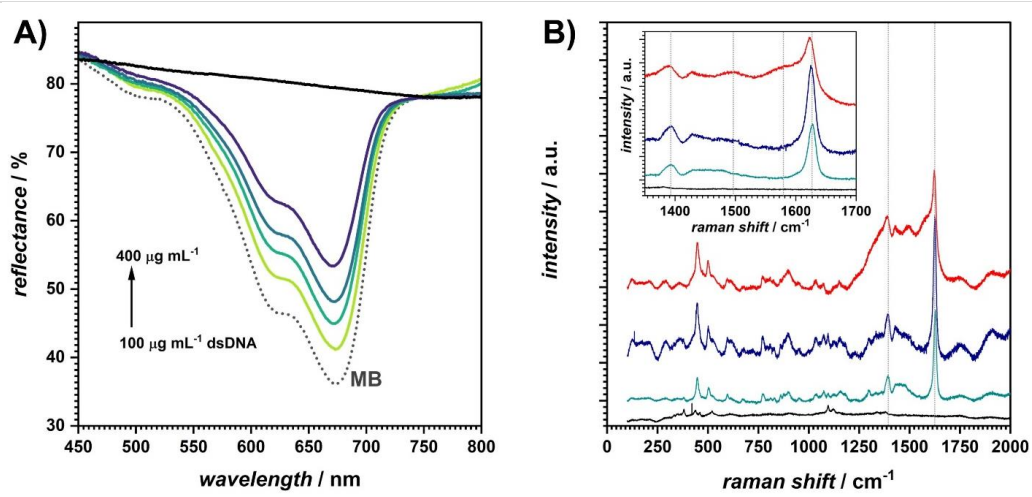

***Figure 3**: Spectroscopic analysis of MB-DNA interaction. (**A**) UV-Vis reflectance spectra of chromatographic paper saturated with 100 µM MB before and after successive additions of dsDNA. (**B**) Raman spectra of paper before and after saturation with MB and after addition of different concentrations of dsDNA. Reproduced from Ref. [1].*

For practical validation, the sensor was optimized for the detection of PCR-amplified products of the methylenetetrahydrofolate reductase (MTHFR) gene, whose mutations are associated with cardiovascular diseases. Optimization studies established optimal conditions: 40 µL of 1 mM methylene

blue in phosphate buffer (pH 7.0), 2 µL sample injection volumes, and 3 minutes equilibration time. Under these conditions, the sensor achieved a limit of detection of 1.38 ± 0.07 ng µL^{-1} (equivalent to 11.5 nM or 4.6 fmol) with a relative standard deviation of 5.3%. The limit of quantification was determined to be 4.6 ± 0.20 ng µL^{-1}. Analysis of spiked serum samples by standard additions method yielded recovery values between 91% and 95%, demonstrating excellent accuracy in complex biological matrices. The calibration curve showed a logarithmic relationship between current density variation and MTHFR concentration, with excellent linearity (R^2 = 0.993) across the tested concentration range (Fig. 4).

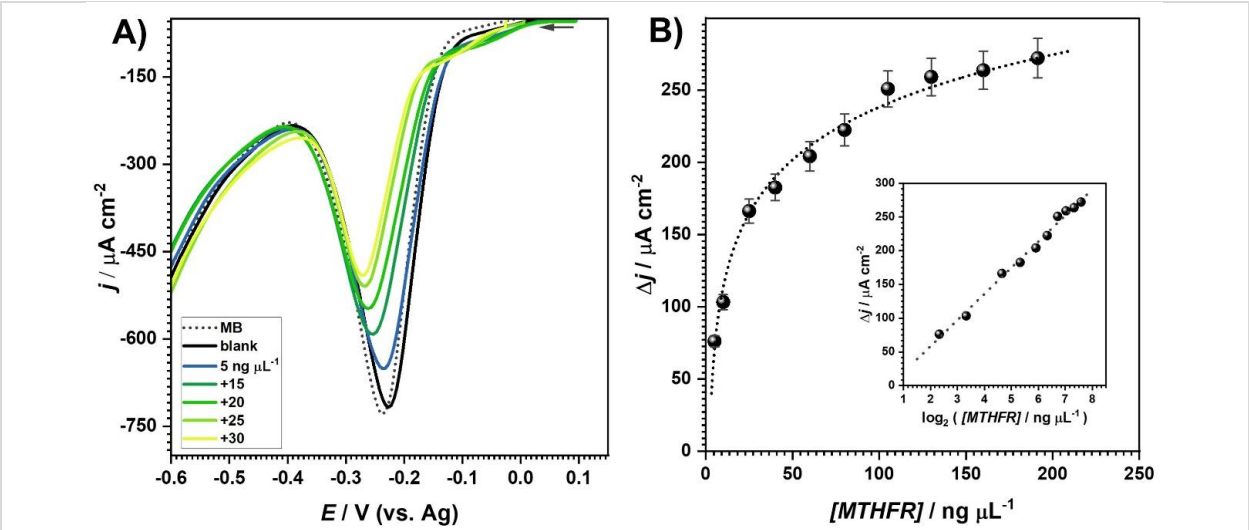

***Figure 4**: Detection of PCR-amplified MTHFR gene. (**A**) Square-wave voltammograms recorded with subsequent additions of PCR-amplified products. (**B**) Calibration curve showing logarithmic relationship between current density variation and MTHFR concentration (linear and semi-log representations). Reproduced from Ref. [1].*

Device reproducibility was rigorously evaluated, with three independently fabricated sensors showing a relative standard deviation of 8.8% in sensitivity and 8.5% in limit of detection, indicating excellent fabrication reproducibility. Long-term stability studies revealed that sensors maintained 85–91% of their initial sensitivity after storage for over one year under normal laboratory conditions.

This paper-based electrochemical sensor represents a significant advancement in point-of-care nucleic acid detection. The device achieves rapid detection (3 minutes) with minimal sample volume (2 µL), making it highly suitable for resource-limited settings and field-deployable applications. The performance metrics are comparable to or better than many reported paper-based sensors that rely on complex surface modifications with nanomaterials and capture probes. Future work will focus on integrating FiberSens with on-chip amplification systems such as loop-mediated isothermal amplification or PCR, enabling complete sample-to-answer diagnostics on a single platform. The scalable fabrication process, combined with the demonstrated analytical performance and stability, positions FiberSens as a promising solution for decentralized genetic diagnostics and point-of-care testing applications.

Reference:

[1] D. Botta, M. Beregoi, I.A. Cepleanu-Pascu, D.N. Crisan, A.-M. Ignat, E. Matei, I. Enculescu, V.C. Diculescu, *A paper-based device with submicronic fiber mesh electrodes for voltammetric quantification of nucleic acids*, Cell Reports Physical Science 6 (2025) 102781.

Amyloid beta peptide fibrils functionalized surfaces for neurological applications

M. Beregoi[1], S. Nistor[1], I.C. Ciobotaru[1], A. Nițescu[1], I. Zgură[1], M.C. Bunea[1], M. Enculescu[1], L. Nedelcu[1], C. Busuioc[2], T.A. Enache[1]

1) *National Institute of Materials Physics, 077125, Măgurele, Romania*
2) *Faculty of Medical Engineering, National University of Science and Technology POLITEHNICA of Bucharest, 011061, Bucharest, Romania*

Amyloid beta (Aβ) peptides are primarily known for their involvement in neurodegenerative disorders, particularly Alzheimer's disease [1,2]. However, beyond their pathological relevance, amyloid fibrils exhibit remarkable physicochemical properties, including nanoscale organization, self-assembly capability, and exceptional resistance to proteolytic degradation [3]. These features make amyloid fibrils promising candidates for biofunctional surface engineering. In this contribution, we report the fabrication and biological evaluation of conductive rigid and flexible substrates functionalized with fibrils from amyloid beta fragment 1–40 (Aβ40), aimed at developing stable and biocompatible biointerfaces for cell-based and neuromorphic applications [4]. The study focuses on gold-coated glass substrates and gold-coated electrospun poly(methyl methacrylate) (PMMA) fibre networks, chosen to represent rigid and flexible conductive platforms. Gold was deposited by DC magnetron sputtering, resulting in uniform conductive layers with low sheet resistance. Aβ40 was induced to form fibrils under controlled conditions and subsequently immobilized onto the conductive surfaces via spontaneous physical adsorption. For comparative assessment, additional surface functionalization using poly-L-lysine, collagen, inverse Aβ40 sequences, and non-Aβ peptides were also prepared. The overall experimental pathway is schematically illustrated in *Fig. 1*.

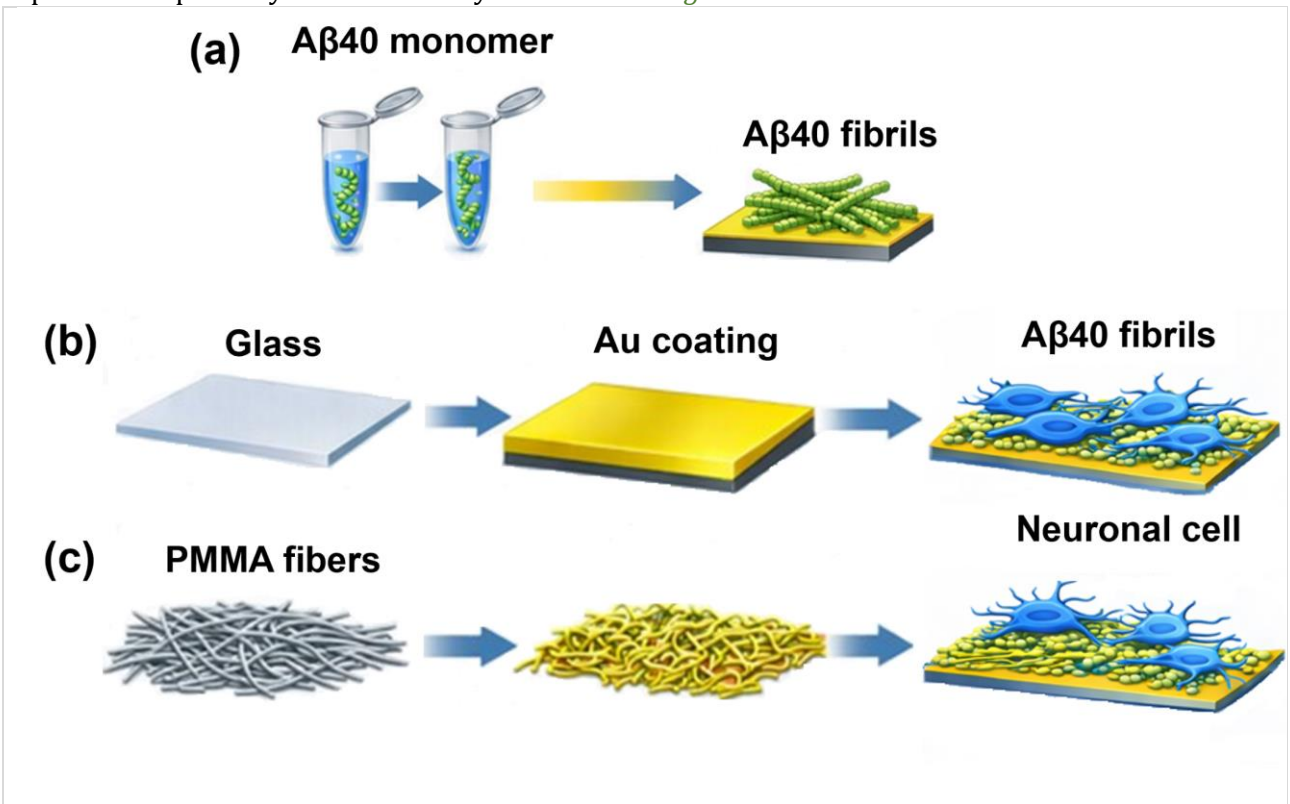

***Figure 1**: Schematic representation of scaffold fabrication, gold coating, amyloid fibril functionalization, and cell interaction workflow.*

Surface morphology and structural properties were investigated using scanning electron microscopy, atomic force microscopy, and X-ray diffraction. Electrical performance was evaluated through four-point probe measurements, confirming the preservation of conductivity after biofunctionalization.

Aβ40 fibril adsorption significantly altered the surface topography, increasing nanoscale roughness and generating fibrillar architectures reminiscent of extracellular matrix features. Importantly, contact angle measurements revealed a pronounced transition from hydrophobic to hydrophilic behaviour upon fibril functionalization, bringing the wettability into an optimal range for mammalian cell adhesion (*Fig. 2*).

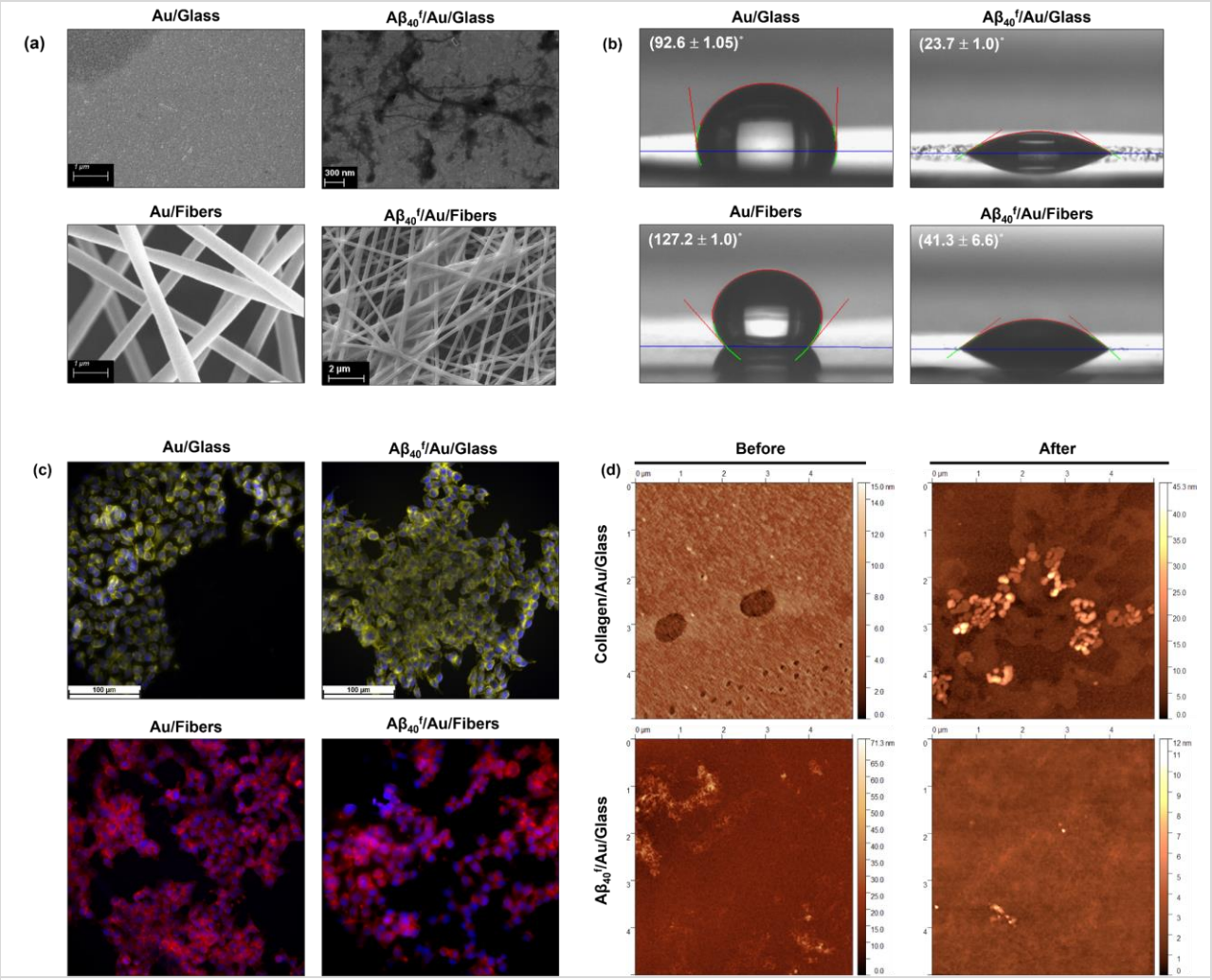

Figure 2: *Correlation between (**a**) surface morphology, (**b**) wettability, (**c**) cell adhesion on amyloid fibril-functionalized conductive substrates, and (**d**) protease resistance. Adapted from Ref. [4].*

The biological performance of the developed scaffolds was evaluated using fibroblast L929 and neuroblastoma SH-SY5Y cell lines. Cell viability organizations was verified using MTS assays, while cell morphology and cytoskeletal organization were assessed by fluorescence microscopy and scanning electron microscopy. Fibroblast cells exhibited high viability and enhanced spreading on Aβ40 fibril-functionalized rigid surfaces, comparable to or exceeding that observed on glass control substrates. In contrast, bare gold-coated surfaces showed reduced cell coverage, highlighting the importance of biofunctional coatings.

Neuronal SH-SY5Y cells cultured on both rigid and flexible amyloid-modified conductive scaffolds displayed viability levels close to 100%, with no signs of cytotoxicity or abnormal morphology. Quantitative image analysis revealed increased cell coverage and clustering on fibril-coated substrates compared to bare gold or non-functionalized controls. Notably, the mechanical nature of the substrate did not significantly influence the overall biological response, indicating that cell behaviour was primarily governed by the chemical and nanoscale characteristics of the amyloid fibril coating (*Table 1*).

***Table 1**: Comparative properties of conductive scaffolds functionalized with amyloid beta fibrils.*

Scaffold Type	Surface Modifications	Contact Angle	Cell Viability	Protease Resistance	Electrical Conductivity
Glass	None (Control)	Low	High	-	No
Au/Glass	None	Moderate	Low	-	Yes
Au/Glass	Aβ40 fibrils	Low	High	Low	Yes
Au/Fibers	None	High	Low	-	Yes
Au/Fibers	Aβ40 fibrils	low	High	High	Yes

A critical advantage of amyloid fibril coatings is their remarkable resistance to enzymatic degradation. Protease digestion experiments demonstrated that, unlike collagen-based coatings, Aβ40 fibrils retained their structural integrity after exposure to trypsin, preserving surface morphology and biofunctionality. This stability underscores the suitability of amyloid-modified conductive scaffolds for long-term bioelectronic and neuromorphic applications, where prolonged exposure to biological environments is unavoidable.

In conclusion, this work demonstrates that amyloid beta fibrils are not harmful for living cells and can be repurposed as robust and biocompatible building blocks for functional biointerfaces. By combining electrical conductivity, optimized surface wettability, enhanced cell adhesion, and exceptional protease resistance, Aβ40 fibril-functionalized scaffolds represent a versatile platform for neuronal culture systems, neuromorphic devices, and advanced biosensing technologies.

References:

[1] M.P. Murphy, H. LeVine III, *Alzheimer's disease and the β-amyloid peptide*, Journal of Alzheimers Disease 19 (2010) 311.

[2] C. Cheignon, M. Tomas, D. Bonnefont-Rousselot, P. Faller, C. Hureau, F. Collin, *Oxidative stress and the amyloid beta peptide in Alzheimer's disease*, Redox Biology 14 (2018) 450–464.

[3] N.P. Reynolds, *Amyloid-like peptide nanofibrils as scaffolds for tissue engineering: Progress and challenges*, Biointerphases 14 (2019) 041001.

[4] M. Beregoi, S. Nistor, I.C. Ciobotaru, A. Nitescu, I. Zgura, M.C. Bunea, M. Enculescu, L. Nedelcu, C. Busuioc, T.A. Enache, *Cells proliferation on surfaces functionalized with amyloid beta peptide fibrils*, International Journal of Biological Macromolecules 309 (2025) 143160.

Phosphorothioated oligonucleotides on gold-coated electrospun polymeric fibres for electrochemical genosensors

A. Aldea, M. Onea, E. Matei, N. Apostol, D. Botta, I. Enculescu, V.C. Diculescu

National Institute of Materials Physics, 077125, Măgurele, Romania

This study explored the benefits of metal-coated electrospun polymeric fibres for the development of electrochemical genosensors, which working principle is based on nucleic acids hybridization reactions [1]. The investigation focused on comparing two electrode architectures: flexible gold-coated electrospun polymer electrodes (Au/PMMA/PET) and conventional planar gold electrodes (Au/Ti/SiO_2/Si), in combination with phosphorothioated oligonucleotide probes, for detection of BCR/ABL fusion gene of chronic myeloid leukemia [2].

The designed synthetic oligonucleotide (ODN) probe sequence has the central part specific to the BCR/ABL junction modified with a thiophosphate group by substituting an oxygen atom in the phosphate moiety with a sulphur atom, an essential change for immobilization at the gold electrode surface [3] which is achieved through gold-sulphur covalent bond formation. *Table 1* presents the oligonucleotide probes designed for the target sequences of the BCR/ABL junction of chronic myeloid leukemia and for the BCR gene. A non-complementary target sequence was used to study the level of specific interaction between target and probes.

***Table 1**: Sequences of oligonucleotides, BCR-ABL junction of chronic myeloid leukemia target, BCR target and control.*

Notation	Sequence
ODNP	5'-GCT GAA GGG C*T*T*T*C*T*T*T* CCT TAT TGA TG-3' The probe; to be immobilized to obtain the biosensor
ODNBCR/ABL	5'-CAT CAA TAA GCA AGA AGC CCT TCA GC-3' The target; the sequence of the BCR / ABL fused gene, specific to the b2a2 form
ODNBCR	5'-CTG TTA TCT GGA AGA AGC CCT TCA GC-3' BCR gene sequence
ODNC	5'-CTG TTA TCT GGA AGA TCT GTA CTG CA-3' Non-complementary control sequence
Notation	Sequence

**phosphorothioated modification*

The morphology and electrochemical behaviour of the Au/PMMA/PET electrodes were evaluated and compared with planar Au/Ti/SiO_2/Si electrodes in order to prove their enhanced performance. SEM analysis (not shown) demonstrated uniform electrospun fibres with an average diameter of ~0.4 µm, preserving the polymer structure. The fibres were homogeneously coated with gold, displaying a granular morphology similar to planar gold, with grain sizes of ~50 nm.

Cyclic voltammetry in a solution of 2 mM $K_4[Fe(CN)_6]$ in pH 7.0 0.1 M phosphate buffer revealed the reversible Fe^{2+}/Fe^{3+} redox behaviour for both electrodes ($\Delta Ep \approx 60$ mV, $|Ipa/Ipc| \approx 1$). However, the Au/PMMA/PET electrodes exhibited ~10-fold higher redox currents, indicating a significantly larger electroactive surface area.

The adsorption of ODNP onto gold surface was investigated by surface plasmon resonance (SPR) (*Fig. 1A*). Increased ODNP concentrations produced progressively higher SPR signals during association, followed by partial signal decrease during the dissociation phase. The post-dissociation baseline shifted upward with increasing ODNP concentration (*Fig. 1B*), confirming stable immobilization on the gold surface. In contrast, control experiments with non-phosphorothioated oligonucleotides (ODNC) showed negligible adsorption. This experiment demonstrated the enhanced adsorption of phosphorothioated oligonucleotides on gold surface when compared with the unmodified counterparts, and their efficiency as probes for the development of electrochemical genosensors.

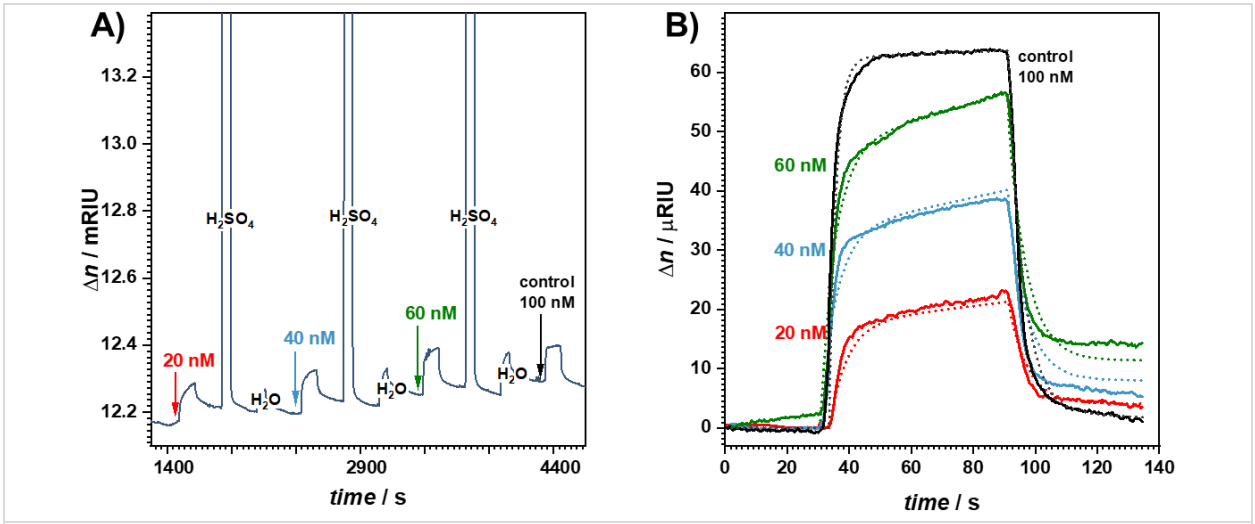

***Figure 1**: SPR signal: (**A**) recorded after consecutive injections of different concentration of ODNP and control experiment with ODNC and (**B**) kinetic analysis. Reproduced from Ref. [2].*

The electrochemical procedure for the identification of the ODNBCR/ABL, involves first the immobilization of ODNP at the electrode surface, followed by the hybridization reaction through incubation of ODNP-modified electrode in a solution of ODNBCR/ABL. Then, the electrode with the duplex formed at its surface is incubated in a solution of methylene blue (MB) electroactive indicator followed by the transduction event in buffer by differential pulse (DP) voltammetry. MB was used as electroactive indicator of the hybridization reaction since it has the property to intercalate between base pairs of the duplex and attached electrostatically to the phosphate-deoxyribose backbone. The DP voltammogram after ODNP immobilization showed a weak MB reduction peak at −0.15 V (*Fig. 2A*). After hybridization with the ODNBCR/ABL target, an increase of the MB reduction peak was observed. Increasing target concentrations resulted in a progressive current enhancement, allowing quantitative detection of the BCR/ABL gene. The biosensor achieved a sensitivity of 379 ± 12 μA cm^{-2} pM^{-1} (RSD 7.4%, n = 3) and a detection limit of ~5.00 ± 0.01 fM (RSD 7.5%, n = 3), demonstrating excellent analytical performance.

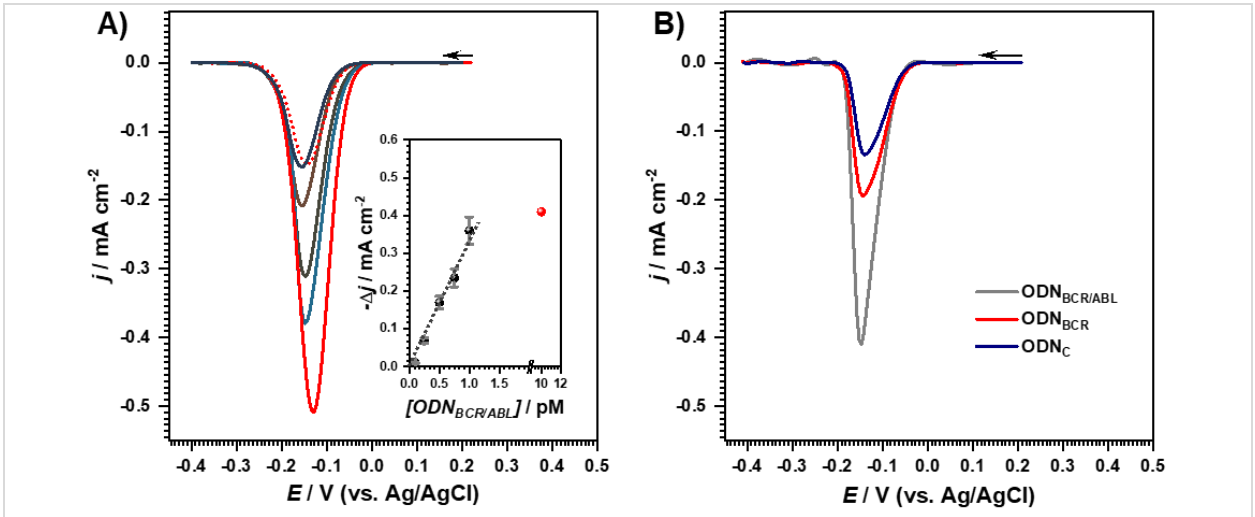

***Figure 2**: DPV obtained with the ODNP-modified Au/PMMA/PET electrode in buffer electrolyte after incubation in: (**A**) 150 μM MB (dotted red curve), and different concentrations of ODNBCR/ABL and 150 μM MB; and (**B**) 1 pM ODNBCR/ABL, ODNBCR, ODNC, and 150 μM MB. Reproduced from Ref. [2].*

Control experiments were conducted by replacing the fully complementary ODNBCR/ABL target with partially complementary ODNBCR or non-complementary ODNC during the hybridization procedure (*Fig. 2B*). For ODNC, no duplex formation occurred, and the MB reduction peak remained similar to that of the ODNP-modified electrode. In contrast, ODNBCR produced a partial duplex, resulting in a (higher

MB reduction peak, though still lower than that obtained with the fully complementary ODNBCR/ABL target, confirming sensor selectivity.

For comparison, BCR/ABL detection was also evaluated using planar $Au/SiO_2/Si$ electrodes. Following the same protocol (*Fig. 3A*), the resulting sensitivity was 8.63 ± 0.85 μA cm^{-2} pM^{-1}, and the detection limit ~0.21 ± 0.01 pM. Nonetheless, SEM analysis (not shown) revealed that ODNP immobilization on $Au/SiO_2/Si$ formed a network-like film exposing regions of bare gold, promoting non-specific adsorption of both target oligonucleotides and the redox indicator. To minimize this effect, a passivation step was introduced after ODNP immobilization (*Fig. 3B*), leading to improved performance with a sensitivity of 34.48 ± 1.68 μA cm^{-2} pM^{-1} and a detection limit of ~0.11 ± 0.01 pM.

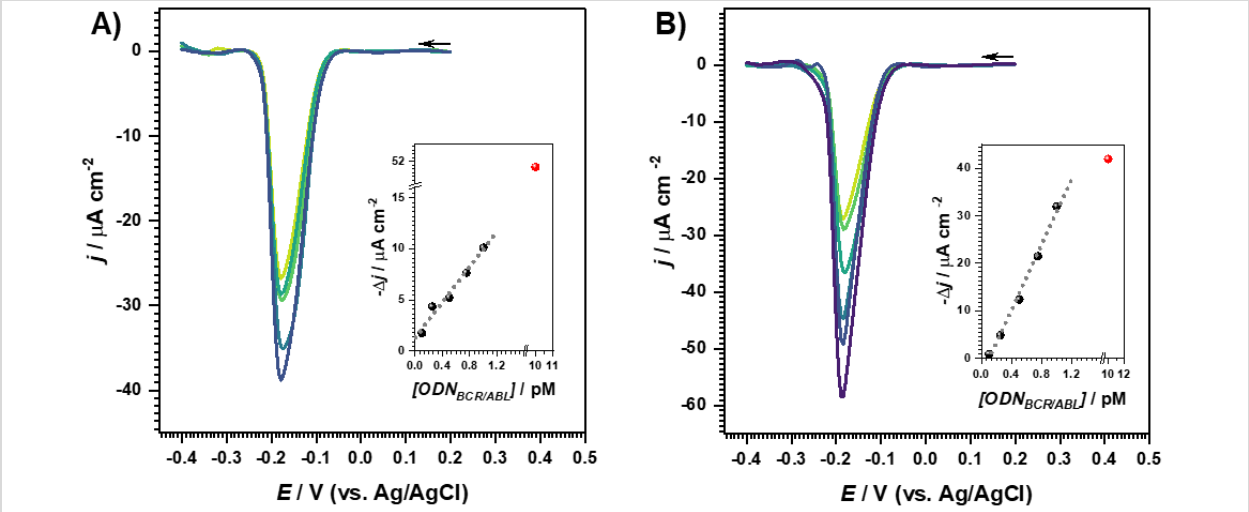

***Figure 3**: DP voltammograms obtained with the ODNP-modified $Au/SiO_2/Si$ electrode in buffer electrolyte after incubation in different concentrations of ODNBCR/ABL and 150 μM MB: (**A**) before and (**B**) after passivation with MUA. Reproduced from Ref. [2].*

Electrochemical measurements confirmed that Au/PMMA/PET electrodes exhibit higher sensitivity and a significantly lower limit of detection than planar electrodes (*Figs. 2* and *3*). This enhancement arises not only from the increased electroactive surface area but also from the electrostatic repulsion of weakly bound species, which improves the signal-to-noise ratio.

The integration of phosphorothioated oligonucleotide probes with gold-coated electrospun fibres provides a robust platform for high-performance genosensors. Structural and spectroscopic analyses confirmed uniform probe coverage and stable Au–S bonding, while SPR demonstrated superior binding affinity compared to unmodified oligonucleotides.

As a result, the Au/PMMA/PET sensors achieved a ten-fold increase in electroactive area and enabled BCR/ABL detection with a sensitivity of 379 ± 12 μA cm^{-2} pM^{-1} and a detection limit of ~5.00 ± 0.01 fM, outperforming conventional planar $Au/Ti/SiO_2/Si$ electrodes. The reduced non-specific adsorption, driven by the electrospun fibre charge, plays a key role in enhancing selectivity and analytical performance.

References:

[1] A. Babaei, A. Pouremamali, N. Rafiee, H. Sohrabi, A. Mokhtarzadeh, M. de la Guardia, *Genosensors as an alternative diagnostic sensing approaches for specific detection of virus species: A review of common techniques and outcomes*, TrAC Trends in Analytical Chemistry 155 (2022) 116686.

[2] A. Aldea, M. Onea, E. Matei, N. Apostol, D. Botta, I. Enculescu, V.C. Diculescu, *Phosphorothioated oligonucleotides on gold-coated electrospun polymeric fibers for electrochemical genosensors*, Electrochimica Acta 524 (2025) 146006.

[3] Y. Xue, X. Li, H. Li, W. Zhang, *Quantifying thiol–gold interactions towards the efficient strength control*, Nature Communications, 5 (2014) 4348.

Electrochemical bienzymatic biosensor for pyruvate kinase activity evaluation and inhibitor screening

R.J. Branco Leote[1,2], C. Sanz[1], M.M. Bârsan[1], V.C. Diculescu[1]

1) *National Institute of Materials Physics, 077125, Măgurele, Romania*
2) *Faculty of Physics, University of Bucharest, 077125, Măgurele, Romania*

This study reports the development of a pyruvate kinase (PyK) biosensor for evaluating PyK activity as a diagnostic tool for early cancer screening and for detecting kinase inhibitors used in cancer therapy. Having a key-role in cancer metabolism [1], the evaluation of PyK activity is of great importance in both medical and pharmaceutical field, being an effective target for therapeutic intervention [2]. While high-throughput assays are commonly employed for PyK activity evaluation, they often suffer from optical interferences [3], while enzyme assays remain valuable for simultaneous activity measurement and inhibitor screening. The here developed electrochemical bienzymatic biosensor combines the enzymes PyK and pyruvate oxidase (P_yO_x), the latter enabling the electrochemical detection of PyK activity. The working principle of the biosensor comprises 4 consecutive reactions, with first two related to the conversion of phosphoenol pyruvate (PEP) to pyruvate, while the last two, catalysed by P_yO_x, enable the electrochemical detection of kinase activity based on the reduction of H_2O_2 produced at the electrode surface. The schematic representation of PyK activity electrochemical detection is illustrated in *Fig. 1*, with the reactions involved as follows:

$$PEP + ADP \xrightarrow{PyK} enolpyruvate + ATP \quad \text{(reaction 1)}$$

$$enolpyruvate + H^+ \rightarrow pyruvate \quad \text{(reaction 2)}$$

$$pyruvate + P_i + O_2 \xrightarrow{PyOx} acetylphosphate + H_2O_2 + CO_2 \quad \text{(reaction 3)}$$

$$H_2O_2 + 2H^+ + 2e^- \rightarrow 2H_2O \quad \text{(reaction 4)}$$

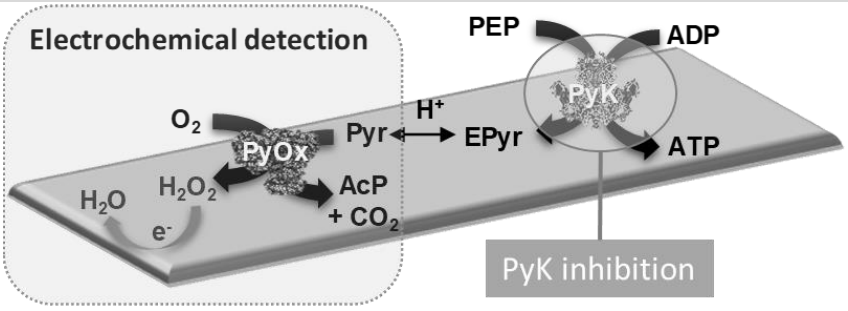

***Figure 1**: Schematic representation of the enzymatic mechanism and working principle of the PyK biosensor. Pyr – pyruvate, EPyr – enolpyruvate, AcP – acetyl phosphate. Reproduced from Ref. [3].*

The optimization of biosensor performance was achieved by analysing the influence of several parameters to maximize the biosensor's sensitivity to the PyK substrates, *e.g.*, applied potential in the fixed potential amperometric measurements, PyK:P_yO_x enzyme ratio, electrolyte pH, ADP and PEP. Maximum sensitivity of ≈2.05 μA mM^{-1} cm^{-2} was achieved at −0.20 V, corresponding to efficient H_2O_2 reduction. Increasing the PyK:P_yO_x ratio, the biosensor signal rises, with optimal performance at 10:1, while lower ratios produced negligible responses. Sensitivity decreased with increasing pH due to pyruvate keto–enol equilibrium effects, leading to the selection of pH 7.0 for further studies. A typical CA response of the PyK biosensor is presented in *Fig. 2*. The optimized PyK biosensor exhibited a sensitivity of 2.11 ± 0.08 nA μM^{-1} cm^{-2} (RSD = 4.1%, n = 3) over a linear PEP range of 1.0–6.0 mM, with a detection limit of 142 ± 9.5 μM (RSD = 4.8%). At lower PEP concentrations (0.1–0.5 mM), the biosensor showed reduced sensitivity (1.5 ± 0.05 nA μM^{-1} cm^{-2}) but a significantly lower detection limit of 12.0 ± 9.5 μM. As mitochondrial ADP and PEP levels exceed 100 μM, subsequent studies were conducted at PEP concentrations above 1.0 mM. The biosensor demonstrated good repeatability (RSD = 5.2%, n = 3), retained 78% of its initial sensitivity after 14 days of storage at 4 °C, and maintained 85% sensitivity after 20 consecutive amperometric measurements.

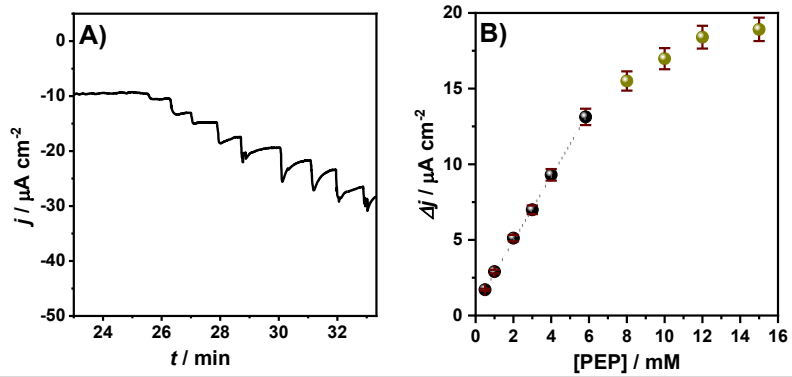

Figure 2: *(**A**) Chronoamperometric response of the PyK biosensor (0:1 PyK:PyOx enzyme ratio) at –0.20 V in the presence of 1.0 mM ADP upon successive additions of increasing concentration of PEP and (**B**) corresponding calibration plot. Reproduced from Ref. [3].*

Inhibition studies at the PyOx:PyK biosensors were performed using CA following two protocols:
(*i*) The biosensor was immersed in a solution containing ADP (1.0, 2.0, or 5.0 mM) and 1.0 mM PEP, and the steady-state current was recorded (Δj_0) followed by incubation in 1 nM inhibitor for 1–20 min; the response to 1.0 mM PEP was measured (Δj). The inhibition degree was calculated as:

$$I\% = \frac{\Delta j_0 - \Delta j}{\Delta j_0} \times 100$$

(*ii*) The response to 1.0 mM PEP was measured at ADP concentrations of 1.0, 2.0, and 5.0 mM (Δj_0), followed by measurements in the presence of increasing shikonin concentrations (0.1 fM–0.1 mM). Dose–response curves were obtained by plotting activity (%) versus log[inhibitor concentration]:

$$\text{Activity}\% = \frac{\Delta j_0}{\Delta j} \times 100$$

IC_{50} was determined experimentally, and K_i was calculated using:

$$\frac{IC_{50}}{K_i} = 1 + \frac{K_m}{[S]}$$

where K_m is the Michaelis–Menten constant and [S] is the substrate concentration.
Full inhibition was achieved after >10 min for 1:1 and 5:1 PyK:P_yO_x ratios, while residual activity below 2% remained for the 10:1 ratio. At shorter times (<5 min), inhibition decreased with increasing PyK content. Inhibition plots are displayed in *Fig. 3* with the constants of inhibition summarized in *Table 1*. Dose–response curves confirmed that shikonin is an efficient PyK inhibitor and a suitable positive control for screening PyK-targeting anticancer drugs. Sigmoidal dose–response profiles were obtained, showing complete inhibition at low PEP and residual activity at higher PEP concentrations, due to PyK allosteric activation. Increasing IC_{50} values with PEP concentration indicated competitive inhibition versus PEP, whereas IC_{50} values were independent of ADP, consistent with non-competitive inhibition relative to ADP in a Bi–Bi random mechanism. Shikonin–PyK binding exhibited negative cooperativity (Hill coefficient, h ≈ 0.5). The K_i values in the low-picomolar range were obtained from dose–response, Dixon, and Cornish–Bowden analyses, all in good agreement, and aabsorbance assays confirmed the inhibition trend [4].
The P_yO_x:PyK biosensor, was further used for enzyme inhibition studies of other four kinase inhibitors: CPG77675, Nilotinib, Ruxolitinib, and Cerdulatinib. The inhibitors exhibit a non-competitive behavior (α ≈ 1), indicating similar affinities for both PyK and the PyK–substrate complex, with a higher affinity toward the PyK–PEP complex. Maximum inhibition was achieved at 1.0 mM PEP and ADP, conditions that were therefore used for the calculation of inhibitor parameters shown in *Table 1*. The Hill coefficient values (0.42–0.45) indicate negative cooperativity within the non-competitive inhibition mechanism. Notably, non-competitive inhibitors are favored in pharmacology due to their *increased in vivo* potency, as they are not affected by competition with cellular ATP, which is present at concentrations much higher than the K_m of most kinases.

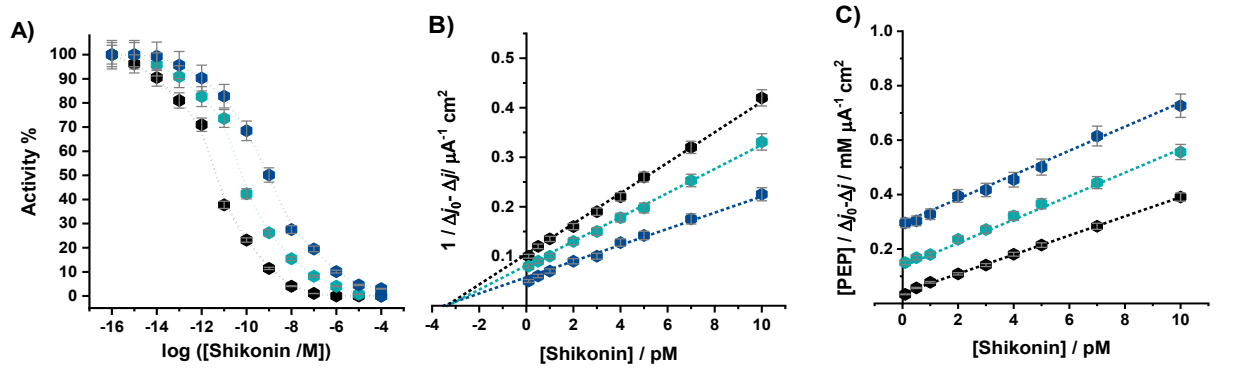

***Figure 3**: Inhibition plots constructed based on PyOx:PyK biosensor CA response over the concentration ranges from 0 to 10 pM shikonin (1.0 mM ADP and different PEP concentration): (**A**) Dose-response; (**B**) Dixon, and (**C**) Cornish-Bowden plots. Reproduced from Ref. [3].*

***Table 1**: Constants of inhibition for the PyK inhibitors, calculated from dose-response curves for 1 mM ADP and 1 mM PEP.*

Compound	α	IC_{50} / pM	K_i / pM	h	RSD/ % (n=3)
Shikonin	1	540	450	0.50	3.9
CPG77675	1	17	17	0.45	4.5
Nilotinib	1	80	80	0.42	3.6
Ruxolitinib	1	45	45	0.49	5.2
Cerdulatinib	1	120	120	0.43	4.8

The PyK/P_yO_x electrochemical biosensor was successfully applied for inhibitor detection by monitoring the chronoamperometric responses at −0.2 V following sequential injection of PEP, ADP, and inhibitors. PEP addition generated a cathodic current due to enzymatically produced H_2O_2 reduction, while inhibitor injection caused a concentration-dependent decrease in current. Calibration plots derived from these responses enabled determination of analytical parameters, including LODs calculated as 3×SD/slope. Most inhibitors showed low-picomolar LODs and wide linear ranges, demonstrating the high analytical performance of the biosensor [5].

Compared to chromatographic and spectroscopic approaches, this electrochemical assay brings several advantages, the main being greater selectivity and sensitivity, cost-effectiveness and ease of operation, while allowing the electrochemical detection simultaneously. Moreover, paring the electrochemical assay with artificial intelligence (AI)-driven data analysis will greatly increase the impact and the importance of the here developed electrochemical assay in several fields of pharmacology and medicine, especially in drug discovery, pharmacokinetic screening, point-of care diagnosis.

References:

[1] X. Chen, S. Chen, D. Yu, *Protein kinase function of pyruvate kinase M2 and cancer*, Cancer Cell International 20 (2020) 523.

[2] P. Cohen, D. Cross, P.A. Jänne, *Kinase drug discovery 20 years after imatinib: progress and future directions*, Nature Reviews Drug Discovery 20 (2021) 551–569.

[3] M. Koresawa, T. Okabe, *High-throughput screening with quantitation of ATP consumption: a universal non-radioisotope, homogeneous assay for protein kinase*, Assay and Drug Development Technologies, 2 (2004) 153–160.

[4] R.J. Branco-Leote, M.M. Barsan, C.G. Sanz, V.C. Diculescu, *Electrochemical bienzymatic biosensor for pyruvate kinase activity evaluation and inhibitor screening*, Talanta 291 (2025) 127886.

[5] R.J. Branco Leote, C.G. Sanz, V.C. Diculescu, M.M. Barsan, *Electrochemical assay for the quantification of anticancer drugs and their inhibition mechanism*, Methods 241 (2025) 13–23.

Exploring the fabrication, properties, and morphology of fluorine substituted hydroxyapatite coatings

D. Predoi[1], S.L. Iconaru[1], S.C. Ciobanu[1], K. Rokosz[2], Ş. Ţălu[3], S.-A. Predoi[4,5,6], S. Raaen[7], M. Motelica-Heino[8]

1) *National Institute of Materials Physics, 077125 Măgurele, Romania*
2) *Faculty of Electronics and Computer Science, Koszalin University of Technology, PL 75-453, Koszalin, Poland*
3) *The Directorate of Research, Development and Innovation Management (DMCDI), Technical University of Cluj-Napoca, 400020, Cluj-Napoca, Romania*
4) *École Normale Supérieure Paris-Saclay, Département de Physique, 91190, Gif-sur-Yvette, France*
5) *Université Paris-Saclay, Physique Fondamentale, 911190, Gif-sur-Yvette, France*
6) *École des Hautes Études Commerciales de Paris, 78350, Jouy-en-Josas, France*
7) *Department of Physics, Norwegian University of Science and Technology (NTNU), NO 7491, Trondheim, Norway*
8) *Department of Civil Engineering and Environment, Université d'Orléans, 45071, Orléans, France*

Hydroxyapatite (HAp), resembling human bone tissue, is a promising biomaterial for dental and hip prosthetics. Incorporating fluorine ions enhances HAp properties, particularly in dental restoration. This study examines the physicochemical and biological properties of fluorine substituted hydroxyapatite (FHAp) coatings [1]. Structural and morphological properties of the coatings were investigated by X-ray diffraction (XRD), scanning electron microscopy (SEM), and atomic force microscopy (AFM) [1]. The elemental composition of the FHAp coatings was studied using energy-dispersive X-ray spectroscopy (EDXS) and X-ray photoelectron spectroscopy (XPS) [1]. Fourier Transform Infrared (FTIR) spectroscopy investigations were also conducted [1]. The typical peaks identified in XRD patterns of the FHAp were associated with pure hydroxyapatite with hexagonal structure [1]. The general XPS spectrum of FHAp coatings showed peaks corresponding to the constituent elements of stoichiometric HAp as well as the presence of F that was used as a substituent [1]. Consequently, the FTIR spectroscopy results underlined the presence of hydroxyapatite in the FHAp coatings. The SEM images revealed the presence of a uniform and continuous layer of particle conglomerates evenly distributed across the FHAp surface [1]. Valuable information about the FHAp coating's wettability, adhesion, and coating thickness were also obtained. Furthemore, the AFM images suggested the absence of the significant irregularities from the surface of the FHAp coatings. Investigations of FHAp coatings highlighted promising outcomes for cell viability and proliferation [1]. A detailed analysis of FHAp's 3D surface characteristics and roughness, performed in accordance with the ISO 25178-2:2012 standard, highlighted its favorable suitability in supporting MG63 cell proliferation [1]. The surface roughness parameters of FHAp coatings were found to vary, with S_a values spanning from 0.029 ± 0.004 µm to 0.778 ± 0.007 µm, while S_q ranged from 0.035 ± 0.005 µm to 0.907 ± 0.011 µm [1]. Furthermore, FHAp exhibits skewness (S_{sk}) from -0.048 ± 0.006 to 0.195 ± 0.009, kurtosis (S_{ku}) from -0.600 ± 0.011 to -1.050 ± 0.021, and fractal dimension from 2.14 ± 0.01 to 2.19 ± 0.01, indicating consistent surface complexity and favourable properties. The Minkowski Functionals mirror the morphological observations from AFM images, emphasizing their dynamic influence on the samples' surfaces [1]. In this context, the primary objective of this study was to develop FHAp coatings on silicon (Si) substrates using a tailored methodology [1]. To this end, we report for the first time the fabrication of FHAp coatings by a vacuum deposition technique [1].

The XRD patterns of the FHAp coating are shown in *Fig. 1a* [*1*]. Typical (002), (102), (210), (211), (300), (202), (310), (222), (2130, and (004) reflections associated with a hexagonal hydroxyapatite structure were observed in agreement with the ICDD-PDF5: 00-09-0432 reference file [1]. No impurity phases were observed [1].

The general XPS spectrum of the FHAp coatings (*Fig. 1b*) shows the presence of typical elements of FHAp, *i.e.*, calcium (Ca), phosphorus (P), oxygen (O), and fluorine (F) [1]. The peak at 284.6 eV attributed to C 1s was also observed in the general XPS spectrum (*Fig. 1b*) [1]. On the other hand, in the general XPS spectrum of FHAp, no peaks corresponding to other elements were observed [1]. Moreover, XPS measurements reveal that Si substrates coated with FHAp are fully covered as no Si peaks appear in the XPS spectra [1].

The survey XPS spectrum of the FHAp coatings (*Fig. 1b*) confirmed the presence of the characteristic elements of FHAp, namely calcium (Ca), phosphorus (P), oxygen (O), and fluorine (F) [1]. A C 1s peak at 284.6 eV is also observed, typically attributed to adventitious carbon [1]. No additional elemental signals are detected in the survey spectrum [1]. Furthermore, the absence of Si-related peaks indicates that the FHAp layer fully covers the Si substrate [1].

Additional information was obtained by performing second derivative analysis of the FTIR spectroscopy data recorded for the FHAp coatings [1]. The second-derivative spectra of the FHAp coatings, performed in two spectral domains (450–700 cm^{-1} and 900–1200 cm^{-1}), are presented in *Fig. 1c* [1]. As shown in *Fig. 1c*, the vibrational bands associated with the symmetric ν_1 stretching and ν_2 bending modes of the phosphate group appear unsplit [1]. In the 1000–1100 cm^{-1} region, characteristic of the ν_3 asymmetric stretching modes of phosphate groups, one intense band accompanied by several weak bands can be observed. In the 550–620 cm^{-1} range, corresponding to the ν_4 asymmetric bending vibration of the phosphate group in HAp, two intense bands and several weaker bands are identified [1]. In addition, a weak band attributed to the librational mode of the hydroxyl (OH^-) group is detected [1]. No additional intense vibrational bands indicative of impurities in the FHAp coating are observed in the second-derivative spectra [1]. These findings are in good agreement with the study previously reported by Leung *et al.* [2].

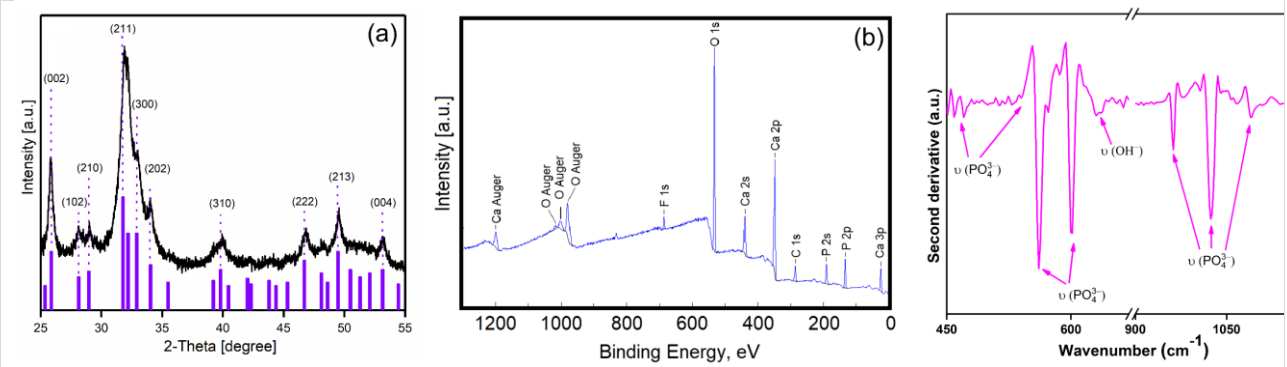

***Figure 1**: (a) XRD pattern; (b) Survey XPS spectrum; and (c) FTIR second derivative spectrum of the fluorine substituted hydroxyapatite coating. Reproduced from Ref. [1].*

The AFM topography of the FHAp coating surface is depicted in *Fig. 2a* [1]. AFM analysis revealed that the surface topography of the FHAp coatings consists of a uniformly and continuously deposited layer, with particle conglomerates evenly distributed across the surface [1]. The 2D AFM images indicate the absence of significant surface irregularities [1]. Furthermore, the 3D topographical representation shown in *Fig. 2b* confirms the homogeneous nature of the coating and the uniform distribution of the particle conglomerates [1].

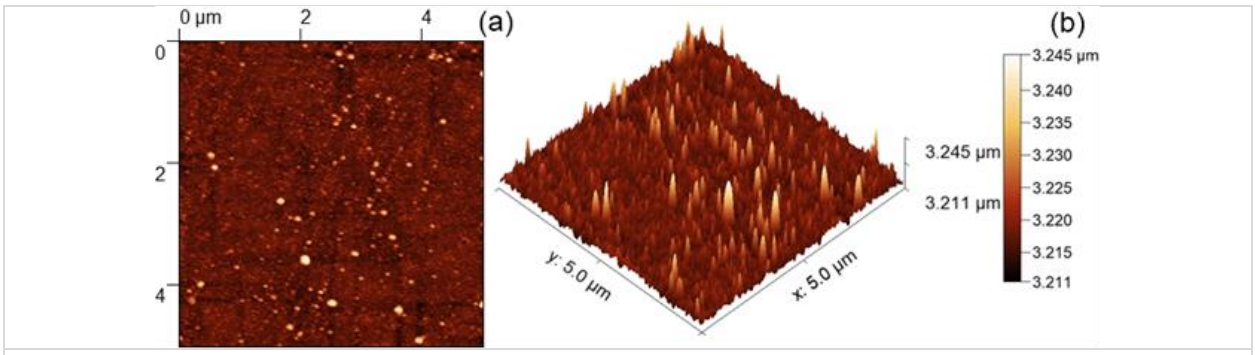

***Figure 2**: (**a**) 2D and (**b**) 3D representation of the AFM surface topography of the FHAp coating, collected for a 5 × 5 µm² scanned area. Reproduced from Ref. [1].*

The adhesion and proliferation of *Pseudomonas aeruginosa* (ATCC® 27853) on the surface of the FHAp coatings were investigated by AFM analysis [1]. To this end, AFM topographies were recorded after incubating the coatings with *P. aeruginosa* bacterial suspensions for different time intervals (24, 48, and 72 h) under atmospheric conditions at room-temperature [1]. 2D surface topographies were acquired in non-contact mode over an area of 10 × 10 μm² [1]. The corresponding 2D AFM images of the coatings incubated for 24, 48, and 72 h, together with their 3D representations, are presented in *Fig. 3a–f* [1].

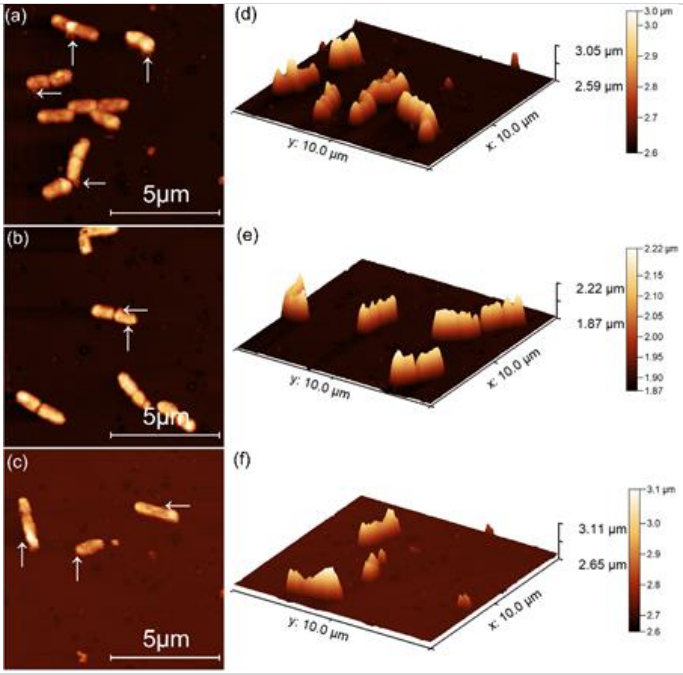

***Figure 3**: (**a–c**) 2D and (**d–f**) 3D AFM surface topography of P. aeruginosa cells on FHAp coatings after (**a**) 24, (**b**) 48, and (**c**) 72 h of exposure. White arrows in (**a–c**) indicate sites of cell membrane damage. Reproduced from Ref. [1].*

AFM analysis of the 2D surface topography of the FHAp coatings revealed that the films effectively inhibited *P. aeruginosa* adherence and growth, even at the early stages of bacterial development. The study also showed that the FHAp coatings prevented biofilm formation on their surfaces. The adhered bacterial cells exhibited the characteristic rod-shaped morphology of *P. aeruginosa*, with lengths ranging from 1.41 to 2.17 μm and widths between 0.5 and 0.68 μm. AFM data indicated that bacterial attachment and proliferation on the FHAp surfaces were significantly reduced within the first 24 h of incubation. Furthermore, both the 2D and 3D topographies suggested a time-dependent antibacterial effect, with the number of attached cells decreasing progressively over time [1]. After 72 h of exposure, only a few isolated cells remained on the FHAp coatings [1]. These results confirm that the FHAp coatings effectively inhibit biofilm formation, highlighting their potential as novel antibacterial materials for biomedical applications [1].

References:

[1] **D. Predoi, S.L. Iconaru, S.C. Ciobanu, K. Rokosz,Ş. Ţălu,, S.-A. Predoi, S. Raaen, M. Motelica-Heino, *Exploring the fabrication, properties, and morphology of fluorine substituted hydroxyapatite coatings*, Ceramics International 51 (2025) 1929–1948.**

[2] Y. Leung, M.A. Walters, R.Z. LeGeros, *Second derivative infrared spectra of hydroxyapatite*, Spectrochimica Acta Part A: Molecular Spectroscopy 46 (1990) 1453–1459.

New nanobioceramics based on hydroxyapatite for biomedical applications: Stability and properties

C.S. Ciobanu[1], D. Predoi[1], S.L. Iconaru[1], C.C. Negrilă[1], D. Leduc[2], L. Ghegoiu[1,3], C. Bleotu[4,5,6], M. Ech Cherif El Kettani[2], R. Trușcă[7], P. Zelmar[2], M.V. Predoi[3]

1) *National Institute of Materials Physics, 077125 Măgurele, Romania*
2) *Laboratoire Ondes et Milieux Complexes (LOMC), University Le Havre Normandy, 76600, Le Havre, France*
3) *Department of Mechanics, National University of Science and Technology POLITEHNICA of Bucharest, 011061, Bucharest, Romania*
4) *Department of Cellular and Molecular Pathology, Stefan S. Nicolau Institute of Virology, Romanian Academy, 030304, Bucharest, Romania*
5) *Research Institute of the University of Bucharest (ICUB), University of Bucharest, 060023, Bucharest, Romania*
6) *The Academy of Romanian Scientist, 050711 Bucharest, Romania*
7) *National Centre for Micro and Nanomaterials, National University of Science and Technology POLITEHNICA of Bucharest, 011061, Bucharest, Romania*

To develop ceramic materials with enhanced properties for compact biocompatible materials or coatings, this study aimed, for the first time, to obtain HAp and zinc-doped HAp powders (xZn = 0.05) by lyophilizing the precipitates produced via an adapted co-precipitation method [1]. By employing lyophilization as a drying technique for the first time in the production of HAp and 5ZnHAp powders, this approach yielded materials with improved physicochemical and biological properties [1]. Thus, the dispersion of nanometric particles of HApLF and 5ZnHApLF powder (in water), based on their stability, can lead to the formation of a homogeneous and dense consolidated material with minimal defects [1]. Valuable information about the HApLF and 5ZnHApLF stability was obtained through non-destructive ultrasound measurements [1]. The X-ray diffraction (XRD) studies revealed the phase and the effects of the incorporation of Zn ions into the HAp structure. The chemical composition of the samples was evaluated by energy dispersive X-ray analysis (EDXS) and X-ray photoelectron spectroscopy (XPS) [1]. Information about the functional groups present in the HApLF and 5ZnHApLF was obtained using Fourier Transform Infrared (FTIR) [1]. The morphology of HApLF and 5ZnHApLF pellets was observed by scanning electron microscopy (SEM). The surface topography of HApLF and 5ZnHApLF pellets was studied with the aid of atomic force microscopy (AFM). A complementary study was also carried out on a larger analysis surface using a Scanning Acoustic Microscope (SAM). The SAM was used for the first time to analyse the surface of HAp and 5ZnHAp pellets.

The biological properties of the HApLF and 5ZnHApLF pellets were evaluated using MG63 osteoblast-like cells and human gingival fibroblasts (HGF-1) [1]. Cell viability assays indicated that both HApLF and 5ZnHApLF pellets exhibited good biocompatibility. SEM and AFM analyses further demonstrated that the pellet surfaces supported attachment and proliferation of both MG63 and HGF-1 cells [1]. Additionally, the antimicrobial activity of the HApLF and 5ZnHApLF pellets was assessed against *Escherichia coli* (ATCC® 25922), *Staphylococcus aureus* (ATCC® 25923), and *Candida albicans* (ATCC® 10231). The results showed that 5ZnHApLF exhibited strong antimicrobial activity against all tested strains [1].

In *Fig. 1 a-d*, the deconvoluted FTIR spectra for two important spectral regions are presented: 450–700 cm^{-1} (domain specific to the ν_2 and ν_4 of [PO_4^{3-}] symmetric and asymmetric bending vibrations in HAp) and 950–1200 cm^{-1} (domain specific to the ν_1 and ν_3 of [PO_4^{3-}] symmetric and asymmetric stretching vibrations in HAp) [1]. For the HApLF sample, seven components were needed to obtain a good fit in the 450–700 cm^{-1} spectral domain. Meanwhile, for the 950–1200 cm^{-1} spectral domain, the use of six subbands allowed to produce a satisfactory fit. For the HApLF sample, seven components were required to achieve a good fit in the 450–700 cm^{-1} spectral domain, while six subbands were sufficient to produce a satisfactory fit in the 950–1200 cm^{-1} region. For the 5ZnHApLF sample, seven components were necessary in the 450–700 cm^{-1} region, corresponding to the ν_2 and ν_4 vibrations of the [PO_4^{3-}] groups [1], whereas nine subbands were required in the 950–1200 cm^{-1} region, characteristic of the ν_1 and ν_3

vibrations of the [PO_4^{3-}] groups [1]. The main functional groups contributing to the absorbance in both spectral regions for HApLF and 5ZnHApLF are the phosphate [PO_4^{3-}] groups from the HAp structure. In addition, in the 450–700 cm^{-1} domain, a vibration band assigned to the hydroxyl group appears at around 634 cm^{-1} alongside the phosphate bands [1]. Furthermore, a slight decrease in the intensity of the component centered at approximately 962 cm^{-1} was observed for the 5ZnHApLF sample, as shown in *Fig. 1c–d* [1].

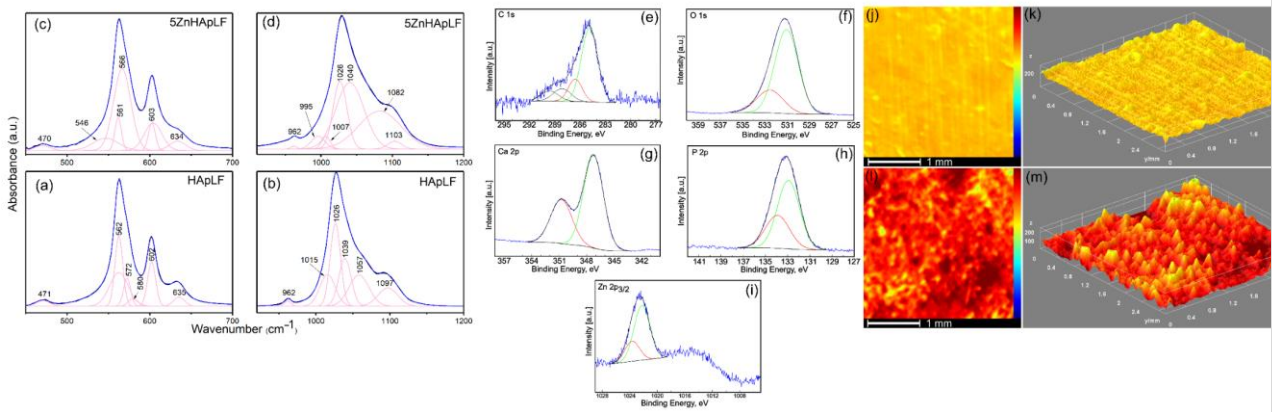

***Figure 1**: FTIR deconvoluted spectra of the ν_4, ν_3, ν_2, and ν_1 regions for the (**a,b**) HApLF and (**c,d**) 5ZnHApLF samples. High-resolution XPS spectra of (**e**) C 1s, (**f**) O 1s, (**g**) Ca 2p, (**h**) P 2p, and (**i**) Zn $2p_{3/2}$ for the 5ZnHApLF sample. Evolution of the maximum reflected signal from the pellet surfaces (C-scan, SAM) of (**j**) HApLF and (**l**) 5ZnHApLF over an area of 3 × 3 mm^2, along with the corresponding (**k,m**) 3D representations. Reproduced from Ref. [1].*

The high-resolution XPS spectra of C 1s, O 1s, Ca 2p, P 2p, and Zn $2p_{3/2}$ for 5ZnHApLF are presented in *Fig. 1e–l* [1,2]. The C 1s spectrum (*Fig. 1e*) revealed four components. The peak at a binding energy (BE) of 284.86 eV is assigned to C–C single bonds [2]. The component at 286.56 eV corresponds to O–C–O single bonds, while the peak at 288.13 eV is attributed to C=O double bonds [2]. The contribution at 289.59 eV is associated with –COOR-type contaminants [2]. The Zn $2p_{3/2}$ spectrum (*Fig. 1i*) confirmed the presence of zinc in the sample [1]. The O 1s spectrum (*Fig. 1f*) exhibited two components located at 531.04 eV and 532.53 eV [1]. The lower-BE peak is attributed to oxygen in the HAp lattice and includes contributions from C–O bonds, whereas the higher-BE component is assigned to O=C–O and C=O groups [1]. The Ca 2p spectrum (*Fig. 1g*) showed the characteristic doublet corresponding to Ca $2p_{3/2}$ and Ca $2p_{1/2}$ at 347.24 eV and 350.84 eV, respectively [1]. The spin–orbit splitting is approximately 3.6 eV, with an area ratio close to 2:1, as expected for Ca in hydroxyapatite [1]. The P 2p spectrum (*Fig. 1h*) also displayed a doublet, with the $2p_{3/2}$ and $2p_{1/2}$ components located at 132.94 eV and 133.84 eV, respectively [1]. The spin–orbit splitting of approximately 0.9 eV and the area ratio of 2:1 are characteristic of phosphate groups in hydroxyapatite [1].

AFM and SEM analyses suggested that Zn incorporation into the HAp matrix induced structural perturbations and variations in grain size, leading to increased surface roughness [1]. Acoustic microscopy results (*Fig. 1j–m*) further supported these findings [1].

The adhesion and proliferation of human osteosarcoma MG63 (*Fig. 2a–d*) and human gingival fibroblast (HGF-1) (*Fig. 2e–h*) cells incubated for 72 h on the surfaces of HApLF and 5ZnHApLF pellets were further evaluated by AFM [1]. The 2D AFM topographies and their corresponding 3D representations after 72 h of incubation revealed distinct morphological features of MG63 cells attached to both pellet surfaces (*Fig. 2a,c*). These analyses provide valuable insights into cell–material interactions and the influence of surface characteristics on cellular behaviour. The AFM results demonstrate that MG63 cells adhered successfully to both tested surfaces [1]. For the HApLF sample, the AFM topographies showed that the adhered cells retained their typical elongated, fibroblastic morphology without significant structural alterations [1,3]. The corresponding 3D representations (*Fig. 2b,d*) further support these observations, highlighting the alignment and distribution of cells across the surface. Similarly, both the 2D and 3D AFM images indicate that MG63 cells spread uniformly over the 5ZnHApLF surface, forming a well-defined monolayer with elongated and aligned morphology. This spreading behaviour is characteristic of favourable cell–material interactions and suggests that the 5ZnHApLF surface provides a suitable environment for cell attachment and proliferation [1].

Furthermore, the AFM topographies shown in *Fig. 2e–h* revealed the characteristic morphological features of HGF-1 cells adhering to the pellet surfaces [1]. While HApLF exhibited a relatively smooth surface, 5ZnHApLF displayed increased roughness due to zinc incorporation. This enhanced surface texture likely provides additional anchoring sites, promoting protein adsorption and facilitating cell attachment and spreading [1]. These findings were consistent with the SEM results (not shown) and further emphasized the superior cytocompatibility of 5ZnHApLF [1]. The 2D AFM images showed (*Fig. 2e,g*) that fibroblast cells on both surfaces exhibit flattened morphologies ranging from spindle-like to tile-like forms, characteristic of well-adhered fibroblasts [4]. Moreover, both 2D (*Fig. 2e,g*) and 3D (*Fig. 2f,h*) representations confirm excellent fibroblast adherence to the HApLF and 5ZnHApLF pellets after 72 h of incubation.

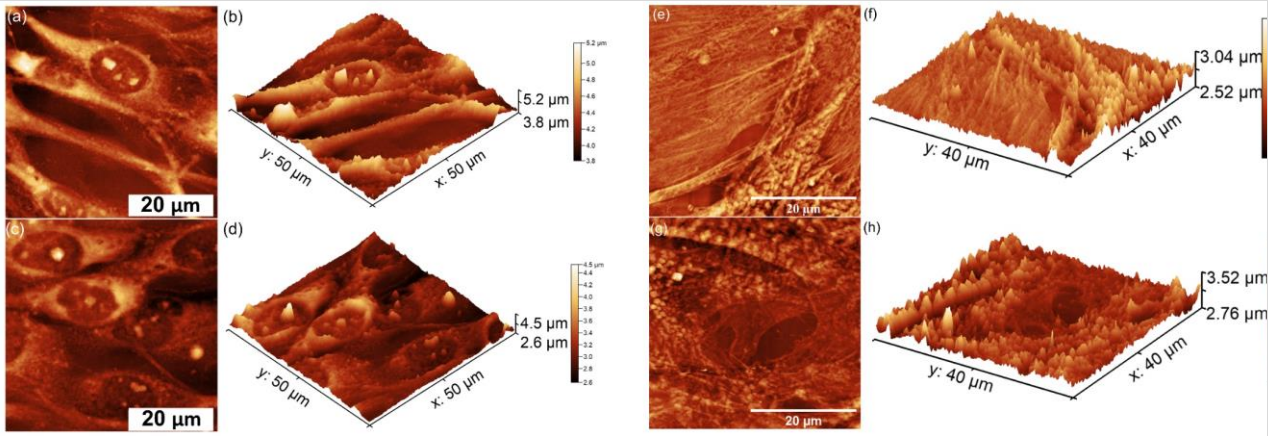

Figure 2: ***(a,c)*** *2D and* ***(b,d)*** *3D AFM topographies of MG63 cells after 72 h of incubation on* ***(a,b)*** *HApLF and* ***(c,d)*** *5ZnHApLF pellets.* ***(e,g)*** *2D and* ***(f,h)*** *3D AFM topographies of HGF-1 cells after 72 h of incubation on* ***(e,f)*** *HApLF and* ***(g,h)*** *5ZnHApLF pellets. Reproduced from Ref. [1].*

References:

[1] **C.S. Ciobanu, D. Predoi, S.L. Iconaru, C.C. Negrila, D. Leduc, L. Ghegoiu, C. Bleotu, M. Ech Cherif El Kettani, R. Trusca, P. Zelmar, M.V. Predoi, *New Nanobioceramics based on hydroxyapatite for biomedical applications: Stability and properties*, Nanomaterials 15 (2025) 224.**

[2] http://www.xpsfitting.com/2011/01/what-is-adventitious-carbon.html

[3] R.J. Chung, M.F. Hsieh, C.W. Huang, L.H. Perng, H.W. Wen, T.S. Chin, *Antimicrobial effects and human gingival biocompatibility of hydroxyapatite sol-gel coatings*, Journal of Biomedical Materials Research Part B 76 (2006) 169–178.

[4] F. Braet, R. de Zanger, C. Seynaeve, M. Baekeland, E. Wisse, *A comparative atomic force microscopy study on living skin fibroblasts and liver endothelial cells*, Microscopy 50 (2001) 283–290.

Enhanced photocatalytic performance of V_2O_5 NRs/RGO nanocomposites for Rhodamine-B decolorization under solar irradiation: Experimental and theoretical study

I. Boukhoubza[1], M. Achehboune[2,3], O. El Khouja[1], M.A. Basyooni-M. Kabatas[4,5], M. Mîndroc[1], I. Derkaoui[6], M. Enculescu[1], E. Matei[1]

1) *National Institute of Materials Physics, 077125, Măgurele, Romania*
2) *Laboratoire de Physique Du Solide, Namur Institute of Structured Matter, University of Namur, 5000, Namur, Belgium*
3) *Institute of Applied Physics, Mohammed VI Polytechnic University, 43150, Hay Moulay Rachid Ben Guerir, Morocco*
4) *Department of Precision and Microsystems Engineering, Delft University of Technology, 2628 CD, Delft, The Netherlands*
5) *Department of Nanotechnology and Advanced Materials, Graduate School of Applied and Natural Science, Selçuk University, 42030, Konya, Turkey*
6) *Faculty of Sciences Dhar El Mahraz, University Sidi Mohammed Ben Abdellah, 30000, Fez, Morocco*

The industrial sector has become an essential engine for economic development. However, this improvement is accompanied by the negative consequence of manufacturing many types of waste that significantly influence the environment, particularly the discharge of organic pollutants [1]. In this context, different types of metal oxide nanostructures and their nanocomposite-based graphene derivatives have been employed in efforts toward the advancement of sustainable photocatalytic technologies. The combination of V_2O_5 with graphene derivatives has recently received much attention in the scientific community to achieve higher activity. Reduced graphene oxide-based photocatalyst nanocomposites enabled the availability of high surface area, abundant functional surface groups, superior electrical conductivity, strong thermal stability, enhanced charge transfer efficiency, and improved photogenerated charge carrier mobility in the photocatalytic approach with variable bandgap [2,3]. In this work, an essential advance in the preparation of novel nanocomposites based on functionalized V_2O_5 nanostructures with reduced graphene oxide by hydrothermal method, which has great potential for use in photocatalytic processes related to environmental remediation (*Fig. 1*) [4].

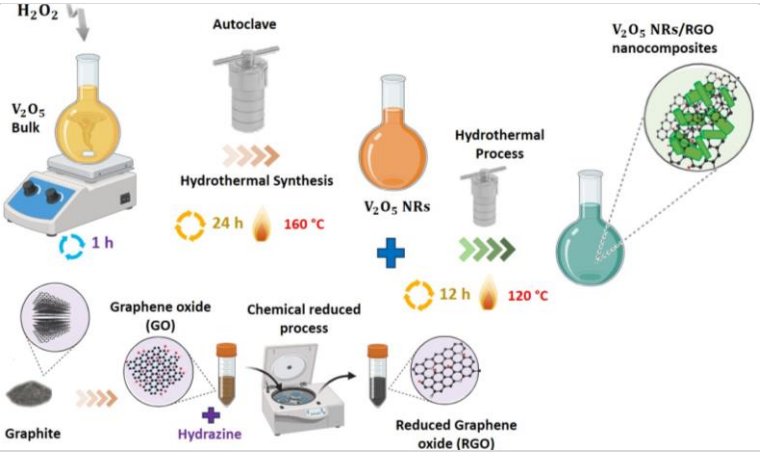

Figure 1: *Representation of V_2O_5 NRs, RGO, and V_2O_5 NRs/ RGO nanocomposites growth by hydrothermal process Reproduced from Ref. [4].*

The XRD structural analysis confirmed the orthorhombic crystal structure of V_2O_5, while SEM revealed that RGO layers were well anchored and homogeneously distributed on the surface of V_2O_5 nanorods, having an average length of approximately 60–100 nm and a diameter of about 15 nm. Raman spectroscopy provided evidence of strong hybridization between V_2O_5 and RGO, indicating effective composite formation (*Fig. 2a–h*). The experimental data was complemented by first-principles density

functional theory (DFT) simulations. These were conducted to probe the electronic interactions at the V_2O_5-graphene interface. These simulations revealed a strong interaction between V_2O_5 and graphene, characterized by an adsorption energy of approximately –1.673 eV and notable charge transfer of around 0.367 electrons from V_2O_5 to RGO. This interaction modulates the electronic structure of the composite, introducing semi-metallic behaviour near the Fermi level and increasing the density of active sites available for photocatalytic reactions. Such electronic modification facilitates improved charge carrier dynamics and thus enhances catalytic activity (*Fig. 2i*).

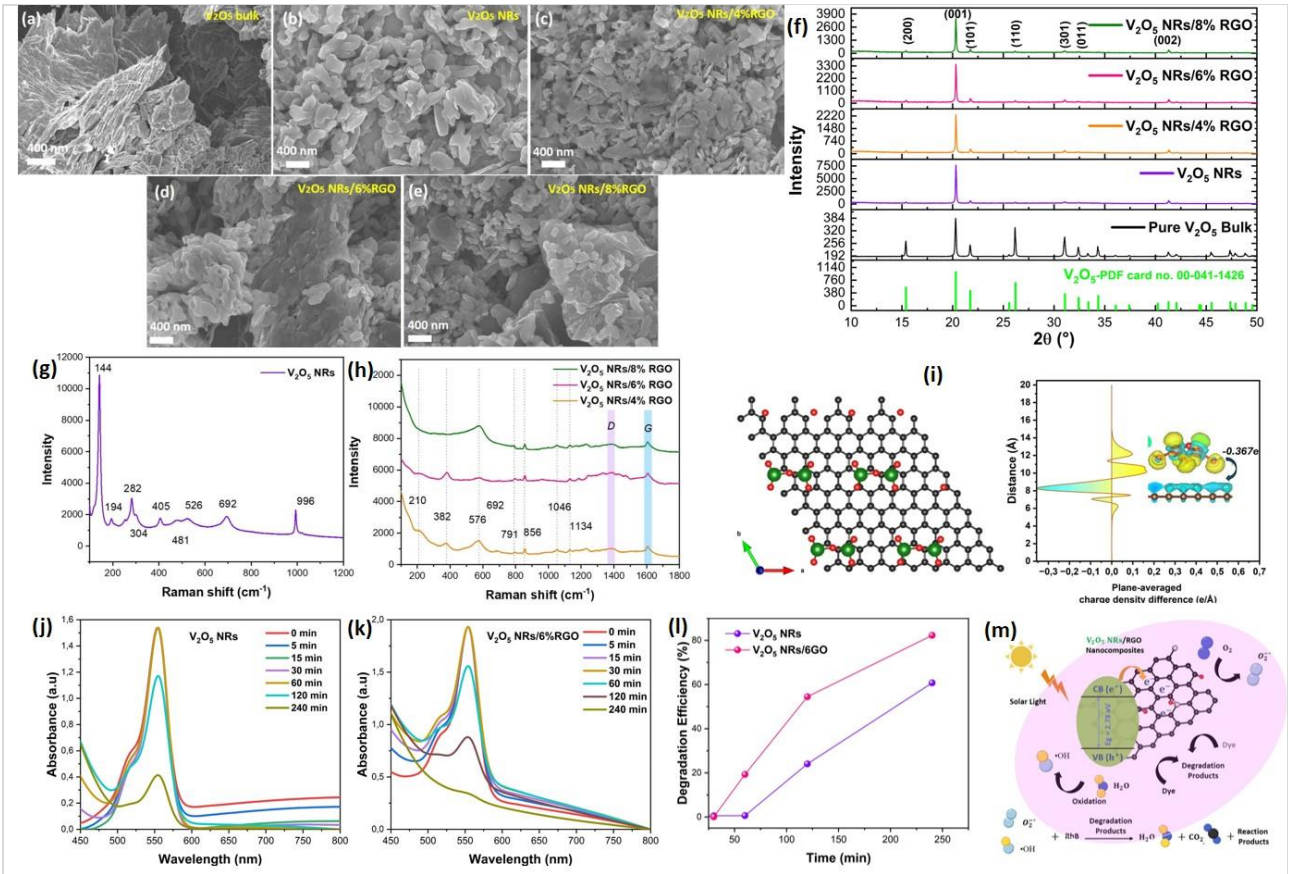

***Figure 2**: (**a–e**) SEM images, (**f**) XRD patterns, and (**g,h**) Raman spectra of V_2O_5 NRs and V_2O_5 NRs/RGO nanocomposites at different concentrations of RGO (4%, 6%, and 8%). (**i**) Schematic of V_2O_5 cluster adsorbed on reduced graphene oxide (top view) and plane-averaged charge density difference. (**j,k**) Absorption spectra, (**l**) degradation efficiency of RhB solutions after irradiation with visible light of a solar simulator for different times in the presence of V_2O_5 NRs and V_2O_5 NRs/6%RGO nanocomposites. (**m**) Schematic illustration of the mechanism of photocatalytic activity. Reproduced from Ref. [4].*

The V_2O_5 NRs/6% RGO nanocomposite was synthesized and evaluated for photocatalytic decolorization of Rhodamine-B (RhB) under simulated solar irradiation (*Fig. 2j–m*). UV–visible absorption measurements showed that pure V_2O_5 nanorods achieved approximately 60% decolorization of a 10 mg/L RhB solution after 240 minutes, whereas the V_2O_5 NRs/6% RGO nanocomposite reached 82% decolorization under identical conditions, highlighting the beneficial role of RGO incorporation. The enhanced performance is attributed to the presence of oxygen-containing functional groups on RGO, which increase surface oxygen content, reduce the effective bandgap, improve light absorption, and facilitate charge transfer while promoting dye adsorption through a higher surface area. From a mechanism perspective, photoexcitation generates electron–hole pairs, with conduction-band electrons forming reactive oxygen species such as superoxide and hydroxyl radicals, while valence-band holes contribute to hydroxyl radical generation; these reactive species efficiently degrade RhB into less harmful products. The RGO layers effectively suppress charge recombination and enhance interfacial electron transport, leading to improved photocatalytic efficiency. Overall, the photocatalytic performance of the V_2O_5/RGO nanocomposite compares favourably with previously reported systems, confirming its potential for efficient dye degradation under solar light.

References:

[1] E. Aawani, N. Memarian, H.R. Dizaji, *Synthesis and characterization of reduced graphene oxide–V_2O_5 nanocomposite for enhanced photocatalytic activity under different types of irradiation*, Journal of Physics and Chemistry of Solids 125 (2019) 8–15.

[2] R. Hatel, I. Boukhoubza, I. Derkaoui, M.A. Basyooni-M. Kabatas, E. Matei, M. Enculescu, *M. Baitoul, Synthesis and photocatalytic activity of WO_3 nanocomposites incorporating GO and MWCNTs for enhanced Rhodamine-B degradation*, Colloids and Surfaces A: Physicochemical and Engineering Aspects 711 (2025) 136395.

[3] I. Boukhoubza, I. Derkaoui, M.A. Basyooni, M. Achehboune, M. Khenfouch, W. Belaid, M Enculescu, E. Matei, *Reduced graphene oxide-functionalized zinc oxide nanorods as promising nanocomposites for white light emitting diodes and reliable UV photodetection devices*, Materials Chemistry and Physics 306 (2023) 128063.

[4] I. Boukhoubza, M. Achehboune, O. El Khouja, M.A. Basyooni-M. Kabatas, M. Mindroc, I. Derkaoui, M. Enculescu, E. Matei, *Enhanced photocatalytic performance of V_2O_5 NRs/RGO nanocomposites for Rhodamine-B decolorization under solar irradiation: Experimental and theoretical study*, Journal of Physics and Chemistry of Solids 201 (2025) 112654.

Reusable PDMS sponge composites incorporating TiO_2 nanoparticles for solar driven photocatalytic degradation of water pollutants

M. Enculescu, M. Beregoi, M-C. Bunea, M-M. Trandafir, I. Enculescu

National Institute of Materials Physics, 077125, Măgurele, Romania

Water pollution resulting from industrial effluents, dyes, petroleum derivatives, and other organic contaminants represents a major environmental challenge, with direct consequences for ecosystems and human health. Conventional wastewater treatment technologies such as membrane filtration, chemical coagulation, or biological treatment are often associated with high operational costs, limited efficiency for persistent pollutants, or poor long-term reusability [1]. As a result, the development of sustainable, low-cost, and efficient purification strategies has become a priority.

Among advanced oxidation processes, photocatalysis has emerged as a promising approach for the degradation of organic pollutants, relying on the generation of reactive oxygen species under light irradiation [2]. Titanium dioxide (TiO_2) remains one of the most extensively studied photocatalysts due to its chemical stability, non-toxicity, and strong oxidative capability. However, practical applications of TiO_2 are limited by nanoparticle aggregation, low affinity toward organic pollutants, and difficulties in catalyst recovery from treated water.

To address these challenges, polymer-based porous supports have gained increasing attention. Polydimethylsiloxane (PDMS) sponges combine flexibility, chemical inertness, high porosity, and mechanical robustness, making them attractive candidates for reusable water purification systems [3]. Embedding TiO_2 nanoparticles within three-dimensional (3D) PDMS sponge architectures enables the synergistic combination of adsorption and photocatalysis, while ensuring easy handling and recovery of the photocatalyst.

Our study presents the fabrication, characterization, and photocatalytic performance of reusable 3D TiO_2@PDMS sponge composites designed for solar-driven water purification [4]. The 3D TiO_2@PDMS sponge composites were fabricated using a sacrificial template method based on water-soluble sugar particles [5]. This approach enables precise control over the pore morphology and interconnected structure of the sponge by adjusting the size distribution and ratio of the sacrificial grains. Two types of sugar particles were employed: large grains (200–1100 μm) and small grains (50–600 μm), mixed in different proportions (10/90, 30/70, and 50/50 w/w). PDMS was prepared by mixing the base elastomer and curing agent in a 10:1 ratio, followed by dilution with cyclohexane to improve processability. TiO_2 nanoparticles (anatase/rutile mixture) were incorporated into the PDMS matrix at concentrations of 1%, 5%, and 10% (w/w). The resulting mixtures were cast into moulds and thermally cured. Subsequent removal of the sugar template by immersion in hot water generated highly porous, interconnected sponge structures (*Fig. 1*).

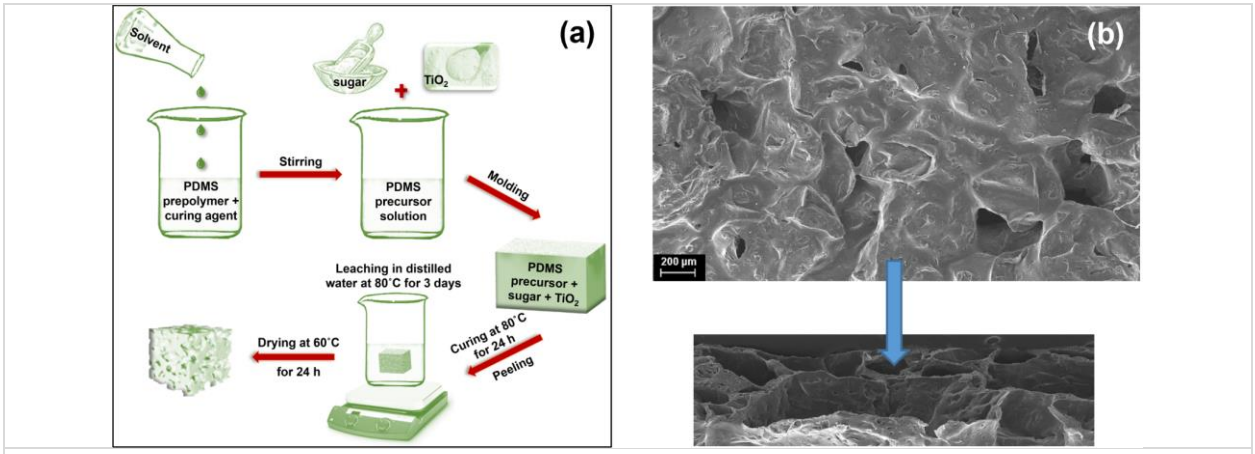

***Figure 1**: (**a**) Schematic diagram of the sponge structures' fabrication; (**b**) SEM images of TiO_2@PDMS sponge structure with interconnected pores obtained by fabrication route presented (**a**) Reproduced from Ref. [4,5].*

This fabrication route presented offers several advantages: (*i*) tuneable pore size and distribution; (*ii*) homogeneous incorporation of photocatalytic nanoparticles; (*iii*) mechanical robustness and compressibility; and (*iv*) scalability using low-cost and environmentally friendly materials.
The morphology of the pristine PDMS and TiO_2-functionalized sponges was investigated by scanning electron microscopy (SEM). All samples exhibited well-defined interconnected pore networks reflecting the size distribution of the sacrificial sugar particles. Increasing the fraction of large sugar grains led to larger pores and a more open structure, while higher contents of small grains resulted in denser networks with smaller pores, as depicted in *Fig. 1b*. Energy-dispersive X-ray spectroscopy (EDXS) confirmed the presence and homogeneous distribution of TiO_2 nanoparticles within the sponge architecture. The intensity of the Ti characteristic peaks increased proportionally with the TiO_2 loading, indicating effective incorporation during fabrication. X-ray diffraction (XRD) analysis revealed the characteristic diffraction peaks of anatase and rutile TiO_2 phases, confirming that the crystalline structure of the nanoparticles was preserved after embedding into the PDMS matrix. Importantly, SEM observations at higher magnifications showed that TiO_2 nanoparticles decorated the internal pore surfaces of the sponges. This configuration maximizes the contact area between photocatalyst and polluted water, which is essential for efficient photocatalytic degradation.

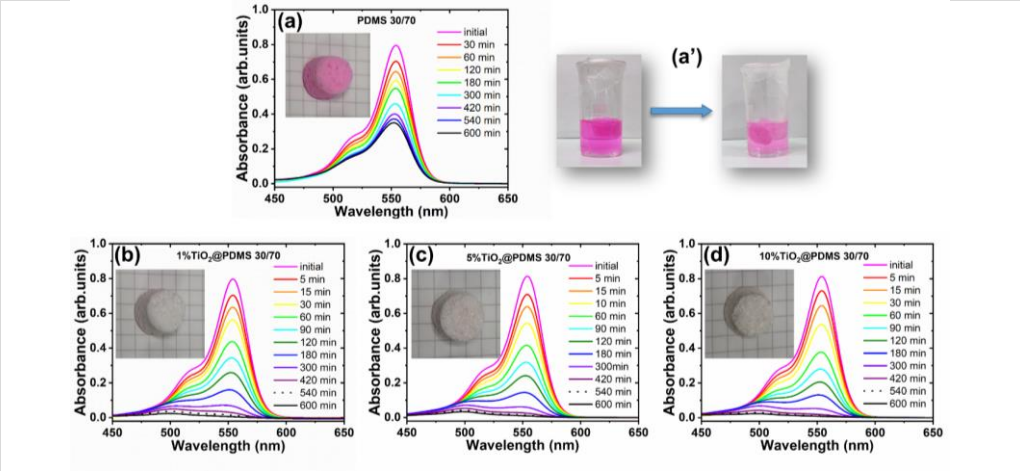

***Figure 2**: Adsorption and photocatalytic degradation of RhB under solar light irradiation using (**a,a'**) pristine and (**b,c,d**) TiO_2-functionalized PDMS sponges. Reproduced from Ref. [4].*

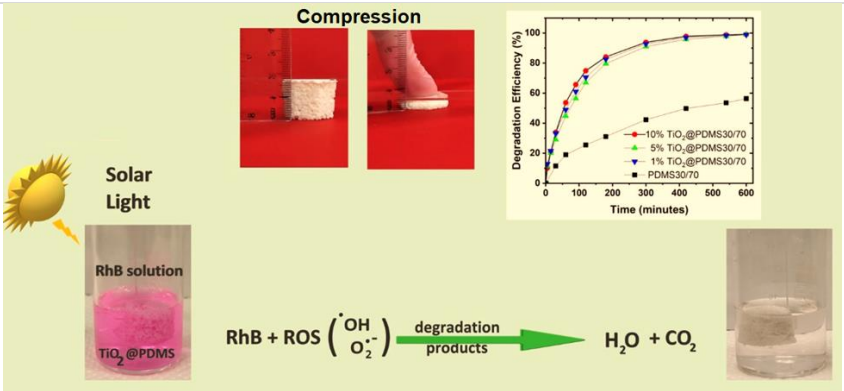

***Figure 3**: Degradation mechanism of RhB with high efficiency using compressible and floating 3D TiO_2@PDMS sponges. Reproduced from Ref. [4].*

The photocatalytic activity of the 3D TiO_2@PDMS sponges was evaluated using Rhodamine-B (RhB) as a model organic dye under simulated solar light irradiation. Cylindrical sponge samples were immersed in RhB aqueous solutions, and degradation was monitored by measuring the decrease in absorbance at 554 nm. Pristine PDMS sponges exhibited partial dye removal due to adsorption on the pore surfaces, but no complete degradation was observed, either in the dark or under solar irradiation (*Fig. 2a,b*). In contrast, all TiO_2-functionalized sponges achieved nearly complete RhB degradation within 600 minutes of solar exposure, even at low TiO_2 concentrations (1% w/w) (*Fig. 2c–e*). The floating and compressible

nature of the sponges played a crucial role in the photocatalytic process. Compression and release allowed efficient uptake of the polluted solution into the pores, while floating ensured continuous exposure of the photocatalyst to incident light (*Fig. 3*). The synergistic combination of adsorption by the PDMS matrix and photocatalytic oxidation by TiO_2 nanoparticles resulted in highly efficient pollutant removal.

Reusability is a key requirement for practical water treatment applications. The stability of the 3D TiO_2@PDMS sponges was evaluated over four consecutive photocatalytic degradation cycles using the same sponge samples. After each cycle, the sponges were rinsed, dried, and reused without any additional treatment. The results demonstrated consistent photocatalytic performance across all cycles, with complete RhB degradation. TiO_2-functionalized sponges remained clean after irradiation, while pristine PDMS sponges retained adsorbed dye molecules (*Fig. 4*).

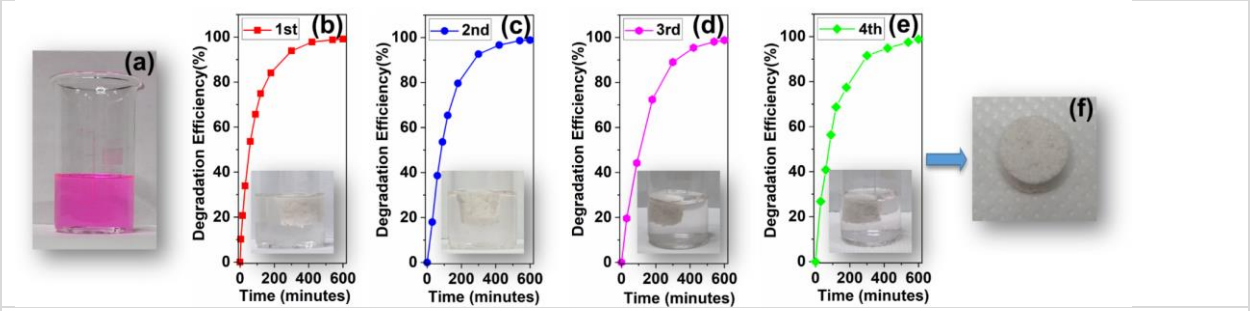

***Figure 4**: Reusability and stability of 3D TiO_2@PDMS sponge composites during repeated degradation cycles. Reproduced from Ref. [4].*

The performance of the 3D TiO_2@PDMS sponge composites can be attributed to several key factors: (*i*) controlled pore architecture enabling efficient mass transport; (*ii*) homogeneous dispersion of photocatalytic nanoparticles; (*iii*) synergistic adsorption–photocatalysis mechanism; and (*iv*) mechanical robustness and reusability.

By adjusting the sacrificial template composition and TiO_2 loading, the sponge properties can be tailored for specific pollutants or operational conditions. This versatility positions the TiO_2@PDMS sponge platform as a promising candidate for scalable and sustainable water purification technologies.

Reusable 3D TiO_2@PDMS sponge composites were successfully fabricated using a sacrificial sugar-template method, enabling precise control over pore morphology and photocatalyst loading. Structural and compositional analyses confirmed the effective incorporation of TiO_2 nanoparticles within the PDMS matrix. The composites exhibited excellent photocatalytic performance under solar irradiation, achieving complete degradation of Rhodamine-B even at low TiO_2 concentrations. Reusability tests and ICP-MS analysis demonstrated high stability and negligible nanoparticle leaching over multiple cycles. These results highlight the potential of 3D TiO_2@PDMS sponges as efficient, low-cost, and sustainable materials for water purification applications.

References:

[1] B.J. Singh A. Chakraborty, R. Sehgal, *A systematic review of industrial wastewater management: Evaluating challenges and enablers*, Journal of Environmental Management 348 (2023) 119230.

[2] D. Zhu, S. Handschuh-Wang, X. Zhou, *Recent progress in fabrication and application of polydimethylsiloxane sponges*, Journal of Materials Chemistry A 5 (2017) 14142–14162.

[3] I.M. Sosnin, S, Vlassov, L.M. Dorogin, *Application of polydimethylsiloxane in photocatalyst composite materials: A review*, Reactive and Functional Polymers 158 (2021) 104781.

[4] M. Enculescu, M. Beregoi, M.-C. Bunea, M.-M. Trandafir, I. Enculescu, *Efficient and reusable 3D TiO_2@PDMS sponge composites for solar driven photocatalytic degradation of water pollutants*, Results in Engineering 27 (2025) 107083.

[5] M. Enculescu, M. Beregoi, M-C. Bunea, I. Enculescu, OSIM atent request A00088/2024.

Tailoring surface defects and faceting in SnO_2 nanocrystals to improve their NO_2 sensing potential

C. Ghica[1], M. Ștefan[1], A. Stănoiu[1], C.E. Simion[1], I.D. Vlaicu[1], N.G. Apostol[1], C.G. Mihalcea[1,2], A.C. Iacoban[1,3], O.G. Florea[1], Ș. Bulat[1], D. Ghica[1]

1) *National Institute of Materials Physics, 077125, Măgurele, Romania*
2) *Faculty of Physics, University of Bucharest, 077125, Măgurele, Romania*
3) *Interdisciplinary School of Doctoral Studies, University of Bucharest, 050107, Bucharest, Romania*

SnO_2, a wide bandgap (E_g = 3.6 eV) n-type semiconductor, has been intensively investigated for applications in lithium/sodium-ion batteries, supercapacitors, electrocatalysts, solar cells, gas sensors, due to its low cost, low toxicity and high physical and chemical stability. To boost the SnO_2 sensor characteristics (*i.e.*, by increasing the selective sensitivity and lowering the operation temperature), several strategies were approached: tailoring the morpho-structural properties, the concentration and nature of the point defects (dopants or lattice defects) and the surface loading with noble metals [1]. The impact of surface defects on the gas sensing performance has yet to be elucidated, as it is difficult to separate the effect of oxygen vacancies from the contributions of various factors responsible for the improved sensing performance. Targeted investigations are needed to better understand the relationships between synthesis, active defects and gas-sensing performances of SnO_2, including in-depth fundamental studies at atomic/nanometric scales, to complete rigorous application-oriented research [2]. We endeavoured a complex atomic-level analysis of the material properties associated with an enhanced sensor response of the SnO_2 nanoparticles to NO_2, a primary air-pollutant gas. Correlated electron paramagnetic resonance (EPR), X-ray photoelectron spectroscopy (XPS) and transmission electron microscopy (TEM/HRTEM) techniques were used to investigate SnO_2 nanoparticles obtained by a clean, base-free hydrothermal synthesis [3].
SnO_2 nanoparticles were obtained using a $SnCl_2$ precursor, with small variations in the temperature synthesis (120, 140 and 160 °C, respectively). The TEM/HRTEM analysis showed that the SnO_2 – 120 and SnO_2 – 140 samples consisted of smaller quasi-isotropic nanoparticles (< 20 nm), while the SnO_2 – 160 sample additionally contained elongated grains (up to 50 nm) with well-developed {110} facets (*Figs. 1, 2*).

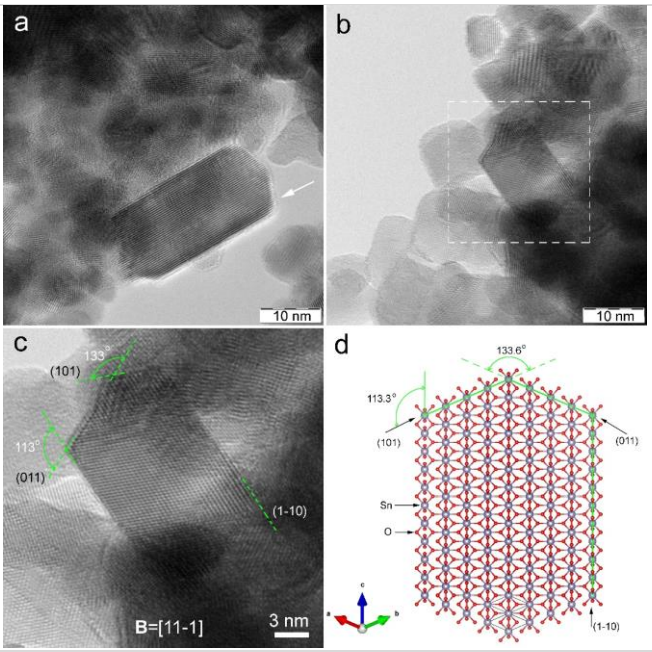

*Figure 1: Examples (**a**,**b**) of elongated faceted nanograins in the SnO_2 – 160 sample; (**c**) enlarged image of the faceted grain in (**b**) along the B=[11–1] zone axis; (**d**) atomic structural model of a SnO_2 grain along [11–1]. Reproduced from Ref. [3].*

The interaction with the target gas takes place by ion exchange involving the weakly bound oxygen ions in bridging positions – $O_{(b)}$, more numerous for the {101} versus the {110} facets (*Fig. 2*). Consequently, the proportion of the more active, higher-index facets over the less active {110} facets exposed to gases in the samples prepared at the lower temperatures is significantly larger than for the sample prepared at 160 °C, which would explain the better sensing properties of the low temperature samples.

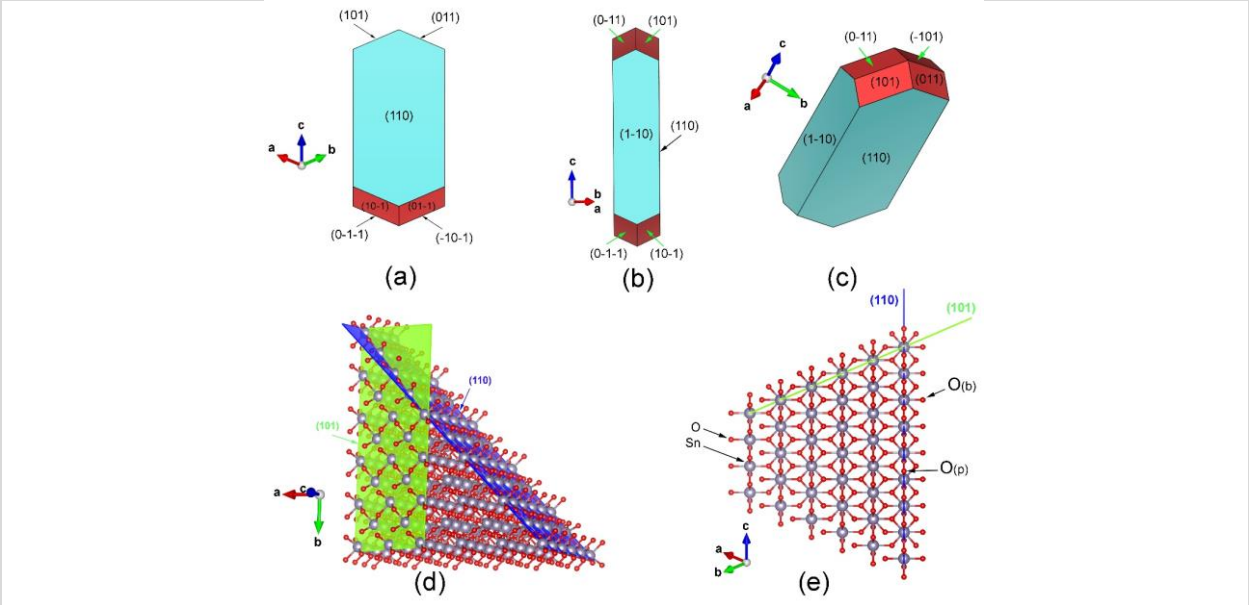

***Figure 2**: 3D representations of a SnO_2 grain delimited by {110} and {101} planes viewed along (**a**) [11–1], (**b**) [1–10], (**c**) close to [101]; the crystallographic planes pointed by black arrows are edge-on oriented; (101) and (110) sections through the crystal structure in 3D representation (**d**) and along the [–111] direction (**e**). Reproduced from Ref. [3].*

The EPR spectra of all samples evidenced the presence of complexes of oxygen vacancies ordered in the (101) planes at the surface of the SnO_2 structure. The concentration of surface oxygen vacancy complexes was higher in the sample prepared at 120 °C, inducing a higher reactivity to oxidizing gases such as NO_2 (*Fig. 3*).

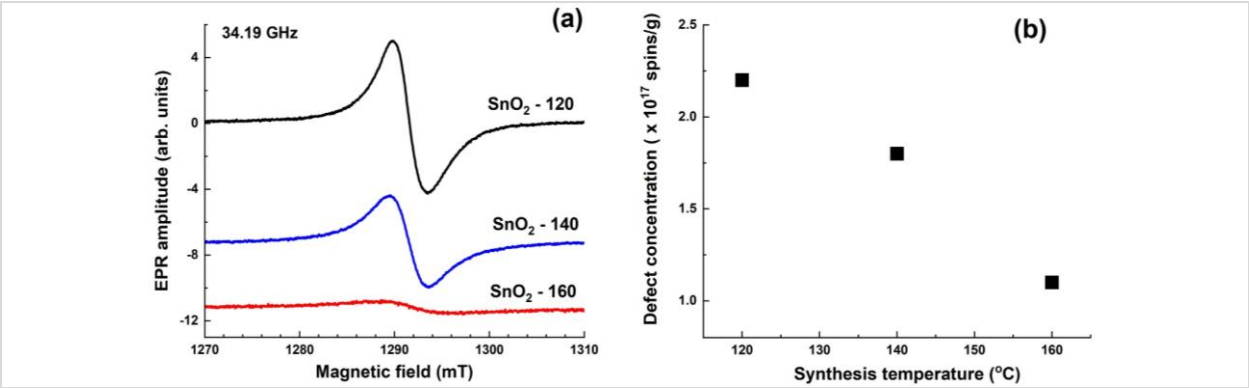

***Figure 3**: (**a**) Q-band spectra measured at room-temperature of the indicated SnO_2 powder samples; (**b**) paramagnetic defect concentrations of the three samples as a function of the synthesis temperature. Reproduced from Ref. [3].*

A sensor signal of 74 for the NO_2 detection limit of 3 ppm, at the operating temperature of 100 °C, under dynamic air flow with in-field-like relative humidity (RH) of 50 %, was obtained for the sample grown at 120 °C. The sensor signal was about four times higher compared to the 140 °C sample and about nine times higher than in the case of the 160 °C sample. In addition to its high NO_2 sensitivity, the 120 °C sample had a low sensor response for potential interfering gases as CH_4 and CO_2 and was relatively stable over a period of 20 months (*Fig. 4*). As the SnO_2 – 120 and SnO_2 – 140 samples have almost similar

nanoparticle size and morphology, the difference in their sensing response emphasizes the direct correlation between the sensing properties and the surface oxygen vacancy complexes.

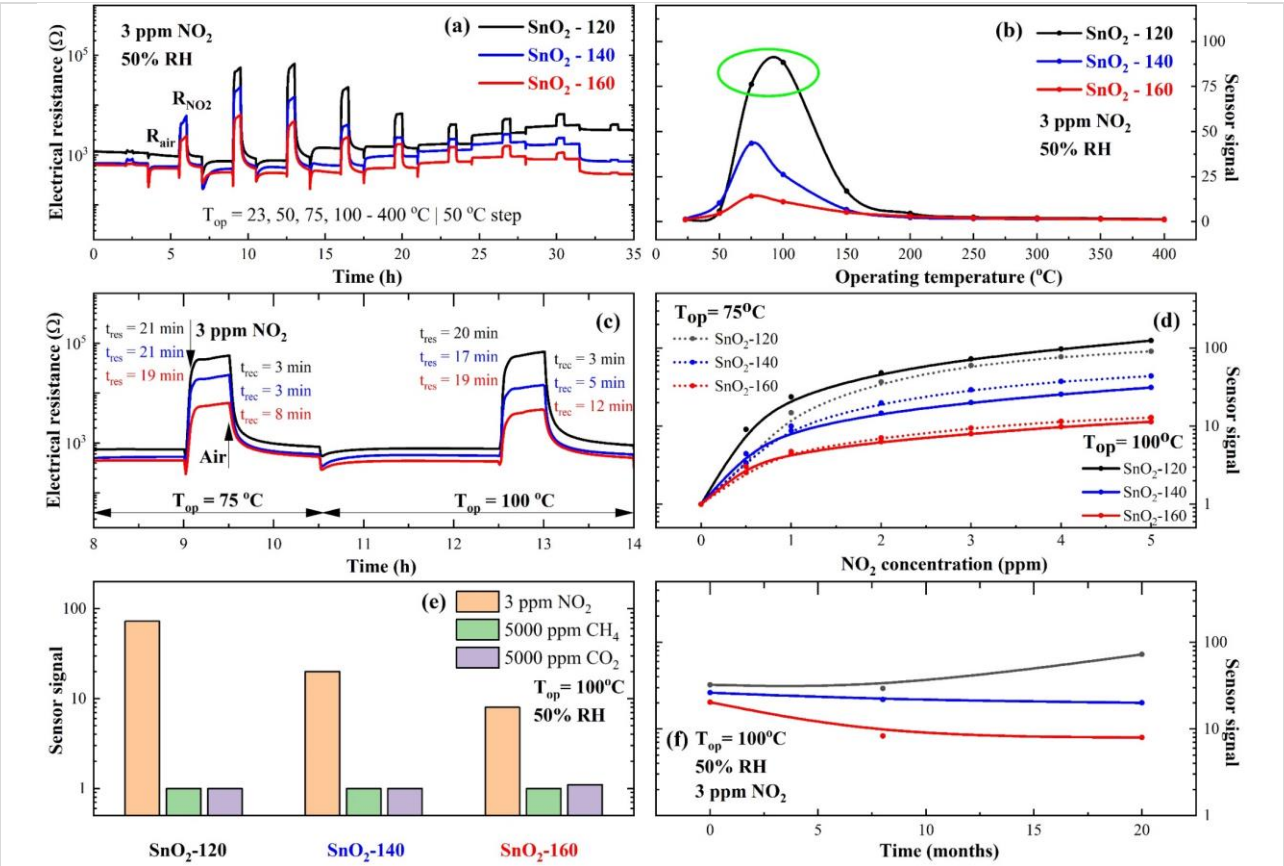

***Figure 4**: (**a**) Electrical resistance behaviour and (**b**) sensor signal dependence on the operating temperature; (**c**) transients and (**d**) signals for a wide NO_2 range at selected operating temperatures; (**e**) selectivity and (**f**) stability at the optimum operating temperature and in-field RH. Reproduced from Ref. [3].*

Our work highlighted the importance of an in-depth atomic-level investigation approach for the controlled synthesis of application-oriented materials and adheres to the ongoing efforts to identify new cleaner, low-cost synthesis of defective SnO_2 nanomaterials, with reasonable sensing response for in-field conditions at low-temperature, without resorting to the use of critical/noble metals for doping.

References:

[1] C. Ghica, C.G. Mihalcea, C.E. Simion, I.D. Vlaicu, D. Ghica, I.V. Dinu, O.G. Florea, A. Stanoiu, *Influence of relative humidity on CO_2 interaction mechanism for Gd-doped SnO_2 with respect to pure SnO_2 and Gd_2O_3*, Sensors and Actuators B: Chemical 368 (2022) 132130.

[2] C.G. Mihalcea, M. Stefan, C. Ghica, O.G. Florea, A. Stanoiu, C.E. Simion, S. Somacescu, D. Ghica, *In-depth insight into the structural properties of nanoparticulate NiO for CO sensing*, Applied Surface Science 651 (2024) 159252.

[3] C. Ghica, M. Stefan, A. Stanoiu, C.E. Simion, I.D. Vlaicu, N.G. Apostol, C.G. Mihalcea, A.C. Iacoban, O.G. Florea, S. Bulat, D. Ghica, *Tailoring surface defects and faceting in SnO_2 nanocrystals to improve their NO_2 sensing potential*, Surfaces and Interfaces 72 (2025) 107212.

Key Scientific Achievements & Breakthroughs in *Theoretical and Computational Materials Physics*

Second-order Floquet topological phases in the presence of spin-orbit coupling

A. Pena, C. Radu, B. Ostahie

National Institute of Materials Physics, 077125, Măgurele, Romania

In recent years, topological phases of matter [1] have attracted significant attention due to their potential applications in quantum computing and (opto)electronic and spintronic technologies. Time reversal symmetry (TRS) breaking is the key mechanism underlying topological phases, leading to the Quantum Hall effect. Traditionally observed in 2D materials under strong magnetic fields and discovered by von Klitzing in 1980, it was later shown that circularly polarized light can also break TRS, generating a Floquet topological insulator (FTI) phase [2,3] with quantized Hall conductance. In first order topological phases, an ND system hosts $(N-1)D$ boundary states, while second order phases [4] generate $(N-2)D$ states protected by crystalline symmetries—for example, $0D$ corner states in 2D systems.

In our previous works [5,6], we investigated spin-orbit coupling (SOC) effects in a 2D FTI based on the Kane–Mele model [7], revealing the interplay between spin and charge Floquet topological phases. Here, we extend that analysis to explore second-order Floquet topological (SOFT) phases [8,9] in the presence of SOC, focusing on spatial symmetries. The model exhibits chiral symmetry along a preferential momentum space direction, resembling a Su-Schrieffer-Heeger (SSH) chain. In Fourier space, the system also possesses C_2 and C_3 symmetries, motivating the study of rhombic (C_2) and triangular (C_3) geometries. In both cases, symmetrically localized corner states emerge. When C_2 and C_3 symmetries are broken, the corner states persist, but redistribute toward specific corners, resulting in corner polarization.

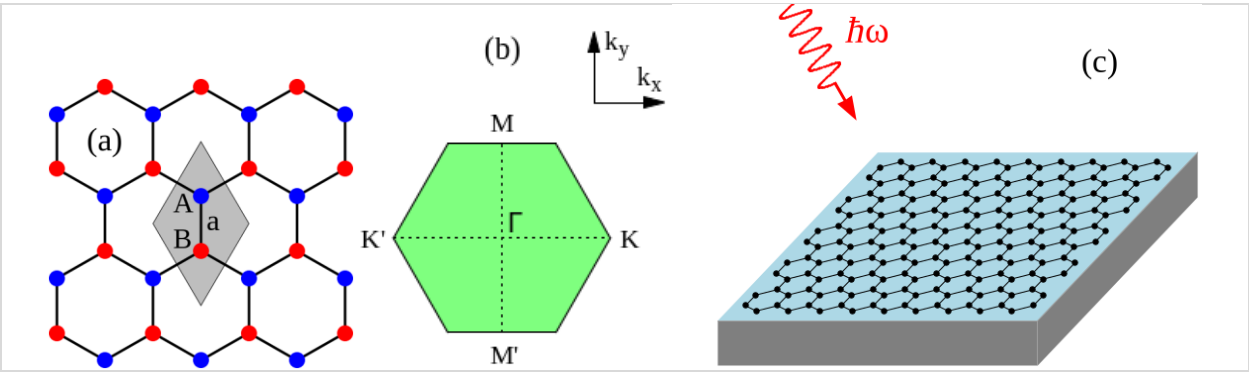

***Figure 1**: FTI model. (**a**) Honeycomb lattice with two-atom unit cell (A/B); nearest-neighbour distance a. (**b**) Corresponding BZ. (**c**) FTI induced by circularly polarized light. Reproduced from Ref. [9].*

As a model, we consider a bipartite honeycomb lattice, illustrated in *Fig. 1a*. The unit cell (grey rhombus) contains two atoms, labelled A (blue) and B (red). The nearest neighbour distance is denoted by a, corresponding to the hexagon side length. The associated Brillouin zone (BZ) is shown in *Fig. 1b*. The FTI phase is induced by irradiating the honeycomb lattice with circularly polarized light of frequency ω, as depicted in *Fig. 1c*.

In a finite size regime (sheet geometry), we expect the bulk topology to manifest through the emergence of isolated corner states inside the quasienergy gap. We first consider the hexagonal sheet geometry. In *Fig. 2a*, we display a specific quasienergy spectrum, sorted in ascending order, corresponding to both spin states. As anticipated from the bulk analysis, a pair of states clearly appears inside the quasienergy gap, for σ =↓ (spin down) state, see the two states indexed with 240 and 241. To further clarify their topological origin, in *Fig. 2b*, we present the local density of states (LDOS) associated with state 240.

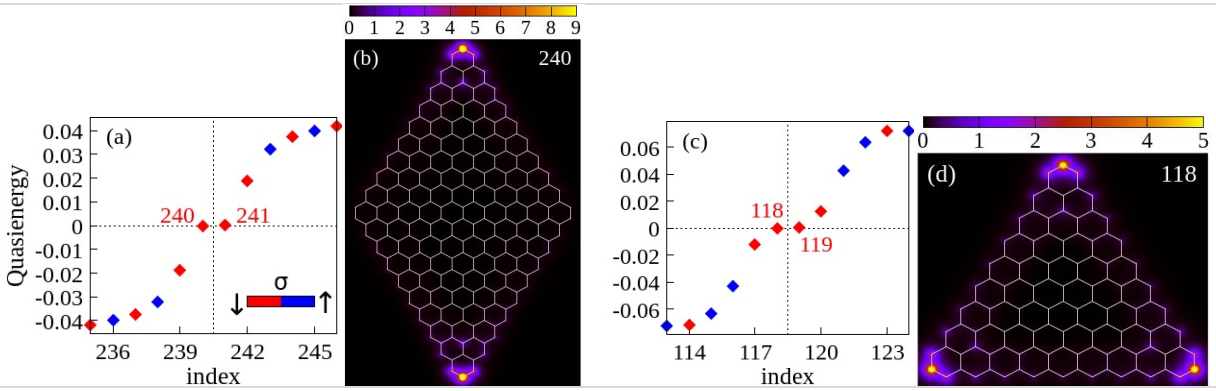

***Figure 2**: SOFT phase in finite geometries. (**a,c**) Quasienergy spectra (ascending order) for rhombic and triangular sheets, respectively. (**b,d**) Corresponding LDOS profiles for states 240 and 118 indicated in (**a**) and (**c**), evidencing corner localization. Reproduced from Ref. [9].*

The spatial profile exhibits a pronounced localization at the system corners, with negligible weight in the bulk and along the edges. This strongly confined 0D character confirms their interpretation as SOFT states. This behaviour is in sharp contrast with the first order Floquet topological (FOFT) phase, where the topological modes are 1D and extend along the system edges. Therefore, the finite geometry clearly distinguishes between first- and second-order topological phases through the dimensionality of the boundary modes.

We next analysed the triangular geometry. The corresponding quasienergy spectrum is shown in *Fig. 2c*, for the same parameters as in *Fig. 2a*. In this case, four in-gap states emerge. The LDOS profile, presented in *Fig. 2d* for state 118, again revealed strong 0D confinement at the system corners, providing additional evidence for the higher order topological nature of the SOFT phase.

The mid-gap corner modes are fully spin polarized and appear in pairs as a direct consequence of chiral symmetry. Indeed, chiral symmetry enforces spectral symmetry around zero quasienergy, implying that each in-gap state has a chiral partner. Moreover, in the present model, eigenstates with mixed spin components cannot occur due to the block-diagonal structure of the Hamiltonian, which decouples the spin up and spin down sectors. Consequently, each corner mode belongs to a well-defined spin block, allowing for an unambiguous definition of the corresponding topological invariant.

By contrast, if a spin-mixing interaction such as Rashba spin-orbit coupling were introduced, the two spin sectors would become coupled and the eigenstates would generally form superpositions of spin components. In that situation, the block-diagonal structure would be lost, and the spin resolved topological invariant could no longer be rigorously defined, since its construction relies on the independent topological characterization of each spin sector. Thus, the existence and robustness of the spin polarized corner states are intrinsically linked to the symmetry protected block structure of the Hamiltonian.

In what follows, we investigated the impact of breaking spatial C_3 symmetry, induced by disordered on-site potentials, for the triangular shape. We defined the corner polarization independently for each corner as P_α with $\alpha =$ up, left, right indicating the corner position.

In the presence of C_3 symmetry, the three corners are equivalent, implying $P_{\mathrm{up}} \equiv P_{\mathrm{left}} \equiv P_{\mathrm{right}}$. Once the C_3 symmetry is broken, this equivalence no longer holds and the corner polarizations P_{up}, P_{left}, and P_{right} become distinct.

Fig. 3a presents the corner polarization for states 118 (upper panel) and 119 (lower panel) highlighted in *Fig. 2c*. In the upper panel, an interesting situation emerges: the state predominantly localizes at the up and right corners, with a combined polarization $P_{\mathrm{up}} + P_{\mathrm{right}} \approx 92\%$ (see the red marker). The corresponding LDOS profile is displayed in *Fig. 3b*.

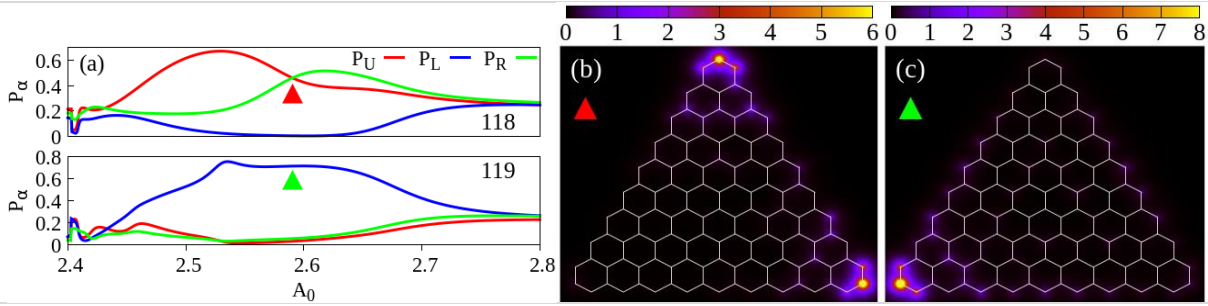

***Figure 3**: Effect of random on-site potential on triangular sheet corner states. (**a**) Corner polarization P_α for states 118 and 119 highlighted in **Fig. 2** (**c**). (**b,c**) LDOS corresponding to the red and green markers indicated in (**a**), respectively. Reproduced from Ref. [9].*

In contrast, the lower panel showed a markedly different distribution. The previously favoured up and right corners are now depleted, while the polarization concentrates at the left corner, reaching $P_{\text{left}} \approx 70\%$ (see the green marker). The resulting left corner localization is illustrated in *Fig. 3c*.

In this work, we analysed SOFT phase transitions in a FTI realized by circularly polarized light in the presence of SOC, focusing on the role of spatial symmetries. Owing to chiral symmetry along the $M' - \Gamma - M$ direction (see *Fig. 1b*), the system can be mapped onto an effective SSH model, while C_2 and C_3 symmetries determine the appropriate finite geometries (rhombic and triangular sheets). SOFT phases were confirmed through the emergence of 0D corner states in the LDOS, in contrast to 1D edge states in FOFT phases. Upon breaking spatial symmetries, the corner states persist but become preferentially localized. The topology of the model is entirely controlled by circularly polarized irradiation.

References:

[1] J.E. Moore, *The birth of topological insulators*, Nature 464 (2010) 194–198.
[2] P.M. Perez-Piskunow, G. Usaj, C.A. Balseiro, L.E.F. Foa Torres, *Floquet chiral edge states in graphene*, Physical Review B 89 (2014) 121401(R).
[3] G. Usaj, P.M. Perez-Piskunow, L.E.F. Foa Torres, C.A. Balseiro, *Irradiated graphene as a tunable Floquet topological insulator*, Physical Review B 90 (2014) 115423.
[4] W.A. Benalcazar, B.A. Bernevig, T.L. Hughes, *Electric multipole moments, topological multipole moment pumping, and chiral hinge states in crystalline insulators*, Physical Review B 96 (2017) 245115.
[5] A. Pena, C. Radu, *Floquet topological insulators with spin-orbit coupling*, Physical Review B 109 (2024) 075121.
[6] A. Pena, C. Radu, *Floquet topological spin filters*, Physical Review B 110 (2024) L241113.
[7] C.L. Kane, E.J. Mele, *Quantum spin Hall effect in graphene*, Physical Review Letters 95 (2005) 226801.
[8] M. Rodriguez-Vega, A. Kumar, B. Seradjeh, *Higher-order Floquet topological phases with corner and bulk bound states*, Physical Review B 100 (2019) 085138.
[9] **A. Pena, C. Radu, B. Ostahie, *Second-order Floquet topological phases and corner states based on spatial symmetries in honeycomb lattices in the presence of spin-orbit coupling*, Physical Review B 111 (2025) 155128.**

Antichiral edge states in finite diatomic square lattices: Quantum transport properties

B. Ostahie, A. Aldea

National Institute of Materials Physics, 077125, Măgurele, Romania

Recent advances in the study of topological phases of matter have revealed a rich variety of unconventional boundary phenomena, with edge states playing a crucial role in determining transport properties. While chiral edge states in Chern insulators are well understood and exhibit unidirectional, backscattering robust transport, increasing attention has recently been devoted to antichiral edge states, a distinct and less explored class of boundary modes. Unlike chiral edge states, antichiral edge states propagate in the same direction along opposite edges of a finite system and typically arise in gapless or semimetallic phases, where current conservation is ensured by compensating counter-propagating bulk currents [1].

The emergence of antichiral edge states is closely linked to the breaking of chiral symmetry, which induces an asymmetry in the energy spectrum. Their spatial localization and robustness depend sensitively on lattice geometry and edge termination. A prototypical example is the modified Haldane model, in which next-nearest-neighbour hopping shifts the Dirac cones in energy without altering their momentum-space positions [1]. Motivated by this mechanism, antichiral edge states have been theoretically proposed in a wide range of platforms, including strained systems, periodically driven lattices, magnetic insulators with Dzyaloshinskii–Moriya interactions, electron-phonon and exciton-polariton coupled systems, and twisted multilayer graphene [2–8]. Experimentally, although their realization in solid-state materials remains elusive, antichiral edge states have been successfully demonstrated in engineered platforms such as photonic crystals and electrical circuits [9,10].

In this work, we introduced a diatomic square lattice model composed of two coupled square sublattices connected through complex nearest-neighbours hopping that breaks time-reversal symmetry. The inclusion of next-nearest-neighbours hopping within each sublattice enabled the formation of antichiral edge states. A key advantage of this model is its tunability with respect to atomic edge configurations. We analysed the formation, localization, and spectral signatures of antichiral edge states, as well as their impact on transport properties in finite systems with different boundary geometries. Furthermore, we examined the effects of disorder to clarify ongoing debates regarding the robustness of antichiral edge states [11].

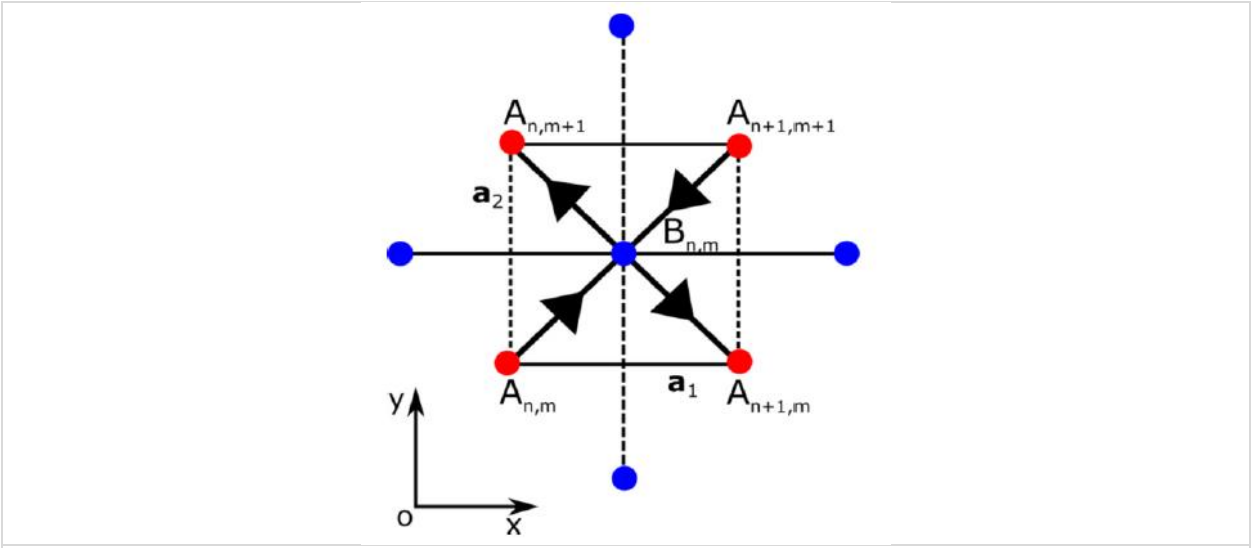

***Figure 1**: Diatomic square lattice unit cell: Atoms A and B are connected by the hopping parameter, t_1, which carries a phase γ (depicted by black arrows). The hopping parameters between A–A and B–B sites, t_{2A} and, t_{2B}, are real, but take a positive or negative sign along solid and dashed lines, respectively. Reproduced from Ref. [11].*

We considered a square lattice with two atoms, A and B, in each unit cell, defined by the primitive vectors $\vec{a}_1$ and $\vec{a}_2$. We introduced the creation $(a^{\dagger}_{n,m}, b^{\dagger}_{n,m})$ and respectively the annihilation $(a_{n,m}, b_{n,m})$ operators corresponding to the atoms in the unit cell located at the lattice position $\vec{R}_{n,m} = n\vec{a}_1 + m\vec{a}_2$. We considered the following model Hamiltonian defined on the diatomic square lattice (see *Fig. 1*):

$$H = H_1 + H_2,$$

$$H_1 = t_1\left[\sum_{n,m} e^{-i\gamma}\, b^{\dagger}_{n,m}\left(a_{n,m+1} + a_{n+1,m}\right) + \sum_{n,m} e^{i\gamma}\, b^{\dagger}_{n,m}\left(a_{n,m} + a_{n+1,m+1}\right)\right] + H.c.$$

$$H_2 = t_{2A}\sum_{n,m} a^{\dagger}_{n,m}\left(a_{n+1,m} - a_{n,m+1}\right) - t_{2B}\sum_{n,m} b^{\dagger}_{n,m}\left(b_{n+1,m} - b_{n,m+1}\right) + H.c. \quad (1)$$

where t_1 is the nearest-neighbor hopping parameter and is taken as the energy unit ($t_1 = 1$) and the terms t_{2A}, t_{2B} act as the next-nearest-neighbour (NNN) hopping parameters. Similarly, to the Haldane model, the γ phase linked to the t_1 can be interpreted as arising from an internal magnetic field.

We analysed the ribbon geometry of the Hamiltonian introduced in *Eq. (1)* by imposing open boundaries along the O_x direction and considering different atomic terminations at the edges. Two distinct ribbon configurations are studied: the AA/BB ribbon, in which A-type atoms occupy the lower edge and B-type atoms the upper edge, and the AA/AA ribbon, where both edges are terminated by A-type atoms. In this geometry, translational invariance along the x −direction allows the Hamiltonian to be expressed in momentum space as $H(kx) = H_1(kx) + H_2(kx)$. Numerical calculations of the energy spectrum as a function of kx reveal different edge-state behaviours depending on the ribbon termination. For the AA/BB configuration, when the ratio $t_{2A}/t_{2B} = 1$, a bulk energy gap opens due to next-nearest-neighbor hopping, leading to a topological insulating phase characterized by gapless chiral edge states *Fig. 2a*. In contrast, for $t_{2A}/t_{2B} = -1$, the system becomes semimetallic, featuring energy-shifted Dirac points connected by dispersive edge states. The unidirectional propagation of these states along both edges identifies them as antichiral edge states *Fig. 2b*. Interestingly, the AA/AA ribbon exhibits a hybrid response: despite satisfying the antichiral condition $t_{2A}/t_{2B} = -1$, the edge states displayed opposite velocities characteristic of chiral modes, while the bulk spectrum remains semimetallic *Fig. 2c*.

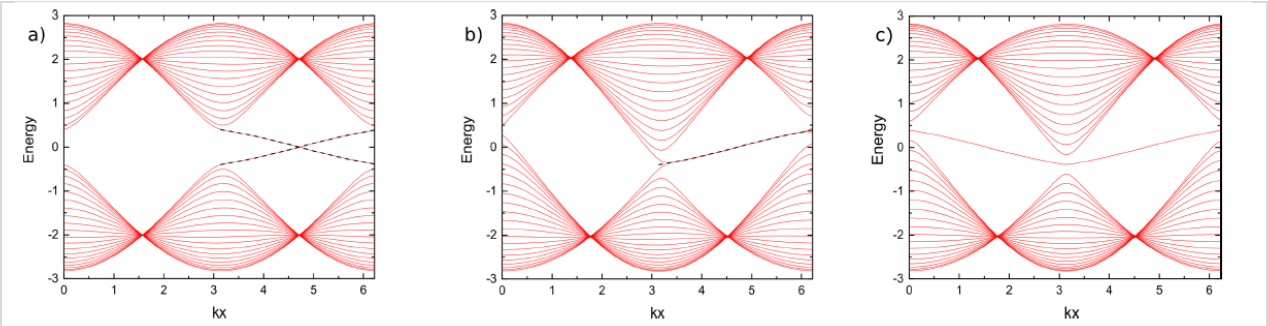

***Figure 2**: Comparison of the energy spectra for ribbons in the AA/BB and AA/AA configuration. The panels (**a**) and (**b**) correspond to the Chern insulator phase ($t_{2A}/t_{2B} = 0.1$) and the semimetallic antichiral phase ($t_{2A}/t_{2B} = -0.1$) of the AA/BB ribbon, respectively. One observes that in both the Chern insulator (**a**) and semimetallic antichiral phase in the AA/AA geometry (**c**), the edge states exhibit opposite chiralities, whereas in panel (**b**), they display the same chirality. Reproduced from Ref. [11].*

Following the analysis of ribbon energy spectra and edge-state chirality, we now investigate how these distinct edge modes manifest in quantum transport and how robust they remain against disorder and finite-size effects. *Fig. 3* presents the Hall resistance calculated for a finite plaquette geometry, highlighting the contrasting behaviour of chiral and antichiral edge states. In the clean limit (*Fig. 3a*), both the chiral phase $t_{2A} = t_{2B} = 0.05$ and the antichiral phase $t_{2A} = -t_{2B} = 0.05$ exhibit a quantized Hall resistance $R_{Hall} = 1\,(h/e^2)$ in the topological energy range. This indicates that, despite the absence of a bulk gap in the antichiral regime, edge transport remains well defined in the pristine system. The situation changes significantly when disorder is introduced, as shown in *Fig. 3b*. While the Hall resistance in the chiral phase remained robust and essentially unaffected by disorder, the antichiral phase displayed a strong sensitivity. This behaviour reflects the semimetallic nature of the antichiral regime, where bulk states coexist with edge modes. Unlike chiral edge states, antichiral edge transport

lacks topological protection in finite systems, emphasizing its fragility against disorder and finite-size effects.

We have proposed a diatomic square lattice model that support chiral and antichiral edge states through the interplay of complex nearest-neighbour hopping, next-nearest-neighbour couplings, and edge termination. By tuning these hopping parameters, we demonstrated the emergence of antichiral edge states in a semimetallic phase, highlighting the essential role of lattice geometry and boundary conditions in determining edge-state chirality. Furthermore, our transport analysis showed that although antichiral edge states support quantized Hall conductance in clean finite systems, they lacked the robustness associated with topologically protected chiral states. The presence of bulk states in the semimetallic regime makes antichiral transport fragile to disorder and finite-size effects.

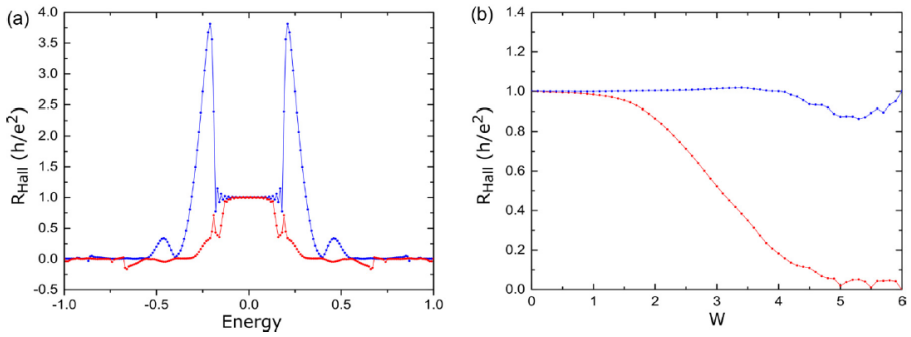

***Figure 3**: Hall resistance for clean and disordered plaquettes. (a) In the clean case, the Hall resistance is quantized at $R_{Hall} = 1\ (h/e^2)$ for both the chiral and antichiral regimes in the topological energy range. (**b**) At zero energy, disorder strongly suppresses the Hall quantization in the antichiral phase, while the chiral case remains robust. Data are averaged over 1000 disorder realizations. Reproduced from Ref. [11].*

References:

[1] E. Colomés, M. Franz, *Antichiral edge states in a modified Haldane nanoribbon*, Physical Review Letters 120 (2018) 086603.

[2] M. Mannaï, S. Haddad, *Strain tuned topology in the Haldane and the modified Haldane models*, Journal of Physics: Condensed Matter 32 (2020) 225501.

[3] K.W. Lee, M.J.A. Calderon, X.-L. Yu, C.H. Lee, Y.S. Ang, P.-H. Fu, *Floquet engineering of topological phase transitions in a quantum spin Hall α-T_3 system*, Physical Review B 111 (2025) 045406.

[4] D. Bhowmick, P. Sengupta, *Antichiral edge states in Heisenberg ferromagnet on a honeycomb lattice*, Physical Review B 101 (202) 195133 (2020).

[5] Y. Su, G. Li, *Topological origin of antichiral edge states induced by a nonchiral phonon*, Physical Review B 109 (2024) 155410.

[6] J. Medina Dueñas, H.L. Calvo, L.E.F. Foa Torres, *Copropagating edge states produced by the interaction between electrons and chiral phonons in two-dimensional materials*, Physical Review Letters 128 (2022) 066801.

[7] S. Mandal, R. Ge, T.C.H. Liew, *Antichiral edge states in an exciton polariton strip*, Physical Review B 99 (2019) 115423.

[8] M.M. Denner, J.L. Lado, O. Zilberberg, *Antichiral states in twisted graphene multilayers*, Physical Review Research 2 (202) 043190.

[9] X. Xi, B. Yan, L. Yang, Z.-X. Zhu, J.-M. Chen, Z. Wang, P. Zhou, P.P. Shum, Y. Yang, H. Chen, S. Mandal, G.-G. Liu, B. Zhang, Z. Gao, *Topological antichiral surface states in a magnetic Weyl photonic crystal*, Nature Communications 14 (2023) 1991.

[10] Y. Yang, D. Zhu, Z. H. Hang, Y. Chong, *Observation of antichiral edge states in a circuit lattice*, Science China Physics, Mechanics & Astronomy 64 (2021) 257011.

[11] **B. Ostahie, A. Aldea, *Antichiral edge states in diatomic square lattice and quantum transport properties*, Physical Review B 112 (2025) 085416.**

Major R&D Projects

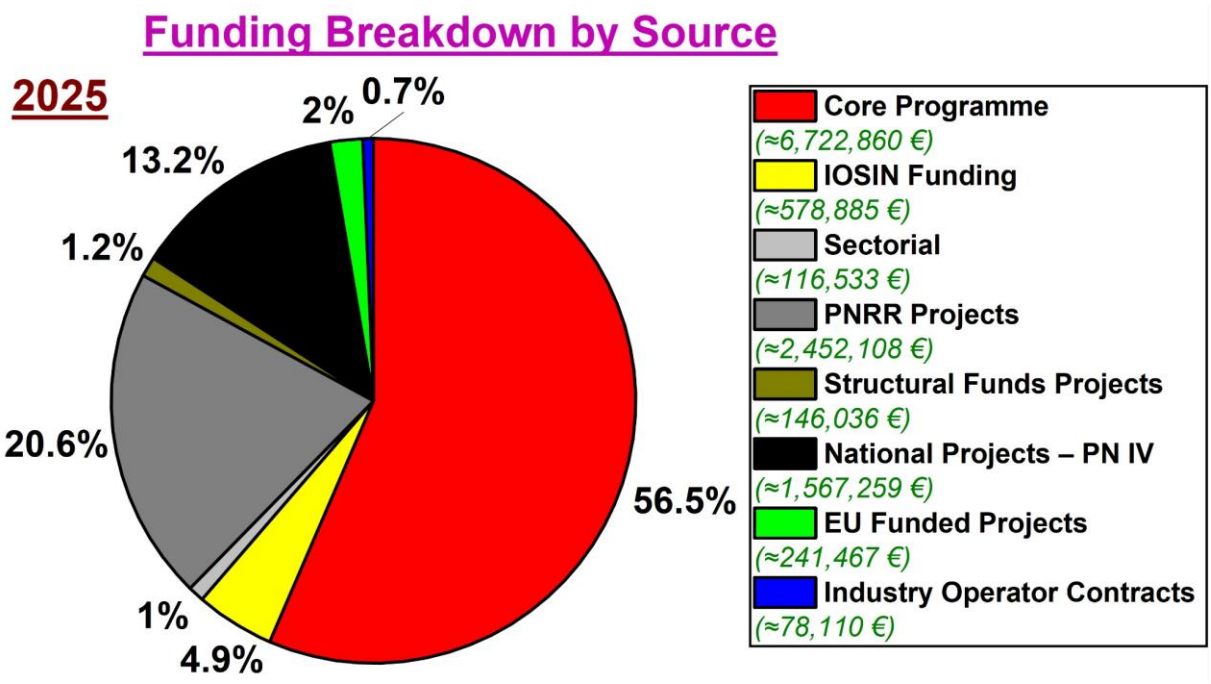

NEutrino properties through use of nuclei

1. Project identification

- ***Acronym:*** *NEPTUN*
- ***Project code / Contract no.:*** *760100/23.05.2023*
- ***Funding program / Competition type:*** *National/PNRR-I8*
- ***Funding authority / Sponsor:*** *MCID-DGGCPNRR*
- ***Project duration:*** *36 months (2023.07.01 – 2026.06.30)*
- ***Total budget / CIFRA (branch of NIMP) share:*** *1,417,290.95 € / 1,417,290.95 €*

2. Consortium

- ***Coordinating institution:*** *Centre International de Formation et de Recherche Avancées en Physique – CIFRA, branch of National Institute of Materials Physics, Măgurele, Romania*
- ***Partners institutions:*** *n/a*

3. Project summary (including objectives, estimated results, progress beyond the state-of-the-art)

Neutrinos are neutral, elementary particles that play a major role in different domains of physics, such as particle and nuclear physics, astrophysics, and cosmology. Their fundamental properties remain insufficiently understood and elucidating them would represent a significant advancement in knowledge, with far-reaching implications for science, technology, and society. In this project we develop new theoretical methods and advanced computational programs for investigating the properties of neutrinos produced in the beta decay (BD) and neutrinoless double-beta decay (NDBD). The overall objectives of the project are: (*i*) formation of a strong internationally recognized research group for providing advanced theory tools and analyses to the theoretical and experimental nuclear-, particle-, and neutrino physics communities; (*ii*) supporting the national fundamental research at frontier, in leading scientific fields; (*iii*) offering young researchers training and research programs, within a highly internationally competitive environment. The specific objectives of the project aim to make a significant contribution to the clarification of the following hot topics: (*a*) effective value of the axial-vector coupling strength g_A; (*b*) existence of sterile neutrinos; (*c*) reliable nuclear matrix elements (NMEs) for NDBD; and (*d*) neutrino masses from BD and NDBD. The project is based on the joint expertise, internationally recognized, of the Jyvaskyla, Bucharest, and Michigan theory groups, complemented by direct, close collaborations with important experimental research groups. Furthermore, this project is envisioned as the starting point of a sustainable, long-term international collaboration, with potential expansion through applications to other EU programs.

4. Role of CIFRA (branch of NIMP)

- ***Role in the project:*** *Coordinator*
- ***Main responsibilities:*** *Logistic support & Education.*
- ***Key personnel involved:*** *1 principal investigator, 1 project manager, 3 senior researchers, 4 junior researchers, 4 PhD students.*

5. Summary of results obtained in 2025

i. Calculation of phase space factors for double-beta decay and EC processes

We develop an advanced method to calculate phase space factors (PSFs) for double-beta decay, including the two-neutrino ($2\nu\beta\beta$) and neutrinoless ($0\nu\beta\beta$) decay modes and transitions with electron emission, positron emission and electron capture. The calculations are performed with an adapted Dirac-Hartree-Fock-Slater method and include accurate treatment of the electron and positron wave functions as well as of key atomic features like screening, finite nuclear size, exchange corrections and

phase shift effects. In addition, the procedure for obtaining orthogonality between electron bound and continuum states is applied. We provide tables with updated PSFs calculated both in the closure approximation and using the Taylor expansion method, for a large class of nuclei. We also discuss the impact of each atomic correction and compare our results with other values reported in literature. Then, we also provide numerical values for electron energy spectra for the isotopes ^{76}Ge, ^{130}Te, and ^{136}Xe, which are used in the currently most sensitive DBD experiments. Similar data for other isotopes can also be provided at request. This work is useful both to theorists and to experimentalists, for planning their set-ups, detector calibration, background characterization and data interpretation.

Table 1: Phase space factors for $2\nu\beta^-\beta^-$ transitions from ground state to ground state, the first excited 0^+, and first 2^+ state, obtained in the Closure approximation. Empty entries correspond to energetically forbidden processes. Phase space factors G and H are displayed in units of $10^{-21}y^{-1}$.

	$0 \to 0^+$			$0 \to 0_2^+$			$0 \to 2^+$		
Nucleus	$G_{2\nu}^{\beta^-\beta^-}$	$H_{2\nu}^{\beta^-\beta^-}$	$K_{2\nu}^{\beta^-\beta^-}$	$G_{2\nu}^{\beta^-\beta^-}$	$H_{2\nu}^{\beta^-\beta^-}$	$K_{2\nu}^{\beta^-\beta^-}$	$G_{2\nu}^{\beta^-\beta^-}$	$H_{2\nu}^{\beta^-\beta^-}$	$K_{2\nu}^{\beta^-\beta^-}$
^{48}Ca	16211.064	−12170.658	−0.751	0.379	−0.145	−0.382	4460.281	−849.043	−0.190
^{76}Ge	51.368	−26.214	−0.510	0.077	−0.021	−0.275	0.473	−0.053	−0.112
^{82}Se	1705.062	−1076.413	−0.631	4.919	−2.026	−0.412	84.735	−12.427	−0.147
^{96}Zr	7349.061	−4840.951	−0.659	192.044	−100.736	−0.525	890.059	−140.388	−0.158
^{100}Mo	3519.398	−2201.674	−0.626	65.307	−30.945	−0.474	694.412	−106.732	−0.154
^{110}Pd	147.713	−72.531	−0.491	0.005	-8.266×10^{-4}	−0.156	0.560	−0.056	−0.101
^{116}Cd	2950.066	−1755.011	−0.595	0.968	−0.284	−0.293	2.562	−0.278	−0.108
^{124}Sn	605.949	−318.976	−0.526	0.024	−0.004	−0.178	11.066	−1.284	−0.116
^{128}Te	0.305	−0.074	−0.241				1.214×10^{-6}	-3.680×10^{-8}	−0.030
^{130}Te	1643.051	−912.710	−0.555	0.087	−0.018	−0.205	98.149	−12.715	−0.130
^{136}Xe	1540.125	−838.947	−0.545	0.410	−0.100	−0.243	10.925	−1.224	−0.112
^{148}Nd	352.204	−161.717	−0.459	0.012	−0.002	−0.132	2.352	−0.226	−0.096
^{150}Nd	38953.965	−24939.916	−0.640	4660.103	−2607.767	−0.560	37239.786	−6198.920	−0.166
^{154}Sm	13.455	−4.378	−0.325	0.035	−0.005	−0.150	0.263	−0.021	−0.081
^{160}Gd	213.467	−89.583	−0.420	0.008	-8.757×10^{-4}	−0.113	28.483	−3.102	−0.109
^{198}Pt	17.960	−4.746	−0.264				0.002	-7.303×10^{-5}	−0.040
^{232}Th	12.703	−2.543	−0.200	4.735×10^{-5}	-4.482×10^{-7}	−0.009	0.082	−0.004	−0.047
^{238}U	166.697	−45.379	−0.272	6.162×10^{-4}	-1.391×10^{-5}	−0.023	4.732	−0.321	−0.068

ii. Novel way of evaluating g_A quenching in β^+/EC decays: Introducing the Branching-Ratio Method (BRM)

The novel Branching-Ratio Method (BRM) is introduced for determining the effective value $g_A^{\text{eff}}$of the weak axial coupling $g_A$in forbidden non-unique (FNU) β^+/electron-capture (EC) decays. This method provides new opportunities to test the suitability of nuclear Hamiltonians in modeling the complex physics of β^+/ECtransitions. By simultaneously reproducing the branching ratios for both $\beta^+$and EC decays, BRM introduces an additional constraint that improves the determination of g_A^{eff}. In this approach, the ambiguity in choosing $g_A^{\text{eff}}$and the small relativistic vector nuclear matrix element (s-NME) is resolved by applying the branching-ratio constraints.

As a demonstration, the present work applies BRM to the second FNU β^+/ECdecay of ^{59}Ni. This decay is analyzed using three different nuclear shell-model (NSM) Hamiltonians, illustrating how variations in nuclear structure affect the application and results of the BRM.

Table 2
GX1APN-computed s-NME ($^{V}\mathcal{M}^{(0)}_{KK-11}$) values, $sNME_{\beta^+/EC}(1)$ and $sNME_{\beta^+/EC}(2)$, columns 2 and 4, which reproduce the experimental total half-life (rows 2 - 6) or the β^+ half-life (rows 8 - 12) for a given g_A^{eff} of the 2nd FNU β^+/EC decay transition of ^{59}Ni. The respective relative BR, $BR_{\beta^+:EC}$, are also given in columns 3 and 5. The last row gives the CVC value of sNME.

g_A^{eff}	$sNME_{\beta^+/EC}(1)$	$BR_{\beta^+:EC}$	$sNME_{\beta^+/EC}(2)$	$BR_{\beta^+:EC}$
0.6	$0.00839^{+0.00163}_{-0.0018}$	$2.52^{+0.38}_{-0.37}$e-7	$0.10703^{-0.00163}_{+0.00179}$	$2.87^{+0.12}_{-0.12}$e-6
0.8	$0.02543^{+0.00164}_{-0.00181}$	$3.60^{+0.50}_{-0.48}$e-7	$0.12344^{-0.00164}_{+0.00181}$	$3.19^{+0.14}_{-0.14}$e-6
0.818	$0.02697^{+0.00163}_{-0.00182}$	$3.71^{+0.50}_{-0.50}$e-7	$0.12491^{-0.00164}_{+0.00181}$	$3.21^{+0.14}_{-0.14}$e-6
1.0	$0.04260^{+0.00165}_{-0.00183}$	$4.89^{+0.63}_{-0.61}$e-7	$0.13972^{-0.00165}_{+0.00183}$	$3.51^{+0.15}_{-0.16}$e-6
1.2	$0.05992^{+0.00167}_{-0.00185}$	$6.41^{+0.78}_{-0.76}$e-7	$0.15585^{-0.00167}_{+0.00185}$	$3.85^{+0.17}_{-0.17}$e-6
	$sNME_{\beta^+}(1)$		$sNME_{\beta^+}(2)$	
0.6	$-0.08301^{+0.00673}_{-0.01127}$	$4.70^{-0.81}_{+1.33}$e-8	$0.01720^{-0.00673}_{+0.01127}$	$5.39^{-2.37}_{+9.37}$e-7
0.8	$-0.07414^{+0.00673}_{-0.01126}$	$4.21^{-0.74}_{+1.24}$e-8	$0.02616^{-0.00673}_{+0.01126}$	$3.81^{-1.58}_{+5.56}$e-7
0.818	$-0.07334^{+0.00673}_{-0.01125}$	$4.17^{-0.73}_{+1.23}$e-8	$0.02697^{-0.00647}_{+0.01123}$	$3.71^{-1.54}_{+5.31}$e-7
1.0	$-0.06524^{+0.00673}_{-0.01126}$	$3.80^{-0.69}_{+1.15}$e-8	$0.03509^{-0.00673}_{+0.01126}$	$2.82^{-1.12}_{+3.61}$e-7
1.2	$-0.05632^{+0.00673}_{-0.01126}$	$3.44^{-0.63}_{+1.07}$e-8	$0.04400^{-0.00673}_{+0.01126}$	$2.17^{-0.82}_{+2.50}$e-7
	$sNME_{CVC} = 0.175$			

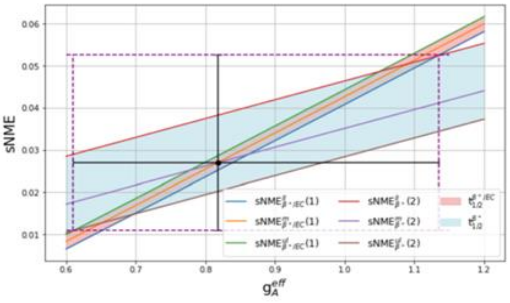

Fig. 3. Experimental mean values and error bands for the half-lives $t^{\beta^+/EC}_{1/2}$ (red) and $t^{\beta^+}_{1/2}$ (blue), and the resulting lower limits (ll), mean values (m) and upper limits (ul) for $sNME_{\beta^+/EC}$ and $sNME_{\beta^+}$. The overlap region defines the physically relevant values of sNME and g_A^{eff}, as indicated by the horizontal and vertical bars centered at the mean values of the involved sNME(1) and sNME(2).

iii. <u>High-precision direct decay energy measurements of the electron-capture decay of ^{97}Tc</u>

A direct, high-precision ground-state–to–ground-state (g.s.–to–g.s.) electron-capture (EC) Q-value measurement of ^{97}Tc $(9/2^+) \rightarrow$ ^{97}Mo $(5/2^+)$ was performed using the PI-ICR technique at the JYFLTRAP Penning-trap mass spectrometer. The measured Q value of 324.82(21) keV improves the precision by a factor of ∼19 compared to previous literature. This measurement also refined the mass excess of ^{97}Tc to –87219.88(26) keV/c^2, a 15-fold improvement over earlier results.

With this precise g.s.–to–g.s. Q value, the candidate transition ^{97}Tc $(9/2^+) \rightarrow$ ^{97}Mo* (320.0 keV) was confirmed to be energetically allowed. Consequently, all possible lines in the EC spectrum of this transition can now be unambiguously characterized at a significance level of at least 2σ. The transition to the 320.0 keV excited state corresponds to a small energy difference of 2.0(1.0) keV between the g.s.–to–excited-state Q $^{*}_{EC}$ and the binding energy of electrons in the allowed L1 shell of the daughter atom. To further verify whether this emitted neutrino energy is indeed ultralow, the excitation energy must be measured with higher precision and accuracy. Additionally, to determine the transition type (allowed or forbidden), spectroscopic measurements of the angular momentum of the final state are required.

Future improvements will employ a highly charged ion Penning trap to refine the g.s.–to–g.s. Q $_{EC}$ to a few eV and cryogenic detectors, such as transition-edge sensors or metallic magnetic calorimeters at low temperatures, to measure the 320.0 keV excitation energy with an uncertainty on the order of tens of eV. This will reduce the Q $^{*}_{EC}$ uncertainty to ≈ tens of eV. Phase-space factor analysis combined with gamma-coincidence measurements will further constrain decay rates, ensuring sensitivity at the sub-eV level, analogous to studies on ^{159}Dy.

The atomic self-consistent many-electron Dirac–Hartree–Fock–Slater method, together with the nuclear shell model, was used to predict partial decay half-lives and energy distributions of g.s.–to–excited-state EC transitions in ^{97}Tc with low Q values. A pseudo-experiment technique was introduced to propagate errors in half-lives and to define the 68% confidence interval for normalized energy distributions. Multiple corrections, including exchange, overlap, shake-up, and shake-off effects, were incorporated in these calculations to accurately model the spectral shape near the endpoint.

TABLE III. Computed half-lives for the EC decay of ^{97}Tc to the excited state (320.0 keV) in ^{97}Mo, with the Q^*_{EC} value shown in Table II. The errors are computed according to the approach presented in Sec. IV A. The used interaction is jj45pnb. LCS denotes lowest captured shell.

LCS	Decay type	Total half-life (10^4yr)	L1 (10^4yr)	L2 (10^7yr)	M1 (10^4yr)	M2 (10^6yr)	N1 (10^5yr)	N2 (10^7yr)	O1 (10^6yr)	
L1	Allowed	$19^{+17}_{-0.7}$	46^{+120}_{-26}	$2.2^{+5.0}_{-1.2}$	47^{+32}_{-17}	26^{+18}_{-10}	20^{+12}_{-7}	13^{+8}_{-4}	42^{+25}_{-15}	
L2	Allowed	93^{+7}_{-6}	–	570^{+4000}_{-340}	169^{+50}_{-34}	91^{+27}_{-18}	60^{+18}_{-12}	38^{+11}_{-8}	127^{+40}_{-25}	
		Total half-life (10^{16}yr)	L1 (10^{23}yr)	L2 (10^{24}yr)	L3 (10^{18}yr)	M1 (10^{21}yr)	M2 (10^{23}yr)	M3 (10^{18}yr)	M4 (10^{21}yr)	M5 (10^{16}yr)
L1	Second UF	$11^{+6.1}_{-3.4}$	$1.0^{+50}_{-0.92}$	$3.1^{+84}_{-2.7}$	$5.3^{+38}_{-4.0}$	$4.4^{+15}_{-3.1}$	$2.3^{+7.2}_{-1.6}$	$2.0^{+3.1}_{-1.1}$	$1.1^{+1.7}_{-0.62}$	$11^{+6.2}_{-3.4}$
L2	Second UF	$33^{+2.5}_{-1.9}$	–	$4.9^{+2326}_{-4.5} \times 10^7$	$4.1^{+21}_{-2.7} \times 10^4$	215^{+59}_{-38}	98^{+26}_{-17}	$24^{+4.0}_{-2.8}$	$12^{+1.9}_{-1.4}$	$35^{+2.6}_{-2.0}$
		Total half-life (10^{21}yr)	L1 (10^{28}yr)	L2 (10^{30}yr)	L3 (10^{24}yr)	M1 (10^{26}yr)	M2 (10^{28}yr)	M3 (10^{23}yr)	M4 (10^{26}yr)	M5 (10^{21}yr)
L1	Fourth NUF	$10^{+10}_{-3.6}$	$5.7^{+1066}_{-5.5}$	$1.4^{+116}_{-1.3}$	$2.6^{+58}_{-2.3}$	$5.0^{+31}_{-4.0}$	$2.5^{+1.4}_{-2.0}$	$2.6^{+8.4}_{-1.8}$	$1.4^{+4.2}_{-0.10}$	$7.2^{+11}_{-3.9}$
L2	Fourth NUF	$74^{+11}_{-8.3}$	–	$6.1^{+25320}_{-5.9} \times 10^9$	$1.9^{+26}_{-1.5} \times 10^6$	900^{+340}_{-210}	380^{+140}_{-87}	110^{+29}_{-19}	$51^{+12}_{-8.4}$	$78^{+12}_{-8.8}$

iv. Half-life and precision shape measurement of the 2νββ decay of ^{130}Te

A new measurement of the two-neutrino double-beta decay (2νββ) half-life of ^{130}Te, $T^{2\nu}_{1/2}$, was performed using the first complete model of the CUORE data, based on a total exposure of 1038 kg·yr. Optimized data selection enabled a twofold improvement in precision, yielding $T^{2\nu}_{1/2} = 9.32 \times 10^{20}$yr. The signal-to-background ratio increased by 70% compared to previous results, allowing the first application of the improved 2νββ formalism to ^{130}Te. Within this framework, we determined a credibility interval for the effective axial coupling g_A^{eff}in the nuclear medium as a function of nuclear matrix elements. Our group was responsible for the theoretical analysis, presenting the first study of the 2νββ spectral shape of ^{130}Te within this improved formalism. Values for higher-order nuclear matrix element ratios were extracted: the second-to-first ratio agrees with nuclear model predictions, while the third-to-first ratio shows deviations from theoretical expectations. These results provide critical tests of nuclear structure models and constitute key inputs for future neutrinoless double-beta decay ($0\nu\beta\beta$) searches.

6. Dissemination and visibility

- ***2025 published/submitted articles/manuscripts:***
  - Z. Ge, T. Eronen, V.A. Sevestrean, M. Ramalho, O. Nitescu, S. Ghinescu, S. Stoica, J. Suhonen, *et al.*, *High-precision direct decay energy measurements of the electron-capture decay of ^{97}Tc*, Physical Review C 112 (2025) 035501.
  - O. Nitescu, F. Simkovic, *Radiative and exchange corrections for two-neutrino double-β decay*, Physical Review C 111 (2025) 035501 (2025).
  - A.S. Barabash, …, O. Nitescu, …, *Double-beta decay of ^{150}Nd to excited levels of 150Sm*, European Physical Journal C 85 2025) 174.
  - A. Agnihotri, J. Suhonen, *Novel way of evaluating g_A quenching in β⁺/EC decays: Introducing the Branching-Ratio Method (BRM)*, Physics Letters B 868 (2025) 139627.
  - D.Q. Adams, …, J. Kotila, O. Nitescu, …, *Half-life and precision shape measurement of the 2νββ decay of ^{130}Te*, Physical Review Letters 135 (2025) 082501 (2025).
  - S. Ghinescu, S. Stoica, *Updated results for kinematic factors in DBD*, arxiv: 2601.1024v2[nucl-th]19Jan.2026 (submitted to European Physical Journal C).
- ***Conference contributions:***
  - "*Matrix Elements for Double-beta Decay Experiments (MEDEX'25)*" event organized by J. Suhonen (Univ. Jyvaskyula & CIFRA), O. Civitarese (Univ. La Plata), and Ivan Stekl (IEAP, CTU in Prague).
  - S. Stoica, S. Ghinescu, O. Nitescu, *Kinematic factors for beta and double-beta decay* (Invited lecture) at Matrix Elements for Double-beta Decay Experiments (MEDEX'25), Prague, Czechia, 23–27 June 2025.

- J. Suhonen, *New probes of rates of neutrinoless double beta decays* (Invited lecture) at Matrix Elements for Double-beta Decay Experiments (MEDEX'25), Prague, Czechia, 23–27 June 2025.
- V.A. Sevestrean, *Theoretical analysis of ^{97}Tc electron capture with applications to neutrino mass studies* (Oral presentation) at Matrix Elements for Double-beta Decay Experiments (MEDEX'25), Prague, Czechia, 23–27 June 2025.

- ***Impact in the scientific community:***
  - More than 100 citations within approximately one year, appearing in high-impact WoS® journals such as Physical Review Letters, Journal of High Energy Physics, Physics Letters B, Journal of Physics G, and Physical Review A, C, and D
  - Our calculations of electron spectra and weak decay rates are required by leading international large experiments for background characterization, calibration of detectors, data analysis and interpretation of the results. The CIFRA research group is currently providing such precise and detailed calculations for international experiments like NEMO3, EXO-2000; nEXO, CUORE, CUPID, MAJORANA, XENON-1t/nt, Lux-Zepelin, PANDA, etc. These experiments were carried out by researchers from leading institutions from around of world.
- ***Project website:*** https://cifra-c2unesco.ro/projects/neutrino-properties-through-use-of-nuclei-neptun/

7. Contact information

- ***Contact person:*** Dr. Sabin Stoica
- ***E-mail*:** sabin.stoica@cifra-c2unesco

Physics of viromimetic particles

1. Project identification

- ***Acronym:*** *–*
- ***Project code / Contract no.:*** *760099 / 2023.05.23*
- ***Funding program / Competition type:*** *National/PNRR-I8*
- ***Funding authority / Sponsor:*** *MCID-DGGCPNRR*
- ***Project duration:*** *36 months (2023.07.01 – 2026.06.30)*
- ***Total budget / CIFRA (branch of NIMP) share:*** *1,417,290.94 € / 1,417,290.94 €*

2. Consortium

- ***Coordinating institution:*** *Centre International de Formation et de Recherche Avancées en Physique – CIFRA, branch of National Institute of Materials Physics, Măgurele, Romania*
- ***Partners institutions:*** *n/a*

3. Project summary

The project seeks to initiate a program of studies in emergent properties of viruses and viromimetic particles. The scientific questions addressed here are of fundamental importance: How do viruses assemble? What physical properties account for their effective targeted delivery and responsivity to chemical and physical cues? How can we harness their unique properties to elicit new function? For instance, to create virus-like particles with laser-like emissive properties. To tackle specific aspects of these questions, we will employ a twin pronged strategy that combines experiments in nanoparticle-directed self-assembly with computational modelling. The proposed work will build a solid foundation for future experimental testbeds for theoretical models. The long-term intent is to create a world-class hub in predictive physical virology at Măgurele, by leveraging local strengths in computational physics.

4. Role of CIFRA (branch of NIMP)

- ***Role in the project:*** *Coordinator*
- ***Main responsibilities:***
  - *Thermodynamics and mechanical pre-stress in nano-particle directed virus shell assembly; testing the hypothesis that mechanical properties of the self-assembled virus shell are reflected in the thermodynamics (and kinetics) of virus shell assembly. This idea will be used to determine the intrinsic radius of curvature and elastic pre-stress at assembly from thermodynamic equilibrium co-assembly reactions of Au NP BMV with BMV coat proteins;*
  - *Modelling phonons and polarons in dye-conjugated virus shells; the question of internal stresses is central to understanding virus stiffness, dynamics, and non-linear responsiveness to chemical cues. It is an important question because it reflects upon virus ability to switch between cargo protection and cargo delivery modes, and might also be crucial, as we shall see below, for hybrid particle photonic properties.*
- ***Key personnel involved:*** *1 principal investigator, 6 senior researchers, 4 junior researchers, 5 PhD students.*

5. Summary of results obtained in 2025

i. The microspectrometer.

One of the objectives was the development of a microfluidic fluorescence detection system. A microspectrometer was developed by combining a spectrograph/cooled CCD, computer, UVLED source (280 nm), temperature-controlled microscope stage, vibration isolation table, optics and mounts in order to monitor the assembling of proteins both in the absence and presence of gold nanoparticles (hereafter referred to as GNPs) (*Fig. 1*). Activities were carried out to optimize the spectroscopic system used for detecting protein fluorescence during assembly. The optical path, consisting of lenses and mirrors with three degrees of freedom, was assembled on an optical table. A 261 nm light source (UV-

FN-261-10 mW, pulse stability <10%, noise <10%, PSU-H-LED power supply, linewidth <0.1 nm, equipped with TC-02-FS heatsink; CNILaser) was tested and positioned so that the excitation beam was precisely focused onto the focal plane of the inverted Cassegrain objective of the RM21 Versa microscope, where the sample holder is mounted.

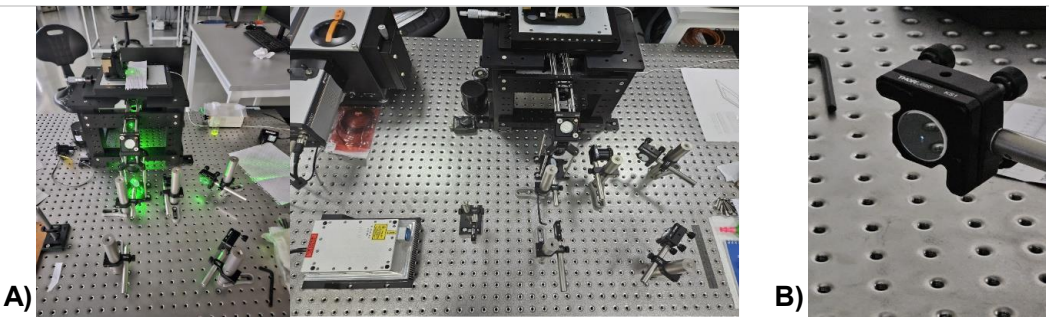

***Figure 1**: (**A**) The optical path from the light source to the microscope. (**B**) Example of a mirror used in the protein detection setup.*

ii. Microfluidics.

The interaction between gold nanoparticles and proteins was evaluated in microchannels with bifurcated and trifurcated geometries. Since particle motion is governed by fluid dynamics, primarily by the velocity distribution and the presence of vortical structures, a coupled simulation framework was developed to extract these quantities from previously performed flow simulations. The imposed inlet flow rates defined the initial conditions, while the numerically computed velocity field subsequently determined particle trajectories. Particles were introduced into separate branches of the microchannels; in the case of the trifurcated geometry, only water was introduced through the central branch. The inlet conditions included the material properties of the two particle types (radius and density). Particle–wall interactions were modeled as elastic collisions, while interparticle interactions were described using a Lennard–Jones potential. Buoyancy effects were included via the Saffman lift model, whereas viscous drag exerted by the fluid was assumed to be negligible. Particle injection into the channels was randomized within the time interval (0–1) s, with three emission events, each consisting of three particles. Particle trajectories were analyzed at different time points (*Fig. 2*) to identify regions with a high probability of interaction.

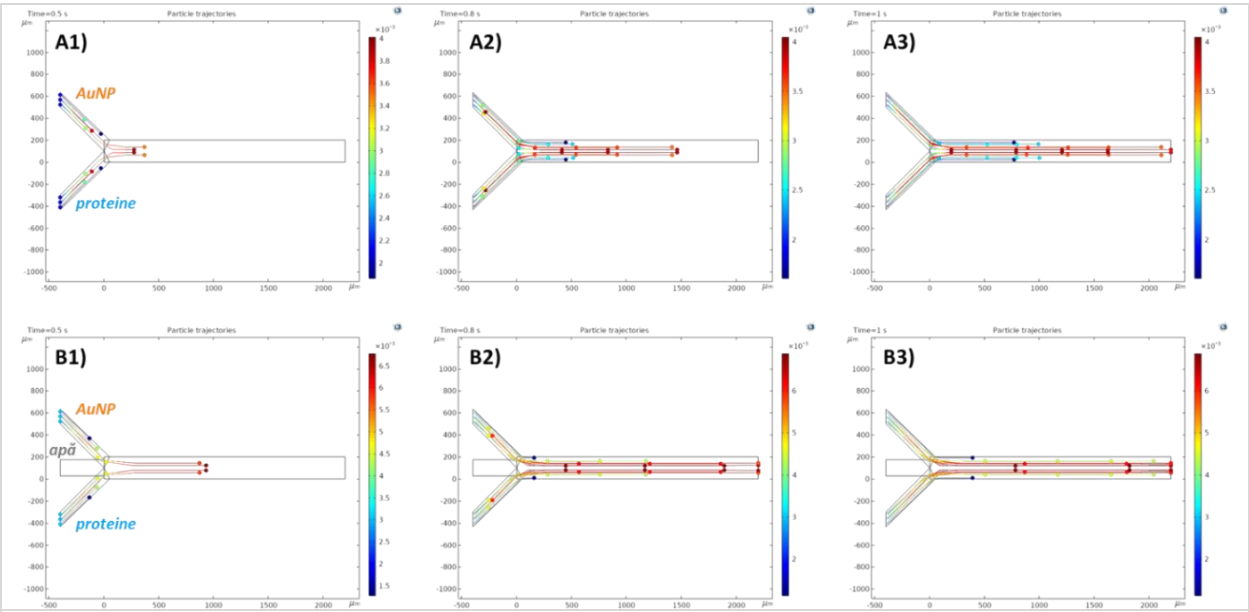

***Figure 2**: Numerical results showing the particle distributions in microchannels with (**A**) bifurcated and (**B**) trifurcated geometries, evaluated after flow times of (**A1, B1**) 0.5 s, (**A2, B2**) 0.8 s, and (**A3, B3**) 1.0 s.*

From experimental point of view, the design of the inlet and outlet ports was also optimized. A strategy for fabricating the microfluidic channels was adopted, based on the use of polymeric threaded

connectors embedded in the PDMS. This design enables the direct insertion of tubing connected to the syringe pump, ensuring improved sealing and mechanical stability.

iii. The viromimetic particles.

The investigation of the the assembly of gold nanoparticles with the BMV protein was carried out through titration experiments using UV–Vis and fluorescence (photoluminescence) spectroscopies (*Fig. 3*). The assembly experiments were performed as a function of the curvature radius of gold nanoparticles. For this investigation an excitation wavelength of 280 nm was employed, and three nanoparticle size categories were selected: 12.1 nm, 16.16 nm, and 20.3 nm. A comparative analysis of the spectra demonstrated that an increase in AuNP size leads to a progressive decrease in emission intensity. This effect can be correlated with the enhancement of non-radiative energy transfer processes and fluorescence quenching, which are more efficient in the presence of larger nanoparticles. In addition, larger nanoparticles exhibit an extended plasmonic resonance and higher effective optical absorption and scattering cross-sections, which promote reabsorption of photons emitted by the protein and consequently reduce the observed fluorescence quantum yield. Overall, these results demonstrate that the fluorescence response of the BMV protein is governed by a complex interplay between protein concentration, gold nanoparticle size, and the chemical environment. This pronounced sensitivity to system parameters confirms the potential of AuNPs as optical signal modulators, relevant for the development of analytical platforms based on controlled fluorescence quenching in protein–nanoparticle systems.

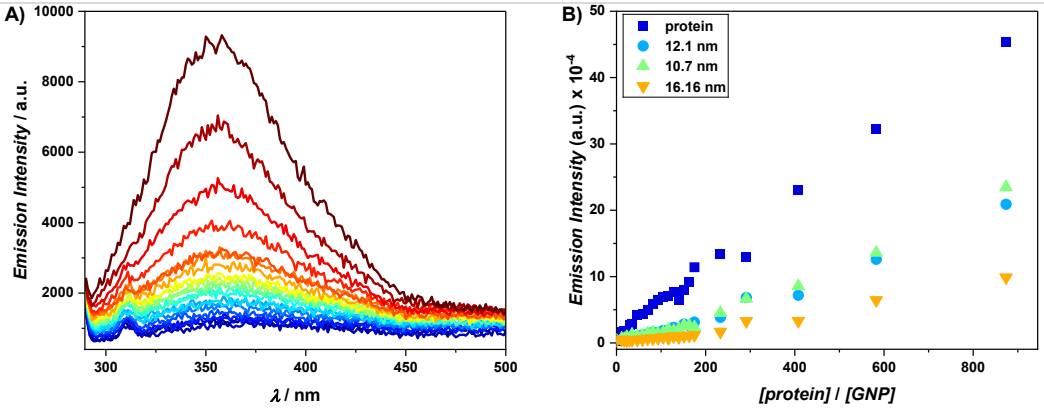

***Figure 3**: (**A**) Emission spectra obtained for different volumes of protein and gold nanoparticles, and (**B**) the emission–concentration dependence for GNP dimensions.*

iv. Molecular simulations.

The objective was to perform Monte Carlo simulations of the interaction between a spherical molecule and a gold surface and to evaluate the corresponding Helmholtz free energy using the LAMMPS simulation package. The developed algorithm estimates the Helmholtz free energy using a histogram-based method that relies on potential energy values recorded during Monte Carlo simulations carried out with LAMMPS. This approach is based on sampling the probability distribution of the observed energy, P(E), as a function of the Monte Carlo steps associated with repositioning the spherical molecule within the simulation box. Brownian dynamics simulations were performed for small, tractable systems in order to demonstrate that the Monte Carlo method yields realistic dynamical behavior (*Fig. 4*). The development of the new model and the associated data processing required considerable effort but provided significant added value. Based on these new results, a manuscript has been resubmitted for evaluation.

Monte Carlo simulations were carried out under various conditions, allowing the identification of optimal parameters for self-assembly as well as the major defects that hinder proper assembly.

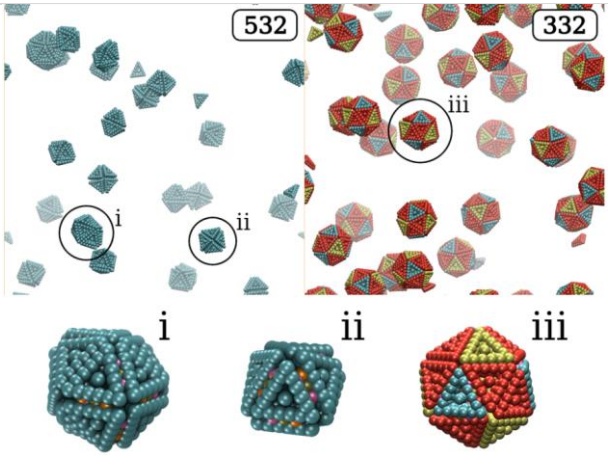

***Figure 4**: A rigid subunit model with Brownian dynamics exhibits the same assembly defects as the Monte Carlo model under realistic conditions in the canonical ensemble.*

6. Dissemination and visibility

- ***2025 published/submitted articles/manuscripts:***
  - C. Ault, C. Simon, I.B. Tsvetkova, P.J. De Pablo, B. Dragnea, *Nanotribology of viruses reveals their adhesion strength and modality of motion on surface*s, Frontiers in Biophysics (2025) 1623880.
  - P. der Schoot, R. Zandi, A. Amjad, B. Dragnea, *Encapsulation of fragmented cargo by virus coat proteins*, Journal of Physical Chemistry 164 (2026) 044906.
- ***Conference contributions:***
  - T. Botond, B. Dragnea, *et al.*, *Magic sizes enable minimal-complexity, high-fidelity assembly of programmable shells* (Oral presentation) at Physical Virology: Across length scales. EMBO/FEBS/Lecture Course and Conference, Sant-Feliu de Guixols, Spain, 01–06 June 2025.
  - D. Botta, V.C. Diculescu, B. Dragnea, *Fabrication and characterization of microfluidic channels for investigating protein-nanoparticle interactions within viromimetic assemblies* (Poster presentation) at Physical Virology: Across length scales. EMBO/FEBS/Lecture Course and Conference, Sant-Feliu de Guixols, Spain, 01–06 June 2025.
  - L. Jinga, A. Aldea, M. Enculescu, V. Diculescu, I. Tsvetkova, B. Dragnea, *Synthesis, assembly and characterization of plasmonic viromimetic nanoparticles* (Poster presentation) at Physical Virology: Across length scales. EMBO/FEBS/Lecture Course and Conference, Sant-Feliu de Guixols, Spain, 01–06 June 2025.
  - I. Tsvetkova, T. Li, B. Dragnea, *Room-temeperature superradiance from a virus supported multi-chromophore antenna* (Poster presentation) at Physical Virology: Across length scales. EMBO/FEBS/Lecture Course and Conference, Sant-Feliu de Guixols, Spain, 01–06 June 2025.
  - T. Botond, B. Dragnea, *et al.*, *Failure modes of icosahedral nanocages upon compression* (Poster presentation) at Physical Virology: Across length scales. EMBO/FEBS/Lecture Course and Conference, Sant-Feliu de Guixols, Spain, 01–06 June 2025.
- ***Project website:*** https://cifra-c2unesco.ro/projects/physics-of-viromimetic-particles/

7. Contact information

- ***Contact person:*** Prof. Bogdan Dragnea
- ***E-mail:*** dragnea@indiana.edu; dragnea@iu.edu

3D magnetic nanostructures for advanced technologies

1. **Project identification**
   - ***Acronym:*** *–*
   - ***Project code / Contract no.:*** *760083/23.05.2023*
   - ***Funding program / Competition type:*** *National/PNRR-I8*
   - ***Funding authority / Sponsor:*** *MCID-DGGCPNRR*
   - ***Project duration:*** *36 months (2022.06.030 – 2026.6.30)*
   - ***Total budget / INCDFM share:*** *1,417,290.34 € / 1,417,290.34 €*

2. **Consortium**
   - ***Coordinating institution:*** *National Institute of Materials Physics, Măgurele, Romania*
   - ***Partners institutions:*** *n/a*

3. **Project summary** (including objectives, estimated results, progress beyond the state-of-the-art)

This project advances research in 3D nanomagnetism by developing and validating cylindrical and pillar-like magnetic nanostructures as building blocks for next-generation spintronic devices, sensors and energy-efficient information technologies. Moving beyond planar (2D) lithographic media, we exploit 3D geometry to unlock complex magnetic textures and domain-wall states (including Bloch-point–type configurations) and to enable novel functionalities without relying on exotic material stacks. We integrate template-assisted electrodeposition and thin-film multilayer growth with micro/nanofabrication (photolithography, ion-beam etching) to produce: (*i*) soft-hard cylindrical nanostructures for spin-valves and nano-oscillators; (*ii*) Ni and CoNi nanowires and nanofibers with tunable anisotropy; and (*iii*) vertically oriented 3D nanopillar arrays. The nanostructures are studied through correlative structural and magnetic characterization (SEM/EDX, TEM/HRTEM/SAED, MFM), magnetoresistance and broadband ferromagnetic resonance, supported by micromagnetic simulations. By the end of 2025, key milestones included optimized complex architectures and their transfer to filamentary/cylindrical geometries, the fabrication of nanopillar matrices nanowires and magnetic nanofibers, and integrated structure-magnetism-dynamics datasets that fuel device-relevant design rules. The outcomes provide a scalable materials-to-device pipeline for future 3D magnetic media and sensor concepts.

4. **Role of INCDFM**
   - ***Role in the project:*** *Coordinator*
   - ***Main responsibilities:***
     - *Synthesis of 3D cylindrical and nanopillar magnetic nanostructures by template-assisted electrodeposition (AAO/track-etched membranes), multilayer thin-film growth (magnetron sputtering) and nanofiber, nanoparticle synthesis and functionalization.*
     - *Modelling of magnetization states and field-driven dynamics in 3D cylindrical nanostructures (nanowires/nanopillars and multilayered spin-valve geometries) by micromagnetic simulations (finite-difference/finite-element approaches) using experimentally measured materials parameters and geometry-accurate meshes to reproduce domain configurations, switching processes, and spin-transport–relevant states.*
     - *Analysis of structure–magnetism–transport correlations in 3D magnetic nanostructures by electron microscopy (SEM/EDX, TEM/HRTEM/SAED), magnetic force microscopy, 3D magnetic imaging, and magneto-transport measurements.*
     - *Fabrication of magnetic nanowires arrays grown in anodic alumina (AAO) templates, vertical magnetic nanopillar matrices, and filamentary/cylindrical multisegment/multilayer spin-valve nanostructures, electroless/electrochemical Ni coating of electrospun polymer nanofiber meshes (nylon 6,6), multilayer magnetron*

sputtering, and photolithography/ion-beam etching for device definition and contacting.

- *Development of integrated 3D nanomagnetic platforms and device-relevant test structures by combining, template-assisted electrodeposition (AAO) of Ni/CoNi nanowires and nanopillars, multilayer spin-valve stack deposition, electrospinning-based fiber scaffolds and lithography/e-beam processing for precise geometry control and electrical contacting.*

- ***Key personnel involved:*** *1 principal investigator, 4 senior researchers, 4 junior researchers, 3 PhD students.*

5. Summary of results obtained in 2025

During 2025 the project consolidated a fabrication–characterization–modelling approach for 3D magnetic nanostructures aimed at the development of cylindrical spintronic elements (nanowires/nanopillars and filamentary multilayer "spin-valve" architectures). The progress shows a clear transition to fully completed work packages, followed by deeper optimization and device-relevant integration. A first major result was the fabrication and validation of multiple classes of cylindrical magnetic nano-objects, including soft–hard ("biphase") cylindrical nanostructures for spin-valves and magnetic nano-oscillators, together with Ni and CoNi nanowires engineered for longitudinal *vs.* perpendicular anisotropy. These structures were iteratively adjusted in geometry/architecture based on the measured magnetic response, with systematic morphology/structure/property feedback.

For CoNi nanowires grown in templates, advanced microstructural and compositional control was reached. TEM observations and electron diffraction indicate a high crystallinity level, including micrometre-scale single-crystalline growth along the wire length, while the wire end can exhibit a nanocrystalline (≈5 nm crystallite) nucleation region that precedes the single-crystal segment. Elemental EDS mapping confirms Co and Ni as the dominant constituents, with an atomic Co/Ni ratio consistent with Co-rich compositions and highlights a non-ideal but practically important feature: oxygen enrichment at the nanowire perimeter, forming an oxide sheath of few nm, relevant for electrical contacting and subsequent current-driven experiments. In parallel with the experimental optimization (including efforts to mitigate surface insulating layers that can hinder robust contacts), geometry-matched micromagnetic simulations (MuMax) were performed in parallel with magnetometry and local magnetic imaging (MFM) to access texture and domain-wall behaviour in truly cylindrical geometries.

A second result thread in 2025 was the development of vertically oriented nanopillar/nanocylinder arrays (*Fig. 1*). Ni nanopillars were fabricated by electrochemical deposition into the pores of anodic aluminium oxide (AAO) membranes, from a Watts-type electrolyte and under controlled potential (optimal value found of −1 V *vs.* reference), with pillar length governed by deposition time and diameter defined by the template pore size. A practically important process improvement should be explicitly noted: pre-wetting/exposing the anodic membrane to the electrolyte for extended time (reported as 2 h) prior to deposition leading to increased pore filling efficiency and to stabile deposition current, supporting reproducibility and scalability of nanopillar arrays. These nanopillar systems were fully characterized and modelled morphology/structure/magnetism, micromagnetic simulations, FMR and magnetoresistance, indicating that the nanopillar platform is being treated as a candidate for device-type test structures rather than only a materials demonstration.

A third major 2025 outcome deals with multilayer "spin-valve" thin-film stacks and their translation toward non-planar/wire like geometries. The results include multilayers of the type $FePt_1/W/FePt_2$ (and exploratory variants using Cu as the spacer), deposited by sputtering and then investigated morpho-structurally by XRD, GIXRD, and TEM, and magnetically by vector MOKE (*Fig. 2*); in selected cases AFM/MFM were also applied. A key technological constraint is described: conventional FePt growth often requires elevated substrate temperature (up to hundreds of °C), which is incompatible with polymeric/resist templates used for lithographically patterning planar wire like structures; therefore, 2025 efforts targeted low-temperature deposition routes (≤100 °C substrate temperature), alternative buffers (*e.g.*, Ti to improve adhesion), and spacer replacement strategies (W→Cu) to preserve the required spin-valve functionality while expanding process compatibility.

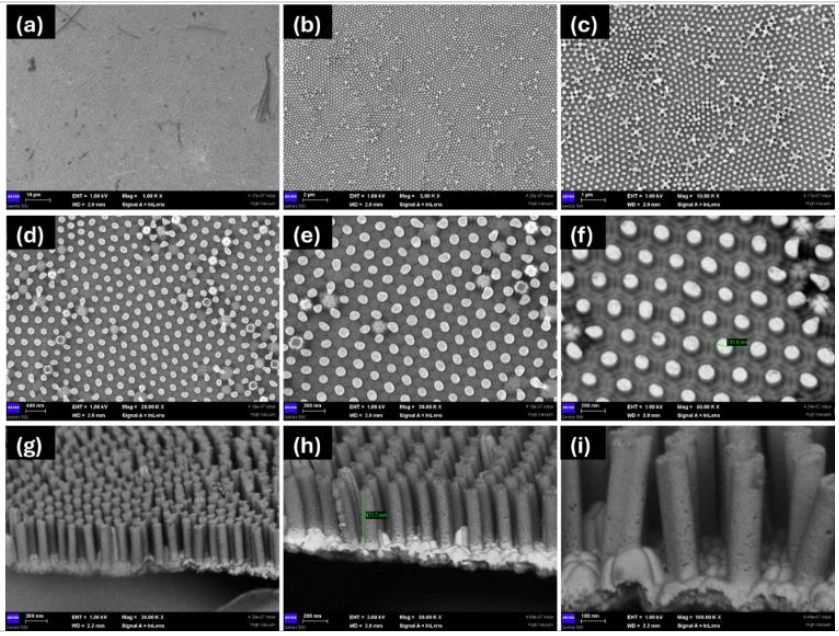

***Figure 1**: Arrays of highly uniform nickel nanorods arrays (**a–f**) top view, (**g–i**) transversal view. Microscopy analysis performed after the sample was transferred on silicon substrates and the anodic alumina template was dissolved.*

These multilayers were not only structurally optimized but also quantified in terms of magnetic properties and dynamical response. Consequently, magnetoresistance measurements will be therefore performed on a PPMS platform in two geometries (field in-plane *vs.* out-of-plane) using a linear four-point configuration; for samples where the magnetic behaviour was additionally modelled analytically in a Stoner–Wohlfarth framework and hysteresis loops were simulated numerically to connect measurements with effective anisotropy and switching mechanisms.

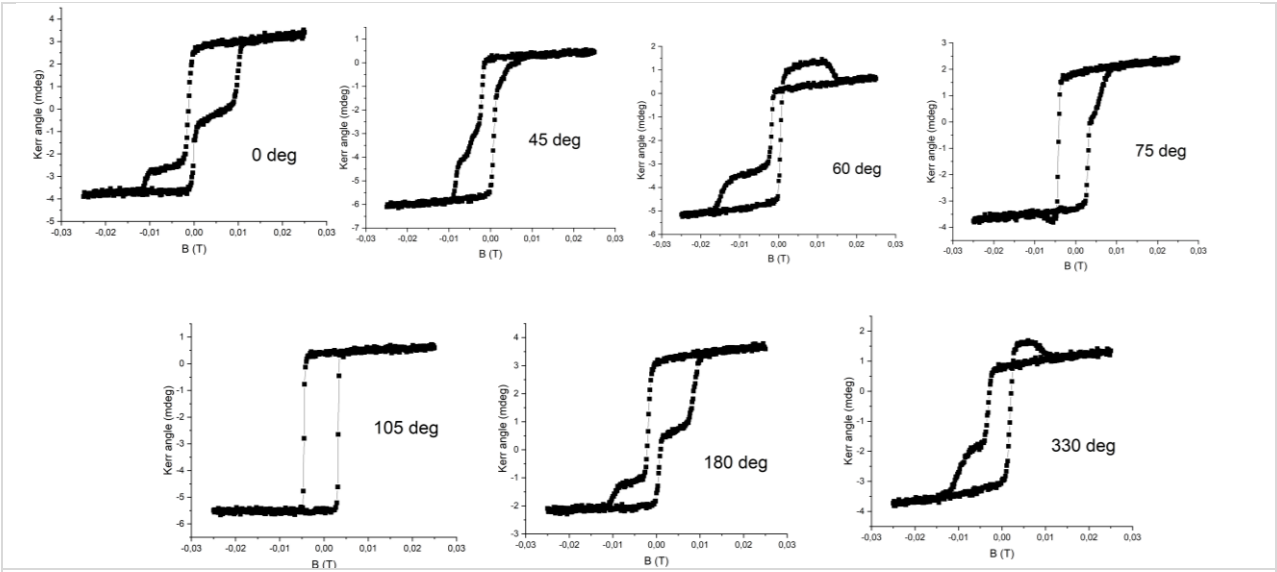

***Figure 2**: MOKE measurements recorded for various directions for a soft/hard magnetic (SM/HM) bilayer spin valve structure with SM Fe grown on a buffer of W_2N and with the HM layer being FePt.*

The project also established a methodology for extracting magnetic anisotropies by ferromagnetic resonance (FMR), including identification of resonant fields and linewidths that differentiate anisotropy contributions between layers. Complementary measurements on orthogonally magnetized spin-valve-type structures (CIP geometry) showed metallic temperature dependence and signatures consistent with progressive spin rotation; importantly for applications, a quasi-linear magnetization response in a narrow field range around zero was highlighted as attractive for sensor concepts.

The optimized multilayer concepts were implemented in filamentary ("filiform") configurations: $FePt_1$/conducting-layer/$FePt_2$ stacks were deposited onto templates patterned and later electrically contacted by lithography, enabling the transition from stack design toward measurable device-like test structures in 3D geometries. This is a nontrivial step because it forces simultaneous control over materials integrity, adhesion, geometry and contact reliability—exactly the bottlenecks that usually stall spintronic demonstrators at the "nice SEM image" stage.

A fourth result expands the materials palette with fibrous, high-surface-area scaffolds. Electrospun nylon 6,6 nanofibre meshes (40–50% optical transmittance) metallized with Ni via an electroless route were fabricated, while deposition temperature and activation/pre-activation/deposition times were systematically varied to improve coating uniformity along fibres. In addition, an electrochemical Ni deposition approach was developed for electrospun meshes: fibres were first metallized with an Au layer (≈150 nm) to serve as a working electrode, transferred to stainless frames to avoid contamination from copper supports, and then plated from a Ni precursor solution (Watts-type composition) under controlled potential/time; SEM/EDX and XRD were used to assess coverage, composition and crystallinity. Finally, the fibre platform was pushed to deep microstructural validation: TEM/HRTEM/STEM, SAED and EDS mapping were performed on FIB-prepared cross-sections extracted from individual metallized fibres, revealing a polymer core (≈60 nm diameter) and two distinct external metal layers with reported thicknesses on the order of ~130 nm and ~150 nm, giving an overall metallized fibre diameter around ~620 nm. The structural detail was needed to link magnetic/transport behaviour to real geometry in fibrous networks.

Beyond these core platforms, chemical synthesis was performed with optimization for cobalt nanostructures, phase/morphology control being linked to reaction temperature and toluene concentration; SEM and XRD evidence includes Co nanostructures with tens-of-nanometres diameters and sub-100-nm lengths as well as micron-scale dendritic morphologies, broadening the library of magnetic nano-building blocks available to the project.

Taken together, in 2025 it was demonstrated an increasingly integrated capability to (*i*) fabricate cylindrical nanowires/nanopillars and fibrous magnetic scaffolds; (*ii*) tailor and verify crystallinity/composition (including oxide-related contacting issues); (*iii*) characterize static and dynamic magnetism (MFM, MOKE, FMR, SQUID) and transport (MR); and (*iv*) connect experiments to modelling (MuMax, Stoner–Wohlfarth + numerical hysteresis).

6. Dissemination and visibility

- ***2025 published/submitted articles/manuscripts:***
  - M. Onea, N. Iacob, G. Schinteie, M.E. Toimil Molares, E. Matei, V. Kuncser, I. Enculescu, *Novel insights into the distinct magnetic configurations of polycrystalline Ni nanowires produced by a template approach at varying electrodeposition potentials*, Journal of Alloys and Compounds 1044 (2025) 183959.
- ***Conference contributions:***
  - R. Grigore, R. Lavric, E. Matei, C. Ghica, L. Nedelcu, V. Kuncser, G. Schinteie, I. Enculescu, *Fabrication and characterization of Ni nanostructures* (Poster presentation) at 22nd International Conference on Nanosciences & Nanotechnologies, Thessaloniki, Greece, 7–12 July 2025.
  - R. Lavric, R. Grigore, E. Matei, V. Kuncser, C. Ghica, L. Nedelcu, G. Schinteie, C. Busuioc, I. Enculescu, *Synthesis and characterization of CoNi alloy nanowires* (Poster presentation) at 22nd International Conference on Nanosciences & Nanotechnologies, Thessaloniki, Greece, 7–12 July 2025.
- ***Project website:*** https://infim.ro/project/3d-magnetic-nanostructures-for-advanced-technologies-nanostructuri-magnetice-3d-pentru-tehnologii-avansate/

7. Contact information

- ***Contact persons:*** Dr. Elena Matei, Dr. Ionuț Enculescu
- ***E-mail:*** elena.matei@infim.ro, encu@infim.ro

Artificial synapses based on ferroelectric tunnel junctions for neuromorphic and analogue computing

1. **Project identification**
   - ***Acronym:*** *ARSYF*
   - ***Project code / Contract no.:*** *760239/28.12.2023*
   - ***Funding program / Competition type:*** *National/PNRR-I8*
   - ***Funding authority / Sponsor:*** *MCID-DGGCPNRR*
   - ***Project duration:*** *30 months (2024.01.01 – 2026.06.30)*
   - ***Total budget / NIMP share:*** *1,206,612.13 € / 1,206,612.13 €*

2. **Consortium**
   - ***Coordinating institution:*** *National Institute of Materials Physics, Măgurele, Romania*
   - ***Partners institutions:*** *n/a*

3. **Project summary** (including objectives, estimated results, progress beyond the state-of-the-art)

Recent studies have estimated that a neuron from the human brain grey matter uses about 2×10^{-9} W, corresponding to an overall brain power consumption of about 20 W. By comparison, a laptop typically consumes around 80 W or more, while a desktop computer can reach power consumptions of up to 175 W. The remarkable ability of the human brain to operate with extremely low power consumption over a wide temperature range has attracted growing interest within the scientific community, particularly in the search for alternatives to conventional binary computing systems. In current computing architectures, energy consumption tends to increase as device dimensions shrink and computational power rises, with a significant fraction of the energy being used for cooling. Consequently, substantial efforts are directed toward mimicking the human brain by developing artificial synapses for neuromorphic and analog computing systems capable of operating with low energy consumption. Among the candidate devices for artificial synapses, the memristor has emerged as a particularly promising solution. A memristor is a two-terminal electrical component that regulates the flow of current in a circuit while retaining memory of the total charge that has previously passed through it. Its key feature is non-volatility, meaning that it preserves its resistance state even in the absence of power. Various material systems have been investigated for memristive applications, including metal oxides, two-dimensional materials, metal–organic frameworks (MOFs), and ferroelectric perovskites.

In this project, a new type of artificial synapse is proposed, namely ferroelectric tunnel junctions (FTJs) based on ferroelectric binary compounds such as $HfZrO_2$ (HZO) or AlScN, combined with a semiconductor bottom electrode to enhance functionality and improve device performance. The underlying concept relies on the modulation of the tunnelling current by ferroelectric polarization, enabling memristive behaviour with synaptic functionality. A major advantage of these materials over alternative systems is their compatibility with silicon technology, facilitating integration into existing semiconductor platforms.

The Principal Investigator builds upon previous collaborations with NIMP in related research areas and will contribute his expertise to the NIMP team, supporting the development of a new research direction within the host institution, which already possesses strong expertise in ferroelectric materials. The ARSYF project is expected to enhance NIMP's international visibility and improve its success rate in EU-funded research calls.

4. **Role of NIMP**
   - ***Role in the project:*** *Coordinator*
   - ***Main responsibilities:***
     - *Synthesis of materials using various thin-film deposition techniques, including pulsed laser deposition (PLD), RF magnetron sputtering, and wet-chemistry methods;*
     - *Modelling of capacitor-like devices;*
     - *Analysis of experimental data;*

- *Fabrication of capacitor-like devices;*
- *Development of memristor devices based on HZO.*

- ***Key personnel involved:*** *1 principal investigator, 7 senior researchers, 4 junior researchers, 2 PhD students.*

5. Summary of results obtained in 2025

i. 7.5 nm-thick $Hf_{0.5}Zr_{0.5}O_2$ (HZO) thin films were investigated. The films were deposited on Si/TiN substrates using low-temperature pulsed laser deposition (PLD), followed by rapid thermal annealing (RTA). Notably, the as-grown film at 400 °C already exhibits a stabilized orthorhombic phase and strong ferroelectricity, achieving a remnant polarization (P_r) of 12.5 μC/cm^2 at an applied field of 1.9 MV/cm (*Fig. 1*). In contrast, RTA at 600 °C induces a transition to the monoclinic phase and reduces overall crystallinity. Compared to atomic layer and chemical solution deposition methods, PLD enables superior crystallinity and phase control. Our results highlight that low-temperature PLD facilitates orthorhombic phase stabilization via kinetic control of oxygen vacancies, eliminating the need for high-temperature annealing or wake-up cycling to achieve robust ferroelectric behaviour.

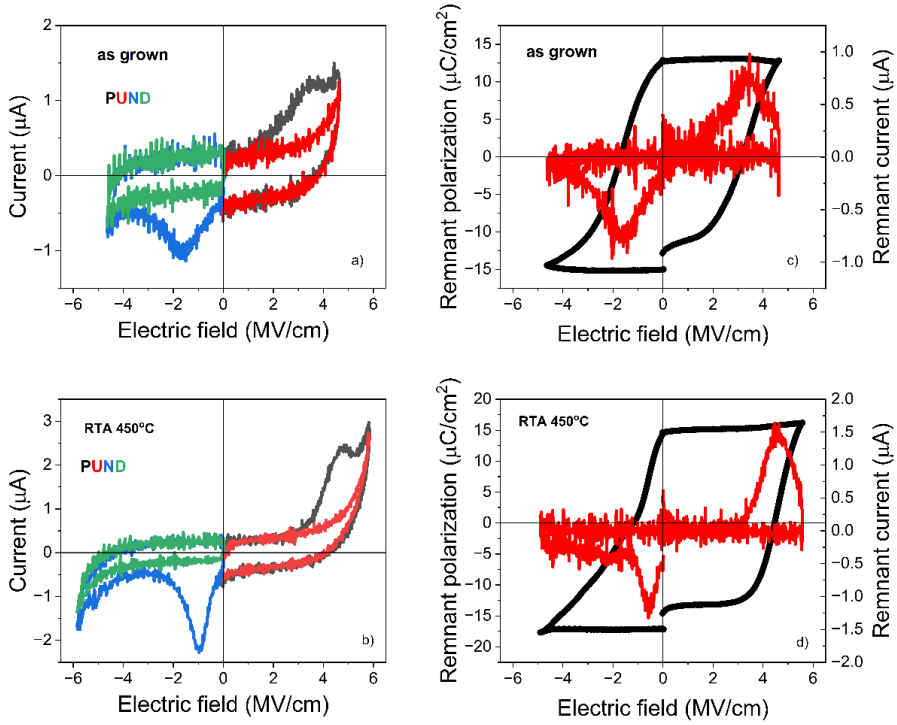

Figure 1*: The current-voltage characteristics determined by PUND pulse sequence (left-side column). Remnant polarization for the as-grown and 450 °C RTA structures (right-side column).*

ii. Nano-crystalline HfO_2 and $(Hf,Zr)O_2$ thin films were synthesized *via* direct liquid injection atomic layer deposition and a comprehensive set of structural, chemical, and electrical characterizations was employed to elucidate their phase composition and functional behaviour. X-ray photoelectron spectroscopy revealed a compositional contrast between the films: $(Hf,Zr)O_2$ layers contained up to 45% stoichiometric oxide, while pure HfO_2 films were dominated by sub-oxides – especially under strongly reducing conditions, in which exclusively sub-oxide phases and p-type semiconducting behaviour was revealed. Electrical measurements indicated room-temperature stabilization of polar phases and a clear tetragonal-to-orthorhombic phase transition with a Curie temperature near 200 K. FTIR spectroscopy confirmed the presence of tetragonal and orthorhombic HfO_2 phases (both polar and antipolar), providing insight into diffraction features observed around 30° (2θ) in GIXRD patterns. Notably, devices incorporating an AlN interlayer demonstrated a significant enhancement – up to 70% – in pyroelectric performance compared to those using SiO_2 alone, as consequence of AlN polar nature and its capability to induce more oxygen vacancies in hafnia (*Fig. 2*).

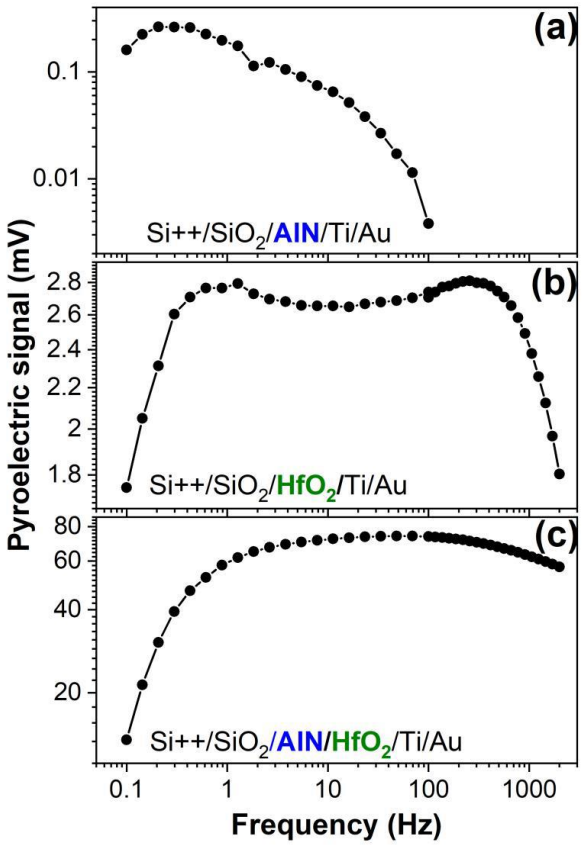

***Figure 2**: The frequency dependence of the pyroelectric signal for (**a**) Si⁺⁺/SiO₂/AlN; (**b**) Si⁺⁺/SiO₂/HfO₂-2.2; and (**c**) Si⁺⁺/SiO²/AlN/HfO²-2.2 devices.*

iii. W/$Hf_{0.5}Zr_{0.5}O2$/p-Ge capacitors were investigated, with top electrode sizes ranging from 10 µm down to 0.1 µm lateral dimensions using conductive atomic force microscopy (C-AFM). Frequency-dependent measurements reveal that peak switching currents increase with sweep rate, yet the total switched charge remains nearly constant, demonstrating full polarization reversal in micro- and submicron devices. PUND analysis further isolates the genuine switching current, allowing reconstruction of polarization–voltage (P–V) loops and quantification of remnant polarization (*Fig. 3*). Interestingly, the smallest devices (0.01 μm^2) exhibit switching currents below the detection threshold due to parasitic capacitance, masking intrinsic ferroelectric behaviour. In contrast, submicron capacitors display an enhanced apparent polarization arising from the larger perimeter-to-area ratio, emphasizing the role of edge-dominated switching. Together, these findings establish C-AFM as a powerful, spatially resolved technique for probing ferroelectric switching in realistic device geometries, providing essential insights for non-volatile memory and neuromorphic applications.

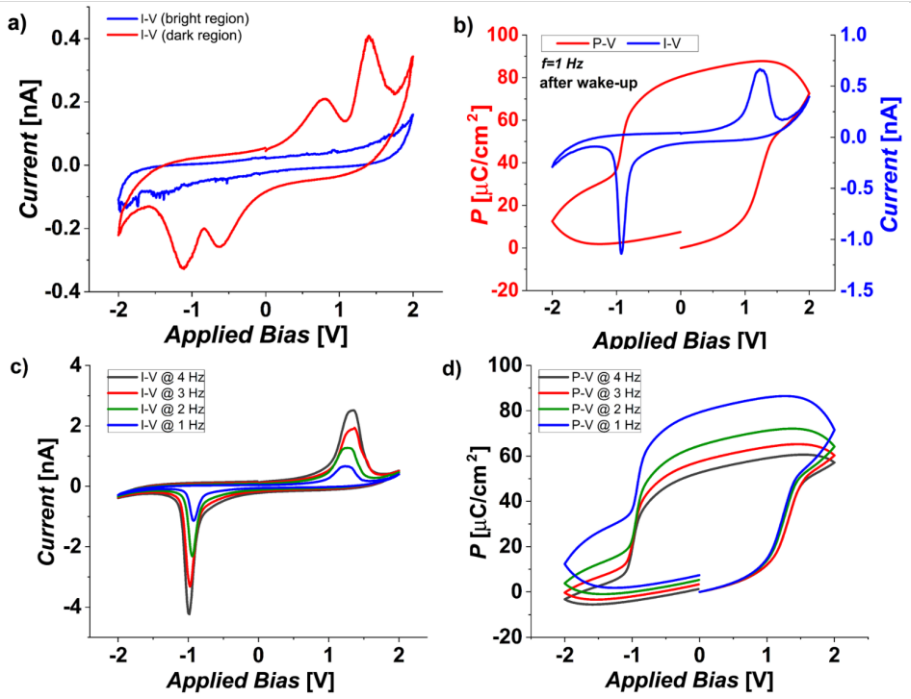

***Figure 3**: (**a**) I–V characteristics measured by C-AFM at two specific locations with different conductivities: the red curve corresponds to the higher conductivity region, while the blue curve represents the lower conductivity region; (**b**) The P–V hysteresis loop (red curve) and the I–V characteristic (blue curve) measured after the wake-up process in region with enhanced current response; (**c**) The I–V characteristics; and (**d**) P–V hysteresis loops measured in higher conductivity region at 1, 2, 3 and 4 Hz after the wake-up process.*

6. Dissemination and visibility

- ***2025 published/submitted articles/manuscripts:***
  - C.F. Chirilă, G.A. Boni, D.G. Popescu, C.M. Istrate, M.A. Husanu, L.D. Filip, C. Beşleagă, L. Pintilie, A. Dimoulas, *Ferroelectric $Hf_{0.5}Zr_{0.5}O_2$ thin films on TiN/Si substrates grown by pulsed laser deposition at CMOS-compatible temperatures*, Ceramics International 51 (2025) 50941–50950.
  - G.A. Boni, P. Tsipas, D. Popescu, C. Radu, S. Laafar, L. Pintilie, A. Dimoulas, *Tailoring polarization and dielectric properties in HZO multilayers: Electrostatic effects vs. structural instabilities*, Journal of Alloys and Compounds 1044 (2025) 184617.
- ***Conference contributions:***
  - C. Istrate, *Transmission electron microscopy studies of ferroelectric AlScN thin films deposited on different substrates* (Poster presentation) at 6th Quantitative Electron Microscopy Conference (QEM 2025), Port-Bacares, France, 11–23 May 2025.
  - C. Chirilă, *Stabilizing orthorhombic $Hf_{0.5}Zr_{0.5}O_2$ thin films on TiN/Si substrates via low-temperature pulsed laser deposition* (Oral presentation) at EMRS Spring Meeting 2025, Strasbourg, France, 26–31 May 2025.
  - G.A. Boni, *Steady-state negative capacitance in ferroelectric bilayer thin film structures* (Oral presentation) at EMRS Spring Meeting 2025, Strasbourg, France, 26–31 May 2025.
  - G.A. Boni, *Development of ferroelectric-based multilayer thin-film structures for advanced applications* (Oral presentation) at Materials Today Conference, Sitges, Spain, 22–27 June 2025.
  - L.M. Bălescu, *Sputtering of wurtzite III-V materials for ferroelectric component in heterostructures* (Poster presentation) at EMRS Spring Meeting 2025, Strasbourg, France, 26–31 May 2025.
- ***Others (e.g., awards/distinctions; outreach activities; theses; media coverage/press releases, etc.):***

- C. Istrate, *Structural and spectroscopic information in nanostructured materials* (completed), PhD thesis, Doctoral School of Physics, University of Bucharest, Bucharest, Romania, 2025.

- ***Project website:*** https://infim.ro/project/sinapse-artificiale-bazate-pe-jonctiuni-tunel-feroelectrice-pentru-calcul-neuromorfic-si-analog-artificial-synapses-based-on-ferroelectric-tunnel-junctions-for-neuromorphic-and-analogue-computing-ar/

7. Contact information

- ***Contact person:*** Dr. Lucian Pintilie
- ***E-mail:*** pintilie@infim.ro

Implementation of novel terahertz spintronic technologies for next generation nanodevices and THz broadband communications

1. Project identification

- ***Acronym:*** *–*
- ***Project code / Contract no.:*** *760085/23.05.2023*
- ***Funding program / Competition type:*** *National/PNRR-I8*
- ***Funding authority / Sponsor:*** *MCID-DGGCPNRR*
- ***Project duration:*** *36 months (2023.07.01 – 2026.06.30)*
- ***Total budget / NIMP share:*** *1,417,277.79 € / 1,417,277.79 €*

2. Consortium

- ***Coordinating institution:*** *National Institute of Materials Physics, Măgurele, Romania*
- ***Partners institutions:*** *n/a*

3. Project summary (including objectives, estimated results, progress beyond the state-of-the-art)

The purpose of the present project is to develop a new direction of THz spintronics within the host institution by building up onto existing strong foundations in the magnetism of nanostructures spintronic technologies. Based on the Principal Investigator's extended expertise in the field of terahertz emission, combined with the host institution highly developed skills in developing multilayered magnetic heterostructures and nanomagnet-logic integrated platforms, it has been foreseen a unique opportunity to go beyond these findings and complementary develop a multipurpose terahertz spintronic technology as well as demonstrators of multilayer structures capable of emitting tuneable terahertz radiation. This technology will serve as a future well-established field of research for the host institution, enabling its role as a major actor in this domain. By implementing this technology, we foresee good perspectives for potential submission of joint proposal under Horizon Europe, growing potential for developing further competencies for young researchers as well as building blocks for other spintronic technologies in the field of random-access memories, non-destructive testing and other promising new applications in 5G communications.

4. Role of NIMP

- ***Role in the project:*** *Coordinator*
- ***Main responsibilities:***
  - *Synthesis of magnetic heterostructures made of ferromagnetic (FM) and non-magnetic (NM) layers;*
  - *Structural and magnetic characterization of the magnetic heterostructures;*
  - *Spin excitation and detection of THz radiation emission in FM/NM heterostructures;*
  - *Demonstration of optimized optically driven spintronic THz emitter and development of spin-based modulation algorithms for potential applications in communication devices.*
- ***Key personnel involved:*** *2 principal investigators, 2 senior researchers, 4 junior researchers.*

5. Summary of results obtained in 2025

The study of ultrafast electron spin dynamics and the spin-dependent parameters governing the spin Hall effect (SHE) and the inverse spin Hall effect (ISHE) on ultrafast timescales is an emerging research topic in spintronics, with the potential to impact various fields beyond physics. One notable example is spintronic terahertz (THz) structures, where ultrafast spin dynamics intersect with optics, photonics, and the THz community. This novel class of THz sources is based on ultrafast spin dynamics, spin currents, and spin Hall effects. Spintronic THz emitters (STEs) represent a new class of THz radiation sources, consisting of a ferromagnetic (FM) layer and a non-magnetic (NM) layer, typically a metal with

strong spin-orbit coupling and thus a large spin Hall angle. THz radiation in spintronic emitters originates from ultrafast spin transport phenomena induced when an FM/NM heterostructure is illuminated by femtosecond (fs) laser pulses (*Fig. 1*). The pulse excites a spin-polarized current in the FM layer, which is subsequently injected into the NM layer. There, it can be converted into a transverse charge current via the relativistic ISHE. This ultrafast transient charge current generates thus THz radiation. STEs hold great potential for next generation THz technologies, offering high field strengths, spatiotemporal modulation of the THz beam and an exceptionally broad spectrum extending up to 30 THz. Various materials and layer combinations have been explored as potential STEs. Current knowledge indicates that the most efficient THz sources based on the inverse spin Hall mechanism are FM/NM bilayers and trilayers structured as NM1/FM/NM2. The most prominent choice is the W/CoFeB/Pt heterostructure, where the two NM layers, tungsten (W) and platinum (Pt), exhibit large and opposite spin Hall angles. THz emission from trilayers surpasses that of bilayers, as the emitted waves from NM1 and NM2 layers are in phase and thus interfere constructively. In this stage of the project, we reevaluated the efficiency of trilayer structures. Specifically, we replaced W with tantalum (Ta), which also exhibits a negative spin Hall angle but has been seldomly used in STEs. The highlight of the research activities for this year was the successful exploration of the THz emission efficiency of ultrathin Ta/Fe/Pt trilayers and its correlation with their structural properties, using THz Time-Domain Spectroscopy (THz-TDS) The THz experiments were performed using a standard THz-TDS system, where the trilayers were used as THz emitters. (*Fig. 1*).

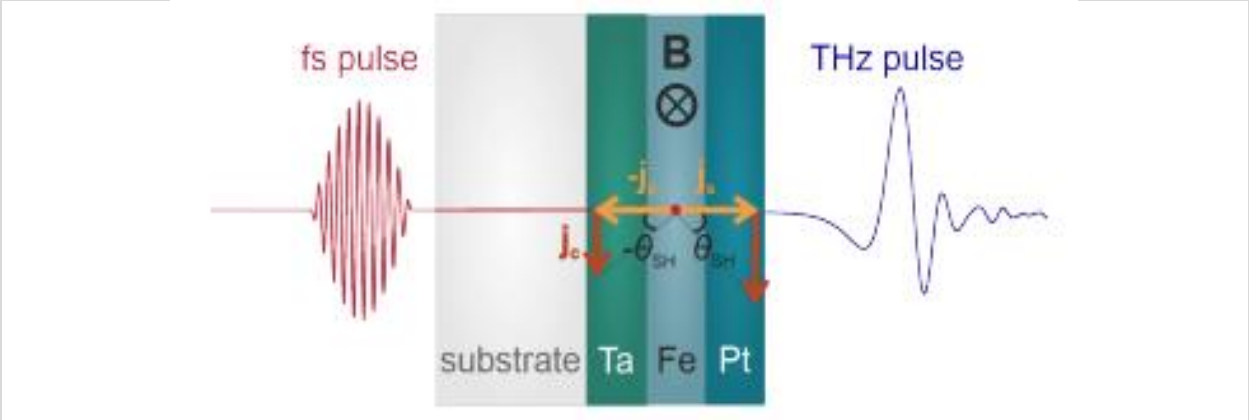

Figure 1*: Schematics of THz emission by optically exciting the trilayer structure with a femtosecond laser pulse, based on the Inverse Spin Hall Effect (ISHE). The FM layer (Fe) is sandwiched between NM1 (Ta) and NM2 (Pt) with opposite spin Hall angles ΘSH.*

In the THz-TDS setup the fs Ti:Sa laser produces optical pulses of 22 fs length at a wavelength of 800 nm with a repetition rate of 75 MHz and a maximum average output power of 1W. The probe beam is used to excite a photoconductive antenna (PCA) with a dipole length of 20 μm that acts as a THz detector. The spintronic emitter is magnetized by a constant external magnetic field of maximum value of 20 mT that was able to saturate the samples. The measurements were performed at room-temperature under dry air conditions. The pump beam was focused on the trilayer from the substrate side and the sample surface was facing the detector. *Fig. 2* presents a comparison of THz emission between Fe (2 nm)/ Pt (1 nm) and Ta (1 nm)/ Fe 2 nm) bilayers, as well as a trilayer Ta (1 nm)/ Fe (2 nm) /Pt (1 nm). Notably, in the Ta/Fe bilayer, the Ta layer is directly grown on the MgO substrate, whereas in the Fe/Pt bilayer, Pt serves as the top layer. The direct deposition of Ta on the substrate ensures the correct growth sequence for trilayer fabrication. To prevent Fe oxidation in Ta/Fe bilayers, a 5 nm MgO capping layer is introduced. Regarding the THz measurement geometry in *Fig. 2*, the incident light pulse impinges first on the substrate while the THz pulse is detected from the sample side. The recorded voltage (y-axis) is proportional to the instantaneous electric field amplitude of the emitted THz wave. The observed pulse represents the THz signal, reflecting the underlying spin and charge carrier dynamics. The THz signal strength is highest in the trilayer configuration, validating the concept we originally proposed, illustrated in *Fig. 1*. While the signal from the Ta/Fe bilayer is lower, it remains comparable to that of the Fe/Pt bilayer, despite reports in the literature indicating a low spin Hall angle for Ta. Similar results

were obtained when reversing the sample orientation with the substrate facing the detector. This confirms that the observed effect is independent of the detection geometry (*Fig. 2*).

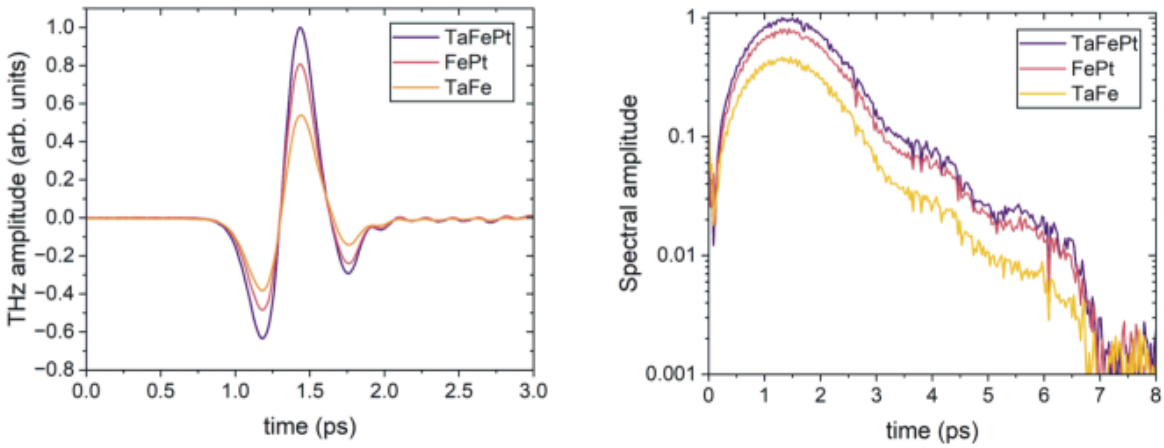

***Figure 2**: THz emission and corresponding bandwidth from Fe (2 nm) / Pt (1 nm) bilayer, Ta (1nm) / Fe (2nm) bilayer and Ta (1 nm) / Fe (2 nm) / Pt (1 nm) trilayer. The trilayer exhibits the highest emission, confirming the advantage of using two NM materials with opposite spin Hall angles.*

To optimize the THz emission of the trilayers, we systematically studied the dependence of the THz amplitude on the thickness of the Pt and Ta layers. All trilayers were grown in the form Ta (t1 nm) /Fe(2 nm)/ Pt (t2 nm) where t1 and t2 were between 1 and 3 nm. The results show important THz signal as a function of the total Ta and Pt t1+ t2. The measured samples include Ta (1 nm) / Fe (2 nm)/ Pt (1 nm), Ta (1.5 nm) / Fe (2 nm) / Pt (1.5 nm), Ta (1.5 nm) / Fe (2 nm)/ Pt (2 nm), Ta (2 nm) / Fe(2 nm)/ Pt (2 nm), Ta (3 nm) / Fe(2 nm)/ Pt (3 nm). The THz signal strength was evaluated using the peak-to-peak amplitude of the THz pulse oscillations. The signal increases starting from Ta (1 nm) / Fe (2 nm)/ Pt (1 nm) and reaches its maximum for Ta (1.5 nm) / Fe (2 nm)/ Pt (2 nm).
In conclusion, during this stage of the project, we have demonstrated high THz emission in several classes of FM/NM magnetic heterostructures, bilayers, and trilayers, containing Ta, Fe, Pt. Of particular importance were the successfully fabricated single-crystalline ultrathin NM1/FM/NM2 trilayers in the form Ta (t1 nm) / Fe (2 nm) / Pt (t2 nm), with t1 and t2 ranging from 1 nm to 3 nm. THz-TDS spectroscopy measurements demonstrate a significant enhancement in THz emission compared to equivalent thickness Fe/Pt and Ta/Fe bilayers. Moreover, the increase in THz signal is highly sensitive to the thicknesses of the Ta and Pt layers, reaching maximum values for Ta+Pt thicknesses of 3–4 nm. Modeling the thickness dependence of THz emission highlights the necessity of introducing effective thicknesses to justify secondary spin current excitations, arising from multiple spin current reflections at the NM/air and NM/FM interfaces, as well as absorption during diffusion within the Ta and Pt layers.

6. Dissemination and visibility

- ***2025 published/submitted articles/manuscripts:***
  - B. Das-Mohapatra, R. Rouzegar, E.Th. Papaioannou, T. Kampfrath, G. Schmidt, *Controlling charge dynamics in nanopatterned spintronic terahertz emitters*, Physical Review Applied 23 (2025) 014024.
  - E.Th. Papaioannou, L. Scheuer, G. Torosyan, G.P. Dimitrakopouls, S. Kret, A.D. Crisan, O. Crisan, R. Beigang, T. Kehagias, *Enhanced Thz emission from ultrathin Ta/Fe/Pt spintronic trilayers*, Advanced Optical Materials 13 (2025) e00874.
  - C. Locovei, G. Torosyan, E.Th. Papaioannou, A.D. Crisan, R. Beigang, O. Crisan, Structural, *Magnetic and THz emission properties of ultrathin Fe/L10-FePt/Pt heterostructures*, Nanomaterials 14 (2025) 1099.
- ***Conference contributions:***
  - O. Crisan, A.D. Crisan, E.Th. Papaioannou, *Enhanced THz emission in magnetic hybrid nanostructures with L10 interfacial FePt layer* (Oral presentation) at the 16th Joint

Magnetism and Magnetic Materials – Intermag Conference, New Orleans, USA, 13–17 January 2025.

- E.Th. Papaioannou, *Enhanced spin-to-charge conversion at graded ferromagnetic/ /non-magnetic interfaces* (Oral presentation) at the 12th International Symposium on Ultrafast Dynamics and Ultrafast Bandgap Photonics, Crete, Greece, 11–18 June 2025.

- ***Project website:*** https://infim.ro/project/implementarea-de-noi-tehnologii-terahertz-spintronice-pentru-nanostructuri-emisive-de-generatie-urmatoare-si-telecomunicatii-in-banda-larga/

7. Contact information

- ***Contact person:*** Dr. Ovidiu Crișan
- ***E-mail:*** ovidiu.crisan@infim.ro

Composite materials for the applications in the water management field

1. **Project identification**
   - ***Acronym:*** *CMAWMF*
   - ***Project code / Contract no.:*** *760270/26.03.2024*
   - ***Funding program / Competition type:*** *National/PNRR-I8*
   - ***Funding authority / Sponsor:*** *MCID-DGGCPNRR*
   - ***Project duration:*** *27 months (2024.03.26 – 2026.06.31)*
   - ***Total budget / NIMP share:*** *1,214,820.68 € / 1,214,820.68 €*

2. **Consortium**
   - ***Coordinating institution:*** *National Institute of Materials Physics, Măgurele, Romania*
   - ***Partners institutions:*** *n/a*

3. **Project summary** (including objectives, estimated results, progress beyond the state-of-the-art)

This project aims to develop a technology to manufacture a filtration device for the treatment of contaminated water with a high pollutant (P) decontamination efficiency. The strategy addressed aims at preparing membranes (MEMs) by the phase inversion process method, which will allow the incorporation of decontamination agents (DA) into the poly(vinyl chloride) (PVC) matrix combined with the deposition of the DA colloidal dispersion on the MEM surface by aerosol spraying, followed by a fusion process of inorganic nanoparticles achieved by a thermal treatment to increase the adhesion of the nanoparticles to the PVC MEM. The expected impact of this project and the potential benefits are: (*i*) the realization of a filtration device based on a set of MEMs, which successively removes organic compounds, various anions and heavy metals ions; (*ii*) the preparation of new optical sensors using surface enhanced Raman scattering (SERS) as analytical technique for monitoring of the Ps concentration in wastewaters; (*iii*) the training of a new generation of young people with expertise in polluted water management; and (iv) the dissemination of results through publication in WoS® Q1 journals and patent applications.

4. **Role of NIMP**
   - ***Role in the project:*** *Coordinator*
   - ***Main responsibilities:***
     - *Preparation of decontamination agents based on TiO_2 and carbon nanoparticles such as carbon nanotubes (CNT), reduced graphene oxide (RGO), and carbon nanohorns (CNH);*
     - *Preparation of polyvinyl chloride membranes modified with decontamination agents and their optimization for pollutant removal;*
     - *Development of SERS supports for monitoring the concentration of pollutants in wastewater.*
   - ***Key personnel involved:*** *1 principal investigator, 7 senior researchers, 4 junior researchers, 4 PhD students.*

5. **Summary of results obtained in 2025**

In 2025, the activity was focused on: (*i*) testing photocatalysts based on TiO_2 and carbon nanoparticles such as carbon nanotubes (SWNT), reduced graphene oxide (RG) and carbon nanohorns (CNH) for the removal of dyes and pharmaceutical compounds; (*ii*) development of membranes based on polyvinyl chloride and photocatalysts for the evaluation of dye pollution and anions such as sulfate, nitrate, *etc.* but also of heavy metal cations; and (*iii*) development of new SERS supports for the monitoring of organic and inorganic pollutants in wastewater.

Among the most important results obtained in 2025, the following can be listed: (*a*) development of photocatalysts based on TiO_2 and single-walled carbon nanotubes separated in semiconductor tubes (S-SWNT) for the removal of the dye rhodamine 6G (*Fig. 1a*); the dye photodegradation efficiencies

reported for these photocatalysts are superior to those for photocatalysts based on TiO_2 and single-walled carbon nanotubes in a mixture of metallic and semiconductor tubes (M+S-SWNT); (*b*) demonstration of the potential of TiO_2 and RGO-based composites as photocatalysts for the removal of the pharmaceutical compound metoclopramide (MET, *Fig. 1b*); (*c*) development of polyvinyl chloride (PVC) membranes modified with photocatalysts based on TiO_2 and single-walled carbon nanotubes whose photodegradation efficiency of the rhodamine G dye reaches approximately 89% (*Fig. 2*, Milestone: MS1); (*d*) development of PVC membranes and carbon nanoparticles functionalized with polyaniline in order to remove inorganic compounds containing nitrate and sulphate anions as well as heavy metal cations such as Pb^{2+} and Cd^{2+} (Milestone: MS2); (*e*) development of active supports in surface enhanced Raman scattering (SERS) based on free PVC films modified with carbon nanostructures decorated with plasmonic nanoparticles for testing the optical response in the case of organic compounds (Milestone: MS3); and (*f*) preparation of SERS supports based on free films of PVC and polyaniline decorated with plasmonic nanoparticles for evaluating the optical response regarding the concentration of inorganic compounds containing nitrate and sulphate anions and heavy metal cations, respectively (Milestone: MS3).

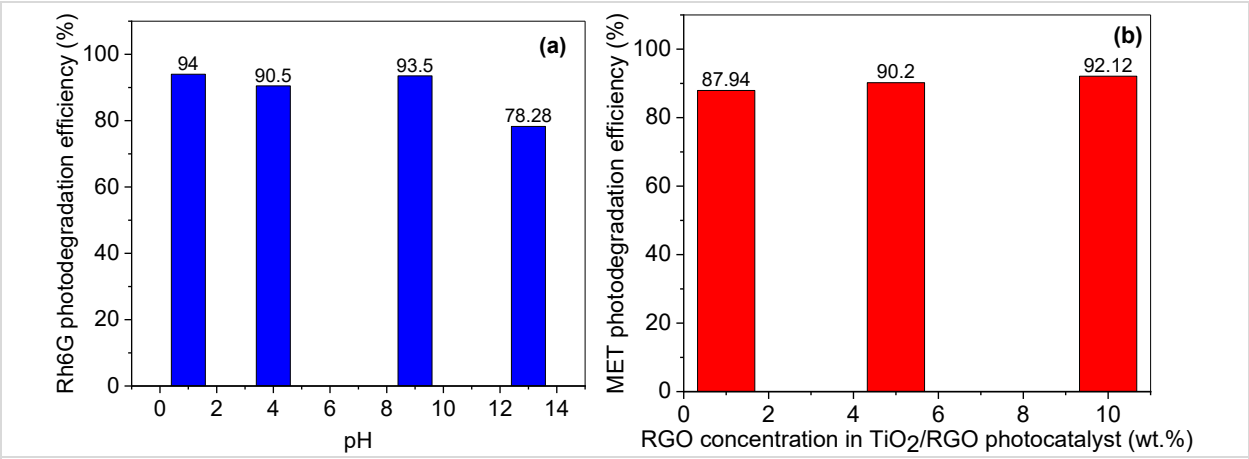

***Figure 1**: (**a**) Dependence of Rh6G photodegradation efficiency on the pH of the Rh6G solution in the presence of the TiO_2/S-SWNT photocatalyst. (**b**) Dependence of the photodegradation efficiency of MET as a function of the RGO concentration in the mass of the TiO_2/RGO photocatalyst.*

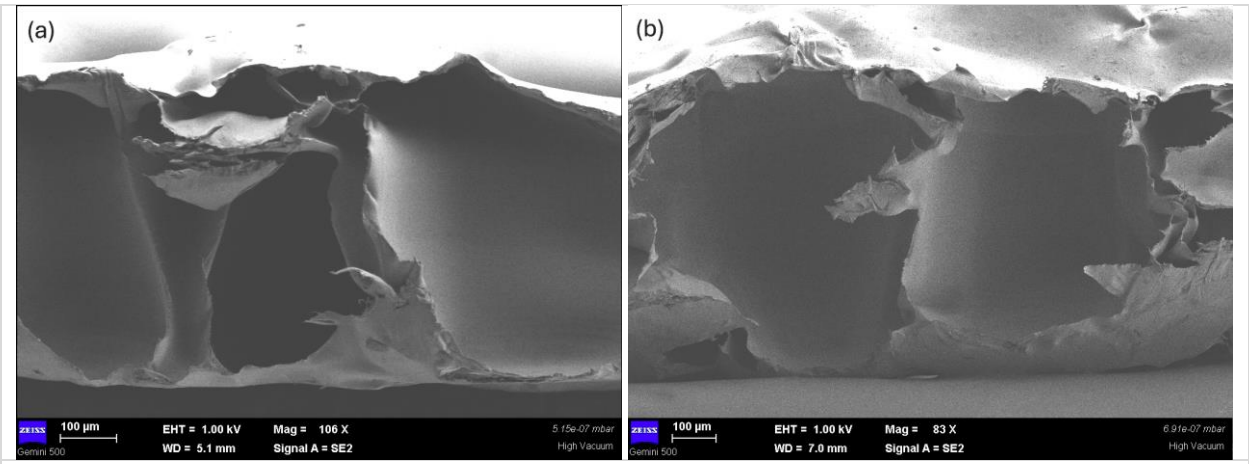

***Figure 2**: Membranes of the (**a**) PVC/TiO_2/S-SWNT and (**b**) PVC/TiO_2/M+S.*

6. Dissemination and visibility

- ***2025 published/submitted articles/manuscripts:***
  - F. Khammar, S. Boukerche, S. Djaber, A. Boublia, A. Messabhia, A. Gharbi, H. Ferkous, C.V. Gomez, S. Bellucci, M. Albrahim, M. Alam, Y. Benguerba, *Synthesis, characterization and photocatalytic efficiency of Mg-doped ZnO nanoparticles for basic Fuchsin dye degradation: Experimental and theoretical insights*, Inorganic Chemistry Communications 176 (2025) 114274.

- R. Cercel, A. Androne, C. Bartha, C. Negrila, M. Baibarac, S. Bellucci, *Photochemical behavior of metoclopramide hydrochloride in the presence of alkaline media and hydrogen peroxide*, Scientific Reports (submitted in 2025, currently under revision).

- ***IPR status – Filed patents/patent applications; prototypes/demonstrators:***
  - I. Smaranda, A. Udrescu, A. Nila, S. Bellucci, M. Baibarac, *Method for preparing composites based on TiO_2 and carbon nanotubes with high efficiency for the photodegradation of the dye rhodamine 6G*, OSIM patent application, No. A00120, 13.05.2025.
  - M. Baibarac, A. Androne, C.S. Florica, *Method for preparing composites based on polyaniline and carbon nanohorns*, OSIM patent application, No. A00276, 30.06.2025.
  - I. Smaranda, T. Burlanescu, S. Florica, A. Androne, M. Baibarac, M. Vaduva, *Method for preparing polyvinyl chloride membranes modified with photocatalysts for use in the adsorption and photodegradation of the dye rhodamine 6G*, EPO patent application, No. 25465574.9, 30.10.2025.
- ***Conference contributions:***
  - A. Androne, T. Burlanescu, I. Smaranda, A. Udrescu, R. Cercel, A. Nila, M. Vaduva, M. Baibarac, *Composite materials for multifunctional applications* (Oral presentation) at the 26th YUCOMAT 2025 Conference, Herceg Novi, Montenegro, 1–5 September 2025.
  - A. Udrescu, A. Androne, S. Florica, I. Smaranda, M. Chivu, A. Nila, M. Baibarac, *Applications of composites based on carbon nanotubes and TiO_2 in photocatalysis* (Oral presentation) at the 6th International Conference on Powder Metallurgy & Advanced Materials, Cluj-Napoca, Romania, 29 October – 1 November 2025.
  - I. Smaranda, A. Udrescu, A. Nila, R. Cercel, A. Androne, M. Baibarac, *Composites based on carbon nanostructures and TiO_2 as photocatalysts for removal of rhodamine 6G* (Poster presentation) at the 6th International Conference on Powder Metallurgy & Advanced Materials, Cluj-Napoca, Romania, 29 October – 1 November 2025.
- ***Others (e.g., awards/distinctions; outreach activities; theses; media coverage/press releases, etc.):***
  - R. Cercel, *Degradation of pharmaceutical compounds and their detection in the presence of optical and/or electrochemical sensors* (ongoing), PhD thesis, University of Bucharest, Romania, expected completion: 2026.
  - T. Burlanescu, *Composites based on reduced graphene oxide, conductive polymer and WS_2 for applications in energy storage and medical sensors* (ongoing), PhD thesis, University of Bucharest, Romania, expected completion: 2026.
  - C.S. Florica, *Composite materials based on conductive polymers and carbon nanostructures for applications in the field of electrochemical supercapacitors* (ongoing), PhD thesis, University of Bucharest, Romania expected completion: 2027.
  - A. Androne, *Composite materials for applications in monitoring and photodegradation of water pollutants* (ongoing), PhD thesis, University of Bucharest, Romania, expected completion: 2028.
- ***Project website:*** https://infim.ro/en/project/composite-materials-for-the-applications-in-the-water-management-field/

7. Contact information

- ***Contact person:*** Prof. Stefano Bellucci
- ***E-mail:*** stefano.bellucci@infim.ro

Radiation damage in Si and SiC based sensors

1. **Project identification**
   - ***Acronym:*** *RADASS*
   - ***Project code / Contract no.:*** *CERN-RO/CDI/2024- 007/26.11.2024*
   - ***Funding program / Competition type:*** *National/CERN-RO*
   - ***Funding authority / Sponsor:*** *IFA/ RD50 - CERN and DRD3-CERN Collaborations*
   - ***Project duration:*** *25 months (2024.11.26 – 2026.12.31)*
   - ***Total budget / NIMP share:*** *329,820 € / 278,655 €*

2. **Consortium**
   - ***Coordinating institution:*** *National Institute of Materials Physics, Măgurele, Romania*
   - ***Partners institutions:***
     - *P1: Horia Hulubei National Institute for R&D in Physics and Nuclear Engineering Măgurele, Romania (R & D partner);*
     - *P2: University of Bucharest, Faculty of Physics, Măgurele, Romania (Academic partner);*
     - *P3: Institute of Space Science – INFLPR Subsidiary, Măgurele, Romania (R & D partner).*

3. **Project summary** (including objectives, estimated results, progress beyond the state-of-the-art)

The project is embedded as part of the research efforts in DRD3 working groups: WG3 – Radiation damage characterization and sensor operation at extreme fluences; WG4 – Simulation; WG6 – Wide Band Gap and innovative sensor materials. It directly maps into the work package WP3 – Sensors for extreme fluences covering the Roadmap DRDT 3.3 on extreme fluence operation and reaches into all four Roadmap DRDTs for solid-state detectors. The goal of the project is to achieve a fundamental scientific understanding of radiation damage in Si and SiC detector materials at low, high, and extreme fluences. It aims to increase the radiation tolerance of various detector types under development within the DRD3-CERN collaboration through defect and material engineering, device engineering and optimization of operational conditions.

Specific objectives: (*O1*) Characterize the radiation damage at the microscopic level in SiC and build up data sets on defect formation; (*O2*) Establish the role of B, C, O and P in the formation of electrically active defects in Si diodes exposed to various irradiation fluences; (*O3*) Model the defects formation, dynamics and metastabilities in irradiated Si and SiC in connection with doping and extrinsic impurities; and (*O4*) Device modelling and parametrization of radiation effects in Si and SiC.

4. **Role of NIMP**
   - ***Role in the project:*** *Coordinator/ WP3 leader in DRD3-CERN Collaboration*
   - ***Main responsibilities:***
     - *Electrical characterization of irradiated samples:*
       - *Detection and characterization of radiation induced defects in Si and SiC by various techniques (DLTS, TSC, TSCap);*
       - *Measure the electrical performance of Si and SiC sensors;*
       - *Resistivity and Hall effect measurements.*
     - *Modelling of defect kinetics and establishing the role of B, C, O and P in the formation of electrically active defects in Si;*
     - *Structural characterization – Investigations by Fourier Transform Infra-Red spectroscopy;*
     - *Evaluation of irradiated electronic devices based on fluence, irradiation type, annealing and develop parametrization models;*
     - *Management and involvement in DRD3 strategic projects: NIMP holds the positions of joint Convener of WG3 (Radiation damage characterization and sensor operation at*

extreme fluences) and Leader of WP3 (Sensors for extreme fluences) in DRD3 Collaboration.

- ***Key personnel involved:*** *1 principal investigator, 6 senior researchers, 2 junior researchers, 1 PhD student.*

5. Summary of results obtained in 2025

With respect to the project objectives outlined above, the progress achieved in 2025 is summarized as follows:

O1. (*a*) Investigations of defects in n type 4H-SiC grown in different conditions (C/Si ratio, Nitrogen flow, growth rate) induced by irradiation with 6 MeV electrons, fluences up to $6 * 10^{14}$ e/cm^2 ; (*b*) thermal stability studies aimed to bring evidence for chemical identity of $Z_{1,2}$ and $EH_{6,7}$ centres; (*c*) As-grown samples provided by DRD3 or by NIMP were also investigated, especially for following the correlation between $Z_{1,2}$ and $EH_{6,7}$ as they both are associated with Carbon Vacancy in 4H-SiC. We have investigated these centres in 4H-SiC grown in both, Carbon rich, and Carbon lean conditions and follow their annealing behaviour. The study aimed to investigate the correlation between the $Z_{1,2}$ and $EH_{6,7}$ centers and their possible assignment to V_C . These experiments revealed that the $Z_{1,2}$ and $EH_{6,7}$ centres do not exhibit the expected good correlation. More specific:

- these centres are sometimes observed even under C-rich growth conditions, where the formation of V_C should be strongly suppressed;
- their thermal stability varies inconsistently in irradiated samples; in some studies, the centres anneal already at relatively low temperatures, although isolated V_C should remain stable up to growth temperatures (~1400 °C);
- $Z_{1,2}$ and $EH_{6,7}$ exhibit imperfect correlation - their concentrations do not maintain the expected 1:1 ratio if they originate from the same defect.

The different behaviour for $Z_{1,2}$ and $EH_{6,7}$ signals can be observed in *Fig. 1*. DLTS measurements showed that the concentration of these defects increases after irradiation; additional, less stable centres also appear but anneal out after heating at 375 K or 750 K. Due to multiple overlapping peaks with close activation energies, the evaluation of individual defect parameters just after performing the irradiation does not provide unique results. Thus, after the final annealing step, when adjacent defects are removed, clearer extraction of activation energies and concentrations becomes possible. Additional, DLTS spectrum simulation provides an even more reliable approach. By using simulated defect levels to estimate concentrations and the $Z_{1,2}$:EH_7 ratio after annealing-out of other radiation induced defects. Such examples of reconstructing the DLTS spectra by simulations are given in *Fig. 2*.

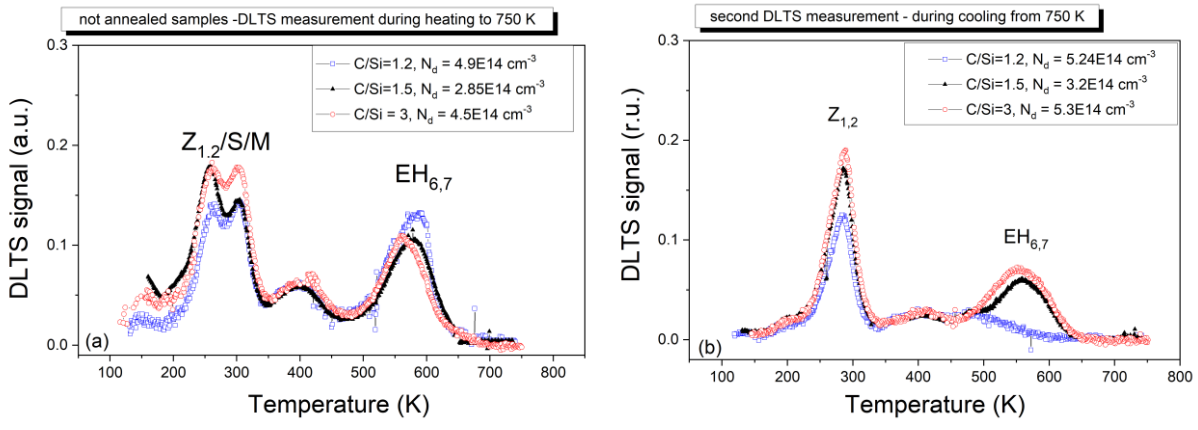

Figure 1*: DLTS spectra obtained on samples grown with different C/Si ratios and having similar level of doping with Nitrogen (Nd) and irradiated with 1.5× $10^{14} e/cm^2$, during : (**a**) the first heating ; (**b**) the first cooling.*

Thus, defect spectroscopies performed on as-grown samples and after irradiation with 6 MeV electrons followed by annealing experiments brought evidence for establishing the nature and introduction rates of radiation induced defects in relation with the growth conditions of 4H-SiC. Especially the generation

of $Z_{1,2}$ and $EH_{6,7}$centers was investigated with respect to the literature controversies concerning the identification of both signals with Carbon Vacancy (V_C). We demonstrate that such identification holds only in some cases and such we conclude that $Z_{1,2}$ and $EH_{6,7}$ signals cannot come from the same defect, namely V_C.

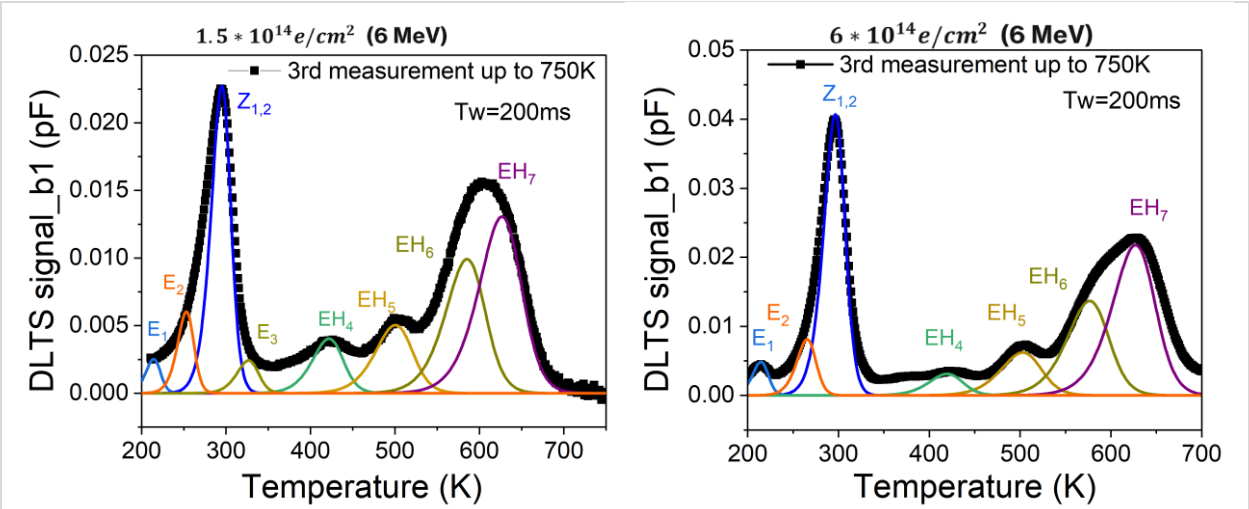

***Figure 2**: Simulation/reconstruction of DLTS Data in irradiated 4H-SiC, different fluences.*

O2. (*a*) Electrical investigations (resistivity, Hall, CV/IV, DLTS) on Si diodes mimicking the gain layer in LGADs (DRD3 project in WP3), fabricated with different flavours of B, C, O and P impurities. These samples, mimicking the gain layer in LGADs were fabricated especially for exploring the high to extreme fluence range in Silicon. The fabrication of such defect engineered samples, has been fully funded by RD50-CERN Collaboration (now part of the DRD3 Collaboration). In 2025 these samples, labelled in the following as GL diodes, were produced, summing up to 19050 diodes. One diode of each flavour has been characterized prior any irradiation, examples in *Fig. 3* for Carbon implantations with doses of 5×10^{12} C/cm^2 and 5×10^{13} C/cm^2, respectively. All the GL diodes present an intrinsic hole trap having and activation energy of 0.27 eV, except for the GL diodes co-implanted with Carbon in the highest dose (5×10^{14} C/cm^2) where very disturbed spectra are recorded. In this latter case the samples do not behave as PiN diodes anymore.

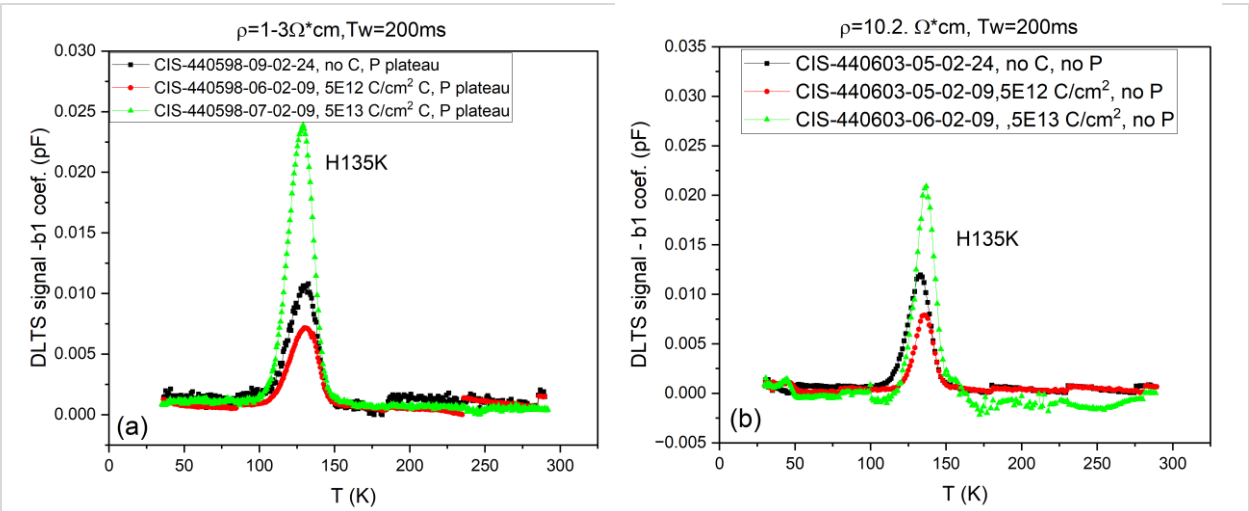

***Figure 3**: DLTS spectra measured on not irradiated GL diodes fabricated on oxygenated Silicon of (**a**) 1–3 Ωcm and (**b**) 10.2 Ωcm resistivities, different levels of carbon and phosphorous implantations.*

(*b*) defect investigations and annealing studies in n type LGADs exposed to local ion beam irradiation with low-penetrating 1.285 MeV Gallium ions, p-type LGADs exposed to low-energy X-ray photons (around 2 keV) and deep-LGADs with and without C-implantation at the request of DRD3 collaborators (CNM Barcelona and PSI). On LGADs, we succeed in correlating the defect investigations with the

observed macroscopic damage. For example, the C implantation induces mid-gap energy level (MGL) responsible for the high leakage current and the slight decrease in the gain layer depletion voltage (*Fig. 4*).

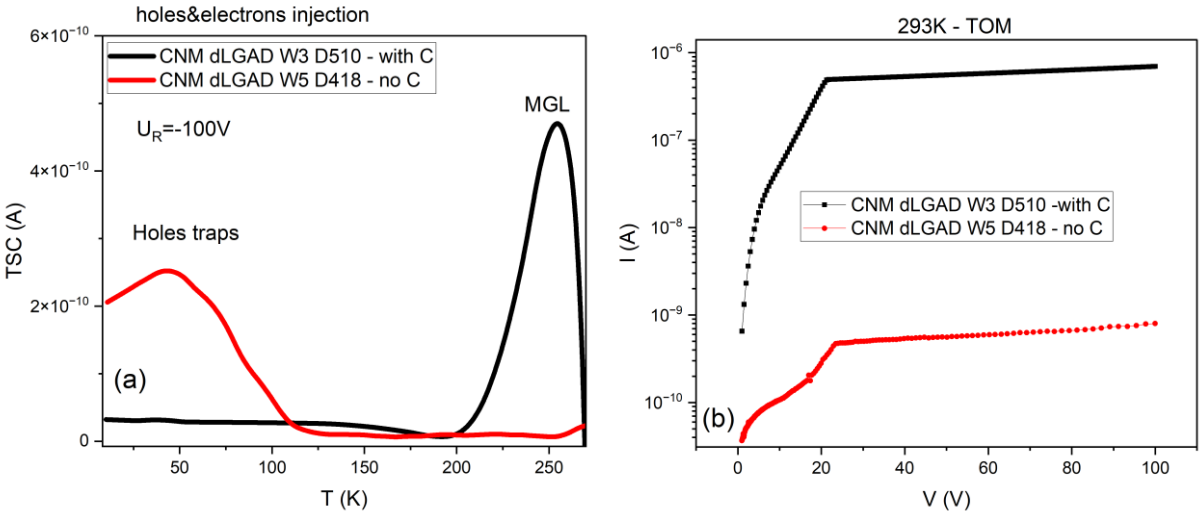

***Figure 4**: Measurements performed on deep LGADs with and without C-implantation: (**a**) TSC spectra revealing some shallow hole traps in non-implanted specimen and a midgap defect level (MGL) present in C-implanted sample; (**b**) Corresponding I–V characteristics of the devices at 293 K.*

(*c*) Elucidation of the chemical nature of X defect in low resistivity p-type Si – a centre with enhanced field emission, tentatively explained through the Poole-Frenkel mechanism. Contrary to the expected impact on the effective doping concentration (N_{eff}) the center proved unharmful. Therefore, in-depth investigations of the emission rate were performed. We demonstrated a phonon-assisted tunnelling mechanism for charge emission from the X defect, pointing out that it does not impact on the device performance. Moreover, the defect' characteristics identify it with the donor state of the singly charged di-vacancy in Silicon, $V_2(+/0)$.

6. Dissemination and visibility

- ***2025 published/submitted articles/manuscripts:***
  - A. Himmerlich *et al.*, including co-authors A. Nitescu and I. Pintilie, *Defects and acceptor removal in 60Co γ-irradiated p-type silicon*, Nuclear Instruments and Methods in Physics Research Section A: Accelerators, Spectrometers, Detectors and Associated Equipment 1081 (2026) 170886.
  - M. Manojlović, A. Crnjac, N. Moffat, J. Villegas, I. Pintilie, E. Cabruja, *Gain response and ion beam-induced donor removal in nLGAD detector: Global gain quenching*, IEEE Sensors Journal 25 (2025) 43985–43996.
  - N.G. Sorgenfrei, Y. Gurimskaya, A. Himmerlich, M. Moll, U. Parzefall, I. Pintilie, J. Schwandt, *On the nature and charge state of the X-Defect, a radiation-induced Silicon defect with field-enhanced charge carrier emission*, Nuclear Instruments and Methods in Physics Research Section A: Accelerators, Spectrometers, Detectors and Associated Equipment 1083 (2026) 171133.
- ***Conference contributions:***
  - C. Besleaga, R.E. Boni, A. Nitescu, N.G. Sorgenfrei, Y. Gurimskaya, F. Rizwan, M. Moll, I. Pintilie, *Characterization of electrically active defects in unirradiated epitaxial 4H-SiC p+-n diodes* (Oral presentation) at the 3rd DRD3 week, Amsterdam, Netherland, 2–6 June 2025.
  - N.G. Sorgenfrei, Y. Gurimskaya, A. Himmerlich, M. Moll, I. Pintilie, J. Schwandt, *Hunting the X-defect* (Oral presentation) at the 3rd DRD3 week, Amsterdam, Netherland, 2–6 June 2025.

- J. Schwandt, I. Pintilie, K.Lauer, M. Moll, *Update on the "Defect engineering in PAD diodes mimicking the gain layer in LGADs" project* (Oral presentation) at the 3rd DRD3 week, Amsterdam, Netherland, 2–6 June 2025.
- N. Filipoiu, M. Cosinschi, C.-A. Pantis-Simut, A.T. Preda, I. Pintilie, G.A. Nemnes, A. Danu, *Investigation of point defects in silicon supercells using density functional theory* (Oral presentation) at the 4th DRD3 week, Geneve, Switzerland, 10–14 November 2025.
- A.G. Boni, A. Nitescu, C. Besleaga, C.D. Geambasu, R.E. Patru, I. Pintilie, *Defect investigation on n-type Schottky diodes based on 4H-SiC before and after irradiation with 5 MeV electrons* (Oral presentation) at the 4th DRD3 week, Geneve, Switzerland, 10–14 November 2025.
- M. Manojlovic, A. Crnjac, N. Moffat, J. Villegas, I. Pintilie, C. Besleaga, A. Nitescu, E. Cabruja, G. Pellegrini Salvador Hidalgo, *Donor removal and Global Gain Quenching (GGQ) in n-type LGAD detector* (Oral presentation) at the 4th DRD3 week, Geneve, Switzerland, 10–14 November 2025.
- N.G. Sorgenfrei, A.R. Altamura, C. Besleaga, A.G. Boni, C.F. Chirila, T. Ceponis, P. Erberk, M. Ferrero, E. Fretwurst, C.D. Geambasu, Y. Gurimskaya, K. Lauer, L. Massaccesi, L. Menzio, M. Moll, M. Mühlnikel, L. Nedelcu, A. Nitescu, R.E. Patru, J. Pavlov, I. Pintilie, F. Rizwan, J. Schwandt, V. Sola, G.E. Stan, *Gain-Layer project* (Oral presentation) at the at the 4th DRD3 week, Geneve, Switzerland, 10–14 November 2025.

- ***Others (e.g., awards/distinctions; outreach activities; theses; media coverage/press releases, etc.):***
  - 13 visits to the DUROCERN Centre;
  - Participation in the "European Researcher Night 2025" in Măgurele (26 September 2025) and Bucharest (27 September 2025);
  - Contribution to organizing the 5th EPS-TIG hands-on session "Frontiers of Quantum Technologies" – satellite event at the 12th Congress of the Balkan Physical Union, 9–12 July 2025;
  - Provided material, device, and scientific support for the 5CBees team applying to "Beamline for Schools" (www.cern.ch/bl4s) with the project "5CB Liquid Crystal Particle Detector." The team was shortlisted among 50 applicants and received a special prize, including a DIY kit to build their own particle detector.
  - A. Niţescu, *Multilayer semiconductor architectures with applications in electronics and sensing* (completed), PhD thesis, University of Bucharest, Romania, thesis defence scheduled for 2026."
- ***Project website:*** https://infim.ro/en/project/radiation-damage-in-si-and-sic-based-sensors-radass/

7. Contact information

- ***Contact person:*** Dr. Ioana Pintilie
- ***E-mail:*** ioana@infim.ro

Romanian participation at EUROfusion WPMAT and complementary research

1. **Project identification**
   - ***Acronym:*** *WPMAT-RO*
   - ***Project code / Contract no.:*** *EURATOM-RO/CDI/2024-2-002*
   - ***Funding program / Competition type:*** *PNCDI IV/5.9/5.9.2/Modul EURATOM-RO + GA101052200*
   - ***Funding authority / Sponsor:*** *MEC*
   - ***Project duration:*** *23 months (2025.02.261 – 2026.12.31)*
   - ***Total budget / INCDFM share:*** *472,400 € / 404,400 €*

2. **Consortium**
   - ***Coordinating institution:*** *National Institute of Materials Physics, Măgurele, Romania*
   - ***Partners institutions:***
     - *P1: Nat. Inst. for Plasma Laser and Radiation Physics (INFLPR) (R & D partner).*

3. **Project summary** (including objectives, estimated results, progress beyond the state-of-the-art)

NIMP's proposed contribution for the Work Package MAT is focused on HHFM processing and characterization. The processing activities encompass the fabrication of materials, such as K-doped W foils, using the already demonstrated FAST-based technology, as well as joining techniques for dissimilar materials, including FAST, diffusion bonding, and brazing methods. With the available equipment, NIMP can support small-scale component manufacturing. In terms of characterization, NIMP can contribute, as demonstrated in previous work, to the assessment of thermo-physical properties (thermal and electrical transport properties, thermal expansion) as well as microstructure investigations using XRD, SEM, HRTEM and various spectroscopic techniques (XRF, XPS, SIMS-TOF, ICP-MS, FTIR, *etc*.). Both joining technologies and materials characterization methods can accommodate also investigations for other tasks, like steels or functional materials. The complementary part aims to develop new materials processing routes and investigation techniques Development of non-destructive investigation of different joint types using X-ray computer micro tomography or micro XRF from INFLPR-Tiseanu partner might provide an additional tool for ND testing for components including dense materials like W. However, due to the high W absorption of X-rays, the specimens investigated until now, in spite of the incremental progress obtained (from sub millimetre to a few millimetres) are still small and usually not relevant for real scale divertor components. Based on the recent results obtained on layered materials containing at least one W part and benefiting from the new developed techniques by INFLPR-Tiseanu group, we aim to further refine these techniques. Moreover, new materials are emerging as promising for fusion applications, *e.g.*, HEAs containing one or several high Z components, whose 3D microstructural characterizations poses increasing challenges. In terms of the materials interactions with energetic particles, we have already collaborated with INFLPR-Ticos group to investigate irradiated surfaces aiming to detect possible elements expelled from inside of composites or deteriorations of joint in multi-material structures. However, the experimental setup could be further improved in two directions: (*i*) expanding the beam to cover a larger area, or (*ii*) focusing the beam to a smaller spot to study the effects on adjacent regions subjected to high thermal stresses, thereby enabling the analysis of local thermal shock effects. In terms of processing and joining technology development, we aim to establish a SPS-based method for embedding interfaces in monoblock-type components. Finally, we plan to enhance our capabilities in producing novel materials, with particular emphasis on HEAs. Many of these HEAs can be fabricated via arc melting and casting, providing a simpler and more scalable production route while also allowing a direct comparison of material properties with those obtained by powder metallurgy techniques, such as mechanical alloying followed by sintering.

4. **Role of INCDFM**
   - ***Role in the project:*** *Coordinator*

- ***Main responsibilities:***
  - *Synthesis of different High Heat Flux (HHF) materials;*
  - *Modelling of thermophysical properties in ITER type divertor armour components;*
  - *Analysis of thermophysical properties of HHF materials produced in EUROfusion WPMAT;*
  - *Fabrication of W-based monoblocks;*
  - *Development of new processing and joining technologies.*
- ***Key personnel involved:*** *1 principal investigator, 3 senior researchers, 2 junior researchers.*

5. Summary of results obtained in 2025

NIMP's contribution to the Work Package MAT is focused on HHFM processing and characterization. In 2025 the processing part covered materials fabrication from K-doped W foils (KdWL) using the already demonstrated FAST-based technology (specimens for HHF, tensile and neutron irradiation tests and also ultrasound calibration specimens with artificial engineered defects) as well as other W materials for IPP-CR and CEA research units. With the available equipment, NIMP can cover laboratory scale component manufacturing. Thus, also a study regarding the processing up-scaling to industrial level was initiated. In terms of characterization NIMP contributed to thermo-physical properties characterization, in 2025 participating in the "W stress relieved" characterization campaign. Also, investigations on KdWL own materials and materials from KIT, SCK, IST and CIEMAT have been performed. Supporting the task MAT-T.03.04-T070, in 2025 new tools have been developed in NIMP in order to improve the quality of the joints produced using our FAST equipment. INFLPR-Tiseanu partner work was focused on the assessment of the quality of the W-Cu composite produced by AM and Cu infiltration using X-ray Microtomography (XCT) as a non-destructive imaging solution for specific challenges like cracking and porosity. The analysis employed a multi-phase strategy, utilizing a 320 kV microfocus X-ray generator for the initial overview scan of relatively large rod samples. INFLPR-Ticos partner work was focused to obtain a very narrow electron beam profile at the ALID accelerator. This would increase the electron density on the surface, and it would subject the materials to a harsher test under radiation.

6. Dissemination and visibility

- ***2025 published/submitted articles/manuscripts:***
  - K. Poleshchuk, D. Terentyev, A. Galatanu, K. Verbeken, *Investigation of neutron irradiated W/CuCrZr joints*, Journal of Nuclear Materials 604 (2025) 155496.
  - A. Iveković, G.K. Muralidharan, A. Galatanu, G. Li, K. Vanmeensel, J. Vleugels, *Liquid-copper infiltration and characterization of additively manufactured W-lattice structures*, Journal of Alloys and Compounds 1011 (2025) 178411.
  - A. Pereira, R. Martins, B. Monteiro, J.B. Correia, A. Galatanu, N. Catarino, P.J. Belec, M. Dias, *Thermal stability and irradiation resistance of (CrFeTiTa)70W30 and VFeTiTaW high entropy alloys*, Materials 18 (2025) 01030.
  - R. De Luca, E. Cacciotti, M. Cerocchi, F. Crea, S. Roccella, H. Greuner, K. Hunger, C. Bonnekoh, A. Galatanu, A. Ivekovic, P. Jenus, M. Wirtz, *Non-destructive ultrasonic inspections of small-scale mock-ups provided with advanced tungsten armours for DEMO divertor target*, Fusion Engineering and Design 215 (2025) 115007.
- ***Conference contributions:***
  - A. Galatanu, M. Galatanu, *Advanced tungsten materials produced in NIMP for divertor armor application in thermo-nuclear fusion reactors* (Poster presentation) at the 23rd International Balkan Workshop on Applied Physics and Materials Science (IBWAP 2025), Constanța, Romania, 9–12 July 2025.

7. Contact information

- ***Contact person:*** Dr. Andrei Galațanu
- ***E-mail:*** gala@infim.ro

Romanian participation at EUROfusion WPPRD and complementary research

1. **Project identification**
   - ***Acronym:*** *WPPRD-RO*
   - ***Project code / Contract no.:*** *EURATOM-RO/CDI/2024-2-001*
   - ***Funding program / Competition type:*** *PNCDI IV/5.9/5.9.2/Modul EURATOM-RO + GA101052200*
   - ***Funding authority / Sponsor:*** *MEC*
   - ***Project duration:*** *23 months (2025.02.261 – 2026.12.31)*
   - ***Total budget / NIMP share:*** *118,430 € / 89,890 €*

2. **Consortium**
   - ***Coordinating institution:*** *National Institute of Materials Physics, Măgurele, Romania*
   - ***Partners institutions:***
     - *P1: Nat. Inst. for Plasma Laser and Radiation Physics (INFLPR) (R & D partner).*

3. **Project summary** (including objectives, estimated results, progress beyond the state-of-the-art)

Activities under Prospective R&D (PRD) are aimed at providing alternative, risk-mitigating, options for DEMO and/or a fusion power plant, targeting the delivery of commercially viable fusion energy. NIMP proposed contribution for the Work Package PRD is focused on HHFM processing and characterization. The processing part covers bulk W-composites with various dispersed powders consolidated using FAST (field assisted sintering technique) and HPS (hot press sintering). Metallic or ceramic nanometric particle dispersions will be included in W, aiming to decrease BDTT of the material and also to increase its fracture toughness. Such dispersions are also expected to increase the recrystallization temperature of the material, thus making it more suited for extended high temperature exposure without a significant degradation of its properties. After an initial fast forward screening of ZrC, diamond, Sic, Cr and Fe, the materials based on ZrC and Cr dispersoids have shown interesting properties. The other have been down-selected. Optimization of the morphology of W-ZrC material has led to a plastic behaviour observed at temperatures as low as 300 °C, while the recrystallization temperature was estimated at more than 1400 °C. Also, after optimization of the grain-size ratio of the Cr/W powders, a uniform dispersion of Cr particles has been observed after the SPS consolidation. Work is in progress to evaluate the thermal stability of such materials. Also work with V is in progress aiming to test the possibility to obtain an in-situ coating of W grains. Other possible dispersoids as HEA or Zr are foreseen for investigations in the present project. The best materials obtained will be further developed and tested in fusion relevant conditions. The complementary part of the project is focussed on testing materials behaviour under severe conditions, closer to that expected in a fusion reactor. IAP has an adequate infrastructure to produce various types of materials and components following the task specifications of the HHFM work group in WPPRD while INFLPR has facilities for sample irradiation using high and low energy electrons beams and also plasma guns.

4. **Role of NIMP**
   - ***Role in the project:*** *Coordinator*
   - ***Main responsibilities:***
     - *Synthesis of different new W-based materials;*
     - *Analysis of thermophysical properties of HHF materials produced in EUROfusion WPPRD.*
   - ***Key personnel involved:*** *1 principal investigator, 1 senior researcher, 2 junior researchers.*

5. Summary of results obtained in 2025

The 2025 work was focused on W-ZrC, W-Cr and W-V composites produced with powders with different W grain sizes and nanometric dispersions. A complicated interdependence between W grain sizes (as produced and after annealing/recrystallization) and the dispersoids size/content is driving the mechanical behaviour of the samples in the case of W-ZrC material.

For the best W-ZrC material a flexural strength up 1.7 GPa is obtained from 300 °C upward which outperforms the pure W material by a factor of 3. From this point of view, our W-ZrC material produced by a powder metallurgy route is one of the top materials considered in the frame of EUROfusion as possible alternative for divertor armour in DEMO. Further test will be performed in the next years.

For W-V material it was demonstrated that the partial coating of W grains by the nm V powder is preserved also after the thermomechanical treatment performed to increase the density.

6 MeV electron irradiation of the W-V specimens showed that the exposed surface is more affected when the V content increases.

6. Dissemination and visibility

- ***Conference contributions:***
  - A. Galatanu, M. Galatanu, *Advanced tungsten materials produced in NIMP for divertor armor application in thermo-nuclear fusion reactors* (Poster presentation) at the 23rd International Balkan Workshop on Applied Physics and Materials Science (IBWAP 2025), Constanța, Romania, 9–12 July 2025.
  - M. Galatanu, M. Enculescu, I. Assahsahi, A. Galatanu, *Morphology and microstructure of advanced Tungsten materials with Cr and V dispersoids intended for nuclear fusion applications* (Oral presentation) at the 23rd International Balkan Workshop on Applied Physics and Materials Science (IBWAP 2025), Constanța, Romania, 9–12 July 2025.
  - M. Galatanu, W. Pantleon, M. Enculescu, M. Grigoroscuta, A. Galatanu, *Tuning thermophysical and mechanical properties of tungsten materials with dispersed nanometric ZrC processed by powder metallurgy route* (Oral presentation) at MRS Fall Meeting 2025, Boston, MA, USA, 29 November – 7 December 2025.

7. Contact information

- ***Contact person:*** Dr. Magdalena Galațanu
- ***E-mail:*** magdalena.galatanu@infim.ro

Quasi-1D materials for advanced thin-film photovoltaics

1. Project identification

- ***Acronym:*** *LightCell*
- ***Project code / Contract no.:*** *19/2024*
- ***Funding program / Competition type:*** *International/ERANET-M-3-ERANET-Light*
- ***Funding authority / Sponsor:*** *Innovation Fund Denmark (DTU and LightNovo), Executive Unit for Financing the Higher Education, Research, Development and Innovation (UEFISCDI, Romania), Estonian Research Council (TALT), Korean Institute for Advancement of Technology (DGIST and Ultech).*
- ***Project duration:*** *29 months (2024.03.15 – 2026.07.31)*
- ***Total budget / NIMP share:*** *2,124,390 € / 200,000 €*

2. Consortium

- ***Coordinating institution:*** *Technical University of Denmark (DTU), Lyngby, Denmark*
- ***Partners institutions:***
  - *P1: LightNovo APS, Birkerød, Denmark (R & D partner and Industrial)*
  - *P2: National Institute of Materials Physics, Măgurele, Romania (R & D partner)*
  - *P4: Tallinn University of Technology, Tallinn, Estonia (R & D partner)*
  - *P5: DGIST, Daegu, South Korea (R & D partner)*
  - *P6: ULTECH, Daegu, South Korea (R & D partner and Industrial)*

3. Project summary (including objectives, estimated results, progress beyond the state-of-the-art)

LightCell aims to demonstrate a new generation of all inorganic, environmentally-friendly and stable, quasi-1D $Sb_2S(Se)_3$ solar cells featuring efficiencies beyond state of the art, providing a green alternative to the commercial CdTe thin-film solar cells. The joint research and innovation activities proposed by LightCell will advance several areas of quasi-1D solar material synthesis, spectroscopy, and thin-film photovoltaics through the following actions:

i. Design of functionalized substrates for quasi-1D growth of solar materials featuring efficient charge transport;

ii. Achieving efficient control over the recombination in quasi-1D $Sb_2S(Se)_3$ by defect engineering;

iii. Development of a new tool for the rapid and non-destructive mapping of 2D and 3D crystallographic orientation of quasi-1D photovoltaic materials;

iv. Implementation of advanced solar device architectures using passivation layers with nano-sized openings for reduced recombination and controlled growth of quasi-1D layers;

v. Demonstration of environmentally-friendly Cd-free $Sb_2S(Se)_3$ solar cells with a power conversion efficiency of up 15% on a lab scale and up to 10% with all industrial processes.

vi. Starting from the technology readiness level (TRL) of 3, it aims to validate new PV technologies in demonstrators of industrial partners targeting building-integrated photovoltaic applications (BIPV), reaching a TRL 5 at the end of the 3-year project.

4. Role of NIMP

- ***Role in the project:*** *Partner; WP leader.*
- ***Main responsibilities:***
  - *New recipes and methods for the synthesis of Sb^2X^3 thin films;*
  - *Characterisation methods employed for the determination of materials' physico-chemical properties;*
  - *Design and fabrication of photovoltaic devices;*
  - *Methodologies and procedures used for electrical assessment of new devices;*
  - *Studies on aging factor for Sb_2X_3-based solar cells.*

- ***Key personnel involved:*** *1 principal investigator, 5 senior researchers, 5 junior researchers, 3 PhD students.*

5. Summary of results obtained in 2025

In 2025, the LightCell project entered Stage 2 of the Work Plan, during which four major activities were undertaken:

- Activity 2.1 – Optimization of deposition conditions for obtaining uniform Sb_2X_3 (X = S and/or Se) thin films on large-area substrates. → 100% Completed: Deposition of Sb_2X_3 (X = S, Se) thin films on large substrates: 10 × 2.5 cm by RF magnetron co-sputtering, and 5 × 5 cm by spin-coating, achieving thickness uniformity of up to ~95% (*Figs. 1 and 2*).
- Activity 2.2 – Determination and correlation of structural, electrical, and optical properties of the obtained Sb_2X_3 (X = S and/or Se) layers. → 100 % Completed: The obtained Sb_2X_3 films were analysed structurally, electrically, and optically, and the results were correlated to optimize the fabrication process. Adjusting the composition toward optimal stoichiometry and identifying electrically active defects using DLTS (Deep Level Transient Spectroscopy) are key steps for achieving high-performance solar cells.

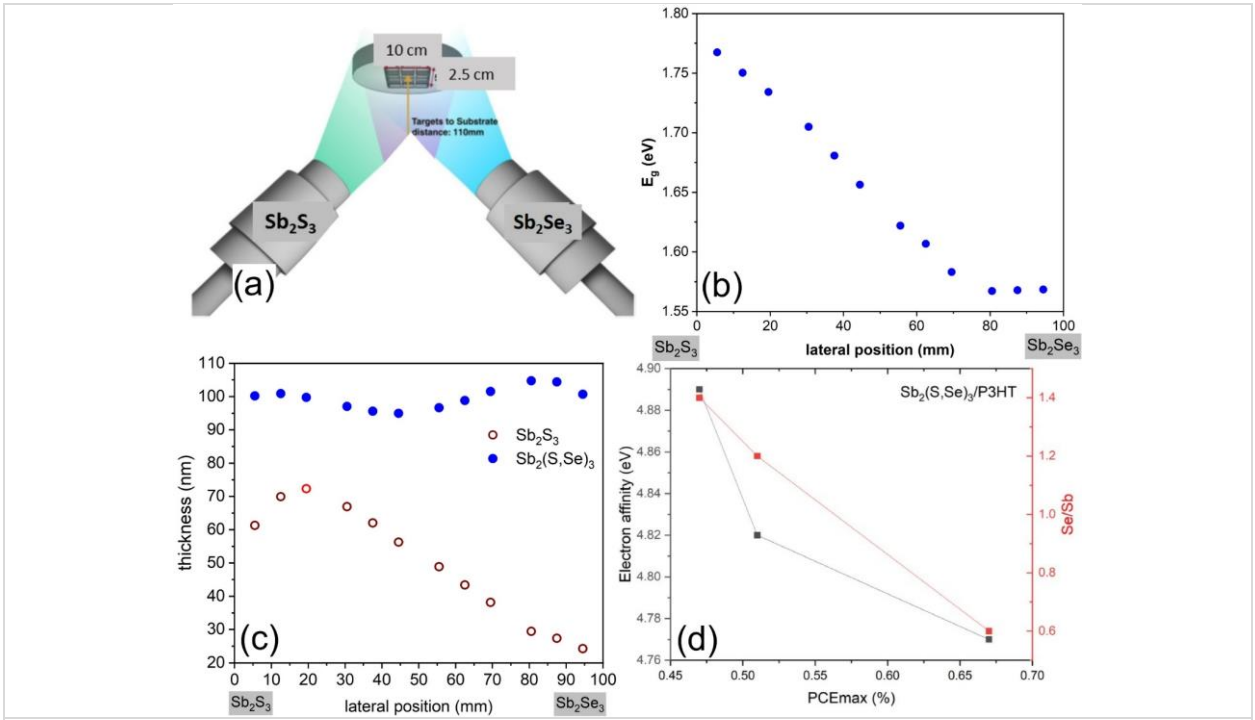

Figure 1*: (**a**) Schematic representation of the RF magnetron co-sputtering set-up; (**b**) band gap values of $Sb_2(S,Se)_3$ film vs. substrate position related to the Sb_2S_3 and Sb_2Se_3 targets; (**c**) thickness variation of $Sb_2(S,Se)_3$ film vs. substrate position related to the Sb_2S_3 and Sb_2Se_3 targets; (**d**) external conversion efficiency of $Sb_2(S,Se)_3$-based solar cells vs. electron affinity of $Sb_2(S,Se)_3$ layer and vs. Se/Sb ratio in $Sb_2(S,Se)_3$ films.*

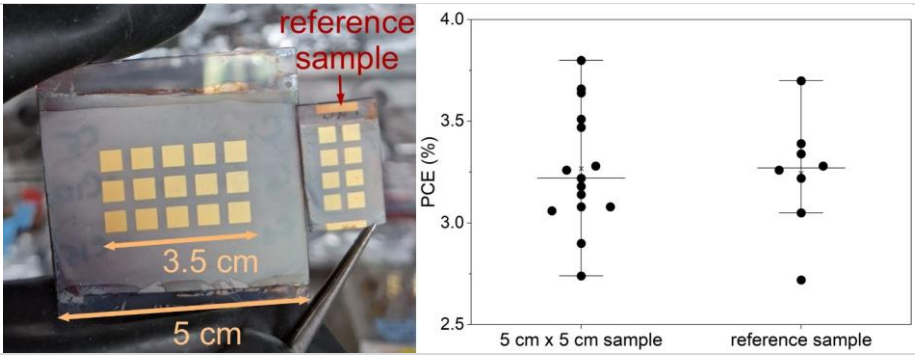

Figure 2*: (**a**) Pictures of large area (5 × 5 cm²) and standard (2 × 1.5 cm²) solar cells samples with Sb_2S_3 absorber deposited by spin-coating; (b) power conversion efficiency of solar cells fabricated on 5 × 5 cm² and reference substrates.*

- Activity 2.3 – Fabrication of solar cells with optimized Sb_2X_3 (X = S and/or Se) absorber layer and evaluation of photovoltaic characteristics. → 100% Completed: Solar cells with optimized Sb_2X_3 absorber layers were fabricated and their performance was evaluated. Cells based on Sb_2X_3 deposited by RF magnetron sputtering showed external conversion efficiencies (PCE) below 1%; cells based on solution-processed Sb_2S_3, deposited by spin-coating, reached PCE values between 3% and 5.3% (*Fig. 3*). The maximum efficiency was achieved after optimizing the interface between Sb_2S_3 and the hole-transport layer (P3HT).

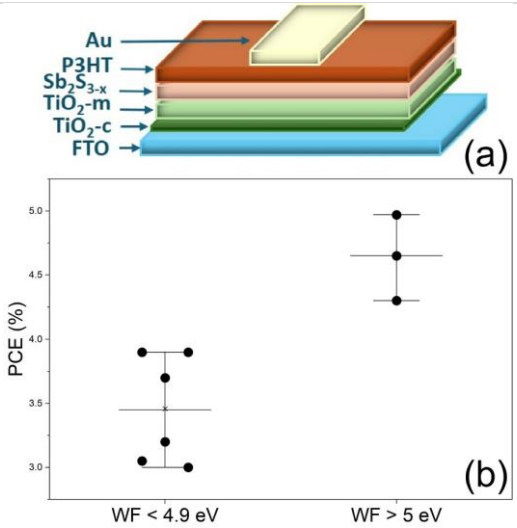

***Figure 3**: (**a**) Schematics of Sb_2S_3-based solar cell design; (**b**) power conversion efficiency of fabricated solar cells vs. work function of the hole transporter layer (P3HT).*

- Activity 2.4 – Management and dissemination. → 100% Completed: The project team participated at internal meetings, at monthly consortium online meetings organized by the coordinator (DTU) and at bi-annual consortium meetings which took place at DTU, Denmark and at DGIST, South Korea. Seven articles indexed in Web of Science were published, and two articles were submitted for publication in Materials & Design and Applied Surface Science. Team members contributed to work presented at 13 international conferences. The project also included educational activities: five PhD students carried out research internships on topics related to solar cells.

6. Dissemination and visibility

- ***2025 published/submitted articles/manuscripts:***
  - C. Besleaga, V. Stancu, A. El Kanouny, S. Laafar, I.C. Ciobotaru, A.-E. Bocirnea, L.N. Leonat, C.-A. Pescaru, I.-D. Simandan, A.G. Tomulescu, G.E. Stan, I. Pintilie, A.C. Galca, *Intrinsic and extrinsic stability factors in Sb_2S_{3-x}-based solar cells*, Materials & Design, in press (submitted in 2025, accepted in 2026).
  - V. Stancu, A. El Kanouny, S. Laafar, A.G. Tomulescu, C. Besleaga, A.C. Galca, L.N. Leonat, *Partially replacing DMF with eco-friendly solvents in the fabrication of Sb_2S_3 photoactive layer for solar cells*, submitted at Applied Surface Science (2025).
  - M. Tamin, O. El Khouja, M. Guemmaz, C. Tamin, A.E. Bocirnea, I. Assahsahi, D. Chaumont, A.C. Galca, *Towards a wide bandgap absorber: structural, morphological, and optical investigation of Ag-alloyed Cu_2ZnSnS_4 thin films*, Sustainable Energy & Fuels 9 (2025) 6751–6760.
  - A. El Kanouny, R. Elotmani, A. El Manouni, O. El Khouja, I. Assahsahi, A. Almaggoussi, A.C. Galca, *Electrodeposition of SnSe nanosheets: Effect of deposition potential on structural, morphological, and optical properties*, Applied Physics A–Materials Science & Processing 131 (2025) 979.
  - O. El Khouja, B. Popescu, I. Assahsahi, C.C. Negrila, L.N. Leonat, K. Nouneh, M. Ebn Touhami, A. Galatanu, A.C. Galca, *Improved sulfurization process for enhancing the*

microstructure and transport properties of spray pyrolysis-deposited Cu_2ZnSnS_4 films, Ceramics International 51 (2025) 47818–47829.

- E. Gilshtein, H.M. Gupta, A.M.P. Enevoldsen, C. Besleaga, A.C. Galca, S. Canulescu, *Superstrate structured Sb_2S_3 thin-film solar cells by magnetron sputtering of Sb and post-sulfurization*, Materials & Design 258 (2025) 114621.
- M. Dolcet Sadurni, K. Timmo, V. Mikli, J. Krustok, M. Danilson, A. Suchodolskis, C. Radu, A.E. Bocirnea, A.C. Galca, M. Grossberg-Kuusk, M. Kauk-Kuusik, *Effects of cationic substitution on the properties of $Sb_{1-x}Bi_xSeI$ (x = 0–1) compounds*, Journal of Alloys and Compounds 1037 (2025) 182292.
- O. El Khouja, Y.C. Gong, A. Jimenez-Arguijo, M.J. Guerra, A. Gon Medaille, R. Scaffidi, A. Basak, C. Radu, D. Flandre, B. Vermang, S. Giraldo, M. Placidi, Z. Jehl Li-Kao, A.C. Galca, E. Saucedo, *Exploring the synthesis of $Cu_2(Zn, Cd)SnS_4$ at high temperatures as a route for high-efficiency solar cells*, Progress in Photovoltaics 33 (2025) 628–643.
- I.C. Ciobotaru, C.C. Ciobotaru, C. Bartha, M. Enculescu, M. Secu, S. Polosan, C. Besleaga, *Phase transitions in dimer/layered Sb-Based hybrid halide perovskites: An in-depth analysis of structural and spectroscopic properties*, Advanced Optical Materials 13 (2025) 2402242.

- ***Conference contributions:***
  - E. Gilshtein, A. Tsekou, D. Komisar, H.M. Gupta, O. El Khouja, C. Besleaga, A.C. Galca, M. Grossberg-Kuusk, D.-H. Kim, S.-J. Sung, O. Ilchenko, S. Canulescu, *Antimony sulfide (Sb_2S_3) with tailored crystallographic orientation* (Invited presentation) at 2025 MRS Spring Meeting & Exhibit, Seattle, WA, USA, 7–11 April 2025.
  - E. Gilshtein, H.M. Gupta, R. Kahuure, A. Tsekou, K.E. Dehm, R.W. Crisp, T. Tran, N. Pryds, C. Besleaga, A.C. Galca, M. Grossberg-Kuusk, H. Van Quy, D.-H. Kim, S.-J. Sung, S. Canulescu, *Optimizing charge transport and crystal orientation in Sb_2S_3 thin-film solar cells: Strategies of doping and using the seed layer to improve device performance* (Oral presentation) at 2025 MRS Spring Meeting & Exhibit, Seattle, WA, USA, 7–11 April 2025.
  - A.C. Galca, O. El Khouja, Y. Gong, A. Jimenez-Arguijo, I. Assahsahi, I. Caño, A.E. Bocirnea, C. Radu, S. Giraldo, C. Besleaga, M. Placidi, Z. Jehl Li Kao, E. Saucedo, *Solution-processed CZCTS solar cells with efficiencies beyond 10% via atomic-level defect control with Ag alloying and Li passivation* (Oral presentation) at the 15th European Kesterite+ and 3rd ReNewPV Workshop, Berlin-Wannsee, Germany, 11–13 June 2025.
  - A. El Kanouny, V. Stancu, A. El Manouni, S. Laafar, C.A. Pescaru, A.G. Tomulescu, A. Almaggousi, C. Besleaga, A.C. Galca, *Optimization of TiO_2/SnS heterojunctions for hybrid n-i-p solar cells* (Oral presentation) at the 15th European Kesterite+ and 3rd ReNewPV Workshop, Berlin-Wannsee, Germany, 11–13 June 2025.
  - A.C. Galca, V. Stancu, O. El Khouja, K.E. Dehm, A. El Kanouny, E. Gilshtein, A.G. Tomulescu, S. Kern, C.A. Pescaru, S. Laafar, A.E. Bocirnea, L.N. Leonat, V. Toma, O. Rasoga, G.E. Stan, S. Canulescu, R.W. Crisp, C. Besleaga, Reproducibility and stability of Sb_2S_3 based solar cells (Poster presentation) at the 15th European Kesterite+ and 3rd ReNewPV Workshop, Berlin-Wannsee, Germany, 11–13 June 2025.
  - M. Tamin, O. El Khouja, D. Chaumont, M. Guemmaz, A.C. Galca, *Synthesis and characterization of CZTS and AZTS thin films for indoor and tandem photovoltaic applications* (Poster presentation) at the 15th European Kesterite+ and 3rd ReNewPV Workshop, Berlin-Wannsee, Germany, 11–13 June 2025.
  - E. Gilshtein, C. Besleaga, S. Canulescu, A.M.P. Enevoldsen, A.C. Galca, H.M. Gupta, *Superstrate structured Sb_2S_3 thin-film solar cells by magnetron sputtering of Sb and post-sulfurization* (Poster presentation) at the 15th European Kesterite+ and 3rd ReNewPV Workshop, Berlin-Wannsee, Germany, 11–13 June 2025.
  - M. Tamin, O. El Khouja, D. Chaumont, M. Guemmaz, C. Tamin, A.E. Bocirnea, A.C. Galca, *Substitution cationique et traitement thermique de $(Ag_xCu_{1-x})_2ZnSnS_4$: Vers des absorbeurs à large bande interdite pour le photovoltaïque tandem et indoor* (Poster

presentation) at the Journées Nationales du PhotoVoltaïque 2025 (JNPV), Strasbourg, France, 4–7 July 2025.

- M. Tamin, O. El Khouja, D. Chaumont, M. Guemmaz, A.E. Bocirnea, A.C. Galca, *Tuning the optoelectronic properties of CZTS thin films via ag alloying for next-generation tandem and indoor photovoltaics* (Oral presentation) at Nanotechnology for Next Generation High Efficiency Photovoltaics (NEXTGEN 2025), Mallorca, Spain, 9–12 September 2025.
- A. El Kanouny, V. Stancu, A. El Manouni, C.A. Pescaru, S. Laafar, A.G. Tomulescu, C. Radu, O. El Khouja, L.N. Leonat, A. Almaggousi, A.C. Galca, C. Besleaga, *Antimony sulfide absorbers from molecular inks: process optimization and performance of PV cells* (Oral presentation) at Nanotechnology for Next Generation High Efficiency Photovoltaics (NEXTGEN 2025), Mallorca, Spain, 9–12 September 2025.
- N. Ilić, C. Radu, T. Barudžija, A.C. Galca, I. Validžić, *Synthesis and characterization of Sb_2S_3 nanoparticles for application as absorber in solar cells* (Oral presentation) at the 5th International Meeting on Materials Science for Energy Related Applications (5IMMSERA), Belgrade, Serbia, 25–26 September 2025.
- R. Merah, N. Benaissa, A. El Kanouny, M. Tamin, A.G. Tomulescu, L.N. Leonat, W. Darenfad, A.C. Galca, *Influence des paramètres de dépots et du recuit sur les cellules solaires à couches minces de Sb_2S_3 par pulvérisation pyrolytique sous vide* (Oral presentation) at the 4eme édition du Symposium de la Recherche Scientifique Francophone en Europe Centrale et Orientale, Iaşi, Romania, 30–31 October 2025.
- M. Tamin, O. El Khouja, A.C. Galca, *Substitution cationique dans $(Ag,Cu)_2ZnSnS_4$: Vers des absorbeur à large bande interdite* (Oral presentation) at the 4eme édition du Symposium de la Recherche Scientifique Francophone en Europe Centrale et Orientale, Iaşi, Romania, 30–31 October 2025.

- ***Project website:*** https://infim.ro/en/project/quasi-1d-materials-for-advanced-thin-film-photovoltaics/

7. Contact information

- ***Contact person:*** Dr. Cristina Beşleagă Stan
- ***E-mail:*** cristina.besleaga@infim.ro

New gas sensing materials with working temperature close to or at room temperature

1. **Project identification**
   - ***Acronym:*** *GasSensingMat-RT*
   - ***Project code / Contract no.:*** *72/2024*
   - ***Funding program / Competition type:*** *International / M-Era.Net -M3*
   - ***Funding authority:*** *Executive Unit for Financing the Higher Education, Research, Development and Innovation (UEFISCDI, Romania)*
   - ***Project duration:*** *36 months (2024.05.01 – 2027.04.30)*
   - ***Total budget / NIMP share:*** *250,000 € / 90,000 €*

2. **Consortium**
   - ***Coordinating institution:*** *National Institute of Materials Physics, Măgurele, Romania*
   - ***Partners institutions:***
     - *P1: National Institute for Lasers, Plasma and Radiation Physics, Măgurele, Romania (R & D partner)*
     - *P2: Caloris Group SRL, Bucharest, Romania (Industrial / End-user partner)*
     - *P3: University of Debrecen, Debrecen, Hungary (Academic partner)*
     - *P4: University of Trabzon, Trabzon, Turkey (Academic partner)*
     - *P5: NanoMagnetic Instruments, Ankara, Turkey (Industrial / End-user partner)*

3. **Project summary** (including objectives, estimated results, progress beyond the state-of-the-art)

In this project we aim to continue our previous original work published in Chemosensors 8 (2020) 134 (https://doi.org/10.3390/chemosensors8040134), to create an added value to the recently developed new nanocomposite materials, which is sensitive for methane at room temperature.
It is a challenge to find alternative gas sensing materials to the SnO_2, which has an operating temperature for methane as high as 600 °C. The high value of the operating temperature is a serious drawback in the case of remote in-field applications. As such, room temperature (RT) sensing materials are highly desired.
The major novelty of these nanocomposite gas sensing materials as thin films is that they proved to be sensitive to methane (CH_4) in concentrations as low as 1000 ppm at RT of about 25 °C, without the need for heating the sensing element.
Through this project we aim to develop further on similar nanocomposites, suitable to signal the presence of different other gases, like propane and butane, hence the liquid petroleum gas (LPG) as well.

4. **Role of NIMP**
   - ***Role in the project:*** *Coordinator, Partner, WP leader.*
   - ***Main responsibilities:***
     - *Synthesis of the gas sensing nanocomposites working at environmental temperature;*
     - *Fabrication of gas sensing elements based on interdigitated electrodes and the above nanocomposites;*
     - *Contributing to the technology transfer to the industrial / end-user partners.*
   - ***Key personnel involved:*** *1 principal investigator, 4 senior researchers, 2 junior researchers, 2 PhD students.*

5. **Summary of results obtained in 2025**

When preparing the nanocomposites, we started on the one hand from the precursors of metal chalcogenide compounds (MeCh): 1 – SnSe; 2 – Sb_2Te_3, and 3 – WSe_2 respectively from the additions for

adjusting the resistance, consisting of 1 – Au_NP; 2 – PANI-EB, and 3 – Carbon black (C-black), resulting in several series of samples, consisting of sensor elements with four types of interdigital distances, 10, 100, 300, and 500 microns.
For easy and clear evidence of sensor element samples, we introduced a coding in the following form: Sab_n, where S denotes the sensor element, a and b can take one of the values 1, 2, or 3, and n identifies the type of electrode by interdigital distance, and can take the values 10, 100, 300, or 500.
The following sensor elements were produced:

***Table 1**: Produced sensor elements.*

S10_10	S10_100	S10_300	S10_500
S11_10	S11_100	S11_300	S11_500
S12_10	S12_100	S12_300	S12_500
S13_10	S13_100	S13_300	S13_500
S20_10	S20_100	S20_300	S20_500
S21_10	S21_100	S21_300	S21_500
S22_10	S22_100	S22_300	S22_500
S31_10	S31_100	S31_300	S31_500
S32_10	S32_100	S32_300	S32_500
S33_10	S33_100	S33_300	S33_500

It was found during the gas response testing of these nanocomposites that only a relatively small number of variants cumulatively satisfy the conditions of resistance and systematic response to LPG.
In a new series of samples were also those with the codes S12_10L (based on SnSe, and PANI-EB) and S33_10_L (based on WSe_2 and Carbon Black). Their response to the presence of LPG gas was this time relevant, repetitive and consistent.
The results are presented in *Fig. 1*, where in *Fig. 1a* we have an image from the screen of the resistance measuring device for the response of the S12_10_L sensor element, and in *Fig. 1b* we have the response of the S33_10_L sensor element in the form of an Origin graph.

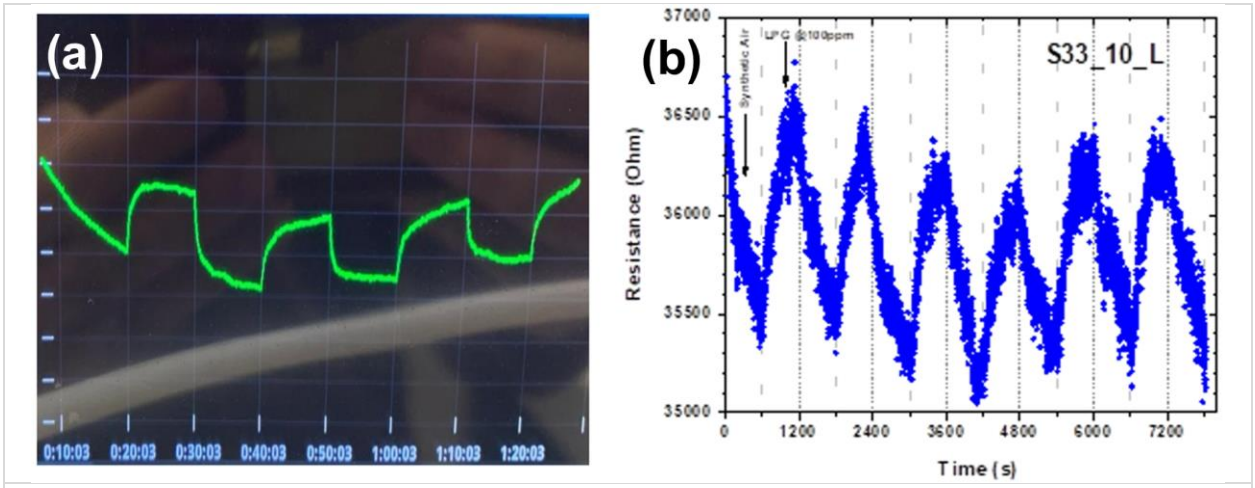

***Figure 1**: Consistent response to LPG gas of sensors (**a**) S12_10_L and (b) S33_10_L.*

The sensor elements produced these responses in *Fig. 1* at LPG gas concentration of 100 ppm at ambient temperature. On the other hand, LPG gas is known to be explosive in air at concentrations between approximately 1.8% (equivalent to 18×10^3 ppm) and 9.5% (equivalent to 95×10^3 ppm). (https://factories.wb.gov.in/main/files/contents/eodb/lpg_hazard_safety_measure.pdf)
Therefore, the nanocomposite materials developed at this stage can be a basis for further developments for early warning systems in areas with LPG risk (vehicles, warehouses, *etc.*).

6. Dissemination and visibility

- ***2025 published/submitted articles/manuscripts:***
  - A manuscript is under preparation based on the results obtained during November/December 2025 period.
- ***IPR status – Filed patents/patent applications; prototypes/demonstrators:***
  - A patent application is under preparation based on the results obtained during November/December 2025 period.
- ***Conference contributions:***
  - A. Pătruț, *New gas sensing materials working at or close to environmental temperatures* (Oral presentation), at the RoEnergy: International Renewable Energy Fair 2025, Timișoara, Romania, 1–3 October 2025.
  - A.M. Popa, A. Stochioiu, L.I. Toderascu, O. Gherasim, V.A. Antohe, E. Manaila, G. Craciun, G. Socol, I. Antohe, *The influence of electron beam irradiation on polyaniline-based chemiresistive sensors for ammonia detection* (Poster presentation) at E-MRS Spring Meeting 2025 (Section J.: Engineered nanomaterials for energy and environment: From synthesis to applications), Strasbourg, France, 26–30 May 2025.
- ***Project website:*** https://infim.ro/en/project/new-gas-sensing-materials-with-working-temperature-close-to-or-at-room-temperature/

7. Contact information

- ***Contact person:*** Dr. Adam Lőrinczi
- ***E-mail:*** adam.lorinczi@infim.ro

Recycling of the cathodes, based on carbon nanotubes and conducting polymers, from spent rechargeable Li batteries

1. **Project identification**
   - ***Acronym:*** *RCLIB*
   - ***Project code / Contract no.:*** *13/2024*
   - ***Funding program / Competition type:*** *International / COFUND-LEAP-RE-RCLIB-1.*
   - ***Funding authority / Sponsor****: European Commission & Executive Unit for Financing the Higher Education, Research, Development and Innovation (UEFISCDI, Romania) within PNCDI IV – Program 5.8 – European and International Cooperation 2022 Joint call of the European Partnership 101060874 – LEAP-RE; Ministry of University and Research (MUR, Italy); Ministry of Higher Education and Scientific Research (MESRS, Algeria); Ministry of National Education, Professional Training, Tertiary Education and Scientific Research (MENFPESRS, Morrocco).*
   - ***Project duration:*** *24 months (2024.03.01 – 2026.02.28)*
   - ***Total budget / INCDFM share:*** *837,600 € / 250,000 €*

2. **Consortium**
   - ***Coordinating institution:*** *National Institute of Materials Physics, Măgurele, Romania*
   - ***Partners institutions:***
     - *P1: IT Center for Science and Technology, Bucharest, Romania (SME partner)*
     - *P2: Istituto Nazionale di Fisica Nucleare, Italy (R & D partner)*
     - *P3: Mohammed VI Polytechnic University, Morocco (Academic partner)*
     - *P4: Badji Mokhtar University, Algeria (Academic partner)*
     - *P5: University Cadi Ayyad, Morocco (Academic partner)*

3. **Project summary** (including objectives, estimated results, progress beyond the state-of-the-art)

The innovation of this project lies in the life-cycle analysis of novel emerging cathodes containing carbon nanotubes (CNs) and conducting polymers (CPs) from rechargeable lithium-ion batteries (RLIBs), as well as in the development of new strategies for recycling cathode constituents at end of life. The main objectives of the project are: (*i*) Collection of spent RLIBs incorporating CP/CN composite electrode materials; (*ii*) Recovery of the cathode and separation of the spent electrode components, namely: CP/CN composites (where CP is in a semi-doped state), polyvinylidene fluoride (PVDF), CN–Li^+ species, undoped CP (CPu), LiCl, $LiPF_6$, and Super P carbon (C); (*iii*) Development of strategies to improve the physico-chemical properties of CP/CN/PVDF, CP/CN, and CP/oxidized CN (OCN) composites. These strategies include protonic acid doping of CP, chemical polymerization of monomers in the presence of CN or OCN, and processing into fibers obtained by electrospinning; (*iv*) Synthesis and characterization of CP/Biochar/CN composites; (*v*) Application and evaluation of the prepared composites as electrode materials for supercapacitor cells and RLIBs, using both conventional fabrication methods and electrospinning, followed by a comparative analysis of their electrochemical performance.

4. **Role of NIMP**
   - ***Role in the project:*** *Coordinator*
   - ***Main responsibilities:***
     - *The collection of spent RLIB recovery of the cathode and the separation of spent electrode constituents.*
     - *The development of various strategies for improvement of physico-chemical properties of the CP/CNs/PVDF, CP/CNs, and CP/oxidized CN (OCN) composites.*
     - *Application of composite as electrode active materials for supercapacitor cells.*
   - ***Key personnel involved:*** *1 principal investigator, 4 senior researchers, 3 junior researchers, 7 PhD students, 1 MSc student.*

5. Summary of results obtained in 2025

In 2025, the project activities were focused on testing electrodes containing composites of the type polydiphenylamine/multi-wall carbon nanotubes grafted with carboxyl groups (PDPA/MWNT-COOH) as active electrode materials in supercapacitor cells and optimization of supercapacitor cells. The PDPA/MWNT-COOH composites were prepared starting from the *in-situ* chemical polymerization of diphenylamine. Briefly, this method involves the dissolution of 1.12 mM DPA in a solution of 50 mL H_2SO_4 0.5 M and 10 mL of DMF, resulting in a colorless solution, and 2.678 mM $K^2Cr^2O^7$ in 50 mL H_2SO_4 0.5 M, when an orange solution results. The two solutions are mixed and homogenized under ultrasonic treatment for 5 minutes, during which the solution turns green. The reaction mixture is then allowed to react under magnetic stirring for 2 hours, resulting in the formation of a dark green precipitate. The precipitate is subsequently filtered, washed with 500 mL of H_2O and 100 mL of CH_3CN, and dried to constant weight. For the preparation of the PDPA/MWCNT-COOH-1 composite, 0.04 g of MWNT was added to the solution of diphenylamine (DPA) in H_2SO_4 and DMF, after which the synthesis proceeded as described above. The final product corresponds to the PDPA/MWCNT-COOH composite.

The electrochemical performance of this composite prepared with commercial materials was compared to that of a similar composite obtained under identical conditions using MWNT-COOH-0 recovered from electrodes of end-of-life rechargeable lithium batteries (denoted below as PDPA/MWNT-COOH-1). Electrode preparation involved 80 wt.% active material, 5 wt.% polyvinylidene fluoride (PVDF) as binder, 15 wt.% Super P carbon, two drops of dibutyl phthalate (DBP), and 1 mL of acetone. The components were mixed for 12 hours to obtain a homogeneous paste. The paste was spread onto a glass slide, and after acetone evaporation, the resulting film was peeled off and washed with diethyl ether to remove DBP. The film was then cut into circular electrodes with a diameter of 8 mm.

Using the composite materials, electrodes with active material contents of 82 and 84 wt.% were also fabricated. The electrodes were assembled in Swagelok-type cells for electrochemical testing.

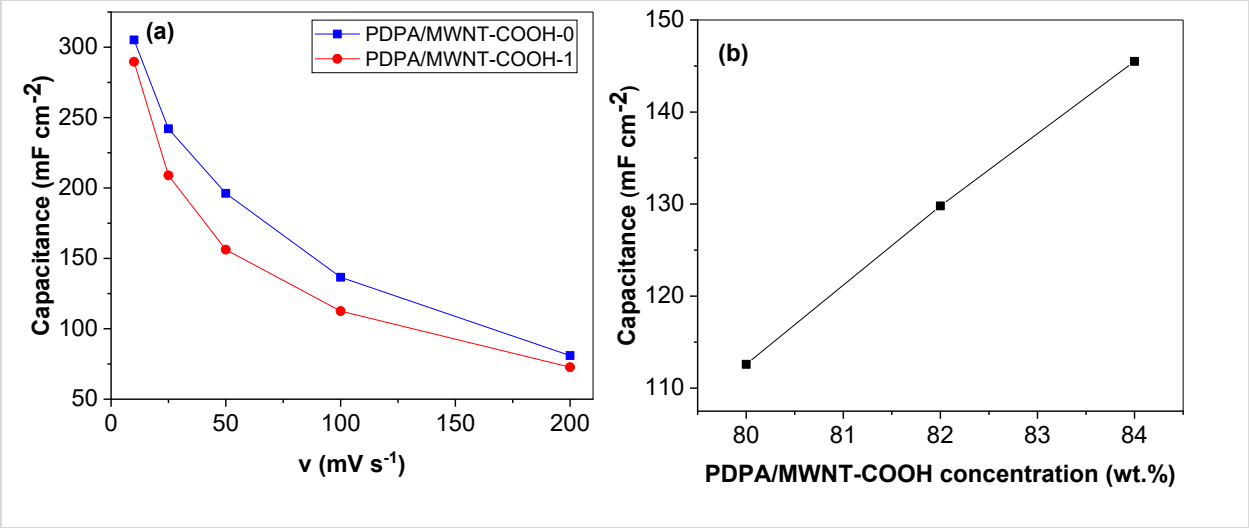

***Figure 1**: (**a**) The dependence of capacitance of supercapacitors having the composites PDPA/MWNT-COOH-0 and PDPA/MWNT-COOH-1 as electrode active material. (**b**) The dependence of the capacitance of symmetrical supercapacitors having electrodes based on the PDPA/MWNT-COOH-2 composite as a function of the concentration of active material.*

According to *Fig. 1a*, at a potential scan rate of 100 mV s^{-1}, the capacitance of symmetric supercapacitors based on electrodes containing PDPA/MWNT-COOH-0 and PDPA/MWNT-COOH-1 composites as active materials is 136.6 mF cm^{-2} and 112.59 mF cm^{-2}, respectively, when the active material content in the electrode is 80 wt.%. Increasing the concentration of PDPA/MWNT-COOH-1 active material in the electrode from 80 wt.% to 82 wt.% and 84 wt.% (*Fig. 1b*) results in a corresponding increase in the capacitance of the symmetric supercapacitors from 112.59 mF cm^{-2} to 129.8 mF cm^{-2} and 145.5 mF cm^{-2}, respectively (Milestone M4.1). The successful achievement of these results ensures the fulfilment of KPI 4, which requires the active material content in the supercapacitor electrodes to remain below 85 wt.%. The activities carried out in 2025 enabled the Technology Readiness Level (TRL) to advance from 2 to 3.

6. Dissemination and visibility

- ***2025 published/submitted articles/manuscripts:***
  - C.S. Florica, A. Nila, M. Vaduva, C. Negrila, C. Bartha, M. Aannir, I. Saadoune, S. Bellucci, O. Cramariuc, M. Baibarac, *Comparative analysis of polydiphenylamine/MWNT-COOH composites for supercapacitors: Recovered vs. commercial nanotube electrodes*, submitted to RSC Advances 2025.
  - F. Djefaflia, O. Guellati, A.N. Merzoug, A. Harat, J.E. Haskouri, I. Janowska, M. Baibarac, *Exploring the synergistic effects of ultrafine polyaniline nanofibers and oxygen-modified multi-walled carbon nanotubes to enhance intercalated electrochemical performance for advanced flexible supercapacitors*, submitted to Materials 2025.
  - I.G. Lupu, O.T. Cramariuc, M.R. Zvonaru, D.I. Stanciu, M.C. Grosu, E. Codau, M. Baibarac, D.L. Chicet, *Comparative analysis of electrospinning geometries of PEO nanofiber optimization*, submitted to Journal of the Textile Institute 2025.

Conference contributions:

- T. Burlanescu, S. Florica, M. Vaduva, A. Udrescu, M. Chivu, M. Baibarac, *Composites materials for applications in the supercapacitors field* (Poster presentation) at 6th International Conference on Powder Metallurgy & Advanced Materials, Cluj-Napoca, Romania, 29 October – 1 November 2025.
- C.S. Florica, M. Vaduva, T. Burlanescu, M. Baibarac, *Composite materials for applications in energy storage* (Poster presentation) at 6th International Conference on Powder Metallurgy & Advanced Materials, Cluj-Napoca, Romania, 29 October – 1 November 2025.

- ***Others (e.g., awards/distinctions; outreach activities; theses; media coverage/press releases, etc.):***
  - C.S. Florica, *Composite materials based on conductive polymers, carbon nanotubes, and graphene quantum dots for applications in the field of supercapacitors and sensors* (ongoing), PhD thesis, University of Bucharest, Romania, expected completion: 2027.
- ***Project website:*** https://infim.ro/en/project/rclib-leap-re/

7. Contact information

- ***Contact person:*** Dr. Mihaela Baibarac
- ***E-mail:*** barac@infim.ro

Ultra-sensitive optical sensor system for simultaneous, *in-situ* detection of multiple pesticides in surface and ground waters

1. **Project identification**
   - ***Acronym:*** *STARDUST*
   - ***Project code / Contract no.:*** *55/2024*
   - ***Funding program / Competition type:*** *International/COFUND-WATER4ALL-STARDUST-1*
   - ***Funding authority / Sponsor****: European Commission & Executive Unit for Financing the Higher Education, Research, Development and Innovation (UEFISCDI, Romania) within Program 5.8 - European and International Cooperation/ 2022 Joint call of the European Partnership 101060874 – Water4All); The Research Council of Norway; Environmental Protection Agency, Innovation Fund Denmark, NCBR.*
   - ***Project duration:*** *36 months (2024.03.01 – 2027.02.28)*
   - ***Total budget / NIMP share:*** *1,249,526 € / 90,000 €*

2. **Consortium**
   - ***Coordinating institution:*** *SINTEF AS, Oslo, Norway (R & D)*
   - ***Partners institutions:***
     - *P1: National Institute of Materials Physics, Măgurele, Romania*
     - *P2: Instytut Chemii Fizycznej Polskiej Akademii Nauk (Institute of Physical Chemistry Polish Academy of Sciences), Warsaw, Poland (R & D partner)*
     - *P3: Dublin City University, Dublin, Ireland (Academic partner)*
     - *P4: Technical University of Denmark, KGS LYNGBY, Denmark (Academic partner)*
     - *P5: National Institute for Research and Development in Microtechnologies, Voluntari, Romania (R & D partner)*

3. **Project summary** (including objectives, estimated results, progress beyond the state-of-the-art)

Hydro-climatic extremes such as droughts and floods, exacerbated by climate change, significantly affect socio-economic and environmental sectors. Current models indicate that pesticides can contaminate waterways during heavy rainfall, but monitoring methods are insufficient to assess their effects on water quality and biodiversity. The STARDUST project aims to develop a real-time optical system for monitoring pesticides in water using surface-enhanced Raman spectroscopy and microfluidics. By incorporating rainfall forecasts and citizen science for sample collection, the project will build on existing monitoring efforts. Key objectives include: (*1*) Understanding the effects of intense rainfall on water quality; (*2*) Developing and validating an integrated sensor prototype; (*3*) Maximizing implementation impacts. (*4*) Democratizing data through citizen science. STARDUST aims to ensure a continuous supply of clean water (SDG 6) by delivering: (*i*) a low-cost sensor system to detect multiple pesticides in water; (*ii*) event-based sampling informed by weather forecasts; (iii) insights into pesticide accumulation during extreme events; (*iii*) a new algorithm for recognizing complex pesticide mixtures and a database; (*iv*) validation of sensor technology at key hotspots; (*v*) enhanced collaboration among EU water analysis experts through research and innovation activities.

4. **Role of NIMP**
   - ***Role in the project:*** *Partner*
   - ***Main responsibilities:***
     - *Process metrology that covers the characterization of the sensor prototypes fabricated using electron beam lithography (EBL) and Nanoimprint Lithography (NIL) by RAMAN spectroscopy, scanning electron microscopy (SEM), atomic force microscopy (AFM), etc;*

- *Testing the SERS sensor performance for Raman signal enhancement, sensitivity, and LOD for selected relevant pesticides and pesticide mixtures using stationary Raman spectrometers;*
- *Development of Data Management Plan (DMP)- a living document ensuring data outputs are stored in a FAIR-compliant manner and updated as the project progresses. Create and update the project website during implementation.*

- ***Key personnel involved:*** *1 principal investigator, 5 senior researchers, 3 junior researchers, 1 MSc student.*

5. Summary of results obtained in 2025

During the second stage of project implementation in 2025, the following activities were conducted:

- Activity 2.1: Characterization of SERS Substrates Fabricated by EBL and NIL with the sub-activity 2.1.1 involved the characterization of Electron Beam Lithography (EBL) and Nanoimprint Lithography (NIL) SERS substrates through Scanning Electron Microscopy (SEM), Atomic Force Microscopy (AFM), and reflection measurements, continuing from task T2.3. This phase extended measurements initiated in the previous year on both SERS substrates and flat gold substrates. Thiabendazole and clotrimazole were utilized as pesticide models and were dissolved in both ethanol and aqueous solutions. Notably, the layers deposited from the aqueous solution exhibited a stronger Raman signal than those derived from ethanol.
- Activity 2.2: Performance Evaluation of the SERS Sensor with the sub-activity 2.2.1 focused on the characterization of the SERS sensor for Raman applications, encompassing signal enhancement, sensitivity assessment, and detection limit determination for relevant pesticides as well as pesticide mixtures, utilizing stationary Raman spectrometers (task T2.5 - partial). Samples supplied by the Danish partner were analysed, revealing a detectable Raman signal and indicating that the sensor proposed within the project represents a reliable detection method (*Fig. 1*).

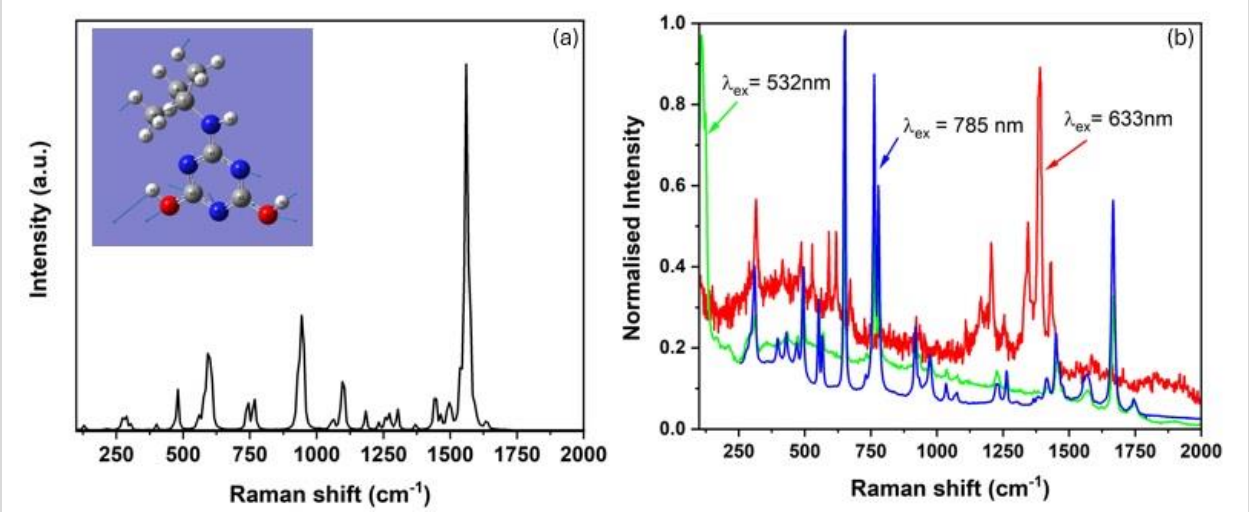

Figure 1*: Terbuthylazine-TP MT23 (LM5) simulated Raman spectra using (**a**) DFT calculation and (**b**) experimental Raman spectra at different excitation wavelengths.*

For all relevant metabolites, we extracted and compared the simulated with the experimental Raman spectra. In particular, the spectra for terbuthylazine-TP MT23 (LM5), the most prevalent metabolite, are illustrated in *Figs. 1* and *2*.

- Activity 2.3: Feasibility of Multiplexed Detection with the sub-activity 2.3.1 assessed the feasibility of multiplexed detection (task 3.3 - initiation) and 4. Activity 2.4: Sensor Implementation Demonstration, with Sub-activity 2.4.1 outlining the sensor implementation demonstration (partially related to T3.4). These activities are associated with Work Package 3 (WP3), which focuses on developing an integrated sensor system. The preliminary studies conducted aimed to establish a microfluidic system for pesticide detection utilizing Surface-

Enhanced Raman Spectroscopy (SERS) sensors. Additionally, a comprehensive review concerning optical sensors for pesticide detection is being finalized for journal submission.

6. Dissemination and visibility

- ***2025 proceeding papers:***
  - I.-A. Baragau, O. Rasoga, A. Costas, H.-J. Albrechtsen, K. Gizynski, K. Milenko, E. Vereshchagina, J. Jose, F. Regan, *Establishing a Raman spectra database for the detection of Terbuthylazine metabolites using SERS-based optical sensors*, Proceedings EUROSENSORS XXXVII (2025) 347–348. Publisher: AMA Service GmbH, ISBN 978-3-910600-07-2.
  - A.M. Baracu, A. Dinescu, K. Milenko-Kuszewska, O. Rasoga, I.-A. Baragau, *Metasurface development for SERS-based optical sensors*, Proceedings EUROSENSORS XXXVII, (2025) 363–364. Publisher: AMA Service GmbH, ISBN 978-3-910600-07-2.
- ***Conference contributions:***
  - A.M. Baracu, A. Dinescu, K. Milenko-Kuszewska, O. Rasoga, I.-A. Baragau, *Metasurface development for SERS-based optical sensors* (Poster presentation) at the 37th European Conference on Solid-State Transducers Eurosensors 2025 (EUROSENSORS XXXVII), Wrocław, Poland, 7–10 September 2025.
  - I.-A. Baragau, O. Rasoga, A. Costas, H.-J. Albrechtsen, K. Gizynski, K. Milenko, E. Vereshchagina, J. Jose, F. Regan, *Establishing a Raman spectra database for the detection of Terbuthylazine metabolites using SERS-based optical sensors* (Poster presentation) at the 37th European Conference on Solid-State Transducers Eurosensors 2025 (EUROSENSORS XXXVII), Wrocław, Poland, 7–10 September 2025.
- ***Others (e.g., awards/distinctions; outreach activities; theses; media coverage/press releases, etc.):***
  - Promotion article in the MSP Magazine, no. 11, pages 36–37.
  - "European Researchers' Night 2025", 26–27 September 2025 – The European Researchers' Night is an event organized under the Marie Skłodowska-Curie Actions, which is part of the Horizon 2020 framework program at the European Union level. The event aims to raise public awareness about the role of researchers and to showcase the fascinating and impactful nature of scientific research.
  - Water Blitz at Mølle Å, in Denmark, on Saturday, 27 September 2025, to investigate pesticides, held by DTU partner as part of the STARDUST project.
  - STARDUST Citizen Science Water-Blitz, in Ireland, 26–28 September 2025, held by DCU partner as part of the STARDUST project.
- ***Project website:*** https://water4all.ro/stardust/

7. Contact information

- ***Contact person:*** Dr. Oana Raşoga
- ***E-mail:*** oana.rasoga@infim.ro

A green approach in the frame of circular economy: Robocasted photocatalysts for wastewater treatment and use of reclaimed water in agriculture

1. **Project identification**
   - ***Acronym:*** *WaterGreenTreat*
   - ***Project code / Contract no.:*** *59/2024*
   - ***Funding program / Competition type:*** *International / COFUND-WATER4ALL-WATER Green Treat-1*
   - ***Funding authority / Sponsor:*** *European Commission & Executive Unit for Financing the Higher Education, Research, Development and Innovation (UEFISCDI, Romania) within PNCDI IV - Program 5.8 - European and International Cooperation 2022 Joint call of the European Partnership 101060874 – Water4All; National Research, Development and Innovation Office (NKFIH, Hungary); State Research Agency (AEI, Spain); French National Research Agency (ANR, France).*
   - ***Project duration:*** *36 months (2024.04.01 – 2027.03.31)*
   - ***Total budget / NIMP share:*** *1,119,988.53 € / 125,000 €*

2. **Consortium**
   - ***Coordinating institution:*** *National Institute of Materials Physics, Măgurele, Romania*
   - ***Partners institutions:***
     - *P1: University of Bucharest, Faculty of Physics, Bucharest, Romania (Academic partner)*
     - *P2: Magyar Agrar – Es Elettudomanyi Egyetem, Institute of Aquaculture and Environmental Safety, Godollo, Hungary (Academic partner)*
     - *P3: Universidad de Extremadura, Department of Mechanical, Energy and Materials Engineering, Badajoz, Spain (Academic partner)*
     - *P4: Centre National de la Recherche Scientifique CNRS, GEPEA UMR6144, Saint-Nazaire, France (R & D partner)*

3. **Project summary** (including objectives, estimated results, progress beyond the state-of-the-art)

The aim of this proposal is to develop macroporous photocatalysts based on eco-metal oxide composites (ZnO/CuO) obtained *via* the robocasting technique and to evaluate the synergistic effect between these 3D-printed photocatalytic structures and microalgae for wastewater treatment and agricultural reuse. The project focuses on green synthesis routes for ZnO and CuO nanoparticles, their integration into 3D-printed architectures, and their application in the removal of emerging pollutants such as drugs and dyes from industrial wastewaters. The main objectives include: (*i*) phytosynthesis and comprehensive physicochemical characterization of metal oxide nanoparticles and their composites; (*ii*) fabrication of macroporous structures by robocasting; (*iii*) laboratory-scale photocatalytic degradation of organic contaminants; (*iv*) mitigation of secondary toxic by-products through microalgae cultivation; and (*v*) evaluation of the synergistic performance of photocatalysts and microalgae under laboratory, semi-industrial, and greenhouse conditions, using both synthetic and real wastewaters. Ecotoxicological assessment will be conducted using standardized *in vitro* and *in vivo* assays covering multiple trophic levels including microalgae, bacteria, crustaceans, fish embryos and plants growth tests. No studies have reported robocasted photocatalysts based on eco-ZnO/CuO composites. Within a circular economy framework, the proposed approach aims to enable the safe reuse of treated wastewater for irrigation, thereby enhancing the resilience of water management systems under hydroclimatic stress and promoting greater sustainability in agriculture.

4. Role of NIMP

- ***Role in the project:*** *Coordinator*
- ***Main responsibilities:***
  - *Green synthesis of metal oxide (~0.5 Kg of ZnO eco-powder) using aqueous plant extracts in order to print (in Spain) 3D structures based on ecogenic metal oxides by robocasting;*
  - *Optical, structural, and morphological ccharacterization of the commercial and ecological metal oxides and their composites (powder and robocasted samples);*
  - *Application of composite based on commercial and ecogenic metal oxide nanoparticles (powder or robocasted samples) in laboratory-scale photocatalysis experiments to treat synthetic and real wastewaters containing organic pollutants (dyes, drugs, etc.).*
- ***Key personnel involved:*** *1 principal investigator, 8 senior researchers, 1 junior researcher, 1 PhD student.*

5. Summary of results obtained in 2025

In 2025, the project activities were focused on the preparation and comprehensive characterization of phyto-synthesized metal oxide–based samples. In order to fulfil the objectives, set for 2025, green synthesis approaches were applied for the preparation of metal oxide nanoparticles (ZnO, CuO) and their composite powders. Furthermore, the synthesis conditions were optimized to obtain nanometric ZnO and CuO powders with increased yield per synthesis batch. The project coordinator obtained approximately 0.5 kg of eco-ZnO powder, and the UB partner obtained around 0.1 kg of eco-CuO powder. Both materials were subsequently employed by the Spanish partner to fabricate 3D structures based on eco-synthesized metal oxides (EcoMOs) using the robocasting technique. The synthesized powders were evaluated in terms of their morphological, structural, and optical properties, both as single-component systems (ZnO, CuO) and as composite materials (ZnO–CuO). Structural characterization by X-ray diffraction (XRD) confirmed that the phyto-synthesized powders exhibited diffraction peaks corresponding to hexagonal wurtzite ZnO and monoclinic CuO phases. Morphological properties were assessed by scanning electron microscopy (SEM), revealing particles with an average size below 200 nm, in good agreement with the partner's dynamic light scattering (DLS) measurements. Optical investigations including reflectance and Fourier-transform infrared (FTIR) spectroscopy revealed characteristic optical fingerprints of both ZnO and CuO components within the composite materials. Eco-impact (ecotoxicological) evaluations including greenhouse and laboratory plant tests, urease activity assays, and photosynthesis and respiration analyses revealed that: i) among the tested samples (EcoMOs and their composites), only two materials-EcoZnO95%–CuO5%NP and EcoZnO99%–CuO1%NP-exhibited pronounced urease inhibition at a concentration of 1 g/L. The anti-ureolytic activity reached 53.90% for EcoZnO95%–CuO5%NP and 43.33% for EcoZnO99%–CuO1%NP. A slight inhibitory effect was also observed for EcoZnO100%NPs and EcoCuO100%NPs; ii) all samples exhibited antioxidant activity attributed to the presence of bioactive compounds capable of scavenging free radicals. The highest antioxidant activity (AA%) values were recorded for EcoCuO100%NPs and EcoZnO99%–CuO1%NPs.

Photocatalytic activity investigations demonstrated that composite powders exhibited superior performance compared to monocomponent ZnO or CuO materials (*Fig. 1a,b*). The highest degradation efficiency was obtained for the composite containing 3% CuO. Overall, EcoZnO97%–CuO3%NPs were identified as the most efficient materials for the photodegradation of both Rhodamine B (RhB) and paracetamol.

Analysis of synthetic wastewater with phyto-synthesized metal oxide powders prior to photocatalytic degradation showed that residual RhB accelerated plant senescence, ultimately causing premature plant death, similarly to observations reported in Stage I (2024). Consequently, these plants could not be used for further photosynthesis or respiration assessments.

The respiration of basil plants (*Ocimum basilicum* L.) fed with water containing RhB photocatalytically degraded in the presence of EcoMOs and their composites showed a pronounced decrease after irrigation with water treated using eco-synthesized metal oxide powder photocatalysts, namely EcoZnO99%–CuO1% and EcoZnO97%–CuO3%. When assessing RhB photodegradation using 3D-printed structures, longer irradiation times and significantly higher photocatalyst loadings were required. This is attributed to the substantially lower specific surface area of the 3D-printed structures

compared to eco-synthesized metal oxide powder photocatalysts. Although higher photocatalyst amounts are required, the implementation of 3D-printed structures in dye-containing wastewater treatment provides clear technological benefits, such as simplified process flow through the elimination of filtration steps, facile catalyst recovery and reuse, and the production of high-quality treated water without solid residues.

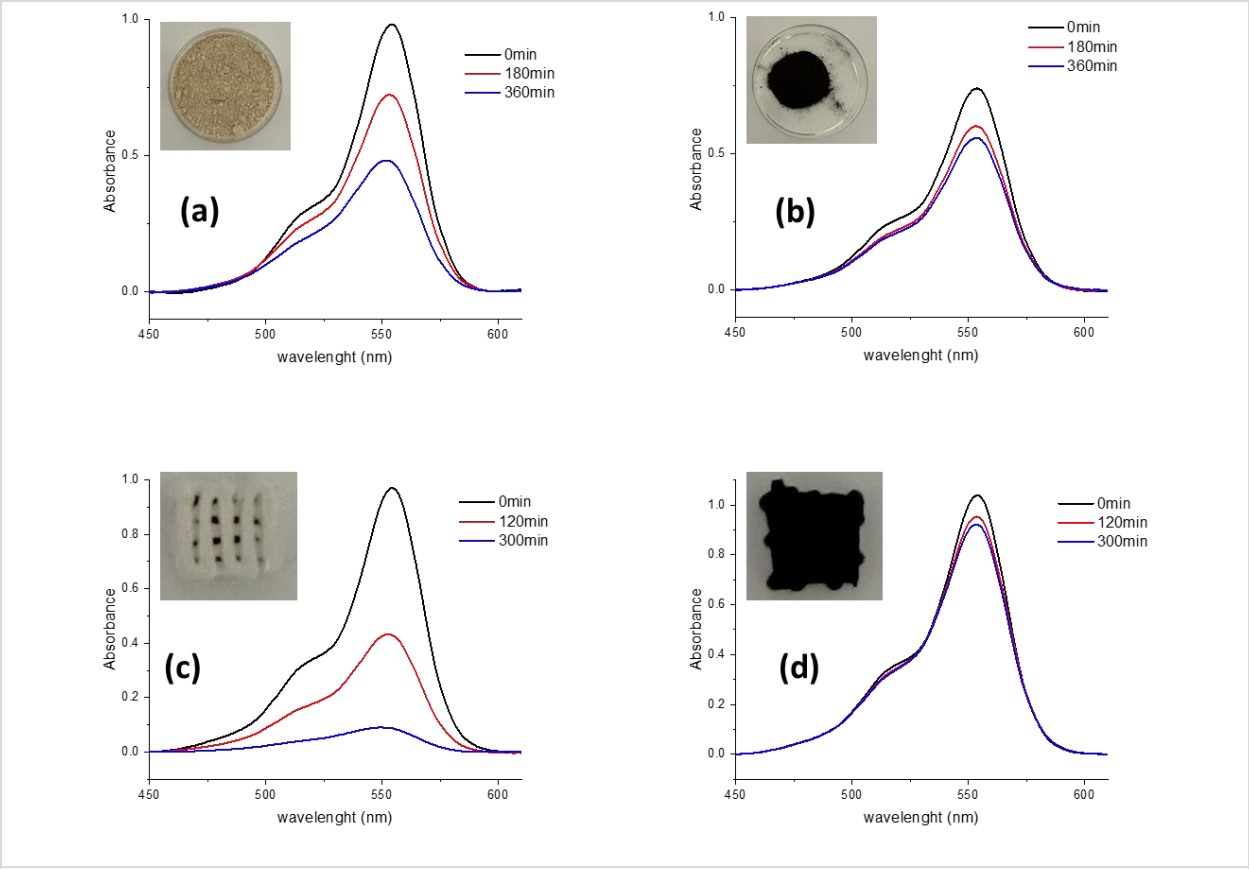

***Figure 1**: Photographs and time-dependent UV–Vis absorption spectra of Rhodamine B (RhB) under photocatalytic conditions for the following samples: (**a**) EcoZnO100% nanoparticles; (**b**) EcoCuO100% nanoparticles; (**c**) 3D-printed EcoZnO100%; and (**d**) 3D-printed EcoCuO100%.*

3D-printed composite-based samples exhibited superior photocatalytic activity (Milestones: M3.1) compared to monocomponent 3D EcoZnO100% or 3D EcoCuO100% samples (*Fig. 1c,d*). The effects of synthetic wastewater treated with robocasted structures on plants were evaluated by analysing photosynthesis and respiration. The applied treatments did not affect plant photosynthesis. Moreover, no alteration in respiration was observed following irrigation with RhB-contaminated water treated using 3D EcoCuO100% and 3D EcoZnO99%–CuO1%. In contrast, a slowdown in respiration was detected for the remaining samples. Ecotoxicological assessments (Milestones: M3.1) further indicated the absence of toxic effects and supported the potential use of these materials in agricultural applications. The project progress was monitored using clearly defined key performance indicators (KPIs) covering scientific excellence (structure, controlled morphology, optical properties), technical performance (photocatalytic performance), ecotoxicological validation (absence of toxic effects of treated synthetic wastewater on plants), dissemination, and TRL advancement. The project successfully achieved an increase in TRL from 2 to 3 while delivering validated, reproducible results aligned with the project milestones.

6. Dissemination and visibility

- ***2025 published/submitted articles/manuscripts:***
  - I. Zgura, C.P. Ganea, L. Nedelcu, C. Bartha, M. Enculescu, L. Frunza, *Unveiling a weak surface interaction in composites based on nematic liquid crystal mixture and semiconducting nanoparticles*, Romanian Reports in Physics, in press.

- A. Udaondo, P. Miranda, I. Zgura, A. Pajares, *Direct ink writing of porous ZnO structures for wastewater treatment: Effect of sintering temperature*, submitted to Ceramics International 2025.

- ***Conference contributions:***
  - M.-E. Barbinta-Patrascu, C. Nichita, B.C. Mitrea, B. Bita, I. Zgura, I. Stamatin, *Eco-toxicological aspects regarding phytogenic copper oxide nanoparticles for wastewater treatment* (Poster presentation) at the 23th International Balkan Workshop on Applied Physics and Materials Science, Constanta, Romania, 9–12 July 2025.
  - I. Zgura, M. Enculescu, N. Preda, L. Nedelcu, O. Rasoga, M. Cercel, M. Dinescu, M.-E. Barbinta-Patrascu, C. Nichita, A. Udaondo, P. Miranda, A. Pajares, *Developing metal oxide-based photocatalysts as powders or robocasted 3D structures for degradation of organic pollutants in water* (Invited lecture) at the 17th International Conference on Physics of Advanced Materials (ICPAM-17) and 8th Autumn School on Physics of Advanced Materials (PAMS-8), Hamamatsu, Japan, 16–23 November 2025.
- ***Others (e.g., awards/distinctions; outreach activities; theses; media coverage/press releases, etc.):***
  - Best presentation Award was offered by Photochem Journal to Irina Zgură from National Institute of Materials Physics, Măgurele, Romania, for the Developing metal oxide-based photocatalysts as powders or robocasted 3D structures for degradation of organic pollutants in water *(Invited lecture) at the 17th International Conference on Physics of Advanced Materials (ICPAM-17) and 8th Autumn School on Physics of Advanced Materials (PAMS-8), Hamamatsu, Japan, 16–23 November 2025.*
  - "European Researchers' Night 2025", 26–27 September 2025 – The European Researchers' Night is an event organized under the Marie Skłodowska-Curie Actions, which is part of the Horizon 2020 framework program at the European Union level. The event aims to raise public awareness about the role of researchers and to showcase the fascinating and impactful nature of scientific research. https://water4all.ro/watergreentreat/wp-content/uploads/2025/09/INCDFM-NC.pdf
  - The project was promoted to the general public also through dissemination activities carried out by partners from France, Spain, and Hungary: Oct 25 Fête de la Science in Saint-Nazaire (open fair for the citizens, the scholars and the students during 3 days). Demonstration of microalgae cultivation and WaterGreenTreat poster presentation; https://www.elperiodicoextremadura.com/extremadura/2025/04/23/universidad-extremadura-logra-nuevos-materiales-depurar-aguas-residuales-reaprovecharlas-agricultura-116652468.html; Project exhibition on Girls' Day Festival (powered by Association of Hungarian Women in Science), 25.04.2025, MATE Gödöllő, Hungary, https://lanyoknapja.hu/program-reszletek/?pid=1259&fbclid=IwY2xjawNTsHRleHRuA2FlbQIxMABicmlkETBRVWVVQ0g1aG15dGEzUjY4AR7UMxK25wYD8lodCRMOitiO88NXDOU893Ejf0-PDw_POr5HyrhdufAP53Gxkw_aem_4kGU7aFMVnNyq7Di_JRJyw;
  - Additionally, a collaboration protocol was signed (21.10.2025) with SC MAJUTEX SRL, a Romanian textile company, enabling access to real dyeing wastewater for testing and supporting applied research and technology transfer activities within WaterGreenTreat.
- ***Project website:*** https://infim.ro/en/project/a-green-approach-in-the-frame-of-circular-economy-robocasted-photocatalysts-for-wastewater-treatment-and-use-of-reclaimed-water-in-agriculture/; https://water4all.ro/watergreentreat/.

7. Contact information

- ***Contact person:*** Dr. Irina Zgură
- ***E-mail:*** irina.zgura@infim.ro

Contributions to Education and Society

UNESCO at the National Institute of Materials Physics, Romania

8. Project identification

- ***Acronym:*** *UNESCO*
- ***Funding program / Competition type:*** *International / Revitalizing STEM education to equip next generations with STEM competency, launched by UNESCO-Venice*
- ***Sponsor:*** *Huawei*
- ***Project duration:*** *36 months (2024.01.01 – 2026.12.31)*

9. Short description

The National Institute of Materials Physics (NIMP) holds a unique position in Romania as the only institution hosting both a UNESCO Category 2 Centre (CIFRA) and a UNESCO Chair (TRRISE), serving as hub for advanced research excellence, international cooperation, and science education. Through its dual role as a hub for scientific excellence and international cooperation, NIMP, together with CIFRA and TRISSE, plays a key part in building scientific capacity, fostering innovation, and contributing to UNESCO's mission for inclusive, high-quality science education worldwide and provides an ideal environment for integrating research excellence with science education, science diplomacy, outreach, and societal impact.

10. Project summary (including objectives, estimated results, progress beyond the state-of-the-art)

The *Centre International de Formation et de Recherche Avancées en Physique* (CIFRA) is a UNESCO Category 2 Centre hosted by the National Institute for Materials Physics in Măgurele, Romania. It was established under an agreement between the Government of Romania and UNESCO and has been operational since February 2017. CIFRA is the only UNESCO Category 2 Centre in Romania and the Balkan region dedicated to the field of basic sciences. Its mission is to promote international research collaboration and capacity building in science and education. The Centre's main objectives include:

i. conducting advanced research in physics and related interdisciplinary fields;
ii. providing scientific training for students and young researchers from Southeastern Europe, the Balkan region, and developing countries;
iii. fostering the formation of and participation in regional scientific networks;
iv. organizing and facilitating high-level scientific meetings;
v. promoting gender equality in science; and
vi. offering expertise to decision-makers in science and education, as well as to the general public, with the aim of strengthening national research and development capacity.

The *UNESCO Chair on STEM Education — TRRISE (Transfer of Research Results into STEM Education)* was officially launched in 2025 at National Institute for Materials Physics with the objective of bridging cutting-edge scientific research and formal education systems. The Chair is dedicated to enhancing the inclusiveness and relevance of quality STEM education by equipping educators with modern, research-based teaching tools and reducing disparities in access to STEM learning.

Its vision is to empower educators, inspire learners, particularly in underserved regions, and integrate research advances into educational practice, thereby fostering curiosity, critical thinking, and future-ready STEM competencies.

11. Role of NIMP

- ***Role in the project:*** *Coordinator*
- ***Main responsibilities:*** *Logistic support and partner in various activities for promoting STEM Education.*

- ***Key personnel involved:*** *3 principal investigators (Sabin Stoica, Mihaela Florea, Andrei Neacşu), 4 senior researchers, 4 junior researchers, and 3 PhD students.*

12. Summary of results obtained in 2025

CIFRA UNESCO

A. Programs/Projects

- *Training and Research in Romanian Labs (TRROL)*. This program offers students and young researchers, mainly from African and Southeastern European countries, the opportunity to undertake training and research stages, on different topics of physics and related domains, in Romanian labs. This program is running in collaboration with ICTP-Trieste. To date, over 100 students have benefited from internships at NIMP and CIFRA, 26 students accomplishing internships during 2024 – 2025.
- "*Integrating and Supporting STEM in the Educational Curriculum through UNESCO Microscience Experiments Project*". This is a hands-on education project that provided opportunities for middle- and high-school students, assisted by teachers, to conduct practical works in basic sciences using educational Kits describing scientific experiments in basic sciences (physics, chemistry, and biology). The project was carried out by CIFRA in collaboration with UNESCO-Venice and in partnership with NIMP and schools from Bucharest and province.

B. Projects Results

- Designing and developing from scratch unique experimental kits in physics, chemistry, and biology to support the teaching and learning of basic sciences in schools;
- Training master trainers, followed by the training of school teachers in the effective use and integration of these kits into classroom activities;
- Establishing and strengthening collaboration between researchers (CIFRA, NIMP) and school teachers to improve curricula and to co-design and produce selected experimental kits;
- Enhancing teacher–student collaboration by engaging them in proposing, designing, and producing experimental kits within schools for hands-on activities in basic sciences;
- Creating a self-sustaining project framework based on teacher–student cooperation, enabling the development of low-cost, personalized experimental kits produced in schools using local resources;
- Increasing students' interest in practical laboratory work, thereby fostering critical thinking, creativity, and problem-solving skills, while simultaneously enhancing teachers' professional development in modern STEM teaching methodologies;
- Implementing a pilot project at the local level, with the perspective of scaling up to regional and national levels.

Figure 1*: Hands-on education project.*

C. Outreach Activities

- Summer school of Science and Technology in Măgurele (2024, 2025).

Approximately 80 high school students participate in this two-week event, during which they engage in various research activities. CIFRA was involved both in the organization of the event and in conducting several experimental activities.

- Researchers' night (2024, 2025).

CIFRA was among the organizers and presented various hands-on experiments.

- Faculty of Physics from A to Z (FFAZ) (2024).

Event for attracting students to attend the Faculty of Physics of the University of Bucharest

- Traveling through Universe (2024).

Around 100 high school students from Bucharest participated in a visit to the Faculty of Physics, engaging in discussions with researchers from the national research institutes located in Măgurele and exploring advanced research laboratories. CIFRA contributed as a co-organizer and presented interactive, hands-on experiments.

***Figure 2**: Outreach activities of CIFRA.*

D. Advanced Training & Capacity Building

- Măgurele Summer School for Computing (30 June–11 July 2025), directors Ivan Girotto (ICTP) and Andrei Neacşu (CIFRA).

This event was jointly organized with ICTP-Trieste and NIMP. A major international training initiative on parallel algorithms, GPU computing, and scientific computing paradigms for early-career researchers, strengthening computational research skills in physics and related areas. Participants: about 50 selected students from countries on 4 continents.

- In 2025, CIFRA had current scientific international collaboration with: ICTP-Trieste, University of Jyväskylä, Finland; Central Michigan University, US; Comenius University, Bratislava; University of Zurich; IFN-Frascati, Italy; WAH University, Pakistan; UNESCO Basic Sciences, research, Innovation and Engineering division; UNESCO Regional Bureau in Venice.
- CIFRA is an ICTP-affiliated centre.
- In July 2025, Prof. Atish Dabholkar, Director of the "Abdus Salam" International Centre for Theoretical Physics (ICTP), visited CIFRA and NIMP. The visit strengthened cooperation with ICTP and paved the way for deeper scientific partnerships. It also supported high-level discussions aimed at expanding institutional collaboration between Romania and ICTP.
- Dr. Sabin Stoica was invited to participate as a panel member at the meeting "Shaping the Future through Science Diplomacy", held in Ljubljana, Slovenia, on 18–19 November 2025.
- Dr. Sabin Stoica received an invitation to join the Editorial Board of the UNESCO Science Report.

***Figure 3**: Măgurele Summer School for Computing.*

E. Promotion of Science Networks

CIFRA continued its role in building regional and global research networks through workshops, seminars, and collaborative programs with international institutes. These activities reinforced its profile as a hub for advanced training linked to UNESCO's scientific capacity-building mandates. CIFRA is founder member of the UNESCO network SCIENSA (https://www.unesco.org/en/sciensa-network) and is member (since December 2025) of the SEENET-MTP (Southeastern European Network in Mathematical and Theoretical Physics).

UNESCO Chair TRRISE – Key Achievements in 2025

In 2025, the UNESCO Chair on STEM Education (TRRISE) at the National Institute of Materials Physics was engaged in a series of activities focused on bridging research and education, STEM outreach, teacher development, and public engagement:

A. Official Launch Event – "Creating BONDS for the Future"

The Chair was formally launched on 24 September 2025 at Oteteleşanu Hall, Măgurele. The event brought together academics, policymakers, educators, and civil society to discuss how research can support inclusive, sustainable STEM education, with keynote talks, panels, roundtables, and the Annual Meeting of UNESCO Chairs in Romania.

B. Participation in the European Researchers' Night 2025

On 26–27 September 2025, TRRISE participated with its own exhibition stand at flagship science festivals held in Măgurele and in Bucharest (Lumea Copiilor Park). The UNESCO Chair showcased interactive demonstrations illustrating how cutting-edge research can be effectively integrated into STEM education and sustainability themes, actively engaging children, young people, teachers, and the general public.

***Figure 4**: Researcher Night 2025.*

C. Educator Development & Knowledge Transfer

On 17–18 November 2025, TRRISE co-organized a mini-series of advanced lectures presented by Dr. Doru Constantin (Institut Charles Sadron, CNRS, Strasbourg, France), addressing state-of-the-art experimental methods and contemporary research themes in materials science.

D. Support & Partnership in Scientific Events

- The UNESCO chair collaborated in the International Chemistry Tournament 2025 (IChTo 2025), helping promote scientific debate and mentorship for high-school students.
- The UNESCO chair was a partner in organising the Summer School – APEX CHEMISTRY 2025 (Academic Program of Excellence in Chemistry). APEX-Chemistry 2025 was an intensive, immersive three-week residential program designed to provide participants with direct exposure to organic chemistry research and scientific discovery. The program accommodates a maximum of 36 participants, who experience the research environment from within, exploring advanced chemical concepts under the guidance of internationally recognized university professors. The invited faculty includes Jean-Marie Lehn (University of Strasbourg, Nobel Prize in Chemistry, 1987), Adrian Şalic (Harvard Medical School), Niculina Hădade (Babeș-Bolyai University of Cluj-Napoca), Ivan Huc (Ludwig Maximilian University of Munich), Mihaela Matache (University of Bucharest), and Mihaela Florea (National Institute for Research and Development in Materials Physics, Măgurele).
  The camp follows an intensive format, comprising lectures, seminars, and a broad range of laboratory activities conducted in the laboratories of the Faculty of Chemistry at the University of Bucharest and at the National Institute for Research and Development in Materials Physics.

***Figure 5**: APEXCHEM 2025.*

E. Ongoing Strategic Vision & Education Outreach

Beyond specific events, the Chair's mission includes:

- Organizing STEM outreach workshops, camps, and competitions for students;
- Developing interactive educational tools and platforms;
- Providing teacher training and capacity-building programs in innovative pedagogies;
- conducting research on best practices in STEM education;
- Building national and international partnerships with universities, research centres, and UNESCO networks.

Through its activities, TRRISE worked to enhance teacher skills, promote inclusive educational practices, and advocate for the integration of modern scientific insights into curricula, contributing to UNESCO's goals for equitable, high-quality education.

Together, CIFRA and the UNESCO Chair TRRISE at NIMP made significant contributions in 2025 by:

- Advancing scientific expertise and research capacity through targeted training, international cooperation, and summer schools;
- Strengthening public understanding of science, particularly in STEM education and the integration of research into teaching;
- Fostering inclusive education and knowledge transfer, aligning research excellence with educational transformation and societal needs;
- Enhancing Romania's international scientific and educational engagement within the UNESCO network.

13. Dissemination and visibility

- ***Media coverage:***
  - *X: https://x.com/cifra_c2unesco*
  - *Instagram: https://www.instagram.com/trrise.unescochair/*
  - *LinkedIn: https://www.linkedin.com/company/cifra-c2unesco/; https://www.linkedin.com/posts/incdfm_the-unesco-chair-for-education-in-stem-trrise-activity-7407776073112870912-TFZQ*
  - *Facebook: https://www.facebook.com/p/Transfer-of-the-Research-Results-into-STEM-Education-61578080074142/; https://www.facebook.com/people/Centre-International-de-Formation-et-de-Recherche-Avanc%C3%A9es-en-Physique/61563541726319/*
  - *Press interview published in Gândul newspaper: www.gandul.ro/actualitate/cum-pot-revolutiona-kit-urile-experimentale-procesul-educational-pentru-stem-problema-esentiala-este-cum-se-preda-si-cum-se-invata-20366100*
- ***Project website:***
  - *https://cifra-c2unesco.ro/*
  - *https://cifra-c2unesco.ro/projects/integrating-and-supporting-stem-in-the-educational-curriculum-through-unesco-microscience-experiments-project/*
  - *https://trrise-unesco.infim.ro/*

14. Contact information

- ***Contact person:*** *Dr. Sabin Stoica / Dr. Mihaela Florea*
- ***E-mail:*** *sabin.stoica@cifra-c2unesco.ro / mihaela.florea@infim.ro*

Annual report on the progress of the NIMP collaborations conducted within the framework of the Central European Research Infrastructure Consortium (CERIC-ERIC)

1. Mission and scope

The Central-European Research Infrastructure Consortium (CERIC-ERIC) represents an integrated scientific platform providing open access to some of the most advanced analytical facilities in Europe, contributing to the progress of science and technology in the fields of advanced materials, biomaterials, nanotechnology, and life sciences. With a single entry-point to leading national research organisations in eight European countries, it enables the delivery of innovative solutions to societal challenges such as energy, health, food, cultural heritage and more. As founding member of the consortium, NIMP offers open access to advanced scientific instrumentation of analytical Transmission Electron Microscopy and multifrequency Electron Paramagnetic Resonance spectroscopy to academic or industrial users worldwide, by semesterly calls. In collaboration with external users worldwide, selected on a competitive basis, NIMP performs investigation of atomic structures, interfaces, phase transitions, extended and point defects by microscopic (HRTEM, STEM) and spectroscopic (multifrequency EPR) methods to understand the structure-functionality correlations in advanced application-oriented materials (nanoparticles, thin films, ceramics and special alloys).

2. Overview of research visits

The table below summarizes the research visits hosted by NIMP in 2025, carried out in the framework of 10 CERIC-funded proposals (from CERIC Calls 19 and 20) and 2 Horizon Europe projects in which NIMP participates as a CERIC Partner Facility.

No.	Researcher(s) name	Home institution	Research theme/title	Infrastructure used	NIMP supervisor(s)	Access period
1.	Andrea BRAGA	Università degli Studi di Udine, ITALY	Surface and morphological studies of dual function materials for the CO_2 capture and methanation	TEM	Marian Cosmin ISTRATE Corneliu Ghica	08.04.2025-10.04.2025
2.	Carla CANNAS	Università degli Studi di Cagliari, ITALY	Composition, structure and morphology of nanostructured ceria-based catalysts for CO_2 conversion into dimethyl carbonate and methane	TEM	Valentin Adrian MARALOIU	05.03.2025-07.03.2025
3.	Yuliia SHLAPA	National Academy of Science, UKRAINE	Microscopy examination of Fe_3O_4@CeO_2 nanocomposites: morphology and microstructure vs synthesis conditions	TEM	Valentin Adrian MARALOIU	07.05.2025-09.05.2025
4.	Paolo CENTOMO	Università degli Studi di Padova, ITALY	Correlation among synthesis, structure and performance: Operando XAFS insights into Fe-Cu-SSZ-13 catalysts	TEM	Marian Cosmin ISTRATE	18.03.2025-20.03.2025
5.	Gianluca D'OLIMPIO	Università degli Studi dell'Aquila, ITALY	Exploring the catalytic potential of magnetic metal phosphorus chalcogenides for energy applications	TEM	Corneliu GHICA Marian Cosmin ISTRATE	22.05.2025-23.05.2025
6.	Gianluca D'OLIMPIO	Università degli Studi dell'Aquila, ITALY	Exploring surface oxidation and gas sensing capabilities of two-dimensional indium telluride for NO_2 detection	TEM	Corneliu GHICA Marian Cosmin ISTRATE	18.06.2025-19.06.2025
7.	Viktoriya PODHURSKA	National Academy of Sciences, UKRAINE	Development of an electrically conductive coating for current collectors of lightweight solid oxide fuel cells	TEM	Cristian RADU Marian Cosmin ISTRATE	10.11.2025-12.11.2025
8.	Daniel Pawel JAWORSKI	Gdansk University of Technology, POLAND	Elemental and phase ordering in high-entropy perovskite oxides for energy conversion	TEM	Andrei Cristian KUNCSER	27.10.2025-28.10.2025

No.	Researcher(s) name	Home institution	Research theme/title	Infrastructure used	NIMP supervisor(s)	Access period
9.	Arsenii TYMOSHENKO	National Academy of Sciences, UKRAINE	Study of the influence of Mg^{2+} and Si^{4+} dopants on the growth of YAG:Sm^{3+} single crystals by the SSCG method	TEM	Valentin Adrian MARALOIU	17.11.2025-18.11.2025
10.	Mustafa Saeed Ahmed SHALABY	National Centre for Radiation Research and Technology, EGYPT	Investigating the crystal structure and magnetic properties of doped-BSCCO high-temperature superconductors using neutron diffraction and EPR	EPR	Mariana STEFAN Daniela GHICA	20.10.2025-24.10.2025
11.	Anna WCISŁO	University of Gdańsk, POLAND	Secondment in the frame of the Horizon Europe project "Accelerating ERA by sharing unique talents for healthy life and environment", HORIZON-WIDERA-2022-TALENTS-03/ Project No. 101120502	EPR	Mariana STEFAN	15.09.2025-15.12.2025
12.	Jacinto SA	Duck Technologies AB, SWEDEN	Imaging plasmonic nanoparticles for enhanced heat-reflective nanocoatings, in the frame of Horizon Europe project "ReMade@ARI" HORIZON-INFRA-2021-SERV-01/ Project No. 101058414	TEM	Valentin Adrian MARALOIU Corneliu GHICA	14.07.2025-18.07.2025

The CERIC proposals granted in 2025 addressed a broad spectrum of materials and topics with high societal relevance, including materials for the low-carbon economy, biomedical applications, and energy storage and conversion.

3. Key results and impact

Highlights concerning experiments and preliminary results of CERIC proposals granted in 2025:

A. <u>Materials for Low-carbon Economy</u>

- Dual Function Materials (DMFs) materials (DFMs) for CO_2 capture and valorisation are currently being investigated to reduce emissions from point sources. The studied DFMs consist of Na and Ru phases dispersed on Al_2O_3, prepared by green mechanochemical methods. We are examining the effect of different milling parameters on various Ru and Na precursors, aiming to achieve high CO_2 capture capacities and enhanced CH_4 production rates. Our goal is to elucidate the structure-activity relationships and understand how the synthesis influences the resulting morphologies. TEM-EDXS measurements performed at NIMP have been used to map the distribution of capture and catalytic sites, enabling correlations between milling parameters, surface composition, and the catalytic performance of the materials.
- Ceria-based nanostructured materials are widely investigated for their ability to exhibit high and tunable concentrations of oxygen vacancies at the surface, making them promising heterogeneous catalysts for carbon capture and utilization technologies. Ceria nanomaterials synthesized by various chemical routes (solvothermal, sol-gel, solution combustion, soft-template) have been tested for CO_2 conversion to dimethyl carbonate and methane. Key factors influencing catalytic performance include structural defects, metal substitution, particle morphology, and grain faceting. HRTEM and nanoscale chemical mapping using STEM-EDXS and STEM-EELS were performed at NIMP to characterize the types of defects, exposed crystal facets, and elemental distribution at the nanoscale. These analyses also enabled the study of metal ion incorporation or segregation in substituted ceria and the investigation of interfaces between multiple structural phases.
- Cu-based SSZ-13 zeolites are known to provide excellent catalytic performance in partial oxidation of CH_4 to CH_3OH. The work aimed to investigate the dynamics of Cu and Fe species in Fe-Cu-SSZ-13 zeolites during CH_4-to-CH_3OH oxidation using N_2O as the oxidant. HRTEM

characterization, including analytical capabilities for imaging of the catalyst ionic species at the atomic or near-atomic scale, provided high-resolution structural information which, in connection with XAFS information, helped finding possible correlations between the features of the active sites and the catalytic behaviour of the materials. HRTEM characterization has been applied to provide quantitative information about nanoparticles shape and size distribution, local crystallographic phases and dispersion of the active Fe-Cu phase.

B. Materials for Biomedical Applications

- The goal of the TEM investigations performed at NIMP was to evaluate the morphology of Fe_3O_4@CeO_2 nanocomposites prepared *via* the precipitation of CeO_2 nanoparticles onto the surface of pre-synthesized magnetic Fe_3O_4, thus providing information regarding the type of formed composites and the way in which the functionalization of magnetic nanoparticles and the chemical reagents affected the morphology of the obtained composites. Together with the experimental data obtained after the physicochemical characterization of the developed nanocomposites, a complete picture of the physicochemical and morphological features of the proposed composites will be gained, helping to understand the interplay between their physicochemical and biological properties, while pointing to the optimisation of the synthesis route.

C. Materials for Energy Storage and Conversion

- Metal thiophosphites (MPS_x) have recently attracted significant attention due to their unique layered structures and versatile anisotropic properties such as magnetic and antiferromagnetic behaviour, wide-range band gaps, and promising electrochemical performance in heterogeneous electron transfer, hydrogen evolution reaction (HER), oxygen evolution reaction (OER), and oxygen reduction reaction (ORR). In this work, we focused on the catalytic activity and surface chemical reactivity of $CrPS_4$. The HRTEM investigations performed on exfoliated $CrPS_4$ nanosheets has evidenced the formation of oxide layers, agglomerates, and structural defects that contribute to the enhanced catalytic performance. This comprehensive analysis, combining scanning photoelectron microscopy and *operando* XPS, provided insights into the mechanisms underlying the enhanced catalytic activity, elucidating the structure–activity relationships, and supporting the development of future applications in sustainable energy technologies.
- Solid oxide fuel cells operate at temperatures of 600–800 °C to convert chemical energy into electrical energy with an efficiency of 65–70%. Interconnecting materials based on highly alloyed steels have a significant contribution to the weight of the stacks. Sintered composites based on MAX phases of Ti have recently raised the interest as candidate materials for fuel cell interconnects. Analytical HRTEM has been applied to conduct a comparative analysis of the change in the characteristics of oxidation resistance during long term exposure (1000 h) at 600 °C in air and a mixture of hydrogen and water vapor depending on the chemical and phase composition of the coating system.

These experimental data and preliminary results are currently being processed and analyzed in collaboration with the submitting partners and will be incorporated into manuscripts for publication in peer-reviewed scientific journals.

Results published in 2025 in collaboration with CERIC users:

- Electron paramagnetic resonance (EPR) experiments and density functional theory (DFT) calculations evidenced the possibility of exciting an oxygen molecule from its ground triplet state S = 1 to an excited doublet state S = 1/2 at room-temperature after stable physical adsorption on the defect-free surface of bulk VSe_2, without the need for UV irradiation or radical-like states on the substrate (*Fig. 1*). These findings in collaboration with the team lead by Prof. A. Politano at the University of L'Aquila, Italy, have tremendous potential for various applications, including

organic synthesis and medicine [1]. The investigations have been performed in the frame of CERIC Grant No. 20212215.

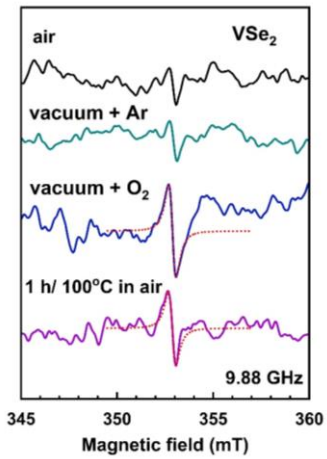

***Figure 1**: Successive EPR spectra recorded on a VSe_2 sample exposed to different atmospheres (air, Ar, and O_2) and after annealing in air at 100 °C for 1 h [1].*

- Analytical HRTEM investigations at NIMP elucidated the distinctive characteristics of garnet formation in Gd-doped yttrium-iron ferrites (YIG) as a function of Gd concentration and thermal treatment temperature (*Fig. 2*). These findings contributed to the fundamental understanding of garnet phase formation and demonstrate a scalable route for producing low-porosity, high-performance polycrystalline ferrites suitable for advanced UHF and microwave device applications. This work also layed the foundation for future studies on dopant-driven phase engineering in garnet systems, bridging the gap between materials synthesis and device optimization.

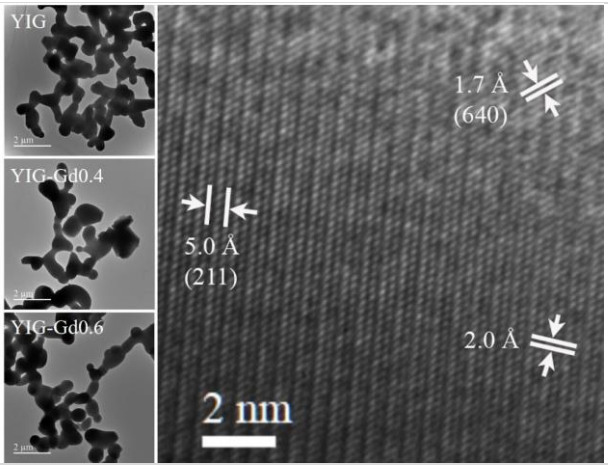

***Figure 2**: Representative CTEM and HRTEM images of selected Gd-doped YIG garnets obtained after 1200 °C [2].*

This work has been performed in collaboration with research groups from the V.I. Vernadsky Institute of General and Inorganic Chemistry of the NAS of Ukraine, V.G. Baryakhtar Institute of Magnetism of the NAS of Ukraine, and the Educational and Scientific Institute of High Technologies, Taras Shevchenko National University of Kyiv [2]. The TEM investigations have been done in the frame of CERIC Grant No. 20247161.

NIMP activity in CERIC-related collaborations within European projects:

- "*Accelerating ERA by Sharing Unique Talents for healThy Life and Environment*" (ERA SHUTTLE), HORIZON-WIDERA-2022-TALENTS-03, Grant Agreement 101120502. CERIC-ERIC is a member of the Project Consortium, while NIMP represents a Project Affiliated Entity as CERIC-ERIC member (https://erashuttle.eu/era-partners/):
  NIMP hosted Dr. Anna Wcislo, Assist. Prof. at the University of Gdansk, Poland for a three-month secondment within the group of Electron Paramagnetic Resonance spectroscopy. Dr. Wcislo acquired theoretical and practical information concerning the EPR spectroscopy, including hands-on training in operating X- and Q-band EPR spectrometers. In collaboration with the members of the EPR group, she used the developed skills in the investigation of various advanced materials, including functionalized magnetite nanoparticles and Au@SiO_2 and Ag@SiO_2 core-shell nanostructures synthesized at the University of Gdansk. As per the project requirements, the knowledge and skills acquired during the secondment will be transferred to her home institution through the implementation of the developed EPR methodology in ongoing and future research on magnetic nanomaterials.
- *"REcyclable MAterials Development at Analytical Research Infrastructures*" (ReMade@ARI) – HORIZON-INFRA-2021-SERV-01, Grant Agreement 101058414. CERIC-ERIC is a member of the Project Consortium, while NIMP represents a Project Affiliated Entity as CERIC-ERIC member (https://remade-project.eu/index.php/what-is-remadeari/partners-and-consortium-members/):
  In 2025, NIMO hosted the proposal "*Imaging Plasmonic Nanoparticles for Enhanced Heat-Reflective Nanocoatings*" submitted by Duck Technologies AB, Sweden, performing microstructural characterisation of silver nanoplatelets for applications in heat management in buildings and vehicles.
- "*Novel Nanotechnology-Enabled Therapeutics to Treat Systemic Disorders and Skin Lesions in Victims of Large-Scale Radiation Injuries*" (SMARTMat-RAD) – NATO Science for Peace and Security, grant G8914:
  As a follow-up of the fruitful collaboration inside CERIC between NIMP and V.I. Vernadsky Institute of General & Inorganic Chemistry, National Academy of Sciences in Ukraine, a new research idea was born, leading to the submission of a project proposal to the NATO Science for Peace and Security call of January 2025, being an international collaboration between:
  - Institute of Experimental Physics, Slovak Academy of Sciences, Kosice, Slovakia (CO);
  - V.I. Vernadsky Institute of General & Inorganic Chemistry, National Academy of Sciences, Kiev, Ukraine (P);
  - R.E. Kavetsky Institute of Experimental Pathology, Oncology and Radiobiology of the National Academy of Sciences, Kiev, Ukraine (P);
  - Basque Centre for Materials, Applications & Nanostructures (BCMaterials), Leioa, Bizkaia, Spain (P);
  - National Institute of Materials Physics (NIMP), Măgurele, Romania (P).

  The proposal was granted in December 2025 and has been formally launched on February 1, 2026.
  The NIMP research team will assess the morphological, structural, and compositional characteristics of synthesized nanomaterials, composites, and hydrogels using the available electron microscopy techniques, including SEM, CTEM, HRTEM, HAADF-STEM, EDXS, and EELS.

NIMP contribution in training and education activities within CERIC:

CERIC promotes and supports training actions for students and researchers. In this context, two PhD students at NIMP have benefited from CERIC support during their doctoral activity [A,B], for research visits at CERIC partner facilities as well as for their participation in training schools and scientific conferences [a–e]. In addition, as a follow-up of the successful collaboration in the CERIC proposals no. 20217169, 20227247, and 20232128 resulting, among others, in one scientific publication [3] and two PhD theses defended in 2024 [C,D], a new PhD program has been agreed with the Laboratory of Molecular Pathology at the University of Trieste, including a 3 months secondment at NIMP to be accomplished by a PhD student

in 2026, in order to acquire new skills in the field electron microscopy for the mineralogical characterization of elongated mineral particles (asbestos, erionite, and antigorite) in interaction with biological fluids [E].

NIMP participation in other CERIC integration activities:
In line with CERIC-ERIC's aims and objectives related to strengthening cutting-edge research in Life Sciences, the scientific workshop "*CERIC's Future in Life Sciences: A Focus on Aging*" has been organised in Warsaw, Poland, on October 13–15, 2025. The workshop was dedicated to exploring the theme of aging through the lens of advanced structural and molecular techniques. Featuring presentations from scientists utilizing methods including cryo-electron microscopy (cryo-EM), nuclear magnetic resonance (NMR), small-angle X-ray scattering (SAXS) as well as emerging approaches in biomaterials research, the event was aimed to strengthen the bridge between the large-scale research infrastructures offers at CERIC and the biomedical research community. In addition, the event hosted a panel discussion focused on the practical aspects of accessing large infrastructures, navigating multi-technique research, and fostering collaboration across disciplines and borders. Three researchers attended the event on behalf of NIMP, Dr. Victor Diculescu, Dr. Valentin Adrian Maraloiu, and Dr. George Stan, highlighting the current interests and research topics approached at NIMP in relation to Life Sciences, opening new collaboration opportunities within CERIC as well as in the coming Horizon Europe calls.

4. Outputs and deliverables

4.1 Publications

[1] D.W. Boukhvalov, M. Stefan, A. C. Joita, C.-N. Kuo, C.S. Lue, A. Politano, *Charge transfer-driven conversion of molecular oxygen to doublet state on vanadium diselenide (VSe_2) surface at room temperature*, Advanced Materials and Interfaces 12 (2025) 2400656.

[2] Y. Shlapa, L. Kovalenko, I. Lisovskyi, V. Zamorskyi, V.A. Maraloiu, A. Tovstolytkin, M. Popov, H. Chumak, A. Belous, *Structure formation and physical properties of Gd-doped Yttrium-Iron Ferrites: Nonlinear concentration–temperature effects and phase-dependent magnetic behaviour*, Ceramics International 53 (2026) 6277–6290.

[3] M. Zangari, F. Piccirilli, L. Vaccari, C. Radu, P. Zacchi, A. Bernareggi, S. Leone, G. Zabucchi, V. Borelli, *Ferritin adsorption onto chrysotile asbestos fibers influences the protein secondary structure*, Heliyon 10 (2024) e38966.

4.2 Theses and academic works

[A] C.G. Mihalcea, *Nanostructured materials for gas sensors: correlations between functional, electronic and microstructural properties* (ongoing), PhD thesis, University of Bucharest, Romania, final year of the research stage.

[B] C. Radu, *Application of electron microscopy techniques in studying materials with semiconductor or ferroic properties* (ongoing), PhD thesis, University of Bucharest, Romania, final year of the research stage.

[C] M. Zangari, *On the role played by protein-asbestos fibre interaction in asbestos toxicity: a multi-technique approach from single fibre to cellular milieu* (completed), PhD thesis, University of Trieste, Italy, 2024.

[D] O.V. Zikrata, *Conversion of n- and i-butanol on metal oxide and zeolite catalysts with the production of alkenes and higher alcohols* (completed), PhD thesis, L. V. Pisarzhevskii Institute of Physical Chemistry of the National Academy of Sciences, Kiev, Ukraine, 2024.

[E] A. Marconato, *Elongated mineral particles in biological fluids: A possible key for modelling their in vivo behaviour* (ongoing), PhD thesis, La Sapienza Università di Roma, Italy, 3rd year of the research stage.

4.3 Other outputs (conferences, white papers, patents, prototypes)

[a] C.G. Mihalcea, C. Ghica, A. Stanoiu, C.E. Simion, D. Ghica, M. Stefan, S. Somacescu, I.D. Vlaicu, A.C. Iacoban, *Morphological and structural characterization of metal oxide semiconductors with applications in gas sensing*, Poster presentation at the Quantitative electron microscopy 2025 – QEM 2025, Port-Barcares, France, 11–23 March 2025.

[b] C. Radu, *Morphological and structural characterization of ferroic materials using electron microscopy techniques*, Poster presentation at the Quantitative electron microscopy 2025 – QEM 2025, Port-Barcares, France, 11–23 March 2025.

[c] C. Ghica, C.G. Mihalcea, D. Ghica, M. Stefan, A. Stanoiu, C.E. Simion, I. D. Kuncser, A.C. Iacoban, O. Florea, S. Bulat, *Contribution of nanoscale morphology in tailoring the gas sensing properties of SnO_2-based nanopowders*, Oral

presentation at the 6th Conference of the Romanian Electron Microscopy Society, Poiana Brasov, Romania, 01–02 October 2025.

[d] C. Radu, *Dipolar interactions influence on magnetic properties of nanoparticle systems: Insights from electron tomography and micromagnetic simulations*, Oral presentation at the 6th Conference of the Romanian Electron Microscopy Society, Poiana Brasov, Romania, 01–02 October 2025.

[e] C.G. Mihalcea, *Correlations between the synthesis route and the morpho-structural properties of nickel oxide nanoparticles with applications in gas sensing*, Oral presentation at the 6th Conference of the Romanian Electron Microscopy Society, Poiana Brasov, Romania, 01–02 October 2025.

Annual report on the hosting of scholarship students and postdoctoral researchers, and collaborative activities at NIMP within the AUF–Eugen Ionescu, ITCP, and other international programs

1. Mission and scope

At NIMP, internationalization is a strategic driver of scientific excellence, innovation, and global competitiveness. By hosting scholarship students, postdoctoral researchers, and engaging in programs such as AUF–Eugen Ionescu, ITCP, and other international initiatives, NIMP attracts top talent, expands its research capabilities, and strengthens its global reputation.

The institute fosters intercultural skills, language proficiency, and access to diverse scientific knowledge, preparing researchers to excel in a globally connected scientific environment. Through collaboration with international partners, participation in joint projects, and integration into global research networks, NIMP enhances its capacity for innovation, builds a qualified talent pipeline, and contributes to solving pressing global challenges.

By combining strategic push factors (such as demographic trends, available funding, and the need for highly qualified teams), with pull factors (like access to global expertise and complementary research capabilities), NIMP positions itself as a hub of world-class science, education, and international collaboration.

2. Overview of research stages and access periods

No.	Researcher name *Academic status*	Home institution	Program	Research theme/title	Infrastructure used	NIMP supervisor(s)	Access period
1.	Marwene OUMEZZINE Postdoc	University of Monastir, Monastir, TUNISIA	COST STSM, CA20116 – OPERA	Epitaxial spin valve structures of functional La–Ba–Mn-Ti-O manganite for memory applications	PLD XRD TEM Electrical measurements lab PPMS	A.C. GÂLCĂ	09.03.2025-08.04.2025
2.	Messaoud TAMIN *PhD student*	Ferhat Abbas University Setif 1, Sétif, ALGERIA	CIFRA/ICTP Trieste grant	Development of wide-bandgap chalcogenide devices for advanced photovoltaic applications	XRD XPS SEM Magnetron sputtering Ellipsometry Raman Spectroscopy Photovoltaics lab	A.C. GÂLCĂ	01.05.2025–30.07.2025
3.	Nouhaila BENAISSA *Postdoc*	Chouaïb Doukkali University, El Jadida, MOROCCO	Co-financing provided by the home university and NIMP-CIFRA	Solution deposited Sb_2S_3 light absorbing thin films: enhancing efficiency in photovoltaic devices	Spray pyrolysis XRD SEM Magnetron sputtering Ellipsometry Photovoltaics lab	A.C. GÂLCĂ	12.05.2025–29.07.2025
4.	Assia KARRAB *Postdoc*	University of Gabes, Gabes, TUNISIA	Eugen Ionescu scholarship–AUF/MAE	Photoelectrochemical generation of H_2 from SiO/CdS/FST photoanodes/nickel-based co-catalyst: application to the photoelectrochemical conversion of ammonia and urea	Electrochemistry lab	M. FLOREA	15.05.2025-31.07.2027
5.	Panupol UNTARABUT *PhD student*	University of Limoges, Limoges, FRANCE	Funding provided by the home university	Ceramic materials characterization	Electrical measurements lab	L. PINTILIE	13.05.2025–16.05.2025

No.	Researcher name *Academic status*	Home institution	Program	Research theme/title	Infrastructure used	NIMP supervisor(s)	Access period
6.	Essodossomondom ANATE PhD student	University of Kara, Kara, TOGO	Eugen Ionescu scholarship–AUF/MAE	Synthesis and characterization of perovskite-based photovoltaic cells	XRD SEM Spray pyrolysis Magnetron sputtering Ellipsometry Photovoltaics lab	L.N. LEONAT	27.05.2025–29.07.2025
7.	Sana HANDOR *PhD student*	Sultan Moulay Slimane University, Béni Mellal, MOROCCO	Eugen Ionescu scholarship–AUF/MAE	Optimization of solar cells based on hybrid perovskite materials $CH_3NH_3PbI_{2.6}Cl_{0.4}$: Towards more efficient and sustainable photovoltaics	XRD SEM Magnetron sputtering Spray pyrolysis Ellipsometry Photovoltaics lab	L.N. LEONAT	28.05.2025–29.07.2025
8.	Rayene MERAH *PhD student*	University Frères Mentouri Constantine 1, Constantine, ALGERIA	COST STSM, CA21148 – RENEW-PV	Optimisation of the performance of spray-deposited Sb_2S_3 absorbing thin films: Enhancing efficiency in photovoltaic devices	Spray pyrolysis XRD SEM Magnetron sputtering Ellipsometry Photovoltaics lab	A.C. GÂLCĂ	31.05.2025–18.08.2025
9.	Florian COTHENET *MSc student*	ISTP Saint-Etienne, Saint-Etienne, FRANCE	Erasmus+ mobility	Realization of a magnetic field controller based on Helmholtz coils for a MOKE equipment		I.A. IVAN	10.06.2025–12.09.2025
10.	Katharina Elena DEHM *PhD student*	Friedrich-Alexander-Universität Erlangen-Nürnberg, Erlangen, GERMANY	COST STSM, CA21148 – RENEW-PV	All-inorganic antimony sulfide solar cells using $CuInS_2$ quantum dots for hole extraction and transport	XRD TEM SEM Magnetron sputtering Ellipsometry Raman Spectroscopy Photovoltaics lab	A.C. GÂLCĂ	13.06.2025–26.06.2025
11.	Selina KERN *PhD student*	Friedrich-Alexander-Universität Erlangen-Nürnberg, Erlangen, GERMANY	COST STSM, CA21148 – RENEW-PV	Advancements in all-inorganic cadmium-free antimony sulfide solar cells	XRD TEM SEM Magnetron sputtering Ellipsometry Raman Spectroscopy Photovoltaics lab	A.C. GÂLCĂ	13.06.2025–26.06.2025
12.	Aagrah AGNIHOTRI *PhD student*	University of Jyväskylä, Jyväskylä, FINLAND	CIFRA/ICTP Trieste grant	Study of nuclear weak interaction processes with implications to physics beyond the Standard Model		S. STOICA	29.06.2025–03.08.2025
13.	Messaoud TAMIN *PhD student*	University of Ferhat Abbas Setif 1, Sétif, Algeria, & Bourgogne Europe University, Dijon, FRANCE	COST STSM, CA21148 – RENEW-PV	Semi-transparent wide band gap kesterite solar cells for indoor and tandem applications	XRD XPS SEM Magnetron sputtering Ellipsometry Spray pyrolysis Photovoltaics lab	A.C. GÂLCĂ	16.08.2025–30.09.2025
14.	Mariem BRAHIM *PhD student*	University of Monastir, Monastir, TUNISIA	Tunisian MESRS mobility grant	Synthesis, characterization and applications of new functional materials based on calcium phosphate		D. PREDOI	01.09.2025–31.10.2025

No.	Researcher name *Academic status*	Home institution	Program	Research theme/title	Infrastructure used	NIMP supervisor(s)	Access period
15.	André Sampaio PEREIRA *PhD student*	Universidade de Lisboa, Lisbon, PORTUGAL	Co-financing provided by the home university and NIMP-CIFRA	W-based high entropy alloys as thermal barriers in future nuclear fusion reactors	Thermoelectrics lab SEM EDX Ceramic sintering lab	A. GALAȚANU	04.09.2025–10.09.2025
16.	Kacper WALCZYK *BSc student*	University of Warsaw, Warsaw, POLAND	Co-financing provided by the home university and NIMP-CIFRA	Organic light emitting diodes: Fabrication and characterization		I.C. CIOBOTARU	08.09.2025–23.09.2025
17.	Anna WCISŁO *Postdoc*	University of Gdańsk, Gdańsk, POLAND	Funding provided by the home university	Advanced oxidative modification processes	EPR	M. ȘTEFAN	15.09.2025–15.12.2025
18.	Aibota KADIRBYEK *MSc student*	Karadeniz Technical University, Trabzon, TURKEY	Erasmus+ mobility	Superconductors for levitation and related applications		P. BĂDICĂ	26.09.2025–03.12.2025
19.	Dumitru UNTILĂ *Postdoc*	Moldova State University, Chisinau, REPUBLIC OF MOLDOVA	Funding provided via EMPOWER RO-MD project	$Sb_2(S,Se)_3$ solar cells	XPS TEM XRD Magnetron sputtering Ellipsometry Photovoltaics lab Tubular furnance	A.C. GÂLCĂ	13.10.2025–28.10.2025
20.	Serghei BÎZGAN *Postdoc*	Moldova State University, Chisinau, REPUBLIC OF MOLDOVA	Funding provided via EMPOWER RO-MD project	Modelling of $Sb_2(S,Se)_3$ solar cells		A.C. GÂLCĂ	24.10.2025–02.11.2025
21.	Abdelbassat KENANE *Postdoc*	Mustapha Stambouli University of Mascara, Mascara, ALGERIA	Co-financing provided by the home university and NIMP-CIFRA	Study of hybrid materials composed of carbon nanotubes embedded in polymer matrices		O. RAȘOGA	26.10.2025–08.11.2025
22.	Dumitru RUSNAC *PhD student*	Moldova State University, Chisinau, REPUBLIC OF MOLDOVA	Funding provided via EMPOWER RO-MD project	Development of $Sb_2(S,Se)_3$ solar cells	Ellipsometry Electrical measurements lab	A.C. GÂLCĂ	30.10.2025–30.11.2025
23.	Achmad NASYORI *PhD student*	Tallinn University of Technology (TALTECH), Tallinn, ESTONIA	Co-financing provided by the home university and NIMP-CIFRA	Development of solution-processed kesterite absorbers for thin film solar cells	TEM XRD	A.C. GÂLCĂ	14.12.2025–20.12.2025

3. Key results and impact

Most collaborative efforts focused on the development of new materials and novel devices for applications in photovoltaic conversion (hybrid perovskite and chalcogenide solar cells), light emission (photodiodes), energy storage (supercapacitors and rechargeable batteries), and catalysis (photocatalysis).

- We reported [1] the successful synthesis of $(Ag, Cu)_2ZnSnS_2$ (ACZTS) thin films *via* a scalable and controllable chemical solution process, facilitating the precise fine-tuning of the Ag/(Ag + Cu) molar ratio, thereby enabling optimal control over the film properties. Higher Ag/Cu ratios led to significant larger bandgaps, from 1.52 eV for the pure CZTS to 1.68–1.71 eV for high Ag alloys, thus by absorber engineering, making those materials suitable for new applications, such as tandem and indoor photovoltaics.

- We demonstrated [2] the critical role of deposition techniques and electron transport layer (ETL) thickness optimization in the performance of perovskite solar cells. The gas-assisted spray deposition under ambient conditions allows for precise tuning of film thickness and quality simply by adjusting the number of spray passes to produce both compact (c-TiO_2) and mesoporous (m-TiO_2) films with precise control, free from defects like cracks or pinholes and for achieving complete surface coverage. The m-TiO_2 layer effectively reduced hysteresis and series resistance, resulting in improved fill factor (FF) and higher power conversion efficiency (PCE). Controlling the thickness of the TiO_2 layers is also critical, as excessively thick electron transport layers (ETLs) can hinder charge transport and increase resistance.
- We characterized [3] thin films of conducting oxides, ITO and AZO, before and after proton irradiation, showing that the high-energy proton environment has a slight negative influence on the properties of transparent conductive oxide thin films, proving they are good candidates as functional layers in space applications.
- We provided [4] detailed insights into how varying Sr levels modulate the band gap, phase transitions, and relaxation dynamics in $Ba_{1-x}Sr_xTiO_3$ ceramics, for optimizing these materials for advanced applications, including self-powered photodetection and photocatalysis, highlighting their significant potential in emerging technologies.
- SnSe thin films with potential use in photovoltaics/photodetectors were successfully fabricated [5] by single-step electrodeposition on ITO/glass substrates, showing that the deposition potential strongly influences their structural, morphological, and optical properties. The main challenge would be to smart wise succeed the electrodeposition on low conductive surface of the electron transport layer, and later to complete and test an optoelectronic device.
- The electrochemical performances of the V_2O_5/FTO/glass systems were evaluated [6] in different aqueous electrolytes at different concentrations, using cyclic voltammetry, galvanostatic charge–discharge, and electrochemical impedance spectroscopy measurements, underlying the case of most favourable supercapacitive performance.
- We highlighted [7] the tuneable optoelectronic properties of $Sb_{1-x}Bi_xSeI$, showing that increasing the Bi relative concentration will reduce nonlinearly the band gap from 1.7 eV (SbSeI) to 1.29 eV (BiSeI), positioning the material within the optimal energy range for photovoltaic absorbers.

4. Outputs and deliverables

4.1 Publications

[1] M. Tamin, O. El Khouja, M. Guemmaz, C. Tamin, A.E. Bocirnea, I. Assahsahi, D. Choumont, A.C. Galca, *Towards a wide bandgap absorber: structural, morphological, and optical investigation of Ag-alloyed Cu_2ZnSnS_4 thin films*, Sustainable Energy & Fuels 9 (2025) 6751–6760.

[2] S. Handor, A.G. Tomulescu, V. Stancu, A. Razouk, A.C. Galca, L.N. Leonat, Gas-assisted spray fabrication of reticulated TiO_2 scaffolds for perovskite solar applications, Micromachines 16 (2025) 685.

[3] K. Ungeheuer, J. Rybak, A.E. Bocirnea, D.A. Pikulski, A.C. Galca, K.W. Marszalek, *Influence of proton irradiation on thin films of AZO and ITO transparent conductive oxides—simulation of space environment*, Applied Sciences 15 (2025) 754.

[4] Y. Zidi, O. Khaldi, R.E. Patru, L.N. Leonat, M. Enculescu, V. Toma, A. Stepanova, R. Ben Younes, A.C. Galca, *Experimental and theoretical perspective on band gap modulation in Sr^{2+} modified $BaTiO_3$ capacitors*, Ceramics International 51 (2025) 18166–18177.

[5] A. El Kanouny, R. Elotmani, A. El Manouni, O. El Khouja, I. Assahsahi, A. Almaggoussi, A.C. Galca, *Electrodeposition of SnSe nanosheets: Effect of deposition potential on structural, morphological, and optical properties*, Applied Physics A-Materials Science & Processing 131 (2025) 979.

[6] L. Akabbouch, O. El Khouja, I. Assahsahi, S. Dassallem, Y. Ait-alla, M. Fahoume, T. Tite, A.C. Galca, K. Nouneh, *Charge storage mechanism and supercapacitive behavior of transparent vanadium pentoxide thin films in various aqueous electrolytes*, Results in Engineering 28 (2025) 107836.

[7] M. Dolcet Sadurni, K. Timmo, V. Mikli, J. Krustok, M. Danilson, A. Suchodolskis, C. Radu, A.E: Bocirnea, A.C. Galca, M. Grossberg-Kuusk, M. Kauk-Kuusik, Effects of cationic substitution on the properties of $Sb_{1-x}Bi_xSeI$ (x = 0–1) compounds, Journal of Alloys and Compounds 1037 (2025) 182292.

4.2 Theses and academic works

[A] R. ElOtmani, *Développement de couches minces de SnS et CZT(S, Se): Croissance, intégration dans des cellules solaires et modélisation numérique* (completed), PhD thesis, Faculté des Sciences et Techniques-Mohammedia, Hassan II University, Mohammedia, Morocco, 2025 (year of defence), research stages in 2023 and 2024.

[B] Y. Zidi, *Ab initio study and experimental characterization of the physical properties of functional oxide-based material alloys* (completed), PhD thesis, University of Gafsa, Gafsa, Tunisia, 2025 (year of defence), research stages in 2022, 2023 and 2024.

[C] A. El Kanouny, *Ternary $Sn(Se_{1-x}S_x)$ thin-film materials for solar cells at low cost and low environmental impact* (ongoing), PhD thesis, Faculté des Sciences et Techniques-Mohammedia, Hassan II University, Mohammedia, Morocco, research stage in 2024.

[D] N.E.H. Bouftila, *Designing competitive solid electrolyte through substitution and element doping for all solid state Li-ion batteries* (ongoing), Ph.D. Thesis, Sidi Mohamed Ben Abdellah University, Fes, Morocco, research stages in 2023 and 2024.

[E] L. Akabbouch, *Development of innovative materials for application in energy storage* (ongoing), Ph.D. Thesis, Ibn Tofail University, Kénitra, Morroco, research stages in 2023 and 2024.

[F] M. Tamin, D*evelopment of wide-bandgap chalcogenide-based semiconductors and devices for advanced photovoltaic applications* (ongoing), Ph.D. Thesis, Ferhat Abbas University (UFAS)-Setif 1, Setif, Algeria & Bourgogne Europe University, Dijon, France, research stages in 2024 and 2025.

[G] R. Merah, *Synthesis and analysis of the electrical properties of thin-film heterojunctions for photovoltaic applications* (ongoing), Ph.D. Thesis, University of Constantine 1, Constantine, Algeria, research stage in 2025.

[H] E. Anate, *Elaboration and characterisation of perovskite solar cells for real-conditions applications* (ongoing), Ph.D. Thesis, University of Kara, Kara, Togo. Research stage in 2025.

[I] S. Handor, *Perovskite based devices* (ongoing), Ph.D. Thesis, Sultan Moulay Slimane University, Beni Mellal, Morocco, research stages in 2024 and 2025.

4.3 Other outputs (conferences, white papers, patents, prototypes)

[a] L. Akabbouch, O. El Khouja, T. Tite, A.C. Galca, K. Nouneh, *Synthesis of V_2O_5 thin films using spin-coating as potential supercapacitor electrode materials*, Poster presentation at the International Symposium on Advanced Coating & Applications (ISCApp 2025), Benguerir, Morocco, 24–26 February 2025.

[b] M. Tamin, O. El Khouja, D. Chaumont, M. Guemmaz, A.C. Galca, *Synthesis and characterization of CZTS and AZTS thin films for indoor and tandem photovoltaic applications*, Poster presentation at the 15th European Kesterite+ and 3rd ReNewPV Workshop, Berlin-Wannsee, Germany, 11–13 June 2025.

[c] L. Akabbouch, O. El Khouja, I. Assahsahi, S. Dassallem, T. Tite, A.C. Galca, K. Nouneh, *Effect of various aqueous electrolytes on the electrochemical performance of V_2O_5 thin films*, Oral presentation at the 8th International Conference on Materials & Environmental Science, Saïdia, Morocco, 12–15 June 2025.

[d] M. Tamin, O. El Khouja, D. Chaumont, M. Guemmaz, A.E. Bocirnea, A.C. Galca, *Tuning the optoelectronic properties of CZTS thin films via ag alloying for next-generation tandem and indoor photovoltaics*, Oral presentation at Nanotechnology for Next Generation High Efficiency Photovoltaics (NEXTGEN 2025), Palma, Mallorca, Spain, 09–12 September 2025.

[e] M. Oumezzine, C.F. Chirila, A. Kuncser, A.C. Galca, *Epitaxial spin valve structures of functional La–Ba–Mn-Ti-O manganite for memory applications*, Oral presentation at 4th Short-Term Scientific Mission Workshop on Innovative and Advanced Epitaxy, (OPERA), COST Action CA-20116, online workshop, 18–19 September 2025.

[f] N. Ilić, C. Radu, T. Barudžija, A.C. Galca, I. Validžić, *Synthesis and characterization of Sb_2S_3 nanoparticles for application as absorber in solar cells*, Oral presentation at 5th International Meeting on Materials Science for Energy Related Applications (5IMMSERA), Belgrade, Serbia, 25–26 September 2025.

[g] S. Handor, A.G. Tomulescu, V. Stancu, A. Razouk, A.C. Galca, L.N. Leonat, Gas-assisted spray fabrication of reticulated TiO_2 scaffolds for perovskite solar applications, Poster presentation at 3rd International Workshop on Lead-Free Perovskite Solar Cells, online workshop, 22–23 October 2025.

[h] M. Tamin, O. El Khouja, A.C. Galca, *Substitution cationique dans $(Ag,Cu)_2ZnSnS_4$: Vers des absorbeur à large bande interdite*, Oral presentation at 4eme édition du Symposium de la Recherche Scientifique Francophone en Europe Centrale et Orientale, Iași, Romania, 30–31 October 2025.

[i] R. Merah, N. Benaissa, A. El Kanouny, M. Tamin, A.G. Tomulescu, L.N. Leonat, W. Darenfad, A.C. Galca, *Influence des paramètres de dépots et du recuit sur les cellules solaires à couches minces de Sb_2S_3 par pulvérisation pyrolytique sous vide*, Oral presentation at 4eme édition du Symposium de la Recherche Scientifique Francophone en Europe Centrale et Orientale, Iași, Romania, 30–31 October 2025.

[j] A. Kenane, O. Rasoga, M.E.B. Bakhti, G. Socol, A.C. Galca, *Films minces à base de nanocomposites fonctionnels déposés par MAPLE: Nouveau concept et application*, Oral presentation at 4eme édition du Symposium de la Recherche Scientifique Francophone en Europe Centrale et Orientale, Iaşi, Romania, 30–31 October 2025.

[k] S. Handor, A. Razouk, A.G. Tomulescu, A.C. Galca, V. Stancu, L.N. Leonat, *Dynamique des antisolvants dans les cellules solaires en pérovskite*, Oral presentation at 4eme édition du Symposium de la Recherche Scientifique Francophone en Europe Centrale et Orientale, Iaşi, Romania, 30–31 October 2025.

[l] Y. Zidi, R.E. Patru, L.N. Leonat, O. Khaldi, V. Toma, R. Ben Younes, A.C. Galca, *Propriétés structurelles et diélectriques des céramiques de titanate de baryum-strontium,* Oral presentation at 4eme édition du Symposium de la Recherche Scientifique Francophone en Europe Centrale et Orientale, Iaşi, Romania, 30–31 October 2025.

[m] M. Tamin, O. El Khouja, D. Chaumont, M. Guemmaz, C. Tamin, A.E. Bocirnea, A.C. Galca, *Substitution cationique et traitement thermique de* $(Ag_xCu_{1-x})_2ZnSnS_4$*: Vers des absorbeurs à large bande interdite pour le photovoltaïque tandem et indoor*, Poster presentation at Journées Nationales du PhotoVoltaïque 2025 (JNPV), Strasbourg, France, 04–07 November 2025.